Low-Angle Radar Land Clutter

Measurements and Empirical Models

J. Barrie Billingsley

Lincoln Laboratory

Massachusetts Institute of Technology

William Andrew Publishing

William Andrew
publishing

Published in the United States of America by William Andrew Publishing / Noyes Publishing
13 Eaton Avenue
Norwich, NY 13815
www.williamandrew.com

President and CEO: William Woishnis
Sponsoring Editor: Dudley R. Kay – SciTech Publishing, Inc.
Production Manager: Kathy Breed
Production services provided by ***TIPS*** Technical Publishing, Carrboro, North Carolina
Copyeditor: Howard Jones
Book Design: Robert Kern
Compositor: Lynanne Fowle
Proofreaders: Maria Mauriello, Jeff Eckert
Printed in the United States

10 9 8 7 6 5 4 3 2 1

SciTech is a partner with William Andrew for high-quality radar and aerospace books.
See www.scitechpub.com for information.

Library of Congress Cataloging-in-Publication Data
Billingsley, J. Barrie.
Low angle radar land clutter : measurements and empirical models / J. Barrie Billingsley.
p. cm.
Includes index.
ISBN 1-891121-16-2 (alk. paper)
1. Radar—Interference. I. Title

TK6580 .B45 2001
621.3848—dc21

2001034284

This book is co-published and distributed in the UK and Europe by:

The Institution of Electrical Engineers
Michael Faraday House
Six Hills Way, Stevenage, SGI 2AY, UK
Phone: +44 (0) 1438 313311
Fax: +44 (0) 1438 313465
Email: books@iee.org.uk
www.iee.org.uk/publish
IEE ISBN: 0-85296-230-4

Other Books Under the SciTech Imprint

How to Speak Radar CD-Rom (2001)
Arnold Acker

Air and Spaceborne Radar Systems: An Introduction (2001)
Philippe Lacomme, Jean-Philippe Hardange, Jean-Claude Marchais, and Eric Normant

Introduction to Airborne Radar, Second Edition (1998)
George W. Stimson

Radar Principles for the Non-Specialist, Second Edition (1998)
John C. Toomay

Radar Design Principles, Second Edition (1998)
Fred Nathanson

Understanding Radar Systems (1998)
Simon Kingsley and Shaun Quegan

Hazardous Gas Monitors (2000)
Jack Chou

The Advanced Communication Satellite System (2000)
Richard Gedney, Ronald Shertler, and Frank Gargione

Moving Up the Organization in Facilities Management
A. S. Damiani

Return of the Ether (1999)
Sid Deutsch

To my wife Mary,
and to our children Jennifer, Michael, and Thomas,
and grandchildren Andrew and Sylvia

Foreword

MIT Lincoln Laboratory was founded in 1951 to develop a strategic air-defense system for the United States. The Laboratory engineers of that era quickly found that ground clutter greatly limited the performance of their radars. Consequently, they pioneered the development of Doppler processing techniques and later digital processing techniques to mitigate the effects of ground clutter. The Laboratory returned to the problem of air defense in the late 1970s with a major program to assess and ensure the survivability of U.S. cruise missiles. Once again ground clutter proved an important issue because a low-flying, low-observable cruise missile could hide in ground clutter and escape radar detection. The new challenge was to confidently predict low-grazing angle ground clutter for any number of specific sites with widely varying topographies. But the understanding of clutter phenomena at this time certainly did not permit these predictions. Therefore, with the early support of the Defense Advanced Research Projects Agency and later with the support of the United States Air Force, the Laboratory set out to make a major improvement in our understanding of ground clutter as seen by ground radars.

Barrie Billingsley was the principal researcher at the start and I was the director of the overall Laboratory program. I recall telling Barrie to archive his data, document his experiments, calibrate his radars, and collect ground truth on his many test sites so that he could write the definitive textbook on low grazing angle ground clutter when our program was finished. I would say that Barrie has delivered magnificently on this challenge. I am delighted to see over 300 directly applicable charts characterizing ground clutter backscatter in this book.

I confess that I had expected this book to appear about 10 years after the start, not 20 years. The long gestation period reflects the enormous technical problem of capturing what really happens at low grazing angles and the fact that Barrie Billingsley is an extremely meticulous and persistent researcher. He did stretch the patience of successive Lincoln Laboratory program managers, but he pulled it off by teasing us each year with additional insights into these complex clutter phenomena. We greatly admired his research abilities and his dedication to the task of unfolding the mystery of low grazing angle ground clutter. We had heard the violins and the horns and the woodwinds before, but now we could understand the whole orchestration—how frequency, terrain, propagation, resolution, and polarization all operated together to produce the complex result we had witnessed but did not understand.

My congratulations to Barrie for this grand accomplishment—a book that will serve engineers and scientists for many years to come. My congratulations also to his collaborators and the long sequence of Lincoln Laboratory program managers who supported Barrie in this most important endeavor. My thanks to the Defense Advanced Research Projects Agency and United States Air Force for their enlightened support and management of this program. It is not very often in the defense research business that we get to complete and beautifully wrap a wonderful piece of scientific research. Enjoy!

— William P. Delaney
Pine Island, Meredith, New Hampshire
November 2001

Preface

Radar land clutter constitutes the unwanted radar echoes returned from the earth's surface that compete against and interfere with the desired echoes returned from targets of interest, such as aircraft or other moving or stationary objects. To be able to knowledgeably design and predict the performance of radars operating to provide surveillance of airspace, detection and tracking of targets, and other functions in land clutter backgrounds out to the radar horizon, radar engineers require accurate descriptions of the strengths of the land clutter returns and their statistical attributes as they vary from pulse to pulse and cell to cell. The problem of bringing statistical order and predictability to land clutter is particularly onerous at the low angles (at or near grazing incidence) at which surface-sited radars illuminate the clutter-producing terrain, where the fundamental difficulty arising from the essentially infinite variability of composite terrain is exacerbated by such effects as specularity against discrete clutter sources and intermittent shadowing. Thus, predicting the effects of low-angle land clutter in surface radar was for many years a major unsolved problem in radar technology.

Based on the results of a 20-year program of measuring and investigating low-angle land clutter carried out at Lincoln Laboratory, Massachusetts Institute of Technology, this book advances the state of understanding so as to "solve the low-angle clutter problem" in many important respects. The book thoroughly documents all important results of the Lincoln Laboratory clutter program. These results enable the user to predict land clutter effects in surface radar.

This book is comprehensive in addressing the specific topic of low-angle land clutter phenomenology. It contains many interrelated results, each important in its own right, and unifies and integrates them so as to add up to a work of significant technological innovation and consequence. Mean clutter strength is specified for most important terrain types (e.g., forest, farmland, mountains, desert, urban, etc.). Information is also provided specifying the statistical distributions of clutter strength, necessary for determining probabilities of detection and false alarm against targets in clutter backgrounds. The totality of clutter modeling information so presented is parameterized, not only by the type of terrain giving rise to the clutter returns, but also (and importantly) by the angle at which the radar illuminates the ground and by such important radar parameters as carrier frequency, spatial resolution, and polarization. This information is put forward in terms of empirical clutter models. These include a Weibull statistical model for prediction of clutter strength and an exponential model for the prediction of clutter Doppler spreading due to wind-induced intrinsic clutter motion. Also included are analyses and results indicating, given the strength and spreading of clutter, to what extent various techniques of clutter cancellation can reduce the effects of clutter on target detection performance.

The empirically-derived clutter modeling information thus provided in this book utilizes easy-to-understand formats and easy-to-implement models. Each of the six chapters is essentially self-contained, although reading them consecutively provides an iterative pedagogical approach that allows the ideas underlying the finalized modeling information of Chapters 5 and 6 to be fully explored. No difficult mathematics exist to prevent easy

assimilation of the subject matter of each chapter by the reader. The technical writing style is formal and dedicated to maximizing clarity and conciseness of presentation. Meticulous attention is paid to accuracy, consistency, and correctness of results. No further prerequisite requirements are necessary beyond the normal knowledge base of the working radar engineer (or student) to access the information of this book. A fortuitous combination of national political, technological, and economic circumstances occurring in the late 1970s and early 1980s allowed the Lincoln Laboratory land clutter measurement project to be implemented and thereafter continued in studies and analysis over a 20-year period. It is highly unlikely that another program of the scope of the Lincoln Laboratory clutter program will take place in the foreseeable future. Future clutter measurement programs are expected to build on or extend the information of this book in defined specific directions, rather than supersede this information. Thus this book is expected to be of long-lasting significance and to be a definitive work and standard reference on the subject of land clutter phenomenology.

A number of individuals and organizations provided significant contributions to the Phase Zero/Phase One land clutter measurements and modeling program at Lincoln Laboratory and consequently towards bringing this book into existence and affecting its final form and contents. This program commenced at Lincoln Laboratory in 1978 under sponsorship from the Defense Advanced Research Projects Agency. The United States Air Force began joint sponsorship several years into the program and subsequently assumed full sponsorship over the longer period of its complete duration. The program was originally conceived by Mr. William P. Delaney of Lincoln Laboratory, and largely came into focus in a short 1977 DARPA/USAF-sponsored summer study requested by the Department of Defense and directed by Mr. Delaney. The Phase Zero/Phase One program was first managed at Lincoln Laboratory by Mr. Carl E. Nielsen Jr. and by Dr. David L. Briggs, and subsequently by Dr. Lewis A. Thurman and Dr. Curtis W. Davis III.

Early site selection studies for the Phase Zero/Phase One program indicated the desirability of focusing measurements in terrain of relatively low relief and at northern latitudes such as generally occurs in the prairie provinces of western Canada. As a result, a Memorandum of Understanding (MOU) was established between the United States and Canada implementing a joint clutter measurements program in which Canada, through Defence Research Establishment Ottawa, was to provide logistics support and share in the measured data and results. Dr. Hing C. Chan was the principal investigator of the clutter data at DREO. Dr. Chan became a close and valued member of the Phase One community; many useful discussions and interactions concerning the measured clutter data and its analysis occurred between Dr. Chan and the author down to the time of present writing. Substantial contracted data analysis support activity was provided to Dr. Chan by AIT Corporation, Ottawa. Information descriptive of the terrain at the clutter measurement sites was provided in a succession of contracted studies at Intera Information Technologies Ltd., Calgary.

The government of the United Kingdom through its Defence Evaluation Research Agency became interested in the Lincoln Laboratory clutter program shortly after its commencement. DERA subsequently became involved in the analysis of Phase One clutter data under the aegis of The Technical Cooperation Program (TTCP), an international defense science technical information exchange program. The U.S./Canada MOU was terminated at the completion of measurements, and the sharing of the measurement data and its analysis was thereafter continued between all three countries under TTCP.

Significant analyses of selected subsets of the Phase One measurement data occurred with DERA sponsorship in the U.K. at Smith Associates Limited and at GEC Marconi Research Centre. The principal coordinator of these interactions at DERA was Mr. Robert A. Blinston. Mr. John N. Entzminger Jr., former Director of the Tactical Technology Office at DARPA, provided much encouragement to these joint U.S./Canada/U.K. clutter study interactions in his role as head of the U.S. delegation to Subgroup K (radar) in TTCP.

In its early years, the Lincoln Laboratory clutter program was followed by Mr. David K. Barton, then of Raytheon Company, now of ANRO Engineering, who stimulated our thinking with his insights on the interrelationships of clutter and propagation and discussions on approaches to clutter modeling. Also in the early years of the clutter program, several interactions with Mr. William L. Simkins of the Air Force Research Laboratory, Rome, N.Y., influenced methodology to develop correctly at Lincoln Laboratory in such matters as clutter data reduction and intrinsic-motion clutter spectral modeling. In the latter years of the Phase One program, Professor Alfonso Farina of Alenia Marconi Systems, Italy, became interested in the clutter data. An informal collaboration was organized by Professor Farina in which some particular Phase One clutter data sets were provided to and studied by him and his colleagues at the University of Pisa and University of Rome. These studies were from the point of view of signal processing and target detectability in ground clutter backgrounds. A number of jointly-authored technical journal papers in the scientific literature resulted.

The five-frequency Phase One clutter measurement equipment was fabricated by the General Electric Co., Syracuse, N.Y. (now part of Lockheed Martin Corporation). Key members of the Phase One measurements crew were Harry Dence and Joe Miller of GE, Captain Ken Lockhart of the Canadian Forces, and Jerry Anderson of Intera. At Lincoln Laboratory, the principal people involved in the management and technical interface with GE were David Kettner and John Hartt. The project engineer of the precursor X-band Phase Zero clutter program was Ovide Fortier. People who had significant involvement in data reduction and computer programming activities include Gerry McCaffrey, Paul Crochetiere, Ken Gregson, Peter Briggs, Bill Dustin, Bob Graham-Munn, Carol Bernhard, Kim Jones, Charlotte Schell, Louise Moss, and Sharon Kelsey. Dr. Seichoong Chang served in an important consultant role in overseeing the accurate calibration of the clutter data. Many informative discussions with Dr. Serpil Ayasli helped provide understanding of the significant effects of electromagnetic propagation in the clutter data. Application of the resultant clutter models in radar system studies took place under the jurisdiction of Dr. John Eidson.

The original idea that the results of the Lincoln Laboratory clutter program could be the basis of a clutter reference book valuable to the radar community at large came from Mr. Delaney. Dr. Merrill I. Skolnik, former Superintendent of the Radar Division at the Naval Research Laboratory in Washington, D.C., lent his support to this book idea and provided encouragement to the author in his efforts to follow through with it. When a first rough draft of Chapter 1 of the proposed book became available, Dr. Skolnik kindly read it and provided a number of constructive suggestions. Throughout the duration of the clutter book project, Dr. Thurman was a never-failing source of positive managerial support and insightful counsel to the author on how best to carry the book project forward. Mr. C.E. Muehe provided a thorough critical review of the original report material upon which much of Chapter 6 is based. Dr. William E. Keicher followed the book project in its later stages and provided a technical review of the entire book manuscript. Skillful typing of the

original manuscript of this book was patiently and cheerfully performed through its many iterations by Gail Kirkwood. Pat DeCuir typed many of the original technical reports upon which the book is largely based. Members of the Lincoln Laboratory Publications group maintained an always positive and most helpful approach in transforming the original rough manuscript into highly finished form. These people in particular include Deborah Goodwin, Jennifer Weis, Dorothy Ryan, and Katherine Shackelford. Dudley R. Kay, president of SciTech Publishing and vice-president at William Andrew Publishing, and the book's compositors, Lynanne Fowle and Robert Kern at TIPS Technical Publishing, ably and proficiently met the many challenges in successfully seeing the book to press.

It is a particular pleasure for the author to acknowledge the dedicated and invaluable assistance provided by Mr. John F. Larrabee (Lockheed Martin Corporation) in the day-to-day management, reduction, and analyses of the clutter data at Lincoln Laboratory over the full duration of the project. In the latter days of the clutter project involving the production of this book, Mr. Larrabee managed the interface to the Lincoln Laboratory Publications group and provided meticulous attention to detail in the many necessary iterations required in preparing all the figures and tables of the book. Mr. Larrabee recently retired after a long professional career in contracted employment at Lincoln Laboratory, at about the time the book manuscript was being delivered to the publisher.

Many others contributed to the land clutter project at Lincoln Laboratory. Lack of explicit mention here does not mean that the author is not fully aware of the value of each contribution or lessen the debt of gratitude owed to everyone involved in acquiring, reducing, and analyzing the clutter data. Although this book was written at Lincoln Laboratory, Massachusetts Institute of Technology, under the sponsorship of DARPA and the USAF, the opinions, recommendations, and conclusions of the book are those of the author and are not necessarily endorsed by the sponsoring agencies. Permissions received from the Institute of Electrical and Electronics Engineers, Inc., the Institution of Electrical Engineers (U.K.), and The McGraw-Hill Companies to make use of copyrighted materials are gratefully acknowledged. Any errors or shortcomings that remain in the material of the book are entirely the responsibility of the author. The author sincerely hopes that every reader of this book is able to find helpful information within its pages.

— J. Barrie Billingsley
Lexington, Massachusetts
October 2001

Contents

1

Overview

1.1 Introduction

The performance of surface-sited radar against low-flying targets has been limited by land clutter since the earliest days of radar. Consider the beam of such a radar scanning over the surrounding terrain and illuminating it at grazing incidence. The amplitudes of the clutter returns received from all the spatially distributed resolution cells within the scan coverage on the ground vary randomly over extremely wide dynamic ranges, as the interrogating pulse encounters the complex variety of surface features and discrete reflecting objects comprising or associated with the terrain. The resultant clutter signal varies in a complex manner with time and space to interfere with and mask the much weaker target signal in the radar receiver. Early ground-based radars of necessity were restricted to operations at relatively long ranges beyond the clutter horizon where terrain was not directly illuminated. The development of Doppler signal processing techniques allowed radars to have capability within clutter regions against larger targets by exploiting the differences in frequency of the signal returned from the rapidly moving target compared to that from the relatively stationary clutter. However, because the clutter signal is often overwhelmingly stronger than the target signal and because of the lack of perfect waveform stability, modern pulsed radars often remain severely limited by land clutter residues against small targets even after clutter cancellation.

The need of designers and analysts to accurately predict clutter-limited radar system performance led to many attempts to measure and model land clutter over the decades following World War II [1–13]. The problem was highly challenging, not just because of the variability and wide dynamic range of the clutter at a given site, but also because the overall severity of the clutter and resulting system performance varied dramatically from site to site. Early clutter measurements, although numerous, tended to be low-budget piece-part efforts overly influenced by terrain specificity in each measurement scene. In aggregate these efforts led to inconsistent, contradictory, and incomplete results. Early clutter models tended to be overly general, modeling clutter simply as a constant reflectivity level, or on a spherical but featureless earth, or as a simple function of grazing angle. As a result, they did not incorporate features of terrain specificity that dominated clutter effects at real sites. Thus there was a logical disconnection between models (overly general) and measurements (overly specific), and clutter-limited radar performance remained unpredictable into the decade of the 1970s. By that time it had become widely acknowledged that "there was no generally accepted clutter model available for calculation," and there was "no accepted approach by which a model could be built up" [8].

The middle and late 1970s also saw an emerging era of low-observable technology in aircraft design and consequent new demands on air defense capabilities in which liabilities imposed by the lack of predictability of clutter-limited surface radar performance were much heightened. As a result, a significant new activity was established at Lincoln Laboratory in 1978 to advance the scientific understandings of air defense. An important initial element of this activity was the requirement to develop an accurate full-scale clutter simulation capability that would breach the previous impasse. The goal was to make clutter modeling a proper engineering endeavor typified by quantitative comparison of theory with measurement, and so allow confident prediction of clutter-limited performance of ground-sited radar.

It was believed on the basis of the historical evidence that a successful approach would have to be strongly empirical. To this end, a major new program of land clutter measurements was initiated at Lincoln Laboratory [14–18]. To solve the land clutter modeling problem, it was understood that the new measurements program would have to substantially raise the ante in terms of level of effort and new approaches compared with those undertaken in the past. Underlying the key aspect of variability in the low-angle clutter phenomenon was the obvious fact that landscape itself was essentially infinitely variable—every clutter measurement scenario was different. Rather than seek the general in any individual measurement, underlying trends among aggregates of similar measurements would be sought.

In ensuing years, a large volume of coherent multifrequency land clutter measurement data was acquired (using dedicated new measurement instrumentation) from many sites widely distributed geographically over the North American continent [14]. A new site-specific approach was adopted in model development, based on the use of digitized terrain elevation data (DTED) to distinguish between visible and masked regions to the radar, which represented an important advance over earlier featureless or sandpaper-earth (i.e., statistically rough) constructs [15]. Extensive analysis of the new clutter measurements database led to a progression of increasingly accurate statistical clutter models for specifying the clutter in visible regions of clutter occurrence. A key requirement in the development of the statistical models was that only parametric trends directly observable in the measurement data would be employed; any postulated dependencies that could not be demonstrated to be statistically significant were discarded. As a result, a number of earlier insights into low-angle clutter phenomenology were often understood in a new light and employed in a different manner or at a different scale so as to reconcile with what was actually observed in the data. In addition, significant new advances in understanding low-angle clutter occurred that, when incorporated properly with the modified earlier insights, led to a unified statistical approach for modeling low-angle clutter in which all important trends observable in the data were reproducible.

An empirically-based statistical clutter modeling capability now exists at Lincoln Laboratory. Clutter-limited performance of surface-sited radar in benign or difficult environments is routinely and accurately predicted. Time histories of the signal-to-clutter ratios existing in particular radars as they work against particular targets at particular sites are computed and closely compared to measurements. Systems computations involving tens or hundreds of netted radars are performed in which the ground clutter[1] at each site is predicted separately and specifically. Little incentive remains at Lincoln Laboratory to develop generic non-site-specific approaches to clutter modeling for the benefit of saving

computer time, because the results of generic models lack specific realism and, as a result, are difficult to validate.

This book provides a thorough summary and review of the results obtained in the clutter measurements and modeling program at Lincoln Laboratory over a 20-year period. The book covers (1) prediction of clutter strength (Weibull statistical model[2]), (2) clutter spreading in Doppler (exponential model), and (3) given the strength and spreading of clutter, the extent to which various techniques of clutter cancellation (e.g., simple delay-line cancellation vs coherent signal processing) can reduce the effects of clutter on target detection performance.

1.2 Historical Review

Although most surface-sited radars partially suppress land clutter interference from surrounding terrain to provide some capability in cluttered spatial regions, the design of clutter cancellers requires knowledge of the statistical properties of the clutter, and the clutter residues remaining after cancellation can still strongly limit radar performance (see Chapter 6, Sections 6.4.4 and 6.5). Because of this importance of land clutter to the operations of surface radar, there were very many early attempts [1–9] to measure and characterize the phenomenon and bring it into analytic predictability. A literature review of the subject of low-angle land clutter as the Lincoln Laboratory clutter measurement program commenced found over 100 different preceding measurement programs and over 300 different reports and journal articles on the subject. There exist many excellent sources of review [19–25] of these early efforts and preceding literature. These reviews without exception agree on the difficulty of generally characterizing low-angle land clutter.

The difficulty arises largely because of the complexity and variability of land-surface form and the elements of land cover that exist at a scale of radar wavelength (typically, from a few meters to a few centimeters or less) over the hundreds or thousands of square kilometers of composite terrain that are usually under radar coverage at a typical radar site. As a result, the earlier efforts [1–9] to understand low-angle land clutter revealed that it was a highly non-Gaussian (i.e., non-noise-like), multifaceted, relatively intractable, statistical random process of which the most salient attribute was variability. The variability existed at whatever level the phenomenon was observed—pulse-to-pulse, cell-to-cell, or site-to-site.

Other important attributes of the low-angle clutter phenomenon included: patchiness in spatial occurrence [3–5]; lack of homogeneity and domination by point-like or spatially discrete sources within spatial patches [6–8]; and extremely widely-skewed distributions of clutter amplitudes over spatial patches often covering six orders of magnitude or more [1, 2, 4, 9]. Early efforts to capture these attributes and dependencies in simple clutter models

1. This book uses the terms “land clutter” and “ground clutter” interchangeably to refer to the same phenomenon. The adjective “land” is more global in reach and distinguishes land clutter from other, generically different types of clutter such as sea clutter or weather clutter. The adjective “ground” is often used when the subject focus is only on ground clutter, and more localized circumstances need to be distinguished, for example, the differences in ground clutter from one site to another, or from one area or type of ground to another.

2. Weibull statistics are used as approximations only—not rigorous fits—to measured clutter spatial amplitude distributions. See Chapter 2, Section 2.4.1.1; Chapter 5, Section 5.2.1 and Appendix 5.A.

based only on range or illumination angle to the clutter cell were largely unsuccessful in being able to predict radar system performance. Figure 1.1 shows a measured plan-position-indicator (PPI) clutter map that illustrates to 24-km range at a western prairie site the spatial complexity and variability of low-angle land clutter. The fact that the clutter does not occur uniformly but is spatially patchy over the region of surveillance is evident in this measurement, as is the granularity or discrete-like nature of the clutter such that it often occurs in spatially isolated cells over regions where it does occur.

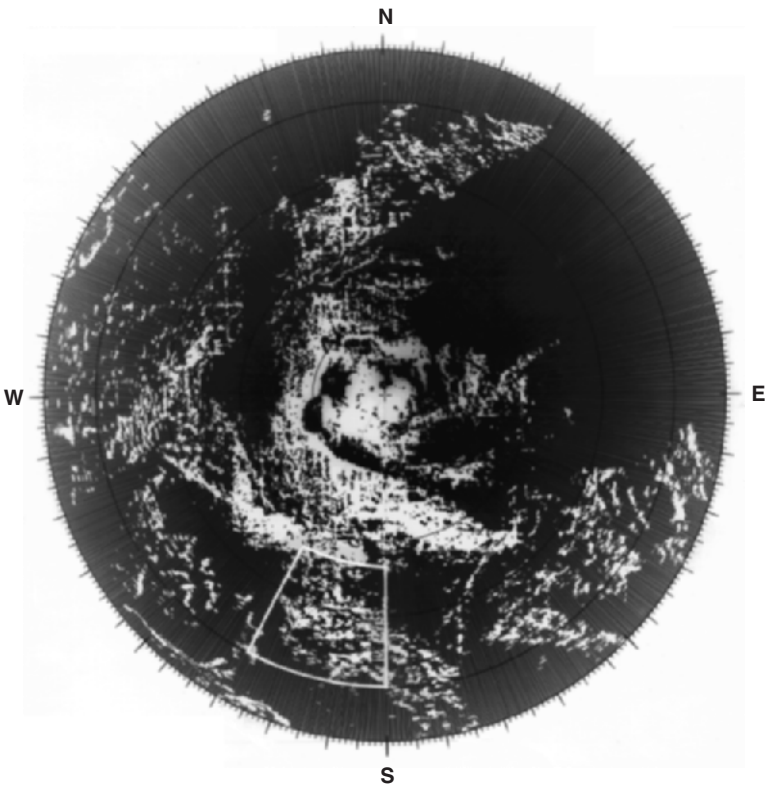

FIGURE 1.1 Measured X-band ground clutter map; Orion, Alberta. Maximum range = 24 km. Cells with discernible clutter are shown white. A large clutter patch (i.e., macroregion) to the SSW is also shown outlined in white.

Although the earlier efforts and preceding literature did not lead to a satisfactory clutter model, they did in total gradually develop a number of useful insights into the complexity of the land clutter phenomenon. Section 1.2 provides a summary of what these insights were, and the general approaches extant for attempting to bring the important observables of low-angle clutter under predictive constructs, as the Lincoln Laboratory program commenced.

1.2.1 CONSTANT σ°

Initially, land clutter was conceptualized (unlike Figure 1.1) as arising from a spatially homogeneous surface surrounding the radar site, of uniform roughness (like sandpaper) at a

scale of radar wavelength to account for clutter backscatter. The backscatter reflectivity of this surface was characterized as being a surface-area density function, that is, by a clutter coefficient σ° defined [20] to be the radar cross section (RCS) of the clutter signal returned per unit terrain surface-area within the radar spatial resolution cell (see Section 2.3.1.1). This characterization implies a power-additive random process, in which each resolution cell contains many elemental clutter scatterers of random amplitude and uniformly distributed phase, such that the central limit theorem applies and the resultant clutter signal is Rayleigh-distributed in amplitude (like thermal noise).

As conceptualized in this simple manner, land clutter merely acts to uniformly raise the noise level in the receiver, the higher noise level being directly determined by σ°. A selected set of careful measurements of σ° compiled in tables or handbooks for various combinations of terrain type (forest, farmland, etc.) and radar parameter (frequency, polarization) would allow radar system engineers to straightforwardly calculate signal-to-clutter ratios and estimate target detection statistics and other performance measures on the basis of clutter statistics being like those of thermal noise, but stronger. Early radar system engineering textbooks promoted this view. However, this approach led to frustration in practice. Tabularization of σ° into generally accepted, universal values proved elusive. Every measurement scenario seemed overly specific. Resulting matrices of σ° numbers compiled from different investigators using different measurement instrumentation operating at different landscape scales (e.g., long-range scanning surveillance radar vs short-range small-spot-size experiments) and employing different data reduction procedures were erratic and incomplete, with little evidence of consistency, general trend, or connective tissue.

1.2.2 Wide Clutter Amplitude Distributions

Clutter measurements that involved accumulating σ° returns by scanning over a spatially continuous neighborhood of generally similar terrain (i.e., clutter patch) found that the resulting clutter spatial amplitude distributions were of extreme, highly skewed shapes very much wider than Rayleigh [2, 4, 9]. Unlike the narrow fixed-shape Rayleigh distribution with its tight mean-to-median ratio of only 1.6 dB, the measured broad distributions were of highly variable shapes with mean-to-median ratios as high as 15 or even 30 dB.

Figure 1.2 shows five measured clutter histograms from typical clutter patches such as that shown in Figure 1.1, illustrating the wide variability in shape and broad spread that occurs in such data. Thus in the important aspect of its amplitude distribution, low-angle land clutter was decidedly non-noise-like. This fact was at best only awkwardly reconcilable with the constant-σ° clutter model. The accompanying shapes of clutter distributions as well as their mean σ° levels required specification against radar and environmental parameters, compounding the difficulties of compilation. As a result of both sea and land clutter measured distributions being wider than Rayleigh, an extensive literature came into being that addressed radar detection statistics in non-Rayleigh clutter backgrounds of wide spread typically characterizable as lognormal, Weibull, or *K*-distributed [26–31]. However, the need continued for a single-point constant-σ° clutter model to provide an average indication of signal-to-clutter ratio which left the user with the nebulous question of what single value of σ° (e.g., mean, median, mode, etc.) to use to best characterize the wide underlying distributions. Some investigators used the mean, others used the median, and it was not always clear what was being used since it did not make much difference under Rayleigh statistics and the question of underlying distribution was not always raised.

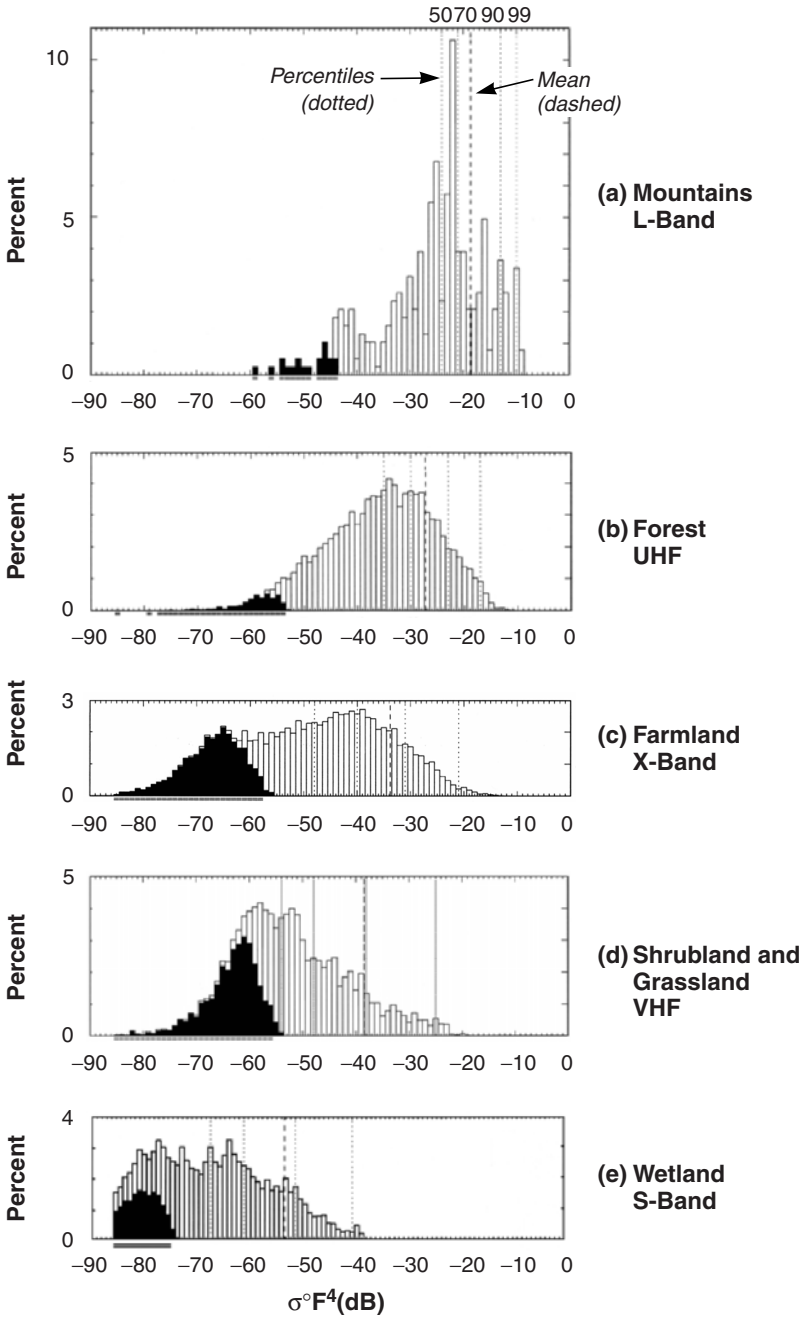

Figure 1.2 Histograms of measured clutter strength $\sigma^\circ F^4$ from five different clutter patches showing wide variability in shape and broad spread. σ° = clutter coefficient (see Section 2.3.1.1); F = pattern propagation factor (see Section 1.5.4). Black values are receiver noise.

1.2.3 Spatial Inhomogeneity/Resolution Dependence

The definition of σ° as an area-density function implies spatial homogeneity of land clutter. The underlying necessary condition for the area-density concept to be valid is that

the mean value of σ° be independent of the particular cell size or resolution utilized in a given clutter spatial field.[3] As mentioned, it was additionally presumed that much the same invariant value of σ° (tight Rayleigh variations) would exist among the individual spatial samples of σ° independent of cell size. Early low-resolution radars showed land clutter generally surrounding the site and extending in range to the clutter horizon in an approximately area-extensive manner. Measurements at higher resolution with narrower beams and shorter pulses showed that clutter was not present everywhere as from a featureless sandpaper surface, but that resolved clutter typically occurred in patches or spatial regions of strong returns separated by regions of low returns near or at the radar noise floor [4]—see Figure 1.1. Thus, clutter was highly non-noise-like not only in its non-Rayleigh amplitude statistics, but also in its lack of spatial homogeneity. High-resolution radars took advantage of the spatial non-homogeneity of clutter by providing some operational capability known as interclutter visibility in relatively clear regions between clutter patches [23].

Within clutter patches, clutter is not uniformly distributed. The individual spatial samples of σ°, as opposed to their mean, depend strongly upon resolution cell size. Thus the shapes of the broad amplitude distributions of σ° are highly dependent on resolution—increasing resolution results in less averaging within cells, more cell-to-cell variability, and increasing spread in values of σ°. In contrast, the fixed shape of a Rayleigh distribution describing simple homogeneous clutter is invariant with resolution. Significant early work was conducted into establishing necessary and sufficient conditions (e.g., number of scatterers and their relative amplitudes) in order for Rayleigh/Ricean statistics to prevail in temporal variations from individual cells, but the associated idea of how cell size affects shapes of spatial amplitude distributions from many individual cells was less a subject of investigation.

One early study got so far as to document an observed trend of increasing spread in clutter spatial amplitude distributions with increasing radar resolution [8], but this fundamentally important observation into the nature of low-angle clutter[4] was not generally followed up on or worked into empirical clutter models. Figure 1.3 shows how the Weibull shape parameter a_w (see Section 2.4.1.1), which controls the extent of spread in histograms such as those of Figure 1.2, varies strongly with radar spatial resolution in low-relief farmland viewed at low depression angle. These and many other such results for various terrain types and viewing angles are presented and explained in Chapter 5.

These two key attributes of low-angle clutter—patchiness and lack of uniformity in spatial extent (Figure 1.1), and extreme resolution-dependent cell-to-cell variability in clutter amplitudes within spatial patches of occurrence (Figures 1.2 and 1.3)—do not constitute extraneous complexity to be avoided in formulating simple clutter models aimed at

3. By "clutter spatial field" is meant a region of [land surface] space characterized by a physical property [clutter strength] having a determinable value at every point [resolution cell] in the region; see American Heritage Dictionary of the English Language, 3rd ed. This book uses the phrase "clutter spatial field" or "clutter field" as so defined to bring to mind when it is a spatially-distributed ensemble of backscattering clutter resolution cells that is of primary interest. The word "clutter" by itself can be vague (e.g., clutter signal vs clutter source; spatial vs temporal vs Doppler distribution), so that its use alone can bring different images to mind for different readers. Use of the phrase "clutter field" in this book does not refer to the strength of the propagating electromagnetic wave constituting the clutter return signal.
4. That is, the effect of resolution on the spatial as opposed to the temporal statistics of clutter.

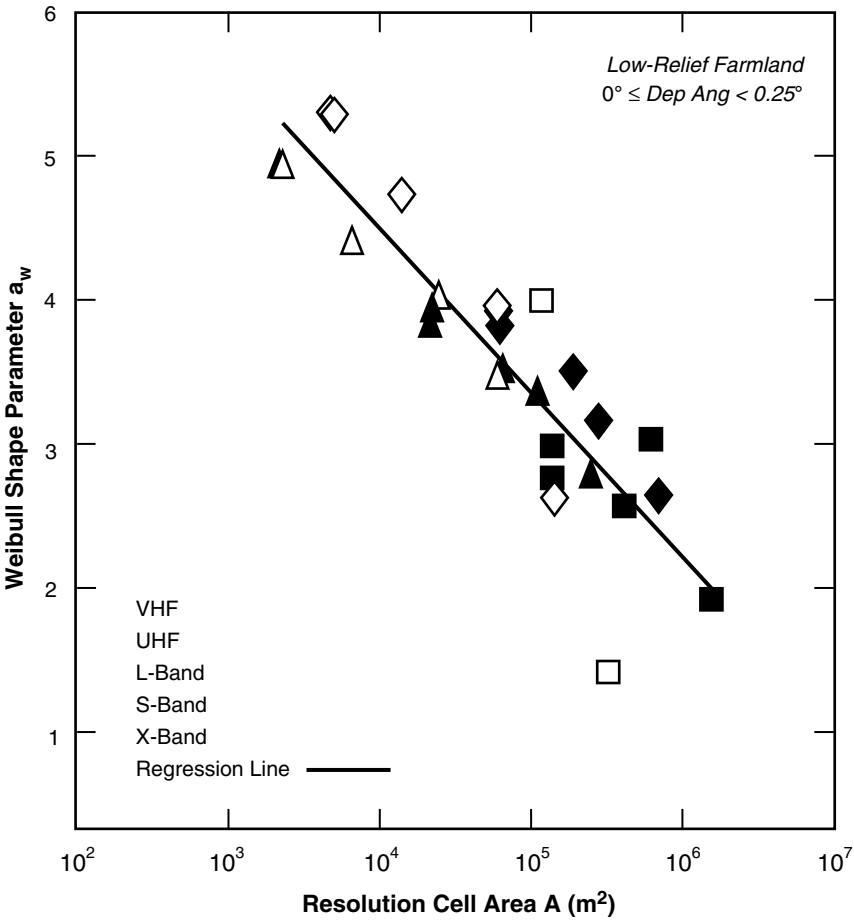

FIGURE 1.3 Weibull shape parameter a_w vs resolution cell area A for low-relief farmland viewed at low depression angle. Plot symbols are defined in Chapter 5. These data show a rapid decrease in the spread of measured clutter spatial amplitude statistics with increasing cell size (each plot symbol is a median over many patch measurements). $a_w = 1$ represents a tight Rayleigh (voltage) distribution with little spread (mean/median ratio = 1.6 dB). $a_w = 5$ represents a broadly spread Weibull distribution (mean/median ratio = 28.8 dB).

generality, but in fact are the important aspects of the phenomenon that determine system performance and that therefore must be captured in a realistic clutter model.

1.2.4 Discrete Clutter Sources

The increasing awareness of the capability of higher resolution radars to resolve spatial feature and structure in ground clutter and see between clutter patches led to investigations using high resolution radars to determine the statistics of resolved patch size and patch separation as a function of thresholded strength of the received clutter signal. It was found that the spatial extents of clutter patches diminished with increasing signal-strength threshold such that in the limit the dominant land clutter signals came from spatially isolated or discrete point sources on the landscape (e.g., individual trees or localized stands of trees; individual or clustered groups of buildings or other man-made structures;

utility poles and towers; local heights of land, hilltops, hummocks, river bluffs, and rock faces) [6, 7]. This discrete or granular nature of the strongest clutter sources in low-angle clutter became relatively widely recognized—this granularity is quite evident in Figure 1.1. It became typical for clutter models to consist of two components: a spatially-extensive background component modeled in terms of an area-density clutter coefficient σ°, and a discrete component modeled in terms of radar cross section (RCS) as being the appropriate measure for a point source of clutter isolated in its resolution cell and for which the strength of the RCS return is independent of the size of the cell encompassing it. The RCS levels of the discretes were specified by spatial incidence or density (so many per square km), with the incidence diminishing as the specified level of discrete RCS increased. Note that in such a representation for the discrete clutter component, although the strength of the RCS return from a single discrete source is independent of the spatial resolution of the observing radar, the probability of a cell capturing zero vs one vs more than one discrete does depend on resolution (i.e., discrete clutter is also affected by cell size). It was usual in such two-component clutter models for the extended background σ° component to be developed more elaborately than the discrete RCS component, the latter usually being added in as an adjunct overlay to what was regarded as the main area-extensive phenomenon.

Although the two-component clutter model seemed conceptually simple and satisfactory as an idealized concept to deal with first-level observations, attempting to sort out measured data following this approach was not so simple. The wide measured spatial amplitude distributions of clutter were continuous in clutter strength over many (typically, as many as six or eight) orders of magnitude and did not separate nicely into what could be recognized as a high-end cluster of strong discretes and a weaker bell-curve background. That is, in measured clutter data, there is no way of telling whether any given return is from a spatially discrete or distributed clutter source [25]. Additional complication arises due to radar spatial resolution diminishing linearly with range (i.e., cross-range resolution is determined by azimuth beamwidth) so that discretes of a given spatial density might be isolated at short range but not at longer ranges. The reality is that, at lower signal-strength thresholds, spatial cells capture more than one discrete and cell area affects returned clutter strength. This difficulty in the two-component model of how to transition in measured data and hence in modeling specification between extended σ° and discrete RCS has been discussed very little in the literature. These matters are discussed more extensively in Chapter 4, Section 4.5.

1.2.5 Illumination Angle

To many investigators, a land clutter model is basically just a characteristic of σ° vs illumination angle in the vertical plane of incidence. The empirical relationship $\sigma^\circ = \gamma \sin \psi$ where ψ is grazing angle (i.e., the angle between the terrain surface and the radar line-of-sight; see Figure 2.15 in Chapter 2) and γ is a constant dependent on terrain type and radar frequency has come to be accepted as generally representative over a wide range of higher, airborne-like angles [24]. However, at the low angles of ground-based radar, typically with $\psi < 1^\circ$ or 2°, it was not clear how to proceed. One relatively widely-held school of thought[5] was that at such low angles in typically-occurring low-relief terrain, grazing

5. The phrase "school of thought" rather than "opinion" is used here to indicate a point-of-view held by a group [more than one investigator] and to which some effort [as opposed to a preliminary idea] along the line indicated took place.

angle was a rather nebulous concept, neither readily definable [e.g., at what scale should such a definition be attempted, that of radar wavelength (cm) or that of landform variation (km)?] nor necessarily very directly related to the clutter strengths arising from discontinuous or discrete sources of vertical discontinuity dominating the low-angle backscatter and principally associated with land cover. From this point-of-view, the radar wave was more like a horizontally-propagating surface wave than one impinging at an angle from above, and it made more sense to separate the clutter by gross terrain type (mountains vs plains, forest vs farmland) than by fine distinctions in what were all very oblique angles of incidence.

Another widely held school-of-thought was to extend the constant-γ model to the low-angle regime by adding a low-angle correction term to prevent σ° from becoming vanishingly small at grazing incidence (as $\psi \rightarrow 0^\circ$). Little appropriate measurement data (for example, from in situ surveillance radars) was available upon which to base such a corrective term. Moreover, the idea of a corrective term tends to oversimplify the low-angle regime. At higher angles, the assumption behind a constant-γ model is of Rayleigh statistics; at low angles, it was known that the shapes of clutter amplitude distributions were broader and modelable as Weibull or lognormal, but following through with information specifying shape parameters continuously with angle for corrected constant-γ models at low angles was generally not attempted.

The gradually increasing availability of digitized terrain elevation data (DTED) in the 1970s and 1980s, typically at about 100 m horizontal sampling interval and 1 m quantization in elevation, quickly led to its use by the low-angle clutter modeling community. The hope was that the DTED would carry the burden of terrain representation by allowing the earth's surface to be modeled as a grid of small interconnected triangular DTED planes or facets joining the points of terrain elevation. Then clutter modeling could proceed relatively straightforwardly in the low-angle regime, as a function of grazing angle (e.g., constant-γ or extended constant-γ) on inclined DTED facets. This approach to modeling low-angle clutter won a wide following and continues to receive much attention. Note that it is usually advocated as a seemingly sensible but unproven postulate, and not on the basis of successful reduction of actual measurement data via grazing angle on DTED facets. As applied on a cell-by-cell (or facet-by-facet) basis, such a model is usually thought of as returning deterministic samples of σ°, thus avoiding the difficult problem of specifying statistical clutter spreads at low angles (although such a model can return random draws from statistical distributions if the distributions are specified). Indeed, when applied deterministically, the cell-to-cell scintillations in the simulated clutter signal caused by variations in DTED facet inclinations appear to mimic scintillation in measured clutter signals. However, this simple deterministic approach to modeling generally does not result in predicted low-angle clutter amplitude distributions matching measurement data. Predicted signal-to-clutter ratios and track errors recorded in radar tracking of low-altitude targets across particular clutter spatial fields using such a model show little correlation with measured data.

The root cause of this failure is that the bare-earth DTED-facet representation of terrain does not carry sufficient information to alone account for radar backscatter; it lacks precision and accuracy to define terrain slope at a scale of radar wavelength and provides no information on the discrete elements of land cover which dominate and cause scintillation in the measurement data. This is illustrated by the results of Figure 1.4. At the

top, Figure 1.4(a) shows X-band measurements of clutter strength vs grazing angle in two short-range canonical situations where the clutter-producing surface was very level—on a frozen snow-covered lake and on an artificially level, mown-grass, ground-reflecting antenna range. In such situations, the computation of grazing angle is straightforward—it is simply equal to the depression angle below the horizontal at which the clutter cell is observed at the radar antenna. In these two canonical or laboratory-like measurement situations, a strong dependence of increasing clutter strength with increasing grazing angle is indicated.

Such results illustrate the thinking that lies behind the desire of many investigators to want to establish a grazing-angle dependent clutter model. However, as shown in Figure 1.4(b), when grazing angle is computed to DTED facets used to model real terrain surfaces, little correlation between clutter strength and grazing angle is seen in the results. Specifically, Figure 1.4(b) shows a scatter plot in which measured X-band clutter strength in each cell at the undulating western prairie site of Beiseker, Alberta is paired with an estimate of grazing angle to the cell derived from a DTED model of the terrain at the site. As mentioned, the reasons that little or no correlation is seen in the results have to do with lack of accuracy in the DTED and in the fact that the bare-earth DTED representation of the terrain surface contains no information on the spatially discrete land cover elements that usually dominate low-angle clutter. Results such as those shown in Figure 1.4(b) are discussed at greater length in Chapter 2 (see Section 2.3.5). Such results illustrate why attempting deterministic prediction of low-angle clutter strength via grazing angle to DTED facets has been an over-simplified micro-approach that fails.

1.2.6 Range Dependence

Return now to the first school of thought mentioned in the preceding discussion concerning illumination angle, namely, that at grazing incidence in low-relief terrain, terrain slope and grazing angle are neither very definable nor of basic consequence in low angle clutter. Within this school of thought, the central observable fact concerning clutter in a ground-based radar is its obvious dissipation with increasing range. Thus some early clutter models for surface-sited radars were formulated from this point of view. Rather than model the clutter at microscale, such models treated the earth as a large featureless sphere, uniformly microrough to provide backscattering, but without specific large-scale terrain feature. Such an earth does not provide spatial patchiness; rather it is uniformly illuminated everywhere to the horizon, and clutter strength is diminished with increasing range via propagation losses over the spherical earth. This appears to be a simple general macroscale approach for providing a range-dependent clutter model for surface-sited radar.

However, like the microscale grazing angle model, the macroscale range-dependent model does not conform to the measurement data. These data show that what actually diminishes with increasing range at real sites is the occurrence of the clutter—with increasing range, visible clutter-producing terrain regions become smaller, fewer, and farther between, until, beyond some maximum range, no more terrain is visible (see Chapter 4, Figure 4.10). Further, the measurement data show that clutter strength does not generally diminish with increasing range, either within visible patches or from patch to patch. To illustrate this, Figure 1.5 shows mean clutter strength vs range in a 20^{o} azimuth sector at Katahdin Hill, Massachusetts, looking out 30 km over hilly forested terrain. The data in this figure scintillate from gate to gate and occasionally drop to the noise floor where visibility to terrain is lost, but the average level stays at ~ –30 dB over the full extent in range with no

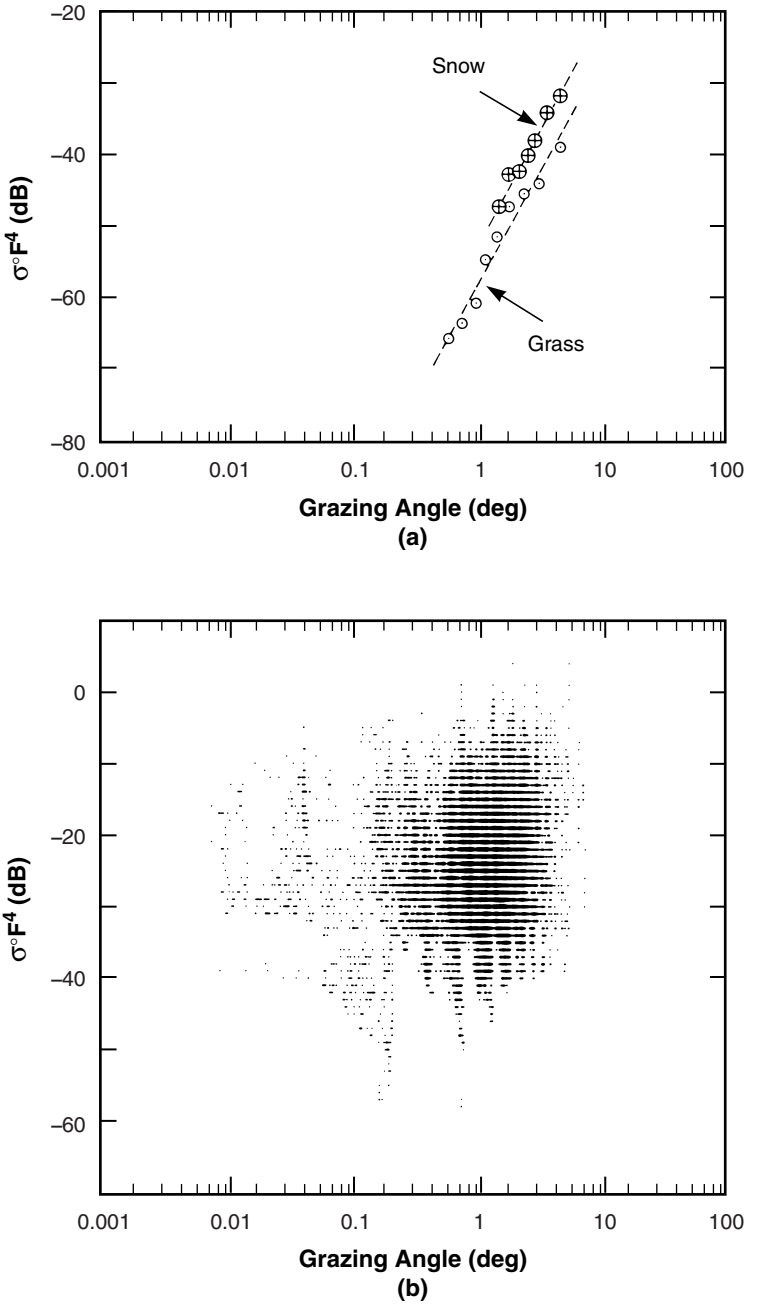

FIGURE 1.4 Measurements of clutter strength $\sigma\,°F^4$ vs grazing angle. (a) Canonically level, discrete-free surfaces; (b) undulating open prairie landscape.

significant general trend exhibited of, for example, decreasing clutter strength with increasing range. Many similar results from Katahdin Hill and other sites are discussed in detail in what follows (see Chapter 2, Section 2.3 and Chapter 4, Appendix 4.A).

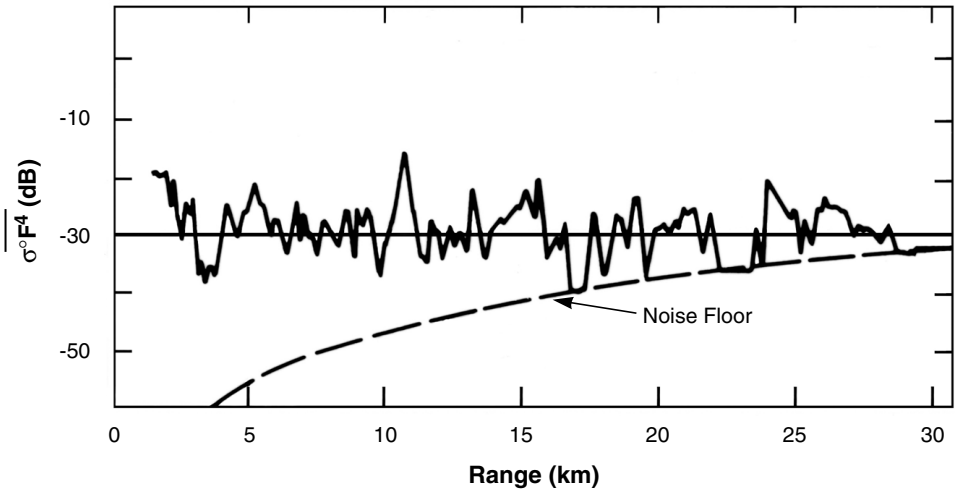

Figure 1.5 Mean clutter strength $\overline{\sigma^\circ F^4}$ vs range at Katahdin Hill. X-band data, averaged range gate by range gate within a 20°-azimuth sector, 80 samples per gate. Range gate sampling interval = 148.4 m. Such results indicate little general trend of clutter strength with range.

Another way of examining the measurement data for range dependence of clutter strength is in PPI clutter maps such as is shown in Figure 1.1. If a gradually increasing threshold on clutter strength is applied to a measured long-range PPI clutter map, the clutter does not disappear at long ranges first, but tends to uniformly dissipate within patches of occurrence over much of the PPI independent of range (see Chapter 4, Figure 4.19). Thus patchiness is necessary in a clutter model, not only to realistically represent the spatial nature of the clutter in local areas, but also to provide the important global feature of diminishing clutter occurrence (not strength) with increasing range.

1.2.7 Status

The preceding discussions give some sense as to the state of understanding of low-angle land clutter and different points of view regarding its modeling when the Lincoln Laboratory clutter program commenced. As has been indicated, various elements of this complex phenomenon were individually understood to greater or lesser degrees, but a useful overall prediction capability was not available. Next, Section 1.3 briefly describes the Lincoln Laboratory measurement equipment for obtaining an extensive new land clutter database of clutter for the development of new empirical clutter models. Then Section 1.4 takes up again the various facets of the clutter phenomenon introduced in the foregoing and shows how the successful predictive approaches developed in this book build on the thinking that went before but extend it in improved ways of analyzing the data and formulating the models.

1.3 Clutter Measurements at Lincoln Laboratory

The Lincoln Laboratory program of radar ground clutter measurements went forward in two main phases, Phase Zero [18], a pilot phase that was noncoherent and at X-band only, followed by Phase One [14], the full-scale coherent program at five frequencies, VHF,

UHF, L-, S-, and X-bands. Photographs of the Phase Zero and Phase One measurement instruments are shown in Figures 1.6 and 1.7, respectively. The basis of the Phase Zero radar was a commercial marine navigation radar, in the receiver of which was installed a precision intermediate frequency (IF) attenuator to measure clutter strength. Phase Zero measurements were conducted at 106 different sites. The Phase One five-frequency radar was a one-of-a-kind special-purpose instrumentation radar specifically designed to measure ground clutter. It was computer-controlled with high data rate recording capability. It utilized a linear receiver with 13-bit analog-to-digital (A/D) converters in in-phase (I) and quadrature (Q) channels, and maintained coherence and stability sufficient for 60-dB clutter attenuation in postprocessing. Phase One five-frequency measurements were conducted at 42 different sites.

FIGURE 1.6 Phase Zero equipment at a western prairie site.

Important system parameters associated with the Phase Zero and Phase One radars are shown in Table 1.1. Both instruments were self-contained and mobile on truck platforms. Antennas were mounted on erectable towers and had relatively wide elevation beams that were fixed horizontally at 0° depression angle. That is, no control was provided on the position of the elevation beam. For most sites and landscapes, the terrain at all ranges from one to many kilometers was usually illuminated within the 3-dB points of the fixed elevation beamwidth. At each site, terrain backscatter was measured by steering the azimuth beam through 360° and selecting a maximum range setting such that all discernible clutter within the field of view, typically from 1 km to about 25 or 50 km in

FIGURE 1.7 Phase One equipment at a northern forested site.

range, was recorded. The Phase Zero and Phase One radars had uncoded, pulsed waveforms.

The Phase Zero and Phase One clutter measurement radars were internally calibrated for every clutter measurement. The Phase One instrument was externally calibrated at many sites, using standard gain antennas and corner reflectors mounted on portable towers. The Phase Zero instrument utilized balloon-borne spheres to provide several external calibrations. More detailed information describing the Phase Zero and Phase One clutter measurement radars is provided in Chapters 2 and 3, respectively.

Several years after the Phase One measurement program was completed, the L-band component of the Phase One radar was upgraded to provide an improved LCE (L-band Clutter Experiment) instrument for the measurement of low-Doppler windblown clutter spectra to low levels of clutter spectral power. The LCE radar is described in Chapter 6.

TABLE 1.1 Clutter Measurement Parameters

	Phase Zero	Phase One				
Frequency						
Band	X-Band	VHF	UHF	L-Band	S-Band	X-Band
MHz	9375	165	435	1230	3240	9200
Polarization	HH	VV or HH				
Resolution						
Range	9, 75, 150 m	15, 36, 150 m				
Azimuth	0.9°	13°	5°	3°	1°	1°
Peak Power	50 kW	10 kW (50 kW at X-Band)				
10 km Sensitivity	$\sigma^\circ F^4 = -45$ dB	$\sigma^\circ F^4 = -60$ dB				
Antenna Control	Continuous Azimuth Scan	Step or Scan through Azimuth Sector (<185°)				
Tower Height	50'	60' or 100'				
Data						
Volume	2 Tapes/Site (800 bpi)	≈ 25 Tapes/Site (6250 bpi)				
Acquisition Time	1/2 Day/Site	2 Weeks/Site				

Figure 1.8 shows results of five-frequency measurements of ground clutter conducted by the Phase One instrument at 35 general rural sites. Each plotted point indicates the mean value of clutter strength $\sigma^\circ F^4$—F is the pattern propagation factor (see Section 1.5.4)—obtained from a particular clutter patch for given settings of radar frequency, polarization, and range resolution, one clutter patch per site from each of the 35 sites (Figure 1.1 shows the outline of a typical clutter patch). These results illustrate the variability in mean strength from measured clutter histograms (e.g., see the vertical dashed lines in Figure 1.2); the cell-to-cell variability within the clutter patches is usually much greater (indicated by the overall extent in $\sigma^\circ F^4$ of the histograms in Figure 1.2). Such variability in mean clutter strength as is indicated in Figure 1.8 occurs both due to variations in the intrinsic clutter coefficient σ° as well as variations in the propagation factor F (e.g., as discussed in Section 3.3.2). The five-frequency results of Figure 1.8 show broad site-to-site variability and increasing variability with decreasing radar frequency (i.e., 20 dB of variability at X-band increasing to 65 dB of variability at VHF); but otherwise indicate little general trend of mean clutter strength with radar frequency when averaged over all rural terrain types. In contrast and as will be demonstrated, significant trends of mean clutter strength with frequency do occur in specific rural terrain types (e.g., farmland vs forest). The results of Figure 1.8 are discussed in much greater detail in Chapter 3 (see Section 3.5.1).

1.4 Clutter Prediction at Lincoln Laboratory

Section 1.4 describes the basic tenets underpinning ground clutter modeling efforts at Lincoln Laboratory and upon which the success of the models fundamentally depends. These tenets are further developed in subsequent sections of this book. Much of the discussion follows from the preceding historical review (Section 1.2) of important ideas

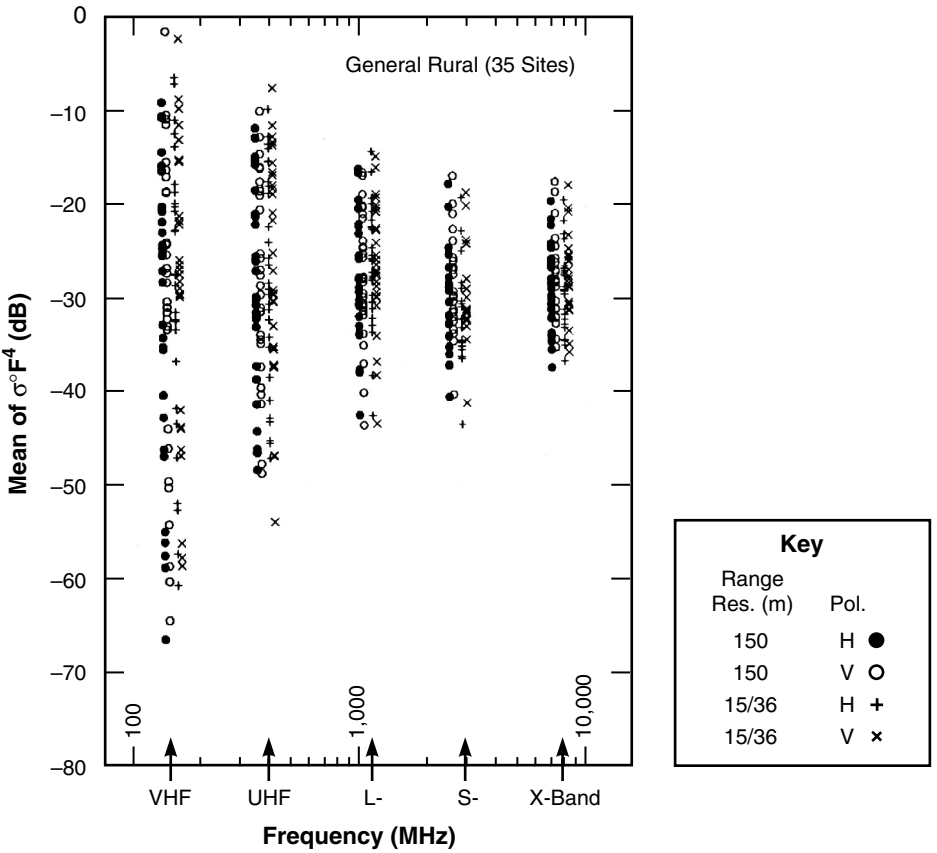

FIGURE 1.8 Mean clutter strength vs radar frequency in general rural terrain, as measured at 35 sites. These data show broad site-to-site variability, and increasing variability with decreasing frequency; but otherwise indicate little overall (e.g., medianized) trend of mean clutter strength with frequency.

that had emerged earlier concerning low-angle ground clutter and previous approaches to its modeling.

1.4.1 EMPIRICAL APPROACH

The approach to solving the problem of bringing order and predictability to low-angle clutter, as carried forward in this book, is based on trend analysis in measurement data. Averaging over large amounts of high-quality, internally self-consistent measurement data allows fundamental underlying trends to emerge which are often obscured by specific effects in individual measurements. No attempts are made to hypothesize and validate theoretical solutions, and any notional dependencies that cannot be demonstrated in the data are also not utilized. Empirical predictive constructs for low-angle clutter in surface radar are developed based on replicating all important general trends observed in the measurement data.

1.4.2 Deterministic Patchiness

As stated previously, the most salient characteristic of ground clutter in a surface radar is variability. One important way that this variability manifests itself is patchiness in spatial occurrence (see Figure 1.1). Clutter does not exist everywhere, and its on-again, off-again behavior is what fundamentally determines system performance at any given site. The main approach of this book presumes the use of DTED to deterministically approximate the site-specific spatial patterns of terrain visibility and hence clutter occurrence at each site of interest. Following this approach, answers about the degree to which clutter limits system performance are obtainable one site at a time. Clutter varies dramatically from site to site, and the extent to which clutter limits radar performance only has deterministic meaning on a site-specific basis. Some effort (coordinated with studies at Lincoln Laboratory) has been made elsewhere [32] to include mathematically-derived stochastic patchiness within a general non-site-specific clutter modeling framework, but in such efforts the statistics of patchiness, dependent upon terrain type, are themselves obtained from processing in DTED for the terrain type of interest. A site-specific deterministically-patchy model allows quantitative comparison between prediction and measurement of given clutter patches at given sites; more general stochastically-patchy or non-patchy models cannot be validated in this direct manner.

1.4.3 Statistical Clutter

Although the visible regions of occurrences of ground clutter (i.e., the macroscale clutter spatial occupancy map—see Figure 1.1) are predicted deterministically using DTED, the clutter amplitudes that occur distributed over such regions are a statistical phenomenon. The information content in DTED is suitable for defining kilometer-sized macroregions of terrain visibility, but this information content—in currently available or any foreseeable database of digitized terrain elevations and/or terrain descriptive information—is insufficient to deterministically predict clutter amplitudes in individual spatial cells. Thus this book characterizes land clutter strength (as opposed to its spatial occupancy map) as a statistical random process and determines predictive parametric trends in the parameters characterizing the statistical clutter amplitude distributions.

1.4.4 One-Component σ° Model

The difficulty in two-component clutter models[6] of how to transition in measured data and modeling specification between extended σ° and discrete RCS was previously brought into consideration in Section 1.2.4. Consider again the key role that spatial resolution plays in low-angle ground clutter (see Section 1.2.3). The shapes of clutter spatial amplitude distributions are highly dependent on resolution over their whole extents (not just their strong-side tails). This results from the fact that at grazing incidence much of the discernible clutter (not just the strongest returns) is discrete-like. This key fact has been relatively unrecognized in the clutter literature, although occasional past remarks may be found that begin to approach the idea. For example, Krason and Randig [3] based the interpretation of their measurements of forest clutter on what appeared to them to be a fundamental "transition from diffuse scattering at large angles to specular scattering at the very shallow angles." Recall that surface clutter as originally conceptualized—wherein all cells, whether large or small, contain large numbers of small scatterers—provides amplitude distributions with unvarying tight Rayleigh shapes and no dependence of shape

6. "Two-component clutter model" is defined in Section 1.2.4.

on resolution. In contrast, what the radar is actually collecting at low angles is a broad continuum of spiky returns from discretes over a wide range of amplitudes, such that there are usually a number of discretes in each cell. This number is small enough that changing cell size strongly affects the statistics of the results.

Recognition of this fact allows the complete spatial field of low-angle land clutter from weakest to strongest cells to be understood and predicted in a unified manner using an area-extensive σ° formulation. The approach properly deals with cells containing a number of relatively weak, randomly-phased discretes as a power-additive density function in the statistical aggregate of many such cells. However, the approach also properly treats occasional cells containing strong isolated discretes, despite the fact that representing isolated discretes with a density function may at first seem inappropriate. For such a cell, a high-resolution radar will contribute a strong σ° into a wide amplitude distribution, and a low-resolution radar will contribute a weaker σ° into a narrower amplitude distribution. Prediction of clutter RCS from these distributions will result in the same RCS for the large discrete in both cells (large σ° times small cell area equals smaller σ° times larger cell area).

Thus a statistical σ° model implementing the fundamental property of spread in amplitude distribution vs resolution can capture and recreate the observed spatial granularity and point-like nature of clutter fields at low angles of observation, without recourse to an additional RCS component that is difficult to implement realistically. The reasoning behind why the density function σ° is the proper way to model clutter even when dominated by discrete sources is considerably expanded upon in Chapter 4, Section 4.5. The clutter modeling statistics provided in this book follow this approach (but see Appendix 4.D).

1.4.5 Depression Angle

Return now to the preceding discussion (Section 1.2.5) of historical perceptions on whether illumination angle might be important in affecting low-angle clutter strength, and if so, how to implement it in a model. Another position on how to use illumination angle to help characterize low-angle clutter, intermediate between that of not using angle at all (following the first approach described in Section 1.2.5) and that based on fine-scale specification of local terrain slopes in DTED (following the subsequent approach described in Section 1.2.5), exists and was utilized in the early literature by Linell [1] to successfully reduce measurement data from a ground-sited radar working over ranges up to 12 km.[7] Although terrain slopes may not be very definable or directly relatable to clutter strengths at grazing incidence (as under the first approach described in Section 1.2.5), this intermediate approach brings a more macroscopic measure of angle to bear on the problem, namely the depression angle at which larger patches of relatively uniform terrain are viewed below the local horizontal at the radar antenna. The use of DTED to define depression angle as a macroparameter in this manner is appropriate to the information content and accuracy of the DTED, in contrast to the use of DTED to define grazing angle as a microparameter associated with individual cells. That is, depression angle depends only on terrain elevations and not their rates of change and hence is a slowly varying

7. That is, at more realistic ranges for surface radar than the several tens or hundreds of meters of many measurements of σ° vs grazing angle reported in the literature and performed, for example, with radars mounted on portable "cherry-pickers" for the purpose of measuring backscatter from small areas of homogeneous ground and for the most part at higher angles [40].

quantity over clutter patches; whereas grazing angle depends also on rates of change of elevation (i.e., the derivative) and hence is a rapidly varying quantity much more susceptible to inaccuracies and error tolerances in DTED. Linell's results [1] showed that levels and shapes of clutter amplitude distributions measured from such macropatches were extremely sensitive to the differences in depression angle (e.g., 0.7°, 1.25°, 5°) at which they were obtained. These data became widely referenced [21, 24, 26], but did not directly lead to clutter models. An important distinction is that such data did not directly provide a simple continuous angle characteristic (like constant-γ), but instead showed how complete clutter amplitude distributions vary in steps or intervals of depression angle regime.

Similar effects with depression angle, as first seen much earlier by Linell, both on the mean levels and shapes of clutter amplitude distributions over large spatial macroregions of low-angle clutter occurrence, constitute a highly pervasive and important parametric influence observed throughout the Phase Zero and Phase One measurements. Figure 1.9 shows these strong effects of depression angle on levels and shapes of clutter amplitude distributions. The curves of Figure 1.9 are plotted from the Phase Zero X-band data in Table 2.4 of Chapter 2; they were first presented in this manner by Skolnik [19]. It is evident in these results that mean and median clutter strengths rise rapidly with increasing depression angle, and that spreads in clutter amplitude distributions as given by either the mean/median ratio (as shown in the lower part of Figure 1.9) or by the Weibull shape parameter a_w rapidly decrease with increasing angle (the upper part of Figure 1.9 plots the inverse of a_w against depression angle). The results shown in Figure 1.9 are described in greater detail in Chapter 2.

Although Linell's results reporting the sensitivity of shape parameter to angle were relatively widely referenced, the corresponding similar sensitivity of shape parameter to radar spatial resolution was less widely recognized, as of course were the consequent interdependent effects of angle and resolution together on shape. These important interdependent effects of both depression angle (Figure 1.9) and radar resolution (Figure 1.3) on the shapes of low-angle clutter amplitude distributions are key elements in the clutter modeling information provided in this book.

1.4.6 Decoupling of Radar Frequency and Resolution

Statistical low-angle clutter amplitude distributions are fundamentally characterized by a mean absolute level, and by the shape or degree of spread (broad or narrow) about the mean level. Results in this book show that the mean level of the distribution depends strongly on radar frequency, depending on terrain type (see Figure 3.38);[8] and that the shape of the distribution depends strongly on radar spatial resolution (as has been discussed, see Figure 1.3). In addition, both the mean level and the shape depend upon depression angle (see Figure 1.9). However, analyses of the clutter measurement data have uncovered an important further fact, fundamental to the development of the modeling information in this book. This further fact is the decoupling of the effects of radar frequency and resolution on

8. To be clear what is meant, this book shows that there exists little or no general dependence of land clutter strength with radar carrier frequency, VHF to X-band, where by "general" is meant averaging across all specific terrain types; but that for specific terrain types the frequency dependence of clutter can be strong, ranging from varying directly with carrier frequency (i.e., strongly increasing with frequency) in open low-relief terrain to varying inversely with carrier frequency (i.e., strongly decreasing with frequency) in forested high-relief terrain (see Chapters 3 and 5).

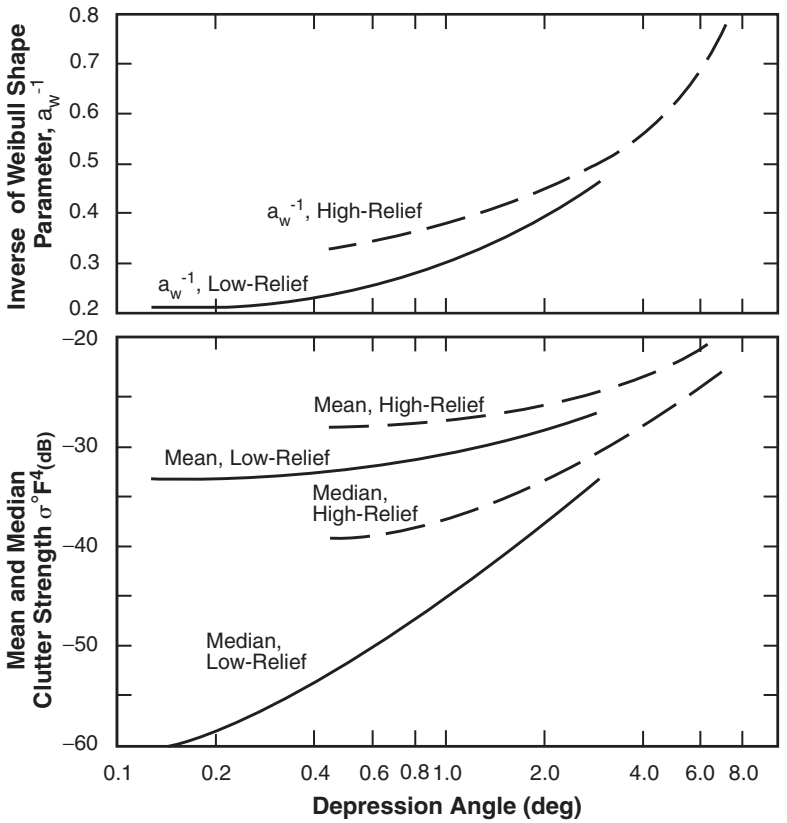

FIGURE 1.9 General variation of ground clutter strength (mean and median) and spread (a_w) in measured ground clutter spatial amplitude statistics vs depression angle, for rural terrain of low and high relief. Clutter strengths increase and spreads decrease with increasing depression angle. X-band data, plotted from Table 2.4 in Chapter 2. (After Skolnik [19]; by permission, © 2001 The McGraw-Hill Companies, Inc.)

the clutter amplitude distributions. Thus, although radar frequency affects mean level, it does not significantly affect shape; and although radar resolution affects shape, it does not affect mean level. The mean level is the only statistical attribute of the distribution unaffected by resolution; for example, the median and other percentile levels are strongly affected by resolution. This decoupling of effects of radar frequency and resolution on clutter amplitude distributions greatly decreases the parametric dimensionality of the consequent clutter modeling construct, such that this construct constitutes a proper empirical model incorporating trends over many measurements, and does not simply degenerate to a table look-up procedure of specific measurements.

1.4.7 Radar Noise Corruption

At the very low angles at which surface radar illuminates the surrounding terrain, typically $< 1^\circ$ or 2°, even within spatial macroregions (i.e., clutter patches comprising many resolution cells) that are under general illumination and not deep in shadow, there usually occurs a subset of randomly occurring radar return samples from low-lying or shadowed terrain cells interspersed within the patch that are at the noise level of the radar (see Figure

1.2; samples at radar noise level shown black). This phenomenon is henceforth referred to as the occurrence of microshadow within macropatches of clutter. Microshadow is inescapable in low-angle clutter statistics. The correct way of dealing with microshadow is as follows: once the boundaries of a spatial clutter patch are defined (for example, by terrain visibility in DTED), all of the samples returned from within the patch boundaries must be included in the clutter statistics, including those at radar noise level. Frequently, in the clutter literature, only the shadowless or noise-free set of samples above radar noise level (shown white in Figure 1.2) is retained to characterize the clutter in the region. Shadowless statistics are dependent on the sensitivity of the measurement radar; that is, radars of differing sensitivity obtain different numbers of noise samples and hence obtain different measures of shadowless clutter strength. The key requirement for determining correct absolute measures of clutter strength over a given spatial patch of clutter (as opposed to relative, sensitivity-dependent measures) is to include all samples from the patch in the computation, including those at radar noise level. Clutter amplitude distributions from spatial patches inclusive of all the returns from the patch (including those at radar noise level) will henceforth be referred to as all-sample distributions.

The necessary existence of noise-level samples in all-sample clutter amplitude distributions is a source of corruption in clutter computation. This corruption is dealt with as follows. All statistical quantities including moments and percentile levels are computed and shown two ways: 1) as an upper bound in which samples at noise level keep their noise power values (for noise samples, the actual clutter power $\leq$ noise power); and 2) as a lower bound in which the samples at noise level are assigned zero or a very low value of power (for noise samples, the actual clutter power $\geq$ zero). The correct value of the statistical quantity, that is, the value that would be measured by a theoretically infinitely sensitive radar for which the upper and lower bounds would coalesce, must lie between the upper bound and lower bound values. Even when the amount of noise corruption is severe, upper and lower bounds to statistical moments are usually close to one another because these calculations are dominated by the strong returns from the discrete clutter sources within the patch. In contrast, moments and percentile levels in the less correct, noise-free or shadowless distributions can be significantly higher than upper and lower bounds to these quantities in the corresponding, more correct noise-corrupted all-sample distributions. Separation of upper and lower bound values by large amounts in all-sample distributions indicates a measurement too corrupted by noise to provide useful information.

The modeling information provided in this book is based on noise-corrupted all-sample clutter amplitude distributions from measured clutter patches with tight upper and lower bounds. As a consequence, the Weibull distributions specified herein for predicting clutter

1.5.2 Two Basic Trends

Two fundamental parametric dependencies exist in low-angle clutter amplitude statistics. The first dependency is that of depression angle as it affects microshadowing in a sea[10] of discrete clutter sources such that mean strengths increase and cell-to-cell fluctuations decrease with increasing angle. The second dependency in low-angle clutter amplitude statistics is that of spatial resolution. In the discrete-dominated heterogeneous spatial field of low-angle clutter, increasing resolution results in increased spread in amplitude distributions. This effect of resolution on shapes of clutter amplitude distributions is key to the understanding and realistic replication of the fundamental texture and graininess of clutter spatial fields.

1.5.3 Measurement-System-Independent Clutter Strength

The measures of clutter amplitude statistics provided in this book are absolute measures not dependent on radar sensitivity. For this to be true, noise-level samples within visible regions are included in the clutter statistics. The Phase Zero and Phase One measurement radars were sensitive enough to measure discernible returns from the dominant discrete clutter sources that occurred within visible regions, regardless of range to the region. For clutter distributions that properly include the noise-level samples, increasing sensitivity merely acts to reduce the relative proportions of cells at radar noise level within such regions, but otherwise is of little consequence in its effect on cumulatives, moments, etc.

1.5.4 Propagation

In land clutter, the intervening terrain can strongly influence the radiation between the clutter cell and the radar. These terrain effects are caused by multipath reflections and diffraction from the terrain. All such effects are included in the pattern propagation factor F, defined (see, for example, [20]) to be the ratio of the incident field strength[11] that actually exists at the clutter cell being measured to the incident field strength that would exist there if the clutter cell existed by itself in free space and on the axis of the antenna beam. The measures of clutter strength provided throughout this book, both in reduction of measurement data and in predictive modeling information, do not separate the effects of propagation over the terrain between the radar and the clutter cell from those of intrinsic terrain backscatter from the clutter cell itself. Thus, the term "clutter strength" as used in this book is defined as the product of the intrinsic clutter coefficient σ° (see Section 2.3.1.1) and the fourth power of the pattern propagation factor F, where F includes all propagation effects, including multipath and diffraction, between the radar and the clutter cell.

Using currently available DTED, it is not generally possible to deterministically compute the propagation factor F at clutter source heights sufficiently accurately to allow cell-by-cell separation of intrinsic σ° in measured clutter data. Difficulties are encountered in attempting to accurately separate propagation effects using any of the currently available

10. This book uses the phrase "sea of discretes" to suggest "a widely extended, copious, or overwhelming quantity," or "a vast expanse," or "a large extended tract of some aggregate of objects;" see Oxford English Dictionary, or Random House Dictionary of the English Language, etc. In other words, at the low illumination angles of surface radar, the number of spatially localized or discrete scattering sources is extremely large and of extremely wide variation in strengths, so as to completely dominate the low-angle ground clutter phenomenon. This is in contrast to the much less frequent occurrence of discrete clutter sources at higher airborne-like angles of illumination, where the nature of the ground clutter phenomenon is generally diffuse.
11. The strength of the electromagnetic field constituting the incident radar wave.

propagation prediction computer codes, such as those based on SEKE [33, 34], Parabolic Equation [35–37], or Method of Moments [38]. For example, since at low angles F varies as the fourth power of clutter source height [10], the illumination of vertical sources increases rapidly with source height, and differences of several meters in source height can cause tens of dB differences in observed clutter strength $\sigma^{\circ}F^4$. Further, reflect that most clutter cells contain a variety of unspecified vertical scatterers of various unknown heights. Theoretical work by Barrick [39] on scattering from rough surfaces is based on the premise that at low angles scattering and propagation influences are intimately interwoven and phenomenologically inseparable. Thus all of the coefficients of clutter strength $\sigma^{\circ}F^4$ tabulated as modeling information in this book include propagation effects. Further illustrating the importance of propagation effects on low-angle clutter, Barton [10] has provided insightful work in modeling clutter in ground-sited radars as a largely propagation-dependent phenomenon over nominally level or nominally hilly terrain.

Although propagation is generally not separable from clutter strength, mentioned here but not further developed in this book are two particular circumstances in which propagation effects can be dominant and to some extent predictable in low-angle clutter. These two circumstances are: 1) at low (VHF) radar frequencies over open low-relief terrain where dominant multipath effects affect clutter strengths by large amounts; and 2) from shipboard radars operating in littoral environments where ground clutter from inland cells is strongly affected by anomalous propagation and ducting.

This book investigates low-angle land clutter from directly illuminated, visible terrain regions. Land clutter from regions well beyond the horizon is usually much weaker than that from directly illuminated regions. Although weak, such interference is not necessarily inconsequential to radars operating against targets beyond the horizon. Long-range diffraction-illuminated land clutter is understood fundamentally as clutter reduced by large propagation losses due to the indirect illumination and is not further considered in this book. Thus all measures of clutter strength provided herein apply to directly—i.e., geometrically—visible terrain and include propagation effects.

1.5.5 Statistical Issues

This book determines fundamental parametric trends in the distributions of clutter amplitudes over kilometer-sized macroregions or patches of directly visible terrain. Low-angle ground clutter is a complex phenomenon, primarily because of the essentially infinite variety of terrain. As a result, there are many influences at work in any specific measurement. Thus the discernment of fundamental trends in clutter amplitude distributions must occur through a fog of obscuring detail. A science is winnowed out, through statistical combination of many similar measurements (i.e., measurements from like-classified patches of terrain at similar illumination angles).

This brings the discussion to technical statistical issues concerning combination of measured data. Simply put, an individual resolution cell (from which a single spatial sample of clutter strength is obtained) may be regarded as the elemental spatial statistical quantity; or the complete terrain patch (from which an amplitude distribution is formed from the clutter returns from the many resolution cells comprising the patch) may be regarded as the elemental spatial statistical quantity. The former approach leads to ensemble amplitude distributions in which measured data from many similar patches are aggregated, sample by sample. The word “ensemble” distinguishes such results obtained by

combining individual cell values—many values per patch—from many patches. The latter approach leads to the generation of many statistical attributes for the amplitude distribution of a given patch, the subsequent combination of a given attribute (e.g., mean strength) into a distribution of that attribute from many similar patches, and the final determination of a best expected value of the attribute from its distribution. The words "expected value" distinguish such results obtained by combining patch values—one value per patch—from many patches.

The advantage of the cell-by-cell ensemble approach is that it not only allows quick determination of trends in amplitude distributions, but also allows simple and straightforward actual specification of resultant general distributions. This is the major approach followed in Chapter 2. However, reduction of data via expected values is the more rigorously correct way to provide clutter modeling information. Thus the finalized results in Chapters 3, 4, and 5, largely based on Phase One data, are presented in terms of expected values. Trends seen in ensemble distributions also occur in expected values; fine adjustment of ensemble numbers to best expected values appropriate to a patch is a higher-order technical issue considered in Chapter 2.

1.5.6 Simpler Models

A considerable amount of clutter modeling information is provided in this book within the context of approximating Weibull coefficients, reflecting the web of basic parametric trends that exist in clutter amplitude distributions. Simpler approaches to ground clutter modeling are often suggested. This book provides a comprehensive base of information upon which alternative clutter modeling constructs may be developed and verified. Realistic and useful models of the low-angle clutter phenomenon need to include the sorts of complex parametric variation discussed in what follows. The empirical modeling information presented herein for describing low-angle clutter amplitude distributions captures the fundamental characteristics of these variations and allows the understanding and quantitative prediction of the limiting effects of ground clutter on the system performance of surface-sited radar.

1.5.7 Parameter Ranges

The ranges in important radar and environmental parameters over which clutter was measured with the Lincoln Laboratory measurement equipment, and to which the clutter modeling information presented in this book is limited, are discussed in this section. Radar frequency in the results of this book ranges from VHF (170 MHz) to X-band (9200 MHz). The behavior of ground clutter at higher or lower frequencies is not addressed. One particular result of the Phase One five-frequency analyses is that clutter strength at the Phase One VHF measurement frequency of 170 MHz for forested terrain illuminated at relatively high depression angles of 1° or 2°[12] is as much as 10 dB stronger than at microwave frequencies. On the basis of recent synthetic aperture radar (SAR) measurement programs at Lincoln Laboratory and elsewhere, it is known that at lower VHF frequencies (e.g., ~50 MHz), the clutter strength from forests drops by ~10 dB as frequency decreases below the resonance range and enters the Rayleigh region of scattering. That is, clutter strength from trees decreases as frequency decreases below

12. Depression angles of 1° or 2°, although small in absolute terms, are relatively high angles [e.g., are at the 84 and 93 percentile positions, respectively, in the overall distribution of depression angles shown in Chapter 2, Figure 2.27(a)] for a surface radar to illuminate the ground.

~100 MHz. However, effects like this outside the Phase Zero/Phase One ranges of parameters are not addressed in this book.

Radar spatial resolution in the results of this book ranges from ~10^3 to ~10^6 m^2. A strong trend in shapes of clutter amplitude distributions with spatial resolution over this range is shown to exist. To what extent this trend can be extrapolated to lower or higher (i.e., SAR-like) resolutions is not addressed. It may be expected that with increasing cell size a limit of Rayleigh statistics is eventually approached, beyond which little additional effect with increasing cell size would be expected. Also, perhaps with decreasing cell size (e.g., appropriate to high resolution SAR radars) a limit in the other direction might be approached wherein most cells resolve individual scatterers so that further effects with resolution diminish. Such speculative limits do not appear within the ranges of spatial resolution available in the Phase Zero/Phase One data.

Radar polarization[13] in the results of this book is largely limited to co-polarized linear transmit/receive states. The Phase One five-frequency radar acquired clutter data only at VV- or HH-polarizations. Some cross-polarized data at VH- and HV-polarization were acquired with the subsequent LCE-upgrade to the Phase One radar and are briefly discussed in Chapter 6. Phase Zero X-band clutter data are limited to HH-polarization.

The clutter data in the results of this book are limited in the depression angle at which the terrain is illuminated to the relatively small angles associated with ground-based radars. Most of the results apply to depression angles less than 1° or 2°. With decreasing rates of occurrences, some results are applicable at somewhat higher angles. Although constrained by narrow elevation beamwidths, some Phase One five-frequency results were obtained up to ~4° (X-, S-bands) or up to ~6° (lower bands). Some Phase Zero X-band results reach up to ~8°. A small amount of X-band SAR clutter data is discussed that shows continuity in the transition with angle that occurs between the Phase Zero ground-based data of depression angles up to ~6° or 8° and airborne clutter data of depression angles ranging from ~4° to 16°.

Land clutter results in this book are based on measurements from many sites widely dispersed over the North American continent and hence covering a variety of terrain types and terrain relief. Modeling information is provided for general rural terrain and various specific terrain types. Ranges at which clutter was measured are relatively long; that is, they begin at 1 or 2 km and extend in some cases to more than 50 km. Patch sizes are relatively large—typically, several kms on a side. Thus the scale at which the clutter results in this book apply is appropriate to surface-sited surveillance and tracking radar typically operating in composite, discrete-dominated, heterogeneous terrain over long ranges and low angles. In contrast, much of the existing ground clutter literature is not relevant to this situation, but rather is concerned with measurements at shorter ranges (< 1 km), higher angles, and homogeneous conditions over small areas of ground [40].

1.6 Organization of Book

This book is organized into six chapters, in which for the most part each chapter is based upon data analysis in a particular subset from the overall database of Phase Zero and Phase

13. VH means transmit vertical polarization, receive horizontal polarization, etc.

One measurements. This section briefly describes the subset of data upon which each chapter is based. Also briefly indicated is how a comprehensive understanding of low-angle land clutter is sequentially built up chapter by chapter to provide a capability for predicting clutter effects in surface-sited radar. In each chapter, technical discussions of subject matter ancillary to the development of the main clutter modeling information of the chapter are included in appendices.

Chapter 2. Chapter 2 is based on the X-band data obtained in the Phase Zero ground clutter measurements program. Many of the Phase Zero results in Chapter 2 are obtained from a basic file of 2,177 clutter patch amplitude distributions obtained from the 12-km maximum range Phase Zero experiment as measured at 106 different sites [18]. Analyses of these data as described in Chapter 2 lead to the first of two major results. This first result is the dependence of low-angle ground clutter spatial amplitude distributions on depression angle, such that the mean strengths of these distributions increase and their spreads decrease with increasing depression angle. These depression angle effects are largely the result of shadowing at low angles in a sea of patchy visibility and discrete or localized scattering sources. This result and its ramifications are developed in Chapter 2.

Chapter 3. Phase One five-frequency clutter measurement data were collected within three different types of experiments, namely, repeat sector measurements, survey experiments, and long-time-dwell experiments. Chapter 3 is based upon repeat sector measurements [14]. The repeat sector at each site was a narrow azimuth sector in which clutter measurements were repeated a number of times during the two or three week time-on-site of the measurement equipment, to increase the depth of understanding and the reliability of the results. The repeat sector database altogether comprises 4,465 measured clutter spatial amplitude distributions. This database—comparable in size to the Phase Zero database but much smaller than the spatially comprehensive 360° survey database to be taken up in Chapter 5—is utilized in Chapter 3 for in-depth investigations of multifrequency parametric effects in low-angle clutter beyond the preliminary X-band effects discussed in Chapter 2. Thus Chapter 3 leads to a second major result, which is the dependence of mean clutter strength on radar frequency, VHF to X-band, in various specific types of terrain. In addition, general trends of variation with frequency,[14] polarization, and resolution are determined, not only for mean clutter strength, but also for the higher order moments and percentile levels in clutter spatial amplitude distributions. Also determined in Chapter 3 are the statistical effects of changing weather and season on clutter strength, the latter based on six seasonally-repeated data collection visits of the Phase One equipment to selected sites.

Chapter 4. The two major results obtained in Chapters 2 and 3 provide an approach for modeling low-angle ground clutter spatial amplitude distributions. In this approach, the mean strengths of clutter amplitude distributions vary with frequency, and the spreads of these distributions vary with spatial resolution, depending on terrain type. For a given terrain type, mean strengths increase and spreads decrease with increasing depression angle. This main approach to clutter modeling as taken in the Lincoln Laboratory Phase Zero/Phase One clutter project is introduced and developed in Chapter 4. A preliminary site-specific model, following this approach and based on Phase Zero X-band and repeat-sector Phase One five-frequency data, is provided. Also included in Chapter 4 are discussions of other, simpler approaches to clutter modeling. Phase Zero clutter data are

14. See footnote, Section 1.4.6.

reduced in various ways to aid in quantifying simple model constructs. Chapter 4 also discusses the interrelationship between geometrically visible terrain and clutter occurrence, and what is involved in separating discrete from distributed clutter in measured data and subsequent empirical models. Illustrative results are provided of the temporal statistics, spectral characteristics, and correlative properties of low-angle clutter.

Chapter 5. Chapter 5 obtains the statistical benefit of analyzing and subsuming within the clutter model the much more voluminous 360° spatially comprehensive survey data at each site. This modeling information is presented in Chapter 5 following the same modeling construct as developed in Chapter 4, but based on 59,804 stored spatial clutter amplitude distributions measured from 3,361 clutter patches at 42 Phase One sites. This large set of stored clutter patch statistics together with associated terrain descriptions and ground truth are reduced to generalized land clutter coefficients in Chapter 5 for general rural terrain and for eight specific terrain types. An example is provided of how this modeling information is used to predict PPI clutter maps in surface-sited radar. Clutter model validation at Lincoln Laboratory is discussed. The modeling information in Chapter 5 is presented within a context of Weibull clutter coefficients.

Chapter 6. Most radar signal processing of target returns embedded in clutter is based on Doppler discrimination and hence is highly dependent not only on the relative strength of the clutter power to that of the target, but also on the spectral spreading of the clutter power away from zero Doppler. Clutter spectral spreading in surface-sited radar of fixed position and stable phase is due to the phenomenologically intrinsic motion of the clutter sources themselves, most commonly that of windblown vegetation. Chapter 6 characterizes intrinsic-motion windblown clutter spectral spreading by means of long-time-dwell clutter experiments, in which long sequences of pulses at low pulse repetition frequency (PRF) were recorded over a contiguous set of range gates with a stationary antenna beam. Long-time-dwell data were obtained both with the Phase One five-frequency radar and with its subsequent, L-band only, LCE upgrade with reduced phase noise levels.

On the basis of Phase One and LCE long-time-dwell data, Chapter 6 develops an empirical model [41–43] for the intrinsic spectral spreading of windblown ground clutter. The model proportions total clutter power between dc and ac terms. The ac term is invested with exponential decay characteristics. The resultant modeling construct is parameterized by wind speed, radar frequency, and terrain type. Chapter 6 includes a discussion of the effect of clutter spectral shape on MTI delay line improvement factor and goes on to show how the exponentially shaped Doppler spectrum of windblown clutter affects coherent radar detection performance compared with corresponding performance under more commonly assumed Gaussian or power-law spectral shapes. These latter results are the work of Professor Alfonso Farina of Alenia Marconi Systems, Italy and his colleagues at the University of Rome and the University of Pisa, who became highly interested in the consequences to radar signal processors of the Lincoln Laboratory clutter spectral findings and model [44–46]. These Italian results include validation of the exponential spectral model by comparison of modeled clutter-cancellation system performance with the system performance obtained using measured clutter data as input to the clutter canceller [47, 48]. Chapter 6 also reviews the historical literature on intrinsic-motion ground clutter spectral spreading and brings it into accord with the Phase One and LCE results.

References

1. T. Linell, "An experimental investigation of the amplitude distribution of radar terrain return," *6th Conf. Swedish Natl. Comm. Sci. Radio,* Research Institute of National Defence, Stockholm, March 1963.

2. E. M. Holliday, E. W. Wood, D. E. Powell, and C. E. Basham, "L-Band Clutter Measurements," U. S. Army Missile Command Report RE-TR-65-1, Redstone Arsenal, AL, November 1964; DTIC AD-461590.

3. H. Krason and G. Randig, "Terrain backscattering characteristics at low grazing angles for X and S band," *Proc. IEEE (Letters)* (special issue on computers), vol. 54, no. 12, December 1966.

4. F. E. Nathanson and J. P. Reilly, "Clutter statistics that affect radar performance analysis," *EASCON Proc.* (supplement to *IEEE Trans.),* vol. AES-3, no. 6, pp. 386–398, November 1967.

5. M. P. Warden and B. A. Wyndham, "A Study of Ground Clutter Using a 10-cm Surveillance Radar," Royal Radar Establishment Technical Note No. 745, Malvern, U.K., September 1969; DTIC AD-704874.

6. H. R. Ward, "A model environment for search radar evaluation," *IEEE EASCON Rec*, pp. 164–171, 1971.

7. C. J. Rigden, "High Resolution Land Clutter Characteristics," Admiralty Surface Weapons Establishment Technical Report TR-73-6, Portsmouth, U.K., January 1973; DTIC AD-768412.

8. M. P. Warden and E. J. Dodsworth, "A Review of Clutter, 1974," Royal Radar Establishment Technical Note No. 783, Malvern, U.K., September 1974; DTIC AD A014421.

9. W. L. Simkins, V. C. Vannicola, and J. P. Ryan, "Seek Igloo Radar Clutter Study," Rome Air Development Center, Technical Rep. RADC-TR-77-338, October 1977. Updated in FAA-E-2763b Specification, Appendix A, May 1988. See also FAA-E-2763a, September 1987; FAA-E-27263, January 1986, July 1985.

10. D. K. Barton, "Land clutter models for radar design and analysis," *Proc. IEEE*, vol. 73, no. 2, 198–204 (February 1985).

11. K. Rajalakshmi Menon, N. Balakrishnan, M. Janakiraman, and K. Ramchand, "Characterization of fluctuating statistics of radar clutter for Indian terrain," *IEEE Transactions on Geoscience and Remote Sensing,* vol. 33, no. 2 (March 1995), 317–323.

12. K. S. Chen and A. K. Fung, "Frequency dependence of backscattered signals from forest components," *IEE Proceedings*, Pt. F, 142, 6 (December 1995), pp. 310–315.

13. V. Anastassopoulos and G. A. Lampropoulos, "High resolution radar clutter classification," in *Proceedings of IEEE International RADAR Conference*, Washington, DC, May 1995, 662–66.

14. J. B. Billingsley and J. F. Larrabee, "Multifrequency Measurements of Radar Ground Clutter at 42 Sites," Lexington, MA: MIT Lincoln Laboratory, Technical Rep. 916, Volumes 1, 2, 3; 15 November 1991; DTIC AD-A246710.

15. J. B. Billingsley, "Ground Clutter Measurements for Surface-Sited Radar," Lexington, MA: MIT Lincoln Laboratory, Technical Rep. 786, Rev. 1, 1 February 1993; DTIC AD-A262472.

16. J. B. Billingsley, "Radar ground clutter measurements and models, part 1: Spatial amplitude statistics," *AGARD Conf. Proc. Target and Clutter Scattering and Their Effects on Military Radar Performance*, Ottawa, AGARD-CP-501, 1991; DTIC AD-P006 373.

17. J. B. Billingsley, A. Farina, F. Gini, M. V. Greco, and L. Verrazzani, "Statistical analyses of measured radar ground clutter data," *IEEE Trans. AES*, vol. 35, no. 2 (April 1999).

18. J. B. Billingsley, "Low-Angle X-Band Radar Ground Clutter Spatial Amplitude Statistics," Lexington, MA: MIT Lincoln Laboratory, Technical Report 958, 2002.

19. M. I. Skolnik, *Introduction to Radar Systems* (3rd ed)*.,* New York: McGraw-Hill, 2001.

20. L. V. Blake, *Radar Range-Performance Analysis* (2nd ed.), Silver Spring, MD: Monroe Publishing, 1991.

21. M. W. Long, *Radar Reflectivity of Land and Sea* (3rd ed.), Boston: Artech House, Inc., 2001.

22. C. Currie, "Clutter Characteristics and Effects," in *Principles of Modern Radar*, J. L. Eaves and E. K. Reedy (Eds.), New York: Chapman & Hall, 1987.

23. D. K. Barton, *Modern Radar System Analysis*, Norwood, MA: Artech House, 1988.

24. F. E. Nathanson (with J. P. Reilly and M. N. Cohen), *Radar Design Principles* (2nd ed.), New York: McGraw-Hill, 1991.Reprinted, SciTech Publishing, Inc., 1999.

25. D. C. Schleher, *MTI and Pulsed Doppler Radar*, Norwood, MA: Artech House, 1991.

26. R. R. Boothe, "The Weibull Distribution Applied to the Ground Clutter Backscatter Coefficient," U. S. Army Missile Command Rept. No. RE-TR-69-15, Redstone Arsenal, AL, June 1969; DTIC AD-691109.

27. M. Sekine and Y. Mao, *Weibull Radar Clutter*, London, U. K.: Peter Peregrinus Ltd., 1990.

28. E. Jakeman, "On the statistics of *K*-distributed noise," *J. Physics A; Math. Gen*., vol. 13, 31–48 (1980).

29. J. K. Jao, "Amplitude distribution of composite terrain radar clutter and the *K*-distribution," *IEEE Trans. Ant. Prop*., vol. AP-32**,** no. 10, 1049–1062 (October 1984).

30. K. D. Ward, "Application of the *K*-distribution to radar clutter—A review," *Proc. Internat. Symp. on Noise and Clutter Rejection in Radars and Imaging Sensors*, pp. 15–21, IEICE, Tokyo (1989).

31. T. J. Nohara and S. Haykin, "Canadian East Coast radar trials and the *K*-distribution," *IEE Proceedings*, Pt. F, 138, 2 (Apr. 1991), 80–88.

32. S. P. Tonkin and M. A. Wood, "Stochastic model of terrain effects upon the performance of land-based radars," *AGARD Conference Proceedings on Target and Clutter Scattering and Their Effects on Military Radar Performance*, AGARD-CP-501, (1991).

33. S. Ayasli, "A computer model for low altitude radar propagation over irregular terrain," *IEEE Trans. Ant. Prop*., vol. AP-34, no. 8, pp. 1013–1023 (August 1986).

34. M. P. Shatz and G. H. Polychronopoulos, "An algorithm for the evaluation of radar propagation in the spherical earth diffraction region," *The Lincoln Laboratory Journal*, vol. 1, no. 2, 145–152 (Fall 1988).

35. G. D. Dockery and J. R. Kuttler, "An improved impedance boundary algorithm for Fourier split-step solutions of the parabolic wave equation," *IEEE Trans. Ant. Prop*., 44 (12), 1592–1599 (1996).

36. A. E. Barrios, "A terrain parabolic equation model for propagation in the troposphere," *IEEE Trans. Ant. Prop*., 42 (1), 90–98 (January 1994).

37. D. J. Donohue and J. R. Kuttler, "Modeling radar propagation over terrain," Johns Hopkins APL Technical Digest, vol. 18, no. 2, 279–287, (April–June 1997).

38. J. T. Johnson, R. T. Shin, J. C. Eidson, L. Tsang, and J. A. Kong, "A method of moments model for VHF propagation," *IEEE Trans. Ant. Prop*., 45 (1), 115–125 (January 1997).

39. D.E. Barrick, "Grazing behavior of scatter and propagation above any rough surface," *IEEE Trans. Ant. Prop*., vol. 46, no. 1, pp. 73–83 (January 1998).

40. F. T. Ulaby and M. C. Dobson, *Handbook of Radar Scattering Statistics for Terrain*, Norwood, MA: Artech House, 1989.

41. J. B. Billingsley and J. F. Larrabee, "Measured Spectral Extent of L- and X-Band Radar Reflections from Windblown Trees," Lexington, MA: MIT Lincoln Laboratory, Project Rep. CMT-57, 6 February 1987; DTIC AD-A179942.

42. J. B. Billingsley, "Exponential Decay in Windblown Radar Ground Clutter Doppler Spectra: Multifrequency Measurements and Model," Lexington, MA: MIT Lincoln Laboratory, Technical Report 997, 29 July 1996; DTIC AD-A312399.

43. J. B. Billingsley, "Windblown radar ground clutter Doppler spectra: measurements and model," submitted to *IEEE Trans. AES*, accepted subject to minor revision, October 2000.

44. J. B. Billingsley, A. Farina, F. Gini, M. V. Greco, P. Lombardo, "Impact of experimentally measured Doppler spectrum of ground clutter on MTI and STAP," in *Proceedings of IEE International Radar Conference* (Radar '97), IEE Conf. Pub. No. 449, pp. 290–294, Edinburgh, 14–16 October 1997.

45. P. Lombardo, M. V. Greco, F. Gini, A. Farina, and J. B. Billingsley, "Impact of clutter spectra on radar performance prediction,"*IEEE Trans. AES*, Vol. 37, no. 3, July 2001.

46. P. Lombardo and J. B. Billingsley, "A new model for the Doppler spectrum of windblown radar ground clutter," in *Proceedings of IEEE 1999 Radar Conference*, Boston, MA: 20–22 April 1999.

47. M. V. Greco, F. Gini, A. Farina, and J. B. Billingsley, "Analysis of clutter cancellation in the presence of measured L-band radar ground clutter data," in *Proceedings of IEEE International Radar Conference (Radar 2000)*, Alexandria, VA, May 8–12, 2000.

48. M. V. Greco, F. Gini, A. Farina, and J. B. Billingsley, "Validation of windblown radar ground clutter spectral shape," *IEEE Trans. AES,* vol. 37, no. 2, April 2001.

2

Preliminary X-Band Clutter Measurements

2.1 Introduction

Chapter 2 provides general information describing the amplitude distributions of X-band land clutter returns received from regions of visible ground, based on Phase Zero measurements at 106 sites. Subsequent chapters provide similar information at other frequencies. In presenting land clutter data and results, Chapter 2 attempts both to do justice to describing a very complex phenomenon, and also to efficiently provide useful and easily accessible modeling information. The result is a chapter that provides increasing insight into the clutter phenomenon by cyclically building up an understanding of the many interacting influences affecting clutter amplitude statistics. As insights are developed, they are accompanied with the presentation of modeling information that generalizes such influences at various levels of fidelity.

2.1.1 Outline

The major results of Chapter 2 are summarized within this section.

Basic Clutter Modeling Information. Chapter 2 provides basic ensemble modeling information describing X-band clutter amplitude distributions over macropatches of visible terrain as a function of depression angle for three comprehensive terrain types—rural/low-relief, rural/high-relief, and urban. Chapter 2 goes on to explain, enlarge upon, and extend the nature of low-angle clutter amplitude statistics as encoded within the basic modeling information.

Angle Characteristic. There traditionally has existed within the body of ground clutter literature the idea that a clutter model could be a simple characteristic of clutter strength vs illumination angle. Such a model is provided in Chapter 2 as an expected-value generalization of all the Phase Zero measurements. However, ground clutter is inherently a statistical phenomenon in which large statistical variation occurs. Thus this simple angle-characteristic model shows two characteristics of clutter strength, mean and median, vs angle. Together these characteristics demonstrate the important fact that clutter is statistical and show not only clutter strength vs angle, but also specify the variability (i.e., mean-to-median ratio) of clutter strength at any given angle.

Worst-Case Situations. The basic X-band modeling information of Chapter 2 provides general information. Chapter 2 also provides upper bounds on how strong ground clutter can become in exceptional circumstances by comparing the amplitude distributions from

the strongest Phase Zero clutter patches (urban clutter, mountain clutter) with those of the basic information.

Fine-Scaled Variations with Terrain. The basic modeling information separates terrain into just three categories, which, simply interpreted, implies that, in general, only "mountains" (rural/high-relief terrain) and "cities" (urban terrain) warrant separation from all other terrain types (rural/low-relief terrain). However, with decreasing significance finer trends occur in the Phase Zero data with more specific description of terrain type. Within rural low-relief terrain, fine-scaled differences in clutter amplitude statistics among wetland, forest, and agricultural land are shown to exist. Within urban terrain, fine-scaled differences between terrain of residential (i.e., low-rise) and commercial (i.e., high-rise) character are illustrated. The effect of trees as discrete scattering sources is discussed. Modeling information in which, on low-relief open terrain, trees are the predominant X-band discrete scattering source, and such that clutter amplitude distributions vary with the relative incidence of occurrence of trees (i.e., percent tree cover), is provided.

Negative Depression Angle. Negative depression angles occur when terrain is observed by the radar at elevations above the antenna. Such terrain is usually rough and steep. Information is provided describing clutter amplitude distributions occurring at negative depression angles.

Non-Angle-Specific Modeling Information. Chapter 2 principally provides generalized X-band modeling information for clutter amplitude statistics as a function of depression angle. However, the chapter also provides some non-angle-specific modeling information. For example, the overall distribution that results from combining all of the Phase Zero measured clutter samples is specified, irrespective of terrain type and depression angle, into one all-encompassing ensemble distribution. Much information concerning frequency of occurrence of various levels of low-angle clutter strength is contained in this overall distribution, as measured from 2,177 clutter macropatches at 96 different sites. Chapter 2 also provides non-angle-specific expected value information by showing distributions of mean patch clutter strength by landform and land cover, respectively. To the extent that the overall terrain at a given radar site may be classified as being of one terrain class, such information can characterize mean clutter strength over the whole site, not only in terms of most likely values, but also in terms of worst-case (strong clutter) and best-case (weak clutter) values.

Appendices. The appendices of Chapter 2 provide discussions of the following subjects: (a) Phase Zero measurement equipment and calibration, (b) formulation of clutter statistics, and (c) numerical computation of depression angle.

2.2 Phase Zero Clutter Measurements

2.2.1 Radar Instrumentation

The pilot phase clutter measurements and modeling program was designated as Phase Zero. The Phase Zero radar was a pulsed system (0.5 μs pulse width for many of the Chapter 2 results) that operated at X-band (9375 MHz) with horizontal polarization. The primary display of this radar was a 16-inch diameter, digitally generated, PPI unit. A precision IF attenuator was installed in the radar receiver as a means of measuring clutter strength. The radar was put under control of a minicomputer, by means of which a raw digital record of clutter strength could be obtained by digitally recording the contents of the PPI display in stepped levels of attenuation (1-dB steps over a 50-dB dynamic range).

For many of the results of Chapter 2, the maximum PPI range was set at 12 km, and the clutter data sampling interval size in the polar PPI display was 37 m in range extent and ~0.25° in azimuth extent.

The radar and digital recording equipment were installed in an all-wheel drive one-ton truck that was equipped with a 50-ft pneumatically extendable antenna mast and self-contained prime power. With this mobile Phase Zero clutter measurement instrument, clutter data were recorded in surveillance mode from all clutter sources within the field-of-view by azimuthally scanning the beam which was narrow (0.9°) in azimuth, wide (23°) in elevation, and fixed horizontally at zero degrees depression angle, through 360° in azimuth. Azimuthally scanned data were acquired at each site for each of seven experiments of increasing maximum range from 1.5 to 94 km. Clutter strength calibration was based on the elevation beam gain applicable at the depression angle at which each clutter patch was measured, not just the boresight gain, even though most patches were measured within the 3-dB elevation beamwidth. Each Phase Zero clutter measurement included internal calibration based on accurate measurement of the minimum detectable signal of the receiver. Occasional external calibrations were performed using balloon-borne spheres as test targets. The Phase Zero radar is more fully described in Appendix 2.A.

2.2.2 Measurement Sites

Figure 2.1 shows the location of all 106 sites at which Phase Zero ground clutter measurements were obtained. Photographs of the terrain at two of the measurement sites are shown in Figure 2.2. Figure 2.2(a) shows low-relief undulating prairie farmland at the Beiseker site located 75 km northeast of Calgary. Figure 2.2(b) shows high-relief mountainous terrain at the Plateau Mountain site located 120 km southwest of Calgary in the Canadian Rocky Mountains. Significantly different backscatter characteristics would be expected, and indeed were measured, from the terrain in Figure 2.2(a) compared with that of Figure 2.2(b). However, later in Chapter 2 it will be shown that a useful first step in clutter prediction is to simply distinguish terrain type by whether it is of low relief, as pictured in Figure 2.2(a), or of high relief, as pictured in Figure 2.2(b).

The Phase Zero radar served in a pilot role in site selection activities for Phase One measurements. It is apparent in Figure 2.1 that many of the measurement sites were in Canada. The Phase Zero and Phase One clutter measurement programs were jointly conducted by the United States and Canada within an intergovernmental Memorandum of Understanding. Coordinated analyses of the measurement data took place in both countries [1, 2].

2.2.3 Terrain Description

Procedures were developed to systematically describe and classify the clutter-producing terrain at each measurement site. It was necessary that these procedures cause the clutter data, as measured from many sites, to usefully cluster within the same terrain class, and separate between different terrain classes. The terrain within each clutter patch at each site was classified both in terms of the characteristics of its land cover [3] and of its landform or surface relief [4]. The land cover and landform categories utilized in this classification are shown in Tables 2.1 and 2.2, respectively. The classification was performed principally through use of topographic maps and stereo aerial photos, usually at 1:50,000 scale. Since clutter producing terrain is often heterogeneous in its character, even within spatial macropatches, terrain classification often proceeded at two or even three levels to adequately capture the terrain characteristics important in the clutter data.

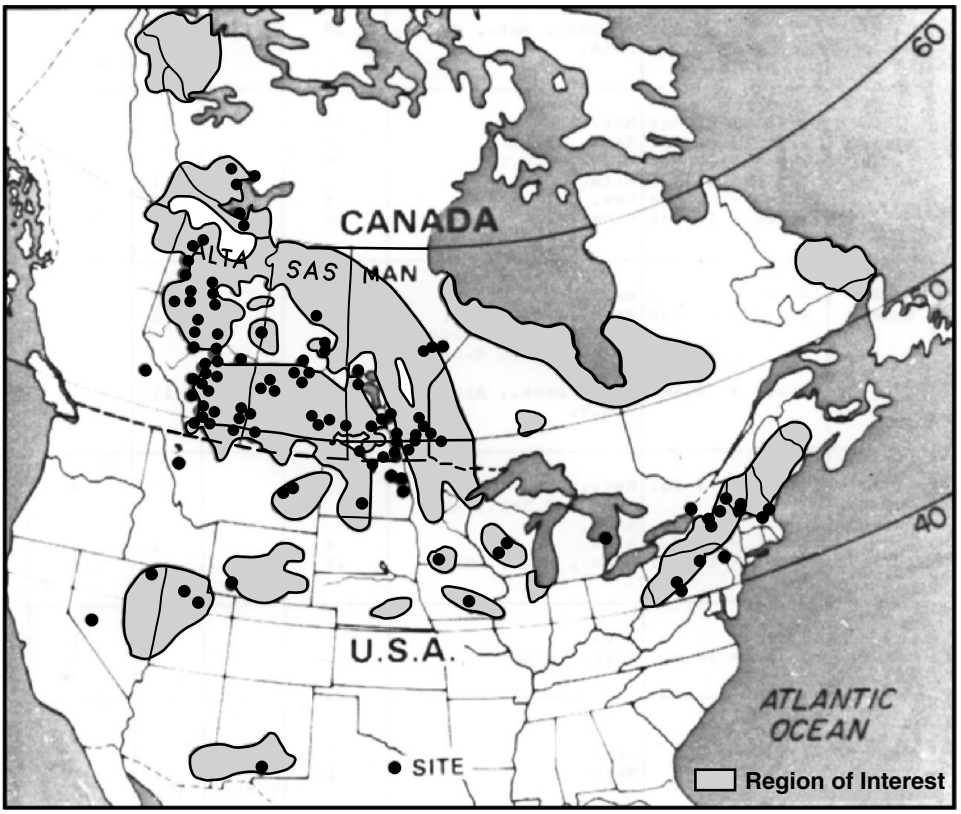

FIGURE 2.1 Map of 106 Phase Zero sites.

In addition to land cover and landform, the height of each site is also important in its effect on the ground clutter measured at that site. High sites see clutter to greater ranges and result in higher depression angles and stronger clutter, compared to low sites. Effective site height is the difference between the terrain elevation of the radar position and the mean of the elevations of all the discernible clutter cells (most of the visible terrain) that occurred at that site. Effective radar height is equal to effective site height plus antenna mast height. By such definition, effective site height and effective radar height are with respect to illuminated terrain only and indicate how high the site or antenna is above the terrain causing clutter backscatter; they are not influenced by masked or shadowed terrain.

The question may be asked as to whether the Phase Zero set of site heights is extensive enough to cover the sorts of height variations that occur in actual radar siting. Figure 2.3 compares site heights for a set of 93 actual radar sites [in Figure 2.3(a)] with Phase Zero site heights [in Figure 2.3(b)], the latter over a set of 93 Phase Zero sites for which effective site height was quantized. In Figure 2.3(a), the 93 actual radar sites were known locations occurring worldwide—of these, 27 occurred around relatively low-relief urban areas, 43 were hilltop sites, and 27 were other sites geographically dispersed (see Appendix 4.B for the definition of "site advantage"). It is seen in Figure 2.3 that this set of other sites provides significantly less extreme siting situations than do the Phase Zero sites. The median Phase Zero site height is 20 m, compared to 10 m for the actual site set. The Phase Zero site set not only encompasses the regime of actual site heights but extends to

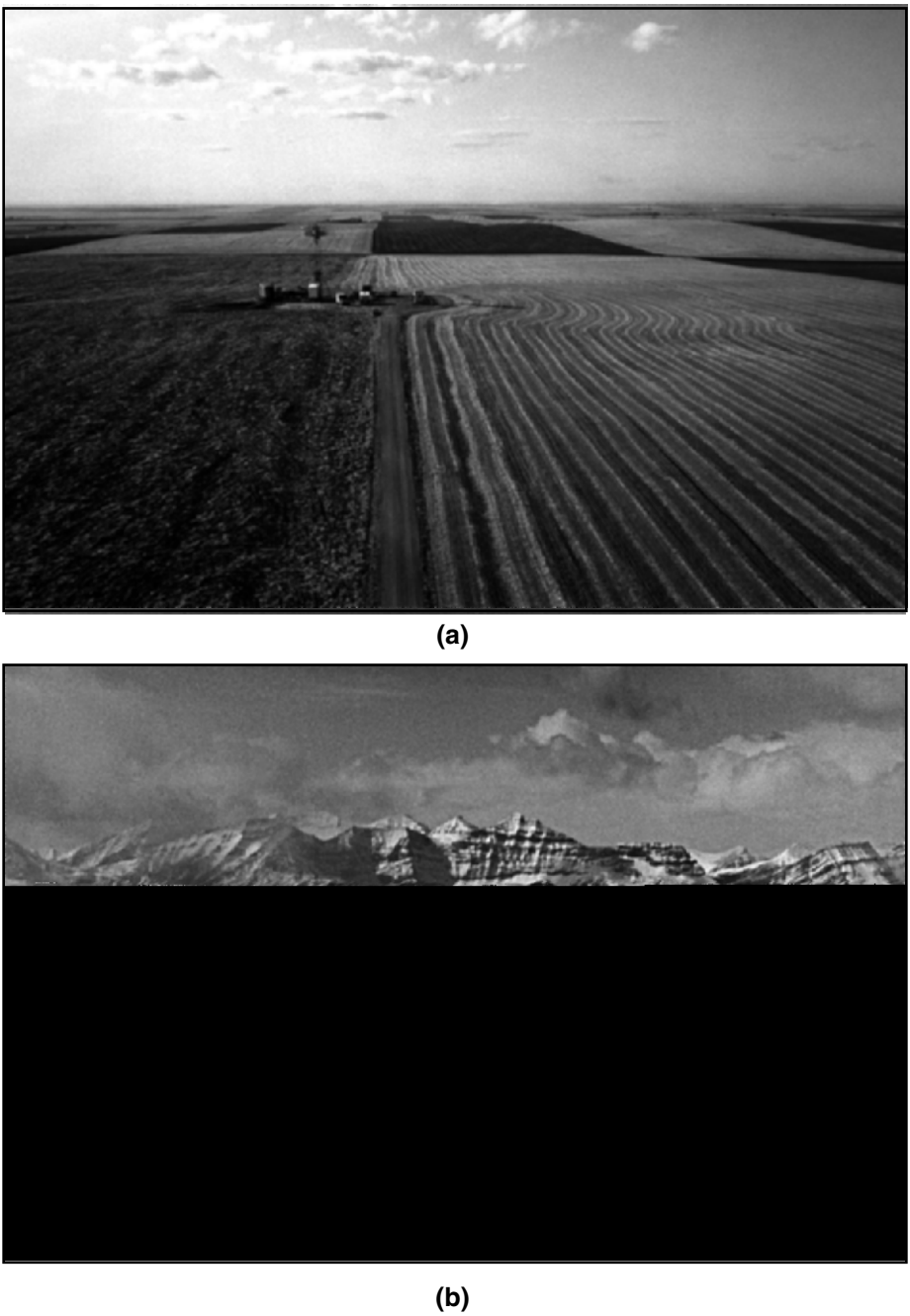

FIGURE 2.2 Two clutter measurement sites in Alberta, Canada. (a) Low-relief farmland at Beiseker. (b) High-relief mountainous terrain at Plateau Mt.

significantly higher and lower sites. This broad expanse of Phase Zero site heights indicates that the database of clutter measurements that results is not constrained in any unrealistic way—for example, in terms of the range of depression angles available, or the range

TABLE 2.1 Land Cover Classes

1	Urban or Built-up Land
	11 Residential
	12 Commercial
2	Agricultural Land
	21 Cropland
	22 Pasture
3	Rangeland
	31 Herbaceous
	32 Shrub
	33 Mixed
4	Forest
	41 Deciduous
	42 Coniferous
	43 Mixed
5	Water
	51 Rivers, Streams, Canals
	52 Lakes, Ponds, Sloughs
6	Wetland
	61 Forested
	62 Non-Forested
7	Barren Land

TABLE 2.2 Landform Classes and Descriptions

Landform Class		Terrain Relief (ft)	Terrain Slope (deg)	Comments
1	Level	< 25	< 1°	
2	Inclined	> 50	1° – 2°	Unidirectional
3	Undulating	25 — 100	< 1°	Regular sequences of gentle slopes; wavelike
4*	Rolling	> 150	2° – 5°	Regular to irregular sequences of moderate slopes
5	Hummocky	25 — 100	< 2°	Complex sequences of slopes
6*	Ridged	50 — 500	2° – 10°	Sharp breaks in slope at tops and bottoms of terrain features
7*	Moderately Steep	> 100	2° – 10°	Unidirectional
8*	Steep	> 100	10° – 35°	Frequently unidirectional
9	Broken	> 50	1° – 5°	Short dissected slopes

* Classes so indicated are "high-relief;" classes not so indicated are "low-relief."

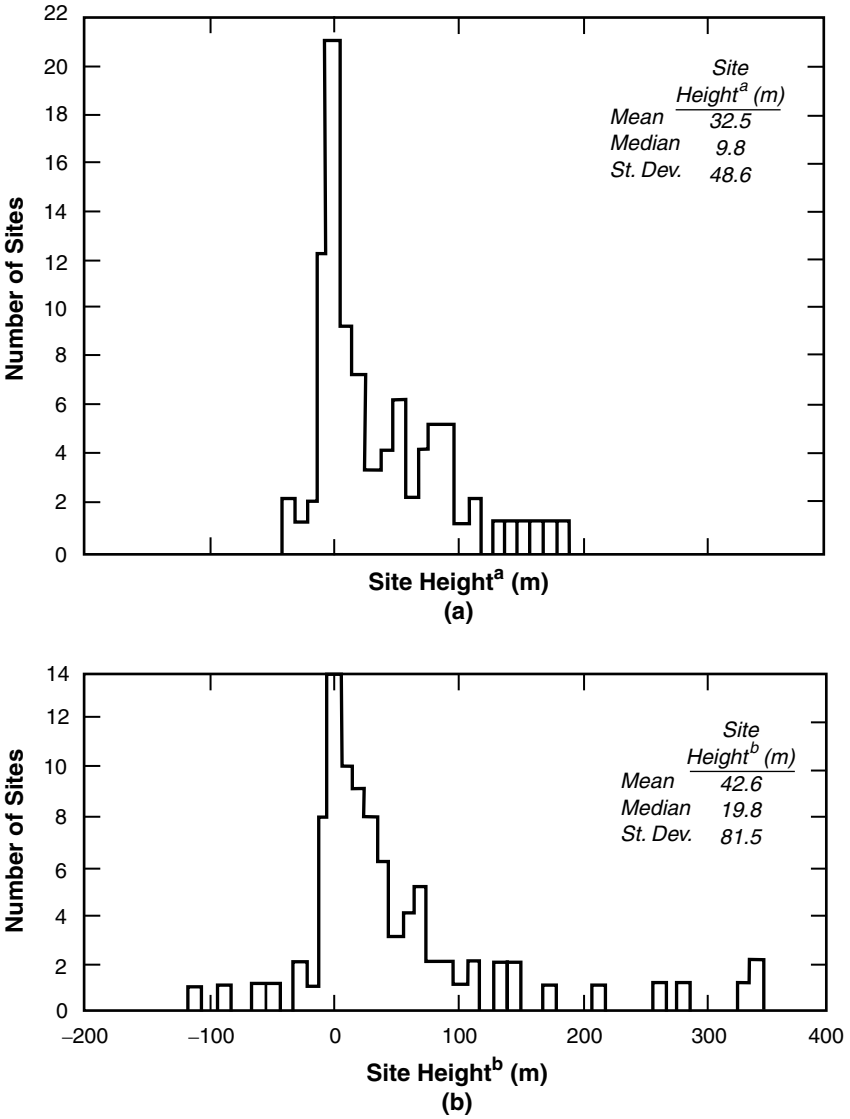

Notes:
a. Site Height = Effective Site Height or Site Advantage
b. Site Height = Effective Site Height

FIGURE 2.3 Comparison of Phase Zero site heights with site heights of radar positions from other geographical regions. (a) 93 radar sites from other regions; (b) 93 Phase Zero measurement sites.

3

Repeat Sector Clutter Measurements

3.1 Introduction

Phase One multifrequency land clutter measurements were conducted during a three-year period at 42 different sites widely dispersed geographically across the North American continent. Many of the sites were in western Canada. The Phase One clutter measurement equipment was self-contained and mobile, principally housed within three, 18-wheel tractor-trailer combination trucks and manned by a five-man crew. The equipment included a transportable antenna tower expandable in six sections to a maximum height of 100 ft. A photograph of the Phase One equipment erected at the Lethbridge West site in Alberta, Canada, is shown in Figure 3.1. At each site, all discernible ground clutter within the field-of-view through 360° in azimuth and from 1 to 25 or 50 km or more in range was measured at each of five frequencies: VHF, UHF, L-, S-, and X-bands. The duration of time that the Phase One equipment spent at each site making these measurements was typically two to three weeks. The amount of raw, digitally recorded, pulse-by-pulse measurement data collected at each site usually filled about 25 to 30 high-density magnetic tapes. Within the measurement program, six repeated data collection visits to a few sites at different times of the year were included to provide seasonal variations in the clutter measurement database.

The objective in conducting the Phase One measurements was to develop a capability for predicting multifrequency variations in ground clutter spatial amplitude distributions in surface-sited radar. Data from each site are analyzed in Chapter 3. From these data multifrequency clutter models are subsequently developed in Chapters 4 and 5. In particular, Chapter 3 shows how ground clutter strength varies with radar frequency, VHF to X-band, in various types of terrain.

The clutter spatial amplitude distributions analyzed in Chapter 3 were measured in what is called the repeat sector at each site. That is, at each site a narrow azimuth sector was selected as a sector of concentration in which measurements were repeated a number of times during the time on site. Typically, the repeat sector is about 20° in azimuth extent and exists at ranges beginning a few kilometers from the radar and extending 5 or 10 km.

FIGURE 3.1 Phase One equipment at Lethbridge West, Alberta. Antenna tower erected to 60 ft.

3.1.1 OUTLINE

This section is a brief introduction to the contents of Chapter 3.

Land Clutter Strength vs Frequency. A major purpose of Chapter 3 is to show how land clutter strength varies with radar frequency, VHF to X-band, in various types of terrain. The best high-level way of showing such variation based on repeat sector measurements is given in Section 3.4 by mean clutter strength data vs frequency for 12 different terrain categories, generalized across a number of similar measurement sites in each category. The remainder of Chapter 3 explains, enlarges upon, and provides background about these generalized multifrequency characteristics, organized within broad terrain groups of urban, mountains, forest, farmland, and desert.

Means and Medians. Each value of mean clutter strength provided in Chapter 3 comes from a clutter amplitude distribution measured over a repeat sector spatial macroregion. These distributions are brought under more complete statistical description by tabulation of their higher moments and several percentile levels, including the median. These additional statistical attributes are generalized within the same terrain categories as are the means.

Polarization and Resolution. The mean clutter strength vs frequency results are combined across measurements of both vertical and horizontal polarization, using both 150-m and 15- or 36-m pulse lengths. Variations of mean clutter strength with polarization

and range resolution are generally small, typically on the order of 1 or 2 dB. Discussion of differences in clutter strength with polarization and resolution is presented in Section 3.5.

Weather and Season. Because low-angle land clutter is dominated by discrete scattering sources, effects with weather and season are also small, usually less than 1.5 dB and 3.0 dB, respectively. Discussion of variability of mean clutter strength with weather and season is given in Section 3.7.

Multipath Propagation. At low angles in open terrain, clutter measurements are dominated by multipath propagation that causes lobing on the free-space antenna pattern and hence introduces strong variations in effective antenna gain to the measured clutter. These propagation-induced variations are generally not removable in assessments of clutter strength. In interpreting many of the measurement results in Chapter 3, it is necessary to estimate the effects of propagation, particularly multipath, in the data. How effects of multipath are estimated is discussed in Appendix 3.B.

Antenna Tower Height. Multifrequency Phase One clutter measurements were obtained with multiple antenna tower heights at four different sites. Results for different Phase One antenna heights are discussed in Section 3.4.1.4. In addition, Section 3.4.1.4 provides a comparison at X-band between Phase Zero and Phase One measurements across many sites in two regimes of antenna height—one where the Phase One radar had similar heights to the Phase Zero radar, and another where the Phase One antenna height was twice as high as that of Phase Zero.

Long-Range Mountain Clutter. A surface-sited radar can occasionally experience strong land clutter from visible terrain at very long ranges, such as 100 km or more. Such clutter comes from mountains because only mountains rise high enough to be within geometric line-of-sight at long ranges. Phase One measurements show that long-range mountain clutter at VHF is significantly stronger than in the microwave bands. In all Phase One bands, the long-range mountain clutter is substantially weaker than mountain clutter observed at shorter ranges due to diffraction over the intervening terrain. Discussion of this matter is included in Appendix 3.B.

Coherency of Clutter Returns. The Phase One measurements were coherent; the phase (provided by in-phase and quadrature samples from 13-bit A/D converters at rates of 1 to 10 MHz) of the clutter return signal was recorded, as well as its amplitude. Clutter may be regarded as partially correlated noise in which the degree of correlation depends on the type of clutter. Pulse-by-pulse coherent integration can increase clutter-to-noise ratios; however, care must be taken not to integrate beyond a correlation period in the clutter, or the quasi-noiselike clutter returns will also be unintentionally reduced. These matters concerning Phase One data reduction are discussed, and examples are given in Appendix 3.C.

3.2 Multifrequency Clutter Measurements

Chapter 2 discusses how, at X-band, variations in clutter amplitude statistics with land cover (for example, between forest and farmland terrains of similar relief and observed at similar viewing angles) are not extreme, and how good modeling headway can be made by combining them as rural/low-relief terrain. Chapter 3 shows that as frequency decreases from X-band to VHF, mean clutter strengths of forested terrain viewed at high angle for surface-sited radar strongly increase; whereas mean clutter strengths of level farmland terrain viewed at grazing incidence strongly decrease. As a result, forested terrain provides

mean clutter strengths at VHF 10 or 15 dB stronger than in the microwave bands; whereas farmland terrain provides mean clutter strengths at VHF 20 or 30 dB weaker than in the microwave bands.

Plots showing mean clutter strength vs frequency at seven different Phase One sites are shown in Figures 3.2 through 3.8. Each plot shows results across the 20-element Phase One parameter matrix (five frequencies, two polarizations, two pulse lengths) based on repeat sector measurements. It is evident in this set of site-specific plots that the frequency dependence of ground clutter is highly variable. Included among this set of plots are forest results (e.g., from Blue Knob, Figure 3.3) and farmland results (e.g., from Corinne, Figure 3.7), as well as results for mountains, rangeland, and wetland. Chapter 3 expands upon and explains these and other variations of mean clutter strength with frequency.

3.2.1 Equipment and Schedule

The Phase One radar [1] was a computer-controlled five-frequency instrumentation radar (see Appendix 3.A). The instrument had uncoded, pulsed waveforms with two pulse lengths available in each band to provide high and low range resolution. Polarization was selectable as vertical or horizontal with transmit and receive antennas always copolarized (the cross-polarized component in the radar return signal could not be received). The Phase One system activated one combination of frequency, polarization, and pulse length at a time for any particular clutter experiment. These three major radar parameters as well as other parameters (e.g., spatial extent in range and azimuth, number of pulses, pulse repetition rate, etc.) were selectable at the onboard computer console for each clutter experiment recorded. The Phase One measurement program consisted of setting up and acquiring clutter measurement data 49 times at 42 different sites [1] (see Appendix 3.A).

3.2.2 Data Collection

Phase One clutter measurement data were collected within three different kinds of experiments, namely, survey experiments, repeat sector experiments, and long-time-dwell experiments. The spatially comprehensive survey data are discussed in Section 3.2.2.1. The more in-depth repeat sector data are discussed in Section 3.2.2.2. Chapters 4 and 6 discuss temporal and spectral characteristics of ground clutter returns based on the long-time-dwell experiments [2]. See Appendix 3.A for more detailed information on all three major types of Phase One experiment.

3.2.2.1 360-Degree Survey Data

One important aspect in Phase One data collection was to record in survey mode all of the discernible clutter within the field-of-view through 360° in azimuth and to 25 or 50 km or more in range. These survey data provide a comprehensive spatial database upon which to base accurate clutter modeling information (see Chapter 5). Figure 3.9 shows ground clutter maps measured in survey mode at all five Phase One frequencies at Gull Lake West in Manitoba. These maps are at high range resolution and horizontal polarization. They are thresholded such that cells in which clutter strength $\sigma°F^4$ is greater than or equal to –35 dB are shown as black. Maximum range in these maps is 15 km. North is zenith. As discussed in Chapter 2 (Section 2.3.3.1), at Gull Lake West the Phase One site is on a 100-ft-high ridge running north-south. This ridge provides good visibility to the west and southwest down onto level composite terrain. The shoreline of Lake Winnipeg is observable in the northwest quadrant with some lake clutter evident at X-band. The X-band Phase One clutter map in

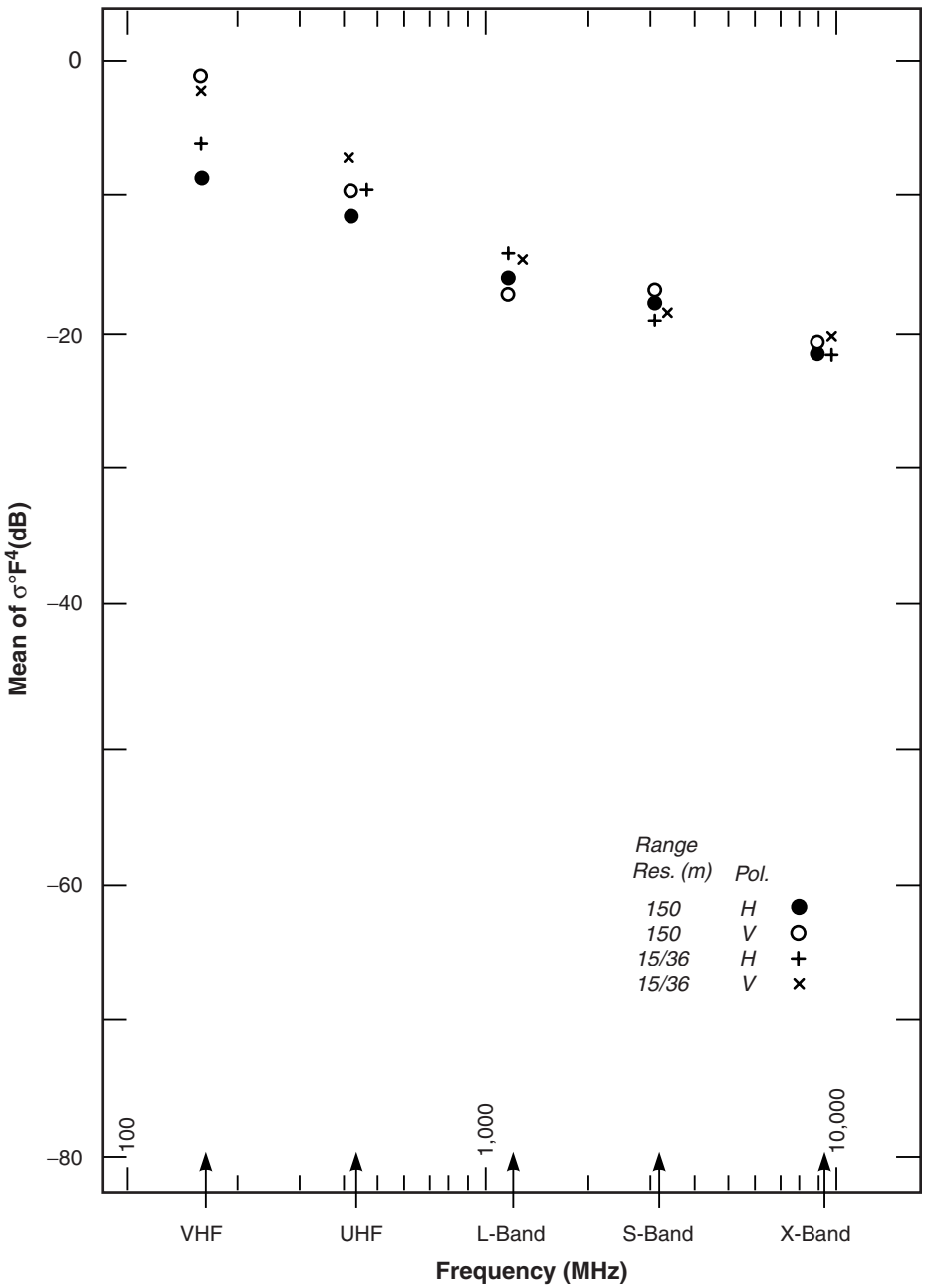

FIGURE 3.2 Mean clutter strength vs frequency at Waterton. For the Waterton repeat sector, depression angle = –1.8 deg, landform = 8-7, land cover = 42-7-41, range = 9 to 14.9 km, azimuth = 175 to 185 deg.

Figure 3.9 obtained with a 100-ft antenna mast may be compared with the Phase Zero Gull Lake West clutter map of Figure 2.7 which was obtained with a 50-ft antenna mast.

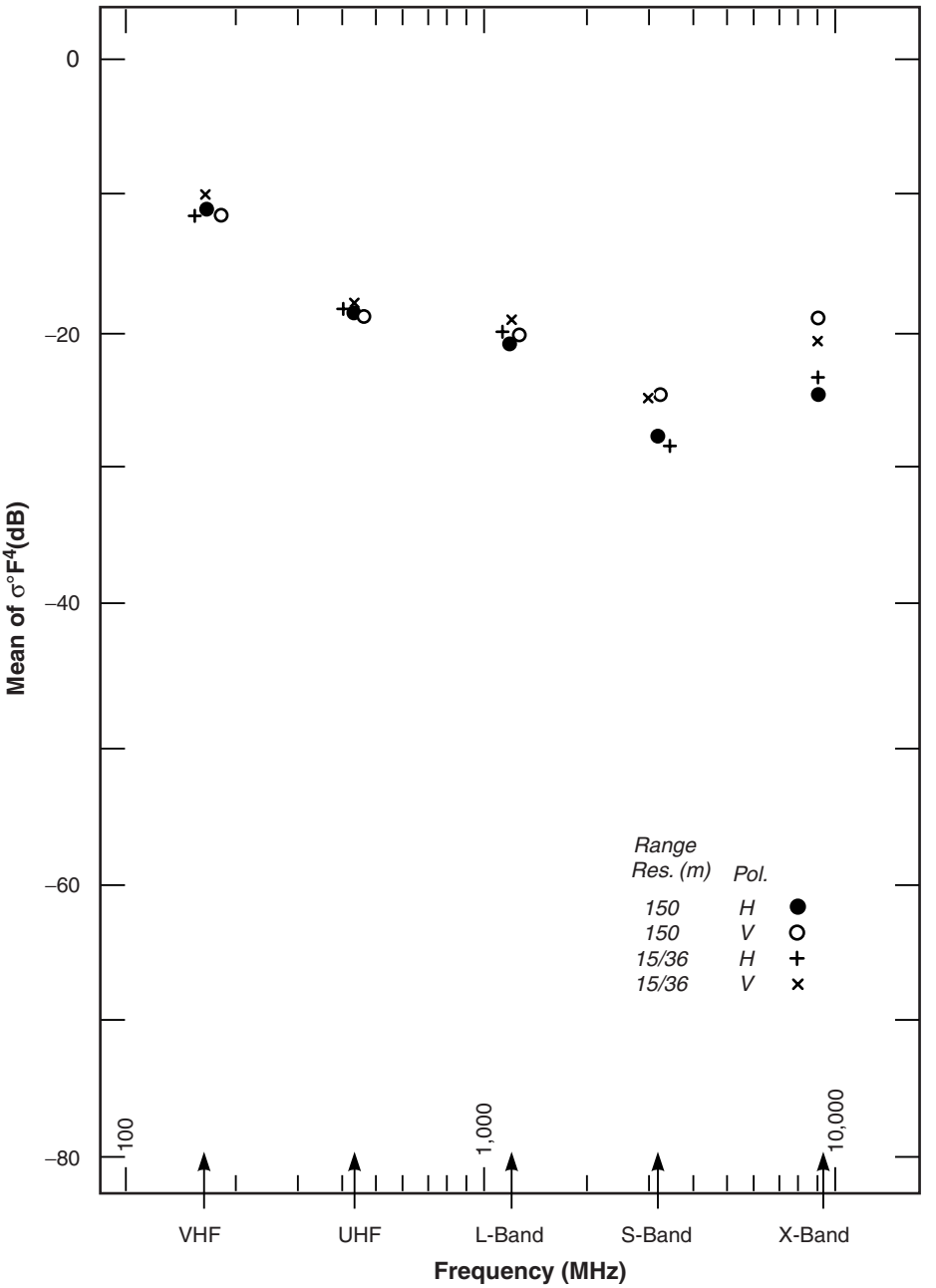

FIGURE 3.3 Mean clutter strength vs frequency at Blue Knob. For the Blue Knob repeat sector, depression angle = 1.6 deg, landform = 4, land cover = 21-43-11, range = 16 to 21.9 km, azimuth = 80 to 100 deg.

The first and most obvious thing to notice in the clutter maps of Figure 3.9 is that, as patterns of spatial occurrence of ground clutter, in overall measure they are quite similar. The reason for this similarity is that the relatively significant or strong clutter being shown comes from visible terrain. Such patterns of spatial occurrence of ground clutter can be

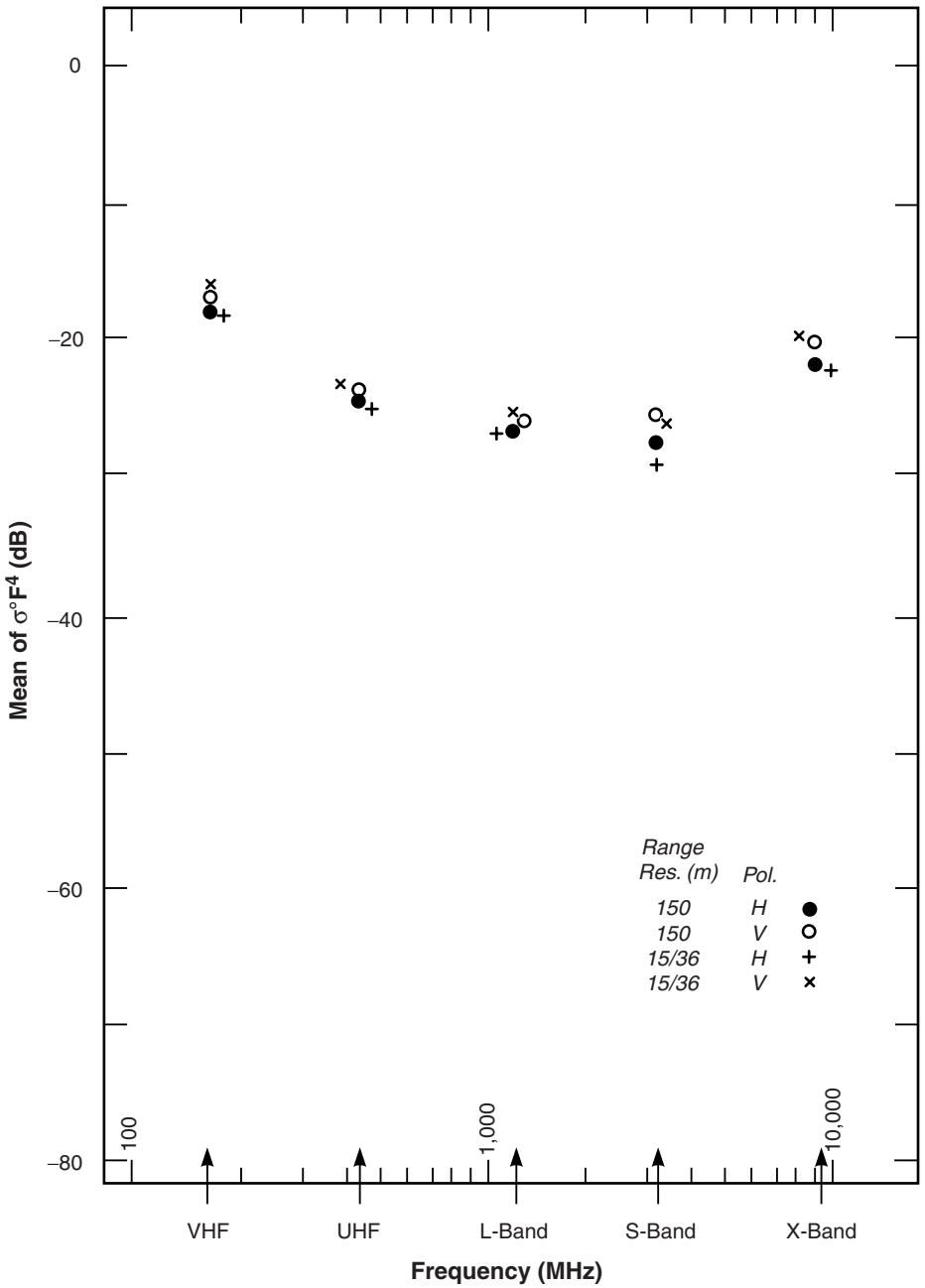

FIGURE 3.4 Mean clutter strength vs frequency at Wachusett Mountain. For the Wachusett Mountain repeat sector, depression angle = 2.1 deg, landform = 5-4, land cover = 43-21-11, range = 8 to 13.9 km, azimuth = 156 to 176 deg.

approximately and deterministically predicted at a given site simply as geometric visibility using available digitized terrain elevation data (DTED).

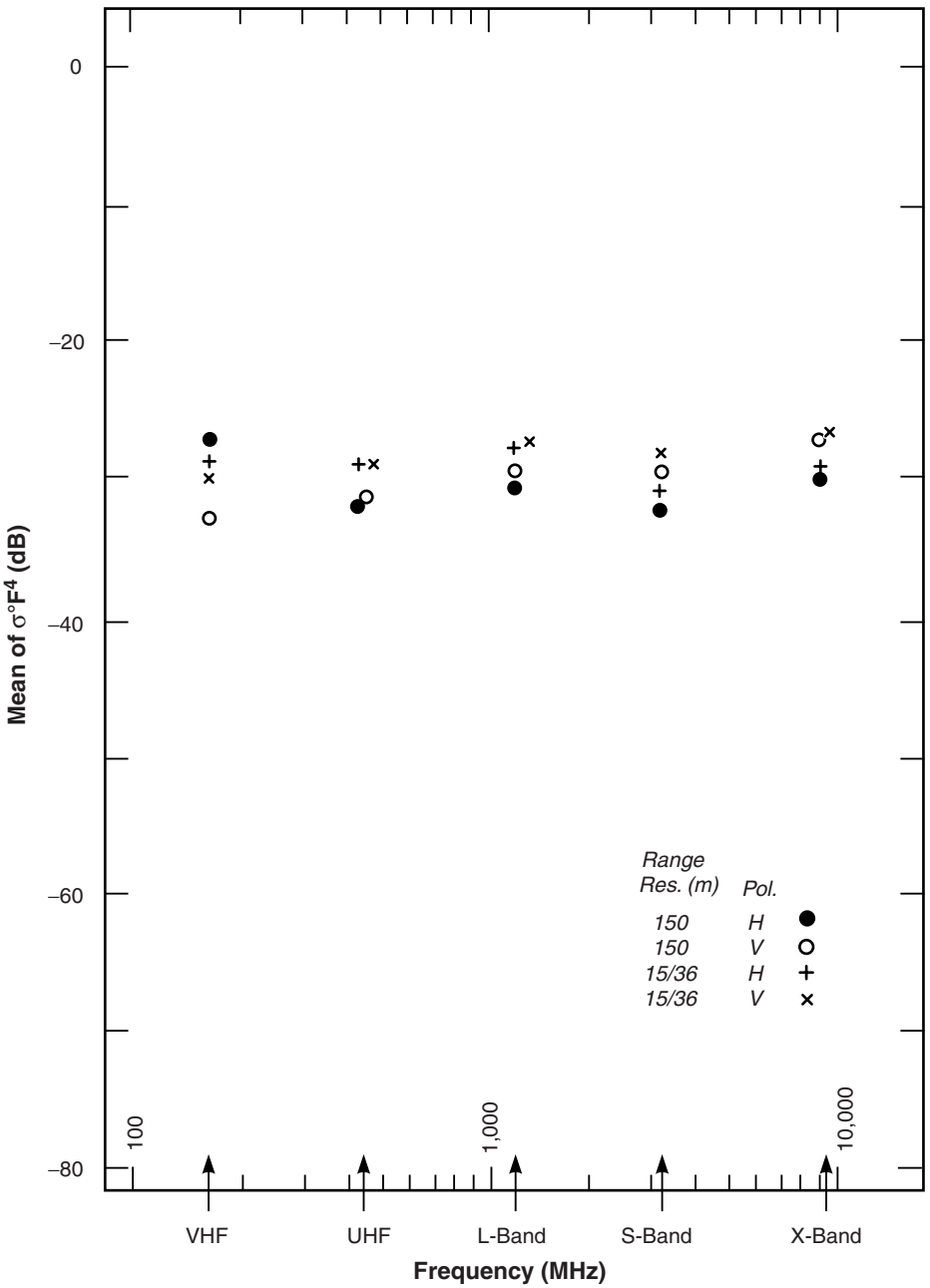

FIGURE 3.5 Mean clutter strength vs frequency at Wainwright. For the Wainwright repeat sector, depression angle = 0.6 deg, landform = 5-3, land cover = 41-32-31, range = 1 to 6.9 km, azimuth = 120 to 150 deg.

The second thing to notice in the clutter maps of Figure 3.9 is the patchy, granular, on-again, off-again nature of the clutter. That is, clutter comes from discrete sources distributed over geometrically visible surfaces and separated by microshadowed cells where the radar is often at its noise floor. As a result, depression angle is of fundamental

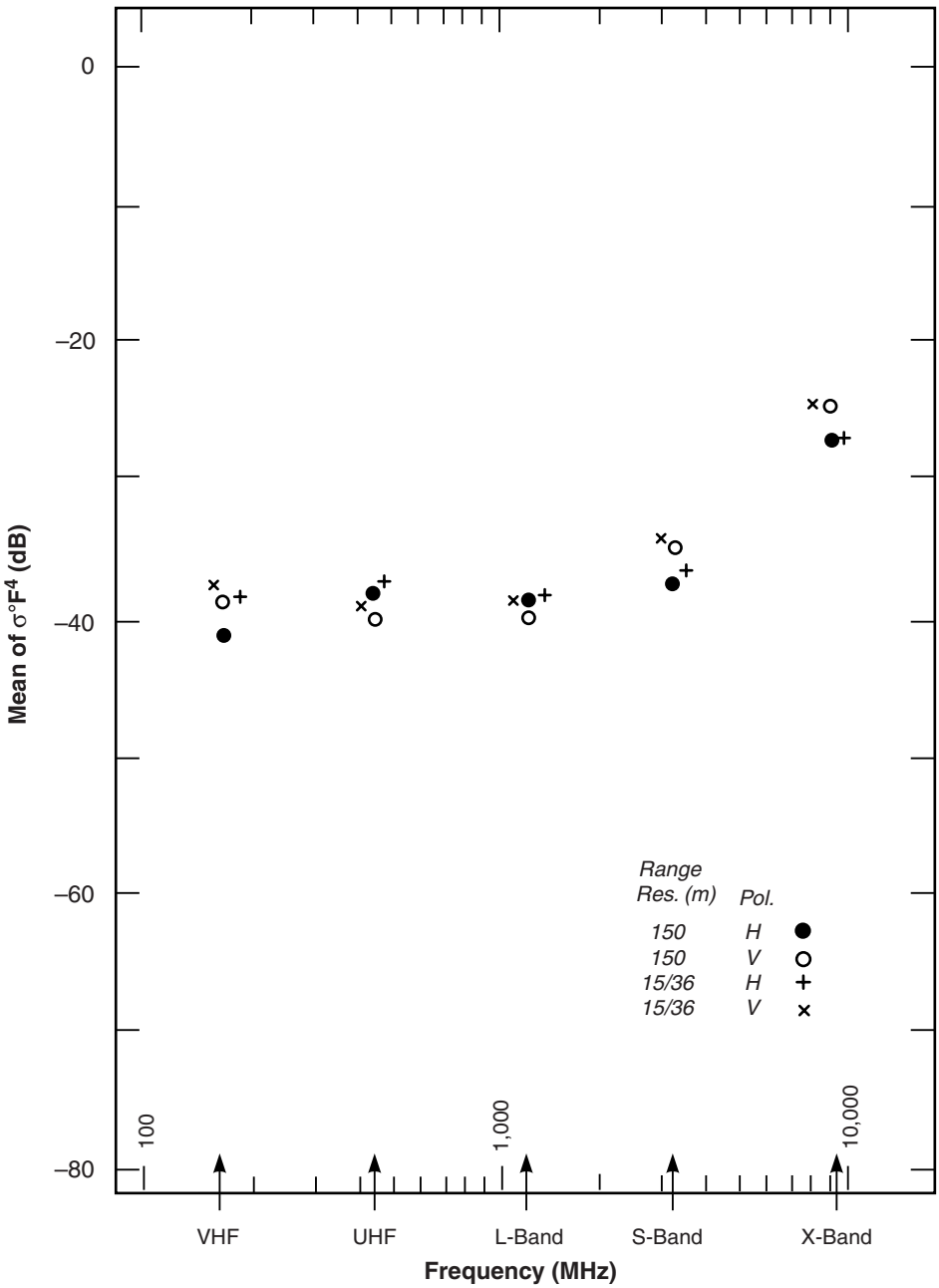

FIGURE 3.6 Mean clutter strength vs frequency at Vananda East. For the Vananda East repeat sector, depression angle = 1.0 deg, landform = 3-5, land cover = 31-32, range = 3.6 to 9.5 km, azimuth = 40 to 60 deg.

parametric importance in clutter modeling investigations because of its influence on shadowing in a sea of patchy visibility and discrete scattering sources. First discussed in the Phase Zero data of Chapter 2, depression angle continues to be of principal influence in the multifrequency measurements of Chapter 3, where mean strengths of clutter amplitude

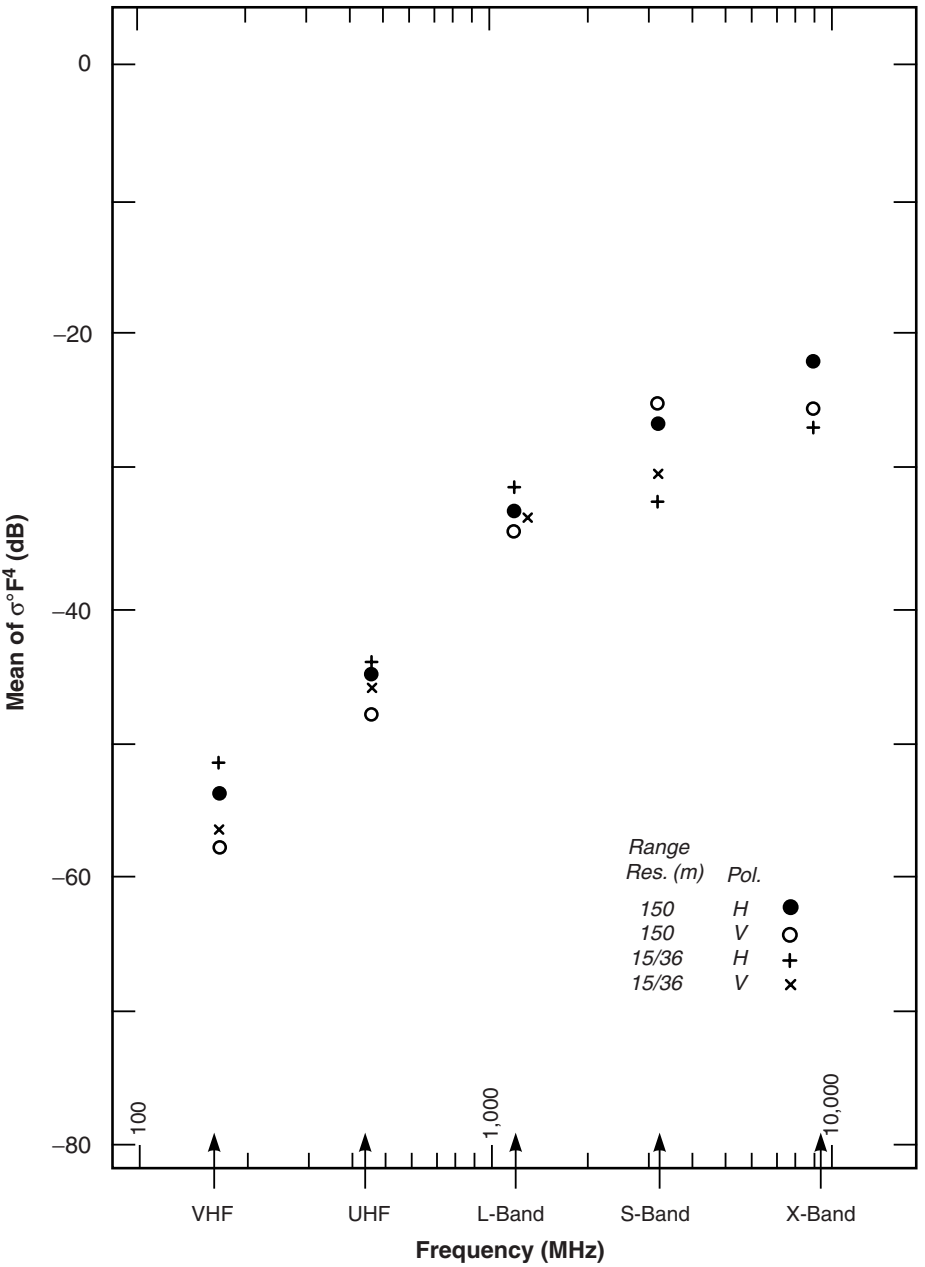

FIGURE 3.7 Mean clutter strength vs frequency at Corinne. For the Corinne repeat sector, depression angle = 0.15 deg, landform = 1, land cover = 21, range = 1 to 8.9 km, azimuth = 330 to 30 deg.

distributions increase, and cell-to-cell variations in these distributions decrease with increasing angle.

The final thing to notice in the clutter maps of Figure 3.9 is the effect of increasing azimuth beamwidth with decreasing frequency (see Table 3.A.2) to smear out the clutter. This illustrates that the role of spatial resolution of the radar is important as it influences spreads

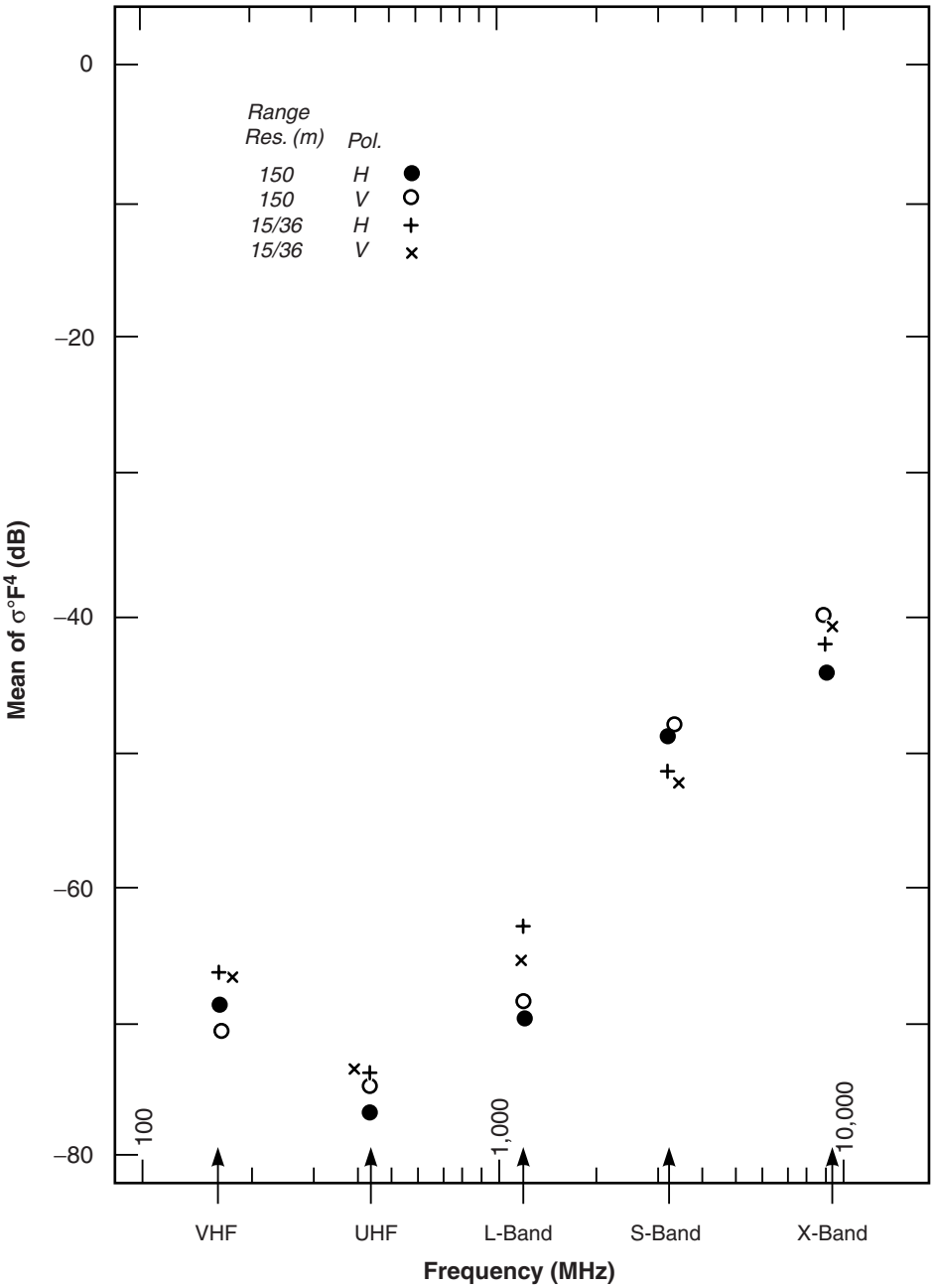

FIGURE 3.8 Mean clutter strength vs frequency at Big Grass Marsh. For the Big Grass Marsh repeat sector, depression angle = 0.2 deg, landform = 1, land cover = 62-22, range = 1 to 6.9 km, azimuth = 350 to 10 deg.

in clutter amplitude distributions. The multifrequency clutter models developed in Chapters 4 and 5 directly implement this important dependency. Chapter 3 documents spreads in measured repeat sector clutter spatial amplitude distributions as ratios of standard deviation-to-mean and ratios of various percentile levels in these distributions. Beyond this,

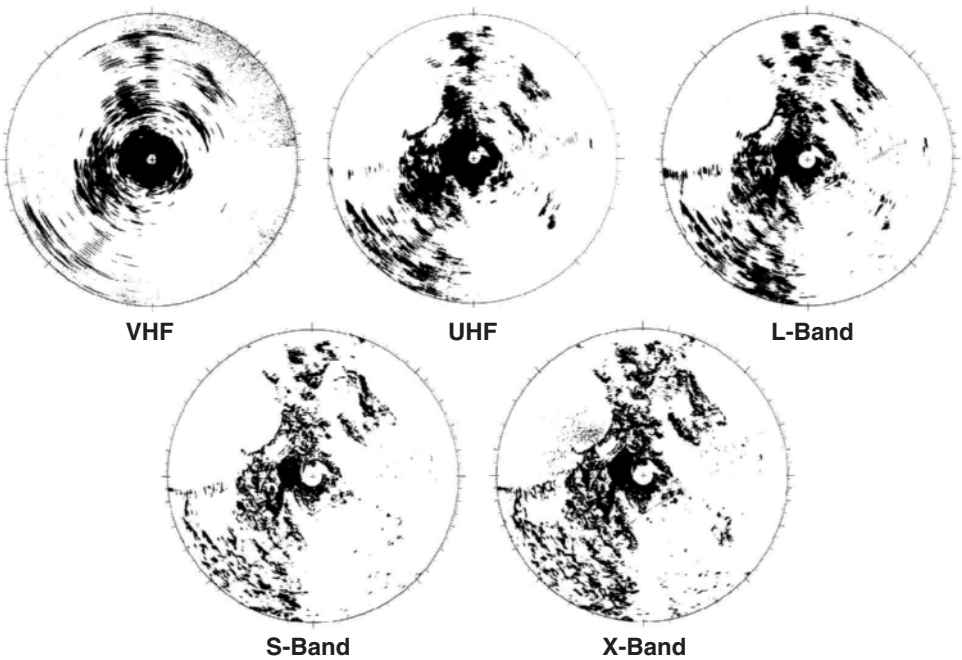

Figure 3.9 Measured multifrequency ground clutter maps at Gull Lake West, Manitoba. Phase One data, 15-km maximum range, $\sigma°F^4 \geq -35$ dB.

however, the primary emphasis in Chapter 3 is to comprehensively discuss and document the important trends observed in mean strength vs frequency, not spreads vs resolution.

3.2.2.2 Repeat Sector Data

One limitation in the Phase One survey data is that, due to limitations in acquisition time and data volume, a long time record could not be established for each spatial clutter cell that was measured in this mode. In much of the survey data, only about 125 pulses were recorded from each cell for each of the 20 data acquisition experiments in the 20-element radar parameter matrix (five frequencies, two polarizations, two pulse lengths). To help overcome this limitation, a second mode of data acquisition was established whereby, at each Phase One site, a series of ground clutter measurements was repeatedly conducted over a specially selected narrow azimuth sector. In total these measurements are referred to as repeat sector measurements. In each repeat sector measurement, many more pulses (e.g., 1,024) per spatial cell were recorded than were recorded in the survey data, and, in addition, each measurement in the repeat sector was repeated a number of times (often four) for each set of radar parameters during the Phase One stay at each site.

The approximately 80 repeat sector measurements at each site (four repeated measurements for each combination of parameters in the 20-element Phase One radar parameter matrix) also encompassed variations of other underlying parameters, such as data rate of recording, pulse repetition frequency, number of pulses recorded, scan and step antenna modes, fixed and variable radio frequency (RF) attenuation schedules, and, occasionally, different antenna mast heights. The objectives in collecting the repeat sector

data were (1) to allow an assessment of quality of data to be made based on comparison of similar measurements, (2) to provide a database with substantially more depth in terms of parameter variations than the mainline survey measurements, and (3) to allow determination of day-to-day temporal clutter variations caused by weather and other natural and cultural processes of change occurring on the landscape.

The analyses of Phase One measurements in Chapter 3 give special attention to the repeat sector measurements. These data provide a manageable subset of the overall data acquired at each site. Descriptions of the terrain within the various repeat sectors are subsequently provided in Table 3.3. Across all repeat sectors, the median azimuth extent is 20°, the median start range is 4 km, the median range extent is 6 km, and the median area is 12 km^2 (compare with the 5.3-km^2 median patch size of the 2,177 patches lying between 2- and 12-km range that constitute the Phase Zero database of Chapter 2). Altogether, 4,465 measurements of pulse-by-pulse clutter backscatter from repeat sector spatial macroregions were obtained in the 49 setups of the Phase One equipment.

Gull Lake West. Repeat sector data are now shown in several formats at Gull Lake West. This discussion continues the Phase Zero Gull Lake West discussion in Chapter 2. Figure 3.10 shows an expanded X-band PPI clutter map at Gull Lake West at a reduced maximum range of 7 km in which the spatial nature of the clutter is apparent. This clutter map shows spatial correlation and texture, both man-made and natural (i.e., clutter does not occur as random salt and pepper). The boundaries of the repeat sector are shown overlaid in Figure 3.10 with heavy black lines. The Phase One antenna looked into this repeat sector from a 100-ft-high ridge, initially over level forested wetland to 3.5-km range, then across a swampy open pond area from 3.5 to 5 km, then to a higher sand dune area along the shoreline of Lake Winnipeg between 5 and 6 km, and then to the open water of Lake Winnipeg.

Figure 3.11 shows mean clutter strength vs range through the Gull Lake West repeat sector at all five Phase One frequencies. These data are shown as range gate-by-range gate sector displays, averaged over the 20°-azimuth sector in each range gate. A comparable Phase Zero sector display at Gull Lake West is shown in Figure 2.10. These Gull Lake West sector displays in Figure 3.11 depict not only the varying spatial nature of the clutter, as does the PPI clutter map, but also the extreme variation in mean clutter strength (40 dB in Figure 3.11) that can occur in a given repeat sector. As is indicated in Figure 3.11, the Phase One radar visited Gull Lake West twice, in winter (February) and late spring (May), as one of six seasonally revisited sites. Discussions of diurnal and seasonal changes in clutter, begun in Chapter 2, Section 2.4.6, continue in Chapter 3, particularly in Section 3.7.

Multifrequency mean clutter strengths over the Gull Lake West repeat sector are shown in Figure 3.12. Results from both winter and spring visits are included. At first consideration, these results seem relatively scattered and trendless. They do not show a strong, clear-cut dependence of mean strength with frequency, except that the S-band data are lower. In terms of seasonal variations in mean clutter strength between winter (snow and ice, deciduous foliage off trees) and spring (no snow or ice, deciduous foliage beginning to emerge), the spring results in Figure 3.12 tend to be a few decibels stronger than winter results, although with considerable overlap within bands except at X-band where a more clear-cut 5-dB seasonal difference is indicated.

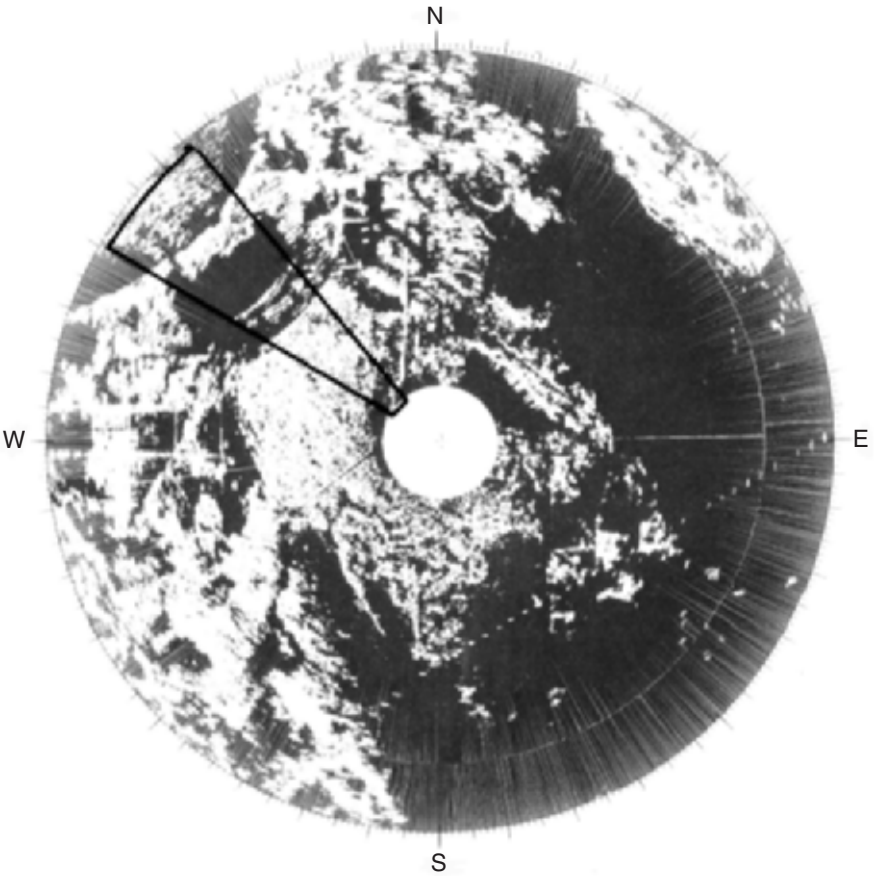

Figure 3.10 PPI clutter map and repeat sector at Gull Lake West. Repeat sector is outlined in black. Max range = 7 km; X-band, 15-m pulse, horizontal polarization; cells with $\sigma\,°F^4 \geq -40$ dB are white. Second visit (May).

It is difficult to know how to generalize from the mean clutter strength results of Figure 3.12. Isolated single-point measurements or even multipoint measurements at a single site are not easily extrapolable to other sites. A solution to this dilemma and the main thrust of Chapter 3 is to obtain results like those of Figure 3.12 at many sites, to combine them within similar terrain categories, to separate them between different terrain categories, and by this means to provide the missing connecting tissue between dissimilar single-point results that leads to generality and predictability. Thus, Chapter 3 provides results like Figure 3.12 for repeat sectors at all the measurement sites and looks for important similarities among them and differences between them.

3.2.3 Terrain Description

Any attempt to investigate and predict ground clutter can only be as successful as its terrain description methodology permits. As an indication of the variability of terrain, Figures 3.13(a) and (b) show terrain elevation profiles and masking in five Phase One repeat sectors [Figure 3.13(a) utilizes an adaptive ordinate that varies from site to site;

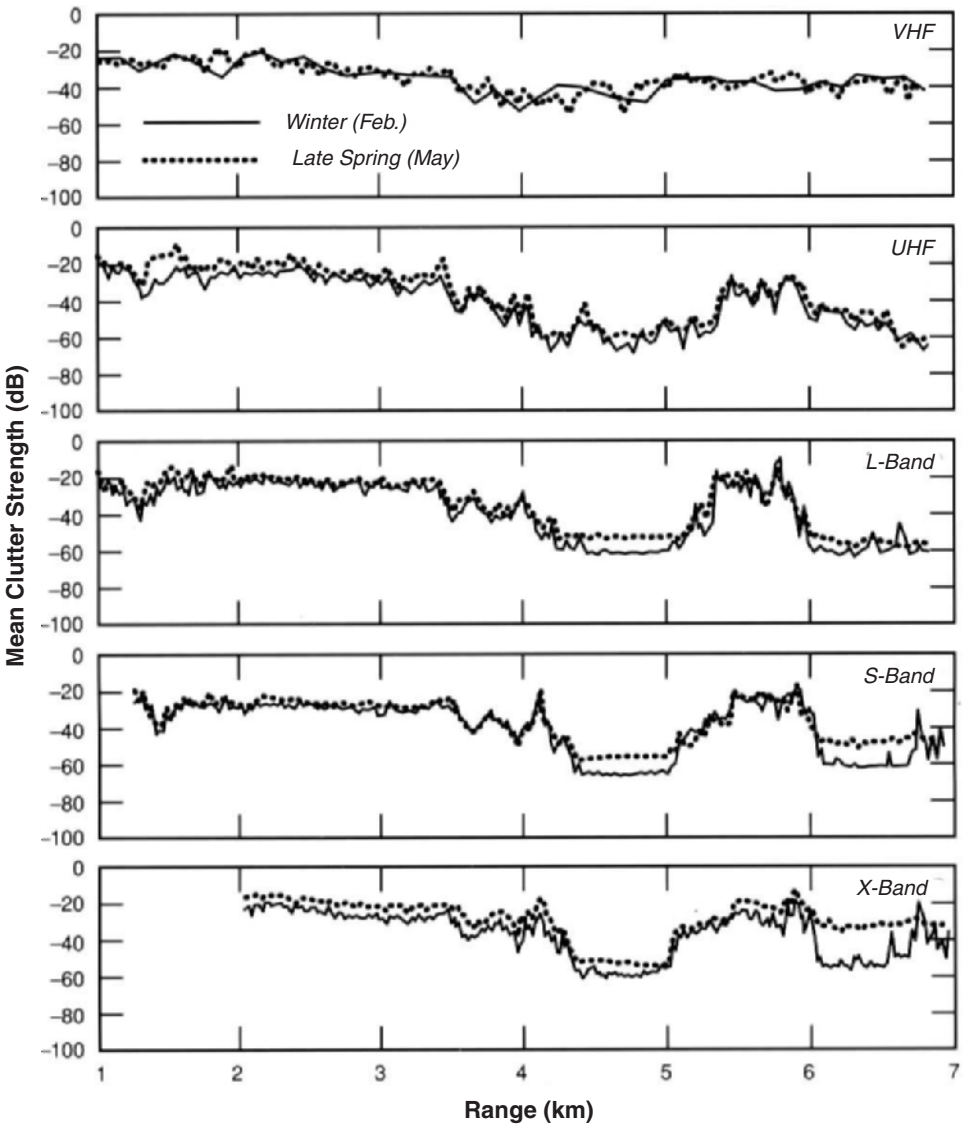

FIGURE 3.11 Seasonal variation in mean clutter strength vs range for five frequency bands at Gull Lake West, Manitoba. Repeat sector data; level forest and forested wetland with lake edges; winter visit in February (solid lines), spring visit in May (dotted lines); vertical polarization, high range resolution data, except VHF winter visit where low range resolution data are shown.

Figure 3.13(b) utilizes a common ordinate; the indicated elevations include the sphericity of a 4/3 radius spherical earth to account for standard atmospheric refraction]. These profiles indicate that terrain visibility and hence clutter is patchy at low angles. Visibility is shown at two antenna heights, 50 ft in Figure 3.13(a) and 100 ft in Figure 3.13(b); these results indicate that visibility is usually not very sensitive to antenna height (see Appendix 4.B). The terrain elevation data of Figures 3.13(a) and (b) were obtained manually from 1:50,000 scale topographic maps.

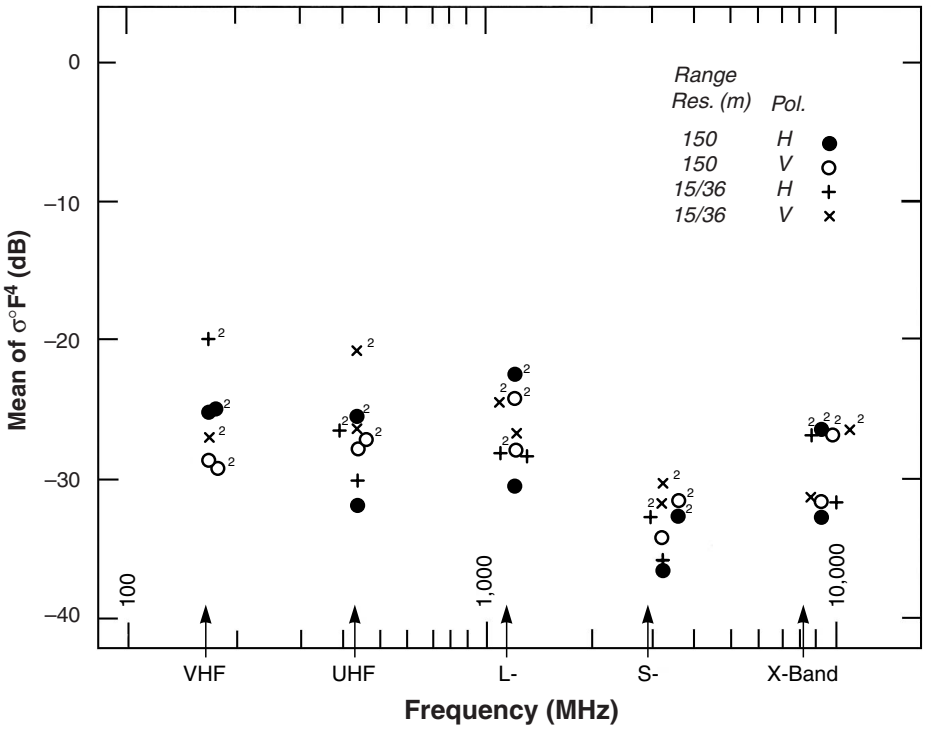

FIGURE 3.12 Mean clutter strength vs frequency at Gull Lake West. Repeat sector data. Two seasonal visits, February (winter) and May (spring). Data from the May visit are indicated with superscript 2's to the upper-right of the plot symbol.

Figures 3.13(a) and (b) illustrate that there is a large range of variation in Phase One site heights. Table 3.1 tabulates Phase One site height above repeat sector midpoint elevation for the 42 Phase One sites, in decreasing order by site height. It is observed that site height varies from 4,021 ft at Plateau Mountain to –1,250 ft at Waterton. Site height strongly affects clutter statistics in that high sites see clutter at higher depression angles and to longer ranges than low sites

The terrain in each repeat sector is classified both in terms of its land cover characteristics and in terms of its land-surface form. The classes of land cover and landform are the same as used in Chapter 2 (see Tables 2.1 and 2.2). Although nine specific landform classes are employed, they are separated into two overview classes; namely, high-relief with terrain slopes > 2° and relief > 100 ft, and low-relief with slopes < 2° and relief < 100 ft (see Table 2.3). As in Chapter 2, repeat sector terrain classification was performed principally through use of stereo air photos and topographic maps. Preexisting available stereo air photos were at 1:50,000 scale. As part of coordinated Phase One studies that took place in Canada in which an emphasis was on a more fine-grained approach to analyzing the data, special aerial photography missions were commissioned and flown over many repeat sectors to provide more accurate color infrared stereo air photographs of repeat sector terrain at 1:10,000 scale. The repeat sectors are large, ranging in area from 4 km^2 (Puskwaskau) to 105 km^2 [Plateau Mountain (a)]. Over such areas, terrain is usually to some extent composite, heterogeneous, or nonuniform. Thus, a single classifier either for land cover or

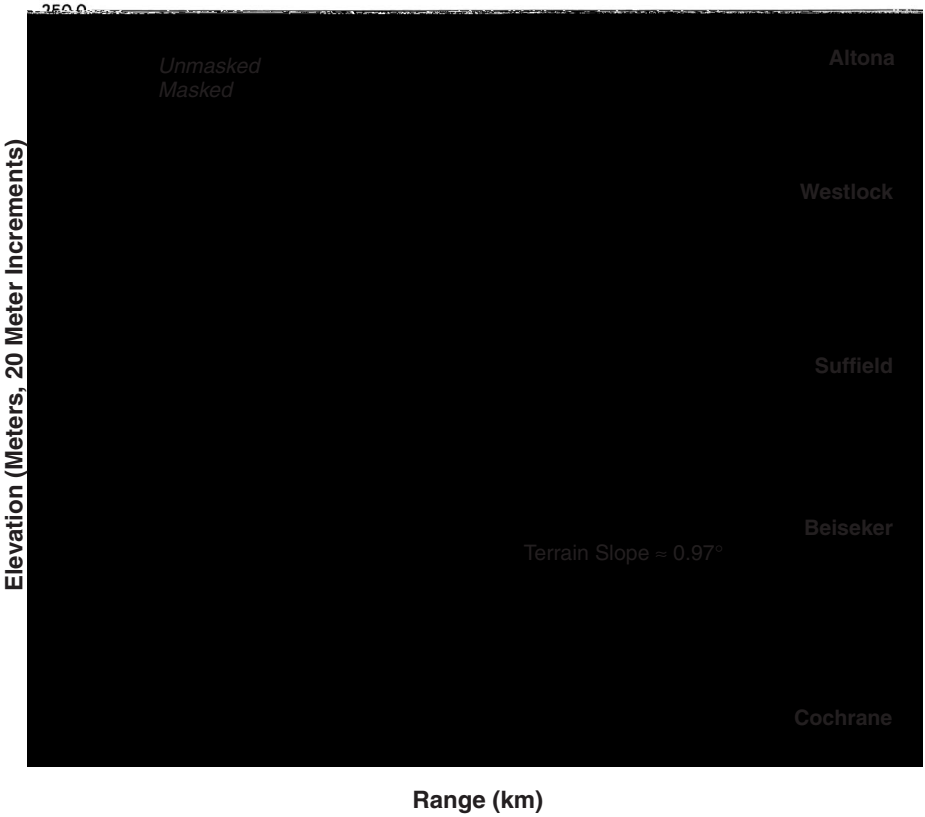

FIGURE 3.13(A) Terrain elevations and masking in five Phase One repeat sectors. Antenna mast height = 50 ft; adaptive ordinate. Data from 1:50,000 scale topographic maps.

landform is usually not sufficient to completely describe the terrain. Usually more than one classifier is used, arranged in order of decreasing percent area of occurrence within the repeat sector. See Table 3.3 for terrain classifications of all repeat sectors.

Additional ground truth information was collected during Phase One data acquisition. To keep track of wind, weather, and seasonal conditions during the measurements, a ground truth file consisting of 60 parameters was written to the raw clutter data tapes in front of each clutter experiment recorded. Weather stations were maintained on site and in the repeat sector to provide information for this file. TV video was recorded in a 360° azimuth scan from an antenna-boresighted TV camera atop the tower. At each site many field photographs were taken of the terrain being measured, where the photography position and direction were keyed to points on maps. The photographs collected included a 360° pan from the top of the Phase One tower. Such terrain descriptive detail can be overwhelming. The approach in Chapter 3 is to funnel all such information down to key macroclassifiers that cause the clutter statistics to cluster within class and separate between classes.

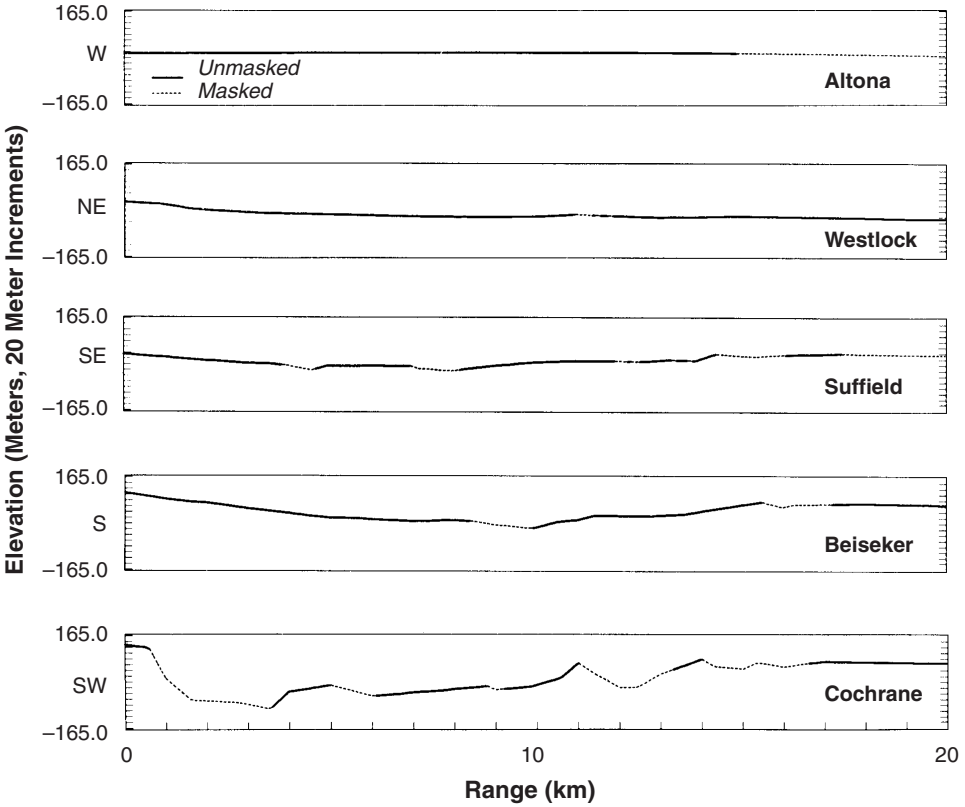

FIGURE 3.13(B) Terrain elevations and masking in five Phase One repeat sectors. Antenna mast height = 100 ft; common ordinate. Data from 1:50,000 scale topographic maps.

3.3 FUNDAMENTAL EFFECTS IN LOW-ANGLE CLUTTER

Section 3.3 reviews the basic mechanisms at work in low-angle ground clutter. The causes of major parametric trends in the Phase One repeat sector results as radar frequency ranges from VHF to X-band are established. Multifrequency examples of measured clutter at forest and farmland sites are provided to illustrate the mechanisms under discussion.

3.3.1 CLUTTER PHYSICS II

The major elements that are involved in low-angle clutter were first discussed in Chapter 2. These are shown again in Figure 3.14. Attention here is focused on Phase One repeat sector patches as the large regions of visible terrain providing directly illuminated clutter. Within the repeat sector patches, as in the Phase Zero patches of Chapter 2, the clutter sources continue to be all the discrete vertical features on the landscape associated with either the land cover or the terrain itself. As a result, the Phase Zero X-band effects of angle of illumination continue to exist at all the Phase One frequencies such that mean clutter strengths measured over repeat sectors increase, and cell-to-cell fluctuations decrease, with increasing angle.

TABLE 3.1 Phase One Site Heights

Site	Site Height above Repeat Sector (ft)	Site	Site Height above Repeat Sector (ft)
Plateau Mt. (a)	4021	Lethbridge West	105
Blue Knob	1710	Wainwright	102
Booker Mt.	1570	Rosetown Hill	98
Wachusett Mt.	1259	Penhold II	68
Plateau Mt. (b)	921	Spruce Home	63
Polonia	576	Pakowki Lake	50
Scranton	555	Turtle Mountain	49
Cochrane	509	Headingley	38
Strathcona	425	Knolls	25
Brazeau	392	Woking	25
Puskwaskau	382	Shilo	20
Vananda East	342	Sandridge	10
Orion	335	Katahdin Hill	5
Magrath	300	Cold Lake	0
Beiseker	255	Big Grass Marsh	–3
Beulah	214	Corinne	–10
Picture Butte II	210	Dundurn	–12
Wolseley	180	Altona II	–22
Westlock	150	Peace River South II	–150
Gull Lake West	147	Neepawa	–340
Suffield	125	Waterton	–1250

Note: Site elevation minus repeat sector midpoint elevation, in feet. In order of decreasing site height.

Multipath reflections interfere with the direct illumination and cause lobing on the free-space antenna pattern. As shown in Figure 3.14, such lobing can act to significantly increase or decrease the effective gain at which the patch is measured, more so at the lower frequencies (particularly VHF for which the lobes are broad, see Figure 3.14) than at higher frequencies (e.g., X-band, narrow lobes, see Figure 2.5). All propagation effects including multipath are included within the pattern propagation factor F (previously defined—see Chapter 1, Section 1.5.4 and Chapter 2, Section 2.3.1.2). Throughout Chapter 3 clutter strength continues to be given by $\sigma^\circ F^4$, where σ° is the intrinsic clutter coefficient (see Chapter 2, Section 2.3.1.1). How clutter strength is computed in the Phase One data is defined in more detail in Appendix 3.C. Section 3.4 determines general variations of clutter strength $\sigma^\circ F^4$ over and above terrain-specific dispersive influences entering via the pattern propagation factor F. This often requires multiple independent measurements of similar terrain from different sites to find underlying parametric trends. The important, often poorly predictable role of propagation in low-angle clutter can be confusing at first consideration. Appendix 3.B provides further discussion of how to deal with propagation in clutter analysis and modeling.

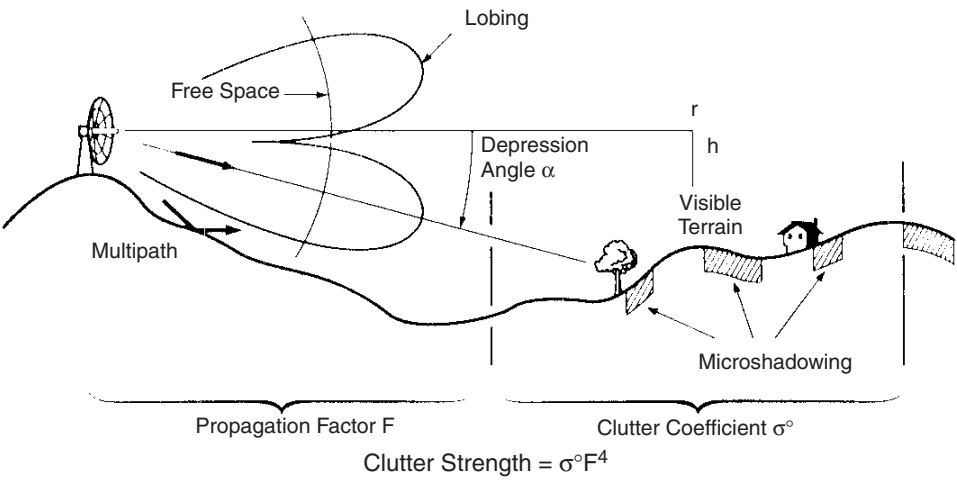

FIGURE 3.14 Clutter physics (VHF).

Within the low-angle clutter phenomenon thus characterized by granularity of sources and specific propagation influences, how are clutter strengths affected by the spatial resolution of the radar? Theoretically, the mean clutter strength from a spatial region such as a repeat sector is independent of the spatial resolution of the measurement radar in situations involving many randomly phased clutter returns per resolution cell (see Section 3.5.3 for details). The theoretical expectation of little dependence of mean strength on resolution is largely borne out in the Phase One results (< 1 dB average variation of mean strength with pulse length, see Section 3.5.3). Although spatial resolution does not usually affect mean clutter strength significantly, because of the heterogeneous nature of low-angle clutter the spatial resolution of the radar plays a fundamental role in the amount of spread in clutter amplitude distributions from large spatial regions (see Chapter 2, Section 2.4.5). Ratios of standard deviation-to-mean for the repeat sectors generally increase both with decreasing pulse length at each Phase One frequency and with decreasing azimuth beamwidth as Phase One radar frequency increases (Tables 3.12, 3.13).

Polarization has very little effect on clutter amplitude statistics. In Section 3.5.2, the distribution of differences of vertically polarized mean clutter strength minus horizontally polarized mean clutter strength across the complete repeat sector database shows a median difference of only 1.5 dB. However, occasional specific measurements can show more significant variation with polarization. For example, repeat sector measurements from both of the steep mountainous sites, Plateau Mountain and Waterton, indicate that at VHF, vertically polarized backscatter can be 7 to 8 dB stronger than horizontally polarized backscatter.

3.3.2 Trends with Radar Frequency

Two strong trends of ground clutter strength with radar carrier frequency occur in particular circumstances. One of these trends is directly the result of the intrinsic backscattering coefficient σ° having an inherent frequency-dependent characteristic. Thus, at high illumination angles in forested terrain, propagation measurements conducted at selected Phase One sites indicate that forward reflections are minimal ($F \approx 1$), and in such terrain σ° is observed to decrease strongly with increasing frequency. This result is due to

the radio frequency (RF) absorption characteristic of forest increasing with frequency, and hence the diffusely radiative characteristic of forest (including the backscatter direction) decreasing with frequency.

The other trend with frequency is the result of a general propagation effect entering clutter strength $\sigma^\circ F^4$ through the pattern propagation factor F. At low depression angles over level open terrain, strong forward reflections cause multipath lobing on the free-space antenna pattern. At low frequencies such as VHF, these lobes tend to be broad for typical antenna heights. As a result, at such low frequencies returns from most clutter sources are received well on the underside of the first multipath lobe, and effective clutter strengths are much reduced. As frequency increases for a given antenna height, from VHF to UHF to L-band, the multipath lobes become narrower, and the first lobe is increasingly squeezed closer to the ground. As a result, the effective gain on the underside of this lobe at which backscatter from clutter sources is received increases, and hence clutter strengths rise with increasing frequency.

Eventually, as frequency increases further to S- and X-band, the multipath lobes become still narrower, and typical clutter sources such as buildings or trees tend to subtend multiple lobes. The result is that at higher frequencies the overall multipath effect on illumination tends to average out and have less dominating influence on the effective clutter strength. Thus, at low angles on level open terrain, a strongly increasing characteristic of mean clutter strength with frequency introduced through the propagation factor is observed. Because this characteristic is caused by the interference between the direct ray and the multipath ray, it depends on geometric factors such as antenna mast height and range to the clutter patch (see Appendix 3.B). In inclined or rolling open terrain of increased relief, multipath is as likely to reinforce as to cancel clutter returns even at low frequencies.

3.3.2.1 Measurement Examples

The frequency dependencies of ground clutter in steep forest and level farmland are now illustrated by measurement example. Results are shown first based on forest data from Blue Knob, Pennsylvania, and on farmland data from Corinne, Saskatchewan. Figures 3.15 and 3.16 show measured ground clutter from Blue Knob and Corinne at X-band and VHF, respectively. First consider the X-band clutter in Figure 3.15. Although the shapes of the forest and farmland histograms are quite different, the mean strengths in these two histograms are nearly the same: –24 dB in forest and –23 dB in farmland. The differences in histogram shape in Figure 3.15 are accounted for in the clutter models of Chapters 4 and 5 by means of the Weibull shape parameter. Figure 3.15 indicates 8-dB mean-to-median ratio at X-band in steep forest vs 33-dB mean-to-median ratio at X-band in level farmland, this latter large value reflecting the extreme spread evident in the farmland histogram.

Now consider the VHF clutter from Blue Knob and Corinne, as shown in Figure 3.16. In the steep forest histogram from Blue Knob, mean clutter strength at VHF has increased by 13 dB from its X-band value to –11 dB; whereas, in the level farmland histogram from Corinne, mean clutter strength at VHF has decreased by 32 dB from its X-band value to –55 dB. In both VHF histograms in Figure 3.16, the mean-to-median ratios indicating spread in the histograms have decreased considerably, from an X-band value of 8 dB to a VHF value of 4 dB in forest and from an X-band value of 33 dB to a VHF value of 15 dB in farmland. This decreased spread is the result of the decreased spatial resolution of the Phase One radar at VHF due to its increased azimuth beamwidth (13° at VHF vs 1° at X-band).

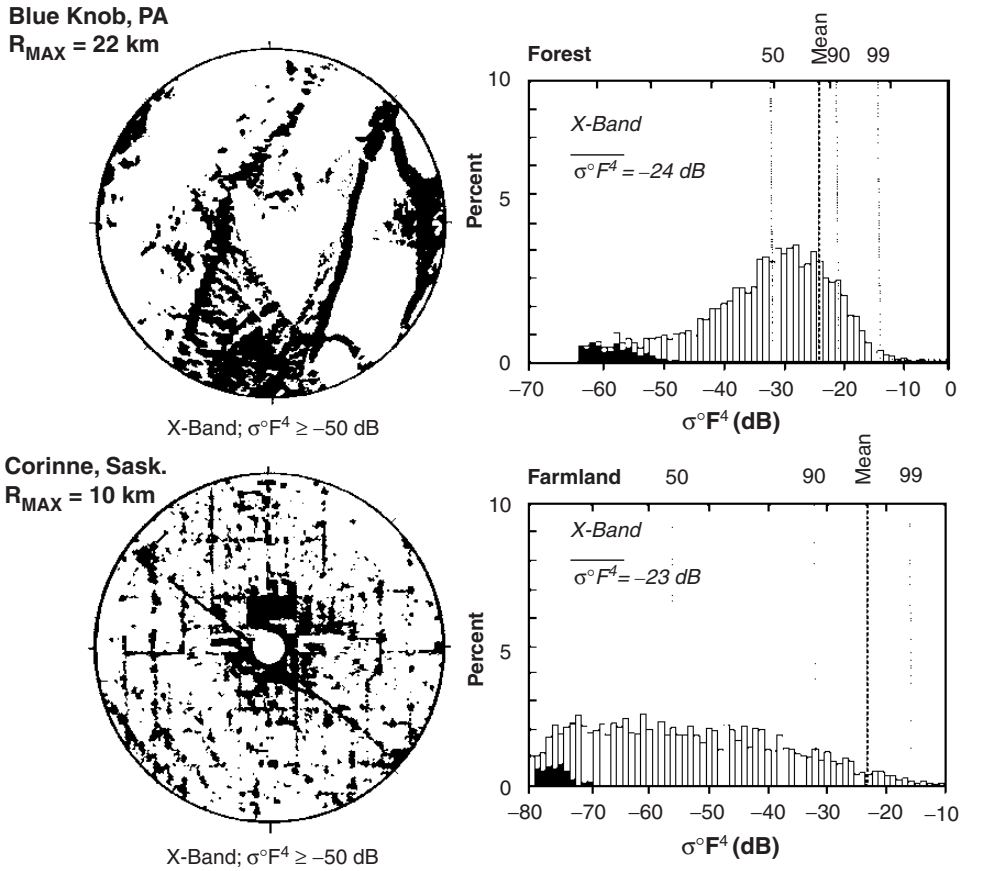

FIGURE 3.15 X-band ground clutter in steep forest and level farmland. Histograms show repeat sector data. In the PPI clutter maps, cells with $\sigma\,°F^4 \geq -50$ dB are shown as black.

Additional forest (Scranton) and farmland (Corinne) histograms are shown in Figure 3.17 for all five Phase One frequency bands. It is evident in these results that the effects of increasing frequency on mean clutter strength and spread for these two terrain types take place continuously across the frequency regime from VHF to X-band. Table 3.2 shows means and ratios of standard deviation-to-mean for the histograms of Figure 3.17. It is clear from Table 3.2 that in steep forest, mean clutter strengths decrease strongly with increasing frequency; whereas, in level farmland, mean clutter strengths increase strongly with increasing frequency. Table 3.2 also shows that spreads (i.e., ratios of standard deviation-to-mean) in clutter amplitude statistics are much greater in level farmland terrain than in steep forest terrain, but that in both terrain types spreads decrease with decreasing spatial resolution as the azimuth beamwidth increases from 1° at X-band to 13° at VHF. Thus there are many influences at work in forested and farmland clutter. These influences include effects of (1) landform—steep vs level, (2) land cover—forest vs farmland, (3) depression angle—at Blue Knob, 1.6°; at Corinne, 0.15°, (4) radar frequency, and (5) spatial resolution.

The set of plots of Figures 3.2–3.8 showing the frequency dependence of ground clutter from repeat sectors at seven different sites include results from Blue Knob (Figure 3.3) and

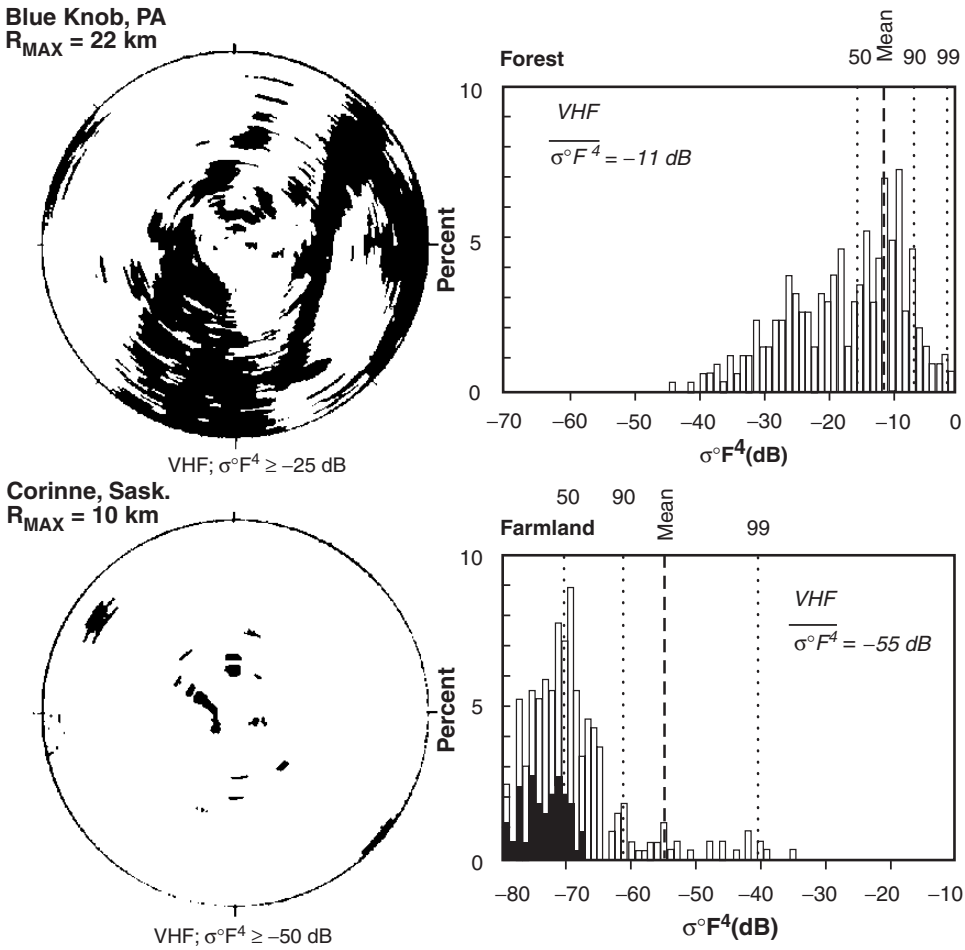

Figure 3.16 VHF ground clutter in steep forest and level farmland. Histograms show repeat sector data. In the PPI clutter maps, cells containing clutter stronger than the indicated threshold are shown as black.

Corinne (Figure 3.7). The data of Figures 3.3 and 3.7 dramatically illustrate that the frequency dependency of mean clutter strength at high angles in steep forest terrain is very different from that at grazing incidence in level farmland terrain. Following sections include dramatic variations in mean clutter strength such as those shown in Figures 3.2–3.8, but within an overall scheme involving finer gradations with terrain type and depression angle so as to provide a continuous matrix of information across all terrain types and measurement scenarios.

3.3.3 Depression Angle and Terrain Slope

As in the X-band data of Chapter 2, depression angle continues to be of major importance in its effects on both strength and spread in the multifrequency low-angle ground clutter spatial amplitude statistics of Chapter 3. Recall that depression angle is rigorously defined to be the complement of incidence angle at the backscattering terrain point under consideration, but that at short ranges depression angle simplifies to be approximately the

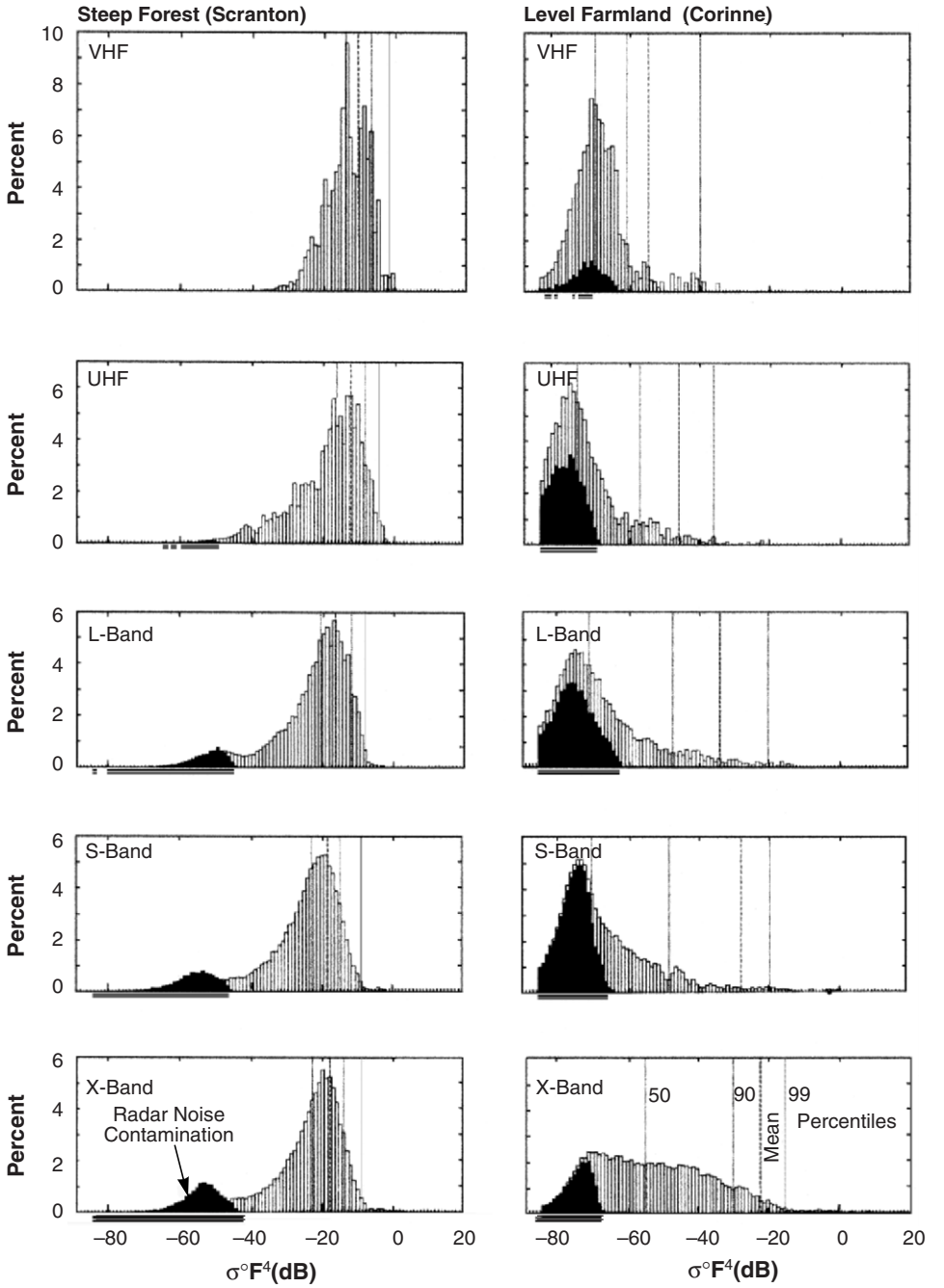

FIGURE 3.17 Five-frequency histograms of clutter strength from steep forest at Scranton, Pennsylvania, and level farmland at Corinne, Saskatchewan. Repeat sector data; 15-m range resolution (36 m at VHF and UHF), vertical polarization at Scranton; 150-m range resolution, horizontal polarization at Corinne. See Table 3.2.

TABLE 3.2 Clutter Strengths for Steep Forest at Scranton and Level Farmland at Corinne

	Mean (dB)	SD/Mean (dB)	Percent of Samples above Noise Floor
Scranton			
VHF	–10.6	1.2	99.8
UHF	–12.3	1.8	99.4
L-Band	–16.7	2.0	92.9
S-Band	–18.5	4.6	89.7
X-Band	–17.9	5.2	86.2
Corinne			
VHF	–54.8	8.1	89.3
UHF	–45.8	11.0	60.8
L-Band	–33.6	10.4	52.8
S-Band	–26.9	12.5	44.6
X-Band	–22.4	13.0	80.9

angle below the horizontal at which the terrain point is viewed from the antenna (see Appendix 2.C). Depression angle includes the effect of earth curvature on the angle of illumination but does not include any effect of the local terrain slope, whereas grazing angle, being the angle between the tangent to the local terrain surface at the backscattering terrain point and the direction of illumination, does take into account local terrain slope. As in Chapter 2, grazing angle is not used in what follows as the measure of angle at which terrain is illuminated because as computed from DTED it does not correlate significantly with clutter returns from terrain cells at the scale of radar resolution. Rather than attempting to assign a single numerical value of terrain slope to each resolution cell, the distribution of terrain slopes contained within each large repeat sector clutter patch is classified in terms of terrain relief (Table 2.2). As in the Phase Zero results, in most terrains much of the statistical significance in the dependency of clutter strength on terrain slope in the Phase One repeat sector results is captured by using just two classes of relief, namely, "high-relief" terrain (terrain slopes > 2°) and "low-relief" terrain (terrain slopes < 2°).

However, the repeat sector results require an important modification to this basic two-class terrain relief descriptive scheme. In low-relief open agricultural terrain supportive of multipath, the general effect of increasing effective clutter strength with increasing frequency requires the terrain to be very level, so that low-frequency clutter returns are always received on the underside of the first multipath lobe. Even relatively low inclinations of terrain at between 1° and 2° of terrain slope are enough to prevent this general illumination effect by directing the multipath lobes more randomly with respect to the clutter sources in the repeat sector. In such terrain, even at low frequencies, clutter returns are received well up on the multipath lobing pattern, not just on the extreme underside of the first lobe, at increased or decreased gain over free space depending on the particular terrain involved. Therefore, in low-relief agricultural terrain, terrain relief is further classified into two subcategories, namely, "moderately low-relief" (terrain slopes that lie between 1° and

2°) and "very low-relief" (terrain slopes < 1°). This refinement in classification is sufficient to distinguish between terrain that is level enough so that multipath results in generally increasing strength of illumination of clutter sources with increasing frequency, and terrain in which multipath effects on illumination are more specific.

3.4 Mean Land Clutter Strength vs Frequency by Terrain Type

Section 3.4 shows how mean land clutter strength varies with radar frequency as measured within Phase One repeat sectors. These results depend on three different categories of descriptive parameter. First, there are parameters descriptive of the radar; namely, frequency, resolution, and polarization. The basic format of data presentation shows mean strength vs frequency across the five Phase One frequency bands for each of four combinations of pulse length and polarization. Second, there are parameters descriptive of the geometry of illumination. Depression angle is the parameter used herein, a quantity relatively simple and unambiguous to determine, depending as it does simply on range and relative elevation difference (Table 3.1) between the radar antenna and the centroid of the repeat sector clutter patch. Third, there are parameters descriptive of the terrain within the repeat sector clutter patch. The terrain within each repeat sector is classified herein both in terms of its land cover (Table 2.1) and its landform (Table 2.2). The terrain classifications were obtained by overlaying and registering measured clutter maps onto stereo aerial photos and topographic maps. All of these parameters have been previously introduced.

Table 3.3 describes the repeat sectors at 38 different Phase One measurement sites in terms of range and azimuth extent from the radar, depression angle, and terrain type by landform and land cover in decreasing order by percent area within the repeat sector clutter patch. It is apparent in Table 3.3 that every repeat sector is different (terrain is essentially infinitely variable). As a result of this variability, the set of 20 multifrequency repeat sector mean clutter strengths is different, at least in detail, for every site. The current objective is to move beyond this abundance of detail to determine useful simple generalizations in the measurement results. The approach taken here to achieve this objective requires the statistical combination of measurements that are reasonably similar within broad classes of terrain type and depression angle, such that the results satisfactorily cluster within each class and significantly separate between different classes.

The repeat sectors in Table 3.3 are grouped within the best such broad classes that were developed in the repeat sector database. Five broadly different terrain classes are defined in Table 3.3, namely, (1) urban, (2) mountains, (3) forest, (4) agricultural, and (5) desert, marsh, or grassland. Except for mountains, these groups are basically distinguished by major land cover type; mountains are distinguished more by landform. Within each class, when terrain relief can vary enough within class to require further subclassification, two subcategories of terrain relief are usually enough, low-relief with terrain slopes < 2°, and high-relief with terrain slopes > 2°. An exception is agricultural terrain, which requires additional subclassification of low-relief terrain into categories of moderately low-relief with terrain slopes between 1° and 2°, and very low-relief with terrain slopes < 1°. For each terrain type/relief category, when depression angle can vary enough within class to be important, usually three categories of depression angle (low, intermediate, and high) are enough to separate effects.

4

Approaches to Clutter Modeling

4.1 Introduction

The historical technical literature on low-angle land clutter includes a number of different past approaches for attempting to model this complex phenomenon, as reviewed in Chapter 1. Thus, most simply, low-angle clutter has been characterized as a single-variable characteristic or functional relationship between the dependent variable σ° and any one of the following three independent variables: (1) illumination angle to the backscattering terrain point; (2) radar carrier frequency; and (3) range to the backscattering terrain point. Chapters 2 and 3 illustrate at some length the strong dependencies of low-angle clutter on illumination (i.e., depression) angle and radar carrier frequency based on Phase Zero X-band data and Phase One five-frequency repeat sector data, respectively.

Although providing new useful clutter modeling information, the results of Chapters 2 and 3 in themselves do not constitute a clutter model generalized to be applicable to any surface-sited radar. The objective of such a model is to provide a description of the amplitude statistics of the clutter returns received by an arbitrary radar in a specified environment. As has been discussed previously in this book, the mean strength (first moment) of the clutter amplitude distribution depends strongly on (1) depression angle and (2) radar frequency. However, the equally important shape parameter (derived from the ratio of second to first moments) of the clutter amplitude distribution is fundamentally dependent on the spatial resolution of the radar. The modeling information of Chapters 2 and 3 is restricted to Phase Zero and Phase One pulse lengths and beamwidths. As such, this modeling information may be used to replicate clutter in radars of Phase Zero or Phase One spatial resolution, but is not generalized there to be applicable to radars of spatial resolution significantly different from the Phase Zero and Phase One radars.

Chapter 4 provides an interim angle-specific clutter model fully generalized to be applicable to radars of arbitrary spatial resolution. This interim model is presented in Section 4.2. It is based on the Phase Zero X-band database (Chapter 2) and the Phase One repeat sector database (Chapter 3) and includes all important trends of variation of low-angle clutter amplitude statistics seen in these two databases, including the general dependency of shape parameter on the spatial resolution or cell size of the radar. The interim clutter model is thus a complete model applicable to any surface-sited radar in any ground environment. This model is labelled “interim” because it does not have the statistical depth of the spatially comprehensive 360° Phase One survey data. The identical

structure of the interim clutter model carries forward to the more comprehensive modeling information of Chapter 5 which is based on the Phase One survey data.

The presentation of material in Chapter 4 is as follows. First, Section 4.1.1 describes an important clutter modeling objective, namely, the prediction or simulation of plan-position indicator (PPI) clutter maps in surface-sited radars. Then Section 4.1.2 discusses the clutter modeling rationale of this book, distinguishing between angle-specific clutter modeling information suitable for site-specific clutter prediction using digitized terrain elevation data (DTED) and non-angle-specific modeling information suitable for more generic clutter prediction. Section 4.1.3 discusses clutter as a statistical random process and briefly describes the scope of included material within the context of available random-process statistical attributes. Section 4.2 presents the angle-specific interim clutter model, which requires specification of the depression angle to each clutter patch. This model explicitly incorporates the interdependent effects on clutter of (1) depression angle and (2) radar frequency, but the effects of (3) range occur implicitly in its site-specific application whereby the occurrences of visible clutter patches decrease with increasing range at each specific site.

PPI clutter maps in surface-sited radars are inherently patchy in character. The details of the patchiness are specific to each site. There remains a need, however, for a generic non-site-specific approach to clutter modeling in which the spatial character of the clutter field is not patchy. An important feature of a PPI clutter map for a surface-sited radar, disregarding the specificities of patchiness in each such map, is the obvious dissipation of the clutter with increasing range. Section 4.3 takes up the subject of non-angle-specific clutter modeling information suitable for use in non-patchy prediction. This naturally leads to the explicit introduction of (3) range as the important independent variable affecting the clutter, in contrast to effects of range occurring implicitly in site-specific modeling. What becomes apparent based on clutter measurements at many sites is that the occurrence of clutter fundamentally depends upon (i.e., decreases with) range, for a given site height; and that the strength of the clutter where it occurs is fundamentally dependent upon terrain type but not upon range. Section 4.3 provides a simple, generic, non-patchy clutter model based upon these observations in the measurement data.

Section 4.4 discusses the intimate interrelationship at low angles between geometrically visible terrain and clutter occurrence. Section 4.5 discusses the difficulties involved at low angles in attempting to distinguish discrete from distributed clutter and takes up the issue of how best to reduce the measurement data. Section 4.6 provides additional insight into the clutter phenomenon and the ramifications in its modeling by providing brief introductory discussions of its temporal statistics, its spectral characteristics, and its correlative properties. Section 4.7 summarizes many of the insights developed in Chapter 4. Appendices 4.A, 4.B, and 4.C further develop the effects of radar height and range in low-angle clutter and discuss the complications introduced by range-dependent sensitivity limitations and the corresponding range-dependent effects of radar noise corruption in clutter measurement data. Appendix 4.D describes a more computationally intensive approach to low-angle clutter modeling in which spatial cells that are locally strong (i.e., “discretes”) compared to their neighbors are modeled separately from the weaker neighboring (i.e., “background”) cells.

4.1.1 Modeling Objective

Figure 4.1 shows measured PPI ground clutter maps for all five Phase One frequencies at the Peace River South measurement site, located high on the east bank of the Peace River in Alberta. The maximum range in these maps is 23 km; north is at zenith. Clutter is shown as white where $\sigma^{\circ}F^4 > -40$ dB. These five-frequency Peace River clutter maps may be compared with the five-frequency Gull Lake West clutter maps previously shown in Figure 3.9. To the west in each map in Figure 4.1 is the well-illuminated river valley; to the east, level terrain is illuminated at grazing incidence. As with the Gull Lake West measurements, as patterns of spatial occurrence of ground clutter, all five clutter maps at Peace River are quite similar. As previously discussed, the reason for this similarity is that the relatively strong clutter shown in Figure 4.1 largely comes from visible terrain. At all five frequencies in the figure, the nature of the clutter tends to be granular and patchy. However, the granularity is greater at grazing incidence to the east, less at the higher depression angles to the west. Also as has been discussed, such effects are principally due to depression angle as it affects microshadowing. Obvious in Figure 4.1 is the effect of increasing beamwidth with decreasing frequency causing increased azimuthal smearing of the clutter. This effect is of spatial resolution, such that decreasing resolution results in decreased spreads in clutter amplitude distributions.

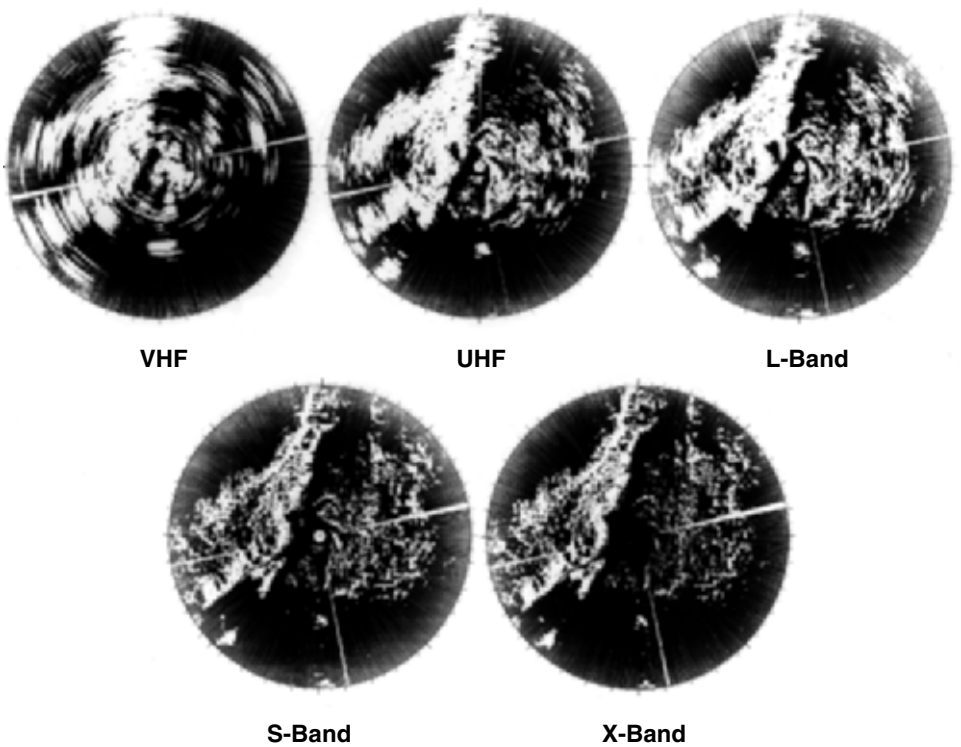

Figure 4.1 Measured multifrequency ground clutter maps at Peace River, Alberta.

A main modeling objective of this book is the site-specific prediction of clutter maps such as those shown in Figure 4.1 using DTED. This objective is illustrated by Figure 4.2 which compares predicted terrain visibility and measured X-band clutter at Katahdin Hill,

Massachusetts. To the left is predicted terrain visibility with a 5-m antenna on the basis of geometric line-of-sight visibility in DTED. To the right is the measured Phase Zero clutter map at the same site. In approximate measure, the two spatial patterns are quite similar;[24] this similarity is borne out in the plot showing percent circumference visible compared with percent circumference in measured clutter vs range. DTED are used to deterministically predict where the clutter occurs, and a statistical depression-angle-specific and terrain-type-specific clutter model is used to predict the strength of the clutter in each visible cell.

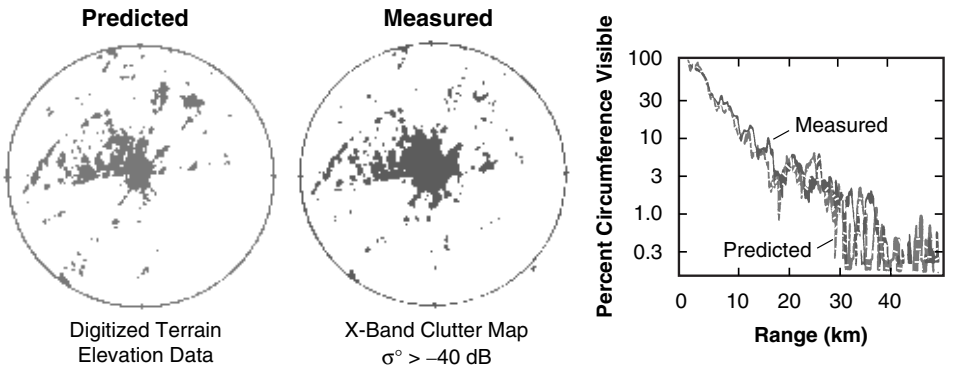

FIGURE 4.2 Predicted clutter visibility at Katahdin Hill. Maximum range = 35 km.

The interim clutter model presented in Section 4.2 is suitable for such site-specific clutter prediction as well as other applications. The interim clutter model structure is illustrated by the schematic diagram of Figure 4.3. To model site-specific clutter, Weibull random numbers are distributed cell-by-cell over visible terrain as determined by DTED. As indicated in Figure 4.3, the Weibull numbers are drawn from distributions characterized by a Weibull mean strength $\overline{\sigma_w^\circ}$ and a Weibull shape parameter a_w. These two coefficients vary with terrain type, depression angle, and the important radar parameters of frequency and resolution. Mean strength $\overline{\sigma_w^\circ}$ varies with frequency, a_w varies with resolution, and both $\overline{\sigma_w^\circ}$ and a_w vary with depression angle and terrain type. The actual interim clutter model matrix of numbers organized as shown in Figure 4.3 is provided in Section 4.2.

4.1.2 Modeling Rationale

Low-angle ground clutter is a patchy phenomenon. Areas of the ground that are directly visible to the radar usually cause relatively strong clutter returns, and areas of the ground that are shadowed or masked to the radar usually cause relatively weak clutter returns, often below the sensitivity of the radar. Using DTED allows the deterministic prediction

24. But see also Figure 2.11, a similar comparison at finer resolution.

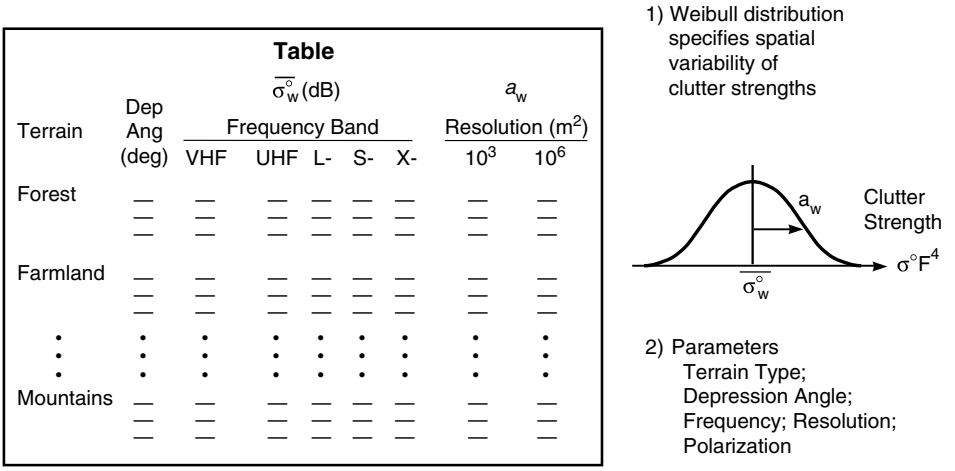

FIGURE 4.3 Interim clutter model structure (table look-up).

and distinction between macroregions of general geometric visibility and macroregions of shadow, where *macro* implies kilometer-sized regions that encompass hundreds or thousands of spatial resolution cells. Such deterministic prediction of the specific pattern of spatial occurrence of ground clutter at a given site is essentially what is meant here by site-specific study.

Predicting, in this manner, the existence of a macropatch of clutter at some site, a description is subsequently needed of the statistics of the clutter returns that are expected from within the patch. Thus Section 4.2 provides modeling information to describe clutter amplitude distributions occurring over macrosized spatial regions of visible terrain. These distributions are characterized by broad spread. The degree of spread in the distribution is fundamentally controlled by depression angle, that is, the angle below the horizontal at which the patch is observed at the radar. Depression angle is a quantity that can be computed relatively rigorously and unambiguously from DTED, depending as it does simply on range and relative elevation difference between the radar antenna and the patch. The fundamental dependence of spread in the clutter amplitude distribution on depression angle is significant even for the very low depression angles (i.e., typically $< 1°$) and small patch-to-patch differences in depression angle (i.e., typically fractions of 1°) that occur in surface-sited radar. The patch-specific modeling information for ground clutter amplitudes presented in Section 4.2 is tied tightly to this basic dependence on depression angle, such that amplitude distributions are specified in terms of small and precise gradations of depression angle for various terrain types.

Let us reflect on this approach to modeling low-angle ground clutter. As a physical phenomenon, the most salient attribute of low-angle ground clutter is variability. This variability is manifested in two important ways: first, as patchiness in spatial occurrence and second, as extremely wide cell-to-cell statistical fluctuation in strength (i.e., spikiness) within a patch. Concerning spatial patchiness, it is emphasized that clutter does not always exist, and it is the patch-specific on-again, off-again macrobehavior of clutter that at first level determines the performance of a given radar against a given low-altitude aircraft at a given site. Concerning wide cell-to-cell variations of clutter strength within macropatches,

it is emphasized that what appears at first consideration to be a phenomenon of extreme variability and little predictability turns out in the end, after much data analysis, to be generally dependent on very fine differences in depression angle.

Use of site-specific DTED allows the capture of both these basic attributes of low-angle ground clutter, its spatial patchiness (approximately computed simply as geometric visibility), and (through depression angle) its expected range of amplitudes within a patch. Therefore, this approach to modeling low-angle clutter is regarded as a major advance over more general non-patchy approaches that do not distinguish between macroregions of clutter occurrence and macroregions of shadow. This approach allows an analyst to predict, within macroregions, where a surface-sited radar can be expected to encounter clutter interference and where the radar will be free of such interference; and, given that the radar is experiencing clutter, what, on the average, the expected statistics of signal-to-clutter ratio will be across the macroregion of clutter.

Clutter returns within patches are often highly spatially correlated. This book discusses the fact that the dominant clutter sources within macroregions of general geometric visibility are usually spatially localized or discrete, such that groups of cells providing strong returns are often separated by cells providing weak or noise-level returns. The occurrence of noise-level returns distributed within macroregions of general geometric visibility is referred to as "microshadowing," where *micro* implies resolution-cell-sized areas (see Figure 2.11 and its accompanying discussion in Chapter 2). The high degree of spatial microcorrelation of strong discrete sources within macropatches results from the fact that such sources exist as vertical features of landscape discontinuity that often occur in definite patterns, for example, along the leading edge of a tree line or the clustering of vertical objects along roads and field boundaries. If an analyst is interested in the actual microstatistics, for example, of break-lock in a surface radar tracking a target across a given clutter patch, the information in this book does not go that far.

The kind of detail and fidelity in terrain description that are required to predict microstatistics of spatial correlation of clutter amplitudes within macropatches are regarded as a second sequential major hurdle to cross in clutter modeling. Limitations encountered in attempting this second advance have been explored. It has been found that prediction of microspatial correlation is a very challenging task that immediately takes exploratory operations out to the limits of current resources in terms of available information and computer processing. In contrast, the first major advance in low-angle clutter fidelity, which is the field-of-investigation of this book, comes relatively easily once DTED are in play.

The above allusion to general non-patchy approaches to clutter modeling does not imply that such approaches are without value. Section 4.3 moves from measurements in which the patch-specific parameter of depression angle is the fundamental controlling parameter to non-angle-specific modeling information based on relatively general parameters such as site height, terrain roughness, and terrain type (e.g., forest, agricultural, etc.). However, it is true that non-patchy approaches to clutter modeling are, indeed, relatively abstract and conceptually vague in quantitative study. This is the logical penalty that non-patchy approaches must pay as the price for generality. This penalty comes about because, instead of aggregating system performance measures after realistic clutter computations at many individual sites, the non-patchy approach attempts to aggregate and generalize clutter influences before a one-time assessment of system performance. That is, the non-patchy

approach takes the easy way of attempting to *a priori* average the clutter first, whereas the site-specific patchy approach takes the harder but more rigorous way of *a posteriori* averaging the actual site-specific performance measures to reach generality.

4.1.3 Modeling Scope

Low-angle radar ground clutter is a complex phenomenon. Nevertheless, as a random process, all of its descriptive attributes must fall somewhere within the list shown in Table 4.1. First, consider variation that occurs from point to point in space. The question of how strong the clutter is across an ensemble of spatial points is answered statistically in terms of a histogram of clutter amplitudes, one from each spatial point. The other pertinent question concerning spatial variation is, how far must the sampling point move for the clutter amplitude to change significantly? This question is answered statistically in terms of correlation distance in the random process. Second, consider variation that occurs at any given point with passing time. As with spatial variation, the question of temporal variation of clutter strength is answered in terms of a statistical histogram of clutter amplitudes measured consecutively in time at a given point. With temporal variation, the remaining question is, how long does it take for the clutter amplitude to change significantly? This question is answered statistically in terms of correlation time. The spatial information contained in correlation distance and the temporal information contained in correlation time are equivalent to the spectral information in the random process in space and time, respectively—i.e., the Fourier transform of the autocorrelation function is the power spectrum.

Table 4.1 Radar Ground Clutter Statistics

Spatial Variations Amplitude Statistics Correlation Distances
Temporal Variations Amplitude Statistics Correlation Times/Spectra

The simple overall scheme illustrated in Table 4.1 for describing low-angle ground clutter becomes complicated because of matters to do with scale. Clutter is spatially nonhomogeneous. That is, it varies spatially in a complex way. As a result, it presents many different observable attributes depending on the scale at which it is observed. For example, consider a wood lot adjacent to an open agricultural field. At microscale, the clutter statistics applicable to the wooded area constitute a different process and need to be investigated separately from those applicable to the open field—where here, as before, the prefix *micro* implies resolution cell-sized areas. But consider the clutter statistics applicable to the important boundary region between wood lot and agricultural field. The strong clutter returns from such boundary regions, and other features of vertical discontinuity that exist pervasively over almost all landscapes, dominate in low-angle clutter. In this regard, the field of low-angle clutter is akin to other modern fields of investigation in which spatial feature is important, such as digitized map processing, synthetic-aperture radar (SAR) image data compression, pattern recognition, and artificial intelligence. All such fields attach more importance to edges of features and to defining, storing, and recognizing such edges than to the more homogeneous regions within bounding edges.

Thus, the field of low-angle clutter leads an investigator from microscale to macroscale, where here, also as before, the prefix *macro* implies kilometer-sized regions encompassing hundreds or thousands of spatial resolution cells and many vertical features. As discussed in Chapter 2, the correct empirical approach in dealing with many edges of features existing as discontinuous or discrete clutter sources is to collect meaningful numbers of them together within macropatches, allowing the terrain classification system to describe their statistical attributes at an overall level of description. This book provides modeling information allowing the prediction of the spatial amplitude statistics of low-angle clutter as they occur for ground-based radar distributed over macroregions of visible terrain. Development of this information requires clutter measurements from many different sites and macropatches to build up an appropriate supportive empirical statistical database. This book does not address statistical issues of patch length and separation, but Chapter 4 and its appendices address how, as a result of spatial patchiness, the occurrence of clutter generally decreases with increasing range. An example showing microscale correlation distance in farmland terrain is provided in Section 4.6. Such microspatial correlation is important, for example, in the detailed processing algorithms of constant-false-alarm rate (CFAR) radars.

Issues of temporal variation of low-angle ground clutter generally stand apart from the more stressing problem of modeling the spatial statistics of clutter. The subjects overlap somewhat in that clutter spatial amplitude statistics vary with long-term temporal variation associated with weather and season. Long-term temporal variation is discussed in Chapter 3. Concerning short-term temporal variation, some brief information describing the relative frequency of occurrence of temporal amplitude statistics between cells with Rayleigh (i.e., windblown foliage) and Ricean (i.e., fixed discretes embedded in foliage) statistics is provided in Section 4.6. Section 4.6 also introduces the subject of intrinsic-motion Doppler frequency spectra of windblown ground clutter; the accurate characterization of windblown clutter spectra is more extensively addressed as the subject of Chapter 6.

4.2 An Interim Angle-Specific Clutter Model

4.2.1 Model Basis

Section 4.2 presents an interim angle-specific clutter model for predicting ground clutter amplitude statistics as they occur over spatial macroregions of directly visible terrain at low depression angles. The interim clutter model is based upon Phase Zero X-band and Phase One five-frequency measurements as discussed in Chapters 2 and 3, respectively. The results of Chapters 2 and 3 apply specifically to cell sizes as defined by Phase Zero and Phase One pulse lengths and beamwidths. The interim model generalizes these results such that the spatial resolution of the radar becomes an important—and, within limits, arbitrarily specifiable—independent variable upon which the clutter statistics strongly depend.

The spread in the clutter amplitude distribution as defined by the shape parameter of the distribution is fundamentally dependent on the spatial resolution of the radar. Spatial resolution or cell size A in m^2 is defined by $A = r \cdot \Delta r \cdot \Delta\theta$ where r is range, Δr is range resolution, and $\Delta\theta$ is beamwidth (see Section 2.3.1.1). The range of cell sizes empirically available in the Phase Zero and Phase One data is determined not only by the different pulse lengths provided by the Phase Zero and Phase One radars (viz., 0.06, 0.1, 0.25, 0.5, and 1.0 μs), but also and very importantly by the different azimuth beamwidths available (viz., 1°, 3°, 5°, 13°) and by the different ranges over which clutter patch amplitude

distributions were acquired (viz., from 1 to > 50 km). Of course, each azimuth beamwidth is generally available in only one radar frequency band in the clutter measurement data, but it turns out that the spread in the clutter amplitude distribution, determined, for example, by the ratio of standard deviation-to-mean, is relatively independent of the radar frequency at which it is measured. The spatial spikiness causing spread in low-angle clutter—a characteristic feature easily observed in A-scope sector displays—is relatively independent of radar frequency because the same large discrete sources causing the spikes exist whatever the frequency band employed in the measurement.

Therefore, observed spreads in clutter amplitude distributions, which are fundamentally and strongly dependent on cell size, may be considered as independent of frequency and thus may be combined and interpolated across the beamwidths available in the various frequency bands to provide a much wider range of spatial resolution than would be available in any one frequency band alone. By this means, the interim clutter model, and also the clutter modeling information provided subsequently in Chapter 5, are generalized such that the highly significant spreads in clutter amplitude distributions apply to radar cell sizes ranging over the relatively wide extent from ~10^3 m^2 to ~10^6 m^2 in any frequency band. This matter is further discussed in Chapter 5.

The Phase Zero X-band results of Chapter 2 underlying the interim clutter model comprise measurements from 2,177 different clutter patches. With this large number of terrain samples, even after separating into different categories of terrain type and depression angle, there are still many samples left in any given category and hence good statistical definition in the results. That is, with a large amount of averaging at work in these data, even small differences in results are statistically significant. In contrast, the Phase One five-frequency results of Chapter 3 underlying the interim clutter model comprise measurements from just 42 repeat sector terrain patches, one per site from each of the 42 Phase One sites. Because backscatter measurements were performed on each repeat sector patch a number of times across a 20-element radar parameter matrix, the Phase One repeat sector database of Chapter 3 constitutes a comparable amount of data to the Phase Zero database and allowed determination of trends of variation with frequency, pulse length and polarization. It is important to realize, however, that when looking for such trends and separating the 42 repeat sector patches into various categories of terrain type and depression angle, in contrast to Phase Zero there often are not very many terrain samples per category. As a result, the interim clutter model reaches for multifrequency characteristics often on the basis of a few examples of an observed trend rather than with the statistical rigor of Phase Zero.

This lack of statistical depth in the interim clutter model is evidenced by the fact that the interim model is presented as a simple one-page table of numbers. There are obvious advantages to this simplicity, both in ease of comprehension and ease of implementation. As a result of such advantages, the interim clutter model has received and continues to receive extensive usage at Lincoln Laboratory and elsewhere. The disadvantages of this simplicity are less statistical rigor and diminished prediction accuracy. Chapter 5 brings all the Phase One 360º survey data at each site under analysis, in addition to the repeat sector data, utilizing the same model construct as employed by the interim clutter model. In doing so, the Phase One modeling information of Chapter 5 obtains the important Phase Zero statistical advantage of many terrain samples and increased prediction accuracy.

4.2.2 Interim Model

The interim angle-specific clutter model is presented in Table 4.2. The clutter modeling information in Table 4.2 is provided within a context of Weibull statistics [1, 2], where $\overline{\sigma_w^\circ}$ is the Weibull mean strength and a_w is the Weibull shape parameter. Weibull statistics are defined and discussed in Appendices 2.B and 5.A. The interim model is based upon the three main categories of descriptive parameter of low-angle clutter previously introduced in Section 3.4. First are parameters which are descriptive of the radar. The important radar parameters affecting clutter statistics as employed in the interim model are radar frequency as it affects $\overline{\sigma_w^\circ}$ and radar spatial resolution as it affects a_w.

Second are parameters descriptive of the geometry of illumination of the clutter patch. As in Chapters 2 and 3, the interim model utilizes depression angle, a relatively simple and unambiguous quantity to determine, depending only on range and relative elevation difference between the radar antenna and the backscattering terrain point. Recall that attempts in Chapter 2 to use grazing angle met with little additional success, partly due to difficulties associated with scale, precision, and accuracy in unambiguously defining local terrain slope and partly because dominant clutter sources tend to be vertical discrete objects associated with the land cover. Use of grazing angle in clutter modeling is further discussed in Appendix 4.D. Formulating the interim clutter model in terms of depression angle involves the possibility of occurrence of negative depression angles wherein terrain is observed by the radar at elevations above the antenna. For terrain to be visible at negative depression angle requires the terrain to be of terrain slope greater than the absolute value of the depression angle at which it is observed.

Third are parameters descriptive of the terrain within the clutter patch. The interim clutter model of Table 4.2 is comprehensive in that, whatever terrain is under consideration, it must fall within one of the terrain types of the model. Most terrain types in the model involve several depression angle regimes. As introduced in Chapter 2, the important general terrain types of the interim model are threefold, namely (1) rural/low-relief terrain in which terrain slopes are $< 2°$; (2) rural/high-relief terrain in which terrain slopes are $> 2°$; and (3) urban terrain.

Within general rural/low-relief terrain, the interim model further distinguishes three specific important subclass terrain types as discussed in Chapter 3, namely, continuous forest, open farmland, and open wasteland (e.g., desert, marsh) or grazing land with very low incidence of large discrete vertical objects (e.g., farmstead buildings, feed storage silos, isolated trees, etc.) such as typically occur in farmland. Within rural/high-relief terrain, particularly separated out are the two subclass terrain types of continuous forest and mountains. Within urban terrain, separated out is the subclass of urban areas as observed over open low-relief terrain supportive of multipath (see Chapter 3). Concerning the several subcategories of terrain contained within each of the three general terrain types in Table 4.2, the general category (a) is applicable only if the terrain in question fails to meet the specification of any of the subsequent specific subcategories within a group. That is, the general category applies to mixed or composite terrain that is neither completely open nor completely tree-covered. The subcategorization of terrain within each major group becomes increasingly important with decreasing frequency. For completeness, a fourth general category comprising terrain observed at negative depression angle is required. Terrain observed at negative depression angle is usually relatively steep.

TABLE 4.2 Multifrequency Weibull Parameters of Land Clutter Amplitude Distributions

Terrain Type	Depression Angle (deg)	$\overline{\sigma_w^\circ}$ (dB) Frequency Band					a_w Resolution(m^2)	
		VHF	UHF	L-	S-	X-Band	10^3	10^6
Rural/Low-Relief								
a) General rural	0.00 to 0.25	-33	-33	-33	-33	-33	3.8	2.5
	0.25 to 0.75	-32	-32	-32	-32	-32	3.5	2.2
	0.75 to 1.50	-30	-30	-30	-30	-30	3.0	1.8
	1.50 to 4.00	-27	-27	-27	-27	-27	2.7	1.6
	> 4.00	-25	-25	-25	-25	-25	2.6	1.5
b) Continuous forest	0.00 to 0.30	-45	-42	-40	-39	-37	3.2	1.8
	0.30 to 1.00	-30	-30	-30	-30	-30	2.7	1.6
	> 1.00	-15	-19	-22	-24	-26	2.0	1.3
c) Open farmland	0.00 to 0.40	-51	-39	-30	-30	-30	5.4	2.8
	0.40 to 0.75	-30	-30	-30	-30	-30	4.0	2.6
	0.75 to 1.50	-30	-30	-30	-30	-30	3.3	2.4
d) Desert, marsh, or grassland (few discretes)	0.00 to 0.25	-68	-74	-68	-51	-42	3.8	1.8
	0.25 to 0.75	-56	-58	-46	-41	-36	2.7	1.6
	> 0.75	-38	-40	-40	-38	-26	2.0	1.3
Rural/High-Relief								
a) General rural	0 to 2	-27	-27	-27	-27	-27	2.2	1.4
	2 to 4	-24	-24	-24	-24	-24	1.8	1.3
	4 to 6	-21	-21	-21	-21	-21	1.6	1.2
	> 6	-19	-19	-19	-19	-19	1.5	1.1
b) Continuous forest	any	-15	-19	-22	-22	-22	1.8	1.3
c) Mountains	any	-8	-11	-18	-20	-20	2.8	1.6
Urban								
a) General urban	0.00 to 0.25	-20	-20	-20	-20	-20	4.3	2.8
	0.25 to 0.75	-20	-20	-20	-20	-20	3.7	2.4
	> 0.75	-20	-20	-20	-20	-20	3.0	2.0
b) Urban, observed on open low-relief terrain	0.00 to 0.25	-32	-24	-15	-10	-10	4.3	2.8
Negative Depression Angle								
a) All, except mountains and high-relief continuous forest	0.00 to -0.25	-31	-31	-31	-31	-31	3.4	2.0
	-0.25 to -0.75	-27	-27	-27	-27	-27	3.3	1.9
	< -0.75	-26	-26	-26	-26	-26	2.3	1.7

The interim clutter model of Table 4.2 consists of 27 combinations of terrain type and depression angle. For each combination, the model provides Weibull mean clutter strength as a function of radar frequency f, VHF through X-band, as $\overline{\sigma_w^\circ}(f)$, and provides the Weibull shape parameter as a function of radar spatial resolution A over the range between 10^3 and 10^6 m^2, as $a_w(A)$. The shape parameter is obtained from linear interpolation on $\log_{10}(A)$ between the values provided for $A = 10^3$ m^2 and $A = 10^6$ m^2. The total matrix of information in Table 4.2 contains all the important trends that are observed in the measured clutter amplitude distributions as discussed in Chapters 2 and 3.

Many of the important trends of variation in the $\overline{\sigma_w^\circ}$ data of Table 4.2 are plotted in Figure 4.4. These trends are now discussed in some detail. This discussion to some extent summarizes and reiterates previous discussions of the clutter measurement data in Chapters 2 and 3. Thus, in Figure 4.4, in general rural terrain of both low and high relief, mean clutter strength increases with depression angle but is invariant with frequency. That is, within the shaded region clutter strength rises with increasing depression angle both within the rural/low-relief and within the rural/high-relief regimes. In continuous forest, however, mean clutter strength depends both on depression angle and frequency; whereas in open farmland, mean clutter strength is invariant both with depression angle and frequency, except at low depression angle on level terrain where a significant multipath propagation loss occurs at low frequencies. Note that at intermediate depression angles in Figure 4.4, both forest and farmland fall in closely with general rural/low-relief terrain in terms of mean clutter strength.

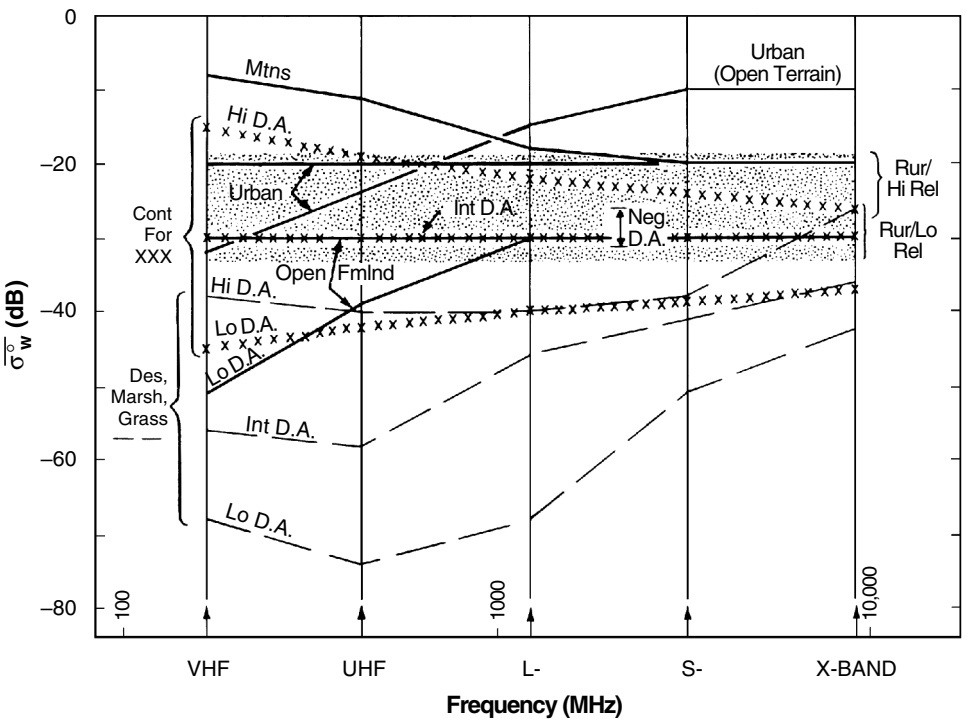

FIGURE 4.4 Weibull mean clutter strength vs frequency for all terrain types.

Urban complexes observed over low-relief open terrain provide large mean clutter strengths at high frequencies partly because of their broadside aspect, but at low frequencies these large returns are decreased significantly through multipath loss. However, in more general

composite terrain, mean clutter strength from urban complexes is 10 dB weaker than at high frequencies on open terrain and is frequency invariant.

On discrete-free desert, marsh, or grassland, mean clutter strength is weaker than for other terrain types. Again, at low and even intermediate depression angles, there is a large multipath loss due to decreased illumination strength at the lower frequencies, and this loss is greater and extends to higher frequencies than in farmland because the clutter sources are much lower in such terrain (e.g., a sagebrush bush) than in farmland (e.g., a silo). Note that, aside from differences in intrinsic σ°, propagation loss by itself would act to continue to decrease mean clutter strength $\overline{\sigma^\circ F^4}$ from UHF to VHF at low and intermediate depression angles on open desert, marsh, or grassland; however, repeat sector data from four different sites and at all parametric variations of polarization and resolution show that mean clutter strength actually rises slightly from UHF to VHF, indicating that intrinsic σ° is considerably greater at VHF than UHF in such terrain.

Next mean clutter strength is compared between desert and forest at X-band. At low and intermediate depression angles, mean strength in desert terrain is 5 or 6 dB weaker than in forest terrain, but at high depression angle >1° (and on the basis of two different desert measurement sites at all combinations of polarization and resolution), mean strength in desert is equal to that in forest terrain (i.e., at X-band, looking down at sagebrush vegetation is equivalent to looking down at a forest canopy).

The data in Figure 4.4 cover 66 dB of variability in mean clutter strength, from mountains at VHF to desert at UHF. Of course, cell-to-cell variability in clutter amplitude statistics is even greater. The trends of variation in the a_w data of Table 4.2 that determine cell-to-cell variability are shown in Figure 4.5 for rural/low-relief terrain. These results illustrate that spreads in clutter amplitude distributions due to cell-to-cell variability decrease both with decreasing spatial resolution and with increasing depression angle. Over and above these basic dependencies, the results in Figure 4.5 and Table 4.2 also show that a_w in open farmland is greater than in general rural/low-relief terrain, whereas a_w in continuous forest is less than in general rural/low-relief terrain; and that a_w in rural/high-relief terrain is less than in rural/low-relief or urban terrain (see Figure 2.47).

4.2.3 Error Bounds

An interim multifrequency ground clutter model is provided in Table 4.2 for determining ground clutter amplitudes from visible regions of terrain in surface-sited radars. This interim model consists of a manageable set of empirically derived numbers that in total establishes an orderly rationale for the specification of such clutter amplitudes over their many order-of-magnitude range of variations, based on terrain type, depression angle, and the important radar parameters of frequency and resolution.

What are the error bounds in the interim modeling information presented in Table 4.2? The discussion of temporal and spatial variation in low-angle ground clutter previously provided in Section 3.7.3 provides some guidance in this matter. On the basis of repeat sector measurements over the two to three week stay at every Phase One site, the 1-σ diurnal variability in mean clutter strength, largely due to changes in weather, is specified in Section 3.7.3 to be 1.1 dB. The Phase One equipment made six repeated visits to selected sites to investigate seasonal variations. On the basis of these measurements, the 1-σ

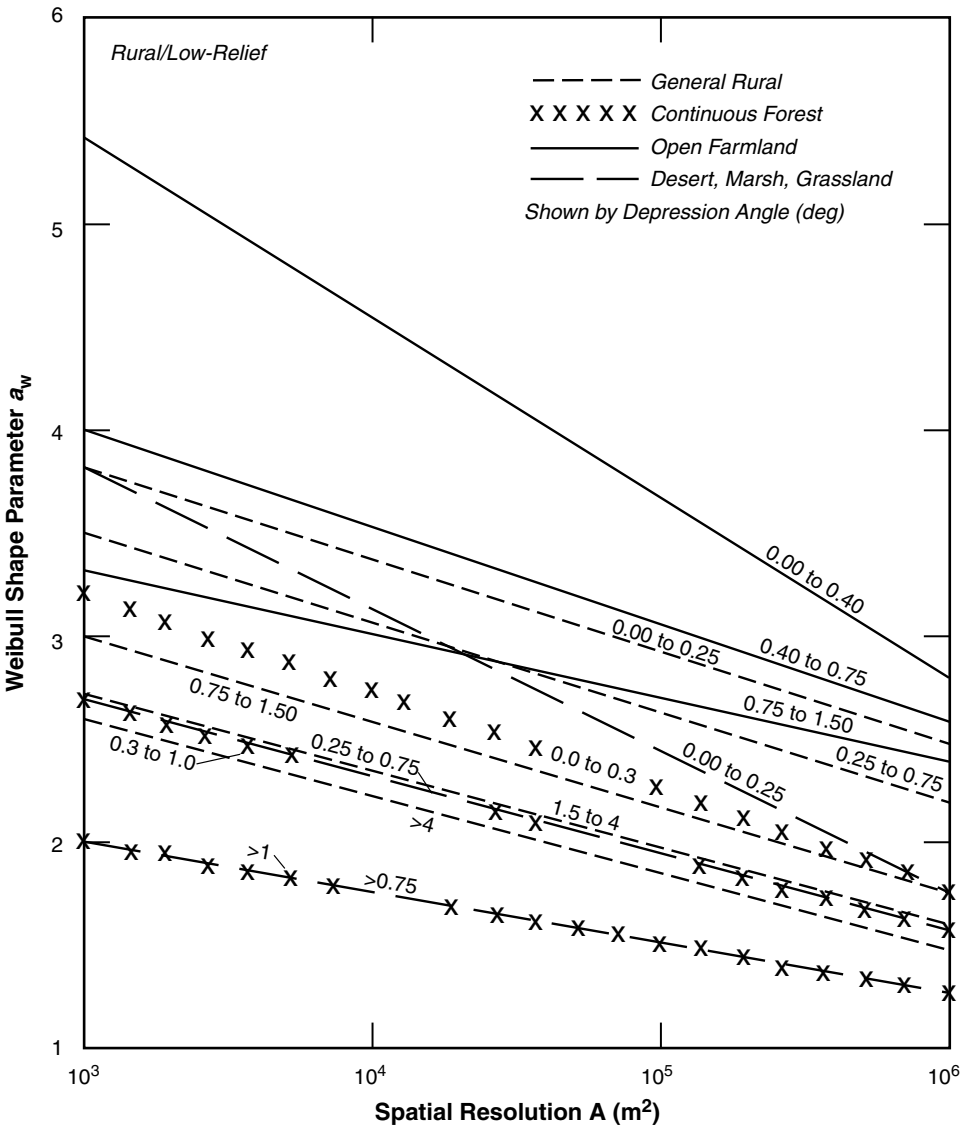

FIGURE 4.5 Weibull shape parameter a_w vs radar spatial resolution for rural/low-relief terrain types.

seasonal variability in mean clutter strength is specified in Section 3.7.3 to be 1.6 dB. Such long-term temporal variations in mean clutter strength from macroregions of terrain may be contrasted with the spatial region-to-region 1-σ variability that is specified in Section 3.7.3 to be 3.2 dB, on the basis of region-to-region variations in repeat sector mean clutter strength within similar regions. Thus, it is apparent that the numbers comprising the interim clutter model are statistical averages. These averages establish important trends, but actual realizations of clutter will deviate from the predicted average numbers of the model.

4.3 Non-Angle-Specific Modeling Considerations

In Section 4.2, the measured data were used to develop an interim clutter model for use in determining site-specific radar system performance, where the actual terrain at the radar site is deterministically represented through digitized terrain elevation data. Such a site-specific clutter model can provide, with reasonable fidelity, detailed measures of clutter-limited radar performance as a particular low-altitude airborne target is engaged by a particular radar at a particular site. At a higher level of abstraction, however, there remains a need for a non-patchy clutter model for use in computing the limiting effects of ground clutter on system performance in a generic sense, independent of how specific terrain features and resulting patchiness varies from site to site. This section brings the large database of Phase Zero ground clutter measurements statistically to bear to provide simple non-patchy clutter modeling information that captures the important statistical and parametric variations in the database. One important characteristic of a PPI clutter map is the obvious dissipation of the clutter with increasing range, which is automatically incorporated in a patchy site-specific model. Consideration of how best to implement this characteristic in a non-patchy non-site-specific model leads to discussion of explicit effects of range on low-angle clutter.

4.3.1 Phase Zero Results

Figure 4.6 shows measured clutter maps to 47-km maximum range for six different sites, in order of increasing effective radar height. Figure 4.7 shows percent circumference in clutter vs range for the same six sites. The details of each pattern of spatial occurrence of clutter in Figure 4.6 are specific to the terrain features at that site. In all such patterns, however, the patches of clutter become fewer and farther between with increasing range so that, as shown in Figure 4.7, the amount of clutter that occurs gradually diminishes with increasing range from the site. These two figures also show that the amount of clutter that occurs is a strong function of the effective height of the radar. Effective radar height is defined with respect to visible terrain and includes both the height of the hill on which the radar is situated and the antenna mast height (see Section 2.2.3). The somewhat differing higher-order effects of hill height and mast height on terrain visibility are discussed in Appendix 4.B. It is apparent in Figures 4.6 and 4.7 that higher radars see clutter to longer ranges.

Figure 4.8 provides general information on clutter extent and strength by averaging measurements like those of Figures 4.6 and 4.7 from many sites. Figure 4.8(a) shows percent of circumference in clutter vs range averaged across 86 sites. The resultant clutter visibility curve is approximately linear over most of its extent as displayed on the logarithmic vertical scale employed in Figure 4.8(a). This linearity indicates that in general the amount of ground clutter that occurs in surface radar decreases exponentially with increasing range, thus quantifying the observations of the preceding paragraph. The curve of Figure 4.8(a) represents the best non-site-specific information that the large Phase Zero database can deliver when brought to bear to answer the general question, how far out does ground clutter go? Because ground clutter diminishes gradually (i.e., exponentially) with increasing range, this question must be answered conditionally in terms of a threshold on how much clutter is of concern. As an example, Figure 4.8(a) indicates that in general 10% of circumference is in clutter at 19-km range.

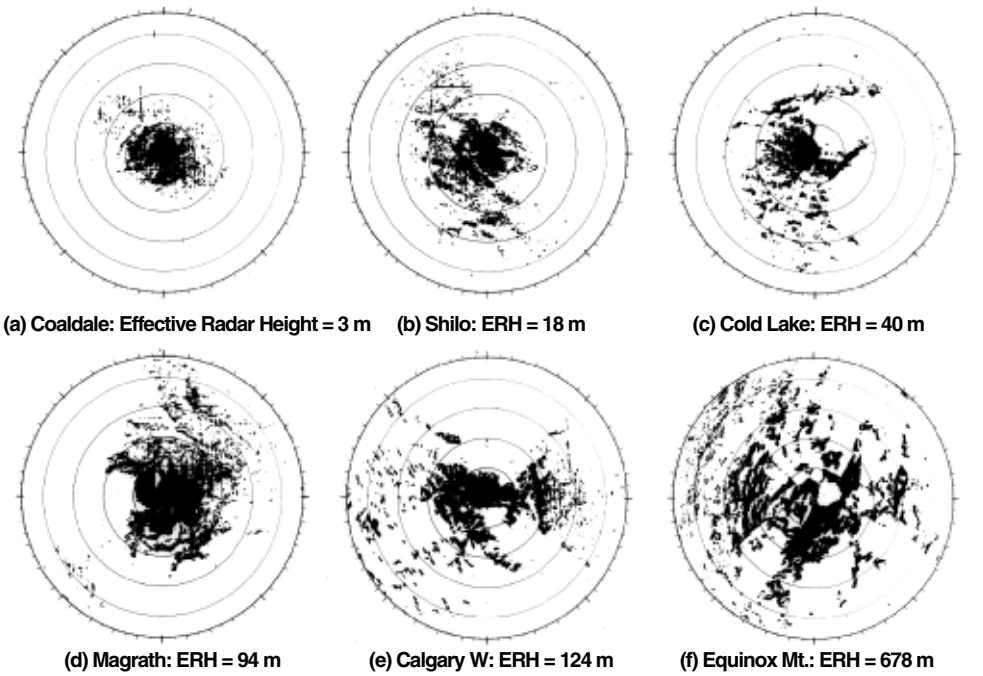

FIGURE 4.6 Phase Zero clutter maps for six sites. In each map, maximum range = 47 km (10-km range rings). Results shown are for full Phase Zero sensitivity.

Percent circumference in clutter represents the probability of discernible clutter P_c vs range r. $P_c(r)$ is dependent on radar sensitivity. If it is assumed that clutter arises only from geometrically visible terrain and that over visible terrain clutter is Weibull-distributed, then it is straightforward to numerically extrapolate the Phase Zero clutter visibility data of Figure 4.8 to radars of higher sensitivity. In this extrapolation, $P_c(r) = P_v(r) \cdot P_D(r)$, where $P_v(r)$ is the probability that the terrain is geometrically visible, and $P_D(r)$ is the probability that the clutter strength is above radar noise level given that the terrain is visible. $P_D(r)$ is simply the Weibull cumulative (integral) distribution function obtained by integrating Eq. (2.B.18) with radar noise level at range r as the lower limit of integration [(cf. Eq. (2.B.21) obtained with zero as the lower limit of integration]. $P_D(r)$ is easily numerically evaluated, once the Weibull coefficients of the clutter and the noise level of the radar are specified. If the ratio of $P_D(r)$ for a radar of increased sensitivity to $P_D(r)$ for Phase Zero sensitivity is computed, then clutter visibility $P_c(r)$ for the radar of increased sensitivity is simply the product of this ratio and $P_c(r)$ for Phase Zero as given by the data in Figure 4.8. The validity of such extrapolation of Phase Zero clutter visibility data to higher sensitivity radars is dependent on the soundness of the assumptions, which deteriorate with large departure from Phase Zero sensitivity.

Discussion now turns to Phase Zero clutter amplitude distributions as obtained within macropatches of visible terrain. Figure 4.8(b) shows the cumulative distribution of mean clutter strengths, one mean value per clutter patch, over all the 2,177 patches for which Phase Zero clutter amplitude distributions were determined. These 2,177 macropatches were selected from 96 different measurement sites. The curve of Figure 4.8(b), as plotted on a logarithmic (i.e., decibel) abscissa, is essentially linear over most of its central extent.

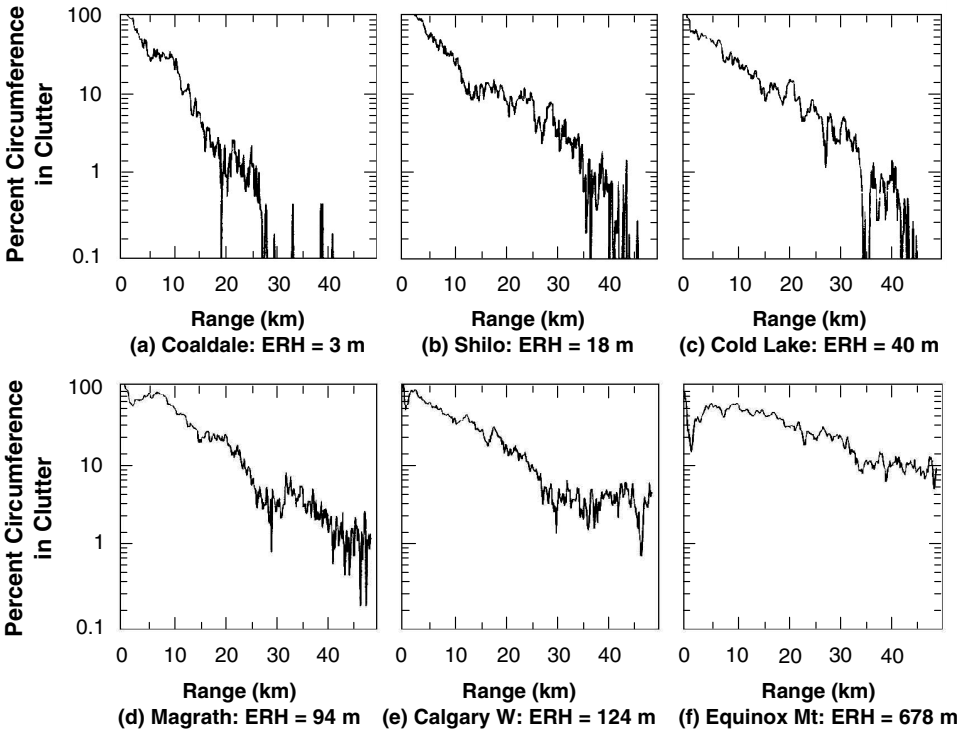

FIGURE 4.7 Percent circumference in clutter vs range for six sites. Phase Zero data, 47-km maximum range, 150-m range resolution, clutter threshold is 3 dB above full sensitivity.

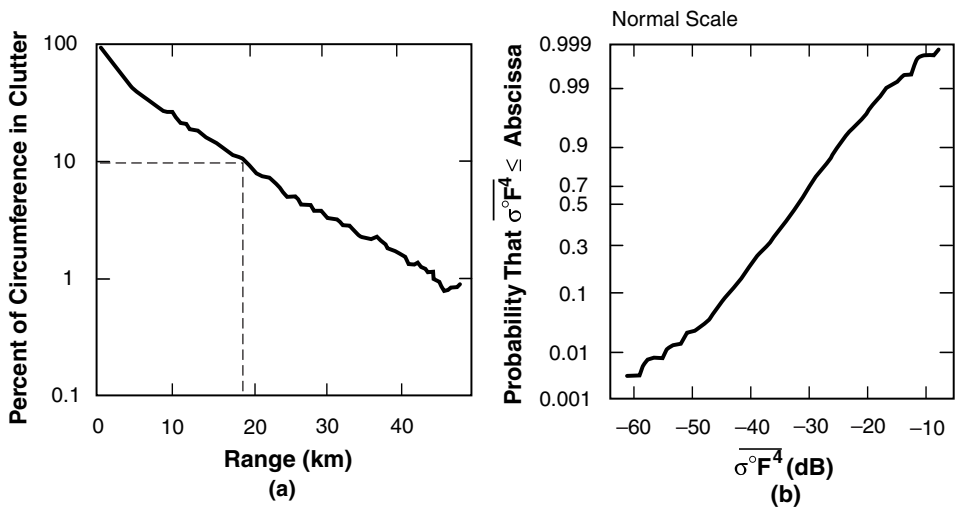

FIGURE 4.8 General spatial extent and strength of low-angle radar ground clutter: (a) decrease of clutter occurrence with range and (b) distribution of mean strengths of ground clutter patches.

This linearity implies that the distribution of mean strengths of clutter patches (in units of m^2/m^2) is lognormal. The data in Figure 4.8(b) represent Phase Zero's best answer to the

next general question, how strong is ground clutter? Figure 4.8(b) indicates that mean ground clutter strength varies over five orders of magnitude. Thus this question also must be answered conditionally in terms of probability of occurrence. The median or 50-percentile value of mean clutter strength in this figure is –31 dB (i.e., half of all measured values of mean clutter strength occur above –31 dB, half below). The mode or most frequently occurring value of mean clutter strength in Figure 4.8(b) is –40 dB.

4.3.2 Simple Clutter Model

In developing a simple non-site-specific clutter model, the first issue that must be confronted is terrain visibility. As previously discussed, from most places on the surface of the real earth, visibility to terrain is spatially patchy. To an observer looking out from the site, high regions are visible and intervening low regions are masked. Most of the relatively significant clutter comes from directly (geometrically) visible terrain. As range increases, the visible terrain patches become fewer and farther between until beyond some maximum range, no more terrain is visible. Thus on the real earth, terrain visibility and hence the spatial occurrence of clutter is a gradually diminishing function of increasing range.

Here, a simple non-site-specific clutter model means a non-patchy model that is spatially homogeneous and isotropic. The sort of earth that provides this kind of clutter is a cue ball earth. That is, if the site-specific macroscopic terrain features that exist at every real site are suppressed, what remains is a cue ball, conceptually devoid of all macrofeature, but uniformly microrough to account for homogeneous and isotropic diffuse clutter backscatter. On such a cue ball devoid of macroscale terrain features, the clutter patches observed at real sites expand to encompass all of the terrain out to a single-valued horizon, R_C. The resulting binary visibility function is imparted to the simple clutter model. There may be a temptation to spatially dilute the clutter amplitude statistics as actually measured within large macropatches of visibility with the large amounts of macroshadow that exist on the real earth between the patches. Such spatial dilution would artificially diminish clutter strengths with increasing range in a way that would certainly not be measured by a real radar, either on a real earth-sized cue ball or on the real earth itself. These matters are discussed at greater length in Appendix 4.C.

Such considerations lead to the simple, non-patchy, non-site-specific clutter model shown in Figure 4.9. This simple model provides homogeneous clutter within a circular region centered at the radar. The mean clutter strength within this region is given by $\overline{\sigma_w^\circ}$, and the radial extent of the region by the clutter cut-off range R_C. The statistically important effect of increasing macroshadow with increasing range shown in Figure 4.8(a) is used to set the radial extent of the homogeneous clutter region R_C. This setting of R_C is done as a statistical threshold on clutter visibility in the measured data. That is, the user first specifies the minimum spatial amount of clutter that begins to degrade the user's systems (e.g., 20%). Then the range at which that amount of clutter generally occurs in the measurements is used as the clutter cut-off range R_C in the simple model (e.g., 12 km).

The effective height of the radar above the surrounding terrain is the major parameter affecting how far ground clutter occurs. This effect is illustrated by the data of Figure 4.10, in which the exponential decrease of clutter occurrence with increasing range shown in Figure 4.8(a) is parameterized in five regimes of effective radar height, using the same 86-site set of data upon which the result of Figure 4.8(a) is based. Figure 4.10 may be compared with Figure 4.7. Again, it is apparent that higher radars see clutter to longer

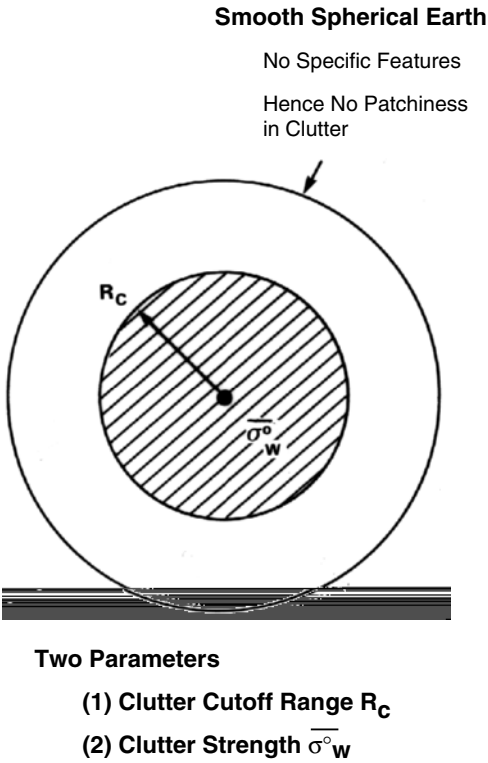

FIGURE 4.9 Non-site-specific clutter model.

ranges. The simple model incorporates this important effect of radar height by parameterizing the statistical procedures for setting clutter cut-off range to be dependent on radar height in the measured data.

The results of these procedures for specifying clutter cut-off range R_C in the non-site-specific model are summarized in Table 4.3. If 20% of circumference in clutter on the real earth is accepted as a baseline threshold above which clutter is expected to have substantial impact on radar system performance, Table 4.3 indicates that at a general radar height of 40 m, this threshold in clutter occurrence will be exceeded at ranges $\leq$ 12 km. If it is known that the radar is substantially lower or higher than this general height of 40 m, the clutter cutoff range decreases to 7 km or increases to 22 km, respectively, for the same baseline threshold in clutter occurrence. If the threshold in clutter occurrence rises to as much as 50%, clutter extents above such a high threshold are relatively benign, 3 or 4 km, whereas if the threshold in clutter occurrence drops to as little as 2%, clutter extents are quite severe, ranging from 21 to 48 km depending on radar height. Note that except for this latter severe situation, clutter extents as derived empirically in Table 4.3 from clutter visibility on the real earth are usually much less than range to the spherical earth horizon on a cue ball, illustrating that on the real earth, terrain relief usually dominates over earth sphericity in influencing terrain visibility and horizons.

With the radial extent of the homogeneous region determined in this manner for the simple model, the mean strength of the clutter $\overline{\sigma_w^\circ}$ that exists within this region must be specified.

percentile probability of occurrence. Proceeding to a worst-case/best-case assessment, if 90- and 10-percentile probabilities of occurrence are accepted as reasonable measures of strong and weak mean clutter strengths, respectively, then by these measures the data in Table 4.4 show that strong mean clutter strength is generally 7 or 8 dB stronger than baseline, and weak clutter is generally 7 or 8 dB weaker than baseline, both in general circumstances and for the three main terrain types.

TABLE 4.4 Mean Clutter Strength for Use in Non-Site-Specific Clutter Modeling

Percent of Measured Patches with $\overline{\sigma_w^\circ} \leq$ Tabulated Value	Mean Clutter Strength $\overline{\sigma_w^\circ}$ (dB)				Clutter Strength Variations
	Terrain Type				
	Rural/ Low-Relief	General	Rural/ High-Relief	Urban	
10	-41	-40	-34	-31	Benign (weakest)
50	-33	-31	-27	-23	Baseline
90	-26	-23	-20	-15	Severe (strongest)

4.3.3 Further Considerations

4.3.3.1 Clutter Strength vs Range

Ground clutter strength depends principally on the depression angle at which the backscattering terrain point is illuminated as it varies with terrain elevation from point to point over a site. The simple, non-patchy, non-site-specific clutter model does not incorporate local variability in terrain elevation and hence would be able to bring in depression angle only as a very slowly diminishing function with increasing range on a spherical earth. Is this small rate of change of illumination angle with range sufficient to cause an observable general dependence of clutter strength with range in measured data?

To begin to answer this question, consider again the measured clutter maps of Figure 4.6. These measurements are shown at full Phase Zero sensitivity. When the clutter in the maps is shown only above a gradually increasing threshold in clutter strength, except at very close ranges the density of the clutter sources within patches gradually diminishes relatively uniformly over the remainder of the map at longer ranges, indicating that within patches of visibility, clutter strength is relatively independent of range beyond the first few kilometers (e.g., see Figure 4.19). That is, the clutter does not disappear at the longer ranges first. Sector display plots of clutter amplitude vs range such as are shown in Figures 2.10, 2.18, 2.20, and 3.11 also do not indicate any general diminishment of clutter strength with range through patches of clutter occurrence. This matter is discussed further in Appendix 4.A, in which similar sector display plots are shown to much longer ranges.

Results generalizing the lack of range dependency in clutter are provided in Figure 4.11. Clutter amplitude statistics combined from 10 different sites are separated into four annular regimes of range—from 5 to 15 km, 15 to 25 km, 25 to 35 km, and 35 to 45 km. Care must be taken to properly normalize the results. First, because the amount of clutter rapidly

diminishes with increasing range, only those cells in which discernible clutter are measured above the radar noise floor are included. Second, because radar sensitivity diminishes with increasing range, the results are normalized to range-independent sensitivity by further conditionally limiting included cells to only those in which clutter signals are stronger than system noise at the longest ranges, that is $\sigma^\circ F^4 > -24$ dB. The results of Figure 4.11 indicate that there is essentially no dependence with range in the resulting clutter amplitude statistics. These results are discussed further in Appendix 4.C.

Because clutter strength shows no major dependence upon range, $\overline{\sigma_w^\circ}$ in the simple non-patchy model abruptly transitions from a constant nonzero m^2/m^2 value within R_C to zero m^2/m^2 beyond R_C. This abrupt transition keeps before the user the simple non-site-specific nature that was initially postulated as a requirement of the model in the results of system studies implementing the model. When step function performance characteristics are unacceptable, it is not realistic to arbitrarily decrease clutter strength $\overline{\sigma_w^\circ}$ with increasing range in the simple model to introduce more acceptable, continuous characteristics with range and avoid step function characteristics. In reality, it is the spatial occurrence of clutter, not its strength, that diminishes with range.

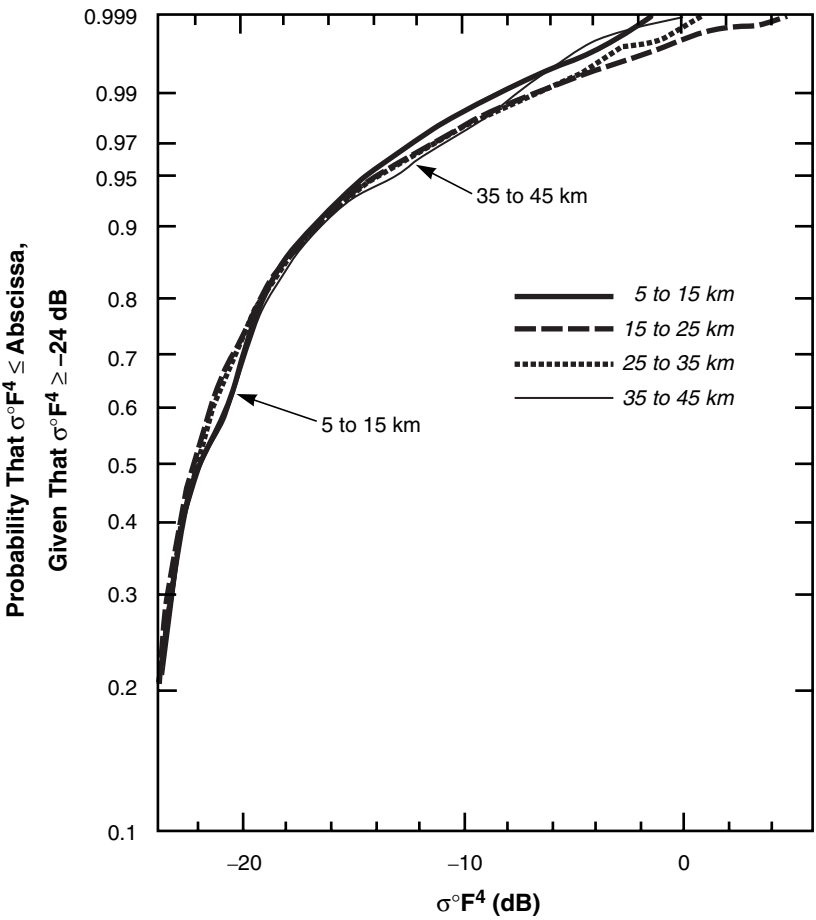

FIGURE 4.11 Clutter amplitude statistics in four regimes of range.

It is certainly incorrect to simply multiply the clutter strength by the visibility function to provide what may be thought to be a more desirable modeling characteristic of diminishing clutter strength with increasing range. Such a procedure involving azimuthal averaging (i.e., spatial dilution of clutter with macroshadow) is only applicable to an unrealistic radar with a 360° omnidirectional azimuth beam [in such circumstances, it is the *shadowless* mean that is multiplied by the visibility function; see Appendix 4.C for further discussion of this matter, in particular, Eq. (4.C.4) and Figures 4.C.16 and 4.C.17)].

Thus when step function performance characteristics are unacceptable, a more sophisticated clutter model incorporating a gradually diminishing clutter occurrence or visibility function must be employed. The site-specific clutter model discussed in Section 4.2 incorporates gradually diminishing terrain visibility with increasing range as determined by line-of-sight geometric terrain visibility in DTED. In addition, a patchy non-site-specific clutter model was developed [3] by the Defence Evaluation and Research Agency/U.K. which conducted analyses of some subsets of Phase One clutter data coordinated with Lincoln Laboratory. The patchy non-site-specific clutter model was based on the empirically observed exponential decrease of clutter visibility with range as shown in Figures 4.8(a) and 4.10 to provide stochastic realizations of random patchiness representative of a particular type of terrain, as opposed to deterministic site-specific realizations of patchiness. In the stochastic approach to patchiness, the characteristics of the terrain that determine the patchiness are obtained by processing DTED over the general terrain of interest. Such stochastic techniques for providing non-site-specific patchiness in a clutter model are more appropriate for low-relief terrain, as high-relief terrain is too specific in terms of dominant terrain features within the radar coverage area to be properly characterized as a random process.

4.3.3.2 Spread in Clutter Amplitude Statistics

Ground clutter amplitude distributions have wide spread resulting from cell-to-cell spatial variation within macropatches of clutter occurrence. This wide spread is illustrated by the data in Figure 4.12, which show percentile levels between 50 and 90 in ground clutter amplitude distributions both for general terrain and for the three primary terrain types. Each percentile value plotted in Figure 4.12 is the median of the set of corresponding individual percentiles from all clutter patches of that class within the overall set of 2,177 clutter patch amplitude distributions. Figure 4.12 typically shows about 16 dB of variation between 50- and 90-percentile levels. Furthermore, this figure also shows that the mean value, indicated by a vertical arrow, is usually close to the 90-percentile level (except for rural/high-relief terrain in which illumination angles are higher and hence the influence of discrete sources, which tend to dominate the mean, are reduced).

Should a percentile level lower than the mean be used in selecting a value for σ_w° in the simple model? This question has no simple answer. The data displayed in Figure 4.12 illustrate the conceptual difficulty of modeling a widely varying dynamic random process with a single deterministic number. However, some guidance may be offered toward answering this question. In a system study simulating the existence of low-altitude targets at a number of Phase One clutter measurement sites, the resultant radar performance, averaged over all sites, was approximately the same as would be computed if a constant clutter strength of σ_w° = –38 dB was used over all visible terrain. This value of clutter strength occurs at the 70-percentile level on the general terrain curve of Figure 4.12, approximately halfway between the mean and the median. Recall that the most probable

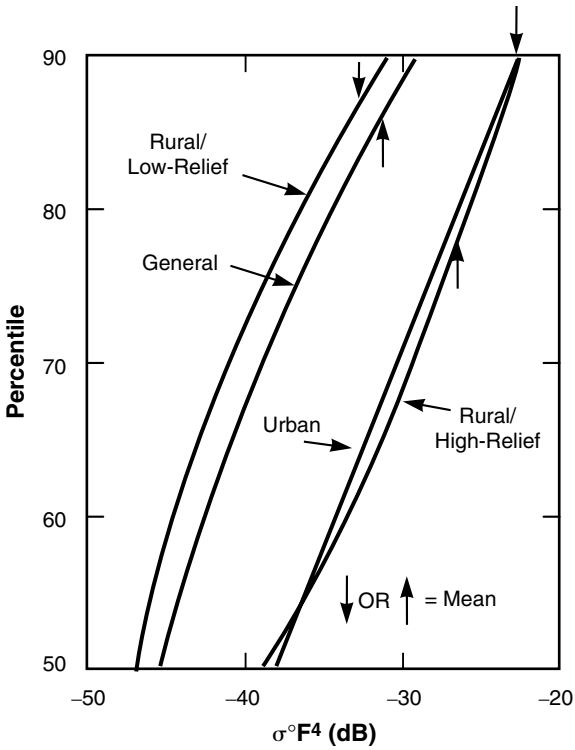

FIGURE 4.12 Clutter strength as a function of percentile level in the amplitude distribution.

value of mean clutter strength in the general data of Figure 4.8(b) is −40 dB, perhaps a fortuitous concurrence. The reader is cautioned that this is a particular result of only one study and that such values of constant-σ° that provide equivalent system performance as real clutter (or site-specifically simulated clutter) are highly specific to the particular radar system and performance parameters under consideration. In any case, the data of Figure 4.12 allow investigators to adjust modeling values of σ_w° away from the mean values shown in Table 4.4, if they so desire.

4.3.3.3 Database Depth

The easy-to-use data for R_C and $\overline{\sigma_w^\circ}$ in Tables 4.3 and 4.4 capture the most important first-level effects contained in the large database of measurements for simple non-site-specific modeling applications. Consideration of higher-order effects can provide ever-increasing specificity of information. For example, consider the distributions of mean strength in six classes of landform and land cover provided earlier in Figures 2.23 and 2.24, respectively. One can imagine similar distributions by landform and land cover for median strength or for other statistical measures of the patch amplitude distributions. The data in Tables 4.5 and 4.6 provide quantitative measures of distributions of means, ratios of standard deviation-to-mean, medians, and various percentile levels, by landform and land cover, respectively. Thus the data of Tables 4.5 and 4.6 may be drawn upon to expand the simplified information of Table 4.4 to other probabilities of occurrence, other measures of strength (e.g., median), and other landform and land cover types

The statistical attributes shown in the second column of Tables 4.5 and 4.6 are now defined more explicitly. Observe in Figures 2.23 and 2.24 that the distributions are approximately lognormal. As a result, it is useful to define the mean and standard deviation of the normally distributed logarithmic quantity. These two quantities are shown as the first (i.e., top-most) and second attributes for each patch amplitude statistic. The third attribute shown is the median, which itself just transforms logarithmically. If the logarithmic quantity is normally and hence symmetrically distributed, its mean and median must be identical. The data in Tables 4.5 and 4.6 indicate that these two quantities (i.e., the first and third attributes, respectively) are, indeed, often nearly equal. Once it is assumed that the distribution is approximately lognormal, all other attributes of the distributions of both the logarithmic quantity and the more fundamental underlying linear quantity immediately follow from the first and second attributes provided in Tables 4.5 and 4.6. However, the fourth and final attribute for each patch amplitude statistic shown is the actual empirical mean of the basic linear quantity, which can be used either directly in its own right or as a further check on the degree of goodness of the approximating lognormal distributions.

Now consider some of the trends with landform contained in the data of Table 4.5, where terrain slopes rise monotonically with landform class, left to right, from less than 1° for level terrain to between 10° and 35° for steep terrain (see Figure 2.23). Consider the median of M samples within a particular landform class of a given statistic (e.g., mean) of a clutter amplitude distribution as an easy-to-understand attribute, in that half the samples occur above the median level and half below. The median attribute is shown in increasing order of landform as the third row of numbers for each patch amplitude statistic in Table 4.5. Thus, as terrain slopes rise from level to steep, the third rows of the table show that (1) mean strengths rise over the 10-dB range from –33 to –23 dB; (2) median strengths rise over the 15-dB range from –48 to –33 dB; (3) spreads in amplitude distributions as measured by ratio of standard deviation-to-mean fall from 7 to 3 dB, spreads as measured by ratio of 99.9- to 50-percentile fall from 33 to 22 dB, and spreads as measured by ratio of mean-to-median fall from 15 to 10 dB. All the trends are monotonic with increasing terrain steepness as specified by the median value from a large number M of individual patch measurements within each landform class.

In considering increasing specificity of information, recall that all the non-site-specific information presented in this section has been derived from X-band measurements. However, when considering that mean strengths from the three general terrain types of rural/low-relief, rural/high-relief, and urban are largely frequency independent, and that the simple model is already averaging out much fine-scaled variation, it is not unrealistic to apply the simple model across the general microwave regime. Investigators who wish to introduce more specific frequency dependence in non-site-specific investigation may, as a beginning, be guided by the multifrequency mean data of Table 4.2.

4.3.4 Summary

The considerations guiding the development of the simple, non-angle-specific clutter modeling information presented in Section 4.3 are now summarized. The objective is to invest a simple clutter model with important general attributes as they have come to be understood in investigating the large database of clutter measurements. Of first-order importance is to distinguish between where the clutter occurs and its strength, given that it occurs. The simple, non-patchy model of Section 4.3.2 maintains this distinction by first specifying clutter cut-off range based on the measurements of clutter visibility, and then

TABLE 4.5 Various Average Measures of Ensembles of Clutter Patch Amplitude Statistics by Landform

Patch Amplitude Statistic	Attribute of Set of Patch Amplitude Statistics over M Patches	Landform					
		Level	Undulating	Inclined	Rolling	Mod Steep	Steep
Mean $\overline{x}^m$	$\overline{\overline{x}}\|_{dB}^{M}$	-33.1	-32.0	-30.2	-28.9	-26.4	-22.8
	$SD\left(\overline{x}\|_{dB}\right)^{M}$	6.9	6.1	5.9	4.8	4.7	5.1
	$\left(\overline{x}\|_{dB}\right)_{50}^{M}$	-33.0	-32.0	-30.0	-29.0	-26.0	-23.0
	$\overline{\overline{x}}^{M}\|_{dB}$	-23.9	-26.6	-26.7	-26.0	-24.5	-19.7
Standard Deviation to Mean x_σ^m	$\overline{x}_\sigma\|_{dB}^{M}$	7.3	7.0	6.0	4.6	3.9	2.9
	$SD\left(x_\sigma\|_{dB}\right)^{M}$	2.9	3.1	2.8	2.1	2.1	1.9
	$\left(x_\sigma\|_{dB}\right)_{50}^{M}$	7.0	7.0	5.0	4.0	4.0	3.0
	$\overline{x}_\sigma{}^{M}\|_{dB}$	8.4	8.2	7.0	5.2	4.5	3.3
Median x_{50}^m	$\overline{x}_{50}\|_{dB}^{M}$	-47.5	-45.8	-42.7	-41.4	-38.1	-35.0
	$SD\left(x_{50}\|_{dB}\right)^{M}$	6.8	7.5	8.7	9.3	10.3	12.6
	$\left(x_{50}\|_{dB}\right)_{50}^{M}$	-48.0	-46.0	-44.0	-42.0	-36.0	-33.0
	$\overline{x}_{50}{}^{M}\|_{dB}$	-41.1	-39.3	-35.1	-33.1	-30.0	-24.5
nth Percentile to 50 Percentile $x_{n/50}^m$ n = 90,99,99.9	$\overline{x}_{n/50}\|_{dB}^{M}$	14.4, 26.2, 32.7	14.9, 25.2, 31.6	14.8, 23.6, 29.1	16.4, 23.1, 27.3	15.6, 21.8, 25.6	16.4, 22.0, 24.1
	$SD\left(x_{n/50}\|_{dB}\right)^{M}$	5.9, 7.0, 8.4	5.2, 6.9, 8.6	5.4, 7.6, 9.2	7.0, 8.0, 8.6	7.7, 9.0, 9.7	10.2, 11.5, 12.2
	$\left(x_{n/50}\|_{dB}\right)_{50}^{M}$	14.0, 26.0, 33.0	14.0, 25.0, 32.0	15.0, 23.0, 29.0	16.0, 23.0, 27.0	14.0, 20.0, 24.0	13.0, 19.0, 22.0
	$\overline{x}_{n/50}{}^{M}\|_{dB}$	19.1, 32.8, 40.6	18.5, 30.6, 39.5	18.1, 30.2, 38.0	22.5, 29.8, 34.7	23.4, 30.6, 36.2	27.2, 34.4, 37.5
Number of Patches M		571	556	338	216	152	94

TABLE 4.6 Various Average Measures of Ensembles of Clutter Patch Amplitude Statistics by Land Cover

Patch Amplitude Statistic	Attribute of Set of Patch Amplitude Statistics over M Patches	Land Cover					
		Wetland	Rangeland	Agricultural	Forest	Barren	Urban
Mean $\overline{x}^m$	$\overline{\overline{x}}\|_{dB}^{M}$	-37.5	-32.0	-31.8	-30.7	-29.1	-22.4
	$SD\left(\overline{x}\|_{dB}\right)^{M}$	4.9	6.0	5.1	7.3	7.8	7.0
	$\left(\overline{x}\|_{dB}\right)_{50}^{M}$	-38.0	-32.0	-31.0	-30.0	-29.0	-23.0
	$\overline{\overline{x}}^{M}\|_{dB}$	-34.6	-27.5	-28.5	-26.2	-22.3	-16.7
Standard Deviation to Mean x_σ^m	$\overline{x}_\sigma\|_{dB}^{M}$	5.5	5.8	7.9	4.3	6.6	7.1
	$SD\left(x_\sigma\|_{dB}\right)^{M}$	2.0	2.8	2.9	2.2	3.4	2.3
	$\left(x_\sigma\|_{dB}\right)_{50}^{M}$	5.0	5.0	8.0	4.0	6.0	7.0
	$\overline{x}_\sigma{}^{M}\|_{dB}$	6.1	6.8	8.9	5.0	8.2	7.7
Median x_{50}^m	$\overline{x}_{50}\|_{dB}^{M}$	-48.3	-44.7	-47.2	-41.5	-42.4	-39.0
	$SD\left(x_{50}\|_{dB}\right)^{M}$	6.6	8.1	6.8	10.3	10.1	8.1
	$\left(x_{50}\|_{dB}\right)_{50}^{M}$	-48.0	-46.0	-47.0	-43.0	-45.0	-38.0
	$\overline{x}_{50}{}^{M}\|_{dB}$	-42.3	-36.6	-41.0	-31.3	-29.4	-32.7
nth Percentile to 50 Percentile $x_{n/50}^m$ n = 90,99,99.9	$\overline{x}_{n/50}\|_{dB}^{M}$	13.5, 22.5, 27.3	15.2, 23.7, 29.0	15.5, 27.1, 34.3	14.4, 21.4, 25.1	14.2, 24.3, 30.2	16.3, 29.2, 34.8
	$SD\left(x_{n/50}\|_{dB}\right)^{M}$	4.7, 5.7, 6.3	6.6, 7.7, 9.0	5.8, 6.5, 7.8	6.4, 7.6, 8.4	7.3, 8.5, 9.8	5.3, 8.2, 9.6
	$\left(x_{n/50}\|_{dB}\right)_{50}^{M}$	13.0, 22.0, 27.0	14.0, 23.0, 29.0	15.0, 27.0, 35.0	13.0, 21.0, 24.0	12.0, 23.0, 31.0	16.0, 29.0, 36.0
	$\overline{x}_{n/50}{}^{M}\|_{dB}$	16.7, 26.2, 31.3	21.9, 31.0, 38.6	19.7, 32.2, 40.6	20.6, 28.4, 33.0	22.6, 31.6, 39.0	20.6, 35.8, 43.4
Number of Patches M		92	371	788	684	115	122

specifying clutter strength based on measurements of clutter amplitude statistics within macropatches of occurrence. Furthermore, this model brings in the important parameters of radar height as it influences clutter extent and terrain type as it influences clutter strength. In this empirical manner, the model maintains its focus on the important first-level parameters in the real clutter phenomenon and statistically provides baseline central values of clutter strength and extent as they occur at real sites.

The simple model does more than this, however. In addition to providing central measures, the model also specifies the distributions. As a result, besides providing information on baseline values of strength and extent of clutter, the model also provides parametric information on how severe (i.e., strong clutter to long-range) or how benign (i.e., weak clutter to short-range) the clutter can become, all in terms of specifiable probability of occurrence. It is this depth of statistical information in the simple model incorporating the extreme variability of the clutter phenomenon in quantitative terms of probability of occurrence, more so than the baseline central values of the model, that sets it apart from other single-point approaches in the literature.

4.4 Terrain Visibility and Clutter Occurrence

Figure 4.10 in Section 4.3.2 shows percent of circumference in discernible clutter as a function of range for five regimes of effective radar height, as measured by the Phase Zero radar with a mast height of 15 m. These clutter occurrence curves of Figure 4.10 may be compared with those of Figure 4.B.3 (in Appendix 4.B) which show percent of circumference over which terrain is visible, also from a mast height of 15 m and as a function of range, for four regimes of site advantage. The occurrence of clutter (Figure 4.10) is strongly tied to line-of-sight visibility to terrain (Figure 4.B.3). That is, clutter occurs primarily within visible terrain macroregions in which discrete clutter sources are separated by randomly occurring microshadowed cells where the radar is at its noise level. Because of the microshadowing that occurs within macroregions of general visibility, the spatial extent of terrain visibility is greater than, and can be much greater than, the spatial extent of discernible clutter, as is apparent in comparing the curves of Figure 4.B.3 with those of Figure 4.10.

Figure 4.13 shows the same terrain characterized by DTED obtained from two different sources, cartographic (maps) and photogrammetric (aerial photos). It is evident that photogrammetric source DTED are more precise and provide fine-scale terrain detail not contained in the cartographic source DTED. The cartographic source DTED capture the basic first-order characteristics of the terrain land-surface form, and are highly suitable for distinguishing macroregions of visible terrain from macroregions of shadow. The increased precision of photogrammetric source DTED may begin to allow deterministic prediction of microshadowed cells within macroregions of visibility. However, land cover elements are much more involved as the predominant sources of microshadow, as is seen in the following Cold Lake results.

4.4.1 Effects of Trees on Visibility at Cold Lake

Trees are often dominant components of land cover affecting low-angle clutter (see Chapter 2, Section 2.4.2.5). Figure 4.14 shows the dramatic effect on clutter visibility of

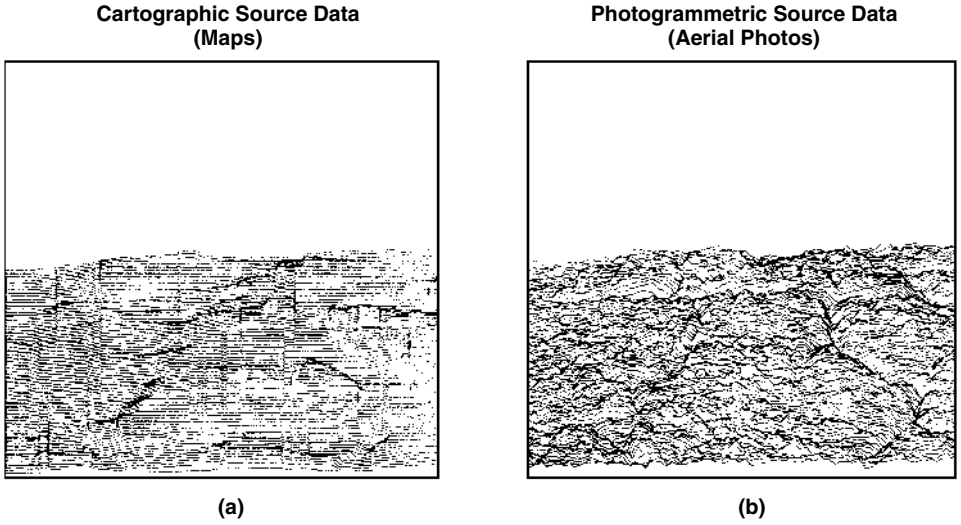

FIGURE 4.13 Three-dimensional oblique views of the same terrain characterized by digitized terrain elevation data derived from two sources: (a) maps and (b) aerial photos. The terrain shown is a common 30 km × 30 km test area.

predicting tree heights in individual spatial cells at the measurement site of Cold Lake, Alberta. These results incorporate cell-specific tree cover information derived from Landsat data to obtain a more precise and accurate clutter map prediction.

Figure 4.14(a) shows terrain elevation contour plots at 20-m intervals at Cold Lake, obtained from cartographic source DTED which does not include tree heights. In the northeast quadrant of this plot, the large level surface at 540-m elevation is water, the surface of Cold Lake. Four small islands are visible in the southern part of the lake. Figure 4.14(b) shows geometric visibility to bare ground (or water) based on these DTED. In Figure 4.14(b), visible areas of the ground are shown as black, and masked or shadowed areas of the ground are shown as white. Large continuous regions of the ground, including much of the surface of Cold Lake itself, are indicated as being within line-of-sight visibility in Figure 4.14(b). Figure 4.14(c) shows the Phase Zero ground clutter measurement at Cold Lake. The Cold Lake area in north-central Alberta is generally forested, although considerable regions have been cleared for farming. Within the large continuous black macroregions of visibility of Figure 4.14(b), actual clutter sources of $\sigma°F^4 \geq -30$ dB occur as black micropatches in Figure 4.14(c), interspersed with a considerable degree of white microshadowing.

Figure 4.14(d) shows how geometric visibility to the ground is modified by cell-specific inclusion of the occurrence of trees on the landscape. Landsat data for the Cold Lake area were classified in a scheme that included deciduous and coniferous tree categories. These data were registered with the terrain elevation data at Cold Lake. Each DTED cell that Landsat indicated as containing trees was increased in effective masking elevation by a statistical increment to account for the tree heights. A Gaussian statistical tree height increment was used such that: (1) mean height = 20 m, standard deviation = 0.9 m, for deciduous classification; and (2) mean height = 25 m, standard deviation = 1.8 m, for coniferous classification.

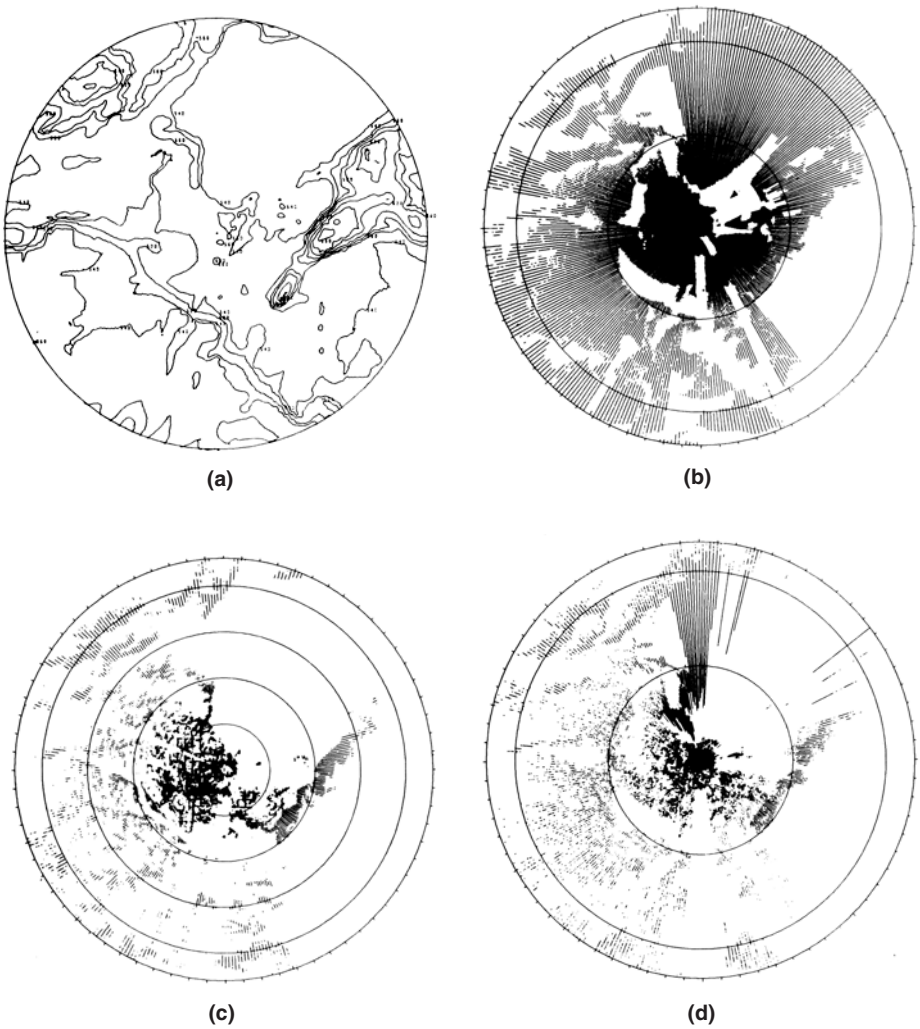

FIGURE 4.14 Effects of tree heights on ground clutter visibility at Cold Lake, Alta. The maximum range in each plot is 23.5 km. (a) terrain elevation contour plot, 20-m intervals; (b) geometric visibility to ground (black), no trees; (c) Phase Zero ground clutter measurement, $\sigma\,°F^4 \geq -30$ dB, 75-m range resolution; (d) geometric visibility to ground (black), with Landsat trees.

Including the effects of tree heights on terrain visibility in Figure 4.14(d) in this way greatly changes the character of the bare ground visibility map of Figure 4.14(b), mainly by introducing cell-specific microshadowing effects within large macroregions of visibility. The bare-earth model at Cold Lake [Figure 4.14(b)] shows much higher terrain visibility than when trees are accounted for [Figure 4.14(d)]. Much of the water surface of Cold Lake itself, indicated as visible without trees in Figure 4.14(b), becomes shadowed when trees are included in Figure 4.14(d). Whether shadowed or not, the water surface of Cold Lake is below the clutter strength threshold in Figure 4.14(c) and is indicated as white there. Thus, careful incorporation of site-specific and cell-specific variations in elevation, for example, due to trees, can account for much detailed feature in a measured

ground clutter map, based on geometric visibility considerations alone without any recourse to propagation or scattering physics.

4.4.2 Decreasing Shadowing with Increasing Site Height

Although there exists much correlation in terms of general features between the measured Cold Lake clutter map of Figure 4.14(c) and the predicted map inclusive of tree height effects of Figure 4.14(d), careful examination indicates that on a more detailed cell-by-cell basis the correlation in these maps deteriorates. Successful reduction of clutter measurement data in a cell-specific manner in which measured clutter strength in a cell is associated with cell-specific geometric effects such as tree height and grazing angle would require terrain descriptive Geographic Information System (GIS) data of very high precision and accuracy.

The reduction of measured clutter data as described in this book uses available DTED more simply to predict boundaries of macroregions of general terrain visibility, which are denoted as clutter patches. Then all of the measured clutter data within the boundaries of the specified patch, including cells at radar noise level, are assembled in a histogram of clutter strengths associated with the patch. Figure 4.15 shows six such measured histograms, one for each of six different sites (including Cold Lake) in order of increasing effective radar height. In these histograms, the 50-, 90-, and 99-percentile levels are shown as vertical dotted lines; the mean strength is shown as a vertical dashed line; and bins to the left side of the histogram that are significantly contaminated by radar noise samples are doubly underlined. Figure 4.16 shows the cumulative distributions above the highest noise contaminated bin for each of these six patches. Table 4.7 shows the incidence of microshadowing within each patch and its effect on the mean clutter strength of the patch. For example, the incidence of microshadowing for the Cold Lake patch for which the clutter strength histogram is shown in Figure 4.15(c) is 35%.

It is evident in these results that the incidence of microshadowing within clutter patches decreases rapidly with increasing effective radar height. At low sites such as Coaldale and Shilo, the incidence of microshadowing can be very high (74% at Coaldale), but even so the mean clutter strength of the patch as determined within the upper- and lower-bound limits remains accurate (to within 0.014 dB at Coaldale). The mean strength of the patch determined in this manner includes the effects of microshadowing and is accurate independent of the sensitivity of the measurement radar; so also is the cumulative distribution for the patch (above the highest noise contaminated bin) as is shown in Figure 4.16 and from which the Weibull shape parameter a_w is obtained. The shadowless mean clutter data shown in Table 4.7 which do not include samples within the histogram at radar noise level are highly dependent on the particular sensitivity of the measurement radar utilized and are not generally useful in clutter modeling (although such data are often inappropriately used in the existing clutter literature).

4.4.3 Vertical Objects on Level Terrain at Altona

Prediction of clutter strengths based on the information provided in this book proceeds on the basis of many measured patch histograms and cumulative distributions of clutter strength such as are shown in Figures 4.15 and 4.16. Given the occurrence of a visible terrain macroregion, the subsequent distribution of modeled clutter over the region is specified as a broad Weibull distribution of appropriate shape parameter a_w that includes the distribution of microshadowed cells at the correct incidence of occurrence as Weibull

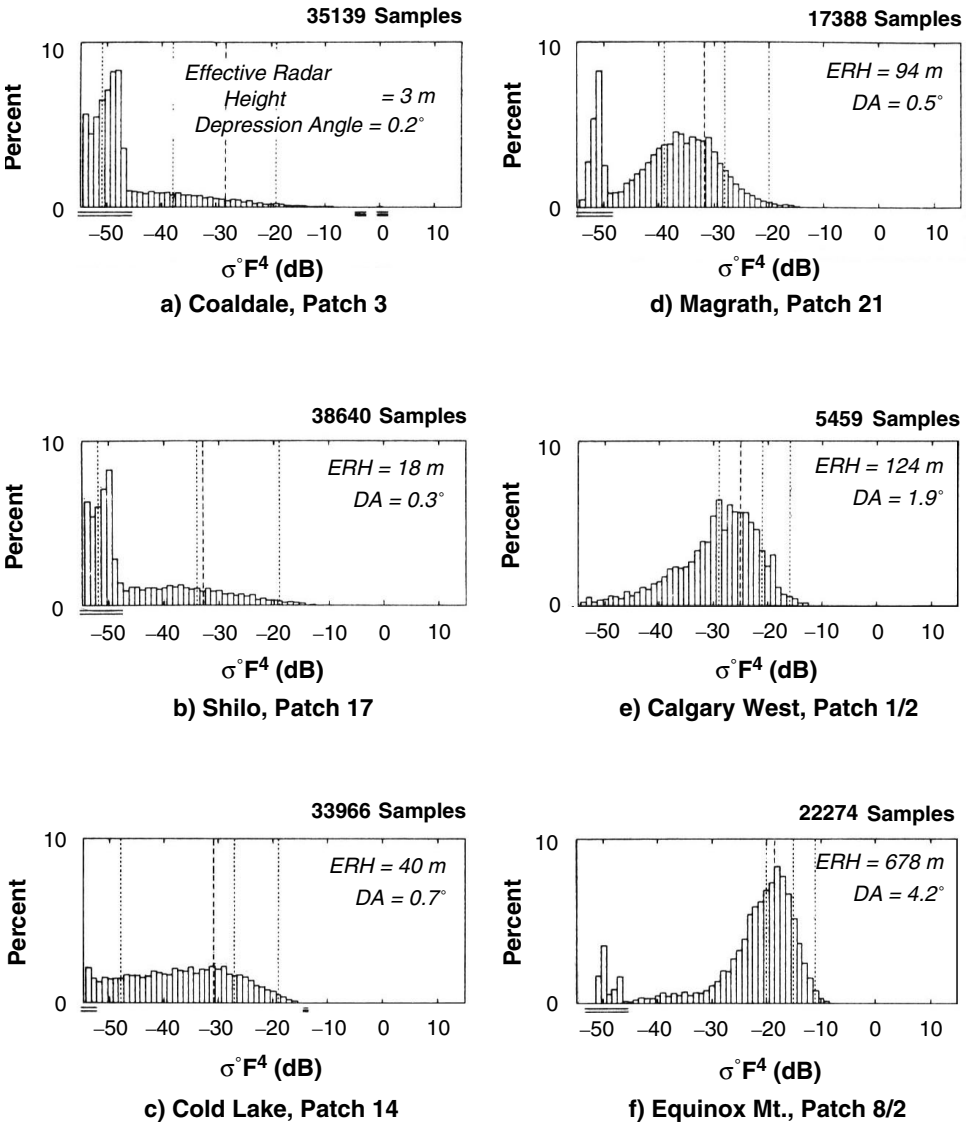

FIGURE 4.15 Clutter strength histograms for six patches selected from sites in different regimes of effective radar height. Phase Zero data, 75-m range resolution.

values below the noise level of the radar under investigation. Not only is the prediction of patch mean strength independent of radar sensitivity, but the incidence of microshadowing that is predicted is appropriate to the sensitivity of the radar under investigation, which can be different from that of the measurement radar. The predicted microshadowed cells within the patch for which clutter is being predicted occur randomly within the patch. Prediction of clutter in this manner thus proceeds accurately without being dependent on the availability of highly precise and accurate cell-specific GIS terrain descriptive data.

For low-relief sites at short ranges where terrain visibility is very high (e.g., Figure 4.B.3, range < 10 km, site advantage regime = 10 to 35 m), visibility of discernible clutter is very

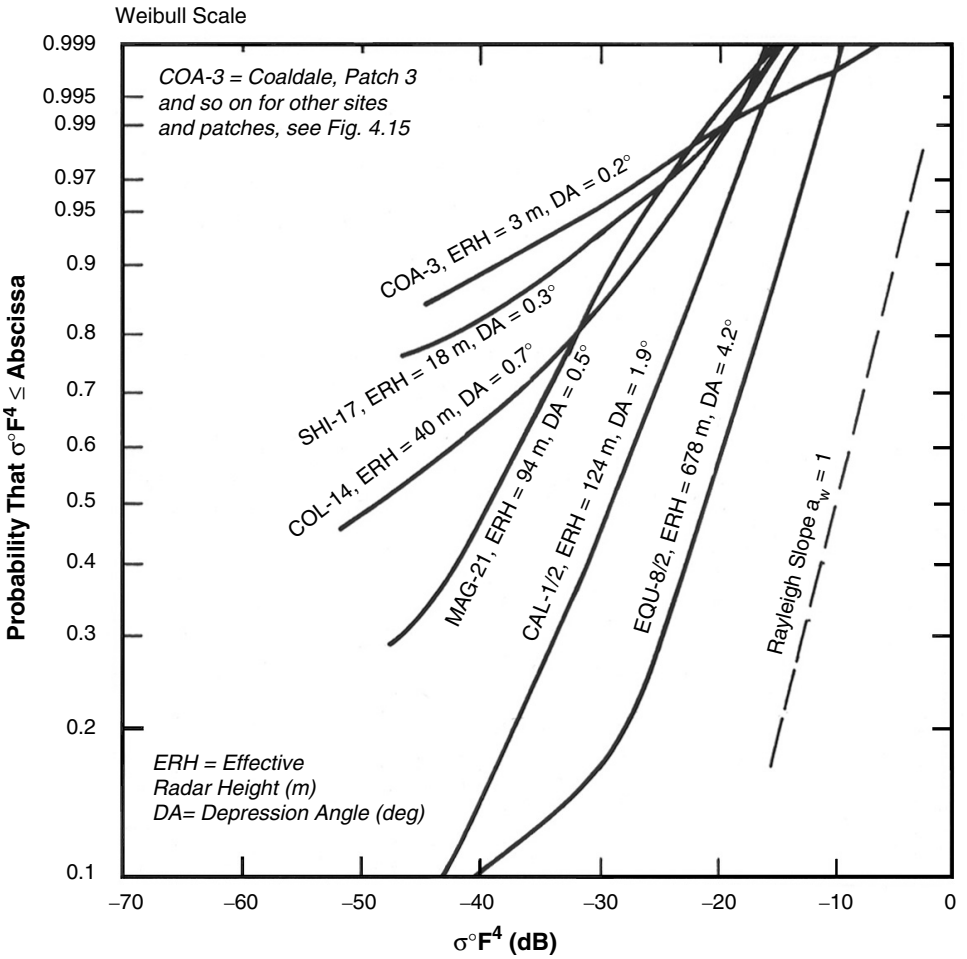

FIGURE 4.16 Six clutter patch cumulative amplitude distributions from sites in different regimes of effective radar height. Phase Zero data, 75-m range resolution.

low (e.g., Figure 4.10, range < 10 km, effective radar height = 0 to 30 m). The reason for this can be seen in the PPI clutter map for Altona II shown in Figure 4.17. The terrain at Altona II is very level cropland, much like that at Coaldale [see Figure 4.15(a)]. From the 15-m Phase Zero antenna mast height, virtually all of the terrain within the 6-km maximum range clutter map of Figure 4.17 is predicted as visible using bare-earth DTED to model the Altona II terrain surfaces. Yet only within the nearest 1 or 2 km is the Phase Zero radar generally sensitive to the backscatter from these terrain surfaces. The several white sectors within the central black region are due to local masking by clusters of trees near the radar site. At longer ranges, it is the vertical objects on the terrain associated with the land cover that constitute strong backscatter sources. Many of these are associated with individual farmsteads and trees around farmsteads, although roads, rail lines, power line pylons, and stream beds are also sources of discernible clutter. The predominant rectangular pattern is associated with vertical objects along field boundaries. The reason backscatter from the field surfaces, as opposed to that from vertical objects on the fields, is weak and generally below the sensitivity of the measurement radar is partly because the illumination occurring

TABLE 4.7 Influence of Effective Radar Height on Incidence of Microshadowing for Six Clutter Patches

Site	Effective Radar Height (m)	Clutter Patch Number	Percent of Micro-shadowed Cells[a]	Mean Clutter Strength $\overline{\sigma^{\circ} F^4}$ (dB)[b]		
				Upper Bound[c]	Lower Bound[d]	Shadow-less[e]
Coaldale	3	3	74.4	-28.332	-28.346	-22.428
Shilo	18	2	62.7	-32.808	-32.831	-28.548
Cold Lake	40	14	34.5	-30.781	-30.784	-28.946
Magrath	94	21	25.2	-31.770	-31.770	-30.517
Calgary West	124	1/2	2.3	-25.270	-25.270	-25.169
Equinox Mt.	678	8/2	8.3	-19.499	-19.499	-19.123

[a] Microshadowed cells are defined to be cells within patches at radar noise level.
[b] Computed in units of m^2/m^2 and subsequently converted to dB.
[c] Assign noise power level to noise cells.
[d] Assign zero power level to noise cells.
[e] Noise cells deleted.

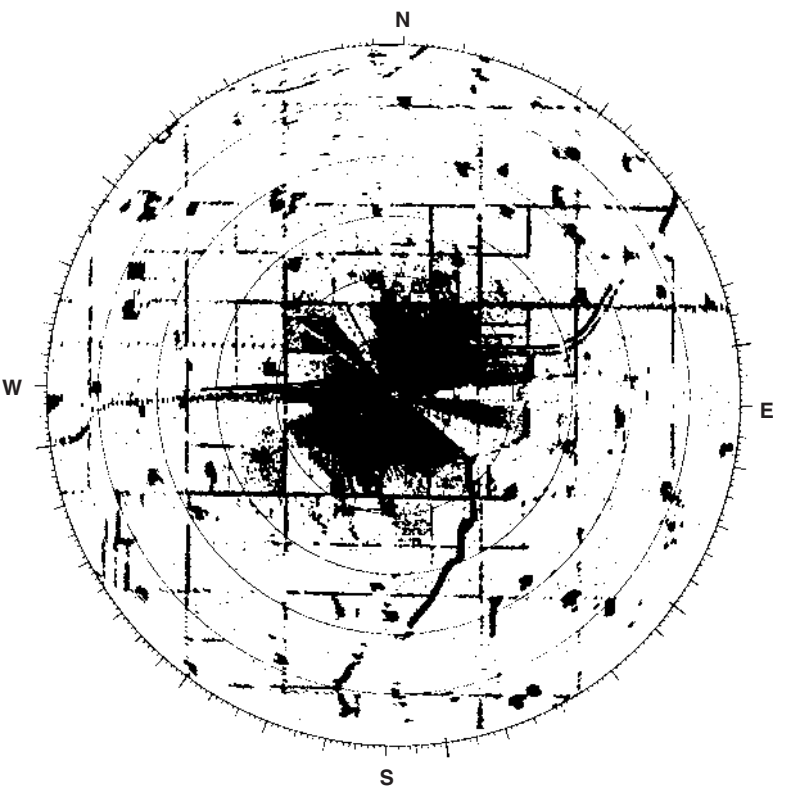

FIGURE 4.17 High resolution clutter map at Altona II, Manitoba. Phase Zero X-band data, 6-km maximum range setting, 9-m range resolution. The clutter map is 3 dB from full sensitivity. Clutter is black. North is zenith.

beyond 1 or 2 km is very close to grazing incidence and partly because many of these low surfaces are shadowed by land cover features not included in DTED (e.g., road and rail beds) that are a few feet higher than the field surfaces proper.

Thus, all of the terrain in Figure 4.17 is within geometric line-of-sight visibility as modeled with DTED, yet the clutter sources are predominantly vertical objects associated with land cover as they exist distributed over this nominally visible terrain. As a result, the extent of discernible clutter (black) in Figure 4.17 is much less than the extent of nominally visible terrain, and a very high incidence of white microshadowed cells occurs between the black clutter cells.

4.4.4 Summary

Determination of geometric terrain visibility in a bare-earth faceted terrain model based on DTED predicts general terrain regions in which clutter sources occur. Predicting the existence of clutter thus arises from a set of conditional probabilities, in which the first and most important condition for the existence of clutter at some spatial position is for that position to be geometrically visible. Consider again (see Section 4.3.1) that the probability of discernible clutter P_c is given by the probability that the terrain is geometrically visible P_v times the probability P_D that the clutter strength is discernible, given that the terrain is visible. As discussed in Section 4.3.1, P_D is easily numerically evaluated, once the Weibull coefficients of the clutter and the noise level of the radar are specified.

Further conditions on clutter discernibility, in addition to the radar sensitivity at the point under consideration, are those associated with land cover, as discussed for Altona II and Cold Lake, or conditions associated with propagation. For example, as discussed in Chapter 3, at low radar frequencies such as VHF, little clutter may be received from low-relief terrain because terrain reflections prevent illumination of the terrain, even though it is within line-of-sight. Or some VHF clutter may be received from regions somewhat beyond geometric visibility due to diffraction, if the radar sensitivity is high enough to discern relatively weak clutter (clutter strength for shadowed terrain depends on depth of shadow; see Appendix 4.D). The Phase One clutter data indicate that determination of bare-earth terrain visibility is the most useful first step in understanding the spatial occurrence of ground clutter, even at VHF. Effective radar height is the single most useful parameter combining site height and mast height for specifying the extent in range to which clutter occurs.

Increasingly precise and accurate terrain descriptive GIS data together with ever more available computational power will allow increasingly accurate future specification of the landform and land cover contents of individual clutter cells. Even with such increased information, the extreme complexity of terrain will likely always require that the prediction of clutter strength from a cell (as opposed to the visibility of the cell) be based on a statistical approach. Whatever the level of fidelity of the available terrain descriptive information, it is evident from the Cold Lake and Altona II results that geometrical considerations dominate the low-angle ground clutter phenomenon, and a realistic approach to clutter prediction needs to involve prediction of geometric terrain visibility as a first step, followed by a statistical determination of clutter strength based on terrain relief and the available land cover information. Although geometry is of first-order importance in this process, once the realistic geometry is specified for a given radar observing the contents of a given visible cell over a given profile, then as a higher-order matter considerations of

propagation, scattering, and absorption physics can be brought to bear to provide increased understanding of the clutter strength phenomenon for that cell. But it is apparent that attempts to model low-angle clutter based on propagation and scattering physics applied as a first step to simplified or canonical representations of the earth that do not take into account specificities of geometry are foreordained to be exercises of the imagination.

4.5 Discrete vs Distributed Clutter

4.5.1 Introduction

It has long been recognized that ". . . dominant land clutter signals are from discrete isolated targets . . . "[4]. This section addresses important considerations involving the modeling of discrete clutter, as opposed to that of distributed clutter. A discrete clutter cell is an occasional, unusually strong, spatially isolated clutter cell for which the strong return is typically associated with some large physical point object in the cell. Discrete clutter is also occasionally referred to as point clutter or specular clutter in the literature. In contrast, distributed clutter is considered to be extensive in area over the clutter-producing surface rather than being associated with particular points on the surface.

Before taking up the subject of approaches to modeling discrete clutter, it is necessary to first distinguish between conceptual models and empirical models. A conceptual clutter model is defined here as a hypothetical construct of the imagination that attempts to match selected important observed features in measured clutter data. On the other hand, an empirical clutter model is tied more tightly to direct trend analyses in actual measured clutter data, where the parametric trends observed in the data and their logical interrelationships and consequences themselves constitute the predictive clutter model. An empirical model is based on reduction and analysis of measured clutter data, whereas a conceptual model can be postulated apart from measured data. In the empirical approach, any preconceived parametric relationships arising from postulated conceptualized modeling constructs that cannot be verified to exist in the measured clutter data are not allowed to have a place in the final empirical modeling apparatus. This book takes an empirical approach to generating clutter modeling information, including the modeling of discrete clutter.

Discrete clutter was early addressed as being of serious systems consequence in land clutter in airborne radar. As discussed in Chapter 2 (see Sections 2.3.4.2 and 2.4.4.3), distributed land clutter occurring at higher depression angles characteristic of airborne radar is a relatively well-behaved quasi-homogeneous, quasi-Rayleigh process of relatively constant return, i.e., exhibiting only small cell-to-cell variability, for example as illustrated in the σ° vs range data shown in Figure 2.20 as measured at Cazenovia. In such a well-behaved, relatively constant clutter background, occasional spatially isolated discrete cells of very much stronger clutter amplitude clearly stand out as being entirely different in kind from the surrounding weaker quasi-homogeneous clutter and are easily capturable in measured data via spatial filtering and amplitude thresholding.

Various measurement programs were established to characterize discrete clutter in airborne radar [5, 6]. An elaborate, largely conceptual clutter model was developed at IIT Research Institute (IITRI) for ground clutter in airborne radar including distributed and discrete components [7, 8]. The distributed component was modeled in terms of the backscattering

ground area density function σ°. The discrete component was modeled in terms of the RCS levels σ of discrete point scatterers, in which σ amplitudes were allowed to vary from 10^2 m^2 to 10^6 m^2 and in which the spatial occurrences of the discrete scatterers was specified to be uniformly random in terms of given numbers per km^2. This discrete model was considerably extended to include temporally varying fluctuation statistics from the discrete sources, their correlation times, etc. The IITRI conceptual approach to modeling land clutter in terms of both a distributed σ° component and a discrete σ component remains intuitively satisfying.

In turning to low-angle clutter as it occurs in surface-sited radar, the conceptual idea of a discrete clutter component separable from a distributed background becomes less clear cut. The complete spatial field of low-angle clutter is inherently a spiky process throughout, with strong and weak cells often closely intermingled and exhibiting extreme cell-to-cell variability, as evidenced for example in the σ° vs range data shown in Figure 2.18 as measured at Shilo. A useful point of view adopted in this book thus has been to conceptualize the complete field of low-angle clutter spatial amplitude statistics as arising from a sea of discretes, where the amplitudes of the discrete scatterers range over orders of magnitude. A similar point of view was previously taken in a brief early paper by Ward [9], in which the whole clutter spatial field was modeled as comprised only of discrete sources σ, without a distributed component σ°. Table 4.8 reproduces Ward's clutter model. The table specifies both the RCS amplitudes σ of the discrete clutter sources in dB with respect to 1 m^2 (i.e., dBsm); the number of discrete sources randomly and uniformly distributed over a half-space 180° in azimuth extent and from 0 to 40 km in range extent; and the resultant spatial density of the discrete sources. If this book envisages low-angle clutter as arising from a sea of discretes, should the clutter modeling information in the book be reduced and presented in terms of σ rather than σ°? This question is answered in Section 4.5.4.

TABLE 4.8 Ward's Discrete Land Clutter Model

RCS Level σ of Point Discrete (dBsm)	Number of Discretes: 0 to 40 km Range, 0 to 180° Azimuth	Density of Discretes (number/km^2)
40	450	0.18
30	900	0.36
20	4500	1.8
10	6800	2.7

After Ward [9]; by permission, © 1971 IEEE.

In the late 1960s and early 1970s, an ongoing series of investigations involving the discrete nature of low-angle land clutter at high resolution was conducted in the United Kingdom, predominantly at Admiralty Surface Weapons Establishment (ASWE) [10] but elsewhere as well [4]. It was very evident in these studies that dominant land clutter signals come from point sources. This fact led to the measured data being reduced to σ rather than σ°. As was stated in these studies, σ was considered to be a more basic quantity for representing a point source, the RCS of which is independent of the size of the cell capturing the point source, in contrast to characterizing the return from the point source by a σ° coefficient that varies with the area of the capturing cell. At first consideration, such argument seems very

reasonable. Again, should the modeling information in this book be presented in terms of σ rather than σ°? Although deferring the answer to Section 4.5.4, we begin to address such matters in what follows.

Although it is possible to postulate a conceptual clutter model comprising both a distributed σ° component and a discrete σ component, it is far from straightforward to separate distributed from discrete clutter in measured low-angle clutter data. The difficulty in meaningfully or usefully effecting such a separation is not widely recognized, although Schleher does so as indicated in the following direct quotation: "Note that most experimental [land] clutter measurements . . . include composite discrete and distributed clutter, which cannot be separated into component parts, and hence measurement statistics of parameters such as σ° . . . represent combined statistical data" [11]. For example, the AWSE measurements of discrete clutter mentioned previously were entirely reduced in terms of σ, without any attempt to reduce a separate σ° component that might be more appropriate at weaker levels.

The inherent spikiness of low-angle clutter is the basic reason why it is difficult to meaningfully separate discrete and distributed components in low-angle clutter simply on the basis of recognizable qualitative differences as exist in higher-angle clutter. Certainly, without recourse to detailed ground truth information, nothing can be said about how point-like any clutter source is beyond the spatial resolution of the measurement. It may be thought from a theoretical point of view that measurements of the same clutter at increasing resolution could find point sources by looking for cells, each providing a constant level of clutter RCS σ independent of the capturing cell size. In practice, Phase One measurements of the same clutter region at both 150-m and 15-m range resolution both reveal cell-to-cell variations in spikiness, with the rate of variation 10 times faster at 15-m resolution than at 150-m resolution, in which it is seldom evident that a particular 15-m cell within any 10-cell neighborhood provides an RCS level clearly standing out from its neighbors and at the same RCS level as in the encompassing 150-m cell. Such a process would not find many discretes, nor would it serve a very useful purpose in simplifying the characterization of low-angle clutter.

Thus we concur with Schleher that for all intents and purposes it is practicably impossible to determine which clutter returns come from point objects and which from distributed surfaces in low-angle clutter, and in fact that it might be equally impracticable to unambiguously frame criteria for capturing what is conceptually meant by "point" and "distributed" over the myriad of physical objects and surfaces constituting landscape, especially as observed at near-grazing incidence. However, it is certainly possible to separate locally strong clutter cells in measured data irrespective of whether or not a determinable point object can be associated with each such strong return. Appendix 4.D goes forward with this approach as a point of departure for defining and separating "discrete" clutter from "background" clutter (as opposed to attempting to distinguish between point objects vs extended surfaces as the physical sources of the clutter) in order to determine what might be gained by such an approach to empirical clutter modeling.

Acknowledging for now the difficulty of separating σ° and σ components in measured low-angle clutter data, it is still possible to follow, for example, the lead of the AWSE studies and the Ward model described above and reduce the measured data only in terms of clutter RCS σ, as opposed to reducing the measured data (as is done elsewhere in this book) only in terms of the normalized clutter RCS (i.e., backscattering coefficient) σ°. Figure

4.18 shows three subsets of Phase Zero X-band clutter data reduced in this manner. The three subsets constitute urban, mountain, and rural data, respectively. Within each subset, the data are shown as cumulative distributions over all the data in each subset in which the ordinate shows the number of cells per km^2 with RCS $\geq$ the value at any given position along the abscissa. Similar to Ward's early discrete model shown in Table 4.8, the Phase Zero results of Figure 4.18 can be tabulated as shown in Table 4.9. The Phase Zero results of Figure 4.18 and Table 4.9 include clutter RCS returns from all the resolution cells within each terrain type; no effort was made to select a subset of cells defined by some criterion to be discrete. Thus, at the larger clutter RCS levels, some of the returns in the figure undoubtedly correspond to cells actually containing large discrete scattering objects, but other returns presumably just come from large cells at long-range. At the lower clutter RCS levels, the returns come from a composite of small cells, discrete-free cells, and microshadowed cells. Such complications must always intrude when attempting to use empirically derived clutter RCS data to attempt specification of a discrete component in a conceptual clutter model.

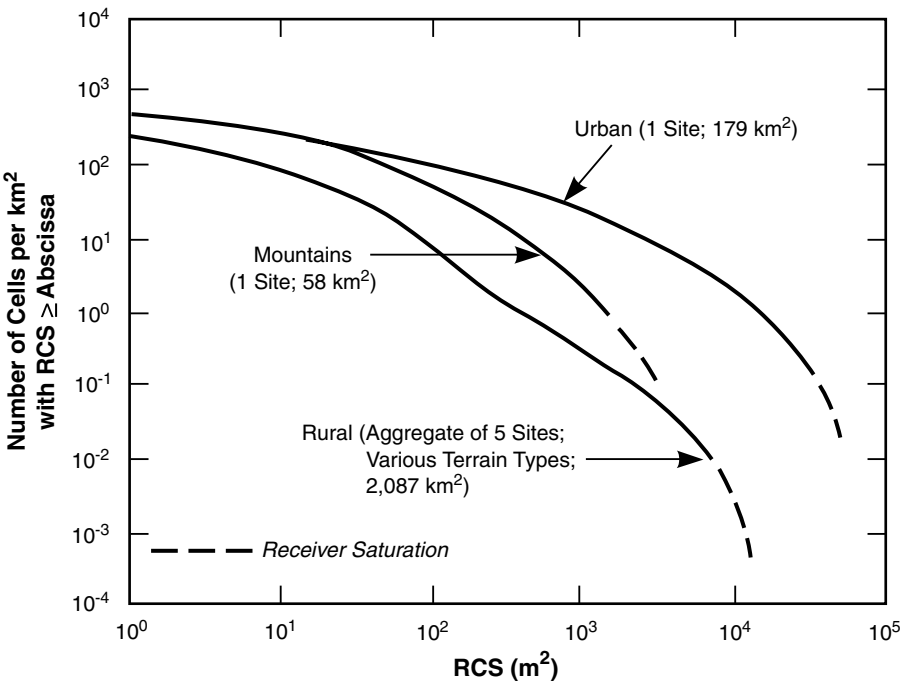

FIGURE 4.18 Number of cells with large RCS in ground clutter. Phase Zero X-band data; 2- to 12-km range; 0.5-μs pulse length.

Consider again that the clutter RCS results shown in Figure 4.18 are based on all the clutter cells within each terrain type. In a similar manner, it would certainly be possible as an alternative approach to reduce all of the Phase Zero and Phase One data in terms of clutter RCS σ rather than in terms of clutter backscattering coefficient σ°. Based on the preceding arguments that low-angle clutter is spiky and discrete, and that the RCS of a point scatterer is independent of the area of the capturing cell, it might be thought, as in the Ward and AWSE studies, that a clutter model based on reducing the measurements to σ statistics

TABLE 4.9 Phase Zero RCS Land Clutter Model

RCS Level σ (dBsm)	Density of Cells (number/km^2)		
	Urban	Mountains	Rural
40	3	0.004	0.004
30	30	3	0.3
20	100	80	10
10	300	300	100

rather than σ° statistics would be the more fundamental approach. To the contrary, Section 4.5.4 will show that σ° is the fundamental quantity to which to reduce clutter measurement data for use in a spatially extensive clutter model, whether the clutter is postulated to arise from discrete or distributed sources over the surfaces involved. Before that, Section 4.5.2 provides examples of thresholded PPI clutter maps at Cochrane, further illustrating how strong isolated discrete cells appear to be embedded in spatially extensive distributed clutter at weaker levels. Then, Section 4.5.3 provides a further example of the spikey nature of low-angle clutter as measured at the prairie grassland site of Suffield and illustrates what is involved in separating one large discrete source from the background clutter when it is known what the discrete is and where it is. Section 4.5.5 provides brief conclusions concerning the practicableness of separating discrete from distributed clutter in measured data and in empirical models.

4.5.2 Discrete Clutter Sources at Cochrane

Figure 4.19 shows PPI clutter maps at Cochrane, Alberta, to 24-km maximum range based on Phase Zero X-band measurement data. The figure shows eight clutter maps at increasing thresholds of clutter strength over a dynamic range of 40 dB, from $\sigma^\circ F^4 \geq -48$ dB to $\sigma^\circ F^4 \geq -8$ dB. In each clutter map, cells exceeding the clutter strength threshold for that map are painted black; cells for which clutter strength is less than the threshold are left white. It is apparent in this figure that at the lowest thresholds, much of the clutter is spatially distributed over contiguous black regions much larger than a resolution cell (resolution cell size = $1^\circ \times 75$ m). With increasing threshold, however, the clutter gradually becomes more spatially granular, such that at the highest thresholds shown it is apparent that the strongest cells at Cochrane are entirely spatially isolated or discrete. Similar measurements by various investigators over the years have led to a concurrence of opinion that land clutter is dominated by discrete sources, and to its often being conceptually modeled as a distributed σ° phenomenon at lower strengths augmented by discrete σ's at higher strengths.

Two additional observations may be made of the data shown in Figure 4.19. First, the strong discrete clutter sources in the figure do not disappear at the long ranges first. This supports evidence and conclusions provided elsewhere in Chapter 4 that clutter strength σ° has no intrinsic dependence on range (for example, see Figure 4.11, and the plots of σ° vs range in Appendix 4.A). Secondly, it is the indication of discrete sources at the highest thresholds such as is shown in Figure 4.19 that motivates investigators to want to determine to what extent clutter modeling can be advanced by separating the effects of discretes at

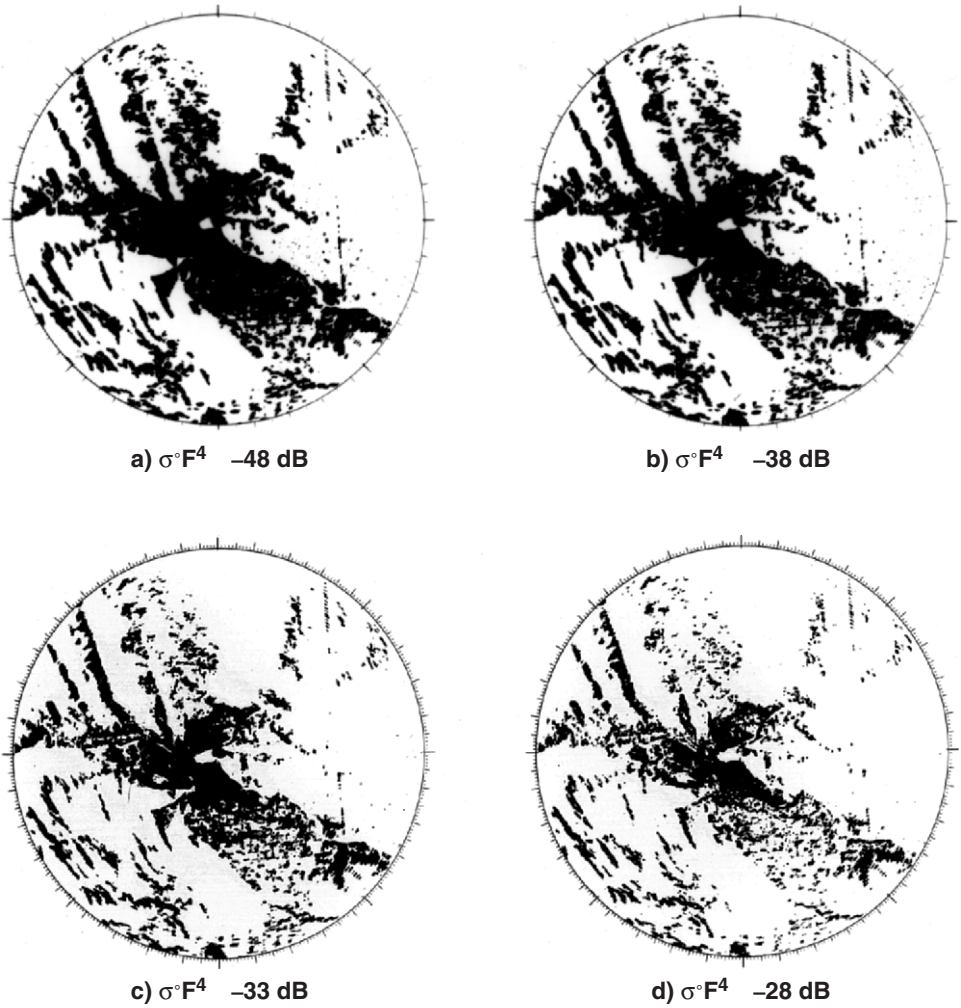

FIGURE 4.19(A-D) Thresholded PPI clutter plots at Cochrane, Alta. Phase Zero X-band data. Maximum range = 24 km; range resolution = 75 m. North is at zenith.

high levels from the more distributed clutter at lower levels. Appendix 4.D provides results obtained by going forward under this motivation and separately analyzing the effects of locally strong "discrete" cells in the measured data.

4.5.3 Separation of Discrete Source at Suffield

This section illustrates that it is complicated to remove the effects of a single large discrete clutter source in measured clutter data, even when it is known what the discrete scatterer is and where it is situated. The investigation is conducted in repeat sector measurement data from the Suffield measurement site in southeastern Alberta. The Suffield terrain is native herbaceous rangeland. Suffield measurements were conducted in winter season with light snow cover. The landform is generally low-relief, although with some variety. From the site center the terrain gradually falls off (by 175 ft) to 7-km range, the start of the repeat sector range interval, and then gradually rises back (by 150 ft) to 13 km, the end of the

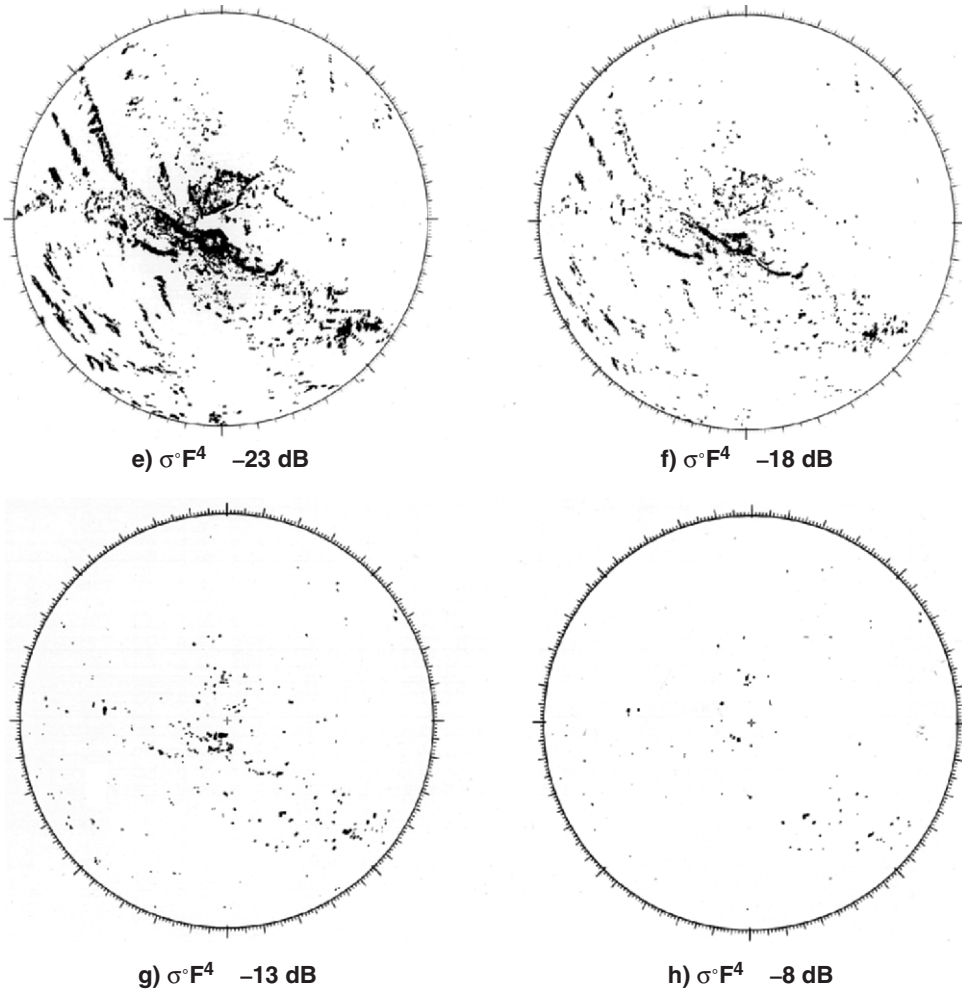

FIGURE 4.19(E-H) Thresholded PPI clutter plots at Cochrane, Alta. Phase Zero X-band data. Maximum range = 24 km; range resolution = 75 m. North is at zenith.

repeat sector. Within the repeat sector, the low-relief terrain is largely undulating, although in places it becomes hummocky or broken. There are some small prairie sloughs or ponds in the sector (2% by area) and some low marshland areas (5% by area) surrounded by sedge and cattails. No trees, cropland, or man-made structures (except as subsequently discussed) are known to exist in the sector.

Thus, at Suffield, discrete-free clutter from winter-season grassland terrain was expected to be measured. However, the measured results appeared to be dominated by some strong discrete returns. Subsequent field surveillance determined that an Alberta Energy Corporation natural gas compressor pumping station had been built since the date of the aerial photos being utilized. The building housing the station was a large, two- to three-story, rectangular metal barn, with smaller outlying buildings and equipment, located at 8.9-km range and 127° azimuth.

The discrete clutter sources comprising the large AEC building complex were sufficient to drive the Suffield repeat sector mean clutter strengths to high levels. This is evident from the results shown in Figures 4.20 and 4.21. These figures show the same measured data reduced and plotted in different ways. Figure 4.20 shows the X-band clutter strength histogram and cumulative distribution for the Suffield repeat sector for the 15-m pulse length and at horizontal polarization. Figure 4.21 shows clutter strength vs range through the Suffield repeat sector, for the same X-band, 15-m pulse, horizontal polarization experiment, for five specific beam positions, namely, for 125.5°, 126.5°, 127.5°, and 128.5°, which are the first four contiguous beam positions in the sector, and for 134.5°, which is the last beam position in the sector (recall that the X-band beamwidth is 1°; see Table 3.A.2).

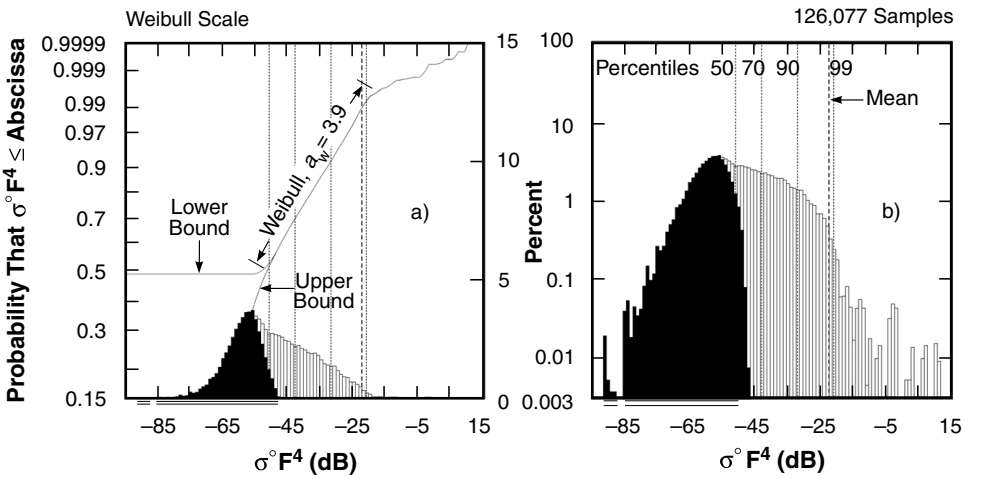

FIGURE 4.20 Clutter histogram and cumulative distribution for Suffield prairie grassland, including large discrete (metal barn). X-band, horizontal polarization, 15-m pulse. (a) Cumulative/Weibull scale and histogram/linear percent scale. (b) Histogram/logarithmic percent scale showing high-side tail.

First consider the clutter histogram and cumulative distribution shown in Figure 4.20. These results were generated from partially integrated data in which each sample was obtained by coherently integrating 32 of the 1,024 pulses collected at a PRF of 2,000 Hz in each range gate with step/scan antenna positioning. In Figure 4.20(a), the histogram is plotted utilizing a linear percent ordinate; Figure 4.20(b) utilizes a logarithmic percent ordinate. The first thing to notice in the histogram is that in the clutter strength region from about –20 dB to about –50 dB, the histogram is very well behaved; the number of samples gradually diminishes with increasing strength in a very regular manner. In fact, over this region from –20 to –50 dB, the distribution of clutter strengths is very accurately represented by a Weibull distribution with a Weibull shape parameter of a_w = 3.9. This well-behaved Weibull distribution of strengths measured from Suffield discrete-free grassland terrain well represents the area-extensive clutter background in these measurements.

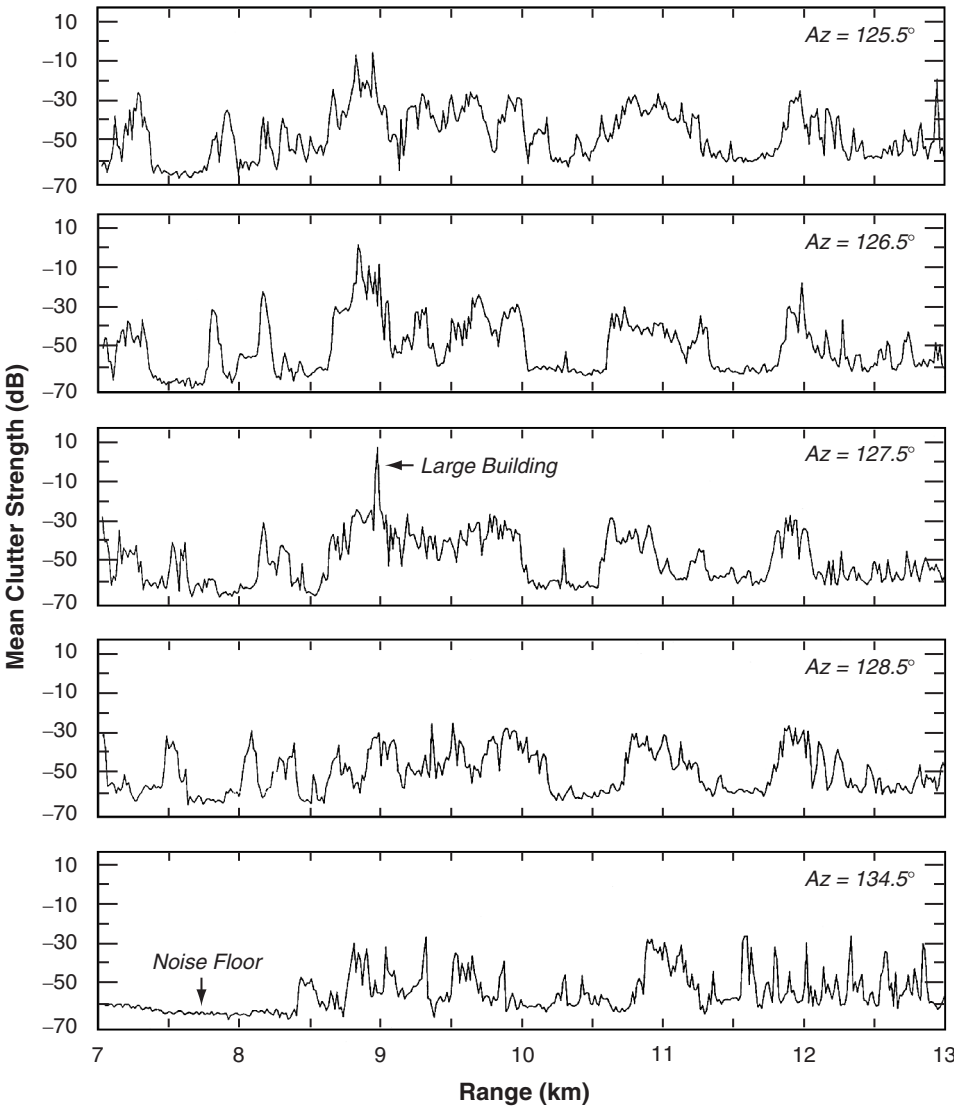

FIGURE 4.21 Mean clutter strength vs range at Suffield. Repeat sector data. X-band, 15-m pulse, horizontal polarization. Individual azimuth beam positions.

However, the next thing to notice in the histogram, particularly as plotted in Figure 4.20(b), is that it contains a long high-side tail over the clutter strength region from –19 to +11 dB, caused by strong discrete returns of low percent occurrence. In fact, from –19 dB to +11 dB inclusive, there are 808 samples in the histogram of Figure 4.20 coming from ~25 different spatial cells, which constitutes 0.64% of the total number of samples in the histogram. If attention is now turned to the sector display of Figure 4.21, it is evident that most of these strong values come from the vicinity of the large AEC building in the Suffield repeat sector.

The data in Figure 4.21 are now described more specifically. These data involve no spatial averaging, but show clutter strength in individual resolution cells, range gate by range gate

and beam position by beam position. In each resolution cell, the clutter strength shown is the temporal mean strength resulting from averaging 32 samples, each of which is a coherent average of 32 pulses recorded at a PRF of 2,000 Hz. Generally, Figure 4.21 indicates that the clutter from this Suffield grassland terrain is of a very spiky nature, with 30-dB fluctuations common, as individual cells drop into and out of direct visibility at the low 0.3-deg depression angle involved. These data are a good example of the statistical nature of low-angle clutter, even from what is relatively homogeneous, discrete-free grassland terrain (i.e., not constant σ° or a tight Rayleigh process). Most of these clutter returns vary over the range from –20 to –50 or –60 dB. The major exception to this range of variation in the data of Figure 4.21 is the set of returns of strength >> –20 dB from cells in the near vicinity of the AEC building in the range interval from 8.8 to 9.0 km and at azimuths from 125.5° to 127.5°. For example, at the 127.5° azimuth position there is a strong specular flash directly from this building that raises the clutter return 30 dB or more above the envelope of the peaks in other cells not near the building. Although in the following beam position (i.e., 128.5°) no indication of the building remains, in the two preceding beam positions there is significant evidence of the building and associated discretes at levels > –20 dB spread over a number of range gates. Altogether, in these data there are 435 samples of strength ≥ –13 dB from the vicinity of the AEC building, which, if deleted, reduce the mean strength in the histogram of Figure 4.20 from –22.6 to –34.9 dB. Note that the general statistical nature of the grassland clutter at 134.5°, the final beam position in the sector, is relatively similar in range of fluctuation to that 6° earlier (i.e., at 128.5°) except over the region from 7 to 8.5 km. This region is shadowed terrain at the noise floor, where the noise level decreases with increasing range because r^4 sensitivity-time-control (STC) attenuation was used in the experiment. The 5-dB discrete-finding algorithm utilized in Appendix 4.D clearly would specify a number of cells in Figure 4.21 as being "discrete," i.e., as being 5 dB stronger than their neighbors, even though no obvious point-like discrete physical scattering sources other than the AEC building are known to exist in the Suffield repeat sector.

Thus, the data of Figures 4.20 and 4.21 indicate that a more appropriate value of X-band mean clutter strength (at 15-m pulse length, horizontal polarization) to represent discrete-free Suffield grassland is –34.9 dB, not the –22.6 dB value actually measured there and driven to be so large by the presence of the AEC building. Next, similar adjustments to Suffield repeat sector mean clutter strengths are performed in other bands. These are done at low resolution (i.e., 150-m pulse length). The low resolution data are more clear-cut as to which samples come from the AEC building. Thus, in the L-band (150-m pulse, horizontal polarization) data there are four cells at $\sigma^\circ F^4$ levels of –4, –8, –16, and –17 dB providing samples (32 each) from the AEC building. When the samples from these four cells are removed from the measured histogram, the mean strength of the histogram drops from –25.0 to –39.9 dB. Similarly in the other bands (at 150-m pulse length, horizontal polarization), it is found that mean strengths adjust as follows: at X-band, from –21.7 to –33.9 dB; at S-band, from –25.3 to –43.2 dB; at L-band, from –25.0 to –39.9 dB; at UHF, from –36.8 to –40.3 dB; and at VHF, from –51.3 to –51.7 dB.

These adjusted Suffield mean clutter strengths (adjusted to be representative of grassland without the large AEC building discrete clutter source) are now compared with the grassland site of Vananda East which has similar landform (i.e., 3–5) but at which a higher depression angle occurred. This comparison is made at 150-m pulse length and horizontal polarization. At UHF, L-, and S-band, the adjusted Suffield values are remarkably close to

Vananda East values (the values are, for Suffield and Vananda East, respectively: at UHF, –40.3 dB vs –38.9 dB; at L-band, –39.9 dB vs –39.5 dB; at S-band, –43.2 dB vs –38.1 dB). Furthermore, in these three bands at both these grassland sites, mean clutter strengths are remarkably invariant with frequency at or near the –40-db level. These –40-db levels are good estimates of mean clutter strength in these bands for canonical discrete-free grassland, and therefore are what would be assigned as mean strengths to Weibull distributions for representing an area-extensive distributed clutter background.

At VHF, although Vananda East mean clutter strength holds near the –40-db level (viz., –41.7 dB), adjusted Suffield mean clutter strength drops to –51.7 dB (i.e., 10 dB weaker than Vananda East). This lower Suffield value is caused by VHF multipath loss from the hillslope local to the antenna at Suffield (see Appendix 3.B, Section 3.B.2), which does not occur for the high-bluff site at Vananda East. Note that, at VHF, the adjusted Suffield mean strength is only 0.4 dB weaker than the unadjusted value. This is because at VHF the cells containing the AEC building, although 25 to 30 dB stronger than surrounding cells, were 5 dB weaker than some cells at longer range which were strong due to multipath enhancement. This resulted in the mean clutter strength, dominated by these strong long-range cells, coincidentally being about equal to the strength of the cells containing the AEC building, so whether the AEC cells are included or not has little effect on mean clutter strength at VHF.

At X-band, the Vananda East mean clutter strength abruptly rises from the –40-db level in lower bands to –27.7 dB. This effect is described elsewhere in this book (viz., see Sections 3.4.1.5, 3.4.2, and 5.4.7.2). The adjusted Suffield X-band mean clutter strength also abruptly rises from –40 dB, but to –33.9 dB, a level 6 dB weaker than measured for grassland at Vananda East but still 11 dB stronger than measured for grassland at Big Grass Marsh.

The repeat sector values of mean clutter strength at Suffield, adjusted to be applicable to relatively discrete-free grassland by removal of cells containing the AEC building, are thus understandable and provide additional information within the context of the other discrete-free grassland sites, Vananda East (same 3–5 landform as Suffield) and Big Grass Marsh (landform = 1, level). The depression angle at Suffield, 0.3 deg, is intermediate between the depression angle at Big Grass Marsh, 0.2 deg, and that at Vananda East, 1.0 deg. As a result, at VHF and X-band, adjusted values of Suffield mean clutter strength for grassland lie intermediate between those at Big Grass Marsh and at Vananda East. At UHF, L-, and S-band, adjusted values of Suffield mean clutter strength are very nearly equivalent to those at Vananda East.

These Suffield results indicate that, in the separation of returns from a known discrete clutter source (viz., large building) in the measurement data, it is not so simple as the finding of a single large value of RCS in a single cell, but instead what is found are multiple returns from the building varying over orders of magnitude from a number of small contiguous cells, each of which partially intersects the building. This technique of separately dealing with large man-made discretes in the clutter data is usually much more demanding than at Suffield because usually many such sources exist in open terrain (e.g., farmland).

4.5.4 σ vs σ° Normalization

Section 4.5.1 raised the idea that a conceptual ground clutter model comprising (1) a σ° component for area-extensive background clutter that is distributed over all cells, augmented by (2) a σ component for discrete clutter arising from large point sources occupying a relatively small proportion of cells, is intuitively satisfying at low or high

angle. However, Sections 4.5.1–4.5.3 further showed that in working with measured low-angle clutter data, which unlike clutter data at higher angles is spiky throughout, it is not readily feasible to separate a distributed σ° component known *a priori* to arise from physically extended surfaces from a discrete σ component known *a priori* to arise from physical point objects. Nevertheless, and also as illustrated in Section 4.5.1, one may choose to reduce all the measured clutter data either to clutter RCS σ per resolution cell or to normalized clutter RCS or backscattering coefficient σ° (where $\sigma^\circ = \sigma/A$, A = cell area $= r \cdot \Delta r \cdot \Delta\theta$; see Figure 2.4). Section 4.5.1 showed that the predilection of some previous investigators was to reduce all the measured clutter data to σ, on the basis that the stronger elements of low-angle clutter were spatially isolated or point-like (see Figure 4.19), and that the RCS σ of a point source is the fundamental quantity independent of the size of the capturing cell, as opposed to σ° which depends on the size of the capturing cell. Is it just a matter of subjective choice or preference on the part of the investigator, or do substantive reasons exist for making either σ or σ° the preferable choice to which to reduce measured low-angle clutter data?

For us to begin to address this question, reference is first made to the results of Section 3.5.3 in Chapter 3 showing that in measured repeat sector clutter data, the mean value of the clutter coefficient $\overline{\sigma^\circ}$ is essentially independent of cell area or spatial resolution (see Table 3.10, small differences with pulse length in all five bands). Independence of mean strength on cell area is necessary for the concept of density function to be true. It is true in the measured data, irrespective of whether descriptive adjectives like "discrete" or "distributed" are associated with the measured data, and also irrespective of whether the nature of the measured clutter is very uniform or very spiky. Thus, as described elsewhere throughout this book, the fact that $\overline{\sigma^\circ}$ is independent of cell area is fundamentally important to the structure of the modeling information presented. In contrast, if all the clutter measurement data are reduced to σ rather than σ°, the mean value of clutter RCS $\overline{\sigma}$ over a spatial region is dependent on cell area, as $\overline{\sigma} = \overline{\sigma^\circ} A$. Clutter modeling information presented in terms of σ rather than σ° would require the mean values $\overline{\sigma}$ of clutter amplitude distributions to be shown as functions of resolution. In other words, σ is not as fundamental a quantity for specifying clutter amplitudes over extended spatial regions as is σ°.

Beyond this, care must be taken not to read too much into the fact that $\overline{\sigma^\circ}$ is independent of cell area A. For example, it is easy to presume that this fact indicates that low-angle clutter is essentially not point-like but from extended surfaces—however, this is an incorrect assumption. What is indicated is that spiky clutter from discrete sources occurs distributed over surfaces; i.e., that in low-angle clutter, both adjectives apply—clutter is both "discrete" and "distributed."

It is easy to appreciate that mean clutter cross section increases linearly with cell area (i.e., $\overline{\sigma} = \overline{\sigma^\circ} A$) in area-extensive clutter. But how does this observation square with the fact that in clutter arising from point sources, the more basic quantity for the cell capturing the clutter source is its RCS σ which is independent of the capturing cell size? A simple example may be illuminating in this regard. Imagine the existence of a hypothetical clutter spatial field in which each cell contains a single point discrete of $\sigma = X$. One might choose to characterize this clutter in terms of its mean clutter RCS such that $\overline{\sigma} = X$. Now suppose the resolution of the radar to change so as to either increase or decrease by a factor of 10. If the resolution increases, one-tenth of the cells will capture a discrete and have $\sigma = X$; the other nine-tenths of cells will miss capturing a discrete and will have $\sigma = 0$. Thus if the resolution increases by

a factor of 10, $\overline{\sigma} = X/10$. If, on the other hand, the resolution decreases by a factor of 10, each cell captures 10 discretes and (under the assumption that the 10 discretes combine as a power-additive process) $\overline{\sigma} = 10X$. Thus even in this hypothetical discrete clutter field, mean clutter RCS $\overline{\sigma}$ varies linearly with cell area similarly as it does in the actual measured data. That is, $\overline{\sigma}$ is not an invariant irreducible quantity suitable for basing a model upon.

Next consider the hypothetical clutter spatial field in σ° space. At the original range resolution, say 150 m, the σ° of each cell (each cell containing a single discrete of RCS = X) is $X/(r \cdot 150 \cdot \Delta\theta)$. Next, allow the range resolution to increase by a factor of 10, to 15 m. Each discrete-capturing 15-m cell still provides RCS = X, and the σ° of each discrete-capturing cell rises by a factor of 10 to $\sigma^\circ = X/(r \cdot 15 \cdot \Delta\theta)$. But in the region around each discrete-capturing cell, there are now nine empty cells with $\sigma^\circ = 0$. Thus the mean value of σ° over each 10-cell region is $\overline{\sigma^\circ} = [X/(r \cdot 15 \cdot \Delta\theta)]/10$ which is the same value of $\overline{\sigma^\circ}$ as measured with the 150-m cell. Similarly, if range resolution is allowed to decrease from its original 150-m value by a factor of 10 to 1500 m, each cell captures 10 discretes; so $\overline{\sigma^\circ} = 10X/(r \cdot 1500 \cdot \Delta\theta)$ which is also the same value of $\overline{\sigma^\circ}$ as measured with the 150-m cell.

Thus in considering ground clutter, all possibilities of cells on the ground must be specified depending on resolution, not just cells capturing single discretes, but including possibilities of cells capturing more than one discrete and cells capturing no discretes. This is the point that is missed when intuition incorrectly suggests that σ is a more basic quantity than σ° for characterizing discrete clutter. Certainly, in a backscatter measurement of any single point object in which concern is only with the cell containing the object and not the surrounding empty cells, the appropriate characterization of the object is by its RCS σ.

This hypothetical situation of a clutter spatial field in which at intermediate resolution each cell contains a single discrete clutter source of RCS = X is handled by a σ° clutter model as follows. At all three resolutions, the mean value of clutter coefficient $\overline{\sigma^\circ}$ remains constant, invariant with cell size (as in the modeling information in this book). The different σ° distributions for the three variations in range resolution are theoretically handled through specification of differently shaped distributions for the three resolutions, but with $\overline{\sigma^\circ}$ for each distribution remaining unchanged (also as occurs in the modeling information in this book). Thus in these hypothetical situations, for the mid-size cell, the shape of the distribution is an impulse allowing no variation in σ°; for the small cell, the shape of the distribution is such as to define a two-impulse bipolar distribution with nine-tenths of the σ° values equal to zero and one-tenth equal to $X/(r \cdot 15 \cdot \Delta\theta)$; and for the large cell, the shape of the distribution is such as to allow the variability associated with 10 interfering scatterers within the cell. For the actual measured clutter data, as opposed to the above hypothetical construct, such extreme shapes of distributions are unnecessary; the Weibull distribution of constant mean strength $\overline{\sigma_w^\circ}$ and varying shape parameter a_w is sufficient to handle the actual variations in shape that occur with changing resolution in the actual measured data.

The above reasoning indicates that when concern is with returns from all the cells defining a surface, the correct way to empirically characterize the phenomenon is to reduce the measured data to σ°, even though each return in itself may arise from a point source. Is this reasoning supported by the observed behavior of the actual measured clutter data? Consider again that since $\overline{\sigma^\circ}$ is independent of cell area, $\overline{\sigma} = \overline{\sigma^\circ} \cdot A$ must increase linearly with

increasing cell area. Thus in observed clutter data, if range is allowed to increase from 1 km to, say, 64 km (that is, by six factors of 2), cell area doubles with each factor of 2 increase in range leading to the expectation that clutter RCS would increase by 18 dB over this range, certainly enough to show a noticeable trend in measured data. That is, larger cells at longer ranges capture more discretes and provide larger cross sections. But in the σ° vs range results shown in this book, for example in the sector displays of Appendix 4.A or in the thresholded PPI displays of Figure 4.19, no strong trends of σ° vs range are observed, indicating that σ° is indeed the appropriate irreducible quantity upon which to base a clutter model. In all observations, σ° within visible clutter regions (although fluctuating strongly from cell to cell) neither increases nor decreases significantly with range, but remains as a fundamental quantity with range effects properly normalized out.

It is apparent from the preceding discussion that σ°, as opposed to σ, is the more fundamental quantity to which to reduce measured low-angle clutter data, despite the fact that low-angle clutter is an essentially spiky phenomenon arising from a sea of discrete clutter sources. A clutter model based on reducing all measured returns to σ is not completely reduced; such a model must include $\overline{\sigma}$ depending on resolution as an extra complicating dimension that is not necessary in a model based on σ°. This fact leads to the clutter data in this book being reduced to σ° as the most basic characteristic of a distributed phenomenon, despite the fact that what is distributed are discrete clutter sources.

4.5.5 Conclusions

The idea behind separating discrete clutter sources in measured clutter data is that objects like water towers act as contaminants in what would otherwise be a statistically well-behaved area-extensive clutter background from the land surface itself, and that a better clutter model results if RCS values of strong discretes are added in a separate σ process to the basic distributed σ° component representing the background clutter. This idea has some validity at higher angles of illumination typical of airborne radar platforms. At the low angles of illumination of ground-based radars, the focus of the idea tends to dissipate for several reasons. First, low-angle clutter is spiky throughout; removal of the largest spikes still leaves a spiky background. Second, it is not possible to deterministically separate clutter arising from point objects from clutter arising from extended surfaces in the measured data. Many spikes occur only because of vicissitudes of visibility and shadowing compounded by extreme propagation variations at very low angles of illumination. Little correlation exists between locally strong clutter returns and known point objects on the ground. Third, even though low-angle clutter appears to arise from a sea of discretes, the proper way to reduce the data is to the normalized clutter coefficient σ°, as opposed to radar cross section σ, irrespective of whether one is examining so-called "distributed" or "discrete" components.

Given these qualifications, if we continue to wish to examine the usefulness of separately analyzing and modeling strong clutter as an overlay to the general clutter background, it is necessary to fall back to a position in which locally strong cells are specified *a posteriori* in the measured clutter data as opposed to their *a priori* specification as the returns from known point objects.

In so doing, the initial premise has changed. Rather than removing and separately modeling the returns from known point discretes such as water towers, the question now being posed is if it is useful to model the total clutter distribution from a given spatial region as two

components, one consisting of the locally strong clutter cells resulting from passing a spatial filter over the data and the other consisting of the residual clutter cells which failed to pass the filter. That is, is it useful to set a threshold so as to separate locally strong σ° from weaker surrounding σ°. The potential benefit of such a procedure hinges on the possibility of there being a difference in kind, not just degree, in the two distributions (even though each consists of spiky returns) such that each might be of a relatively simple shape, whereas their combination is of a more complex shape. Note that both components are broad distributions consisting of spiky returns of strengths differing by orders of magnitude, with the major differences being that the so-called "discrete" component consists of locally strong spiky returns and the so-called "background" component consists of the weaker neighboring spiky returns. Further, note that there is no benefit and indeed needless added complexity in moving to σ space to characterize the locally strong or so-called "discrete" component.

The modeling of clutter based on the two-distribution approach allows the possibility of assigning two random variates to each clutter cell with the resulting total σ° being the phasor addition of the two components. This approach models "discrete" clutter returns statistically rather than attempting to deterministically specify returns from known point targets on the landscape. Appendix 4.D shows results obtained from separating clutter into two σ° components in this manner. The main approach of this book, however, is to characterize the total clutter from a given spatial region as a single Weibull distribution, where the broad extent of the Weibull distribution usually satisfactorily represents the measured distribution, capturing the occasional strong returns from discrete sources at appropriate probabilities of occurrence. The clutter modeling information provided in Chapter 5 and elsewhere (except in Appendix 4.D) in this book is based on the single-distribution approach involving the assignment of a single random variate to represent clutter strength in each resolution cell.

4.6 Temporal Statistics, Spectra, and Correlation

For many years, in radars of low spatial resolution, the in-phase and quadrature components of the spatially varying ground clutter signal were considered to be distributed as Gaussian probability density functions, resulting in the signal amplitude being Rayleigh distributed (see, for example [12], Section 10.2). In modern radar systems, operating at low grazing angles and with resolution capabilities high enough to resolve the surface structure, the statistics of the clutter have been observed to strongly deviate from Gaussianity [13–19]. The clutter is spikier than if it were Gaussian, and the spikes are processed by the radar detector as targets, with increased false-alarm rate. Until now, Chapter 4 and the preceding chapters of this book have been primarily concerned with the characterizations and prediction of the highly non-Gaussian clutter amplitude statistics resulting from cell-to-cell spatial variations in ground clutter signals.

Windblown ground clutter Doppler spectra also in early years were, like the amplitude distributions, erroneously thought to be of Gaussian shape [20–22]. The correct understanding of ground clutter and the accurate modeling of its non-Gaussian behavior, both in the spatial amplitude distribution and in the Doppler spectrum, are problems of fundamental interest to the radar community for successful radar design and performance prediction. The subject now widens to include temporal variations in the received clutter

signals returned from particular spatial cells. Important attributes of temporal statistics are (1) temporal amplitude statistics, (2) spectral characteristics, and (3) correlation times. Correlation distance in the ground clutter spatial process is also discussed. Improved knowledge of these various additional attributes of ground clutter, in addition to its spatial amplitude statistics, is required in the demanding specialized design of modern signal processors required to detect, track, and otherwise operate against ever-smaller radar targets in ground clutter backgrounds. For example, the spectral characteristics of clutter determine the design of moving target indicator (MTI) or space-time adaptive processors (STAP) [23, 24], and the amplitude statistics of clutter affect the design of constant-false-alarm rate (CFAR) processors (see e.g., [12, p. 306; 25]).

Results concerning these additional important attributes of low-angle ground clutter are provided in Section 4.6 at a first or introductory level of analysis. More in-depth analyses of these attributes based on the Phase One clutter data are available elsewhere [26–31]. They show that the temporal and spatial domains of ground clutter are interrelated. However, in the specification of the spatial clutter amplitude statistics which is a principal focus of this book, each individual spatial clutter amplitude so specified may be regarded as the mean level of a temporal process in a given spatial cell. Subsequently, Chapter 6 takes up the subject of the modeling of windblown ground clutter spectral shape as a second principal focus of this book.

4.6.1 Temporal Statistics

Figure 4.22 presents information describing the relative frequency of occurrence of temporal amplitude statistics between cells with Rayleigh (i.e., windblown foliage) and Ricean (i.e., fixed discretes embedded in foliage) statistics. Ricean statistics describe ground clutter temporal variations from a fixed spatial cell quite accurately as the return of a dominant steady reflector or fixed discrete in a varying background [22, 32]. Rayleigh statistics are a limiting case of Ricean statistics with steady signal equal to zero. The quantity m^2 in the Ricean distribution as introduced by Goldstein [22] is the ratio of steady to random average power, or, in other words, the dominant-to-Rayleigh reflector ratio. The ratio of standard deviation-to-mean (sd/mean) in the Ricean process is related to m^2 as sd/mean = $[(1 + 2\,m^2) / (1 + m^2)^2]^{0.5} \cong \sqrt{2}\,/m$ for $m^2 >> 1$.

The data in Figure 4.22 indicate that, over a population of 988 relatively strong clutter cells selected from three rural sites, more than 40% of the cells are Rayleigh (i.e., have ratios of standard deviation-to-mean = 0 dB), and the remainder are generally Ricean (i.e., have ratios of standard deviation-to-mean < 0 dB), with increasingly strong Ricean cells occurring less frequently. For example, Figure 4.22 shows that 1% of cells are strongly enough dominated by fixed discretes to have a dominant-to-Rayleigh reflector ratio as high as 50. The reason that 40% of the clutter cells in the figure contain only windblown foliage with dominant-to-Rayleigh reflector ratio equal to zero is that there are some trees on these farmland landscapes. Where trees occur, even at relatively low incidence of occurrence, they tend to dominate as strong clutter sources (see Chapter 2, Section 2.4.2.5).

4.6.2 Spectral Characteristics

For Rayleigh cells containing windblown trees, the wind-induced motion causes Doppler-shifted energy in the power spectra of the received temporal signals. Figure 4.23 shows two examples of windblown ground clutter spectral results, each computed from a Phase One X-band long-time-dwell experiment measured from the same forested cell at 2.6-km

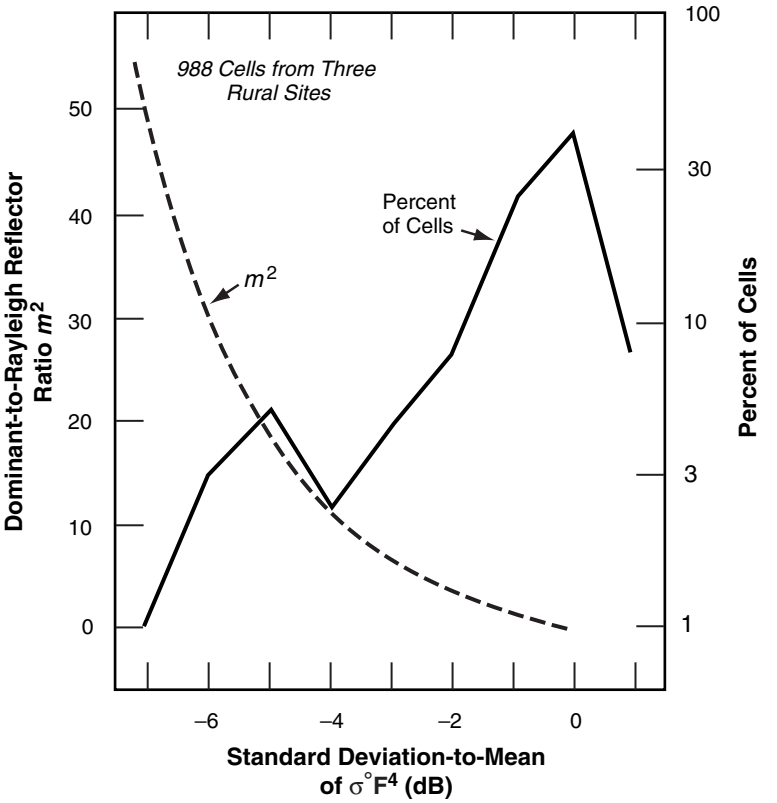

FIGURE 4.22 Frequency of occurrence of Rayleigh vs Ricean cells in X-band ground clutter.

range on two April days about one week apart. This cell contains mixed deciduous and evergreen trees to an approximate height of 60 or 70 ft. On the first day, 17 April, the winds were quite strong; at the time of this X-band experiment, wind speed was recorded at 10 knots, gusting to 20. In contrast, the second day, 25 April, was a very still day and the winds were recorded as calm at the time of the experiment.

The spectra of Figure 4.23 are computed directly as fast Fourier transforms (FFTs) of the temporal pulse-by-pulse return, including the dc component, calibrated in radar cross section (RCS) units of meters squared. The spectral content is displayed in decibels with respect to 1 m^2 (i.e., in dBsm). The method used to generate these spectra is that of modified periodograms [33], where the temporal record of 30,720 pulses is divided into continuous groups of 1,024 samples, a 1,024-point complex FFT is generated for each group, and the amplitudes of the resultant set of FFTs are arithmetically averaged together in each Doppler cell to provide the spectrum illustrated. Thus in Figure 4.23 each spectrum shown is the result of averaging 30 individual spectra from an overall RCS record of 1.024-min duration and 2-ms pulse repetition interval (PRI). In the generation of each spectrum, a 4-sample Blackman-Harris window or weighting function is utilized, with highest sidelobe level at –74 dB and with 6-dB per octave fall-off [34].

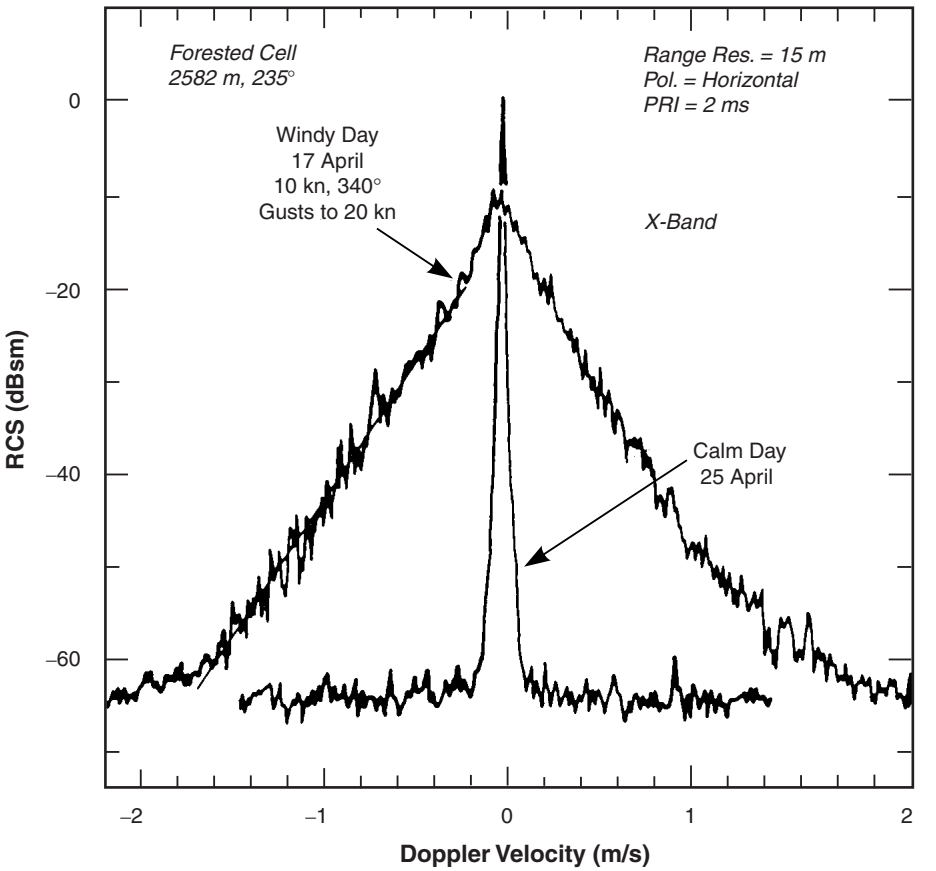

FIGURE 4.23 Power spectra of X-band radar returns from windblown trees.

The results of Figure 4.23 illustrate the differences in spectral content of the X-band reflections from this cell between when the tree branches are relatively motionless and when they are undergoing relatively strong, wind-induced, random motion. It is graphically apparent in these results how much of the dc or zero-Doppler return on the calm day is converted to ac return distributed over Doppler velocities up to 2 m/s on the windy day. The windy day spectrum shown in the figure is one of the wider spectra found in the Phase One long-time-dwell clutter database. In this windy day data, the rate of decay of spectral energy with increasing Doppler velocity in the tail of the spectrum is approximately exponential as indicated by the straight line drawn through the left side of the spectrum. The Phase One system noise levels are evident in both the calm and windy day results of Figure 4.23 at a level of about –64 dBsm. Andrianov, Armand, and Kibardina [35] provide an earlier observation of piece-part exponential spectral decay in windblown radar ground clutter Doppler spectra (see Section 6.6.1.3).

The results of Figure 4.23 are representative of much of the Lincoln Laboratory clutter spectral data, in that rates of decay of spectral power with increasing Doppler velocity in radar returns from windblown trees in these data are often observed to be reasonably well approximated as exponential. One Phase One study [26] involved fitting exponential approximations to 23 different Phase One L-band experiments obtained from nominally

once-a-week measurements over a period of nine months, to provide information on how clutter spectra vary with wind, weather, and season. Chapter 6 takes up the matter of windblown clutter spectral modeling much more extensively and completely.

4.6.3 Correlative Properties

The question now is, how long does it take for radar returns from windblown trees to decorrelate? This question is complementary to that of spectral extent in such returns. The normalized autocorrelation function [36] was computed for all five Phase One frequencies for the returns from the same 2.6-km forested cell as measured on the windy day of 17 April [26] for which spectral results are shown in Figure 4.23. These autocorrelation results are shown in Figure 4.24 over a time lag from 0 to 0.5 sec. The time of day (hr:min) at which data collection commenced for each of these five long-time-dwell experiments was as follows: X-band, 10:24; S-band, 11:30; L-band, 14:12; VHF, 15:50; UHF, 15:27. Each of these five long-time-dwell experiments consisted of 30,720 pulses at PRIs of 2, 10, 10, 6, and 2 ms for VHF, UHF, L-, S-, and X-bands, respectively. For all five experiments, the polarization was horizontal and the range resolution was 150 m. At each of the five Phase One frequencies, the autocorrelation of the return from a stationary water tower reference target remains essentially at unity over the 0.5-s time lag shown in Figure 4.24. Correlation times $\tau_{1/e}$ and $\tau_{1/2}$ are defined as the times required for the normalized autocorrelation function to decrease to $1/e$ (= 0.368) or 1/2 (= 0.5), respectively. Table 4.10 gives these measures of time required for decorrelation of the radar returns from windblown trees, as determined from the data of Figure 4.24.

If the scattering centers and their motion were the same at all five frequencies, simple Doppler considerations would lead to the expectation that correlation times should decrease inversely with radar carrier frequency, all else being equal. There is an approximate trend indicative of this effect in the data of Figure 4.24 and Table 4.10. These results do not scale exactly linearly with frequency, however, because (1) the experiments were conducted at different times and thus under different specific wind conditions on 17 April, (2) the cell sizes and hence scattering center ensembles were different (e.g., due to azimuth beamwidth varying with frequency band), and (3) the scattering centers and their velocities are expected to vary with the radar transmission wavelength (i.e., twigs at X-band, branches at L-band, limbs at VHF).

The correlative properties of radar returns from windblown trees shown in Figure 4.24 and Table 4.10 apply for the particularly windy day of 17 April. Correlation times from windblown trees increase with decreasing wind speed. Figure 4.25 shows the normalized autocorrelation function for the L-band returns from the same 2.6-km forested cell, measured on three different days under three quite different wind conditions. The autocorrelation function is shown in Figure 4.25 only over the correlation interval from 1.0 to 0.9 to emphasize the region where the data just begins to decorrelate. In Figure 4.25, the windy day was 17 April (wind speed = 15 to 25 kn), the breezy day was 10 April (wind speed $\approx$11 kn), and the light air day was 5 June (wind speed $\leq$ 8 kn). Each of these long-time-dwell experiments consisted of 30,720 pulses at pulse repetition intervals of 10, 2, and 10 ms for the windy, breezy, and light air days, respectively. In these results, the correlation times $\tau_{1/e}$ on the windy, breezy, and light air days were 0.95, 2.11, and 5.56 s, respectively. These results show how temporal correlation in L-band radar returns from windblown trees increases with decreasing wind speed.

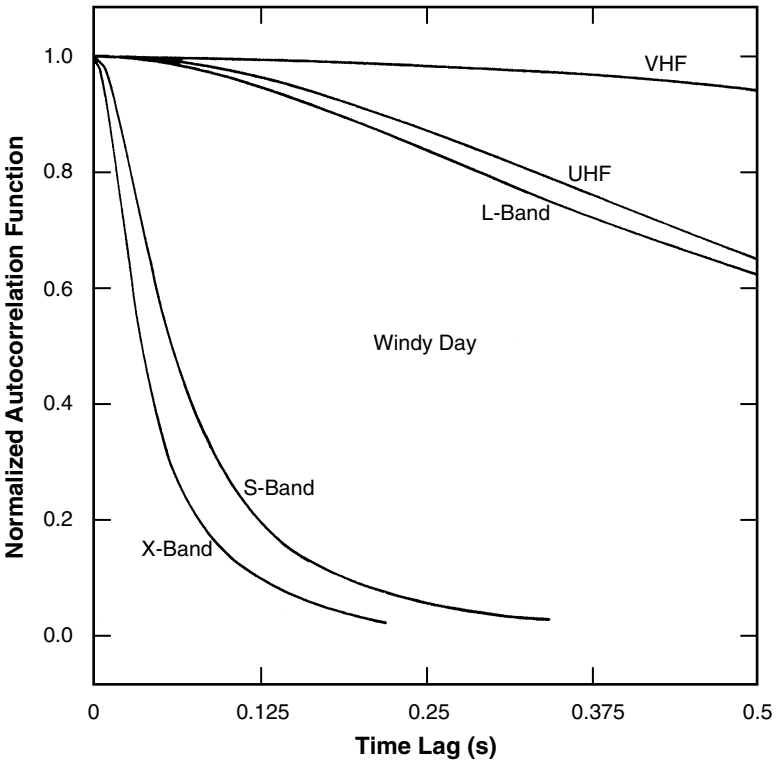

FIGURE 4.24 Autocorrelation functions of radar returns from windblown trees on a windy day at five radar frequencies.

TABLE 4.10 Correlation Times for Radar Returns from Windblown Trees on a Windy Day

Frequency Band	Correlation Time(s)	
	$\tau_{1/2}$	$\tau_{1/e}$
VHF	4.01*	5.04*
UHF	0.69	0.94
L-Band	0.67	0.95
S-Band	0.062	0.081
X-Band	0.033	0.049

Note: * = extrapolated estimate

Spatial Correlation. In contrast to temporal correlation, which addresses the question of duration in time that must pass for a clutter signal from a fixed cell to decorrelate, spatial correlation addresses the question of extent in distance (i.e., number of cell dimensions) that must be traversed in order that the clutter signal from the current cell decorrelates with respect to the signal from the original cell. Because of the general spatial heterogeneity of terrain and the spiky spatial nature of the land clutter phenomenon as observed at low angles, a number of studies over the course of the Phase Zero/Phase One activities have found that low-angle land clutter often spatially decorrelates in about one spatial cell. That is, the physical content (i.e., scattering ensemble) within each cell when observed at low

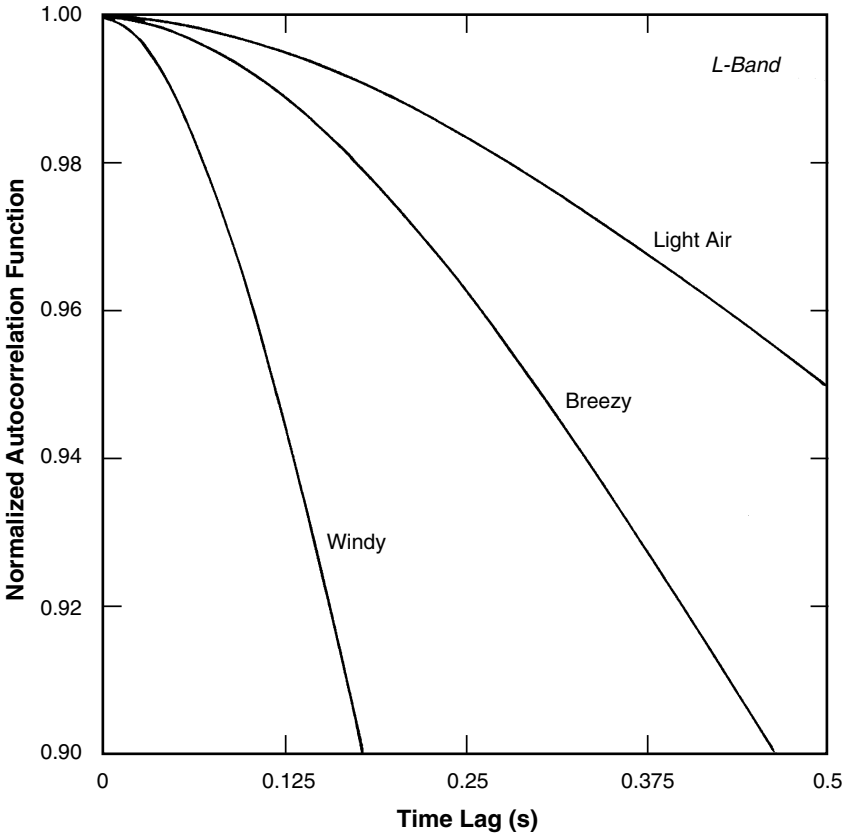

FIGURE 4.25 Autocorrelation functions of L-band radar returns from windblown trees for three different wind conditions.

angles is usually different enough (different set of discrete sources) from cell to cell that the signal from any one cell largely decorrelates from its spatial neighbors. Occasionally, increased correlation is observed from cell to cell, for example, at higher angles over uniform forest.

As an example of cell-to-cell spatial decorrelation, results are summarized here from a statistical study [30] of Phase One X-band open farmland clutter data collected at the Wolseley, Saskatchewan site.[25] Other results from this study are discussed in Appendix 5.A. The data were acquired in slow (2°/s) scan mode through one ~90° azimuth sector in which 703 azimuth samples were collected per range cell. Within the azimuth sector, data were acquired in four contiguous 4.74-km range intervals; each range interval contained 316 range cells of 15 meter sampling interval (i.e., 10 MHz sampling rate). Figures 4.26 and 4.27 show azimuth and range spatial correlation coefficients obtained in processing the fourth range interval in these data. The results were obtained by processing the entire 703 x 416 sample array of data obtained at HH-polarization in the fourth range interval (15.2 to 20.0 km from the radar).

25. Summary provided here of material originally published in [30], by permission of IEEE.

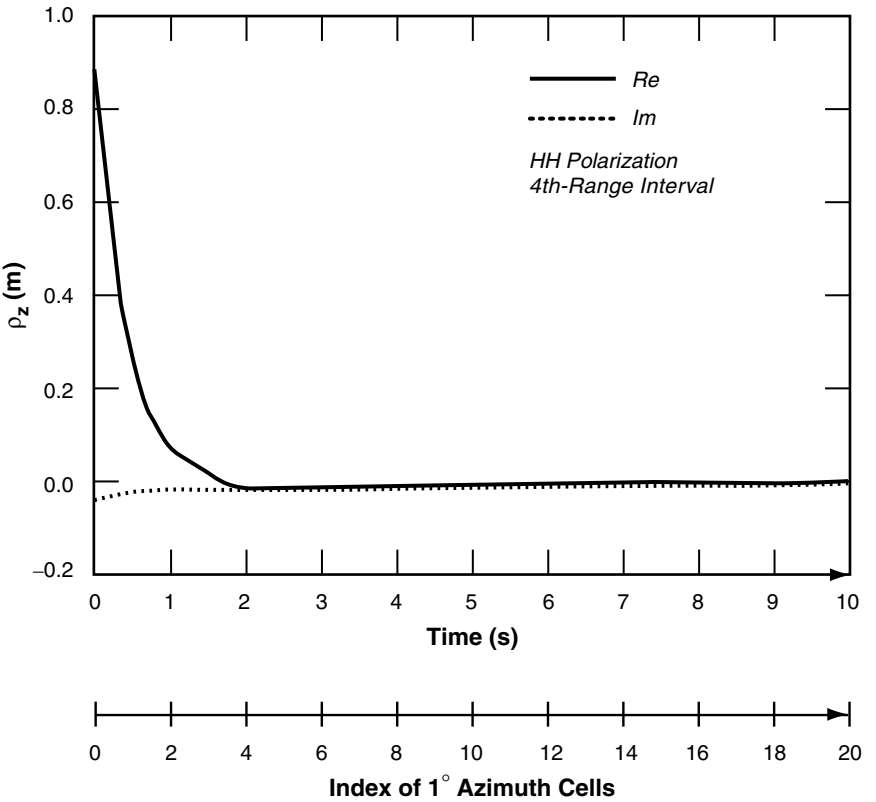

FIGURE 4.26 Azimuthal correlation coefficient, fourth-range interval, HH polarization. (Results provided by F. Gini and M. Greco, Univ. of Pisa. After [30]; by permission, © 1999 IEEE.)

The azimuthal autocorrelation sequence was estimated from the data without making any assumption, other than stationarity, about the structure of the clutter process. The sample estimator processed $M = 316$ records $\{z_k\}_{k=1}^{M}$, one for each range cell, of $N = 703$ complex azimuth samples according to the following algorithm [37, Ch. 9]:

$$\hat{R}_z(m) = \frac{1}{NM}\sum_{k=1}^{M}\sum_{n=0}^{N-m-1} z_k(n)\ z_k^*(n+m) = 2\hat{R}_{z_I}(m) + j2\hat{R}_{z_I z_Q}$$

where $z_I(n)$ and $z_Q(n)$ are the in-phase and quadrature components, $z(n) = z_I(n) + jz_Q(n)$ is the complex envelope of the observed signal, and * represents complex conjugate. In Figure 4.26 the correlation coefficient $\rho_z(m) \triangleq \hat{R}_z(m)/\hat{R}_z(0)$ is shown for the fourth range interval. It is observed that the signal decorrelates to 0.29 in one 1°-beamwidth, and to ~0 in four beamwidths. As expected, the imaginary part of $\rho_z(m)$, i.e., the cross-correlation coefficient $\hat{R}_{z_I z_Q}(m)/\hat{R}_z(0)$, is approximately zero.

To obtain the range correlation coefficient, the correlation for each azimuth cell was calculated, and then the 703 estimates were averaged. The correlation coefficient $\rho_R(m)$ is plotted in Figure 4.27. Comparing this figure with Figure 4.26, the two decorrelation times

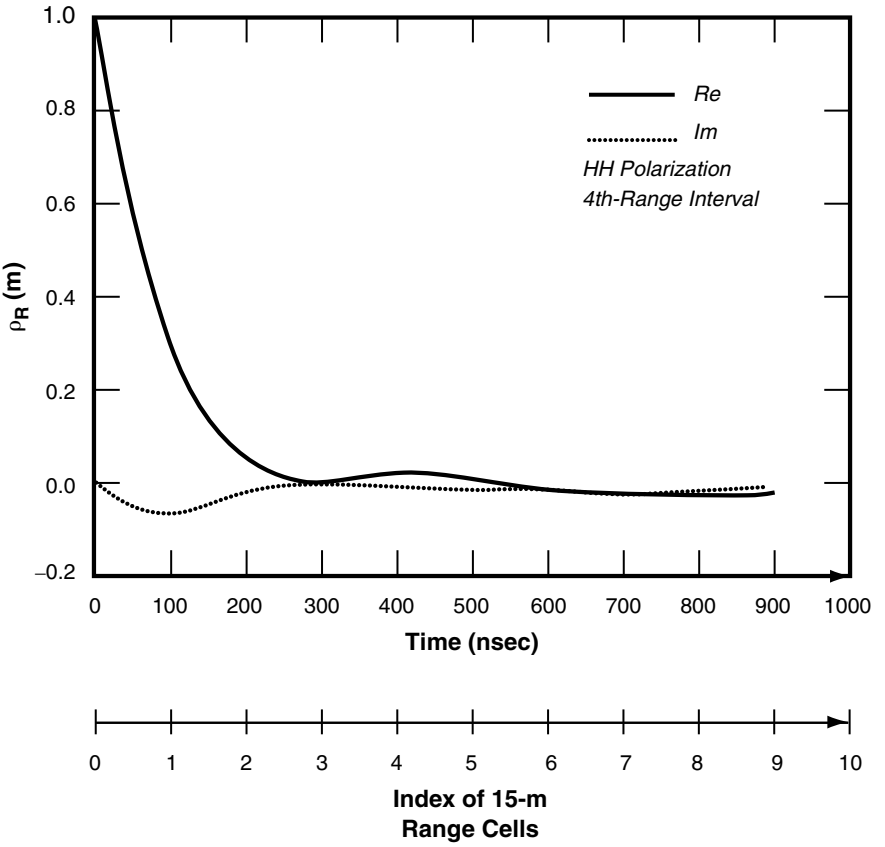

FIGURE 4.27 Range correlation coefficient, fourth range interval, HH polarization. (Results provided by F. Gini and M. Greco, Univ. of Pisa. After [30]; by permission, © 1999 IEEE.)

are observed to be quite different. Along the azimuth direction the coefficient reduces to 0.1 in a few seconds, whereas along the range direction, the same amount of reduction occurs in a few hundreds of nanoseconds. These apparent large differences are merely the result of the different time-sampling frequencies utilized in range (10 MHz) and in azimuth (15.625 Hz). The assumption usually made in adaptive radar detection (see, e.g., [38], Ch. 3) of independence of the data from different range cells is very reasonable in these Wolseley data.

Thus, the important thing to observe in considering Figures 4.26 and 4.27 is that, owing to the heterogeneity of the spatial scattering ensemble in open farmland terrain (strong discrete sources dispersed over a weakly scattering medium), the returned signal from the scanning antenna largely decorrelates from one spatial cell to the next, whether the variation is in the range direction or in the azimuth direction. Consider again the azimuth variation results of Figure 4.26. The azimuth extent of the spatial resolution cell is determined by the beamwidth of ~1°. The scan rate is 2°/s, so the expectation is that the returned signal would decorrelate in ~1 beamwidth or ~0.5 s. Figure 4.26 shows the azimuthal correlation coefficient to drop to 0.29 in 0.5 s (one beamwidth), but to take ~2 s (~4 beamwidths) to decorrelate to zero. This largely meets the expectation of decorrelation in one azimuthal interval, given that the azimuthal cell specified is the 3-dB beamwidth,

with resultant beam overlap between 1° cells. The azimuth sampling rate used in data acquisition was 15.625 samples (pulses) per second. That is, in azimuth, the sampling time (0.064 s, is much less than the cell size (~0.5 s).

Now consider again the range variation results shown in Figure 4.27. The range extent of the spatial resolution cell is determined by the 3-dB pulse length which is specified to be 100 ns. This is matched to the range sampling rate of 10 MHz (i.e., in range, the sampling interval equals the cell size). Therefore, the expectation is that, in range, the returned signal would largely decorrelate, sample-to-sample, in ~100 ns. Figure 4.27 shows the range correlation coefficient to drop to 0.3 in 100 ns (one pulse length), but it takes 300 ns (3 pulse lengths) to decorrelate to zero. Thus the range results of Figure 4.27 very closely match the azimuthal results of Figure 4.26 in terms of equivalent cell-to-cell decorrelation in azimuth and range.

Note that although the azimuthal decorrelation in Figure 4.26 is caused by the antenna pattern, the decorrelation data cannot be simply predicted from the pattern. Perhaps it would be useful to state a simple example as follows: if the pattern were hypothetically purely rectangular (i.e., a simple step function of width ϕ), and if the clutter were simply one large point scatterer, then the azimuthal correlation coefficient would be triangular of base width 2ϕ (i.e., would fall to 0.5 in one cell and to zero in two cells). By contrast, the measured data in Figure 4.26 falls to 0.29 in one cell and to zero in four cells.

4.7 Summary

Chapter 4 describes a number of approaches for modeling low-angle land clutter in surface-sited radar. As a physical phenomenon, the most salient attribute of low-angle clutter is variability. Two important ways in which this variability is evidenced are patchiness in spatial occurrence and extremely wide cell-to-cell statistical fluctuation in clutter strength (i.e., spikiness) within patches. A site-specific approach to clutter modeling is described based on the use of digitized terrain elevation data (DTED) at each site, which captures both of these basic attributes—patchiness, via deterministic computation of geometric terrain visibility from the radar site; and spikiness, via realizations from statistical distributions in which the spread depends on the depression angle to the backscattering terrain point as computed from the DTED.

An interim site-specific clutter model is provided as a table of Weibull coefficients in which the mean value of the distribution of clutter strengths varies with radar frequency, the shape parameter of the distribution varies with radar spatial resolution, and both mean strength and shape parameter vary with depression angle and terrain type. This site-specific approach to clutter modeling in surface radar is highly realistic. Besides capturing the fundamental patchiness and spikiness of low-angle clutter, this approach: (a) ensures that the modeled clutter in surface-sited radar dissipates with increasing range in the same way that clutter actually dissipates with increasing range at real sites, namely, via the deterministic visibility function, whereby the spatial patches of occurrence of clutter become fewer and farther apart with increasing range until, beyond some maximum range, no more clutter patches are visible; and (b) raises clutter modeling to the level of a quantitative science in that a given clutter patch at a given site, and, more specifically, the distribution of clutter strengths over that patch is a real and distinct physical entity that can be measured, parameterized (e.g., by terrain type and depression angle), and modeled, thus

allowing quantitative comparison of the measured and modeled distributions and hence a direct means for clutter model validation.

Dominant sources of low-angle clutter appear to be of a point-like or spatially discrete nature, in that they occur in spatially isolated cells as opposed to being of a spatially extended nature. The basic site-specific approach to clutter modeling does not distinguish between whether clutter returns emanate from discrete or extended sources. A refinement to the basic site-specific clutter model is described involving a more computationally intensive approach that separates the modeling of dominant, locally strong clutter cells (called the discrete component) from weaker surrounding clutter cells (called the background component). Little correlation was found to exist between clutter cells that are locally stronger than their neighbors, and actual physical discrete objects on the terrain that could be identified as the sources of the strong clutter. Furthermore, it is not possible to determine in the measurement data whether a given, locally strong clutter return actually emanates from a definable, physical point object of specifiable RCS, or from a physically extended σ° clutter medium that by chance phasor reinforcement happens to produce a strong clutter return.

Therefore, the separate modeling of locally strong clutter cells under this approach needed to be carried out, not as a deterministic RCS overlay, but as a second statistical σ° process in which, with a specified probability of occurrence, a given cell might have a "discrete" component added vectorally to its "background" component. That is, under this approach an investigator is not provided with a single value of σ° for a given terrain type and illumination angle, but is provided with two values of σ°, one for "discrete" clutter and one for "background" clutter. The total clutter return is comprised of two components requiring two random draws, compared to modeling the total return as a single component obtained from one random draw.

In the separation of locally strong clutter cells from the weaker surrounding cells, the weaker clutter was found to be dependent at the resolution cell level on terrain slope and grazing angle, thus allowing the effect of landform on the weaker clutter to be provided at the cell level via computation of grazing angle using DTED rather than through macropatch classification of terrain relief; the locally strong (i.e., dominant) clutter, like the total clutter in the interim model, did not show correlation with grazing angle at the cell level. Another refinement to the basic site-specific clutter model obtainable with more intensive computation is the softening or blurring of shadow boundaries, as determined geometrically from DTED, whereby clutter is allowed to rapidly diminish into shadowed regions with increasing depth of shadow rather than abruptly terminating right at the shadow boundary.

These site-specific approaches to clutter modeling allow the limiting effects of clutter on radar system performance at any given site to be determined to a high degree of exactitude, thereby meeting much in the way of design- and analysis-related need for quantification and prediction of radar performance in ground clutter. In today's highly evolved and rapidly expanding era of high performance computer capability, the fact that a site-specific approach to clutter modeling is computer-dependent, requiring extensive computation based on accurate DTED for the sites in question, is no longer very restrictive, whether concern is with individual sites or complexes of sites. The nature of ground clutter is that it can affect radar performance very differently from site to site, as a consequence of the

extreme variations in surrounding terrain that can occur from one site to another, and a quantitative approach to the accurate assessment of the effects of clutter needs to reflect this specificity.

Nevertheless, the fact remains that the site-specific approach to modeling clutter provides answers one site at a time. For radar system design/analysis that requires more general information of the impact of ground clutter on system performance, the rigorous way under the site-specific approach is to first compute performance across a set of sites as specified by the particular design or analysis under consideration, and then to generalize (e.g., medianize) performance depending on how site-to-site performance varies across the set. Note that this approach to generality *a posteriori* averages the performance measures obtained from a number of realistic site-specific clutter computations; it does not attempt to *a priori* average the clutter first (a non-verifiable undertaking) followed by a one-time assessment of performance.

As a conceptual alternative to accepting the computational burden required in such a rigorous approach to generality, the idea of a clutter model that retains the important element of spatial patchiness but realizes it by means of a generic stochastic process in which patch extents, separations, and obliquities are statistically representative of general types of terrain rather than specific sites is intuitively attractive. This idea, involving implementation of generalized stochastic patchiness, although beyond the range of subject matter covered in this book, was explored at some length in coordinated studies involving the Lincoln Laboratory clutter data carried out by other investigative agencies ([3] is an early citation from extended research undertaken to develop this idea). However, the specificity of terrain feature at the scale at which terrain feature affects low-angle terrain visibility and clutter patchiness makes it difficult to capture such effects statistically. Unlike the ocean, the terrain at most sites of any significant relief is not very statistical in the sense of generally repeated patterns, but is dominated by a relatively few discrete singular macrofeatures (e.g., a mountain range, a ridge of hills, a river valley, a coastal shoreline). As a result, the parameters affecting the patchiness provided by a general stochastic model could not be related to simple quantifiable measures (e.g., surface relief; correlation distance) associated with generalized terrain types; but rather required that the parameters governing patchiness be acquired by an initialization or conditioning cycle of processing in DTED over a large-scale region encompassing the site of interest.

Such generalized approaches to stochastic patchiness were reasonably successful for terrain of relatively low or moderate relief; high-relief terrain is too specific for a stochastic approach to be appropriate. Since a stochastically patchy non-site-specific clutter model requires initialization using DTED from the terrain region of interest, the sought for advantages of such a model in providing non-site-specific stochastic realizations of patchiness are somewhat diminished compared with more straightforwardly obtained site-specific realizations of patchiness. For such reasons, the initially attractive and deceptively simple notion of a generic non-site-specific clutter model invested with realistic stochastic patchiness becomes more difficult to successfully implement in actual practice than might be presupposed, although a remaining advantage of the stochastically patchy approach is that it can lead to generic analytic formulations of such system performance measures as, for example, signal-to-clutter ratio vs range for the terrain type under consideration.

A spatially patchy clutter model, whether site-specific or non-site-specific, captures the important element of disconnectedness in spatial occurrence of low-angle terrain visibility that leads to a high degree of fidelity in the representation of ground clutter in surface radar. Such a high degree of fidelity is not always required, however, in the representation of ground clutter by radar system engineers. As a first indication of the effects of ground clutter, the radar system engineer may not be interested in the full-blown system effects of patchiness, but may require only a single value of constant σ° indicating how strong the clutter is at a given site for use in the radar range equation to estimate signal-to-clutter ratios against particular targets; and in addition may require only a single value of cut-off range to indicate the maximum extent in range to which the constant σ° applies and beyond which the radar is clutter-free.

From this point of view, the modeling of patchiness in low-angle terrain visibility may be regarded as a higher order (although important) effect in low-angle clutter phenomenology compared with modeling the strength of the clutter (assuming that the ground is visible), and for a beginning all that is required of this higher-order effect is a global estimate of the maximum extent of the patchy terrain visibility in range. Furthermore, this point of view disregards the fact that low-angle σ° occurs as a statistical phenomenon with wide cell-to-cell variations over a local region, but instead focuses on a single measure of strength such as the mean level; it also disregards the fact that σ° varies with depression angle since depression angle varies most significantly only within the first few kilometers of range from the radar, and usually diminishes to very near grazing incidence (e.g., 0.1° or 0.2°) over the much greater extents of clutter spatial occupancy that occur at much longer ranges.

To meet these kinds of less demanding requirements in a clutter model, Chapter 4 also provides a simple, non-patchy, non-site-specific clutter model that specifies mean clutter strength $\overline{\sigma_w^\circ}$ depending only on general terrain type (e.g., rural/low-relief, rural/high-relief, urban) and clutter cut-off range R_c depending only on effective radar height (e.g., low, intermediate, high). Since low-angle clutter is so variable both in strength and extent, these two parameters $\overline{\sigma_w^\circ}$ and R_c are provided not only as baseline central values, but also as worst-case values indicative of severe or heavy clutter situations, and as best-case values indicative of benign or light clutter situations.

A very large step in simplification occurs between the extremes of clutter models (viz., the full-blown site-specific statistical model vs the simple non-site-specific constant-σ° model) described in Chapter 4. Many of the difficulties that face efforts to bring realism to empirical clutter models at intermediate levels of fidelity between these two extremes are explored in ancillary discussions of the measured clutter data both in the body of Chapter 4 and its appendices. These ancillary discussions include considerations of (a) the inherent effects on terrain visibility and clutter strength of radar height and radar range; (b) the proper way to deal with unavoidable noise-level samples in clutter measurements and the important consequent effect on clutter statistics of rapidly decreasing radar sensitivity to clutter with increasing range; and (c) the wide range of variability involved in general clutter amplitude statistics and the attendant difficulty in specifying any particular σ° level for a constant-σ° clutter model.

Discussions are also provided concerning the relationship between terrain visibility and clutter occurrence and concerning discrete vs distributed clutter and the appropriate parameter by which to characterize low-angle clutter. All these discussions serve to more

fully describe the complex, multifaceted nature of low-angle clutter from different perspectives and to bring home the value of the site-specific approach to clutter modeling in that it automatically and accurately incorporates all the complicating factors that are difficult for more general modeling approaches to capture. Although the main subject of Chapter 4 is the consideration of various approaches to modeling the spatial amplitude statistics of low-angle ground clutter, brief consideration is also given to aspects of the phenomenon associated with its temporal variability and its spectral and correlative properties.

References

1. M. Sekine and Y. Mao, *Weibull Radar Clutter*, London, U. K.: Peter Peregrinus Ltd. and IEE, 1990.

2. R. R. Boothe, "The Weibull Distribution Applied to the Ground Clutter Backscatter Coefficient," U. S. Army Missile Command Rept. No. RE-TR-69-15, Redstone Arsenal, AL, June 1969; DTIC AD-691109.

3. S. P. Tonkin and M. A. Wood, "Stochastic model of terrain effects upon the performance of land-based radars," *AGARD Conference Proceedings on Target and Clutter Scattering and Their Effects on Military Radar Performance*, AGARD-CP-501, (1991).

4. M. P. Warden and E. J. Dodsworth, "A Review of Clutter, 1974," Royal Radar Establishment Technical Note No. 783, Malvern, U.K., September 1974; DTIC AD A014421.

5. W. J. McEvoy, "Discrete Clutter Measurements Program: Operations in the Metropolitan Boston Area," MITRE Corporation; Air Force Systems Command, Electronic Systems Division, Deputy for AWACS, Report ESD-TR-72-131, AD 742 298, March 1972.

6. W. J. McEvoy, "Discrete Clutter Measurements Program: Operations in Western Massachusetts," MITRE Corporation; Air Force Systems Command, Electronic Systems Division, Deputy for AWACS, Report ESD-TR-72-132, AD 742 297, March 1972.

7. D. C. Schleher, *MTI and Pulsed Doppler Radar*, Norwood, MA: Artech House, 1991, p. 226.

8. S. Kazel, J. Patten, J. Dabkowski, J. Pipkin, and A. Brindley, "Extensions to the ORT Clutter Model," IIT Research Institute, Chicago, June 1971.

9. H. R. Ward, "A model environment for search radar evaluation," *IEEE EASCON Rec*, pp. 164-171, 1971.

10. C. J. Rigden, "High Resolution Land Clutter Characteristics," Admiralty Surface Weapons Establishment Technical Report TR-73-6, Portsmouth, U.K., January 1973; DTIC AD-768412.

11. D. C. Schleher, *op. cit*., p. 174.

12. C. W. Helstrom, *Elements of Signal Detection and Estimation,* Englewood Cliffs, NJ: Prentice-Hall, 1995.

13. T. Linell, "An experimental investigation of the amplitude distribution of radar terrain return," *6th Conf. Swedish Natl. Comm. Sci. Radio*, Research Institute of National Defence, Stockholm, March 1963.

14. F. E. Nathanson and J. P. Reilly, "Clutter statistics that affect radar performance analysis," *EASCON Proc*. (supplement to *IEEE Trans*.), vol. AES-3, no. 6, pp. 386-398, November 1967.

15. J. K. Jao, "Amplitude distribution of composite terrain radar clutter and the *K*-distribution," *IEEE Transactions on Antennas and Propagation*, AP-32 (Oct. 1984), 1049-1062.

16. J. B. Billingsley and J. F. Larrabee, "Multifrequency Measurements of Radar Ground Clutter at 42 Sites," Lexington, MA: MIT Lincoln Laboratory, Technical Rep. 916, Volumes 1, 2, 3; 15 November 1991; DTIC AD-A246710.

17. K. Rajalakshmi Menon, N. Balakrishnan, M. Janakiraman, and K. Ramchand, "Characterization of fluctuating statistics of radar clutter for Indian terrain," *IEEE Transactions on Geoscience and Remote Sensing*. vol. 33. no. 2 (March 1995), 317-323.

18. V. Anastassopoulos and G. A. Lampropoulos, "High resolution radar clutter classification," in *Proceedings of IEEE International RADAR Conference*, Washington, DC, May 1995, 662-667.

19. K. S. Chen and A. K. Fung, "Frequency dependence of backscattered signals from forest components," *IEE Proceedings*, Pt. F, 142, 6 (December 1995), pp. 310-315.

20. E. J. Barlow, "Doppler Radar", *Proc. IRE,* 37, 4 (1949).

21. J. L. Lawson and G. E. Uhlenbeck (eds), *Threshold Signals*, Vol. 24 in the MIT Radiation Laboratory Series, New York: McGraw-Hill (1950). Reprinted, Dover Publications (1965).

22. H. Goldstein, "The Fluctuations of Clutter Echoes," pp. 550-587, in D. E. Kerr (ed.), *Propagation of Short Radio Waves*, Vol. 13 in the MIT Radiation Laboratory Series, New York: McGraw-Hill (1951). Reprinted, Dover Publications (1965).

23. J. B. Billingsley, A. Farina, F. Gini, M. V. Greco, and P. Lombardo, "Impact of experimentally measured Doppler spectrum of ground clutter on MTI and STAP," in *Proceedings of 1997 International Radar Conference*, Edinburgh, UK, October 14-16, 1997, 290-294.

24. A. Farina, F. Gini, M. V. Greco, and P. Lee, "Improvement factor for real sea-clutter Doppler frequency spectra," *IEE Proceedings*, Pt. F, 143, 5 (October 1996), 341-344.

25. S. Watts, C. J. Baker, and K. D. Ward, "Maritime surveillance radar Part 2: Detection performance prediction in sea clutter," *IEE Proceedings*, Pt. F, 137, 2 (April 1990), 63-72.

26. J. B. Billingsley and J. F. Larrabee, "Measured Spectral Extent of L- and X-Band Radar Reflections from Windblown Trees," Lexington, MA: MIT Lincoln Laboratory, Project Rep. CMT-57, 6 February 1987; DTIC AD-A179942.

27. H. C. Chan, "Radar ground clutter measurements and models, part 2: Spectral characteristics and temporal statistics," *AGARD Conference Proceedings on Target*

and Clutter Scattering and Their Effects on Military Radar Performance, AGARD-CP-501 (1991).

28. G. C. Sarno, "A model of coherent radar land backscatter," *AGARD Conference Proceedings on Target and Clutter Scattering and Their Effects on Military Radar Performance*, AGARD-CP-501 (1991).

29. J. B. Billingsley, "Exponential Decay in Windblown Radar Ground Clutter Doppler Spectra: Multifrequency Measurements and Model," Lexington, MA: MIT Lincoln Laboratory, Technical Report 997, 29 July 1996; DTIC AD-A312399.

30. J. B. Billingsley, A. Farina, F. Gini, M. V. Greco, and L.Verrazzani, "Statistical analyses of measured radar ground clutter data," *IEEE Trans. AES*, vol. 35, no. 2 (April 1999).

31. P. Lombardo, and J. B. Billingsley, "A new model for the Doppler spectrum of windblown radar ground clutter," in *Proceedings of IEEE 1999 Radar Conference*, Boston, MA, 20-22 April 1999.

32. D. P. Meyer and H. A. Mayer, *Radar Target Detection—Handbook of Theory and Practice*, San Diego, CA: Academic Press, 1973, pp. 66, 67.

33. L. R. Rabiner and B. Gold, *Theory and Application of Digital Signal Processing*, Prentice-Hall, Inc., Englewood Cliffs, NJ, 1975.

34. F. J. Harris, "On the use of windows for harmonic analysis with the discrete Fourier transform," *Proc. IEEE*, vol. 66, no. 1, pp. 51-83, January 1978.

35. V. A. Andrianov, N. A. Armand, and I. N. Kibardina, "Scattering of radio waves by an underlying surface covered with vegetation," *Radio Eng. and Electron. Physics* (USSR), vol. 21, no. 9, September 1976.

36. C. M. Rader, "An improved algorithm for high-speed autocorrelation with applications to spectral estimation," *IEEE Trans. Audio Electrocoustic*., vol. AU-18, pp. 439-441, Dec. 1970.

37. S. M. Kay, *Fundamentals of Statistical Signal Processing: Estimation Theory*, Englewood Cliffs, NJ: Prentice-Hall, 1993.

38. S. Haykin and A. Steinhardt, *Adaptive Radar Detection and Estimation*, New York: Wiley, 1992.

5

Multifrequency Land Clutter Modeling Information

5.1 Introduction

Chapter 5 provides land clutter modeling information for surface-sited radar based on comprehensive reduction of extensive multifrequency land clutter measurement data from 42 different sites. The survey clutter measurements upon which this information is based are described in Chapter 3 (see also [1]). The clutter modeling information that follows is provided for general terrain and for eight specific terrain types. For each terrain type, the modeling information is further partitioned by the relief of the terrain and by the depression angle below the horizontal from the radar to the backscattering terrain point.

For each terrain type/relief/depression angle combination of parameters, the modeling information provided specifies the probability distribution encompassing the spatial cell-to-cell variability of clutter amplitude statistics applicable to that combination of parameters. Probability distributions are specified in terms of Weibull statistics. For each terrain type/relief/depression angle combination, Weibull mean clutter strength $\overline{\sigma_w^\circ}$ is provided as a function of radar frequency, VHF to X-band; and Weibull shape parameter a_w is provided as a function of radar spatial resolution, 10^3 m^2 to 10^6 m^2. The number of clutter coefficients $\overline{\sigma_w^\circ}$ applicable to low-angle land clutter specified in Chapter 5 is 864. These coefficients are provided within a parametric structure that allows practical application of them to surface radars sited in various terrains and situations.

Most of the clutter coefficients provided are relatively general, each usually being based on numerous measurements. The number of measurements applicable to each value of $\overline{\sigma_w^\circ}$ is also provided. In the past, authoritative reviews of the subject [2–5] have agreed on the difficulty of characterizing low-angle land clutter with basic questions of radar frequency dependence, the role of illumination angle, and effects of varying terrain type remaining unanswered. The definitive body of new information presented in Chapter 5 now provides a condensed and unified codification of low-angle land clutter's fundamental attributes.

In what follows, Section 5.1.1 reviews the Phase One survey database, the reduction of these data into patch-specific histograms of clutter strength, and the fundamental parametric effects that emerge in the trend analyses of these histograms. Section 5.2 describes how clutter modeling information in terms of Weibull statistics is derived through the combination of many patch measurements. Section 5.3 presents clutter modeling information for general rural terrain, irrespective of land cover. Section 5.4 presents clutter modeling information for eight specific terrain types. Section 5.5 briefly discusses and

provides an example of plan-position indicator (PPI) clutter map simulation using the modeling information of Chapter 5. Section 5.6 is a summary. Appendix 5.A presents additional information on Weibull statistics and compares them with statistics from lognormal and *K*-distributions.

5.1.1 Review

5.1.1.1 Clutter Measurements

The results of Chapter 5 are based on Phase One five-frequency land clutter measurements at 42 different sites as described in Chapter 3. At each Phase One site, all of the discernible land clutter within the field-of-view was measured at each of five frequencies, VHF, UHF, L-, S-, and X-bands, and at both vertical and horizontal polarization and at low and high range resolution. These raw Phase One data were calibrated, pulse-by-pulse and cell-by-cell, into absolute units of clutter strength. The resultant large 475-Gbyte five-frequency land clutter measurement database comprises a unique resource that is planned to be maintained indefinitely at Lincoln Laboratory. These data were provided to government authorities in Canada and the United Kingdom, and coordinated analyses took place in these countries as well as in the United States [6–9]. The results of Chapter 5 are based on the spatially comprehensive 360° survey data from all 42 Phase One sites. Previous Phase One results discussed in Chapters 3 and 4 were based on the relatively narrow (e.g., 20°) azimuth sector of repeated measurement concentration at each site called the repeat sector. Clutter experiments acquired in survey mode, as opposed to repeat sector mode, are further described in Chapter 3, Section 3.2.2.

5.1.1.1.1 Data Reduction

Each raw in-phase (I) and quadrature (Q) sample pair of Phase One measured clutter data is reduced to a clutter strength number. As defined earlier in this book, clutter strength is given by $\sigma^\circ F^4$, where σ° is the intrinsic backscattering coefficient and F is the pattern propagation factor. As previously discussed, the pattern propagation factor includes all terrain effects in low-angle land clutter caused by multipath reflections and diffraction from the terrain. Using available digitized terrain elevation data, it is not generally possible to deterministically compute F at clutter source heights sufficiently accurately to allow cell-by-cell separation of intrinsic σ° in measured clutter data (e.g., see Chapter 1, Section 1.5.4; Chapter 3, Appendix 3.B). All of the coefficients of clutter strength tabulated as modeling information in Chapter 5 include propagation effects. All computations involving $\sigma^\circ F^4$ are performed in units of m^2/m^2. For convenience, the tabulated clutter coefficients have been subsequently converted to decibels with respect to 1 m^2/m^2. The specific computations involved in data reduction are defined more completely in Chapters 2 and 3.

5.1.1.1.2 Stored Clutter Histograms

Within the PPI spatial map of measured clutter strength at each site, terrain macroregions were selected largely within line-of-sight illumination in which a relatively high percentage of resolution cells contain discernible clutter above the radar noise level. These terrain macroregions are referred to as terrain patches or clutter patches. Typically, clutter patches are several kilometers on a side (median size = 12.6 km^2; see Appendix 2.B). Many examples of clutter patches and histograms of clutter strength measured from clutter patches are shown in this book, including several to follow in Chapter 5. By registering measured clutter maps with air photos and topographic maps, landform and land cover descriptive information of the terrain within the patch was provided.

The landform and land cover classification systems utilized in this process are described in Chapter 2, Section 2.2.3. For each clutter patch, the distribution or histogram of clutter strengths occurring within the patch was formed, based upon all of the cells within the patch, including those at radar noise level. This histogram was formed at each of the 20 parameter combinations nominally available within the Phase One radar parameter matrix (five frequencies, two polarizations, two range resolutions; see Appendix 3.A, Table 3.A.2). Various statistical attributes (e.g., mean, median, variance, etc.) of each histogram were computed. The formulas used in these computations are provided in Appendices 2.B and 3.C.

Each histogram together with its statistical attributes and the applicable terrain descriptors of the patch and the radar parameters was then stored in a computer file. Predictive clutter modeling information was developed by establishing general correlative properties between the stored distributions of measured clutter strength and the corresponding terrain descriptions and relevant radar parameters. The results of Chapter 5 are based on 59,804 stored histograms of measured clutter strength from 3,361 clutter patches at the 42 Phase One sites.

5.1.1.1.3 Pure and Mixed Terrain

Classification of the terrain within each of the 3,361 clutter patches in terms of landform (i.e., the relief or roughness of the terrain) and land cover (e.g., urban, forest, agricultural, etc.) occurred at two levels, primary and secondary (see Sections 2.2.3 and 3.2.3 for details). As a result of terrain classification, the results of Chapter 5 are partitioned into two groups, those applicable to pure terrain and those applicable to mixed terrain. Pure terrain is terrain that requires primary classification only. Mixed terrain requires secondary as well as primary classification. Of the 3,361 clutter patches, 1,733 (i.e., 52%) are pure and 1,628 (i.e., 48%) are mixed. For pure terrain, clutter modeling results are provided in Section 5.4 for eight specific terrain types; namely, urban, agricultural, forest, shrubland, grassland, wetland, desert, and mountain categories. These specific terrain types are usually characterized principally by land cover, although mountain terrain is characterized principally by landform. For mixed terrain, general results are provided in Section 5.3.

Most terrain types are further partitioned by relief, usually in terms of high relief (i.e., with terrain slopes $> 2°$) and low relief (i.e., with terrain slopes $< 2°$). Results for pure terrain are suitable for modeling at cell level or in very homogeneous terrain. Results for pure terrain are also useful for setting approximate worst-case/best-case bounds on the severity of land clutter interference. Results for mixed terrain apply more generally to large extents of composite landscape. The results in Section 5.3 for general mixed rural terrain are among the more important results of the Phase One clutter measurements program; these results show how systematic variations in terrain relief and depression angle cause corresponding variations in clutter strength in all five frequency bands for generally occurring composite terrain.

5.1.1.1.4 Clutter Patch Selection at Magrath

Figure 5.1[26] illustrates clutter patch selection at the Phase One measurement site of Magrath, Alberta. The figure shows two Phase One X-band PPI clutter maps in both of which clutter is shown dark gray—the clutter map on the left is to 20-km maximum range, that to the right is to 50-km maximum range. In both clutter maps, the repeat sector clutter patch is shown as a narrow solid black sector to the southeast. Repeat sector clutter

26. All Chapter 5 figures occur consecutively in the figures-only, color section beginning on page 447.

measurements, involving one patch per site at each of 42 different sites, are the basis of the Phase One results provided in Chapters 3 and 4.

Also in both clutter maps, all the survey patches selected at Magrath are shown outlined and shaded to appear light gray. It is evident that the survey patches in total are much more spatially comprehensive in terms of covering almost all of the measured clutter than the repeat sector. As a result, the clutter modeling information of Chapter 5, based on survey measurements at all sites, is of increased statistical certainty and of increased prediction accuracy, both because these survey results are based on many more samples per terrain class and in addition because they are based on more terrain classes.

5.1.1.1.5 Noise Corruption

It was indicated above that, in forming histograms and cumulative distributions of clutter strength $\sigma^{\circ}F^4$ over clutter patches, all of the cells and samples that were measured from the patch, including those at radar noise level, need to be included. It is possible, in forming such histograms and distributions, to include only those samples for which the returned signal strength is greater than radar noise level, and to delete the noise-level samples. Such histograms and distributions have been referred to as "shadowless" previously in this book (e.g., see Section 1.4.7 and Appendices 2.B, 3.C, and 4.C for related discussions). Shadowless statistics are obviously dependent upon radar sensitivity and are thus conditional (not absolute) measures of reflectivity. Use of shadowless clutter statistics can lead to subsequent misinterpretation in analysis and significant misrepresentation of radar system performance.

Thus, in forming the cumulative distribution for a given clutter patch, the noise-level samples are retained and the cumulative is plotted two ways: (1) as an upper bound in which the samples at noise level retain their noise power values, and (2) as a lower bound in which the samples at noise level are assigned zero (or a very low value of) power. These upper bound/lower bound cumulative pairs deviate from each other only over the low-end noise-corrupted interval of the distribution (where the true cumulative must lie between them); they merge to form the single true cumulative at $\sigma^{\circ}F^4$ levels above the highest noise corruption. By true cumulative is meant that which would be measured by a hypothetical radar of infinite sensitivity (or at least sensitivity high enough so that all clutter samples returned from the clutter patch are well above radar noise level). In contrast, the shadowless cumulative can lie significantly apart from the true cumulative over its compete range (see Appendix 4.C).

Similarly, in the computation of the moments of distributions that include noise samples, the moments are computed two ways: (1) as an upper bound in which the samples at noise level retain their noise power values, and (2) as a lower bound in which the samples at noise level are assigned zero power. Upper and lower bounds to moments of noise-corrupted clutter distributions are usually within small fractions of a decibel of each other, even when the amount of noise corruption is high; such tight bounds are the result of the extreme skewness of the distributions such that the moments are dominated by the high-end tails. Of course, the true value of the moment must lie between the upper and lower bounds. In contrast, moments of shadowless distributions are dependent on radar sensitivity (i.e., the amount of noise that was deleted) and can be significantly different from the true value. Separation of upper and lower bound values of moments by large amounts indicates a measurement too corrupted by noise to provide useful information.

The clutter modeling results provided in Chapter 5 are based upon tight upper-bound values of moments of noise-corrupted low-angle clutter distributions and are thus absolute measures independent of radar sensitivity. The correct methodology (as discussed above) for the proper treatment of radar noise and shadowing in low-angle clutter is elaborated in more detail elsewhere (see Section 1.4.7 and Appendices 2.B, 3.C, and 4.C).

5.1.1.1.6 Two Clutter Patch Histograms

The terrain within general rural clutter patches often consists of mixtures of various open (e.g., cropland, rangeland) and tree-covered components. Figures 5.2 and 5.3 show examples of measured clutter histograms and cumulative distributions from two such mixed rural patches. These two examples were selected from the 30,246 such histograms comprising the Phase One general mixed rural clutter modeling database.

Figure 5.2 shows a UHF histogram measured from patch 34/2 at Wachusett Mountain, Massachusetts. Patch WM 34/2 was primarily hilly mixed-forest with secondary occurrences of cropland and lakes, and was observed at 1° depression angle. It was situated beginning at 11.9 km from the radar and extended 11.7 km in range and 35.6° in azimuth. In the histogram of Figure 5.2, 4.1% of the samples are at radar noise level (cells at noise level are indicated as black in the histogram). Figure 5.3 shows an X-band histogram measured from patch 7/1 at Spruce Home, Saskatchewan. Patch SH 7/1 was primarily level cropland with secondary occurrences of trees at 10% incidence of occurrence and was observed at a depression angle of 0.6°. It was situated beginning 2.2 km from the radar and extended 4.8 km in range and 33.6° in azimuth. In the histogram of Figure 5.3, 11.6% of the samples are at radar noise level. The histograms of Figures 5.2 and 5.3 were both measured using 150-m pulse length and horizontal polarization.

The WM 34/2 and SH 7/1 clutter histograms of Figures 5.2 and 5.3 typify the many such measurements in the Phase One database in the extremely wide range of values of clutter strength $\sigma^\circ F^4$ that each exhibits. The WM 34/2 histogram of Figure 5.2 covers over six orders of magnitude in $\sigma^\circ F^4$; the SH 7/1 histogram of Figure 5.3 covers over eight orders of magnitude. In addition to showing these histograms, Figures 5.2 and 5.3 also show the corresponding upper-bound cumulative distributions in which the percent of samples in each histogram bin is accumulated left to right across the histogram.

The cumulative distribution is shown as a solid line and is read on the left ordinate; on the right ordinate is read the percent of samples in each histogram bin. The left ordinate is a nonlinear Weibull probability scale such that theoretical Weibull cumulative distributions plot as straight lines when, as shown, the abscissa is clutter strength in decibels (see Appendix 2.B). Both the WM 34/2 UHF cumulative clutter distribution (Figure 5.2) and the SH 7/1 X-band distribution (Figure 5.3) are relatively linear and hence reasonably well approximated as Weibull distributions over much of their central extents. In this respect also, these two distributions are representative of most of the many such measurements in the Phase One database, which are generally (but not without occasional exception) more Weibull-like than, for example, lognormal-like or *K*-distribution-like. This matter is discussed further in Appendix 5.A.

Also shown in Figures 5.2 and 5.3 is the slope that a theoretical Rayleigh distribution takes in such plots; by Rayleigh, it is meant that the received clutter voltage signal $\sqrt{x}$ is

Rayleigh distributed, which means that the clutter strength $x = \sigma^{\circ}F^4$ (which is a normalized measure of received clutter power) is exponentially distributed. The Rayleigh (voltage) distribution or exponential (power) distribution is a degenerate (one-parameter) case of the more general (two-parameter) Weibull distribution for which the Weibull shape parameter a_w is equal to unity [see Eq. (5.2)]. A simple Rayleigh (voltage) distribution is what is expected for clutter measured at higher airborne-like angles or over more homogeneous surfaces (see discussions in Chapter 2, Sections 2.3.4.2 and 2.4.4.3). It is evident in Figures 5.2 and 5.3 that the measured cumulative distributions are of significantly lower slope and hence are significantly wider than Rayleigh.

The non-Rayleigh nature of the two distributions shown in Figures 5.2 and 5.3 is also apparent from the numbers provided in Table 5.1. This table shows statistical attributes of these two measured clutter distributions and compares them with theoretical Rayleigh values. In Figures 5.2 and 5.3, the vertical dotted lines show the positions of the 50- (or median), 70-, 90-, and 99-percentile levels in the distributions, left to right, respectively; the vertical dashed line shows the position of the mean level in each distribution. For example, whereas a Rayleigh (voltage) distribution has mean/median (power) ratio equal to 1.6 dB [Eq. (5.3)], the measured WM 34/2 and SH 7/1 distributions have mean/median ratios equal to 7.8 and 21.2 dB, respectively.

The other statistical attributes of these measured distributions shown in Table 5.1 are similarly indicative of very wide, highly skewed, non-Rayleigh behavior. A Rayleigh distribution may be envisaged in Figures 5.2 and 5.3 not only to be of the cumulative Rayleigh slope indicated, but also to have a 99-percentile (right-most dotted line) to median (left-most dotted line) extent of only 8.2 dB. Table 5.1 indicates that the measured distributions in Figures 5.2 and 5.3 have 99-percentile/median ratios of 18 and 34 dB, which are more than twice and more than four times the Rayleigh value, respectively.

TABLE 5.1 Clutter Statistics for Two Mixed Rural Terrain Patches

Statistic	Spruce Home Patch 7/1 X-Band	Wachusett Mt. Patch 34/2 UHF	Theoretical Rayleigh Values
a_w	4.2	2.1	1.0
SD/Mean (dB)	7.2	3.7	0.0
Skewness (dB)	10.8	7.2	3.0
Kurtosis (dB)	22.8	16.4	9.5
Mean/Median (dB)	21.2	7.8	1.6
99-percentile/Median (dB)	34.0	18.0	8.2

Of particular interest in Table 5.1 are the values of Weibull shape parameter a_w and the values of ratio of standard deviation-to-mean from which the a_w values derive [Eq. (5.4)]. Again it is evident for the two example histograms of Figures 5.2 and 5.3 that, in terms of a_w, the data depart increasingly from the Rayleigh value of unity in proceeding from the higher angle, more homogeneous WM 34/2 patch (a_w = 2.1) to the lower angle, more heterogeneous SH 7/1 patch (a_w = 4.2). Looking ahead to the empirical clutter modeling information given in Chapter 5, observe that: (1) an important component of the modeling

information is the general specification of a_w as a function of resolution and depression angle, and (2) the values of a_w so specified for general low-angle clutter in ground-based radar over large extents of composite terrain are generally far from Rayleigh and only begin to approach the Rayleigh value of unity when cell size becomes very large or as depression angle increases to airborne-like regimes.

5.1.1.2 Parametric Effects

The following review of parametric clutter dependencies summarizes earlier discussions in this book. As developed in Chapter 2, a fundamental parametric dependence in low-angle clutter amplitude statistics is that of depression angle as it affects microshadowing among dominant discrete clutter sources, such that mean clutter strengths increase and cell-to-cell fluctuations decrease with increasing angle. At very low angles, clutter is to a very great extent caused by isolated discrete sources. Numerous low-reflectivity or shadowed cells occur between cells containing discrete clutter sources, even though the overall region from which the clutter amplitude distribution is formed is under general illumination by the radar. The combination of many shadowed or low-reflectivity weak cells together with many discrete-dominated strong cells causes extensive spread in the resultant low-angle clutter amplitude distribution.

As depression angle increases, the low reflectivity areas between discrete vertical features become more strongly illuminated, resulting in less shadowing and a rapid decrease in the spread of the distribution. As a result, measures of spread in the amplitude statistics such as ratio of standard deviation-to-mean and mean-to-median ratio decrease rapidly with increasing angle as the shadowed and weak samples at the low end of the distribution rise toward the stronger values that dominate the mean. However, the upper tail of the clutter distribution and mean level that is largely determined by the upper tail are still primarily caused by discrete sources and increase more slowly with increasing depression angle. These general effects of depression angle are important at all frequencies in the Phase One measurements.

Because of the heterogeneous process involved, wherein groups of cells providing strong returns are often separated by cells providing weak or noise-level returns, the spatial resolution of the radar fundamentally affects the amount of spread in clutter amplitude distributions from spatial macroregions. Increasing resolution results in less averaging within a cell, more cell-to-cell variability, and hence increased spread in the distributions. This general effect of resolution is also important at all frequencies in the Phase One measurements.

Within the context of the above mechanisms, radar frequency does not generally play as fundamental a role as do depression angle and resolution. However, as discussed in Chapter 3, two strong trends with frequency occur in particular circumstances. One of these is directly the result of the intrinsic backscattering coefficient σ° having an inherent frequency-dependent characteristic. Thus, at high depression angles in forested terrain, propagation measurements show that forward reflections are minimal (i.e., $F \approx 1$). In such terrain, intrinsic σ° decreases strongly with increasing frequency due to the absorption characteristic of forest increasing with frequency.

The other trend with frequency is the result of a general propagation effect entering clutter strength $\sigma^\circ F^4$ through the pattern propagation factor F. At low depression angles in level

open terrain, strong forward reflections cause multipath lobing on the free-space antenna pattern. At low frequencies such as VHF, these lobes tend to be broad so that returns from most clutter sources are received well on the underside of the first multipath lobe, and clutter strengths are much reduced. As frequency increases, the multipath lobes become narrower; typical clutter sources such as buildings or trees tend to extend over multiple lobes, with the result that at higher frequencies the overall multipath effect on illumination has less influence on the clutter strength. Thus, at low angles on level open terrain, there exists a characteristic of strongly increasing mean clutter strength with increasing frequency introduced through the pattern propagation factor. In inclined or rolling open terrain of increased relief, multipath is as likely to reinforce as to cancel clutter returns even at low radar frequencies.

Polarization has little general effect on ground clutter amplitude statistics. On the average, mean ground clutter strength is often 1 or 2 dB stronger at vertical polarization than at horizontal. The reason may be associated with the preferred vertical orientation of many discrete clutter sources. As discussed in Chapter 3, occasional specific measurements can show more significant variation with polarization but almost always less than 6 or 7 dB.

5.1.1.2.1 Discretes

A classical ground clutter model consists of diffuse clutter emanating from area-extensive surfaces with a few large point-like discrete scatterers added in to account for objects like water towers. The Phase One measurements reveal that, at the near grazing incidence of surface radar, over ranges of many kilometers, a more realistic construct is to imagine clutter as arising from a sea of discretes. By discretes are meant here strong, locally isolated clutter cells separated by weak cells often at the noise level of the radar. For example, over forest, it is the cells containing projecting treetops that cause the dominant backscatter, with the in-between shadowed areas of the canopy contributing much lower returns. Over agricultural terrain, it is the few projecting hillocks in the microtopography plus buildings, fence lines, and other obvious cultural discretes that dominate the backscatter.

At low angles, all terrain types, open or forested, natural or cultural, are dominated by discretes that occur at approximately 20% incidence of occurrence independent of land cover. Thus the clutter modeling information of Chapter 5 is based on depression angle as it affects shadowing in a sea of patchy visibility and discrete scattering sources. As depression angle increases, there is a gradual transition from a discrete-dominated, widespread, spiky, Weibull process towards more diffuse clutter and the accompanying, narrow spread, Rayleigh process that exists in airborne radar.

Physical discretes are distinguished from discrete cells in the measured clutter data. By physical discretes are meant isolated vertical objects, structures, and terrain features existing in the landscape. Discrete cells in the measured clutter data are cells which contain stronger clutter than their neighbors. As discussed in Appendix 4.D, discrete cells in the measured clutter data may be specified as 5-db discretes, by which are meant cells in which the clutter is stronger than neighboring cells by 5 dB or more. That is, a 5-db spatial filter separates locally strong cells in a very widespread continuum of clutter amplitudes. The cells that remain (i.e., that fail to pass the 5-db spatial filter) may be called background cells.

To a large extent clutter in background cells also comes from discrete but weaker physical sources in the sea of discretes that tends to make up low-angle clutter (as opposed to area-

extensive diffuse clutter), even though dependency of clutter strength on grazing angle often exists in the residual set of weaker background cells. This dependency of background clutter on grazing angle is of limited advantage since the dominant discrete clutter is not dependent on grazing angle (see Appendix 4.D). Insufficient correlation exists between strong isolated clutter cells and obvious discrete vertical elements on the landscape to allow practicable deterministic prediction of discrete clutter. The clutter modeling information of Chapter 5 does not distinguish between discrete cells and background cells, but applies to the complete spatial amplitude distribution comprising returns from both strong and weak cells.

5.1.1.2.2 Depression Angle

Depression angle is of major importance in its effects on both strength and spread in land clutter spatial amplitude statistics, even for the very low depression angles (typically within a degree of grazing incidence) and small (typically fractional) variations in depression angle that occur in surface radar. Depression angle is formulated mathematically in Appendix 2.D to be the complement of incidence angle at the backscattering terrain point under consideration. Incidence angle equals the angle between the outward projection of the earth's radius at the terrain point and the direction of illumination at that point, assuming a 4/3 earth radius to account for standard atmospheric refraction. As previously discussed, the rigorous definition of depression angle in this book is in a reference frame centered at the terrain point, not at the antenna. For convenience of reference here, the following discussion summarizes material from Chapter 2, Sections 2.3.4–2.3.6, and elsewhere in this book. Thus, if range from radar to backscattering terrain point is r, effective earth's radius (i.e., actual earth's radius times 4/3) is a and effective radar height (i.e., radar site elevation plus radar antenna mast height minus terrain elevation at backscattering terrain point) is h, then depression angle α is given approximately by

$$\alpha \cong \frac{h}{r} - \frac{r}{2a} \tag{5.1}$$

This definition of depression angle includes the effect of earth curvature on the angle of illumination but does not include any effect of the local terrain slope. At short enough ranges that earth curvature is insignificant (i.e., $r << a$), depression angle simplifies to be the angle below the horizontal at which the terrain point is viewed from the antenna (i.e., $\alpha \cong h/r$, see Figure 5.6). Negative depression angle occurs when steep terrain is observed by the radar at elevations above the antenna.

Depression angle is a quantity relatively simple and unambiguous to determine, depending as it does simply on range and relative elevation difference between the radar antenna and the backscattering terrain point. Since depression angle depends only on terrain elevations and not terrain slopes, it is a slowly varying quantity over clutter patches and not highly sensitive to errors in digitized terrain elevation data (DTED). Thus, the complete clutter amplitude distribution from any given clutter patch can usually be associated with one narrow depression angle regime. Grazing angle is the angle between the tangent to the local terrain surface at the backscattering terrain point and the direction of illumination. Thus, grazing angle does take into account the local terrain slope. Attempts to use grazing angle in clutter data analysis met with limited additional success, partly due to difficulties associated with specifying local terrain slope (i.e., rate of change of elevation) accurately in DTED, and partly due to the fact that many clutter sources tend to be vertical discrete objects associated with the land cover (see Section 2.3.5.1 and Appendix 4.D). Thus, the

clutter modeling information of Chapter 5 is presented in fine steps or bins of depression angle in each radar frequency band. The depression angle bins utilized are specified subsequently in Table 5.4, Section 5.2.3.5.

5.2 Derivation of Clutter Modeling Information

5.2.1 Weibull Statistics

In Chapter 5 modeling information for the empirical prediction of land clutter spatial amplitude distributions is presented in terms of Weibull statistics [10, 11]. Weibull statistics are convenient for this purpose both because they can easily accommodate the wide spreads existing in many low-angle measured clutter strength distributions, and because in the limiting, narrow spread case they degenerate to Rayleigh voltage statistics (i.e., exponential power statistics) as do the measured clutter distributions at high angles. The Weibull cumulative distribution function, previously defined in Chapter 2, is repeated here as:

$$P(x) = 1 - \exp\left\{-\frac{\ln 2 \cdot x^{b}}{(\sigma^{\circ}_{50})^{b}}\right\} \tag{5.2}$$

where

σ°_{50} = median value of x,
b = $1/a_w$, and
a_w = Weibull shape parameter.

Here, as elsewhere in this book, the random variable x represents clutter strength $\sigma^{\circ}F^4$ in units of m^2/m^2, i.e., x is a power-like quantity and $y = 10\log_{10} x$. Equation (5.2) degenerates to an exponential power distribution for x (corresponding to a Rayleigh voltage distribution for $\sqrt{x}$) when $a_w = 1$. The mean-to-median ratio for Weibull statistics is

$$\frac{\overline{\sigma^{\circ}_{w}}}{\sigma^{\circ}_{50}} = \frac{\Gamma(1 + a_w)}{(\ln 2)^{a_w}} \tag{5.3}$$

where $\overline{\sigma^{\circ}_{w}}$ is the mean value of x and Γ is the Gamma function. From these relationships, it is seen that a Weibull distribution is characterized by $\overline{\sigma^{\circ}_{w}}$ and a_w. The modeling information in Chapter 5 specifies these two coefficients as a function of the terrain type within the clutter patch, the depression angle at which the radar illuminates the clutter patch, and the radar parameters of radar frequency, polarization, and spatial resolution.

The lognormal distribution is another analytic distribution that can provide wide spread. However, the lognormal distribution often provides somewhat too much spread. That is, the high-end tails of measured low-angle clutter spatial amplitude distributions usually fall off more rapidly than do the tails of lognormal distributions matched to the measurements by, for example, the first two moments (see Appendix 5.A).

Figure 2.28 in Chapter 2 shows five theoretical Weibull cumulative distributions having the same median clutter strength, $\sigma^\circ_{50} = -40$ dB, but having values of shape parameter a_w ranging from $a_w = 1$ to $a_w = 5$. Figure 5.4 shows the same five distributions plotted as histograms of y; i.e., as the probability density function $p(y)$ vs y (see Appendix 5.A). The five Weibull distributions shown in Figure 5.4 graphically indicate how highly skewed distributions of very wide spread rapidly develop as a_w increases from unity. Radar detection performance is seriously degraded in the presence of land clutter as a result of large clutter distribution losses caused by such highly skewed spatial distributions [3]. Appendix 5.A provides further information describing the long high-side tails associated with Weibull distributions with $a_w > 1$.

In a Weibull distribution, the Weibull shape parameter a_w and the ratio of standard deviation-to-mean (sd/mean) are also directly related [see Appendix 2.B, Eq. (2.B.20)], as:

$$\text{sd/mean} = \frac{[\Gamma(1 + 2a_w) - \Gamma^2(1 + a_w)]^{1/2}}{\Gamma(1 + a_w)} \tag{5.4}$$

Thus the shape parameter a_w may be determined from either the ratio of standard deviation-to-mean or the mean-to-median ratio. The modeling information of Chapter 5 specifies a_w both ways, from measured values of ratio of standard deviation-to-mean and from measured values of mean-to-median ratio. To the extent that the measured clutter amplitude distributions are rigorously Weibull, these two evaluations of a_w will be identical. Thus, comparison of the two evaluations provides a first indication of the degree of validity of assuming Weibull statistics.

Although the two evaluations of a_w are often approximately equal, they are seldom identically equal. Low-angle land clutter is a messy statistical phenomenon in which returns are collected from all the discrete vertical scattering sources that occur at near-grazing incidence over composite landscape. Thus, measured low-angle clutter distributions almost never pass rigorous statistical hypothesis tests (e.g., the Kolmogorov-Smirnov test) for belonging to Weibull, lognormal, *K*-, or any other analytic distribution over their complete extents (but see Appendix 5.A). Rather than dwell on statistical rigor, emphasis is given here to engineering approximations to the measured clutter distributions using Weibull statistics. Working in this manner, rigorous Weibull statistics within specified confidence bounds are not guaranteed. However, the one-sigma variability of mean strength (an engineering indication of prediction accuracy) in the measured distributions within a given terrain type/relief/depression angle class is often on the order of 3 dB. Less concern is with specifying exact shapes of low-angle clutter distributions than in correctly establishing the levels of first moments and the amounts of spread that occur in such distributions. Besides providing a_w evaluated two ways, the modeling information of Chapter 5 also includes the measured values of ratio of standard deviation-to-mean and mean-to-median ratio from which these values of a_w were determined.

For Weibull statistics, Figure 5.5 shows plots of the ratios of standard deviation-to-mean and mean-to-median as given by Eqs. (5.3) and (5.4), respectively, vs the Weibull shape parameter a_w. For $a_w = 1$, the Weibull distribution, which is exponential (power) in this case, provides ratio of standard deviation-to-mean = 1 (i.e., 0 dB) and mean-to-median ratio = 1.44 (i.e., 1.6 dB). The results of Figure 5.5 reinforce those of Figure 5.4 in indicating

how distributions of very wide spread (i.e., large ratios of standard deviation-to-mean and mean-to-median) rapidly arise as a_w increases from unity. The plots of Figure 5.5 are useful as graphical aids to provide quick conversion factors in using the Weibull modeling information for a_w provided subsequently in Chapter 5. Information comparing the use of Weibull, lognormal, and *K*-distributions in the representation of measured clutter amplitude statistics is provided in Appendix 5.A.

5.2.2 Clutter Model Framework

For a given clutter patch, measured clutter histograms were collected and stored for all 20 combinations of Phase One radar measurement parameters nominally available (five frequencies, two polarizations, two pulse lengths; see Appendix 3.A). Altogether the file of measured histograms upon which Chapter 5 is based numbers 59,804. Trend analysis of these stored data involved sorting out like-classified sets of patches and looking for clustering within sets and separation between sets. This trend analysis led to a general framework for predicting or modeling clutter in which the fundamental structure is as follows: (1) Weibull mean strength $\overline{\sigma_w^\circ}$ varies with radar frequency and polarization; (2) Weibull shape parameter a_w varies with radar spatial resolution; and (3) both $\overline{\sigma_w^\circ}$ and a_w vary with terrain type and depression angle (cf. Section 4.2.2). Note that within this modeling framework, radar frequency affects $\overline{\sigma_w^\circ}$ but not a_w; whereas spatial resolution affects a_w but not $\overline{\sigma_w^\circ}$. That is, frequency and resolution decouple in their effects on clutter amplitude statistics. The basic criterion imposed in developing this modeling framework was the degree to which an expected trend or dependency was actually borne out in the measured clutter data. This modeling framework is sufficient to capture all of the important trends and dependencies observed in the data.

5.2.2.1 Mean Strength $\overline{\sigma_w^\circ}$

A key attribute of the first moment or mean strength in a low-angle clutter amplitude distribution is that it is independent of radar spatial resolution. This fact and its importance are often unrecognized. It is both theoretically true in power-additive spatial ensemble processes and observed to be empirically true in the Phase One measurements. That it is theoretically true was discussed in Chapter 3, Section 3.5.3, and in Chapter 4, Section 4.5.4. In the Phase One measurement data, differences in mean strength between high (15 m or 36 m) and low (150 m) range resolution across the complete matrix of repeat sector patches were often less than one decibel (i.e., in the distribution of differences of mean strength with resolution, the mean difference was 0.8 dB and the median difference was 0.9 dB; see Figure 3.43).

The fact that the mean is independent of resolution in the modeling construct being utilized here has the important benefit of reducing the parametric dimensionality in this construct. Looking ahead to the tabularized modeling information of Chapter 5, if $\overline{\sigma_w^\circ}$ in these tables had to be further partitioned in several categories of resolution, the number of measurements in any given category would become too small to allow the development of useful general trends, and the modeling information would begin to degenerate to trendless tabularization of data.

The mean is the only attribute of low-angle clutter amplitude distributions that is independent of resolution. A number of early investigations emphasized the median rather than the mean in such distributions, since means usually occur high in the distributions,

often near the 90-percentile level, driven there by occasional strong returns from discrete sources. It was thought that the median might be a better central measure of a discrete-free area-extensive clutter background. However, attempts to characterize the changing shapes of low-angle clutter amplitude distributions using the median instead of the mean as the central measure of each distribution required unwieldy normalization procedures and did not lead to useful general results, since the median central measure of each distribution as well as its shape were strongly dependent on resolution [12]. Because the mean occurs high in a distribution is not a reason to discard standard statistical techniques of using the first two moments of any distribution as the best way to begin to bring it under general description.

5.2.2.2 Shape Parameter a_w

The shapes of low-angle clutter spatial amplitude distributions are strongly and fundamentally dependent on spatial resolution. However, as with the mean strengths, there is a similar savings in model dimensionality with the shape parameter. With a_w, this savings is in the fact that the shapes of distributions, as observed in the clutter data, are not very sensitive to the remaining radar parameters of radar frequency and polarization. This key fact is an empirical observation here that apparently has not been advanced elsewhere. The reason why shapes of clutter amplitude distributions are largely insensitive to frequency and polarization is that essentially the same set of discrete sources on the landscape cause the dominant clutter returns, whatever the radar frequency or polarization. This is observed in PPI clutter plots showing the spatial texture of clutter. Insensitivity of distribution shape to radar frequency allows bringing to bear the varying Phase One azimuth beamwidths with frequency, from 13° at VHF to 1° at X-band, to help provide a combined broad range of spatial resolutions across which to establish trends.

It can be seen in the modeling information of Chapter 5 that, in working across frequency in this manner to establish trends of spread vs spatial resolution, radar frequency is essentially undetectable in the trends observed. That is, looking ahead to Figure 5.9 and the following 18 similar figures showing measured results of sd/mean vs A, it is evident that the different colored plot symbols in each such figure which correspond to different frequency bands contribute much more towards establishing one overall scatter plot through which it is most sensible to define one overall regression line, as opposed to five individual scatter plots with five different regression lines. If it were necessary to separate a_w with radar frequency and/or polarization, there would not be enough available range in resolution in the Phase One data to properly establish a trend, nor would there be enough data to properly fill the matrix.

Thus two important factors upon which the success of the modeling construct employed herein is based are that $\overline{\sigma_w^\circ}$ is dependent on frequency and polarization but is independent of resolution; whereas a_w is independent of frequency and polarization but is dependent on resolution—that is, that the important radar parameters decouple in their effects on low-angle clutter spatial amplitude distributions, much reducing the required parametric dimensionality of the model.

5.2.3 Derivation of Results

5.2.3.1 Derivation of $\overline{\sigma_w^\circ}$ Results

Like-classified groups of measured clutter histograms were formed in which the classifiers were: terrain type, relief, depression angle, radar frequency band (VHF, UHF, L-, S-, or X-band), and radar polarization (HH or VV). For each like-classified group, the mean clutter strengths of all the measured clutter histograms within the group were collected, one value of mean strength per histogram. The median or 50-percentile value from this set of mean strengths was selected as the representative value of mean strength by which to characterize that particular like-classified group of measurements. This 50-percentile value of mean clutter strength for each like-classified group of measurements was tabulated as the Weibull mean clutter strength coefficient $\overline{\sigma_w^\circ}$ in Sections 5.3 and 5.4 of Chapter 5. The number of measurements in each like-classified group was also tabulated in Sections 5.3 and 5.4, as an indication of the degree of generality of each $\overline{\sigma_w^\circ}$ coefficient presented. Color plots of $\overline{\sigma_w^\circ}$ vs frequency by depression angle regime and polarization are provided for each terrain type/relief category in Sections 5.3 and 5.4. The like-classified sets of mean clutter strength, upon which the $\overline{\sigma_w^\circ}$ modeling information of Chapter 5 is based, number 864.

Information Underlying $\overline{\sigma_w^\circ}$. As an example of the derivation of each value of $\overline{\sigma_w^\circ}$ provided as modeling information in what follows, Table 5.2 illustrates the like-classified groups of measured clutter histograms for one terrain type—namely, low-relief forest with depression angle from 0.25° to 0.75°. The data in Table 5.2 are separated by frequency band (VHF, UHF, L-, S-, X-bands), range resolution (F = fat = 150 m; T = thin = 36 m for VHF and UHF bands, = 15 m for L-, S-, X-bands), and polarization (V = vertical, H = horizontal).

Each line in the table corresponds to one group of like classified histograms. In each line, the following information is provided: the number of histograms in the group (Npts) which is also the number of available like-classified values of clutter patch mean strength in dB; the median of these dB values (which is what is selected for $\overline{\sigma_w^\circ}$); the mean of these dB values; the standard deviation of these dB values (i.e., the 1-σ variability of $\overline{\sigma_w^\circ}$); the maximum of these dB values (the strongest like-classified patch measured); and the minimum of these dB values (the weakest like-classified patch measured). Looking ahead to Table 5.27 in Section 5.4.3.1, the values shown in the 0.25° to 0.75° lines in the upper and lower subtables of Table 5.27 come from Table 5.2. For example, lines 5 and 6 in Table 5.2 provide Npts = 113, 113 (4th column) and $\overline{\sigma_w^\circ}$ = –27.1, –28.0 dB (5th column) for vertical and horizontal polarization, respectively, at VHF. Corresponding information to that shown in Table 5.2 lies behind all terrain type/depression angle categories for which $\overline{\sigma_w^\circ}$ values are provided in following Sections 5.3 and 5.4.

5.2.3.2 Derivation of a_w Results

The spread in a clutter spatial amplitude distribution as given, for example, by the ratio of standard deviation-to-mean or by the mean-to-median ratio, is fundamentally dependent on radar spatial resolution. Radar spatial resolution A (see Section 2.3.1.1) is given by

$$A = r\ \Delta\ r\ \Delta\theta \tag{5.5}$$

where

r = range,

Δr = range resolution, and

$\Delta\theta$ = one-way 3-dB azimuth beamwidth.

TABLE 5.2 Information* on Patch Values of Mean Clutter Strength $\overline{\sigma^\circ F^4}$ Underlying $\overline{\sigma^\circ_w}$ for Forest/Low-Relief Terrain at 0.25° to 0.75° Depression Angle, by Frequency Band, Range Resolution, and Polarization

Band	Res	Pol	Npts	$\overline{\sigma^\circ F^4}$ (dB)				
				Median	Mean	St. Dev.	Max.	Min.
VHF	F	V	86	-27.3	-27.4	9.1	-9.1	-54.2
VHF	F	H	82	-29.0	-28.9	9.8	-12.9	-57.8
VHF	T	V	27	-26.9	-26.0	8.0	-10.6	-41.6
VHF	T	H	31	-26.9	-25.4	7.8	-9.3	-44.0
VHF	F+T	V	113	-27.1	-27.1	8.8	-9.1	-54.2
VHF	F+T	H	113	-28.0	-27.9	9.4	-9.3	-57.8
VHF	F+T	V+H	226	-27.5	-27.5	9.1	-9.1	-57.8
UHF	F	V	102	-26.8	-27.2	6.7	-15.0	-46.9
UHF	F	H	100	-29.5	-30.1	6.2	-18.5	-46.3
UHF	T	V	49	-26.1	-26.5	7.1	-15.0	-42.7
UHF	T	H	43	-30.3	-29.5	6.9	-17.5	-44.9
UHF	F+T	V	151	-26.1	-26.9	6.8	-15.0	-46.9
UHF	F+T	H	143	-29.6	-29.9	6.4	-17.5	-46.3
UHF	F+T	V+H	294	-27.8	-28.4	6.8	-15.0	-46.9
L	F	V	109	-27.9	-28.9	4.9	-20.5	-44.8
L	F	H	107	-28.2	-29.6	4.8	-21.7	-47.5
L	T	V	55	-28.5	-28.9	5.1	-21.0	-46.1
L	T	H	55	-28.8	-29.8	5.4	-21.6	-46.2
L	F+T	V	164	-28.2	-28.9	5.0	-20.5	-46.1
L	F+T	H	162	-28.5	-29.7	5.0	-21.6	-47.5
L	F+T	V+H	326	-28.4	-29.3	5.0	-20.5	-47.5
S	F	V	107	-29.4	-30.7	6.3	-20.1	-70.3
S	F	H	108	-32.1	-32.3	3.8	-24.7	-45.4
S	T	V	56	-32.5	-32.7	4.5	-23.5	-45.9
S	T	H	59	-33.8	-34.4	4.6	-25.1	-47.4
S	F+T	V	163	-30.6	-31.4	5.8	-20.1	-70.3
S	F+T	H	167	-32.6	-33.0	4.2	-24.7	-47.4
S	F+T	V+H	330	-31.4	-32.2	5.1	-20.1	-70.3
X	F	V	59	-29.0	-29.3	4.2	-20.4	-39.4
X	F	H	59	-30.1	-29.8	4.5	-14.8	-40.2
X	T	V	33	-28.7	-29.6	4.8	-21.6	-40.9
X	T	H	35	-31.5	-31.5	4.7	-23.4	-41.5
X	F+T	V	92	-28.9	-29.4	4.4	-20.4	-40.9
X	F+T	H	94	-30.3	-30.4	4.7	-14.8	-41.5
X	F+T	V+H	186	-29.8	-29.9	4.6	-14.8	-41.5

* This table shows the number of patch measurements of $\overline{\sigma^\circ F^4}$ available as a set for each combination of parameters, and various statistical attributes (including the median) of each set.

Res = range resolution; F = 150m; T = 36m for VHF and UHF, = 15m for L-, S-, X-bands; F+T = both F and T range res. data combined.

Pol = polarization; V+H = both V and H polarization data combined.

Npts = number of clutter patch histograms.

Like-classified groups of measured clutter histograms were formed in which the classifiers were: terrain type, relief, depression angle, range interval, range resolution, and azimuth beamwidth. Three range intervals were utilized, as: interval 1, 1 to 11.3 km; interval 2, 11.3 to 35.7 km; interval 3, range > 35.7 km. The measured clutter histograms are approximately equally distributed within these three intervals. Two range resolutions are available, wide pulse (i.e., 150 m) or narrow pulse (i.e., 36 m at VHF and UHF, 15 m at L-, S-, and X-bands). Five azimuth beamwidths are available, one per frequency band, as: 13° at VHF, 5° at UHF, 3° at L-band, 1° at S- and X-bands. Although S- and X-bands both have $\approx 1°$ azimuth beamwidth, they are kept separate in spread analysis classification grouping to keep the frequency bands separate in the scatter plots (but not in the regression).

For each like-classified group of measured clutter histograms, three parameters were collected from each of the measured clutter histograms within the group. These three parameters are: (1) the ratio of standard deviation-to-mean, (2) the mean-to-median ratio, and (3) the value of spatial resolution A applicable for the measurement. The median values of each of these three parameters were selected as representative values to characterize the spread in that particular like-classified group of measurements. Spread characterization utilizing these three parameters proceeded as follows. For each terrain type/relief/depression angle category, two scatter plots were formed. The first scatter plot shows the ratio of standard deviation-to-mean vs $\log_{10} A$. The second scatter plot shows the mean-to-median ratio vs $\log_{10} A$.

Each plotted point in the first of these scatter plots shows the median value of ratio of standard deviation-to-mean vs the median value of $\log_{10} A$ for a particular like-classified group of measured clutter histograms. A number of these scatter plots of standard deviation-to-mean vs $\log_{10} A$ are shown in Sections 5.3 and 5.4, one scatter plot for a selected depression angle regime in each terrain type/relief category. Similar to the first scatter plot, each plotted point in the second scatter plot shows the median value of mean-to-median ratio vs the median value of $\log_{10} A$ for a particular like-classified group of measured clutter histograms. The maximum number of points in a scatter plot is 30 (five azimuth beamwidths, two pulse lengths, three range intervals), but little narrow pulse data is generally available in the third range interval.

Regression analysis was performed in each scatter plot. These regression analyses generally show significantly decreasing spread with decreasing resolution (i.e., increasing A) for each terrain type/relief/depression angle category. The regression line for each scatter plot is provided as modeling information for spread in clutter amplitude distributions in Chapter 5. The regression line is generally characterized by its values at $A = 10^3$ m^2 and $A = 10^6$ m^2, with a few noted exceptions.

Modeling information characterizing spread in clutter spatial amplitude distributions based on regression analysis in the scatter plots is provided two ways: (1) based on measured ratios of standard deviation-to-mean and (2) based on measured mean-to-median ratios. For both ways, the regression line values at $A = 10^3$ m^2 and $A = 10^6$ m^2 are converted to the corresponding two values of Weibull shape parameter a_w at $A = 10^3$ m^2 and $A = 10^6$ m^2 by Equations (5.3) and (5.4). These pairs of values of a_w are tabulated by terrain type/relief/depression angle category in Sections 5.3 and 5.4. In addition to the paired values of a_w, the underlying paired values of ratios of standard deviation-to-mean and mean-to-median ratio

are also tabulated. The number of clutter patches and number of measured clutter histograms that each scatter plot (i.e., regression analysis) is based on is also tabulated.

This tabulated modeling information for Weibull shape parameter a_w is used as follows. First, the spatial resolution A of the radar under study is calculated at the terrain point under consideration. Then linear interpolation on $\log_{10} A$ between the values of a_w at $A = 10^3$ m^2 and $A = 10^6$ m^2 for the appropriate terrain type/relief/depression angle category is performed to obtain the value of a_w at the radar spatial resolution A in question. Preference is given to the tabulated values of a_w based on measured ratios of standard deviation-to-mean. The additional provision of tabulated values of a_w based on measured mean-to-median ratios provides a first indication of the degree of validity of modeling the underlying measured data with Weibull statistics, based on how closely a_w computed from measured ratios of standard deviation-to-mean approximates a_w computed from measured mean-to-median ratios. The like-classified sets of measured clutter histograms, upon which the a_w modeling information of Chapter 5 is based, number 1,510. Note that these are different sets than those upon which the $\overline{\sigma_w^\circ}$ modeling information is based.

Information Underlying a_w. As described above, the a_w values provided as modeling information in what follows come from regression in scatter plots. Two scatter plots were formed: one of sd/mean (dB) vs $\log_{10} A$; the other of mean/median (dB) vs $\log_{10} A$. Each scatter plot comes from like-classified groups of measured clutter histograms. As an example of the information underlying the two scatter plots for low-relief forest with depression angle from 0.25° to 0.75°, Table 5.3 is shown here in three parallel parts. Parts (a), (b), and (c) show results for sd/mean (dB), mean/median (dB), and patch mid-range (km), respectively.

Consider first Table 5.3(a) for sd/mean (dB). The data in Table 5.3(a) are separated by frequency band (VHF, UHF, L, S, X), range resolution (Fat or Thin), and range interval (1, 2, or 3, as described previously). Each line in the table corresponds to one group of like-classified histograms and one point in the corresponding scatter plot—note that the groups are different from those of Table 5.2. In each line of Table 5.3(a), the following information is provided: the median value of mid-range cell size A for the group (shown under X as X = $\log_{10} A$ and $A = r\,\Delta r\,\Delta\theta$ in m^2); the number of histograms in the group (Npts), which is also the number of available like-classified values of ratio of sd/mean (dB), one from each clutter patch histogram; the median of these dB values of sd/mean (which forms the ordinate of the point in the scatter plot corresponding to this line); the mean of the dB values of sd/mean; the standard deviation of the dB values of sd/mean (i.e., the vertical 1-σ variability of this point in the scatter plot); the maximum of these dB values of sd/mean (i.e., the maximum patch value of sd/mean in this group); and the minimum of these dB values of mean/median. Thus, each line in Table 5.3(a) corresponds to the ordinate of a given point in a given scatter plot. For example, the scatter plot for low-relief forest, 0.0° to 0.25° depression angle is shown as Figure 5.27 in Section 5.4.3.2 (note: the plot corresponding to the 0.25° to 0.75° depression angle regime of Table 5.3 is not shown).

Table 5.3(b) is similar to Table 5.3(a) except Table 5.3(b) provides underlying information for the ordinate of the plotted points in the scatter plots of mean/median (dB) vs $\log_{10} A$. Examples of the mean/median scatter plots are not shown in this book; they appear similar to the sd/mean scatter plots, except that they employ a different y-scale.

TABLE 5.3A Information* on Patch Values of SD/Mean of $\sigma°F^4$ Underlying a_w for Forest/Low-Relief Terrain at 0.25° to 0.75° Depression Angle, by Frequency Band, Range Resolution, and Range Interval

Band	Res	Rng	X	Npts	Clutter Patch SD/Mean of $\sigma°F^4$ (dB)				
					Median	Mean	St. Dev.	Max.	Min.
VHF	F	1	5.21	70	1.26	1.12	1.73	5.07	-4.62
VHF	F	2	5.93	93	1.88	2.01	1.80	8.82	-1.16
VHF	F	3	6.12	5	0.88	0.92	0.56	1.71	0.27
VHF	T	1	4.55	49	1.94	2.22	1.31	7.29	-0.26
VHF	T	2	5.14	9	3.39	3.43	2.24	6.41	0.08
UHF	F	1	4.79	70	3.32	3.23	1.72	7.47	-0.67
UHF	F	2	5.51	128	3.10	3.10	1.33	7.53	0.27
UHF	F	3	5.70	4	2.47	2.52	0.66	3.29	1.87
UHF	T	1	4.17	70	3.89	4.28	1.85	8.73	0.59
UHF	T	2	4.70	22	4.18	4.51	1.54	8.21	2.21
L	F	1	4.45	70	3.48	3.58	1.92	8.45	-1.08
L	F	2	5.30	138	3.06	3.18	1.22	7.34	0.82
L	F	3	5.48	8	3.63	3.44	0.80	4.72	2.06
L	T	1	3.45	71	4.62	4.88	1.95	11.12	1.53
L	T	2	4.13	39	3.54	3.63	1.36	6.56	0.99
S	F	1	3.98	71	3.48	3.82	2.02	9.74	-0.76
S	F	2	4.82	138	3.97	3.91	1.26	7.41	0.97
S	F	3	5.00	6	4.76	5.12	2.37	9.33	2.77
S	T	1	3.02	77	5.63	5.78	1.75	10.79	1.14
S	T	2	3.65	38	4.43	4.49	1.70	9.00	1.82
X	F	1	4.08	68	3.76	3.69	1.80	8.25	0.18
X	F	2	4.83	48	3.85	3.85	1.19	7.57	1.64
X	F	3	5.00	2	5.81	5.81	0.98	6.50	5.12
X	T	1	3.06	58	5.05	5.75	2.15	13.22	2.75
X	T	2	3.70	10	5.44	4.75	1.69	6.92	1.85

* This table shows the number of patch measurements of SD/Mean of $\sigma°F^4$ available as a set for each combination of parameters, and various statistical attributes (including the median) of each set.
Res = range resolution (m); F = 150m; T = 36m for VHF and UHF, = 15m for L-, S-, X-Bands.
Rng = range interval: 1 (1 to 11.3 km); 2 (11.3 to 35.7 km); 3 (>35.7 km).
X = $\log_{10}$ (A), A = $r \cdot \Delta r \cdot \Delta\theta, \Delta r$ = rang. res. (m), $\Delta\theta$ = az. bw. (rad), r = median range (m).
Npts = number of clutter patch histograms.

Table 5.3(c) is similar to Table 5.3(a) except Table 5.3(c) provides underlying information for the abscissas of the plotted points in both kinds of scatter plots. The abscissa is 10log A where A is cell area in m^2. As discussed above, $A = r\,\Delta r\,\Delta\theta$ where Δr (range resolution) and $\Delta\theta$ (azimuth beamwidth) are fixed within any like-classified group (i.e., any line in the table), but r is the range in km to the center (i.e., mid-range) of each clutter patch in the group. Thus each line in Table 5.3(c) applies to the like-classified set of patch mid-range values, and the median value of mid-range is selected as r in the computation of A and hence the value of $X = \log_{10} A$ shown in each line of Table 5.3(c).

Thus a given point in the scatter plot of sd/mean (dB) vs $\log_{10} A$ for forest/low-relief/depression angle from 0.25° to 0.75° is obtained by selecting the appropriate value of "Median" in Table 5.3(a) as the ordinate, and the corresponding value of X that comes from the corresponding value of "Median" in Table 5.3(c). Scatter plots of sd/mean vs $\log_{10} A$ and mean/median vs $\log_{10} A$ were generated for all terrain type/depression angle categories. Each pair of scatter plots came from corresponding information similar to the three parts of Table 5.3. Shape parameter a_w data obtained from regression in these scatter plots is provided in Sections 5.3 and 5.4.

TABLE 5.3B Information* on Patch Values of Mean/Median of $\sigma^\circ F^4$ Underlying a_w for Forest/Low-Relief Terrain at 0.25° to 0.75° Depression Angle, by Frequency Band, Range Resolution, and Range Interval

Band	Res	Rng	X	Npts	Clutter Patch Mean/Median of $\sigma^\circ F^4$ (dB)				
					Median	Mean	St. Dev.	Max.	Min.
VHF	F	1	5.21	70	3.84	3.89	2.58	9.54	-0.82
VHF	F	2	5.93	93	3.76	4.23	2.33	11.14	-0.18
VHF	F	3	6.12	5	2.07	2.17	0.69	3.03	1.43
VHF	T	1	4.55	49	4.40	4.59	1.76	8.91	1.16
VHF	T	2	5.14	9	5.54	5.23	2.31	7.69	1.23
UHF	F	1	4.79	70	7.40	7.31	3.41	17.60	1.43
UHF	F	2	5.51	128	6.24	6.25	2.46	13.89	1.59
UHF	F	3	5.70	4	4.38	4.49	0.83	5.53	3.66
UHF	T	1	4.17	70	7.96	8.71	3.72	19.58	1.86
UHF	T	2	4.70	22	5.99	6.92	2.41	11.00	3.14
L	F	1	4.45	70	7.09	7.33	3.71	16.96	0.00
L	F	2	5.30	138	6.14	6.70	2.95	18.62	1.45
L	F	3	5.48	8	5.58	6.31	2.04	10.46	4.23
L	T	1	3.45	71	9.73	9.77	4.13	20.21	2.62
L	T	2	4.13	39	5.88	6.51	2.58	11.34	2.70
S	F	1	3.98	71	9.20	9.96	4.40	21.76	3.43
S	F	2	4.82	138	8.42	9.33	4.51	22.35	2.50
S	F	3	5.00	6	9.94	9.39	2.80	11.95	5.36
S	T	1	3.02	77	14.54	14.63	5.71	26.39	2.65
S	T	2	3.65	38	8.43	8.90	3.69	14.86	3.47
X	F	1	4.08	68	8.36	9.10	4.69	22.00	2.05
X	F	2	4.83	48	8.77	9.91	5.09	23.98	3.41
X	F	3	5.00	2	8.52	8.52	0.16	8.63	8.40
X	T	1	3.06	58	14.88	14.98	5.85	29.26	4.30
X	T	2	3.70	10	10.67	9.71	4.19	14.33	3.65

* This table shows the number of patch measurements of Mean/Median of $\sigma^\circ F^4$ available as a set for each combination of parameters, and various statistical attributes (including the median) of each set.

Res = range resolution (m); F = 150m; T = 36m for VHF and UHF, = 15m for L-, S-, X-Bands.

Rng = range interval: 1 (1 to 11.3 km); 2 (11.3 to 35.7 km); 3 (>35.7 km).

X = $\log_{10}$ (A), A = $r \cdot \Delta r \cdot \Delta\theta$, Δr = rang. res. (m), $\Delta\theta$ = az. bw. (rad), r = median range (m).

Npts = number of clutter patch histograms.

5.2.3.3 Statistical Confidence

In Chapter 5, some clutter modeling results are obtained from many similar measurements leading to high statistical confidence, whereas other results are obtained from fewer measurements leading to less confidence. The rationale followed in Chapter 5 is to present all of the results obtained regardless of the degree of trust, confidence coefficient, or generality associated with each. This is in contrast to the interim clutter model of Chapter 4, Section 4.2, where some smoothing of thinner data was employed. In Chapter 5, information specifying the number of like-classified measurements involved for each $\overline{\sigma_w^\circ}$ or a_w number is included as a means of allowing assessment of statistical validity or generality of the result. Statistical sampling populations and associated confidence levels are usually large in the depression angle regimes near grazing incidence. The sampling populations decrease as depression angle moves to outlying positive or negative depression angle regimes. In the color plots of mean clutter strength $\overline{\sigma_w^\circ}$ vs frequency, open symbols are occasionally used to indicate $\overline{\sigma_w^\circ}$ numbers judged likely to be relatively measurement specific and non-representative of the general mean clutter strength applicable to that situation, on the basis of relatively few measurements and clutter strength values far removed from the general trends otherwise observed.

Table 5.3c Information* on Patch Values of "Mid-Range to Clutter Patch" Underlying the Median Range *r* and Resolution *A* Associated with a_w for Forest/Low-Relief Terrain at 0.25° to 0.75° Depression Angle, by Frequency Band, Range Resolution, and Range Interval

					Mid-Range to Clutter Patch (km)				
Band	Res	Rng	X	Npts	Median	Mean	St. Dev.	Max.	Min.
VHF	F	1	5.21	70	4.75	5.20	2.69	10.51	1.67
VHF	F	2	5.93	93	24.90	24.46	6.25	35.48	11.42
VHF	F	3	6.12	5	38.63	37.71	1.90	39.89	35.71
VHF	T	1	4.55	49	4.35	4.73	2.43	10.47	1.61
VHF	T	2	5.14	9	17.08	15.03	3.55	19.23	11.40
UHF	F	1	4.79	70	4.75	5.27	2.74	10.51	1.67
UHF	F	2	5.51	128	24.83	24.67	5.59	35.48	11.42
UHF	F	3	5.70	4	38.63	38.21	1.77	39.89	35.71
UHF	T	1	4.17	70	4.69	5.21	2.74	10.47	1.61
UHF	T	2	4.70	22	15.88	15.89	2.65	19.66	11.40
L	F	1	4.45	70	3.63	4.57	2.37	10.51	1.67
L	F	2	5.30	138	25.51	24.70	5.55	35.48	11.42
L	F	3	5.48	8	38.63	38.21	1.64	39.89	35.71
L	T	1	3.45	71	3.60	4.71	2.52	10.47	1.61
L	T	2	4.13	39	17.07	16.89	2.83	20.57	11.38
S	F	1	3.98	71	3.63	4.62	2.33	10.51	1.67
S	F	2	4.82	138	25.51	24.70	5.55	35.48	11.42
S	F	3	5.00	6	38.63	38.08	1.92	39.89	35.71
S	T	1	3.02	77	4.01	5.03	2.79	11.10	1.61
S	T	2	3.65	38	17.07	17.22	2.48	21.63	11.38
X	F	1	4.08	68	4.56	5.15	2.60	10.51	1.67
X	F	2	4.83	48	25.76	25.96	5.30	35.48	11.42
X	F	3	5.00	2	38.63	38.63	0.00	38.63	38.63
X	T	1	3.06	58	4.35	4.94	2.53	10.47	1.61
X	T	2	3.70	10	19.21	17.79	3.71	21.63	11.38

* This table shows the number of patch measurements of mid-range available as a set for each combination of parameters, and various statistical attributes (including the median) of each set.

Res = range resolution (m); F = 150m; T = 36m for VHF and UHF, = 15m for L-, S-, X-Bands.

Rng = range interval: 1 (1 to 11.3 km); 2 (11.3 to 35.7 km); 3 (>35.7 km).

X = $\log_{10}$ (A), A = $r \cdot \Delta r \cdot \Delta\theta$, Δr = rang. res. (m), $\Delta\theta$ = az. bw. (rad), r = median range (m).

Npts = number of clutter patch histograms.

5.2.3.4 Use of Modeling Information

The Weibull coefficient modeling information may be employed to generate a $\sigma°F^4$ clutter strength number (i.e., realization) for a given spatial cell. First, it is determined if the cell is geometrically visible from the antenna position or if the cell is masked or shadowed by intervening terrain of higher elevation. If masked, as a first approximation, zero clutter power is assigned to the cell (the information of this book is not directly applicable to shadowed cells; but see Appendix 4.D). If visible, the depression angle from the antenna position to the cell is computed, the terrain type and relief for the cell is determined, and the radar spatial resolution *A* at the cell is calculated. This determination of terrain type/relief/depression angle/spatial resolution for the cell leads to the pair of Weibull coefficients, $\overline{\sigma_w^\circ}$, a_w, which specify the clutter amplitude distribution for that combination of terrain type, relief, depression angle, and resolution. A single random variate from this clutter amplitude distribution is assigned as clutter strength to the cell under examination. The modeler then proceeds to the next cell and repeats the process. In this manner, all visible cells at the site are assigned Weibull random variates as clutter strength, each appropriate to the radar parameters, geometry, and terrain type for the cell under consideration. The cell-to-cell spatial correlation that occurs in this process is that

provided by the underlying land cover and DTED information; otherwise, the random variates of clutter strength occur independently from cell to cell, as indeed for the most part do the measured data (see Chapter 4, Section 4.6.3). Further explanation of this terrain-specific modeling rationale is provided in Chapter 4. Techniques for validating and improving this approach to clutter modeling are briefly described in Section 5.5.

For those interested in general clutter levels (e.g., means, medians) exclusive of cell-to-cell variability, use of the modeling information provided in Chapter 5 is more direct. Mean clutter strength $\overline{\sigma_w^\circ}$ is directly tabulated. Median clutter strength σ_{50}° and other percentile levels and moments are dependent on radar spatial resolution A. Median clutter strength σ_{50}° is simply calculated from $\overline{\sigma_w^\circ}$ and the mean-to-median ratio; the mean-to-median ratio may be obtained for the radar resolution A under consideration by linear interpolation on $\log_{10} A$ between tabulated values at $A = 10^3$ m^2 and $A = 10^6$ m^2. The standard deviation may be obtained in a manner directly parallel to that by which the median is obtained. Other percentile levels may be simply calculated from the Weibull cumulative distribution function [Eq. (5.2)].

5.2.3.5 Presentation of Material

Sections 5.3 and 5.4 provide extensive modeling information for low-angle land clutter spatial amplitude statistics within a standard presentation format. The format utilized follows that of the interim clutter model presented in Chapter 4, Section 4.2, and illustrated in Figure 4.3. The format of presentation of mean clutter strength $\overline{\sigma_w^\circ}$ is reviewed here as an aid to the presentation of the extensive modeling information that directly follows.

The clutter modeling information that follows is based on depression angle. Figure 5.6 shows depression angle to be the angle below the horizontal from the radar to the backscattering terrain point. A precise mathematical definition of depression angle is given by Equation (5.1); see also Appendix 2.C of Chapter 2. As shown in Figure 5.6, terrain can occasionally rise to elevations higher than the radar which leads to negative depression angle. Approximately 30% of the clutter modeling information to follow applies to clutter measurements obtained at negative depression angle.

The clutter modeling information that follows is presented within bins (i.e., narrow angular regimes) of depression angle. The depression angle bins utilized are shown in Table 5.4. As is apparent in Table 5.4, different binning is utilized in low-relief terrain (terrain slopes $< 2°$) than in high-relief terrain (terrain slopes $> 2°$). In low-relief terrain, five positive and three negative depression angle bins are used; in high-relief terrain, five positive and two negative bins are used. The bins are very narrow, particularly at low depression angle, and more so for low-relief than high-relief terrain. Each bin typically contains hundreds of clutter measurements. What is plotted is the median value of clutter patch mean strength $\overline{\sigma_w^\circ}$ within each bin.

It will be seen in the clutter modeling information to follow that, as a result of medianizing over many measurements, the small differences in depression angle shown in Table 5.4 can account for systematic differences in mean clutter strength $\overline{\sigma_w^\circ}$ that in total can cover wide ranges. The bins are shown color-coded in Table 5.4; the same color coding is used in plotting mean clutter strength $\overline{\sigma_w^\circ}$ in color figures to follow, with different shaped symbols used to plot $\overline{\sigma_w^\circ}$ at VV-polarization (circles) and HH-polarization (squares). The color

codes are as follows: for increasing positive depression angle, cyan, dark blue, purple, magenta, red for bins 1 to 5, respectively; for increasing negative depression angle, dark green, intermediate green, light green for bins –1, –2, and –3 in low-relief terrain, and dark green, intermediate green for bins –1, –2 in high-relief terrain, respectively. The category of long-range mountains requires a specialized negative depression angle category. Complete data are not always available for all terrain types at outlying depression angles.

TABLE 5.4 Depression Angle Bins

Low-Relief Terrain (Slopes < 2°)				High-Relief Terrain (Slopes > 2°)			
Depression Angle (deg)	Bin Number	Color Code VV	Color Code HH	Depression Angle (deg)	Bin Number	Color Code VV	Color Code HH
> 4°	5			> 6°	5		
1.5° to 4°	4			4° to 6°	4		
0.75° to 1.5°	3			2° to 4°	3		
0.25° to 0.75°	2			1° to 2°	2		
0° to 0.25°	1			0° to 1°	1		
–0.25° to 0°	–1			–1° to 0°	–1		
–0.75° to –0.25°	–2			< –1°	–2		
< – 0.75°	–3						

NOTE: A color version of Table 5.4 appears on page 450.

In the clutter modeling information that follows, for each terrain type mean clutter strength $\overline{\sigma_w^\circ}$ is plotted vs radar frequency against a log-frequency x-axis in order to show results for all five frequency bands together. The plotting methodology is shown representationally in the diagram of Figure 5.7. Within each frequency band, $\overline{\sigma_w^\circ}$ results separated by depression angle bin are plotted by slightly displacing the plot symbols horizontally from bin to bin to avoid symbol overlap. This plot methodology, covering eight depression angle bins, is shown for X-band in an exaggerated way in the diagram of Figure 5.7. The sequential horizontal displacements shown in Figure 5.7 do not imply an in-band frequency shift; the cluster of sixteen plotted values of $\overline{\sigma_w^\circ}$ shown in Figure 5.7 all apply for a single X-band frequency. Similar bin-to-bin horizontal offsetting of plot symbols is also employed in the lower four bands.

Mean clutter strength $\overline{\sigma_w^\circ}$ generally increases both with increasing positive depression angle and with increasing negative depression angle. As a result, the in-band clusters of plotted data in multiple depression angle bins often take on the v-shape shown representatively by the X-band cluster in Figure 5.7. Thus, as a point of departure in interpreting the results, it is suggested that the reader first look for v-shapes indicating

whether or not consistent depression angle effects on clutter strength occur for the particular frequency band and terrain type of interest.

5.3 Land Clutter Coefficients for General Terrain

A radar designer or analyst may often require that the characteristics of land clutter be specified independently of specific terrain type. There are two reasons for this requirement. First, most radars must maintain performance when sited in various terrains and situations. Second, even at individual sites much clutter producing terrain is often composite and mixed over scales of several kilometers. In Section 5.3, modeling information characterizing low-angle land clutter spatial amplitude distributions is provided based on a large set of 30,246 measured clutter histograms from 1,628 clutter patches classified as general mixed rural. These measurements comprise 51% of the multifrequency Phase One clutter measurement data. This set of measurements includes the measurements from all mixed terrain types except those primarily classified as urban. Mixed terrain is generally neither completely open nor completely tree-covered. Because of the large amount of composite terrain clutter measurement data upon which they are based, the results of Section 5.3 are very general. General effects of depression angle, terrain relief, radar frequency, polarization, and resolution are quantified independent of specific terrain type.

5.3.1 General Mixed Rural Terrain

5.3.1.1 High-Relief General Mixed Rural Terrain

Table 5.5 shows the number of patches and measured clutter histograms by depression angle regime and terrain relief for general mixed rural terrain. Table 5.6 presents Weibull mean clutter strength $\overline{\sigma_w^\circ}$ for general mixed rural terrain of high relief, by depression angle, frequency band, and polarization. The number of measured clutter histograms upon which each value of $\overline{\sigma_w^\circ}$ in Table 5.6 is based is also presented in the lower of the two subtables comprising Table 5.6. High-relief terrain has terrain slopes > 2°. The $\overline{\sigma_w^\circ}$ data of Table 5.6 are plotted in Figure 5.8. To avoid obscuring results with overlapping plot symbols, within each frequency band in Figure 5.8 the colored plot symbols are plotted with small increasing horizontal displacements to the right as depression angle decreases from its highest positive regime through zero to its highest negative regime (i.e., top to bottom in Table 5.6). These small artificial displacements do not indicate an in-band frequency shift.

In each frequency band of Figure 5.8, the resultant set of colored plot symbols has a v-shape. The consistent v-shape indicates consistent depression angle effects in each band, where $\overline{\sigma_w^\circ}$ increases with both increasing positive (left side of v-shape, cyan through magenta) and increasing negative (right side of v-shape, dark green through intermediate green) depression angle. In what follows in Chapter 5, the $\overline{\sigma_w^\circ}$ data for each terrain type are plotted in a figure in which the manner of data presentation is similar to that employed in Figure 5.8.

The cyan (i.e., light blue) colored symbols in Figure 5.8 represent the lowest positive depression angle regime (0° to 1°) in high-relief terrain. These results are based on a significantly larger number of measurements than the other depression angle regimes in

TABLE 5.5 Numbers of Terrain Patches and Measured Clutter Histograms for General Mixed Rural Terrain, by Relief and Depression Angle[a,b,c]

Terrain Relief	α = Depression Angle (degrees)	Number of Patches	Number of Measurements
High-relief	$6.0 \le \alpha$	0	0
	$4.0 \le \alpha < 6.0$	5	79
	$2.0 \le \alpha < 4.0$	51	987
	$1.0 \le \alpha < 2.0$	70	1,997
	$0.0 \le \alpha < 1.0$	338	7,003
	$-1.0 \le \alpha < 0.0$	250	2,986
	$\alpha < -1.0$	20	183
	Totals	734	13,235
Low-relief	$4.00 \le \alpha$	1	28
	$1.50 \le \alpha < 4.00$	31	747
	$0.75 \le \alpha < 1.50$	114	2,659
	$0.25 \le \alpha < 0.75$	275	6,130
	$0.00 \le \alpha < 0.25$	292	5,353
	$-0.25 \le \alpha < 0.00$	150	1,758
	$-0.75 \le \alpha < -0.25$	28	285
	$\alpha < -0.75$	3	51
	Totals	894	17,011
Grand Totals		1,628	30,246

[a] Mixed terrain implies primary and secondary terrain classification. Rural terrain includes all classes except urban.
[b] A terrain patch is a land surface macroregion usually several kms on a side (median patch area = 12.62 km^2).
[c] A measured clutter histogram contains all of the temporal (pulse by pulse) and spatial (resolution cell by resolution cell) clutter samples obtained in a given measurement of a terrain patch. A terrain patch was usually measured many times (nominally 20) as RF frequency (5), polarization (2), and range resolution (2) were varied over the Phase One radar parameter matrix.

Table 5.6 and hence may be regarded as the most reliable data shown in Figure 5.8. In moving from cyan through the higher positive depression angles in Figure 5.8, there is a monotonic rise up the left side of the v-shaped cluster from cyan to dark blue (1° to 2°) to purple (2° to 4°) to magenta (4° to 6°). Thus in each frequency band Figure 5.8 shows a strong monotonic increase in $\overline{\sigma^{\circ}_{w}}$ with increasing positive depression angle. The number of measurements falls off with increasing positive or negative depression angle (see Table 5.5). No data are available for depression angle > 6° (red) in any band in Figure 5.8, and no data are available from 4° to 6° (magenta) at S- and X-bands in Figure 5.8 due to the limited Phase One elevation beamwidths in those bands (see Appendix 3.A).

TABLE 5.6 Mean Clutter Strength $\overline{\sigma_w^\circ}$ and Number of Measurements for General Mixed Rural Terrain of High Relief, by Frequency Band, Polarization, and Depression Angle[a]

α = Depression Angle (degrees)	Weibull Mean Clutter Strength $\overline{\sigma_w^\circ}$ (dB)									
	VHF		UHF		L-Band		S-Band		X-Band	
	HH	VV	HH	VV	HH	VV	HH	VV	HH	VV
$6.0 \le \alpha$	- - - -	- - - -	- - - -	- - - -	- - - -	- - - -	- - - -	- - - -	- - - -	- - - -
$4.0 \le \alpha < 6.0$	-17.3	-14.3	-22.9	-19.4	-22.1	-23.0	- - - -	- - - -	- - - -	- - - -
$2.0 \le \alpha < 4.0$	-19.4	-15.3	-21.0	-20.4	-23.0	-23.5	-28.7	-27.1	-25.9	-22.5
$1.0 \le \alpha < 2.0$	-24.0	-20.6	-24.7	-22.8	-26.0	-26.0	-30.3	-28.2	-25.2	-24.0
$0.0 \le \alpha < 1.0$	-27.6	-25.1	-29.0	-27.9	-29.0	-29.0	-31.7	-29.9	-29.5	-28.0
$-1.0 \le \alpha < 0.0$	-26.5	-21.7	-27.0	-25.8	-26.6	-27.7	-30.3	-28.3	-29.6	-28.5
$\alpha < -1.0$	-16.6	-17.0	-19.8	-16.4	-23.1	-21.0	-24.6	-23.6	-24.9	-25.9
α = Depression Angle (degrees)	Number of Measurements									
	VHF		UHF		L-Band		S-Band		X-Band	
	HH	VV	HH	VV	HH	VV	HH	VV	HH	VV
$6.0 \le \alpha$	0	0	0	0	0	0	0	0	0	0
$4.0 \le \alpha < 6.0$	13	11	15	15	9	16	0	0	0	0
$2.0 \le \alpha < 4.0$	136	136	139	141	140	156	66	71	1	1
$1.0 \le \alpha < 2.0$	196	205	203	209	221	227	183	199	174	180
$0.0 \le \alpha < 1.0$	606	626	778	800	760	829	591	593	709	711
$-1.0 \le \alpha < 0.0$	252	278	350	372	321	325	232	235	305	316
$\alpha < -1.0$	21	23	21	21	23	21	11	9	17	16
TOTALS	1,224	1,279	1,506	1,558	1,474	1,574	1,083	1,107	1,206	1,224

[a] Table 5.5 defines the population of terrain patches upon which these data are based.

Values of $\overline{\sigma_w^\circ}$ for negative depression angle are plotted in shades of green. Negative depression angle occurs when steep terrain is observed by the radar at elevations above the antenna. The darkest shade of green shows results in the lowest negative depression angle regime, which is 0° to –1° in high-relief terrain. These dark green (0° to –1°) results in Figure 5.8 are generally close to and usually slightly higher than the cyan (0° to 1°) results, as intuitively would be expected. The shade of green becomes lighter with increasing negative depression angle. In high-relief terrain, only one additional negative depression angle regime is utilized, for depression angle < –1° (intermediate green in Figure 5.8). In every band, the intermediate green values of $\overline{\sigma_w^\circ}$ in Figure 5.8 are significantly stronger than the dark green values, thus providing the right sides of the v-shaped clusters.

There is a general trend of decreasing $\overline{\sigma_w^\circ}$ with increasing radar carrier frequency in Figure 5.8. At the lowest (positive or negative) depression angles, this trend is slight (e.g., for cyan, 0° to 1°, UHF, L-, and X-band results are all remarkably close in the –29 dB vicinity, with VHF slightly stronger and S-band slighter weaker). At higher (positive or negative) depression angles, the trend is stronger. This trend is largely due to increasing

absorption of radio frequency (RF) power from the incident radar wave by tree foliage, VHF to S-band (see Chapter 3). Mixed rural terrain of high relief has a larger component of trees than at low relief. At the highest positive depression angles (magenta and purple) in Figure 5.8, the variation of $\overline{\sigma_w^\circ}$ with radar frequency f VHF to S-band is approximately $\overline{\sigma_w^\circ}(f) \propto f^{-0.94}$. In the historical literature, what little information is available on the subject usually suggests a slight trend of increasing clutter strength with increasing radar frequency, for example, $\overline{\sigma_w^\circ}(f) \propto f^{1/2}$ or $\overline{\sigma_w^\circ}(f) \propto f$ [2–5]. Thus the trend of decreasing clutter strength with increasing radar frequency seen in many of the Phase One high-angle forest measurements is relatively unexpected. Note that at all positive depression angles in Figure 5.8, the trend of decreasing $\overline{\sigma_w^\circ}$ with increasing radar frequency from VHF to S-band reverses from S-band to X-band. That is, at all positive depression angles there is an S-band dip between L-band and X-band in Figure 5.8, indicating that over the range of frequencies shown, maximum RF absorption occurs at S-band. It is probably not entirely coincidental that S-band is also the frequency band in which the common household microwave oven operates (at 2.45 GHz). In Figure 5.8, the differences with polarization are generally small, on the order of several dB or less, with vertical polarization (VV) almost always stronger than horizontal (HH).

Table 5.7 presents the Weibull shape parameter a_w and ratios of standard deviation-to-mean and mean-to-median for general mixed rural terrain of high relief, by depression angle and radar spatial resolution. Whereas the information of Table 5.6 specifies the mean or first moment of the clutter spatial amplitude distribution, the information of Table 5.7 specifies the spread or variability in the distribution as determined by the second moment or other derivative quantities. Table 5.5 shows the number of terrain patches and number of measured clutter histograms for general mixed rural terrain of high relief, broken down by depression angle in a parallel manner to that of Table 5.7; that is, the statistical populations underlying the data of Table 5.7 are available in Table 5.5. The numbers of measured clutter histograms in Table 5.5 are further broken down by frequency band and polarization in Table 5.6. Table 5.5 shows no data available for depression angle > 6° for general mixed rural terrain of high relief. Generally, there is little Phase One data available at such a high depression angle, although Section 5.4 shows that there is one high-relief forest clutter patch and six mountain clutter patches at depression angles > 6°.

In Table 5.7, a_w is calculated two ways: (1) from the ratio of standard deviation-to-mean and (2) from the mean-to-median ratio. In Table 5.7, and in general throughout Chapter 5, no major systematic difference results between these two methods of calculation of a_w, or, including as a third alternative, in the a_w that comes from the least-mean-squares best-fitting true Weibull distribution that is matched to the measured distribution over a large central part (i.e., noise level to 0.999 cumulative probability) of the measured distribution. However, a_w results by two different methods of calculation are shown in Table 5.7 and in all similar tables throughout Chapter 5 as a first indication of the degree to which Weibull statistics approximate the characteristics of the measured distributions; if the measured distributions were exactly Weibull, the two different methods of calculation of a_w would yield identical results.

Each pair of a_w numbers in Table 5.7 comes from a scatter plot in which each individual point plotted shows the median value of spread vs the median value of spatial resolution in a group of like-classified measured clutter histograms. For example, for Table 5.7 the standard deviation-to-mean scatter plot for the 2° to 4° depression angle regime is shown in

TABLE 5.7 Shape Parameter a_w and Ratios of Standard Deviation-to-Mean (SD/Mean) and Mean-to-Median for General Mixed Rural Terrain of High Relief, by Spatial Resolution A and Depression Angle[a]

α = Depression Angle (degrees)	Weibull Shape Parameter a_w			
	from SD/Mean		from Mean/Median	
	$A = 10^3 m^2$	$A = 10^6 m^2$	$A = 10^3 m^2$	$A = 10^6 m^2$
$6.0 \leq \alpha$	- - -	- - -	- - -	- - -
$4.0 \leq \alpha < 6.0$	2.4	1.5	2.9	1.3
$2.0 \leq \alpha < 4.0$	3.0	1.4	3.2	1.7
$1.0 \leq \alpha < 2.0$	3.0	1.6	3.4	1.5
$0.0 \leq \alpha < 1.0$	3.5	1.8	3.8	2.0
$-1.0 \leq \alpha < 0.0$	3.2	1.9	3.8	2.1
$\alpha < -1.0$	3.6	1.9	3.4	2.3
α = Depression Angle (degrees)	Ratios			
	SD/Mean (dB)		Mean/Median (dB)	
	$A = 10^3 m^2$	$A = 10^6 m^2$	$A = 10^3 m^2$	$A = 10^6 m^2$
$6.0 \leq \alpha$	- - -	- - -	- - -	- - -
$4.0 \leq \alpha < 6.0$	4.6	1.9	11.6	2.8
$2.0 \leq \alpha < 4.0$	6.3	1.7	14.3	4.5
$1.0 \leq \alpha < 2.0$	6.4	2.3	15.6	3.8
$0.0 \leq \alpha < 1.0$	7.9	2.9	18.9	6.3
$-1.0 \leq \alpha < 0.0$	6.8	3.2	18.3	7.0
$\alpha < -1.0$	8.1	3.2	15.5	7.7

[a] Table 5.5 defines the population of terrain patches and measurements upon which these data are based.

Figure 5.9. This scatter plot is based on 51 terrain patches and 987 measured clutter histograms, as indicated in Table 5.5. Twelve similar scatter plots underlie the 12 pairs of a_w numbers in Table 5.7.

The major parametric variation of a_w in Table 5.7 is with radar spatial resolution. In every case, a_w is much greater at 10^3 m^2 resolution than at 10^6 m^2 resolution. There is also a weaker trend in Table 5.7 whereby a_w decreases as depression angle increases from the 0° to 1° regime (more so with increasing positive depression angle than with increasing negative depression angle). For cell-by-cell Weibull random clutter strength numbers, a_w for the radar spatial resolution at the cell under consideration is required. The value of a_w applicable at resolution A is obtained by linear interpolation on $\log_{10} A$ between the tabulated values of a_w at $A = 10^3$ m^2 and $A = 10^6$ m^2 shown in Table 5.7. For example, in general mixed rural terrain of high relief in the depression angle regime from 1° to 2°, the applicable value of a_w at $A = 10^4$ m^2 based on: (1) measured ratios of standard deviation-to-mean is $a_w = 2.53$, (2) measured mean-to-median ratios is $a_w = 2.77$, and (3) equal weighting of ratios of standard deviation-to-mean and mean-to-median is $a_w = 2.65$.

The lower subtable of Table 5.7 shows the ratios of standard deviation-to-mean and mean-to-median from which the a_w numbers in the upper subtable come. The large spreads in low-angle land clutter spatial amplitude distributions at high spatial resolution are perhaps more dramatically evidenced by these lower numbers (e.g., mean-to-median ratio = 18.9 dB at 10^3 m^2, compared to 6.3 dB at 10^6 m^2, Table 5.7, depression angle regime from 1° to 2°). Figure 5.5 allows quick conversion between the numbers in the upper and lower subtables of Table 5.7, and similar tables throughout Chapter 5. Interpolation in these lower numbers directly yields general second moment or median values at the spatial resolution under consideration. For example, at $A = 10^4$ m^2, for general mixed rural terrain of high relief in the 1° to 2° depression angle regime, the ratio of standard deviation-to-mean is 5.0 dB and the mean-to-median ratio is 11.7 dB. The applicable mean level $\overline{\sigma^\circ_w}$ is obtained from Table 5.6. If L-band and vertical polarization happen to be the frequency and polarization of the radar in question, then, continuing the example, in general mixed rural terrain of high relief in the 1° to 2° depression angle regime at spatial resolution of 10^4 m^2, the applicable low-angle land clutter spatial amplitude distribution has $\overline{\sigma^\circ_w}$ = –26.0 dB, σ°_{50} = –37.7 dB, and standard deviation equal to –21.0 dB.

5.3.1.2 Low-Relief General Mixed Rural Terrain

Table 5.8 presents Weibull mean clutter strength $\overline{\sigma^\circ_w}$ for general mixed rural terrain of low relief by depression angle, frequency band, and polarization. The lower of the two subtables comprising Table 5.8 shows the number of measurements upon which each $\overline{\sigma^\circ_w}$ value in the upper subtable is based. Low-relief terrain has terrain slopes < 2°. Table 5.5 indicates that, within the Phase One general mixed rural clutter data, low relief occurs somewhat more frequently (viz., 56%) than high relief (viz., 44%).

The low-relief $\overline{\sigma^\circ_w}$ data of Table 5.8 are plotted in Figure 5.10 in a manner similar to that employed with the high-relief $\overline{\sigma^\circ_w}$ data in Figure 5.8. As in Figure 5.8, in each frequency band of Figure 5.10 the set of colored plot symbols continues to have a consistent v-shape indicating consistent depression angle effects in each band. The v-shapes of the low-relief data in Figure 5.10 are, however, considerably more pronounced than those of the high-relief data in Figure 5.8. That is, depression angle effects are stronger at low relief than at high relief.

The cyan colored symbols in Figure 5.10 represent the lowest positive depression angle regime (0° to 0.25°) in low-relief terrain and are based on a large number of measurements (see Table 5.8). In moving from cyan through the higher positive depression angles in Figure 5.10, in general there is a monotonic rise (with a few minor exceptions) up the left side of the v-shaped cluster from cyan to dark blue (0.25° to 0.75°) to purple (0.75° to 1.5°) to magenta (1.5° to 4°) to red (depression angle > 4°). Thus in each frequency band Figure 5.10 shows a strong increase in $\overline{\sigma^\circ_w}$ with increasing positive depression angle. The number of measurements falls off at outlying positive and negative depression angles (see Tables 5.5 and 5.8). No data are available for depression angle > 4° (red) at S- and X-bands in Figure 5.10 due to the limited Phase One elevation beamwidths in those bands.

Values of $\overline{\sigma^\circ_w}$ for negative depression angle are plotted in shades of green. The darkest shade of green shows results in the lowest negative depression angle regime, which is 0° to –0.25° in low-relief terrain. These dark green (0° to –0.25°) results in Figure 5.10 are generally close to and usually slightly higher than the cyan (0° to 0.25°) results. The shade of green becomes lighter with increasing negative depression angle. In low-relief

TABLE 5.8 Mean Clutter Strength $\overline{\sigma_w^\circ}$ and Number of Measurements for General Mixed Rural Terrain of Low Relief, by Frequency Band, Polarization, and Depression Angle[a]

α = Depression Angle (degrees)	Weibull Mean Clutter Strength $\overline{\sigma_w^\circ}$ (dB)									
	VHF		UHF		L-Band		S-Band		X-Band	
	HH	VV	HH	VV	HH	VV	HH	VV	HH	VV
$4.0 \le \alpha$	-17.0	-18.5	-22.5	-21.7	-23.2	-24.8	- - -	- - -	- - -	- - -
$1.50 \le \alpha < 4.00$	-20.5	-18.7	-21.9	-20.4	-23.7	-23.6	-31.8	-28.6	-24.5	-22.5
$0.75 \le \alpha < 1.50$	-26.7	-25.4	-26.0	-23.7	-26.7	-26.5	-31.5	-29.5	-28.4	-26.9
$0.25 \le \alpha < 0.75$	-35.8	-35.9	-32.7	-31.2	-29.6	-29.6	-32.9	-31.1	-30.5	-29.4
$0.00 \le \alpha < 0.25$	-40.7	-40.7	-38.4	-38.1	-32.8	-32.1	-35.3	-33.4	-32.3	-30.8
$-0.25 \le \alpha < 0.00$	-37.5	-39.7	-36.6	-35.4	-33.3	-34.2	-34.1	-32.9	-32.3	-30.6
$-0.75 \le \alpha < -0.25$	-41.3	-39.4	-32.2	-31.7	-30.5	-31.6	-31.2	-28.4	-31.8	-29.8
$\alpha < -0.75$	-31.2	-25.3	-22.3	-19.9	-22.6	-18.8	- - -	- - -	-26.6	-28.4
α = Depression Angle (degrees)	**Number of Measurements**									
	VHF		UHF		L-Band		S-Band		X-Band	
	HH	VV	HH	VV	HH	VV	HH	VV	HH	VV
$4.0 \le \alpha$	4	4	5	5	4	6	0	0	0	0
$1.50 \le \alpha < 4.00$	84	87	90	90	89	97	67	67	38	38
$0.75 \le \alpha < 1.50$	257	270	296	301	296	309	216	218	246	250
$0.25 \le \alpha < 0.75$	566	610	689	710	640	658	458	446	665	688
$0.00 \le \alpha < 0.25$	335	392	614	657	572	595	498	462	589	639
$-0.25 \le \alpha < 0.00$	87	108	188	212	193	199	161	157	225	228
$-0.75 \le \alpha < -0.25$	13	20	32	34	34	37	22	19	37	37
$\alpha < -0.75$	6	6	6	6	8	8	0	0	6	5
TOTALS	1,352	1,497	1,920	2,015	1,836	1,909	1,422	1,369	1,806	1,885

[a] Table 5.5 defines the population of terrain patches upon which these data are based.

terrain, two additional negative depression angle regimes are utilized for depression angles from –0.25° to –0.75° (intermediate green) and for depression angles < –0.75° (light green). In moving from cyan through the three green negative depression angle regimes in Figure 5.10, in general there is a strong monotonic rise (with two minor exceptions) up the right side of each v-shaped cluster.

At VHF in Figure 5.10, at low depression angles (e.g., cyan, 0° to 0.25°) clutter strengths are low due to multipath loss over the open components of the low-relief mixed rural terrain—this effect is not at work in the high-relief data of Figure 5.8. Remaining with VHF in Figure 5.10, at high depression angles (e.g., red, > 4°) clutter strengths are high because of the low RF absorption at VHF by the forested components of the low-relief mixed rural terrain—this effect is at work in the high-relief data of Figure 5.8. As a result of these two effects, the amplitude of the v-shaped cluster of plot symbols at VHF in Figure 5.10 is wide, viz., 24 dB, compared to 13 dB in Figure 5.8. These are the ranges over which small changes in depression angle affect the mean strength $\overline{\sigma_w^\circ}$ of land clutter at VHF in general mixed rural terrain of low and high relief, respectively. In Figure 5.10, as radar carrier

frequency f rises from VHF into the microwave regime, at low depression angle (cyan) $\overline{\sigma_w^\circ}(f)$ rises from VHF to L-band due to decreasing multipath loss with approximate dependence $\overline{\sigma_w^\circ}(f) \propto f^{0.95}$, whereas at high depression angle (red and magenta) $\overline{\sigma_w^\circ}(f)$ falls from VHF to S-band due to increasing RF absorption by tree foliage with approximate dependence $\overline{\sigma_w^\circ}(f) \propto f^{-0.97}$. At intermediate depression angles, the variation with radar frequency is intermediate between these extremes. As a result of these two opposite trends with radar frequency, the data points plotted in Figure 5.10 take on a funnel shape. As in the high-relief data of Figure 5.8, there is an S-band dip between L-band and X-band in the low-relief data of Figure 5.10, with the dip more pronounced at high depression angle (magenta) than at low depression angle (cyan). This dip occurs at all positive depression angles in Figure 5.10. As in Figure 5.8 at high relief, in Figure 5.10 at low relief the differences with polarization are generally small, on the order of several dB or less, with vertical polarization (VV) almost always stronger than horizontal (HH).

Comparison of Figures 5.8 and 5.10 indicates that there exist considerable differences in mean clutter strength $\overline{\sigma_w^\circ}$ between general mixed rural terrain of high relief (terrain slopes > 2°) and low relief (terrain slopes < 2°), respectively. A major reason for this is that low-relief mixed rural terrain allows multipath propagation to occur, which drives down clutter strengths at low depression angle in the lower bands. Multipath propagation does not occur to any significant degree in high-relief terrain or at high depression angles in low-relief terrain. At high depression angles in the lower bands and at all depression angles in the upper bands, mean clutter strengths in high-relief terrain are somewhat greater than in low-relief terrain, within similar depression angle regimes. Such differences are due directly to the effect of terrain relief on intrinsic σ°; they are less than the low depression angle differences in the lower bands caused by multipath. A contributing factor to all the differences in mean clutter strength with terrain relief indicated in Figures 5.8 and 5.10 is that high-relief mixed rural terrain tends to be somewhat more forested whereas low-relief mixed rural terrain tends to be somewhat more open. Classification by terrain relief in two major regimes as shown in Figures 5.8 and 5.10 is a simple and practicable approach for sorting out the complex phenomenological influences at work in low-angle land clutter.

Table 5.9 presents the Weibull shape parameter a_w and ratios of standard deviation-to-mean and mean-to-median for clutter amplitude distributions in general mixed rural terrain of low relief, by depression angle and radar spatial resolution. The statistical populations underlying the data of Table 5.9 are available in Table 5.5. In Table 5.9, a_w is calculated two ways: (1) from the ratio of standard deviation-to-mean and (2) from the mean-to-median ratio. Many of the corresponding a_w numbers resulting from these two methods of calculation are remarkably close in Table 5.9. Each pair of a_w numbers in Table 5.9 comes from a scatter plot in which each individual point plotted shows the median value of spread vs the median value of spatial resolution in a group of like-classified measured clutter histograms. The standard deviation-to-mean scatter plot for the 0.25° to 0.75° depression angle regime in Table 5.9 is shown in Figure 5.11. The major parametric variation of a_w in Table 5.9 is with radar spatial resolution. In every case, a_w is much greater at 10^3 m^2 resolution than at 10^6 m^2 resolution. There is a weak trend in Table 5.9 whereby a_w decreases as depression angle increases from the 0° to 0.25° regime. There is little indication for a_w in terrain of high relief as shown in Table 5.7 to be lower than in terrain of low relief as shown in Table 5.9, as might be expected in these results. The lower subtable of Table 5.9 shows the ratios of standard deviation-to-mean and mean-to-median from which the a_w numbers in the upper subtable come. The large spreads in low-angle land

TABLE 5.9 Shape Parameter a_w and Ratios of Standard Deviation-to-Mean (SD/Mean) and Mean-to-Median for General Mixed Rural Terrain of Low Relief, by Spatial Resolution A and Depression Angle[a]

α = Depression Angle (degrees)	Weibull Shape Parameter a_w			
	from SD/Mean		from Mean/Median	
	$A = 10^3 m^2$	$A = 10^6 m^2$	$A = 10^3 m^2$	$A = 10^6 m^2$
$4.00 \leq \alpha$	2.5	1.6	2.2	1.6
$1.50 \leq \alpha < 4.00$	2.5	1.7	2.5	1.7
$0.75 \leq \alpha < 1.50$	3.1	2.1	3.3	1.9
$0.25 \leq \alpha < 0.75$	3.5	1.8	3.7	1.7
$0.00 \leq \alpha < 0.25$	3.5	1.7	3.7	1.7
$-0.25 \leq \alpha < 0.00$	4.4	1.5	4.3	1.5
$-0.75 \leq \alpha < -0.25$	4.2	1.7	3.6	2.3
$\alpha < -0.75$	2.9	1.7	3.4	1.8
α = Depression Angle (degrees)	Ratios			
	SD/Mean (dB)		Mean/Median (dB)	
	$A = 10^3 m^2$	$A = 10^6 m^2$	$A = 10^3 m^2$	$A = 10^6 m^2$
$4.00 \leq \alpha$	4.9	2.2	7.3	4.0
$1.50 \leq \alpha < 4.00$	4.9	2.5	9.2	4.7
$0.75 \leq \alpha < 1.50$	6.6	3.8	14.8	5.5
$0.25 \leq \alpha < 0.75$	7.9	2.8	17.6	4.7
$0.00 \leq \alpha < 0.25$	7.9	2.6	18.0	4.6
$-0.25 \leq \alpha < 0.00$	10.2	1.9	22.7	3.7
$-0.75 \leq \alpha < -0.25$	9.6	2.6	16.9	7.9
$\alpha < -0.75$	6.1	2.7	15.5	5.2

[a] Table 5.5 defines the population of terrain patches and measurements upon which these data are based.

clutter spatial amplitude distributions at high spatial resolution continue to be dramatically evidenced by these lower numbers.

5.3.2 Further Reduction

The previous results of Section 5.3, although applicable to a single generic terrain type (viz., mixed rural), still require specification of the relief of the terrain (in two categories, viz., high- and low-) and the depression angle at which the terrain is illuminated. A clutter modeler who is unable to specify terrain relief and depression angle may desire that the Phase One clutter measurement data be reduced so as to average together all variations of terrain relief and depression angle. The results of such reduction are presented in what follows. Table 5.10 shows mean clutter strength $\overline{\sigma_w^\circ}$ for general mixed rural terrain by frequency band and polarization, in which all variations with relief and depression angle are subsumed. The $\overline{\sigma_w^\circ}$ results of Table 5.10 are plotted in Figure 5.12. The lower subtable of Table 5.10 shows that the number of measurements upon which the mean clutter

TABLE 5.10 Mean Clutter Strength $\overline{\sigma_w^\circ}$ and Number of Measurements for General Mixed Rural Terrain by Frequency Band and Polarization, Inclusive of Variations with Relief and Depression Angle[a]

Weibull Mean Clutter Strength $\overline{\sigma_w^\circ}$ (dB)									
VHF		UHF		L-Band		S-Band		X-Band	
HH	VV	HH	VV	HH	VV	HH	VV	HH	VV
-29.9	-29.2	-30.5	-29.1	-28.9	-28.9	-32.4	-30.4	-30.1	-28.8
Number of Measurements									
VHF		UHF		L-Band		S-Band		X-Band	
HH	VV	HH	VV	HH	VV	HH	VV	HH	VV
2,576	2,776	3,426	3,573	3,310	3,483	2,505	2,476	3,012	3,109

[a] Table 5.5 defines the population of terrain patches upon which these data are based.

strength results in Table 5.10 are based is large—on the order of 3,000 measurements for each value of $\overline{\sigma_w^\circ}$.

The $\overline{\sigma_w^\circ}$ results of Table 5.10 and Figure 5.12 hover around –30 dB in all five frequency bands and at both polarizations. There is a slight (~2 dB) S-band dip between L-band and X-band; also, results at vertical polarization are usually slightly stronger (on the order of 1 or 2 dB) than at horizontal polarization (except at L-band where $\overline{\sigma_w^\circ}\big|_{VV} = \overline{\sigma_w^\circ}\big|_{HH}$). Such differences with frequency and polarization are small. That is, after incorporating all variations with relief and depression angle, mean clutter strength in general mixed rural terrain is remarkably invariant with frequency and polarization. The results of Table 5.10 and Figure 5.12 corroborate corresponding results obtained with repeat sector data in Chapter 3 (cf. Table 3.7 and Figure 3.40).

Table 5.11 presents the Weibull shape parameter a_w and ratios of standard deviation-to-mean and mean-to-median for clutter amplitude distributions in general mixed rural terrain, inclusive of all variations with relief and depression angle, but retaining the dependence on radar spatial resolution. Figure 5.13 shows the sd/mean scatter plot associated with this table, in which the strong trend of decreasing spread with increasing cell size continues to be seen. The dependence of a_w on spatial resolution cannot sensibly be avoided. However, a radar modeler usually can specify the parameters of his radar, including resolution (as well as frequency and polarization), even if he cannot be specific about terrain relief and depression angle. For example, linear interpolation on $\log_{10}A$ in Table 5.11 indicates that, in general mixed rural terrain independent of relief and depression angle, for a radar that happens to have spatial resolution $A = 10^4$ m^2 for the terrain region in question, the mean-to-median ratio in the amplitude distribution of the land clutter for that region is 13.4 dB. Thus, largely independent of frequency (VHF to X-band) and polarization, the mean clutter strength for that region is $\overline{\sigma_w^\circ} \approx -30$ dB (as per Table 5.10), and the median clutter strength for that region is $\sigma_{50}^\circ \approx -43$ dB (as per Table 5.11). At some other value of spatial resolution significantly different from 10^4 m^2, $\overline{\sigma_w^\circ}$ will remain at ~ –30 dB, but σ_{50}° will vary significantly from ~ –43 dB.

TABLE 5.11 Shape Parameter a_w and Ratios of Standard Deviation-to-Mean (SD/Mean) and Mean-to-Median for General Mixed Rural Terrain by Spatial Resolution A, Inclusive of Variations with Relief and Depression Angle[a]

Weibull Shape Parameter a_w			
from SD/Mean		from Mean/Median	
$A = 10^3 m^2$	$A = 10^6 m^2$	$A = 10^3 m^2$	$A = 10^6 m^2$
3.4	1.8	3.7	1.9
Ratios			
SD/Mean (dB)		Mean/Median (dB)	
$A = 10^3 m^2$	$A = 10^6 m^2$	$A = 10^3 m^2$	$A = 10^6 m^2$
7.6	2.8	17.4	5.5

[a] Table 5.5 defines the population of terrain patches and measurements upon which these data are based.

Does the reduction of clutter strength results inclusive of all variations of terrain relief and depression angle constitute *reductio ad absurdum*? Certainly there is a price to pay for the simplicity of the resulting information. That price is the loss in variability in $\overline{\sigma_w^\circ}$ and a_w that actually occurs with terrain relief and depression angle. The range of variation of $\overline{\sigma_w^\circ}$ in Figure 5.12 is very small compared to the ranges of variation of $\overline{\sigma_w^\circ}$ in Figures 5.8 and 5.10. It is clear from this variability that attempting to characterize low-angle land clutter independently of terrain relief and depression angle must inherently involve large uncertainties in predicting clutter strengths in any real radar operating at a particular depression angle in terrain of particular relief.

5.3.3 Validation of Clutter Model Framework

In the clutter modeling framework of Chapter 5, mean clutter strength $\overline{\sigma_w^\circ}$ varies with radar frequency f as $\overline{\sigma_w^\circ}(f)$, shape parameter a_w varies with radar spatial resolution A as $a_w(A)$, and both $\overline{\sigma_w^\circ}(f)$ and $a_w(A)$ vary with terrain type and depression angle. This modeling framework was developed through evolving examination of clutter measurement data—first, the Phase Zero data at X-band in Chapter 2, and then the Phase One multifrequency repeat sector data in Chapter 3. The repeat sector data were based on one carefully selected clutter patch at each measurement site so as to represent a canonical, uncomplicated, clear-cut terrain type and measurement situation. Thus an important question has been, do the trends observed in the carefully selected 42-patch repeat sector data represent those that exist in more generally occurring composite landscape? Stated differently, were the 42 repeat sector patches selected with too much care, leading to parametric dependencies not generally borne out in the spatially comprehensive 3,361-patch survey data? The results of Section 5.3 confirm that the modeling framework originally developed from preliminary measurement data continues to be appropriate for deriving modeling information from the final complete multifrequency measurement database. As shown in Section 5.3, major empirical dependencies in clutter amplitude statistics with frequency, resolution, terrain relief, and depression angle do indeed exist in general mixed rural terrain and are captured by this modeling framework.

Basing the model framework on $\overline{\sigma_w^\circ}$, in contrast, for example, to σ_{50}°, results in a considerable simplification. In any measured clutter spatial amplitude distribution, $\overline{\sigma_w^\circ}$ is

the only attribute of the distribution not dependent on A. Thus basing the model framework on $\overline{\sigma_w^\circ}$ removes one complete parameter dimension from the model—that is, $\overline{\sigma_w^\circ} = \overline{\sigma_w^\circ}(f)$, whereas $\sigma_{50}^\circ = \sigma_{50}^\circ(f, A)$.

5.3.4 Simplified Clutter Prediction

Digitized terrain elevation data[27] may often be more readily available to radar performance modelers than digitized data descriptive of the land cover. For example, although raw Landsat data descriptive of land cover are readily available by purchase from the USGS EROS Data Center, these raw data require considerable further processing, first for geometric correction, and then for classification into standard land cover categories (e.g., forest, agricultural, etc.), before they are useful for clutter modeling. The clutter modeling information of Section 5.3, applicable to the single general land cover class of "general mixed rural," may be directly used for site-specific clutter prediction using only digitized terrain elevation data—information descriptive of the land cover at the site is not necessary in this simplified approach to clutter modeling.

Through use of the digitized terrain elevation data, (1) depression angle from the radar to the backscattering terrain point can be calculated based simply on the relative elevation differences of the radar and the terrain point, and (2) terrain relief can be estimated as high or low based on whether average terrain slope in the neighborhood of the terrain point is $> 2°$ or $< 2°$, respectively. This information, together with specification of the radar parameters, is sufficient to calculate a Weibull random variate estimate of general mixed rural clutter strength $\sigma°F^4$ for the terrain cell in question from the results of Section 5.3.

Of course the disadvantage of this simplified approach is the loss in prediction fidelity associated with the variations in clutter amplitude statistics that occur with changes in land cover. That such variability can be large is indicated by the clutter modeling information presented in Section 5.4 for a number of specifically different land cover classes. However, simplification to the single "general mixed rural" land cover class (i.e., doing without land cover information) while retaining variations with relief and depression angle is obviously less severe than further simplifying out variations with relief and depression angle (i.e., in addition, doing without digitized terrain elevation data) as in the results of Tables 5.10 and 5.11, and Figures 5.12 and 5.13.

5.4 Land Clutter Coefficients for Specific Terrain Types

In Section 5.4, land clutter coefficients are presented for the following eight specific terrain types—urban, agricultural, forest, shrubland, grassland, wetland, desert, and mountains. These eight terrain types are characterized principally by land cover, except for mountain terrain which is characterized principally by landform. The results of Section 5.4 are based on the set of 1,733 clutter patches for which the terrain classification is pure. Pure terrain classification implies that a single primary classifier was sufficient to describe the patch; secondary classification was unnecessary. This set of 1,733 pure patches is a

27. Digitized terrain elevation data may be acquired from the U. S. Geological Survey (USGS) or the U. S. National Imagery and Mapping Agency (NIMA). Such data are called Digital Elevation Models (DEMs) by USGS, and Digital Terrain Elevation Data (DTED) by NIMA. In the past, the data from both sources were commonly available at 3 arc-seconds (i.e., ≈100 m) sampling interval, but data at smaller sampling intervals (e.g., 1 arc-second) are now increasingly available.

6

Windblown Clutter Spectral Measurements

6.1 Introduction

Moving target indication (MTI) radar utilizes Doppler processing to separate small moving targets from large clutter returns. Any intrinsic motion of the clutter sources causes the clutter returns to fluctuate with time and the received clutter power to spread from zero-Doppler in the frequency domain. As a result, intrinsic clutter motion degrades and limits MTI performance. MTI design objectives can require clutter rejection in the 60- to 80-dB range or more, and can be implemented not only by using conventional fixed-parameter MTI filter design [1, 2] but also through modern adaptive Doppler-processing techniques [3–5]. However implemented, successful clutter rejection to such low levels requires accurate definition of the detailed shape of the intrinsic-motion clutter power spectrum. The most pervasive source of intrinsic fluctuation in ground clutter is the wind-induced motion of tree foliage and branches or other vegetative land cover. The shape of windblown tree clutter power spectra has been a subject of investigation since the early days of radar development. Although this subject continues to be important, it has generally remained rather poorly understood, largely because of the difficulty of accurately measuring clutter spectra to very low spectral power levels.

Radar ground clutter power spectra were originally thought to be of Gaussian shape [6–9]. Later, with measurement radars of increased spectral sensitivity, it became apparent that spectral tails wider than Gaussian existed that could be modeled as power law over the spectral ranges of power—typically 35 to 40 dB below the peak zero-Doppler level—then available [10, 11]. A number of measurements of clutter spectra all generally characterized as power law followed [12–20], and much discussion at the time focused on power-law representation of clutter spectral shape. If real when extrapolated to low levels, power-law spectral tails would severely limit MTI Doppler-processor performance against small targets and would reduce motivation for suppressing radar phase noise to lower levels. Measurements of windblown ground clutter power spectra at Lincoln Laboratory to levels substantially lower (i.e., 60 to 80 dB down) than most earlier measurements indicate spectral shapes that fall off much more rapidly than constant power-law at rates of decay often approaching exponential [21–26]. How are these observations of exponential spectral shape reconcilable with the earlier power-law observations? One purpose of Chapter 6 is to resolve these apparently conflicting results.

The most salient aspect of Lincoln Laboratory's measurements of windblown ground clutter power spectra is their rapid decay to levels 60 to 80 dB down from zero Doppler. Chapter 6

provides a simple model with exponential decay characteristics for the Doppler-velocity power spectrum of radar returns from cells containing windblown trees. This exponential model empirically captures, at least in general measure and occasionally very accurately, the major attributes of the measured phenomenon. The exponential shape (a) is somewhat wider than the historic Gaussian shape, as required by the general consensus of experimental evidence; (b) is very much narrower at lower power levels (i.e., 60 to 80 dB down) than the subsequent power-law representations when they are extrapolated to such low levels; and (c) at higher power levels (35 to 40 dB down) finds approximate equivalence in spectral level and extent with a number of reported results modeled as power law at these higher levels. Important effects of wind speed and radar frequency (VHF to X-band) on windblown ground clutter spectra are also described and incorporated in the model.

Chapter 6 presents the exponential model in Section 6.2. The general validity of the postulated model is demonstrated in Section 6.3 by comparing it with numerous measurements. Section 6.4 briefly discusses (a) how to use the exponential clutter spectral model to calculate the absolute level of clutter power in any radar Doppler cell; (b) differentiation of quasi-dc and ac regions of spectral approximation; (c) how the exponential model can perform adequately not only in forested but also in nonforested terrain (farmland, desert) by suitably adjusting the dc/ac term of the model; and (d) comparison of the MTI improvement factors for a single delay-line canceller in exponential vs Gaussian clutter.

Section 6.5 investigates the impact of assigning the correct shape for the clutter power spectral density (PSD) on modern radar signal processing techniques that use coherent adaptive processing for target detection in clutter; and further validates the exponential clutter spectral model by showing that the differences between using measured windblown clutter data as input to the processor, and using modeled data of various spectral shapes, are minimized when the modeled data are of exponential spectral shape. Section 6.6 is a thorough tutorial review of the historical literature concerning intrinsic-motion ground clutter spectral spreading that compares and contrasts current clutter spectral results with those previously reported. Section 6.7 is a summary.

6.2 Exponential Windblown Clutter Spectral Model

Consider a radar spatial resolution cell containing windblown trees. Such a cell contains both fixed scatterers (ground, rocks, tree trunks) and moving scatterers (leaves, branches). The returned signal correspondingly contains both a constant (or steady) and a varying component. The steady component gives rise to a dc or zero-Doppler term in the power spectrum of the returned signal, and the varying component gives rise to an ac term in the spectrum. Thus a suitable general analytic representation for the total spectral power density $P_{tot}(v)$ in the Doppler-velocity power spectrum from a cell containing windblown vegetation is provided by

$$P_{tot}(v) = \frac{r}{r+1} \cdot \delta(v) + \frac{1}{r+1} P_{ac}(v), \quad -\infty < v < \infty \tag{6.1}$$

where v is Doppler velocity[32] in m/s, r is the ratio of dc power to ac power in the spectrum,[33] $\delta(v)$ is the Dirac delta function, which properly represents the shape of the dc component in the spectrum, and $P_{ac}(v)$ represents the shape of the ac component of the spectrum, normalized such that

$$\int_{-\infty}^{\infty} P_{ac}(v)dv = 1 \ .$$

Since by definition

$$\int_{-\infty}^{\infty} \delta(v)dv = 1 \ ,$$

it follows that normalization in Eq. (6.1) is to unit total spectral power, i.e.,

$$\int_{-\infty}^{\infty} P_{tot}(v)dv = 1 \ .$$

It is apparent from Eq. (6.1) that for $|v| > 0$, $P_{tot}(v) = [1/(r + 1)]P_{ac}(v)$. In considering analytic spectral shapes, $P_{ac}(v)$ is the fundamental quantity, whereas in measured results $P_{tot}(v)$ is the fundamental quantity. On a decibel scale, the level of an analytic spectral shape function $10 \log_{10} P_{ac}$ must be reduced by $10 \log_{10} (r + 1)$ before comparison with directly measured data $10 \log_{10} P_{tot}$, or the level of directly measured data $10 \log_{10} P_{tot}$ must be raised by $10 \log_{10} (r + 1)$ before considering its ac spectral shape. Such normalization adjustments obviously depend on the dc/ac ratio r, a highly variable quantity in measured clutter spectra. In Chapter 6, either P_{tot} or P_{ac} can represent measured or modeled data, depending on context.

6.2.1 AC Spectral Shape

Radar ground clutter spectral measurements at Lincoln Laboratory to levels 60 to 80 dB below the peak zero-Doppler level indicate that the shapes of the spectra often decay at rates close to exponential. The two-sided exponential spectral shape may be represented analytically as

$$P_{ac}(v) = \frac{\beta}{2} \cdot \exp(-\beta|v|) \ , \ -\infty < v < \infty \tag{6.2}$$

where β is the exponential shape parameter. Table 6.1 provides values of β as a function of wind conditions such that spectral width increases with increasing wind speed as generally observed in the measurement data. The exponential shapes specified in Table 6.1 are plotted in Figure 6.1. The terminology used here to describe wind conditions borrows from but does not strictly adhere to that of the Beaufort wind scale [27, 28]. The measurements indicate that the values of β in Table 6.1 and Figure 6.1 are largely independent of radar carrier frequency over the range from VHF to X-band (see Figures 6.10 and 6.11).

32. The term "Doppler velocity" as used herein is equivalent to scatterer radial velocity.

33. In Chapter 6, r represents dc/ac ratio. In preceding chapters, r represents radar range (see Section 2.3.1.1).

TABLE 6.1 Exponential ac Shape Parameter β vs Wind Speed

Wind Conditions	Wind Speed (mph)	Exponential ac Shape Parameter β $(m/s)^{-1}$	
		Typical	Worst Case
Light air	1-7	12	—
Breezy	7-15	8	—
Windy	15-30	5.7	5.2
Gale force (est.)	30-60	4.3	3.8

The basis of the "worst-case, windy" specification of $\beta = 5.2$ is the highly exponential forest/windy spectrum subsequently shown in Figure 6.5, which is among the widest in the current Lincoln Laboratory database of clutter spectral measurements. The basis of the "typical, gale force" specification of $\beta = 4.3$ is the scaled estimate of a forest clutter spectrum in gale force winds subsequently shown in Figure 6.9. Increasing gale force β from its typical specification based on this scaled estimate to a worst-case specification of $\beta = 3.8$ brings it into very close agreement (in terms of spectral extent at the –14-dB level) with the only known measurements of windblown clutter under actual gale force wind conditions, namely, the very early measurements of Goldstein [9] that are further discussed in Section 6.6.3.5. Many measurements similar to the forest/light air spectrum subsequently shown in Figure 6.16 are the basis of the "light air, typical" specification of $\beta = 12$.

Consideration of the β numbers in Table 6.1 reveals that spectral width as given by the quantity β^{-1} varies approximately linearly with the logarithm of the wind speed. Note that $v = \beta^{-1}$ is the point on the spectrum that is $10 \log_{10} (1/e) = -4.34$ dB down from its zero-Doppler peak. Dependency of spectral width on the logarithm of wind speed is directly illustrated in some particular measurements to follow (see Figures 6.8 and 6.9). An algebraic expression for β that incorporates linear dependency of spectral width on the logarithm of the wind speed w as observed in these data is

$$\beta^{-1} = 0.1048 \, [\log_{10} w + 0.4147] \tag{6.3}$$

where w is wind speed in statute miles per hour. Equation (6.3) provides a reasonable match to the values of β shown in Table 6.1 and Figure 6.1. However, β is a highly variable quantity in measured clutter spectra. The tabulated values of β are for the most part medianized values within broad regimes of wind speed and hence portray more realistically than Eq. (6.3) what was actually observed across the spectral database as a whole. The implementation of a rigorous linear dependence of spectral width on the logarithm of wind speed in Eq. (6.3) provides a good fit to the data for windy conditions, but somewhat overestimates the higher wind speeds necessary for given values of β in gale force conditions and slightly underestimates the lower wind speeds necessary for given values of β in breezy and light air conditions. Equation (6.3) can nevertheless be useful in trend analysis studies that require an analytic approximation for the dependency of β on w.

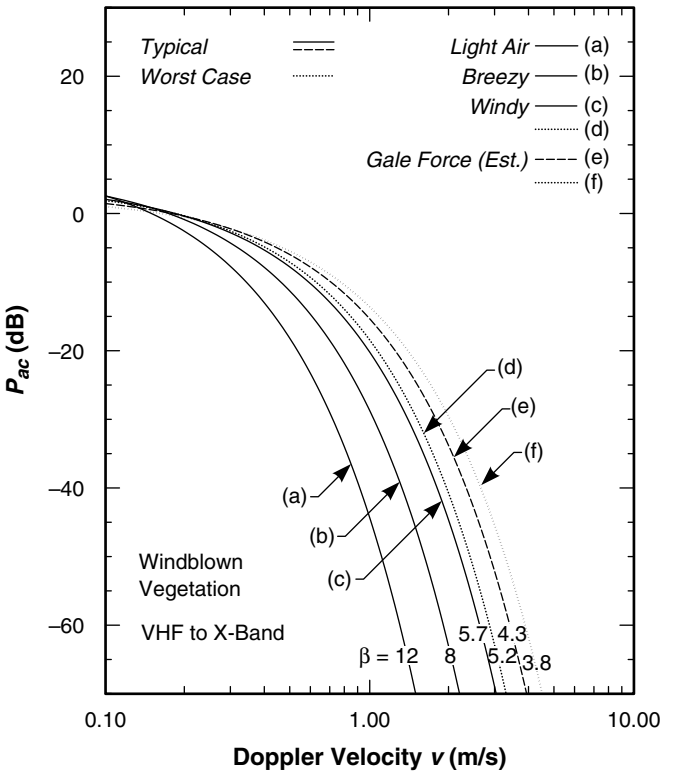

FIGURE 6.1 Exponential model for ac clutter spectral shape from windblown vegetation, parameterized by wind speed. Applicable VHF to X-band.

Doppler frequency f in Hertz and scatterer radial velocity v in m/s are fundamentally related as $f = -2v/\lambda$, where λ is the radar transmission wavelength.[34] It follows that if the Doppler velocity extent of measured clutter spectra from windblown vegetation is largely invariant with radar frequency, the Doppler frequency extent from windblown vegetation must scale approximately linearly with radar frequency. In Chapter 6, clutter spectra are usually plotted using a Doppler velocity abscissa as opposed to the more conventional Doppler frequency abscissa to allow direct comparison of spectral shape and extent at different radar frequencies with the linear scaling factor normalized out. Of course, for any particular radar system, it is the quantity $P_{ac}(f)$, not $P_{ac}(v)$, that is of direct interest. To convert to $P_{ac}(f)$ in Eq. (6.2), i.e., $P_{ac}(f)\,df = P_{ac}(v)\,dv$, replace v by f and β by $(\lambda/2)\,\beta$. To convert from v to f in Eq. (6.1), replace v by f.

6.2.2 DC/AC Ratio

Although $P_{ac}(v)$ is largely independent of radar frequency, the value of dc/ac ratio r in Eq. (6.1) is strongly dependent on both wind speed and radar frequency, as subsequently shown in Figures 6.17 and 6.19. An analytic expression for r empirically derived from such results which generally captures these dependencies is provided by

34. In Chapter 6, f represents Doppler frequency and f_o represents radar carrier frequency. In preceding chapters, f represents radar carrier frequency.

$$r = 489.8\, w^{-1.55} f_o^{-1.21} \tag{6.4}$$

where, as before, w is wind speed in statute miles per hour, and f_0 is radar carrier frequency in gigahertz.[34] Equation (6.4) applies to cells containing windblown trees. The database from which it was derived covers the frequency range from 170 MHz (i.e., VHF) to 9.2 GHz (i.e., X-band) and includes measurements from many forested cells under various wind conditions. The variation of r with wind speed and radar frequency as specified by Eq. (6.4) is plotted in Figure 6.2. The quantity r in Eq. (6.4) is also the ratio of steady to random average power (originally defined as m^2 by Goldstein [9]) in the Ricean distribution describing the temporal amplitude statistics of the clutter (see Chapter 4, Section 4.6.1).

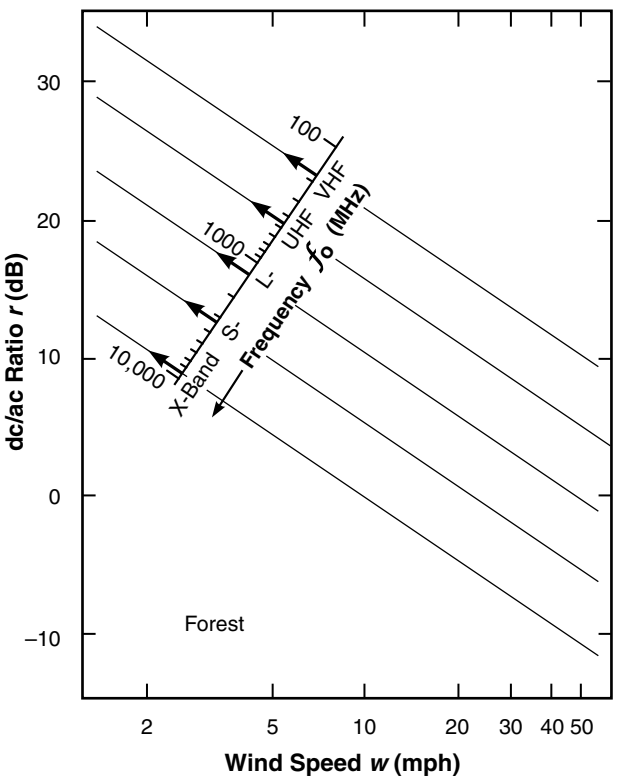

FIGURE 6.2 Modeling information specifying ratio of dc to ac spectral power in windblown forest clutter spectra vs wind speed and radar frequency.

In measured clutter spectra from windblown trees, not only does the maximum spectral power almost always occur in the zero-th Doppler bin, but high spectral power levels are also often resolved in neighboring Doppler bins that are very near but not right at zero Doppler. Hereafter, such near zero-Doppler spectral power is called quasi-dc power. The near zero-Doppler regime of quasi-dc power is usually $0 < |v| < 0.25$ m/s. Excess quasi-dc power exists in the quasi-dc region when the spectral power initially decays rapidly but continuously from the peak power level right at zero Doppler at a rate much faster than the exponential rate evident at lower power levels in the spectral tail. The spectral power that is resolved in the zero-th Doppler bin in such spectra comes from relatively motionless parts

of the tree trunks near ground level as well as from the ground surface itself, whereas the spectral power resolved as quasi-dc comes from higher parts of tree trunks and major limbs flexing slightly at very slow rates. Including the excess quasi-dc spectral power as part of the ac spectral power degrades the goodness-of-fit of the exponential shape function in the spectral tail. That is, in these circumstances even though the value of β in Eq. (6.2) is correctly selected to match the relative shape $P_{ac}(v)$ in the spectral tail, the value of r will be too low, with the result that the absolute level $[1/(r + 1)]P_{ac}(v)$ will be too high. Furthermore, to the extent that windblown clutter statistics are nonstationary, besides being too high, this level can also be dependent on the length of coherent processing interval (CPI) employed.

Therefore, in what follows, where excess (above the approximating exponential) quasi-dc power occurs in the data, it is included with the Dirac delta function as dc power in the model. This approach to quantifying dc/ac ratio r has been followed in the processing underlying the statistics upon which Eq. (6.2) is based (see Section 6.4.2). The major consequence of this approach is that the preceding spectral model approximates the exponential spectral tail region correctly, in both relative shape and absolute level, and independently of the length of CPI employed. Examples of windblown forest clutter spectra containing excess quasi-dc power are presented subsequently, as well as examples of desert and cropland clutter spectra in which a dc component from the absolutely stationary underlying ground surface (as opposed to the moving vegetation) exists as a discrete delta function.

6.2.3 Model Scope

Equations (6.1), (6.2), (6.3), and (6.4) constitute a simple but complete empirical model for characterizing the complex physical phenomenon of radar ground clutter power spectra from windblown trees based on extensive measurements. Total backscattered clutter power is represented including both dc and ac spectral components. The test of any model of a physical phenomenon is the degree to which it generally represents the phenomenon while avoiding complicating detail. The important parameters incorporated in the model of Eqs. (6.1), (6.2), (6.3), and (6.4) are wind speed and radar frequency; others that might be thought to strongly influence clutter spectra from windblown trees, but which appear to be generally subsumed within the ranges of statistical variability over the relatively large cell sizes utilized in the measurement data, include: (a) the types of trees involved (species, density, growth stage), (b) season of the year (e.g., leaves on vs leaves off), (c) wind direction, (d) polarization, and (e) angle of illumination.

It is not possible to generalize information for dc/ac spectral power ratio r for all possible varieties of vegetated (or partially vegetated) ground clutter cells from which significant proportions of backscattered clutter power come from stationary scattering elements. Subsequently discussed Lincoln Laboratory measurements of clutter spectra in scrub desert, rangeland, and cropland terrain, although indicating much larger values of dc/ac spectral power ratio when compared with forest terrain, also indicate that the residual ac spectral shape function $P_{ac}(v)$ is similar to that of forest. Thus the spectral model of Eqs. (6.1), (6.2), and (6.3), although explicitly derived for windblown trees, may be considered generally applicable not only to forested cells but also, at least as a first-order approximation, to cells in partially open or open terrain (desert, rangeland, cropland) as long as the value of r is increased appropriately. However, Eq. (6.4) specifying r was derived only from forested cells, and only some particular examples are provided in what

follows indicating how r increases for cells incompletely filled with trees or in open agricultural terrain.

Although the exponential spectral shapes $P_{ac}(v)$ in Figure 6.1 are modeled to be invariant with radar frequency and vegetation type, two important ramifications are: (1) modeled widths of clutter frequency spectra $P_{ac}(f)$ increase linearly with radar frequency from VHF to X-band, and (2) increasing values of dc to ac ratio r in increasingly open terrain (desert, cropland) and/or with decreasing radar frequency cause absolute ac power levels $[1/(r+1)]$ $P_{ac}(v)$ to decrease even though the $P_{ac}(v)$ shape function itself remains invariant under such circumstances.

An important requirement in the development of the current model was that its predictions of spectral extent be in the correct general Doppler regime at spectral power levels 60 to 80 dB down from zero-Doppler peaks. Much uncertainty has existed concerning the location of this regime. The extensive Lincoln Laboratory database of windblown clutter spectral measurements, without exception, indicates ever increasing rates of spectral decay (i.e., downward curvature) with decreasing spectral power level as observed on log-Doppler velocity axes such that maximum spectral extents 60 to 80 dB down are limited to Doppler velocities of 3 to 4 m/s. The exponential shape function properly reflects this important fundamental feature of the measurements. The exponential model for $P_{ac}(v)$ provides windblown clutter spectra wider than Gaussian as required by experiment and supported by theory [29].

An alternative popular spectral shape function $P_{ac}(v)$ has been power-law [10]. The measurement data clearly indicate that observed rates of decay modeled as power law at upper levels of spectral power do not continue as power law to lower levels of spectral power but fall off much faster at the lower levels. In contrast, an exponential representation generally captures, at least approximately and occasionally highly accurately, the major attributes of the windblown clutter ac spectral shape function over the entire range from near the zero-Doppler peak to measured levels 60 to 80 dB down.

The exponential model for $P_{ac}(v)$ is validated in Section 6.5 (see also [30, 31]) by showing that the differences in matched filter and clutter cancellation system performance between using actual measured in-phase (I) and quadrature (Q) Phase One clutter data as input to the processors, and modeled clutter spectral data of various spectral shapes (viz., Gaussian, power law, and exponential), are minimized when the spectral model employed is of exponential shape. Section 6.5 also evaluates the impact of using the exponential model for $P_{ac}(v)$, as opposed to Gaussian and power-law models, on the prediction of detection performance of airborne and ground-based surveillance radar using coherent adaptive processing [32, 33].

6.3 Measurement Basis for Clutter Spectral Model

6.3.1 Radar Instrumentation and Data Reduction

Lincoln Laboratory has measured and characterized ground clutter power spectra over wide spectral dynamic ranges using the Phase One and LCE (L-Band Clutter Experiment) instrumentation radars [21, 25]. Both of these radars were conventional analog coherent

radars. These two radars are first mentioned in this book in Chapter 1, Section 1.3. The Phase One radar and its program of clutter measurements are subsequently described more completely in Chapter 3.

Important system parameters of these two radars are shown in Table 6.2. As shown in the table, the Phase One radar operated in five frequency bands, whereas the LCE radar operated at L-band only. With both radars, the basic type of clutter experiment suitable for examining temporal and spectral characteristics of ground clutter was the long-time-dwell experiment (see Section 3.2.2) in which relatively long sequences of pulses at low pulse repetition frequency (PRF) were recorded over a contiguous set of range gates with a stationary antenna beam. Each radar activated one combination at a time of frequency, polarization, and pulse length for any particular long-time-dwell clutter experiment. Many of the Phase One clutter spectra shown in Chapter 6 are from long-time-dwell data collected at Katahdin Hill, a forested site in eastern Massachusetts, during April and early May before leaf emergence on deciduous trees. The forested cells from which backscatter was measured at Katahdin Hill are typical of the eastern mixed hardwood forest (oak, maple, beech) with occasional occurrences of conifers (hemlock, pine), all generally 50 or 60 ft high. For the Katahdin Hill measurements, general wind conditions in the neighborhood of the principle cells from which backscatter was recorded were taken from weather information continuously broadcast from a nearby airfield. At other sites, wind conditions were measured by anemometers located at the radar site and, in many instances, also in the clutter measurement sector.

TABLE 6.2 Radar System Parameters

Parameter	LCE	Phase One				
Frequency						
Band	L-Band	VHF	UHF	L-Band	S-Band	X-Band
(MHz)	(1230)	(169)	(435)	(1230)	(3230)	(9100)
Antenna gain (dBi)	31	13	25	28.5	35.5	38.5
Antenna beamwidth						
Az (deg)	6	13	5	3	1	1
El (deg)	3	42	15	10	4	3
Peak power (kW)	8	10	10	10	10	50
Polarization	HH, VV, HV, VH	HH, VV				
PRF (Hz)	500	500				
Pulse width (μs)	1	0.1, 0.25, 1				
Waveform	Uncoded CW pulse	Uncoded CW pulse				
A/D converter						
No. of bits	14	13				
Sampling rate (MHz)	2	10, 5, 1				

The LCE radar was a major upgrade at L-band only of the Phase One measurement equipment with substantially reduced phase noise levels [34, 35]. A primary design objective of the LCE radar was to achieve low enough phase noise such that the low-frequency Doppler components of windblown clutter could be measured to levels ≈ 80 dB below the dc or stationary component of the clutter at zero-Doppler. This objective was met by using a combination of low phase-noise local oscillators (viz., Hewlett-Packard models 8662A and 8663A) locked to a common source, a low phase-noise transmitter, and system clocks with low jitter. The transmitter used two planar triodes (viz., Eimac Y-793F) in a grounded-grid amplifier configuration providing inherently low noise sensitivity [36]. The LCE radar receiver achieved high dynamic range through careful gain distribution and proper choice of mixers and amplifiers, with particular attention paid to maintaining overall system linearity. The two channels of the analog in-phase and quadrature (I/Q) detector, which operated at a receiver IF of 3 GHz, were balanced to within approximately 0.1 dB in amplitude and 1 degree of phase. This balance provided approximately 40 dB of image rejection. The receiver baseband I/Q outputs were digitized by 14-bit analog-to-digital (A/D) converters chosen for their linearity and speed (i.e., maximum clock speed = 10 MHz). The I/Q detector dc bias was temperature-regulated to approximately 100 μV variation (i.e., to less than the least-significant bit of the A/D converter).

Many of the LCE clutter spectra shown in Chapter 6 are from long-time-dwell data collected at Wachusett Mountain, Massachusetts, 32 miles west of Katahdin Hill, with similar tree cover. A photograph of the LCE radar on Wachusett Mountain is shown in Figure 6.3. Another LCE measurement site was in Nevada, where backscatter data were recorded from sparse scrub vegetation typical of the western desert. In contrast with Phase One, the LCE radar could measure both the copolarized and the cross-polarized returns, although not simultaneously. For LCE clutter measurements at Wachusett Mountain, wind conditions were measured simultaneously with the clutter measurements at 10-s update intervals with an anemometer stationed on top of a 75-ft tower in a treed clutter cell along one of the three azimuth positions selected for clutter measurements. These measurements were performed in August with the deciduous trees fully in leaf.

6.3.1.1 Spectral Processing

LCE long-time-dwell clutter data were acquired with a stationary antenna over 70-s data recording intervals called experiments. Each LCE experiment involved the recording of 80 I and Q sample pairs per pulse repetition interval (PRI) at 2- MHz sampling frequency (i.e., 75-m range gate spacing), leading to a 6-km total recorded range swath. Clutter experiments were usually taken in sequential groups covering the various LCE polarization combinations. Phase One long-time-dwell clutter data were acquired similarly to LCE data. Table 6.3 provides the specific Phase One clutter data acquisition and spectral processing parameters applicable to the Phase One spectral results shown herein from Katahdin Hill.

All the LCE clutter power spectra shown subsequently were computed directly as fast Fourier transforms (FFTs) of the sampled temporal pulse-by-pulse return, including the dc component. A four-term Blackman-Harris window function was utilized, with highest sidelobe level at –92 dB [37]. Each temporal record of 30,720 pulses (first 61.44 s of each 70-s experiment) was divided into contiguous groups of 5,120 samples; a 1,024-point complex FFT was generated for each group by utilizing every fifth pulse; and the amplitudes of the resultant set of FFTs were arithmetically averaged together in each

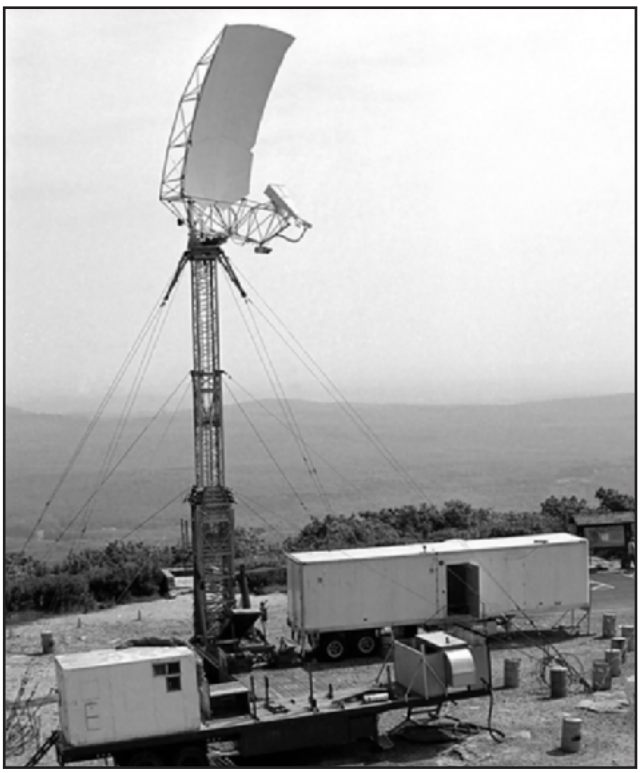

FIGURE 6.3 The LCE radar.

Doppler cell to provide the spectrum illustrated. Thus each LCE spectrum shown is the result of averaging six individual spectra (each from a 1,024-point FFT) from an overall record of 1.024-min duration, using an effective 10-ms PRI and an effective 100-Hz PRF. The CPI for each FFT was 10.24 s.

Table 4.10 in Chapter 4 indicates that the typical correlation time for windblown trees at L-band is $\sim$ 1 s (see also Table 6.3). Thus the CPI utilized in LCE spectral formation, usually being $\sim$ 10 times the correlation time, is more than adequate to allow the random process to fully develop. The Phase One clutter spectra shown were computed similarly to the LCE spectra. Table 6.3 provides the particular Phase One spectral processing parameters utilized in generating the Phase One clutter spectra from Katahdin Hill. Table 6.3 includes both the CPI (i.e., time dwell per FFT) used and the typical correlation time of windblown trees for each Phase One frequency band, as specified by Table 4.10. These numbers indicate that the CPI covers many correlation periods at each of the five Phase One radar frequencies.

6.3.1.2 System Stability

For a steady target, the spectral processing of either the Phase One or LCE radar yields a very narrow spectrum containing only dc power at zero-Doppler velocity. Figure 6.4 shows results from such steady targets. Figure 6.4(a) shows the measured LCE clutter spectrum from a desert terrain cell under very still (0 mph) wind conditions. Figures 6.4(b) and (c) show measured Phase One spectra from a large municipal water tower at L- and X-bands, respectively; in each case, clutter from trees in the same cell as the water tower just

TABLE 6.3 Phase One Clutter Spectra Parameters (Katahdin Hill)

Parameter	Frequency Band				
	VHF	UHF	L-Band	S-Band	X-Band
Polarization	HH	HH	VV, HH	HH	VV
Range resolution (m)	150	150	15	150	150
No. of pulses recorded	30,720	30,720	30,720	30,720	30,720
PRF (Hz)	33.33	33.33	100	167	500
Time dwell(s)					
Total recorded	61.44	307.20	307.20	184.32	61.44
Per FFT	61.44	61.44	20.48	12.29	4.096
Typical correlation time(s)	5.04	0.94	0.95	0.081	0.049
No. of FFTs averaged per spectral plot	1	5	15	15	15

begins to broaden the spectrum near the base of the water-tower dc spike. Figure 6.4(d) shows the measured Phase One VHF spectrum from a cell containing tall grass; the windblown motion of the grass is indiscernible in this VHF measurement. In all these results, the width of the dc spectral component from the steady target is essentially the limit of spectral resolution provided by the Blackman-Harris window function, which is cleanly maintained over the full spectral dynamic range of the radar down to the system noise level (i.e., 71 to 77 dB down for Phase One, 80 dB down for LCE). The window function sidelobes occur below the noise level of either system.

6.3.1.3 Spectral Normalization

Chapter 6 shows measured clutter spectra normalized to compare with analytic representations of clutter spectral density. The first step in spectral normalization is to convert the FFT output from power per spectral resolution cell to power/(m/s) so as to be directly comparable with analytic spectral shapes defining continuous density functions. This conversion is performed by dividing each point in the FFT velocity spectrum by the width of the Doppler velocity resolution cell Δv. The Doppler velocity resolution cell is wider than the sampling interval by a factor equal to the equivalent noise bandwidth *ENBW* of the window function. Thus $\Delta v = (\lambda/2) \cdot (PRF/N) \cdot ENBW$, where N is the number of points in the FFT. For the four-term Blackman-Harris window used here, $ENBW = 2.004$ [37]. The second step in spectral normalization is to bring the power in the measured spectrum to unity for comparison with analytic spectral shapes for which the integral over the entire velocity domain is unity. In some circumstances, total power in the spectrum is brought to unity by dividing each spectral point by total spectral power. In other circumstances, where concern is only with the ac spectral shape and not the particular amount of dc power present, the ac power in the spectrum is brought to unity by dividing each spectral point by total spectral power times $1/(r + 1)$.

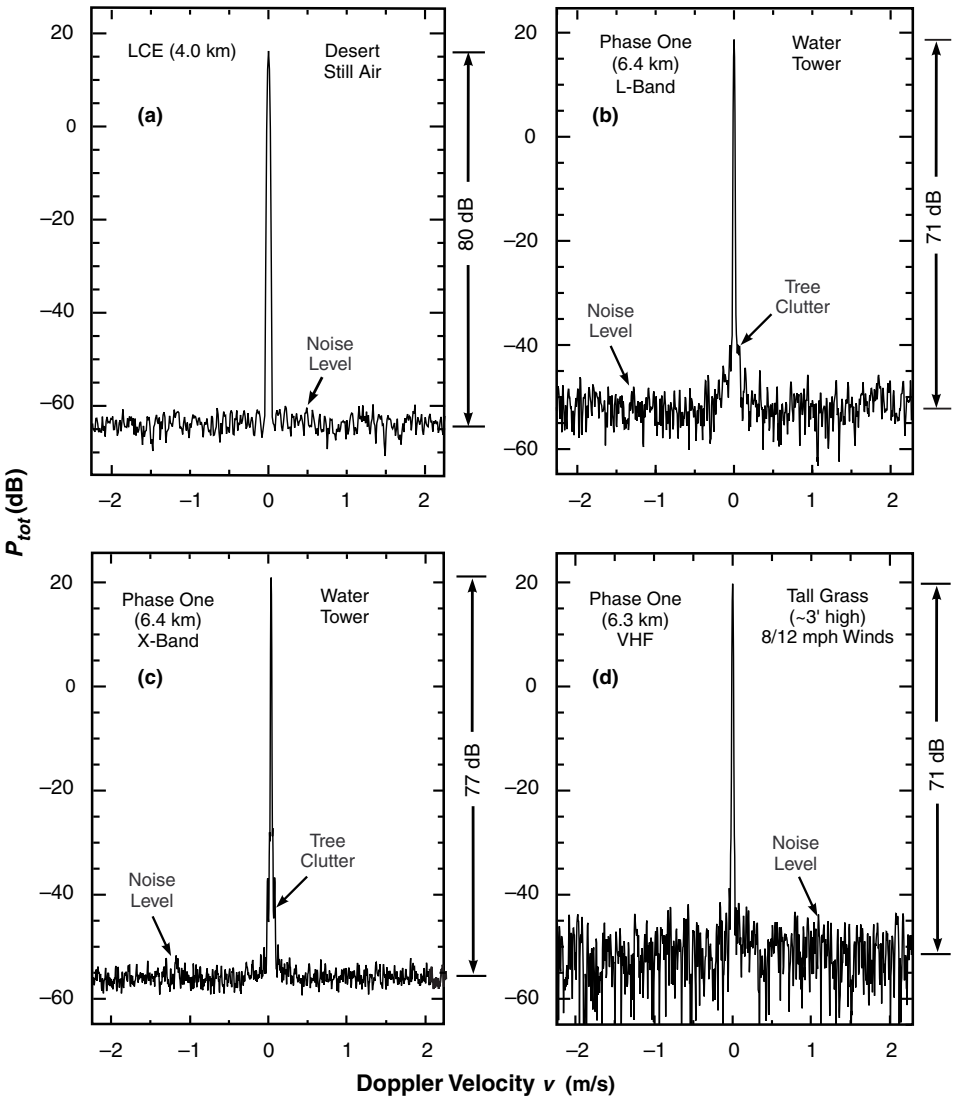

FIGURE 6.4 Four measured power spectra from "stationary" targets exhibiting little or no discernible spectral spreading to levels 70 to 80 dB down: (a) LCE, (b), (c), (d) Phase One L-, X-, VHF bands, respectively.

6.3.1.4 Spectral Power

Total, dc, and ac spectral power were computed in the time domain for the Phase One and LCE spectral results. Total power over the temporal record of each FFT is 1/*N* times the sum of the squares of the I and Q samples of received power. The dc power over the same temporal record is the square of 1/*N* times the sum of the I samples plus the square of 1/*N* times the sum of the Q samples (i.e., coherent sum). The ac power over the same temporal record is total power minus dc power. These computations were performed over each FFT contributing to each spectrum. The final time-domain quantities for total, dc, and ac spectral power are each means of the resulting set of values, one value per FFT, applicable to each spectrum.

The dc power obtained by summing coherently over a temporal record of backscatter from windblown trees depends on the length of the record (the CPI) over which the summation is performed. If the random process were well behaved (i.e., stationary), the coherent sum would converge and be largely independent of record length for lengths much greater than the correlation period of the process. However, windblown clutter backscatter records are not rigorously stationary. The statistics of the process sometimes appear to be characterized as intervals of stability separated by abrupt transitions from one stable state to another. Such abrupt changes can be caused, for example, by large tree limbs suddenly shifting position. Because the coherent sum does not always converge, the ratio of dc/ac power computed in the time domain is dependent on CPI duration.

Table 6.4 provides two examples of the dc/ac ratio obtained as a function of CPI duration for two LCE long-time-dwell backscatter measurements from cells containing windblown trees, one taken under very light wind conditions and the other under very windy conditions. The correlation times for these two experiments are estimated to be $\sim$ 4 s for the light-air data and $\sim$ 1 s for the windy data. The clutter spectra from these two measurements are discussed in Section 6.3.2.1. It is evident that a significant dc component exists in the light-air data in Table 6.4 and very little dc power exists in the windy data. The results in the table may be interpreted in terms of decreasing sampling bandwidth of the zero-velocity Doppler filter with increasing CPI, where sampling interval bandwidth is given by $\lambda/(2 \times \text{CPI})$. Because no weighting is employed in these time-domain computations, the filter has a sin x/x response.

TABLE 6.4 Variation of dc/ac Ratio with Length of CPI for LCE Clutter Measurements from Windblown Trees

CPI (s)	No. of Points per CPI (PRF = 500 Hz)	No. of CPIs Averaged	Ratio of dc to ac Power (dB) (Time-Domain Computation)	
			Light-Air Measurement (5 Sep, 4.7 km)	Windy Measurement (11 Sep, 7.7 km)
0.032	16	2048	47.2	20.8
0.064	32	1024	43.1	15.0
0.128	64	512	37.9	9.8
0.256	128	256	32.4	5.1
0.512	256	128	27.1	1.8
1.02	512	64	22.4	–1.0
2.05	1024	32	18.9	–3.6
4.10	2048	16	15.7	–5.8
8.19	4096	8	14.0	–9.1
16.4	8192	4	13.2	–10.7
32.8	16384	2	12.0	–18.6
65.5	32768	1	10.5	–19.0

In the frequency domain, the zero-th Doppler bin can contain both a singular dc power component existing as a discrete delta function and ac power existing as a continuous density function. The ac power in the zero-th Doppler bin decreases with increasing resolution (i.e., with increasing CPI duration), whereas the singular dc component is

theoretically independent of resolution. However, in all the measured clutter spectra shown here, normalization (division) of power/cell by Δv was performed for all cells, including the zero-Doppler cell. First-order credibility checks of the reasonableness of dc/ac ratios provided herein for spectra containing strong dc components (i.e., strong dc spikes, for example, in desert or cropland or at VHF) should therefore be performed by first decreasing the height of the spike by $|\Delta v|$ dB before estimating the resultant dc/ac ratio. Note that the peak spectral level at zero Doppler (before or after division by Δv) is not itself used in any direct way in Chapter 6 to normalize measured spectral data (measured spectra are never simply aligned by peak level).

One reason that the zero-Doppler cell is not normalized differently from others is to maintain the relative shape of the raw FFT before normalization (whatever is done to one cell is done to all cells). Another reason is that the power in the zero-Doppler cell of windblown foliage spectra is often not dominated by a singular dc (i.e., delta function) component, in which circumstances the continuous power in the zero-Doppler cell requires normalization by Δv similarly to all other Doppler cells. Excess quasi-dc power in Doppler resolution cells near the zero-Doppler cell is included as dc power in computing the dc/ac power ratio used as spectral modeling information in spectra where excess quasi-dc power exists. The dc/ac ratio in which the excess quasi-dc component is included in the singular dc term is obtained in the frequency domain by best-fitting the spectral tail at high Doppler velocities with an exponential ac shape function. The excess quasi-dc power is that which exists above the approximating exponential in cells of very low Doppler velocity close to zero Doppler. The fitting process is largely independent of spectral resolution as long as the resolution is adequate to define the exponential spectral tail. As a result, the dc/ac ratio used herein, which is that required for the ac exponential shape function to match the measured spectral tail both in relative shape and in absolute level, is also largely independent of CPI duration and spectral resolution. This fitting process is discussed in Section 6.4.2.

6.3.2 Measurements Illustrating ac Spectral Shape

6.3.2.1 Variations with Wind Speed

Figures 6.5–6.7 are examples of LCE-measured windblown forest clutter spectra under windy, breezy, and light-air conditions, respectively. The data in these figures are normalized to show ac spectral shape $P_{ac}(v)$ plotted against a logarithmic Doppler velocity axis similar to the modeled curves of Figure 6.1. Each figure compares the measured ac spectral shape with several exponential shape functions of various values of shape parameter β. In Figure 6.5, the measured data follow the exponential curve of shape factor $\beta = 5.2$ remarkably closely over the full spectral dynamic range shown. This match of measured ac spectral shape with exponential is among the best in the Lincoln Laboratory database, although other examples exist both of LCE and Phase One windy-day clutter spectra with equally good fits to exponential. Furthermore, the spectrum of Figure 6.5 is among the widest measured; its shape factor $\beta = 5.2$ is the basis of the "worst case, windy" specification in Table 6.1 and Figure 6.1.

Also shown in Figure 6.5 is a narrower Gaussian spectral shape function. The particular Gaussian shape shown corresponds to Barlow's [7] much-referenced 20-dB dynamic range historical measurement (see Section 6.6.1.1). It is evident in Figure 6.5 that the overall rate of decay in the LCE data is much more exponential than Gaussian in character. Thus these LCE data support the general consensus of agreement subsequently arrived at

[10–20, 27, 28] of spectral tails wider than Gaussian in windblown clutter spectra. Li [19] explains that tails wider than Gaussian are theoretically required by branches and leaves in oscillatory—as opposed to merely translational—motion.

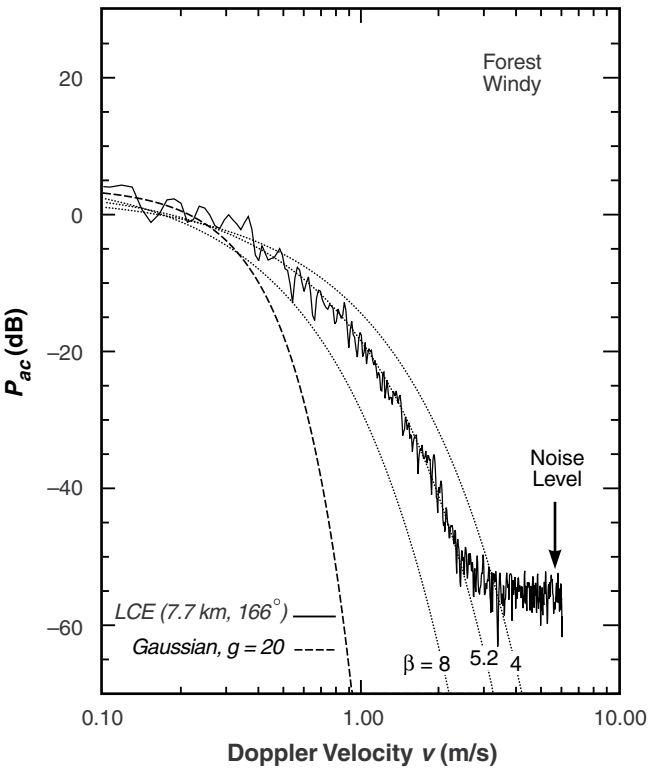

FIGURE 6.5 Highly exponential decay ($\beta = 5.2$) in a forest clutter spectrum measured under windy conditions.

The LCE spectral data of Figures 6.6 and 6.7 indicate that measured ac spectral shapes remain reasonably well represented by exponential shape functions under less windy conditions, with increasing values of exponential shape factor with decreasing winds (i.e., $\beta \cong 8$ for breezy conditions, $\beta \cong 12$ for light-air conditions). The results of Figures 6.6 and 6.7 are representative of many similar spectra measured in other cells on other days. Recall that normalization to $P_{ac}(v)$ requires raising the $P_{tot}(v)$ spectrum by $10 \log_{10} (r + 1)$ decibels on the vertical ordinate. The value of r applicable in Figures 6.5, 6.6, and 6.7 is 0.7, 18.9, and 29.8 dB, respectively. It is evident in Figures 6.6 and 6.7 that the measured data begin to depart from the approximating exponentials for $v < 0.2$ m/s as they begin to rise into the quasi-dc region, contributing to the large values of r in these data. As the amount of dc spectral power increases, less spectral dynamic range is left for measuring the ac power in the spectral tail, indicated by the rapidly rising effective system noise levels with respect to $P_{ac}(v)$ as wind speed decreases and dc/ac ratio increases in Figures 6.5–6.7.

As discussed later (Sections 6.6.1 and 6.6.2), power-law spectral tails plot as straight lines in plots of $10 \log_{10} P$ vs $\log_{10} v$ such as those of Figures 6.5–6.7. Thus a power law of shape $n = 3$ (30 dB/decade) fits the data of Figure 6.6 reasonably well down to the $P_{ac} = -20$-dB level.

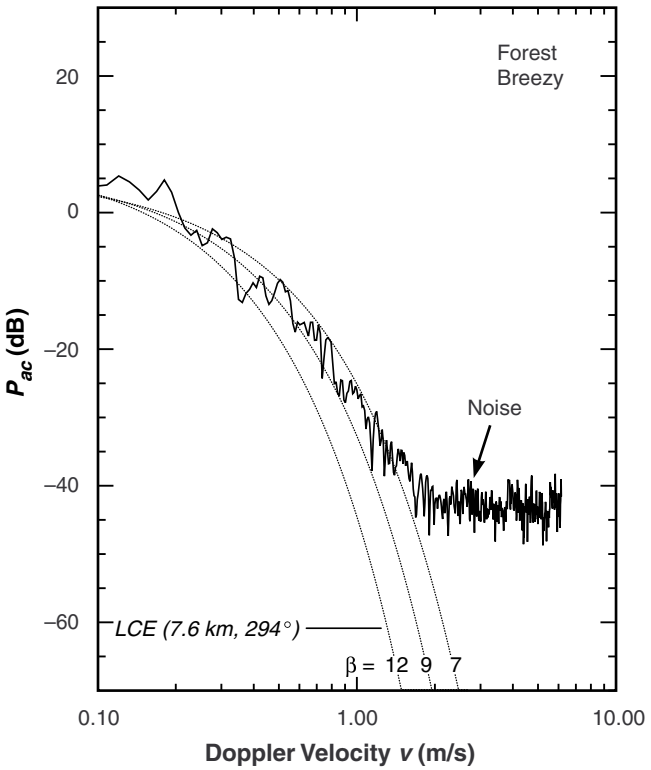

FIGURE 6.6 Approximate exponential decay in a forest clutter spectrum measured under breezy conditions.

However, this $n = 3$ power law cannot be extrapolated to lower levels. The local power-law (local slope tangent to the data curve) rate of decay in Figure 6.6 strongly increases (to $n \cong 6$ or 7) at the lower spectral power levels in Figure 6.6. Likewise, at first consideration, an $n = 4$ power law (40 dB/decade) might be thought to be a reasonable match to the measured data of Figure 6.7. The apparent goodness of this straight-line fit to the data in Figure 6.7 is heightened by the data beginning to rise above the exponential in the low-Doppler quasi-dc region $v < 0.2$ m/s and by the data flaring away from the exponential toward the noise level as they become limited in signal-to-noise (S/N) ratio when approaching to within 10 dB of the noise floor at higher Doppler velocities around 1 m/s. However, these two effects tend to obscure a more fundamental exponential-like rate of decay (increasing local tangent slope with decreasing power level) as shown in the region $0.2 < v < 0.7$ m/s in Figure 6.7, and the upper-level power-law rate of decay can no more be extrapolated to lower levels in the light-air data of Figure 6.7 than in the windier data of Figures 6.5 and 6.6. To do so would lead to physical implausibility as the upper-level light-air power law would extrapolate to lower-level ac power levels (e.g., $P_{ac} = -60$ dB) exceeding in spectral width those measured under windy conditions at the same lower levels.

Not all the Phase One and LCE clutter spectra measured under breezy and windy conditions are as closely exponential as the measured spectrum in Figure 6.5. However, like that spectrum, they all demonstrate increasing downward curvature (convex from above) with increasing Doppler velocity and decreasing power level as their most characteristic general feature in plots of 10 log P vs log v such as that of Figure 6.5. The main reason the

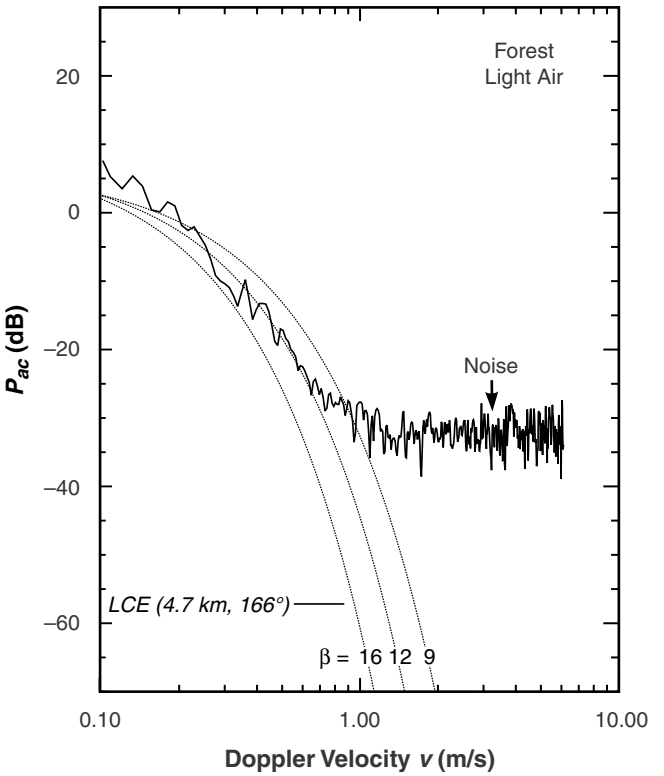

FIGURE 6.7 Approximate exponential decay in a forest clutter spectrum measured under light wind conditions.

exponential form is used herein for modeling clutter spectral shapes is that it, too, when plotted as 10 log P vs log v, possesses this increasingly downward curving shape (see Figure 6.1) while remaining wider than Gaussian as required by the measured data (see Figure 6.5). In contrast, the spectral tails of power-law functions do not have increasing downward curvature on 10 log P vs log v axes but plot linearly (i.e., extrapolate rapidly to excessive spectral width) on such axes. This matter is further discussed in Sections 6.6.1 and 6.6.2.

Most of the Phase One- and LCE-measured clutter spectra are not completely and precisely representable by any simple analytic function over their full spectral ranges. Many of these measured spectra are somewhat wider than exponential (i.e., are concave from above in 10 log P vs v plots), but they are almost always much narrower than power law (i.e., are convex from above in 10 log P vs log v plots). In such circumstances, absorbing excess quasi-dc power in the dc term usually gives the exponential model the flexibility to match the relative shapes and absolute levels of the measured spectra over extensive spectral tail regions.

Gale Force Winds (Scaled Estimate). Figure 6.8 shows a different set of three LCE-measured windblown-forest clutter spectra under light-air, breezy, and windy conditions, displayed as 10 log P_{tot} vs v. In contrast to the light-air, breezy, and windy spectra of Figures 6.5–6.7 (which come from three different range cells) the spectra shown

in Figure 6.8 are from the same 7-km range cell on three different measurement days. These Figure 6.8 spectra clearly indicate that spectral extent from a given range cell increases strongly with increasing wind speed. In approximate measure, the data of Figure 6.8 indicate similar-sized steps of increasing spectral width for wind speeds increasing by approximate factors of 3 (from 1–2 to 6–7 mph, and from 6–7 to 18–20 mph). This observation implies that spectral width increases approximately linearly with the logarithm of wind speed [28, 38]. Such data are the basis of Eq. (6.3) specifying spectral width as a function of wind speed in the clutter model of Section 6.2. In Figure 6.8, the maximum spectral extent in the data 70 dB down from their zero-Doppler peaks is ~ 1, 2, and 3 m/s for the light-air, breezy, and windy spectra, respectively. In these results, as ac clutter power increases and spreads out with increasing wind speed, dc clutter power decreases, as indicated by dc/ac ratios r of 0.1, –1.5, and –4.5 dB for the light-air, breezy, and windy spectra, respectively.

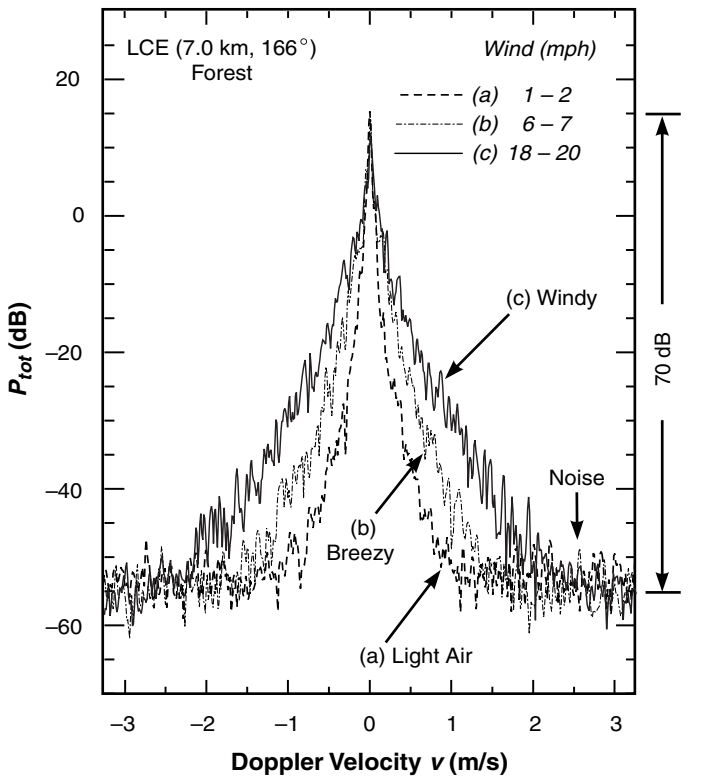

FIGURE 6.8 Variation of LCE windblown forest clutter spectra with wind speed. Common range gate (7 km).

Figure 6.9 shows the same three spectra of Figure 6.8, now displayed as 10 log P_{tot} vs log v. Figure 6.9 also shows a scaled extrapolation to higher wind speeds by a further factor of 3, that is, from the 18–20 mph of the "windy" spectrum to 54–60 mph gale force wind speeds. This estimate was obtained by finite-difference extrapolation of the light-air, breezy, and windy Doppler velocities, say v_a, v_b, and v_c, to v_d, the estimated gale force Doppler velocity, at multiple spectral power levels, assuming constant factors-of-3 increases in wind speed throughout. It is evident in the figure that the gale force spectral estimate is well

modeled by an exponential curve of shape factor $\beta = 4.3$; this is the basis of the "typical" gale force exponential ac shape parameter specification $\beta = 4.3$ in the clutter model of Section 6.2. Increasing gale force β in this model from its typical specification based on the scaled estimate shown in Figure 6.9 to a worst-case specification of $\beta = 3.8$ brings it into very close agreement (in terms of gross spectral extent at the –14-dB level) with the only known measurements of windblown clutter under actual gale wind conditions, namely, the very early measurements of Goldstein [9] that are further discussed in Section 6.6.3.5.

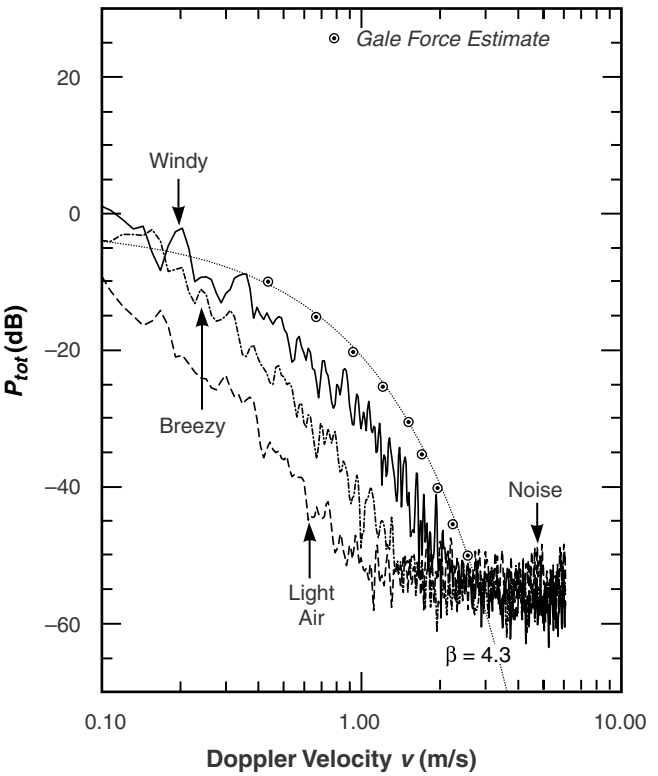

Figure 6.9 Scaled estimate of windblown forest clutter spectrum under gale force winds (54–60 mph).

6.3.2.2 Invariance with Radar Frequency

The idea that spectral extents of windblown ground clutter Doppler-velocity spectra are in large measure invariant with radar frequency, or equivalently, that spectral widths in Doppler-frequency spectra are approximately proportional to radar frequency, has been discussed in the technical literature of the subject since the early days of radar development [6, 8, 9]. For example, early work in comparing spectral widths with radar frequency conducted at the MIT Radiation Laboratory during World War II by Herbert Goldstein and others is summarized by Goldstein's conclusion that "The widths of the [Doppler-frequency] spectra . . . increase with wind speed and . . . appear to be essentially proportional to [radar] frequency" [8, 9]. This idea remains true in the LCE and Phase One spectral results, as indicated in Figures 6.10 and 6.11—Figure 6.10 shows VHF, L-, and X-band Doppler-velocity forest spectra under windy conditions; Figure 6.11 shows UHF, L-, and S-band forest spectra under breezy conditions.

However, the early results were mainly in the 1- to 10-cm range of wavelengths and, by today's standards, over very limited spectral dynamic ranges (~ 20 dB). Results such as those of Figures 6.10 and 6.11 extend the idea of frequency invariance of windblown clutter Doppler-velocity ac spectral shape over very much greater spectral dynamic ranges (> 60 dB) and to very much longer radar wavelengths [from X-band (λ = 3.3 cm) to VHF (1.8 m)]. These results are rather surprising, since the dominant, wavelength-sized scatterers at VHF (large branches, limbs) are presumably different than those at X-band (leaves, twigs). As will be shown, much more dc power exists in VHF windblown clutter spectra than at higher radar frequencies, for one reason because the VHF energy partially penetrates the foliage to reach the underlying stationary tree trunks and ground surface. As a result, the ac spectral power at VHF is measured at lower levels in the available spectral dynamic range. Still, over very many spectral measurements of windblown trees at VHF and UHF, ac spectral spreading caused by internal motion in windblown clutter generally exists at VHF and UHF at lower absolute levels of $P_{tot}(v)$ but roughly equivalently in the relative shape and extent of $P_{ac}(v)$ to that observed in the higher, L, S, and X microwave bands.

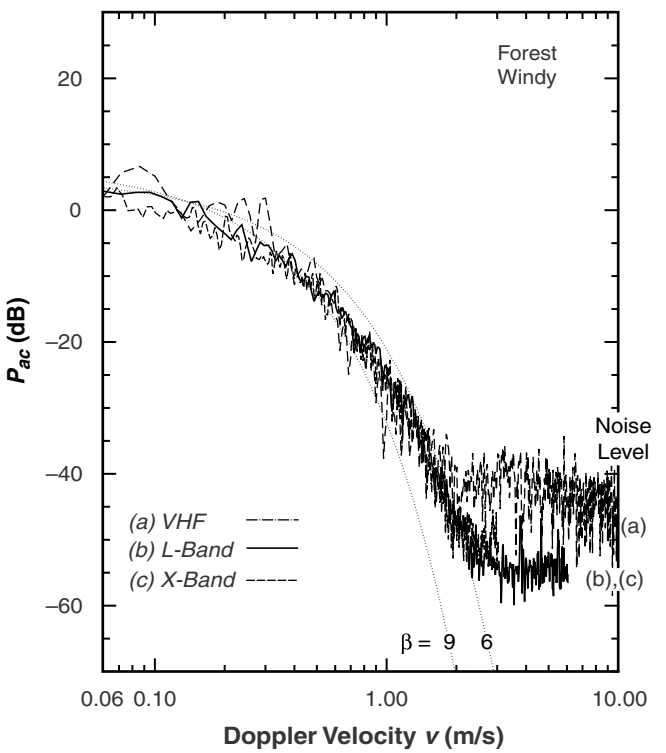

FIGURE 6.10 Variations of windblown forest clutter spectra with radar frequency under windy conditions: (a) VHF, Phase One, (b) L-band, LCE, and (c) X-band, Phase One.

In Figure 6.10, the VHF and X-band spectra were measured by the Phase One radar at Katahdin Hill under windy conditions on two different days in April at 2.8-km range. The L-band spectrum was measured by the LCE radar at Wachusett Mt. on 11 September at 6-km range. The Figure 6.11 spectra were all measured by the Phase One radar at Katahdin Hill also at 2.8-km range under breezy conditions in late April or early May. In general measure, the three windy-day spectra of Figure 6.10 are essentially identical in overall ac spectral

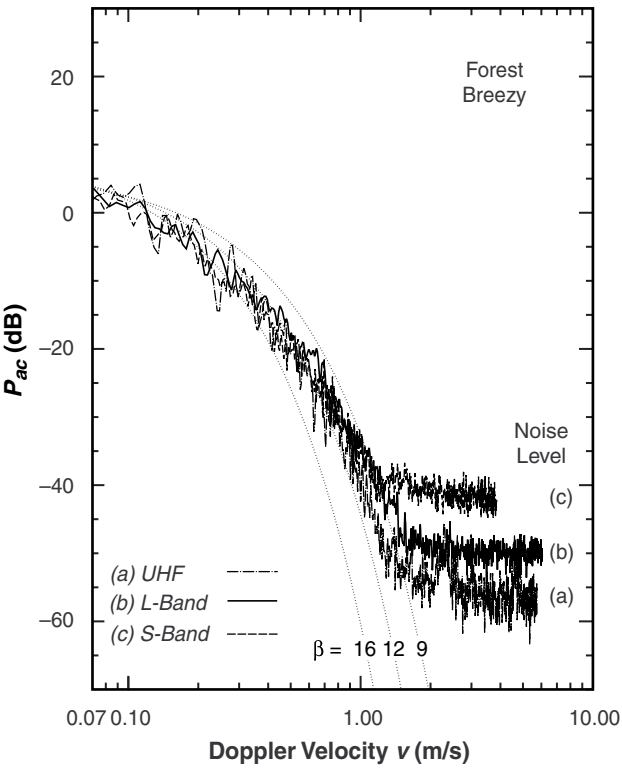

FIGURE 6.11 Variations of Phase One windblown forest clutter spectra with radar frequency under breezy conditions, UHF, L-, and S-bands.

shape, as are the three breezy-day spectra of Figure 6.11. Of course, temporal (minute-to-minute, hour-to-hour) and spatial (cell-to-cell, site-to-site) variability exist in LCE- and Phase One-measured clutter spectra under nominally similar wind conditions, and not all such measurements overlay one another as exactly as those shown in Figures 6.10 and 6.11. Concerning variability, even in the results of Figures 6.10 and 6.11 for which the same nominal range and azimuth apply, the spatial cells still encompass different overlapping ground areas due to the different azimuth beamwidths. Also, ". . . there are the usual uncertainties [because of the lack of]. . . simultaneity of the measurements in time" [9].

In considering possible means by which variations with radar frequency might be introduced in clutter velocity spectra, amplitude fluctuations caused by scatterer rotation and the wig-wag shadowing of background leaves by leaves in the foreground have been discussed [14, 19, 29, 39] as possible mechanisms that might complicate clutter spectra over and above phase fluctuations caused by the scatterer velocity distribution. However, one theoretical model exists [14] that incorporates scatterer rotational and shadowing effects and still provides radar frequency-independent clutter Doppler-velocity spectral shapes (i.e., "to a first approximation, the spectrum . . . depends only on the product λf" [14]). It is not suggested here that if multifrequency spectra could somehow be measured simultaneously from exactly the same spatial assemblage of windblown foliage, fine-scaled specific differences would not be observed in ac spectral shape with radar frequency. However, in looking across all the LCE- and Phase One-measured spectral data and the variations that exist therein, no significant trend is observed in ac Doppler-velocity spectral

shape with radar frequency, VHF to X-band, as opposed, for example, to the strong trend seen in ac spectral shape with wind speed.

6.3.2.3 Invariance with Polarization

The LCE and Phase One clutter spectral data indicate that clutter spectral shape from windblown vegetation is largely independent of radar polarization, to the extent that this can be determined in non-simultaneous measurements. Figure 6.12 shows one set of three sequential LCE measurements of windblown treed-cell ground clutter spectra at VV-, HH-, and HV-polarizations obtained at approximately 2-min intervals, which are of essentially identical spectral shape. The spectral artifact in the HV-pol. spectrum of Figure 6.12 at ~ 2.8 m/s is probably a bird. Many other LCE and Phase One VV- and HH-pol. spectra were compared from common cells selected from other sites and experiments [21]. These usually showed little or no variation in spectral shape with polarization. When variations of spectral shape with polarization did occur, such variations were usually relatively random with little evidence for the existence of any strong general effect on spectral shape with polarization.

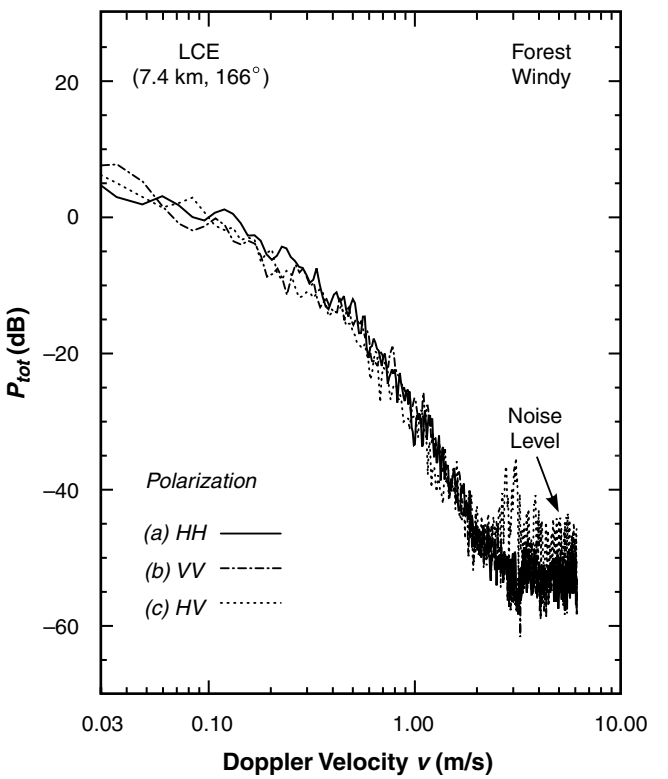

Figure 6.12 Variations of LCE windblown forest clutter spectra with polarization: (a) pol. = HH, winds (mean/gusts) = 10/18 mph; (b) pol. = VV, 2 min later, winds = 13/19 mph; (c) pol. = HV, 4 min later, winds = 10/16 mph.

Other investigators have also found little effect on windblown clutter spectral shape with polarization. For example, Kapitanov et al. [13] observed that "The spectra of [X-band] echo signals from forest for different polarizations [vertical and circular]. . . are on the

average similar." Unpublished X-band windblown clutter spectral results obtained at Lincoln Laboratory by Ewell [20] at VV-, HH-, and circular polarizations in shrubby desert terrain also indicated no consistent differences in the spectral shapes obtained at the various polarizations.

6.3.2.4 Temporal Variation

All LCE clutter spectra in Chapter 6 are averages of six individual 1,024-point FFTs, each formed from a 10.24-s duration temporal backscatter record. Windy-day wind conditions frequently vary considerably from one 10-s interval to the next. Such variability of windy-day conditions within a treed resolution cell from one 10.24-s interval to the next often leads to significant variability in successive individual 10.24-s dwell FFTs [21]. However, the results of Figures 6.13 and 6.14 indicate that over longer periods of 60- to 80-s, windy-day treed-cell clutter spectra can be expected to become more stationary. Figure 6.13 shows LCE treed-cell clutter spectra for three repeated experiments on a windy day, each of which is formed from an overall temporal record of 61.44 s (100-Hz PRF, 1024-point FFTs, 6 FFTs averaged). The shape of the spectrum from the first experiment is essentially identically replicated by the shape of the spectrum from a following experiment begun 65 min later, suggesting that enough averaging of wind variations occurs within 1 min to lead to some degree of convergence in average spectral shape. But wind is an extremely non-stationary dynamic random process with complex short- and long-term variation. For example, on the windy/gusty day on which the data of Figure 6.13 were collected, the gusts happened to die down over the 70-s interval covering the second experiment (begun 9 min after the first), and the spectrum formed from that data is indeed considerably narrower than the other two.

Figure 6.14 shows Phase One L-band clutter spectra for three repeated breezy-day experiments for very nearly the same treed cell at Wachusett Mt. for which the LCE data of Figure 6.13 apply. Each of these Phase One spectra is formed from a temporal record of 81.9-s duration (125-Hz PRF, 2048-point FFTs, 5 FFTs averaged). The spectrum from the first experiment is nearly identical to that of the second experiment, begun 4 min later. The spectrum from the third experiment, begun 9 min after the first, is somewhat narrower. In a similar set of five sequential experiments begun 15 min before those of Figure 6.14, the range of variability of spectral shape was similar. The slightly changing average wind conditions within 81.9-s intervals over 4- or 5-min periods resulted in only very small changes in the measured spectra, such as shown in Figure 6.14. Such results indicate that the range of variability in clutter spectra formed by averaging over 60- to 80-s data intervals under nominally similar wind conditions generally is quite low, compared with the more variable individual FFTs formed from 10- to 16-s data intervals during the same period.

6.3.2.5 Effects of Site/Season/Tree Species/Cell Size

It is not difficult to find Phase One and LCE spectra of essentially identical exponential spectral shape—two are shown in Figure 6.15. The LCE spectrum (a) measured on September 10 (leaves on deciduous trees) at Wachusett Mt. at 7.9-km range, HH-pol., 150-m range resolution, and 2° depression angle essentially overlays and replicates the Phase One spectrum (b) which was measured on May 3 (leaves not yet emerged) at Katahdin Hill at 2.4-km range, VV-pol., 15-m range resolution, and 0.5° depression angle. These two measurements were obtained with different radar receivers, and the two spectra were produced using different data reduction and processing software. Thus commonality can

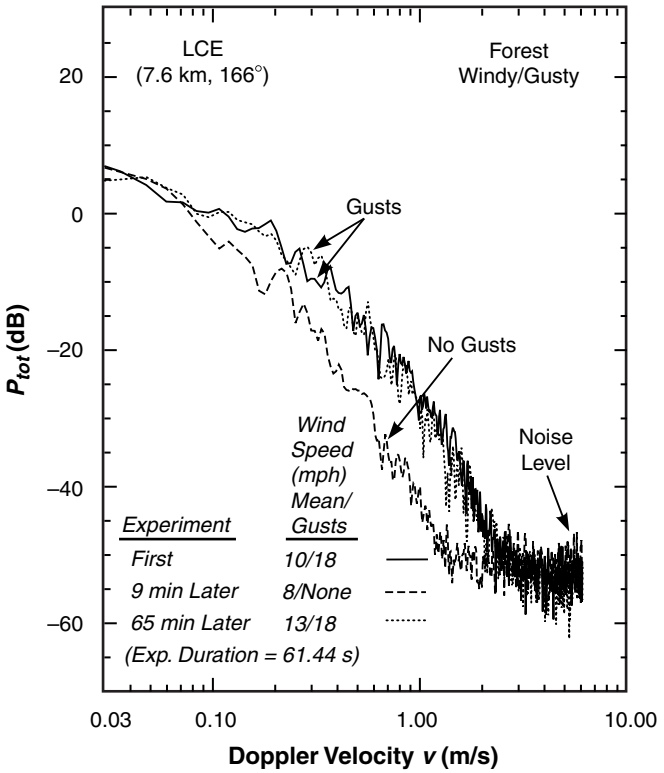

FIGURE 6.13 Variations of LCE windblown forest clutter spectra with time: Wachusett Mt., 11 September.

exist in spectral shape, in large measure because of the large cells and large degree of spatial averaging involved, despite a host of underlying differences including measurement instrumentation and parameters (range, cell size, illumination angle, polarization), site, and time of year.

The Phase One and LCE radars mimic long-range ground-based surveillance radars in the relatively long ranges, large resolution cell sizes, and low illumination angles of their measurements. Cell sizes, typically several hundred meters on a side, are large enough to encompass a large spatial ensemble of scatterers (many trees) as well as variable local wind currents within the cell. Because of the complexity of the scattering ensemble and nonuniform winds within such large cells and the temporal and spatial variability of the ensemble from cell to cell over large numbers of cells, it is difficult to discern significant site-to-site differences or significant trends with season and/or tree species in the Phase One and LCE spectral data. Other, more fine-scaled investigations, both historical [13–16] and recent [40–42], involving small illumination spot sizes (e.g., 1.8-m diameter [42]) on individual trees at short ranges (e.g., 30 m [42], 50 m [16]), provide results showing variation on treed-cell spectral shape with the type or species of trees. However, such small differences are largely absorbed within the general ranges of statistical variability in the Phase One and LCE measurements and are thus of limited consequence for the longer ranges and larger cells of surveillance radars.

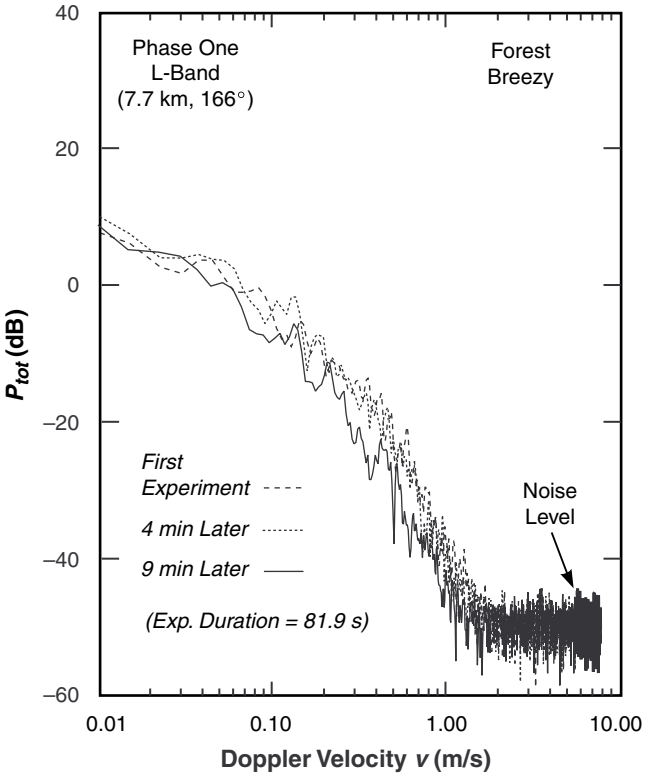

FIGURE 6.14 Variations of Phase One L-band windblown forest clutter spectra with time: Wachusett Mt., 22 August.

From Phase One Katahdin Hill measurements acquired from a specific set of forested cells once a week over a nine-month period [21], L-band spectra were examined for seasonal variations in three wind regimes, viz., calm to light-air conditions, light-air to breezy, and windy. These results marginally showed that in each wind regime, spectral widths 60 to 70 dB down were only very slightly wider by no more than ≈0.5 m/s for summer measurements (leaves on deciduous trees) than for winter measurements (leaves off deciduous trees). An early study of Phase One spectra involved eight forested sites, four in western Canada and four in the eastern U.S. For the western Canadian sites, the dominant tree species were aspen and spruce. For the eastern U.S. sites, the forest was mixed (oak, beech, maple, hemlock, pine). Measured Doppler-velocity spectra generally showed no significant major differences in shape or extent from one forested measurement site to another, either within each group or from group to group. No significant discernible difference has been observed in the shapes of Phase One spectra from cells of 150-m range resolution compared with cells of 15-m range resolution.

6.3.3 Measured Ratios of dc/ac Spectral Power

6.3.3.1 Variation with Wind Speed

Forested ground clutter cells contain many scatterers. Each scatterer is positioned randomly within the cell and hence produces an elemental scattered signal of random relative phase with respect to the other scatterers. Some of the scatterers, such as leaves

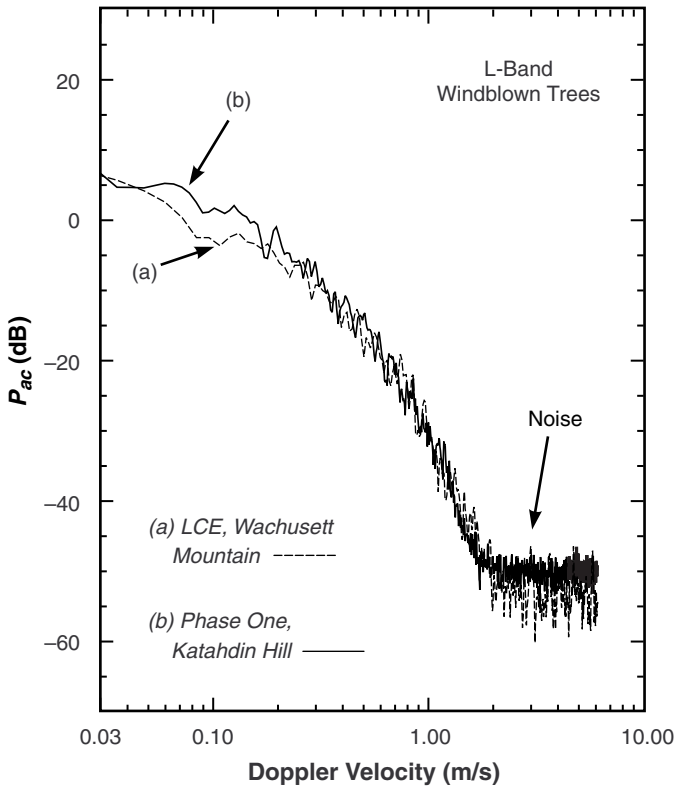

FIGURE 6.15 Similar LCE and Phase One forest clutter spectra measured under windy conditions at two different sites: (a) LCE, Wachusett Mt., 10 September, and (b) Phase One (L-band), Katahdin Hill, 3 May.

and smaller branches, move in the wind, producing fluctuating signals with time-varying phases. Other scatterers, such as tree trunks and larger limbs, are more stationary, producing steady signals of fixed phase. The total clutter signal is the sum of all the elemental backscattered signals, both steady and fluctuating. At high wind speeds, most of the foliage is in motion, and the ratio r of dc to ac power in the clutter spectrum is relatively low. In such circumstances, and in the higher microwave bands where little foliage penetration occurs, the steady component can become vanishingly small, whereupon Eq. (6.1) simplifies to $P_{tot}(v) \cong P_{ac}(v)$. Goldstein correctly anticipated, however, that "As the wind velocity decreases, . . . the steady-to-random ratio [i.e., r] would be expected to increase" [9]. Thus under light winds, a large proportion $r/(r + 1)$ of the clutter power is at dc.

Even so, the small proportion of clutter power $1/(r + 1)$ that, under light winds, remains at ac can still troublesomely interfere with desired target signals. Therefore, it is necessary that a windblown clutter spectral model quantify the dc/ac ratio r expected from forested or other types of vegetated cells as a function of wind speed.

Figure 6.16 shows an LCE-measured clutter spectrum from a treed cell under very light wind conditions. The most striking characteristic of this light winds spectrum is its extreme narrowness, with spectral spreading occurring only at relatively low power levels and to relatively small extent in Doppler. This spectrum contains a large steady or dc component,

and since the spectral density decays smoothly and continuously (albeit rapidly) away from the peak zero-Doppler level, it also contains high levels of quasi-dc power at very low but non-zero Doppler velocities. This spectrum may be approximately modeled utilizing a value of $r = 29.8$ dB, in which excess quasi-dc power is included in the dc term, and an exponential shape function for the spectral tail of shape parameter $\beta = 12$. The spectrum of Figure 6.16 is generally representative of many similarly narrow LCE and Phase One clutter spectra measured in other treed cells and on other light wind days.

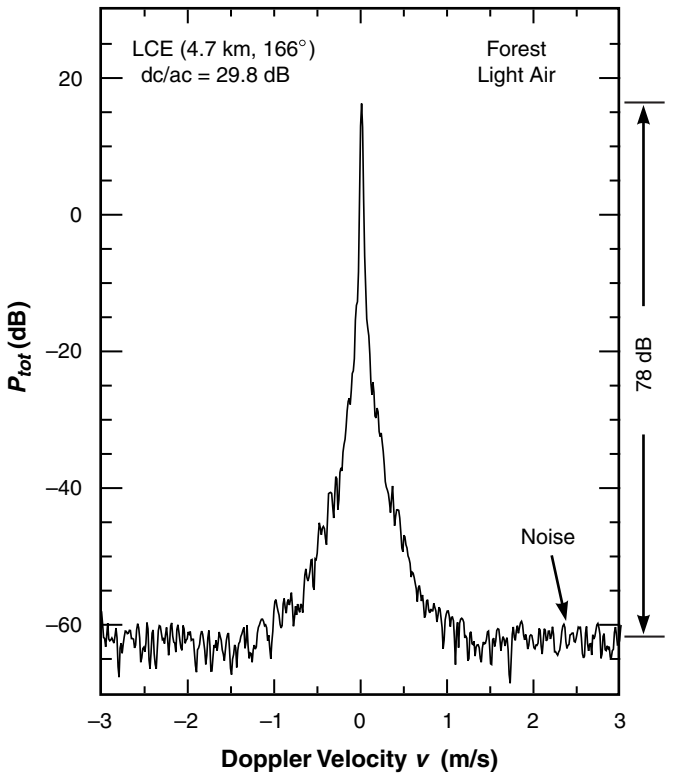

FIGURE 6.16 An LCE windblown forest clutter spectrum measured under light wind conditions.

The particular value of dc/ac ratio r applicable to any given treed clutter cell is highly variable. Such variability is illustrated in the results shown in Figure 6.17, in which ratios of dc to ac spectral power obtained from LCE clutter measurements from many treed cells are shown as a function of wind speed. There is some difficulty in precise specification of wind speed in such results since anemometer measurements usually provide only a one-point-in-space indication of wind conditions for the total test area. Over and above the inherent variability in these data, Figure 6.17 indicates a strong trend such that the ratio of dc to ac spectral power in dB decreases approximately linearly with the logarithm of wind speed w.

6.3.3.2 Variation with Radar Frequency

Whether a scatterer in a forested clutter cell is classified as stationary or in motion depends on the radar wavelength. A back-and-forth scatterer motion of 3 cm would produce a steady signal of essentially fixed phase at VHF, but a fluctuating signal passing through all

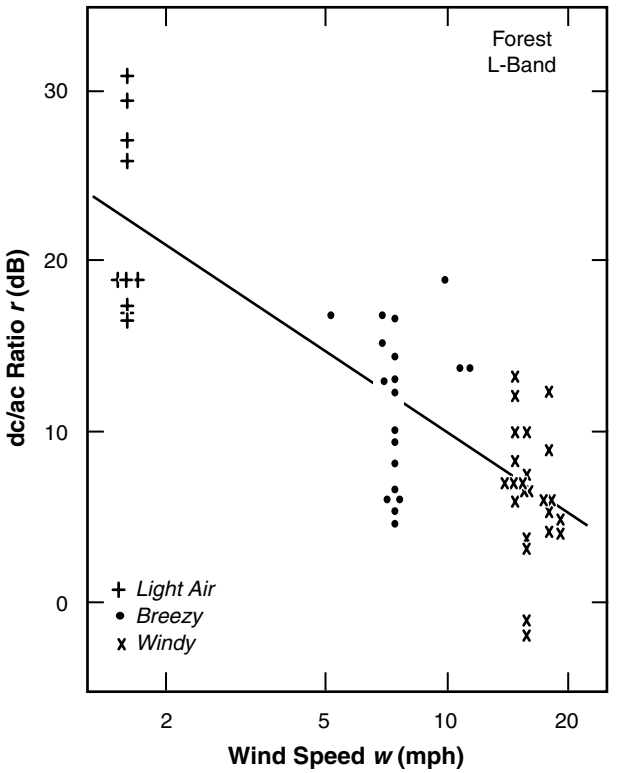

FIGURE 6.17 LCE measurements showing ratio of dc to ac spectral power vs wind speed in L-band windblown forest clutter spectra.

possible phases at X-band. Furthermore, at VHF and UHF, significant energy penetrates the foliage to scatter from the stationary underlying ground surface, whereas at X-band little or no energy reaches the ground. Again, Goldstein correctly anticipated that, because of such effects, the dc to ac ratio in windblown clutter spectra ". . . should therefore decrease with [decreasing] wavelength" [9].

Figure 6.18 shows a Phase One-measured spectrum at VHF from a treed cell under windy conditions (same spectrum as shown in Figure 6.10). It is evident in Figure 6.18 that a large dc component exists in this VHF clutter signal such that the ratio of dc to ac power in the spectrum is 14.8 dB. In contrast to the large dc component in the light winds spectrum of Figure 6.16, in which significant quasi-dc spectral power also occurs, in the lower frequency VHF spectrum of Figure 6.18 the dc component exists largely as a discrete delta function at the spectral resolution of the processing in the zero-Doppler bin. Much smaller dc components occurred in measured spectra at higher radar frequencies from the same forested cell under similarly windy conditions. Although there is a large dc component in the VHF spectrum, it also contains a significant amount of ac power of considerable spectral extent. This VHF spectrum comes from a single FFT of 61.44-s CPI (i.e., no averaging), this relatively long CPI being required to provide adequate spectral resolution at this relatively low radar frequency. The VHF spectrum of Figure 6.18 is representative of many other Phase One-measured VHF clutter spectra from other forested cells and on other windy days.

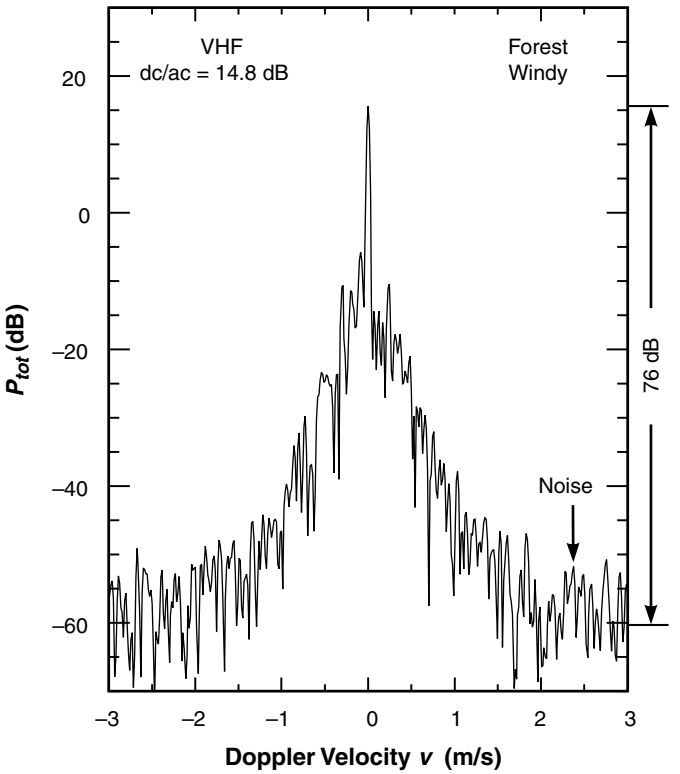

Figure 6.18 A Phase One windblown forest clutter spectrum at VHF.

Figure 6.19 shows ratios of dc to ac spectral power vs radar frequency, VHF to X-band, obtained from Phase One clutter measurements under windy conditions at three forested sites. The solid line in the figure joins the median positions of each in-band cluster of data points; the dashed line joins the median positions of the bounding VHF and X-band clusters only. These lines indicate, over and above the inherent variability in the data, a strong trend such that the dc to ac ratio in dB decreases approximately linearly with the logarithm of the radar carrier frequency f_0. Thus at X-band in Figure 6.19, virtually all the spectral power is ac, whereas at VHF the ac power occurs at levels 15 to 25 dB below the dc power. The information shown in Figures 6.17 and 6.19 substantiates the early expectations [9] in these matters. Such information was used to develop the empirical relationship given by Eq. (6.4), which relates dc to ac ratio in windblown clutter spectra with wind speed and radar frequency.

6.4 Use of Clutter Spectral Model

6.4.1 Spreading of σ° in Doppler

Two important issues concerning the effects of ground clutter on radar system performance are the strength of the clutter, which determines how much interfering clutter power is received, and the spreading of received clutter power in Doppler. Thus predicting ac clutter power in a given Doppler cell requires predicting the backscattering clutter coefficient σ° in the spatial resolution cell under consideration (see Section 2.3.1.1),

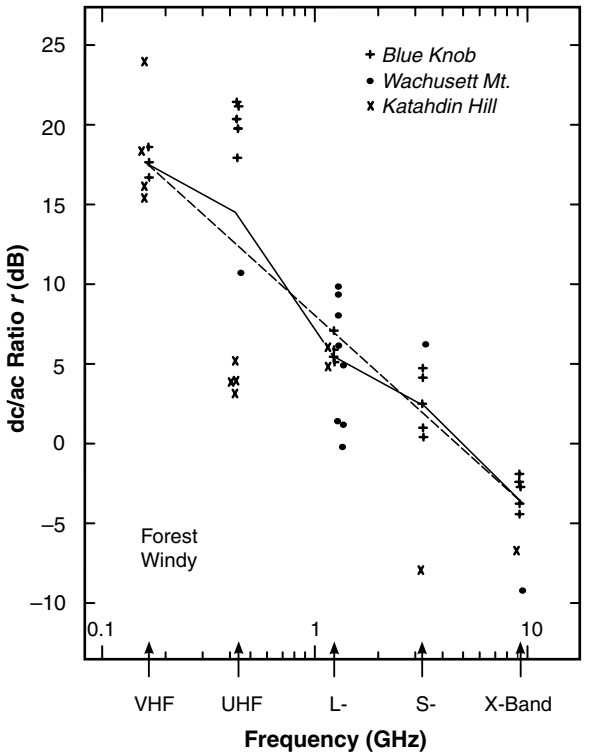

FIGURE 6.19 Phase One measurements showing ratio of dc to ac spectral power vs radar frequency under windy conditions at three forested sites.

predicting the dc to ac power ratio r in the spectrum, and predicting the ac spectral shape factor $P_{ac}(v)$.

Let $\sigma^{\circ}_{\text{trees}}$ be the clutter coefficient for windblown trees. Equation (6.1) shows that $[\sigma^{\circ}_{\text{trees}} \cdot P_{tot}(v)]$ specifies the spreading of $\sigma^{\circ}_{\text{trees}}$ in Doppler, i.e.,

$$\int_{-\infty}^{\infty} [\sigma^{\circ}_{\text{trees}} \cdot P_{tot}(v)]dv = \sigma^{\circ}_{\text{trees}} \ ,$$

so $[\sigma^{\circ}_{\text{trees}} \cdot P_{tot}(v)]$ represents the normalized density of windblown tree clutter power occurring at Doppler velocity v in units of $[(\text{m}^2/\text{m}^2)/(\text{m/s})]$. For $|v| > 0$, $[\sigma^{\circ}_{\text{trees}} \cdot P_{tot}(v)]$ becomes

$$[(\sigma^{\circ}_{\text{trees}} / (r+1)) \cdot P_{ac}(v)] \ .$$

Let $n = 0, 1, 2, \ldots, N$ be the Doppler cell index, where $n = 0$ is the zero-Doppler cell. Then the amount of windblown-tree clutter cross section $\sigma_{\text{trees}}(n)$ that occurs in the nth Doppler cell is given by:

$$\sigma_{\text{trees}}(n) = \frac{\sigma^{\circ}_{\text{trees}}\lambda}{2(r+1)} \cdot \Delta f \cdot A \cdot P_{ac}(f_n), \qquad n > 0 \tag{6.5}$$

where $\sigma_{\text{trees}}(n)$ is in units of [m^2], and f_n is the Doppler frequency [Hz] in the center of the nth Doppler cell. In Eq. (6.5), Δf = Doppler cell width [Hz]; λ = radar wavelength [m]; A = spatial resolution cell area [m^2]; r = ratio of dc/ac spectral power [as given by Eq. (6.4)]; and $P_{ac}(f_n)$ is the value at $f = f_n$ of the ac spectral shape function [as given by Eqs. (6.2) and (6.3)].

Comprehensive information specifying the clutter coefficient $\sigma^{\circ}_{\text{trees}}$ in Eq. (6.5) is provided in earlier chapters for the low illumination angles typical of ground-sited radar, for radar frequencies from VHF to X-band, and for both VV- and HH-polarizations, on the basis of the Phase Zero and Phase One clutter measurement databases. These clutter data are not available at cross-polarization. However, the LCE clutter data at Wachusett Mt. indicate that in forest, cross-pol. clutter coefficients are generally 3 to 6 dB but occasionally as little as 0 dB or as much as 8 dB less than the co-pol. clutter coefficients. Similar depolarization effects in forest clutter data have been observed elsewhere [13, 27, 43].

6.4.2 Two Regions of Spectral Approximation

Figure 6.20 shows an idealized representation of a typical windblown clutter spectrum (solid line). As is often observed in measured clutter spectral data, this representation consists of two distinct regions, namely, a quasi-dc region near zero-Doppler velocity and an ac spectral tail region at greater Doppler velocities. Also shown is a spectral model (dashed lines) as given by Eq. (6.1). The model uses a delta function at $v = 0$ to represent the dc spectral component and the exponential shape function as given by Eq. (6.2) to represent the ac spectral tail. In a plot of 10 $\log_{10} P_{tot}$ vs v such as that of the figure, the exponential shape plots as a straight line of slope 4.34 β (where 4.34 = 10 $\log_{10} e$ and e = 2.718 ...). Also, both the data and the model in Figure 6.20 are normalized to unit total spectral power, i.e.,

$$\int_{-\infty}^{\infty} P_{tot}(v)dv = 1 \ .$$

In these circumstances, the model is matched to the data as follows: first, β is selected so that the slope [i.e., dB/(m/s)] of the model matches that of the data in the ac spectral tail region. Next, the value of dc/ac ratio r in the model is assigned to provide a y-intercept $[1/(r+1)](\beta/2)$ so that the exponential model overlays and matches the ac region of the data in absolute power level $P_{tot}(v)$ (i.e., vertical position) as well as slope. Because of the normalizations involved, this procedure results in the excess power from the quasi-dc region of the data being included in the dc Dirac delta function term $[r/(r+1)]\delta(v)$ of the model, where excess quasi-dc power means the power in the quasi-dc region of the data that exists above the approximating exponential of the model.

Figure 6.21 shows four examples of measured windblown clutter spectra presented as 10 log $P_{tot}(v)$ vs v to illustrate quasi-dc and ac spectral regions in actual measured data. Figure 6.21(a) shows an LCE spectrum; Figures 6.21(b) through (d) show Phase One spectra at L-, X-, and UHF bands, respectively. Each spectrum has an approximating exponential model shown as a straight line through the right side of the data. Each spectrum in Figure 6.21 contains excess power above the approximating exponential in a quasi-dc

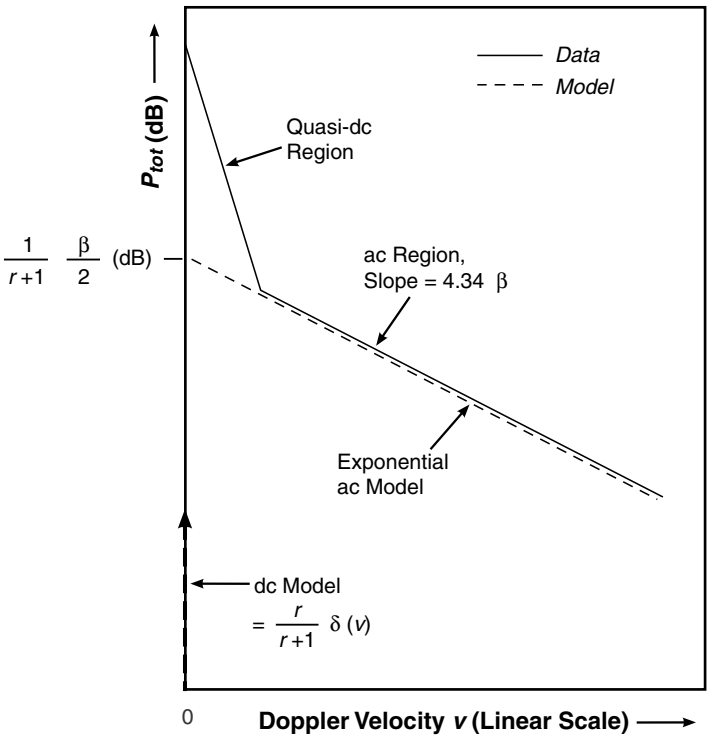

FIGURE 6.20 Modeling of clutter spectra.

region near zero-Doppler. The resolution in these spectra is very fine (≈ 0.01 m/s, see Table 6.3), so in each case quasi-dc spectral power is resolved at levels well above the zero-Doppler window function limiting resolution. It is evident that absorbing the excess quasi-dc power of the data in the delta function dc term of the model in such results allows extremely good fits of the ac spectral tail regions with exponential shape functions over regions of wide Doppler extent in the spectral tails.

As computed directly in the time domain, the zero-Doppler cell contains relatively little dc power compared with the total ac power from all the non-zero Doppler cells, for each of the examples shown in Figure 6.21. However, the quantity r_{modeled} increases compared with r_{measured} as a result of absorbing the excess quasi-dc power in the modeled dc term. For the spectra of Figure 6.21, the values used for r_{modeled} are 0.7, 4.3, 2.9, and 8.0 dB for spectra (a), (b), (c), and (d), respectively. Use of these values causes the exponential straight-line fits to the data in the examples of Figure 6.21 to be shifted downwards by 10 log (r_{modeled} + 1) – 10 log (r_{measured} + 1) decibels, resulting in the exponential models overlaying the measured data in these examples throughout the extensive ac spectral tail regions [25]. Equation (6.4) which specifies r_{modeled} was developed from data in which excess quasi-dc power was absorbed in the dc term to gain the benefit of improved fidelity in modeling spectral tails.

No simple ac model (i.e., analytic expression), including exponential, can adequately represent both the quasi-dc region $|v| < 0.25$ m/s and the ac region $|v| > 0.25$ m/s of the data in Figures 6.20 and 6.21. The objective of Chapter 6 is realistic representation of the ac region or spectral tail of the data. Even the simplest single-delay-line MTI filter can usually

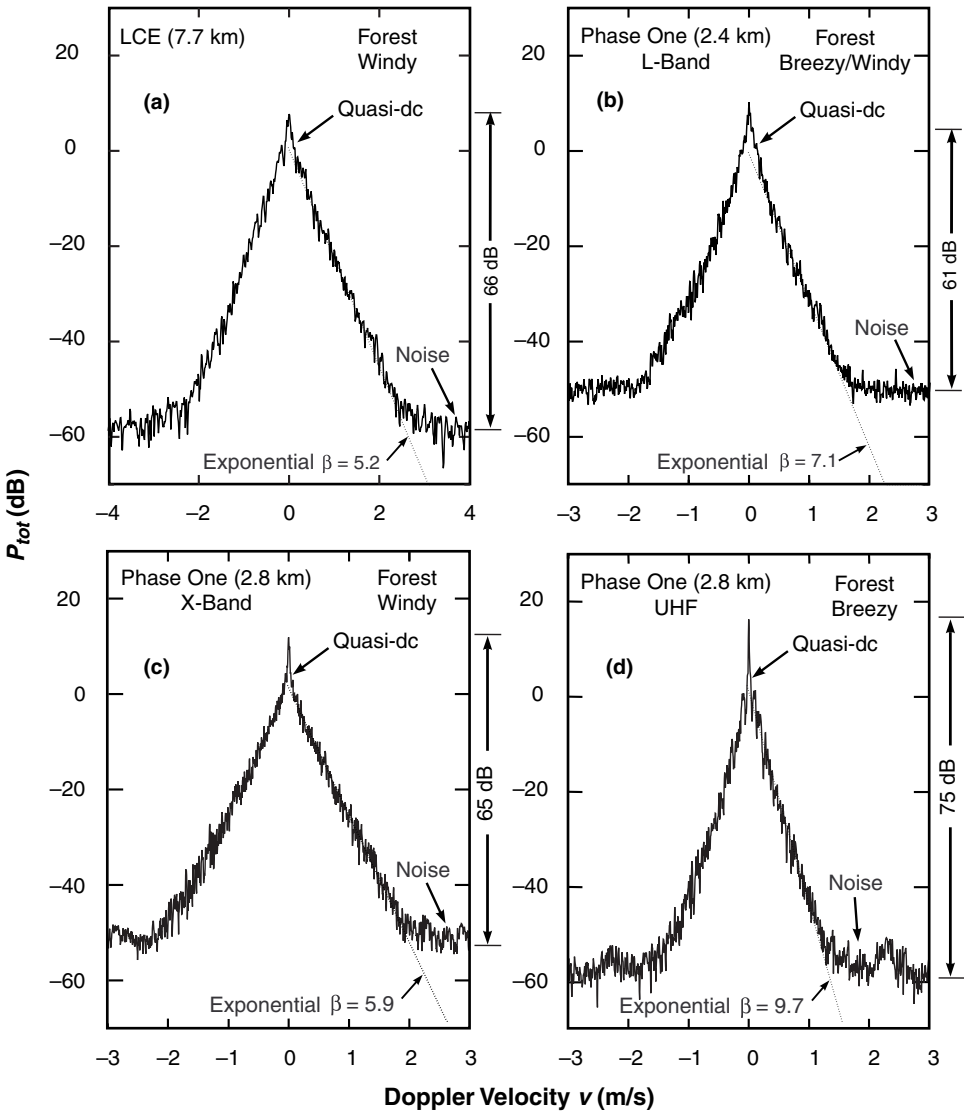

FIGURE 6.21 Highly exponential decay in four measured windblown forest clutter spectra: (a) LCE; (b), (c), and (d) are Phase One L-, X-, and UHF bands, respectively. Regions of excess quasi-dc power are also indicated.

sufficiently reject dc and quasi-dc clutter power in the region $|v| < 0.25$ m/s. It is the tail of the clutter spectrum that requires definition to enable, for example, knowledgeable design of the skirts of MTI filter characteristics or other Doppler signal-processing ground clutter rejection techniques in the region $|v| > 0.25$ m/s (see Section 6.5). In the modeling information provided herein, excess quasi-dc power is included in the dc term in situations where including it as ac power would degrade representation of the ac spectral tail. Users of this information whose interests in clutter spectra may differ from those just stipulated need to be aware that some of the dc power in the delta function of the current model is often spread slightly into a near-in quasi-dc region $|v| < 0.25$ m/s in actual measurements. As an alternative to absorbing the excess quasi-dc power in the dc delta function, the quasi-dc

region in each specific measured clutter spectrum can instead be represented by a second, very sharply declining, measurement-specific exponential function [31]. This alternative can be helpful in analysis situations in which the Dirac delta function is not of sufficient analytic tractability.

6.4.3 Cells in Partially Open or Open Terrain

6.4.3.1 Desert

Ground clutter spatial resolution cells in which some of the backscattered power comes from stationary scattering elements such as the underlying terrain surface itself or large fixed discrete objects (water towers, rock faces) provide correspondingly larger values of dc/ac ratio r in the resulting clutter spectra. In the ground clutter spectral measurements conducted by the LCE radar at its desert site, portions of barren desert floor were visible between the sparse desert bushes (greasewood, creosote) typically of heights of 3 or 4 ft. Figure 6.22 illustrates a typical LCE clutter spectrum measured at this desert site under windy conditions (wind speed ≅ 20 mph). It is evident that this desert clutter spectrum contains a large dc component at zero-Doppler velocity, the result of backscatter from the stationary desert floor.

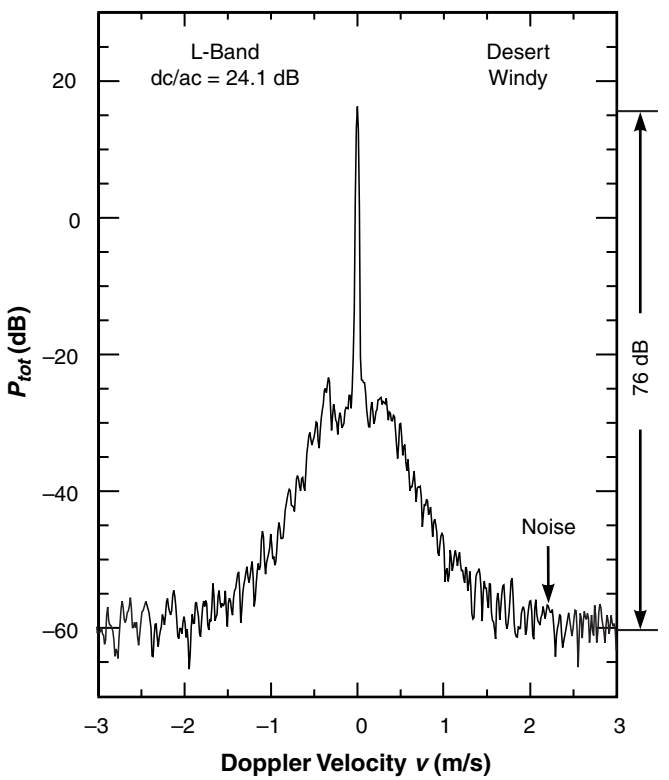

Figure 6.22 An LCE-measured clutter spectrum from desert terrain (scrub/brush, partially open) under windy conditions.

The ratio of dc/ac power computed directly in the time domain for the desert spectrum of Figure 6.22 is 24.1 dB. Normalization of measured spectral data to $P_{tot}(v)$ involves division

of power per resolution cell by the width of the cell Δv. For the data of Figure 6.22, Δv equals –16.22 dB, so this procedure raises the power in each cell by 16.22 dB. For spectra like that of this figure with a large dc component, the power in the zero-Doppler cell is not distributed over Δv but exists as a singular dc component. Reducing the zero-Doppler peak by 16.2 dB allows more straightforward interpretation of $r = 24.1$ dB as simply the ratio of the reduced zero-Doppler peak to the total ac power (i.e., the power level of the step function existing in the unit interval $-0.5 < v < +0.5$ m/s and containing the same total ac spectral power as the measured spectrum).

The desert/windy clutter spectrum of Figure 6.22 contains extensive ac spectral spreading at lower power levels. The low-level ac spectral spreading in these data is due to wind-induced motion of the desert foliage. Other LCE-measured desert spectra from similar cells under light or calm wind conditions showed little or no spectral spreading over as much as 80 dB of spectral dynamic range [see Figure 6.4(a)]. Unlike the forest/light wind spectrum of Figure 6.16, which also contains a large dc component but in which the spectral power decays rapidly but broadens continuously away from the zero-Doppler peak, the dc component in the desert/windy spectrum of Figure 6.22 exists more as a discrete delta function at the spectral resolution of the window function over the higher levels of spectral power.

Figure 6.23 shows the ac spectral tail region of the desert/windy spectrum of Figure 6.22 at higher Doppler velocities as 10 log $P_{ac}(v)$ vs log v. Also shown in Figure 6.23 is the forest/windy spectrum previously shown in Figure 6.5. Both measured spectra in Figure 6.23 are normalized to $P_{ac}(v)$. The 24-dB dc/ac ratio in the desert spectrum (a) of Figure 6.23 results in an effective 24-dB loss of sensitivity (i.e., higher noise level) compared with the forest spectrum (b) in measuring ac spectral shape. Otherwise, the ac spectral shape of the desert/windy spectrum in Figure 6.23 almost exactly overlays that of the forest/windy spectrum over their common interval of available spectral dynamic range.

It was previously shown that the exponential shape factor $\beta = 5.2$ provides an excellent match to the forest/windy spectrum of Figure 6.23. On the basis of these data, the windblown clutter ac spectral shape that applies for densely forest-vegetated clutter cells under windy conditions also applies for more open desert-vegetated cells. That is, these data suggest that the ac spectral shape function caused by windblown vegetation in a cell may be, at least to a first-order approximation, somewhat independent of the type of vegetation in the cell. However, this equivalence does not extend to include dc/ac ratio; the dc to ac ratio of clutter spectral power is much higher in partially open desert than in forest terrain.

Knolls, Utah. Figure 6.24 shows X-band desert clutter spectra measured by the Phase One radar at two western U. S. desert measurement sites—Booker Mt., Nevada, and Knolls, Utah—in summer season. At both sites these spectra were obtained as eight-gate averages, 15 FFTs per gate (2,048-point FFTs, PRF = 500 Hz, hor. pol., gate width = pulse length = 150 m). The Booker Mt. spectrum of Figure 6.24(a) was measured from barren level mud flats under calm wind conditions and light rain at 12- to 13.2-km range and 2.3° grazing angle. This Booker Mt. spectrum shows essentially no spectral spreading beyond the window-function resolution over a 60-dB spectral dynamic range (except for the small residual spur indicated at the base of the dc-spike 56 dB down), and again evidences the field capability of the Phase One radar for making X-band clutter spectral measurements at low Doppler frequencies [compare with Figure 6.4(c)].

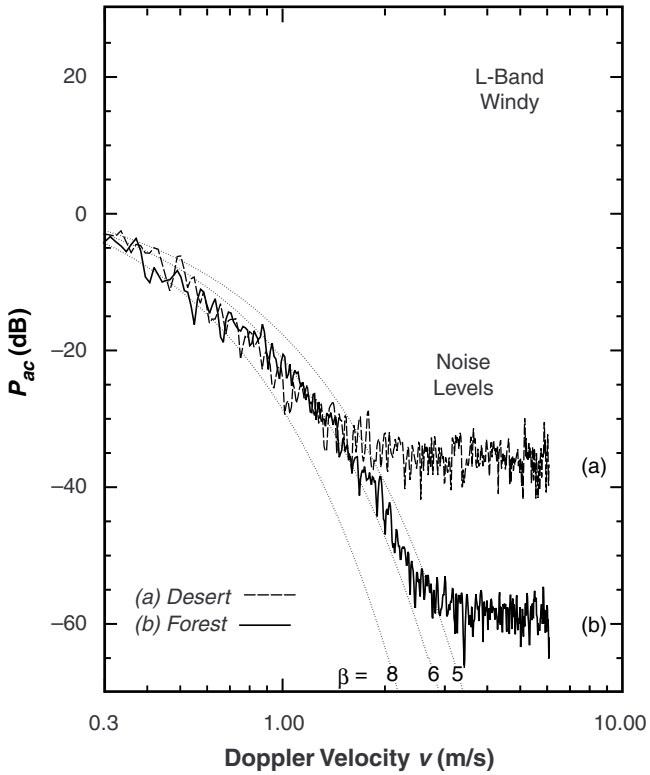

FIGURE 6.23 Comparison of ac spectral shapes of LCE (a) desert (scrub/brush) and (b) forest clutter spectra under windy conditions.

In contrast to no spectral spreading at Booker Mt. in Figure 6.24(a), Figures 6.24(b) and (c) show an X-band desert spectrum from Knolls with significant spectral spreading. The Knolls spectrum was measured from very level terrain containing sparse, low, desert scrub vegetation under 11- to 16-mph wind conditions at 2.5- to 3.7-km range and 0.5° grazing angle. This X-band desert spectrum, although containing a significant dc component, contains less dc power than the LCE L-band Nevada desert spectrum of Figure 6.22. As a result, more ac spectral dynamic range is available for defining the shape of the X-band desert spectrum in Figure 6.24(c) than was available for defining the shape of the L-band desert spectrum in Figure 6.23. This X-band Knolls desert spectrum [Figures 6.24(b), (c)] is very similar to other Phase One and LCE windblown clutter spectra observed at other radar frequencies and from other types of vegetation.

The basic similarities of the Knolls spectrum to other Phase One- and LCE-measured spectra are in the increasing downward curvature with increasing Doppler velocity and decreasing power level displayed in Figure 6.24(c) on 10 log P vs log v axes. This downward curvature also characterizes the exponential shape factor. Thus through a broad central region of increasing downward curvature in the data of Figure 6.24(c), the exponential shape factor $\beta = 11.2$ overlays the data and captures its general shape. At upper levels, the data rise somewhat above the approximating exponential in the quasi-dc region $|v| < 0.21$ m/s; this excess quasi-dc power is included as dc power in the dc/ac ratio of 5.2 dB ascribed in modeling this spectrum. The slight broadening beyond exponential at

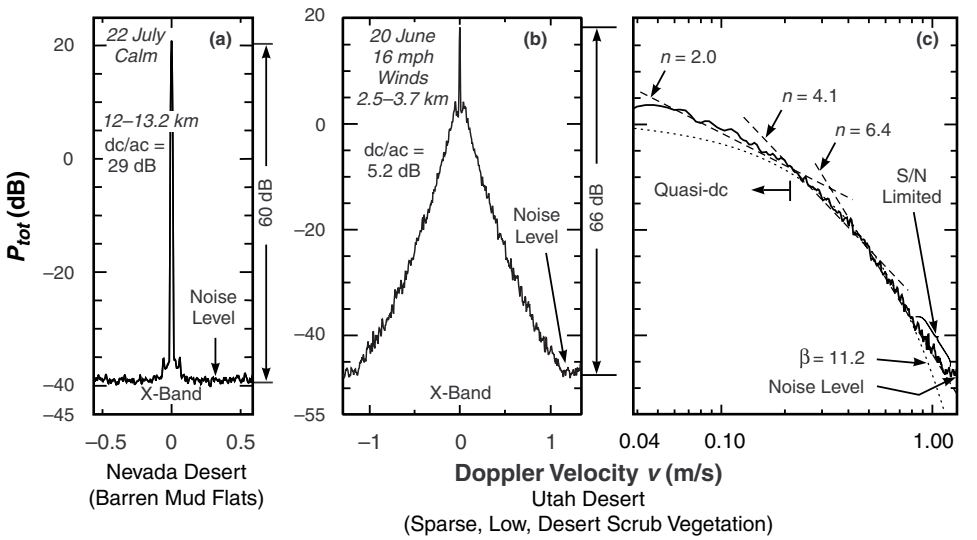

FIGURE 6.24 Phase One X-band desert clutter spectral measurements: (a) Booker Mt., Nevada, and (b), (c) Knolls, Utah.

very low levels in Figure 6.24(c) as the measured data approach to within 10 dB of the noise level is partially the result of S/N limitations in this region. In contrast to the exponential shape factor generally capturing the shape of this spectrum, power-law rates of decay [Figure 6.24(c)] increase from $n \cong 2$ (20 dB/decade) at upper levels to $n \cong 4$ (i.e., 40 dB/decade) at intermediate levels to $n > 6$ (> 60 dB/decade) at the lowest levels; in other words, no single power law comes close to capturing the general shape of the X-band desert spectrum shown in Figures 6.24(b) and (c).

6.4.3.2 Cropland

The Phase One radar acquired clutter measurement data at the farmland site of Beulah, N. Dakota, during the first two weeks of June [44]. The open agricultural fields in the measurement sectors around Beulah were mostly in wheat; in early June, the wheat was not yet very high. Trees occurred at ~1% to 3% incidence by area, for the most part at low-lying elevations along creekbeds. The primary Beulah measurement swath examined comprised 16 contiguous 150-m gates from 4.5- to 6.75-km range. Over this swath, the terrain was well illuminated by the Phase One radar at a depression angle of ~0.4°. Windblown wheatland clutter spectra were generated for all 16 primary-swath gates at vertical polarization and 1-μs pulsewidth in all five Phase One frequency bands. In each band, 2048-point FFTs were generated and averaged to form the spectrum for each gate. The effective PRF and number of FFTs averaged in each band were at X-band, 500-Hz PRF, 15 FFTs; at S-band, 167-Hz PRF, 5 FFTs; at L-band, 100-Hz PRF, 3 FFTs; at UHF, 33.3-Hz PRF, 1 FFT; and at VHF, 12.5-Hz PRF, 1 FFT. Considerable gate-to-gate variation occurred in the resultant clutter spectra.

Six particular gates (10–12 and 14–16) at longer ranges in the primary swath were selected as under strong illumination and essentially containing pure wheat fields within the azimuth main beamwidth in all bands. Spectra from these gates were averaged together in each band to provide a generalized indication of pure windblown wheatland clutter spectra.

Figure 6.25 shows the resultant generalized clutter spectra from pure windblown wheatland in all five Phase One frequency bands. These measurements were obtained on four different days under relatively windy conditions. The results show significant spectral spreading in each of the four upper bands (X, S, L, and UHF) to either side of a strong dc component. Spectral spreading in these bands extends to power levels 60 to 70 dB below zero-Doppler peaks and to corresponding Doppler velocities generally < ~1 m/s. In contrast, the VHF wheatland spectrum shows absolutely no spectral spreading to a level 65 dB down under 12-mph winds. This complete lack of VHF spectral spreading is due to a combination of (a) a high degree of penetration of the VHF radiation through the wheat stalks to the underlying stationary ground, and (b) the amplitude of the 12-mph windblown motion of the wheat stems being << 1λ at VHF (<< 1.7 m). Note that the UHF wheatland spectrum, which shows the greatest degree of spreading of any of the four upper-band spectra to a maximum Doppler velocity of ~1.25 m/s, was measured under much windier conditions (27 mph).

The ac spectral spreading in the four upper-band wheatland clutter spectra of Figure 6.25 is highly exponential in shape, as indicated by the relatively linear decay displayed on the 10 log P vs v axes used in Figure 6.25. The three ac spectral shapes at S-, L-, and UHF-bands are remarkably exponential, and in fact are reasonably well-fitted by the exponential shape factor $\beta = 9$, which is not out of line with the values of exponential shape parameter appropriate for windblown forest at similar wind speeds (see Table 6.1). Each spectrum also shows a strong dc component. However, the X-band spectrum in Figure 6.25 shows a much decreased dc component, such that much of the pure dc power in the lower bands has spread into a quasi-dc region $|v| \leq \sim 0.25$ m/s at X-band. The dc to ac ratios in these spectra for X-, S-, L-band, and UHF are: 4, 17, 21, and 17 dB respectively.

Beiseker, Alberta. Another agricultural site visited by the Phase One radar in summer season was Beiseker, Alberta (see Section 3.4.1.4.2). The Phase One summer visit to Beiseker was in August when the crops (mostly wheat and other grains) were mature and thus higher than for the June visit to Beulah. Figure 6.26 shows an S-band summer Beiseker cropland clutter spectrum measured as a 16- gate average of 150-m range gates at vertical polarization (5 FFTs per gate, 2048-point FFTs, PRF = 500 Hz). The PRF of 500 Hz used to make this spectrum was higher than the 167 Hz generally used at S-band, resulting in somewhat reduced spectral resolution. This Beiseker spectrum is from measurements at 10- to 12.4-km range under 7- to 12-mph winds. The measurement geometry resulted in illumination at a depression angle of ~0.4°. The 2.4-km Beiseker measurement sector was almost entirely in mature wheat, although it was somewhat broken in places and dissected with a stream bed, resulting in small secondary incidences of herbaceous rangeland and minor scrub/brush.

The 16-gate, mature-wheat, Beiseker S-band spectrum of Figure 6.26 is well represented as exponential, although containing less dc power than the 6-gate, young-wheat, Beulah S-band spectrum included in Figure 6.25. The exponential shape factor that best represents the Beiseker spectral shape is $\beta = 13$, greater than the $\beta = 9$ Beulah value as a result of the lighter winds at Beiseker. Power-law rates of decay shown in Figure 6.26(b) increase from $n \cong 3$ (30 dB per decade) at intermediate levels to $n \cong 5$ (50 dB per decade) at lower levels. The dc/ac ratio in which excess quasi-dc power is included as dc power to enable the $\beta = 13$ shape factor to fit the spectral tail in Figure 6.26 is 12.2 dB.

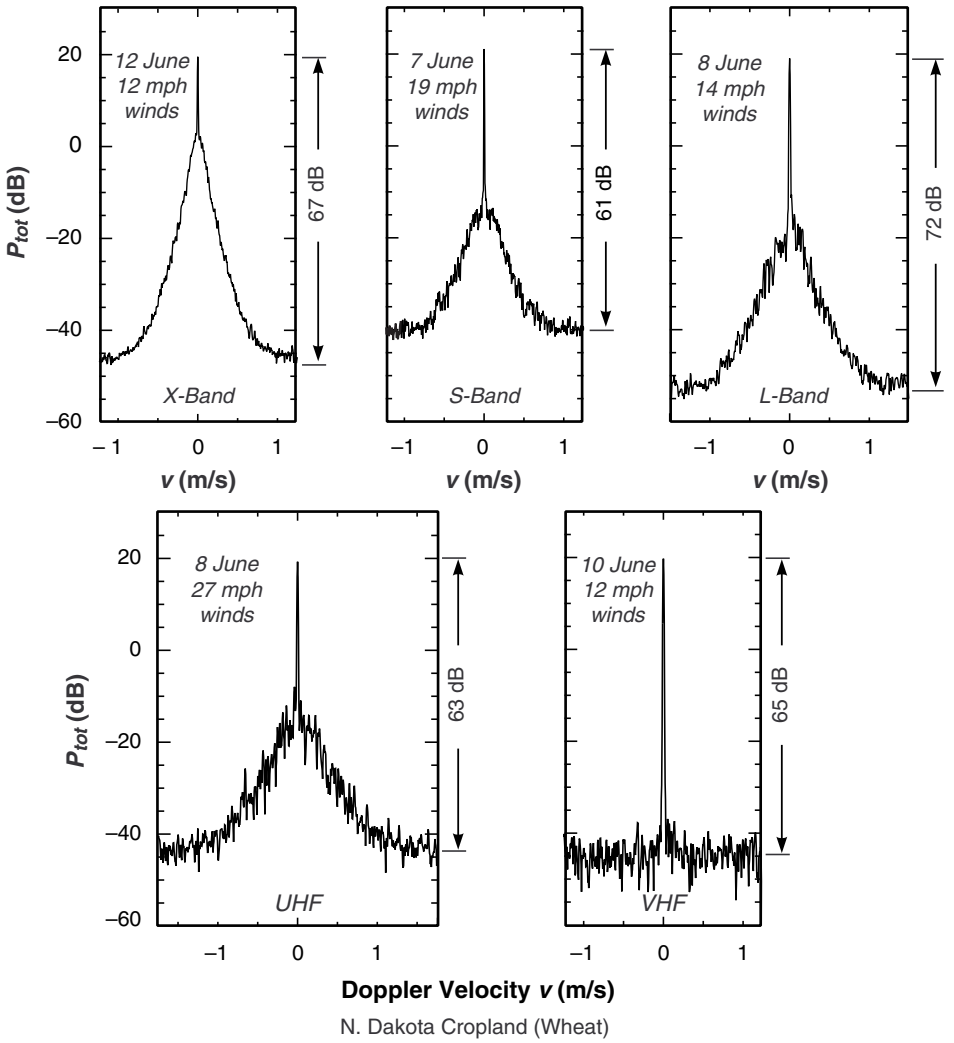

FIGURE 6.25 Phase One five-frequency clutter spectra from North Dakota wheatland measured on four different days in early June under strong breezy or windy conditions.

The Beiseker 16-gate spectrum of Figure 6.26 is essentially identical in all respects to a corresponding Beulah wheatland 16-gate spectrum[35] (not shown). That is, although detailed gate-to-gate differences exist in these data caused by variations in topography, crops, and wind speeds, when averaged over broad 2.4-km swaths these results indicate that exponential spectral spreading generally occurs in open cropland terrain without much site-specific variation.

de Loor's Results. Much earlier measurements of clutter spectra from windblown crops (including wheat) made with a noncoherent X-band system were reported by de Loor, Jurriens, and Gravesteijn [45]. The one example shown by de Loor et al. is an ac spectrum for full-grown wheat under 5- to 7-mph winds of ~ 40-dB spectral dynamic range. This

35. Formed from all 16 primary-swath gates at Beulah, not just the six pure-wheat gates for which results are shown in Figure 6.25.

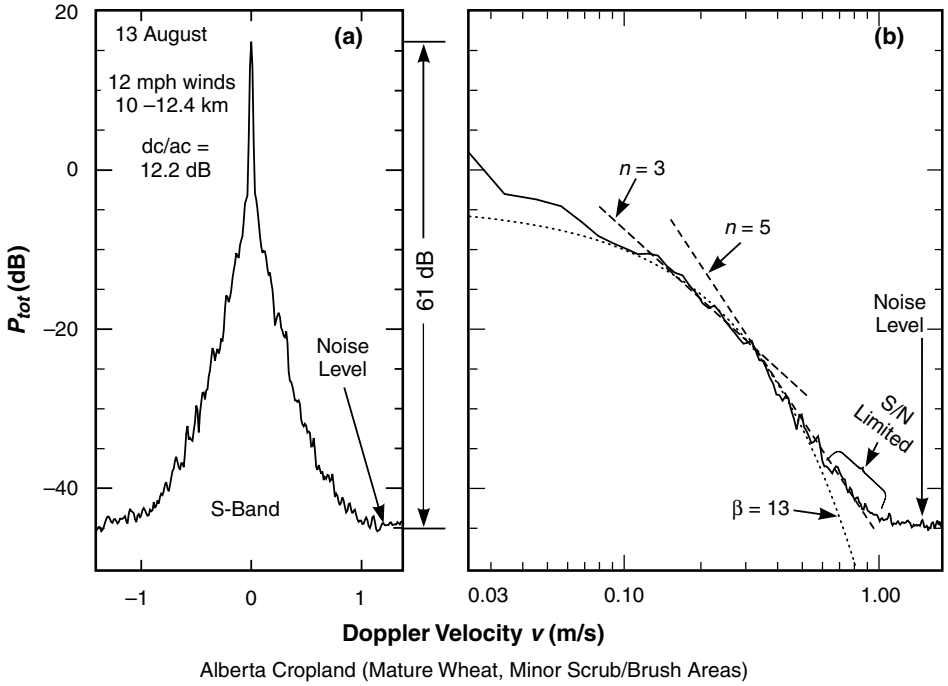

FIGURE 6.26 Phase One S-band cropland clutter spectrum from Beiseker, Alberta.

spectrum appears to be highly exponential and is very similar in shape to the Phase One-measured Beulah pure-wheat spectra of Figure 6.25. Spectral widths at the –3- and –10-dB levels as a function of wind speed for winds up to 22 mph are also provided by de Loor et al. in composite plots covering four different crop types (wheat, alfalfa, sugar beets, potatoes). The maximal extent points in these results fall in closely with the predictions of the current windblown clutter exponential model at corresponding –10- and –25-dB levels under windy conditions (see Figure 6.1), after taking into account that de Loor's results are noncoherent (i.e., wider spectra by a factor of ~1.4, see Section 6.6.1.1). However, de Loor et al. "could not conclusively [show] significant [spectral] differences between different crop types." Detailed comparisons of Phase One spectral results with those of de Loor et al. reinforce Phase One indications suggesting no large differences in ac spectral shape or extent at microwave frequencies between windblown tree spectra and windblown crop spectra, or indeed, between windblown crops at different stages of maturity, from different sites, and of different crop types, under windy conditions.

6.4.3.3 RANGELAND

Clutter spectral results were obtained for rangeland terrain in which patches of trees (45-ft high aspen) and patches of shrubs (15-ft high willow) occurred over open areas of herbaceous (grassy) rangeland [24, 25]. Five-frequency spectra were obtained, each averaged over 76 contiguous 15-m range gates, in which a number of FFTs per gate were also averaged. A significant dc component existed in these spectra (e.g., of dc/ac ratio as much as 15 to 20 dB), largely the result of geometrically visible open ground occurring between the patches of trees and shrubs. "Shoulders" were evident in the spectral shapes at the onset of the ac spreading just at the base of the dc spikes [cf. Figures 6.22, 6.24(b),

6.25]. Such shoulders in spectral shape have been associated with the natural resonant frequency of the trees (see Section 6.6.1.3). Beyond these shoulders, the rates of decay over the ac spectral tail regions in the rangeland spectra were highly exponential. See [25] for plots of these rangeland spectra, as well as other considerations involved in their modeling including their dc/ac ratios.

6.4.4 MTI Improvement Factor

A significant advantage of an exponential spectral model for clutter is its analytic tractability. Here an example of this tractability is provided by deriving the MTI improvement factor of a single delay-line canceller operating in an environment of windblown clutter exponentially distributed in Doppler. Also derived is the single delay-line canceller MTI improvement factor that results under the more traditional assumption of Gaussian-distributed clutter, which is then compared with the improvement factor pertaining to exponentially distributed clutter. In deriving those improvement factors, the earlier approaches of Skolnik [1] and Narayanan et al. [42] are followed for deriving improvement factors for Gaussian spectral shapes. However, also explicitly included in the derivations here is the effect of the dc spectral component on the improvement factor. The expression for n cascaded delay-line cancellers operating in exponential clutter is also presented.

Note that the power-law function [see Eq. (6.18)] is not so analytically tractable as the exponential and Gaussian functions. For example, attempting to follow the preceding approach to obtain the single delay-line canceller improvement factor for power-law-distributed clutter leads to an infinite integral expression that cannot be simply evaluated analytically.

6.4.4.1 Preliminary Analysis

The input clutter power within one pulse repetition interval T entering the single delay-line canceller is given by

$$P_{ic} = \int_{-f_p/2}^{f_p/2} P_{tot}(f)\,df$$

where $f_p = 1/T$ is the PRF and $P_{tot}(f)$ is the total clutter spectral power density as given by Eq. (6.1) (transformed from Doppler velocity v to Doppler frequency f). Since f_p must be much greater than the clutter spectral extent of $P_{tot}(f)$ for successful MTI operation, the limits of integration in the preceding integral can be further expanded to $\pm\,\infty$ without practical consequence on P_{ic}, whereupon

$$P_{ic} = \int_{-\infty}^{\infty} P_{tot}(f)\,df = 1$$

The equivalence of the infinite integral expression to unity in this equation is required by the definition of $P_{tot}(f)$ in Eq. (6.1). The frequency response function in the power domain for a delay line of time delay T is given [1] by

$$|H(f)|^2 = \sin^2(2\pi fT)$$

Thus the residual clutter power after cancellation is given by

$$P_{oc} = \int_{-\infty}^{\infty} P_{tot}(f)|H(f)|^2 df$$

In this equation, the sine function in $|H(f)|^2$ may be replaced by its small-angle approximation (i.e., its argument), again because $f_p = 1/T$ greatly exceeds the practical spectral extent of $P_{tot}(f)$. The result of this substitution is

$$P_{oc} = 4\pi^2 T^2 \int_{-\infty}^{\infty} f^2 P_{tot}(f) df$$

The total clutter spectral power density $P_{tot}(f)$ is given by Eq. (6.1) as

$$P_{tot}(f) = \frac{r}{r+1}\delta(f) + \frac{1}{r+1}P_{ac}(f)$$

where r is the ratio of dc to ac power in the clutter spectrum and $P_{ac}(f)$ is the ac spectral shape factor. Substituting this expression for $P_{tot}(f)$ into the above equation for P_{oc} and recognizing that the term involving integration over the delta function term vanishes, the general result is that the output clutter power from a single delay-line canceller is given by

$$P_{oc} = \frac{4\pi^2 T^2}{r+1} \int_{-\infty}^{\infty} f^2 P_{ac}(f) df \tag{6.6}$$

The MTI improvement factor I of the single delay-line canceller is given [1,42] by

$$I = \overline{G}\frac{P_{ic}}{P_{oc}}$$

where $\overline{G}$, the average gain of the canceller, can be shown [1] to equal 2. Therefore, I of the single delay-line canceller is given by

$$I = \frac{2}{P_{oc}}$$

where P_{oc} is given by Eq. (6.6).

6.4.4.2 Exponential Clutter

Clutter distributed exponentially in Doppler frequency f is given by Eq. (6.2) as

$$P_{ac}(f) = \frac{\beta'}{2}\exp(-\beta'|f|)$$

where $\beta' = (\lambda/2)\beta$ and β is as specified in Eq. (6.3) or Table 6.1. It follows that

$$P_{oc} = \frac{4\pi^2 T^2}{r+1}\beta' \int_{0}^{\infty} f^2 \exp(-\beta' f) df$$

Using the standard result $\int_0^\infty x^2 \exp(-ax)dx = 2a^{-3}$, the preceding equation reduces to

$$P_{oc} = \frac{8\pi^2 T^2}{(r+1)\lambda^2} \cdot \left(\frac{2}{\beta}\right)^2$$

Representing *I* of the single delay-line canceller in exponentially distributed clutter as I_β, it follows that

$$I_\beta = (r+1)\left(\frac{v_p}{\pi}\right)^2 \left(\frac{\beta}{2}\right)^2 \tag{6.7}$$

where $v_p = (\lambda/2)f_p$. Skolnik has extended Eq. (6.7) to apply to *n* delay line cancellers in cascade (see [1], p. 158), as:

$$I_\beta(n) = (r+1)\left(\frac{v_p \beta}{\pi}\right)^{2n} \frac{1 \times 3 \times 5 \times \ldots (2n-1)}{2^n n!(2n)!} \tag{6.8}$$

6.4.4.3 Gaussian Clutter

Clutter distributed Gaussianly in Doppler frequency *f* is given by Eq. (6.17) as

$$P_{ac}(f) = \sqrt{\frac{g'}{\pi}} \exp(-g' f^2)$$

where $g' = (\lambda/2)^2 g$. It follows that

$$P_{oc} = \frac{8\pi^2 T^2}{r+1} \sqrt{\frac{g'}{\pi}} \int_0^\infty f^2 \exp(-g' f^2) df$$

Using the standard result $\int_0^\infty x^2 \exp(-a^2 x^2)dx = \frac{\sqrt{\pi}}{(4a^3)}$, the preceding equation reduces to:

$$P_{oc} = \frac{8\pi^2 T^2}{(r+1)\lambda^2} \cdot \frac{1}{g}$$

If *I* of the single delay-line canceller in Gaussianly distributed clutter is represented as I_g, it follows that

$$I_g = (r+1)\left(\frac{v_p}{\pi}\right)^2 g \tag{6.9}$$

Except for the inclusion of the term $(r+1)$, which explicitly shows the effect on I_g of nonzero dc/ac spectral power ratio *r*, this expression for I_g is otherwise identical to that provided elsewhere [1,42]. Both Eqs. (6.7) and (6.9) reduce to

$$I = (r+1)\left(\frac{v_p}{\pi}\right)^2\left(\frac{1}{2\sigma^2}\right) \tag{6.10}$$

where σ is the standard deviation in the respective spectrum [i.e., in Gaussian-distributed clutter, $\sigma = \sigma_g = 1(\sqrt{2}g)$; in exponentially distributed clutter, $\sigma = \sigma_\beta = (\sqrt{2}/\beta)$].

6.4.4.4 Numerical Examples

It is evident from Eqs. (6.7), (6.9), and (6.10) that I obtained in Gaussian clutter exceeds that obtained in exponential clutter by a decibel amount given by

$$10\log_{10}(I_g/I_\beta) = 10\log_{10}(4g/\beta^2) = 10\log_{10}(\sigma_\beta/\sigma_g)^2 \tag{6.11}$$

assuming that the radar parameters λ and f_p and the clutter dc/ac ratio r are the same in both cases. As a numerical example, consider Barlow's [7] much-referenced Gaussian clutter spectrum under windy (20-mph) conditions for which $g = 20$ (see Section 6.6.1.1). The value of β from the exponential clutter model of Section 6.2 for similar windy (15- to 30-mph) conditions is specified in Table 6.1 as $\beta = 5.7$. Applying Eq. (6.11) using these clutter parameters shows that the single delay-line canceller improvement factor obtained in $g = 20$ Gaussian clutter is 3.9 dB greater than that obtained in $\beta = 5.7$ exponential clutter, independent of radar frequency and processing-specific parameters such as pulse repetition frequency. That is, the fact that exponential clutter spreads the clutter in Doppler beyond that of the more usually assumed Gaussian clutter results in a 3.9 dB loss in improvement factor.

As a further numerical example, the values of I_β obtained by an X-band radar (i.e., λ = 3 cm) of $f_p = 1000$ Hz operating in exponential clutter are shown in Table 6.5 as computed from Eq. (6.7). The exponential clutter for which Table 6.5 applies is that of the model of Eqs. (6.1), (6.2), (6.4) and Table 6.1 under various wind conditions.

Table 6.5 Improvement Factor I_β in Exponential Clutter for an X-Band Radar (λ = 3 cm) with PRF = 1000 Hz

Wind Speed (mph)	Exponential ac Spectral Shape Factor β[a]	Ratio of dc/ac Spectral Power r(dB)[b]	Single Delay-Line Canceller Improvement Factor I_β (dB)[c]
5	12	40	34.6
10	8	–0.7	28.3
20	5.7	–5.4	23.8
40	4.3	–10.0	20.6

a. From Table 6.1
b. From Equation (6.4)
c. From Equation (6.7)

6.5 Impact on MTI and STAP

6.5.1 Introduction

The shape of the windblown radar ground clutter Doppler spectrum is important in determining the performance of target detection in ground clutter. In modern radar that operates with wide dynamic range and low noise floor, the decay of the spectral tails of ground clutter has significant impact on the detection of small moving targets. In such systems, detection performance can be clutter limited, even to relatively high Doppler frequencies. Therefore, the rate at which the clutter spectral tails decay (i.e., the spectral shape) with increasing Doppler frequency is an essential issue for the realistic prediction of detection performance.

The preceding section (Section 6.4.4) shows that the use of a realistic exponential ground clutter spectral shape causes significant loss in single-delay-line improvement factor *I*, e.g., 3.9 dB, compared to use of the more conventional Gaussian ground clutter spectral shape. Section 6.5 expands this previous discussion to consider the impact of ground clutter spectral shape on the prediction of detection performance of ground-based and airborne surveillance radar using modern coherent signal processing. It is shown that, with such processing, detection losses much greater than 3.9 dB can occur using incorrect clutter spectral shapes for performance prediction. The results presented summarize the work in this area of Professor Alfonso Farina of Alenia Marconi Systems, Rome, Italy, and his Italian colleagues, Professor Fulvio Gini and Dr. Maria V. Sabrina Greco at the University of Pisa and Professor Pierfrancesco Lombardo at the University of Rome, who took up the Lincoln Laboratory findings concerning ground clutter spectral shape and investigated the impact of these findings on radar signal processing techniques for target detection in clutter. What follows summarizes[36] these investigations; for more extensive discussion and results describing this work, refer to the original technical journal articles [30–33].

Following subsections first review the derivation of how ground clutter spectral shape affects the performance of optimum coherent detectors, both for ground-based and airborne early-warning (AEW) surveillance radars, when such radars operate in a ground clutter environment of Rayleigh clutter amplitudes (i.e., I and Q components of Gaussian pdf). It has previously been shown in this book that temporal clutter amplitude statistics from windblown vegetation (particularly, windblown trees) indeed tend to be Rayleigh distributed—see Figure 5.A.16. The expressions for detection performance in Gaussian clutter, as discussed in what follows, can also apply to adaptive coherent detection in nonhomogeneous and nonstationary clutter environments, providing the I and Q clutter pdf's remain Gaussian [46].

Numerical results are provided both at X-band and L-band in which the predicted performance of the MTI improvement factor *I* is compared between using an exponential shape for the ground clutter spectrum, as illustrated and modeled heretofore in Chapter 6, and using Gaussian and power-law shapes for the ground clutter spectrum, such as have been previously employed in the technical literature and which are defined and discussed subsequently in Section 6.6.1. This allows evaluation of the sensitivity of detection system performance prediction to the use of incorrect ground clutter spectral models. It is shown

36. The summary provided here includes material originally published in [30, 31, and 33] by permission of IEEE, and in [32] by permission of IEE.

that the Gaussian shape can significantly overestimate system performance, whereas the power-law shape can significantly underestimate system performance, compared to the more correct exponential clutter spectral shape.

6.5.2 Impact on Performance of Optimum MTI

To evaluate the impact of the measured clutter Doppler spectrum on the detection performance, we proceed as follows. Consider a ground-based surveillance radar in which the radar receiver demodulates, filters the incoming narrowband waveform, and uniformly samples each pulse return, thus obtaining N complex samples $\{z[i]\}_{i=0}^{N-1}$ spaced by T seconds, where $T = 1/\text{PRF}$ is the PRI. The N samples are assembled into the N-dimensional vector $\mathbf{z} = \mathbf{z}_I + j\mathbf{z}_Q = [z[0] \ldots z[N-1]]^T$, where $\mathbf{z}_I$ and $\mathbf{z}_Q$ represent the vectors of the I and Q components, and the superscript "T" stands for "transpose of." Assuming an exact knowledge of the clutter covariance matrix, the optimum MTI processor is a coherent linear transversal filter with complex coefficient vector $\mathbf{w} = [w_1, w_2, \ldots, w_N]^T$. To test a range cell for detection, the quantity $\mathbf{w}^H\mathbf{z}$ is evaluated (where the superscript "H" stands for "conjugate transpose of"), and the envelope of the result is compared to a detection threshold, thus ascertaining whether a target is present or not. The target signal is modeled by the N-dimensional complex-valued vector $\mathbf{s} = \alpha\,\mathbf{p}$, where α is a complex parameter accounting for target amplitude and initial phase and $\mathbf{p}_i = e^{j2\pi i f T}$, $0 \le i \le N-1$; f being the target Doppler frequency. The interference (i.e., clutter plus noise) is given by the vector $\mathbf{d}$, where P_C is clutter power; and P_N is white noise power. The parameters that characterize the clutter interference are: the clutter to noise power ratio (*CNR*), the shape of the clutter spectrum, and the width of the clutter spectrum for given shape. In the results to follow, the shape of the clutter spectrum is specified to be either Gaussian, exponential, or power law; and the width of the clutter spectrum is characterized by either the one-lag autocorrelation coefficient ρ (X-band results), or by the –3-dB spectral width (L-band results). In all results, the mean Doppler frequency of the clutter spectrum is assumed to be zero.

The signal to interference power ratio SIR_o at the output of the filter is given by:

$$SIR_o = \frac{\mathbf{w}^H\mathbf{S}\mathbf{w}}{\mathbf{w}^H\mathbf{M}\mathbf{w}} \tag{6.12}$$

where $\mathbf{S} = E\{\mathbf{s}\mathbf{s}^H\}$ is the covariance matrix of the target signal and $\mathbf{M} = E\{\mathbf{d}\mathbf{d}^H\} = (P_C + P_N)\,\mathbf{M}_n$ is the covariance matrix of the interference $\mathbf{d}$ (i.e., clutter and noise). $\mathbf{M}_n$ is the normalized covariance matrix, i.e., $[\mathbf{M}_n]_{i,i} = 1$; $i = 0, 1, \ldots, N-1$. The performance of the filter is described by the definition of clutter improvement factor I, as

$$I = \frac{SIR_o}{SIR_i} \tag{6.13}$$

where SIR_i is the signal-to-interference power ratio referred to a single pulse at the input of the filter. For the optimum MTI processor (i.e., one having the weight vector $\mathbf{w} = c\mathbf{M}^{-1}\mathbf{p}$), the improvement factor is given by

$$I_c = \mathbf{p}^H\mathbf{M}_n^{-1}\mathbf{p} \tag{6.14}$$

The above discussion is applicable to the one-dimensional (1-D) ground-based case (i.e., single antenna) parameterized by f only, as opposed to the two-dimensional (2-D) airborne case (i.e., multiple effective antenna elements) parameterized by f and direction-of-arrival θ discussed in Section 6.5.3. As will be shown, Eq. (6.14) also applies to the airborne (2-D) case and to Kelly's adaptive processor [46], for expressions of $\mathbf{p}$ and $\mathbf{M}_n$ extended to apply to these cases (see Section 6.5.3).

To obtain assigned values of probability of detection P_D and probability of false alarm P_{FA}, a specified level of SIR_o at the output of the detection filter must be provided. The SIR_i which is required at the input of this filter (in dB) to ensure the required performance is given by $SIR_i|_{dB} = SIR_o|_{dB} - I_c(f)|_{dB}$. The improvement factor of the filter is different for any Doppler frequency, while SIR_o is constant. Thus a normalized visibility plot is provided by showing $[-I_c(f)|_{dB}]$ for given N. In what follows, two sets of plots are used to represent performance:

(i) *visibility curves*: the inverse of I_c (i.e., SIR_i required to leave $SIR_o = 0$ dB) as a function of the Doppler frequency f for given N;

(ii) *improvement factor plots*: I_c as a function of N, for given Doppler frequency f.

The *visibility curve* (the inverse of I_c) is a scaled (normalized) version of the required SIR_i for given N as a function of target Doppler frequency necessary to provide a specific SIR_o as required, for any given detector and target model, to ensure an assigned performance level (for example $P_D = 0.8$ with $P_{FA} = 10^{-6}$), for the differing clutter spectral shapes. That is, the visibility curve allows the determination for given N of the SIR_i that is required at the input of the radar detector to ensure the desired performance as given by $SIR_i = SIR_o/I_c$, where SIR_o is a constant. The *improvement factor plot* allows the determination of the minimum number of radar pulses N for given f that is required to provide a desired value of I_c, also for the differing clutter spectral shapes.

6.5.2.1 X-Band Results (1-D)

The X-band results to follow compare optimum MTI filter performance as given by Eq. (6.14) for corresponding Gaussian and exponential windblown ground clutter spectral shapes under breezy wind conditions. The model utilized for clutter power spectral density (PSD) is that specified in Section 6.2, particularly by Eq. (6.1) which specifies $P_{tot}(v)$ in terms of dc/ac ratio r and the ac shape factor $P_{ac}(v)$. The exponential spectral shape is modeled as specified in Section 6.2.1, particularly by Eq. (6.2) which specifies exponential spectral shape in terms of the exponential shape parameter β,β being specified as a function of wind speed (e.g., breezy, windy) in Table 6.1 and Figure 6.1. The Gaussian spectral shape is modeled as specified by Eq. (6.17) in Section 6.6.1.1, where the Gaussian shape parameter g is that required to give the same one-lag temporal autocorrelation coefficient ρ as that of the exponential spectrum under given wind conditions. This procedure is one way of normalizing the Gaussian and exponential shapes to be of equivalent extent in Doppler as a function of wind speed, the autocorrelation function being the inverse Fourier transform of the clutter power spectrum. The dc/ac ratio r in the clutter spectrum is modeled as specified in Section 6.2.2, particular by Eq. (6.4) which models r as a function of wind speed w and radar carrier frequency f_o (see also Figure 6.2). In the results to follow, $f_o = 9.2$ GHz (X-band), PRF = $1/T = 500$ Hz, and $CNR = 50$ dB.

Figure 6.27 shows two visibility curves, corresponding to exponential and Gaussian clutter spectra under breezy conditions with dc/ac ratio r = unity, and for N = 16 coherently integrated pulses. For the exponential spectrum, β = 8 s/m; for both spectra, ρ = 0.9908, and r = 0 dB. Each curve shows the SIR_i necessary to obtain $P_D = 0.8$ and $P_{FA} = 10^{-6}$ vs normalized Doppler separation fT. Both curves decay from large required values of SIR_i at low values of fT, where clutter strength is high, to bottom out at a much lower floor value of $SIR_i \cong -61$ dB at higher values of fT, the floor level being determined by the thermal noise limit. The curve for the Gaussian PSD decays much faster than the curve for the exponential PSD. That is, the MTI filter operating under the standard assumption of Gaussian clutter spectral shape significantly outperforms the MTI filter operating under the more realistic assumption of exponential clutter spectral shape. The loss in detection performance due to the exponential PSD is given by the signal power increase required by the disturbance with exponential PSD to match the performance of the disturbance with Gaussian PSD. It is evident in Figure 6.27 that this loss in detection performance caused by the exponential PSD is significant over a wide range in fT (i.e., for $0.05 < fT < 0.3$) and at its maximum becomes as large as 15 dB. Corresponding results under windy conditions (not shown here) show larger differences in performance between Gaussian and exponential PSDs, with significant detection loss due to the exponential PSD spanning $0.07 < fT < 0.4$, and becoming as large as 18 dB [32]. It is apparent that the predicted performance of the MTI processor is very sensitive to the assumed shape of the clutter Doppler spectrum.

Figures 6.28 and 6.29 show improvement factor plots under assumptions of exponential and Gaussian clutter spectra, respectively (i.e., corresponding to the visibility curves of Figure 6.27). As in Figure 6.27, wind conditions for the results of Figures 6.28 and 6.29 are breezy. Comparison between the two figures indicates that, for a normalized target Doppler frequency of $fT = 0.2$, (i.e., well within the main clutter spectral region), to obtain $I_c = -50$ dB in the presence of an exponential spectrum requires the coherent integration of N = 10 pulses, while integration of only 6–7 pulses is sufficient for a Gaussian spectrum. In passing from breezy to windy conditions, the achievable improvement factor significantly degrades (i.e., under the assumption of an exponential PSD and close to zero Doppler at $fT = 0.1$, the loss in improvement factor in passing from breezy to windy is on the order of 9 dB [32]).

6.5.2.2 L-Band Results (1-D)

The L-band results that follow parallel the X-band results of the previous subsection, except that the comparison of optimum MTI filter performance [Eq. (6.14)] is now extended to include power-law—as well as Gaussian and exponential—windblown ground clutter spectral shapes. The power-law PSD is modeled as specified by Eq. (6.18) in Section 6.6.1.2; i.e., as parameterized by the power-law exponent n which typically takes on values of n = 3 or 4. Equivalent spectral extent for given wind conditions among the three spectral shapes of Gaussian, exponential, and power-law is now specified in these L-band results in terms of equal –3-dB frequency bandwidth in the three shapes, rather than specifying equal temporal correlation coefficients as in the X-band results. A further distinction is that the L-band results are provided for "windy" (as opposed to "breezy") wind conditions, with wind speed specified at 30 mph. In the L-band results to follow, f_o = 1.23 GHz, PRF = 500 Hz, and CNR = 70 dB (as opposed to 50 dB in the X-band results). These parameters are appropriate for an L-band ground-based surveillance radar.

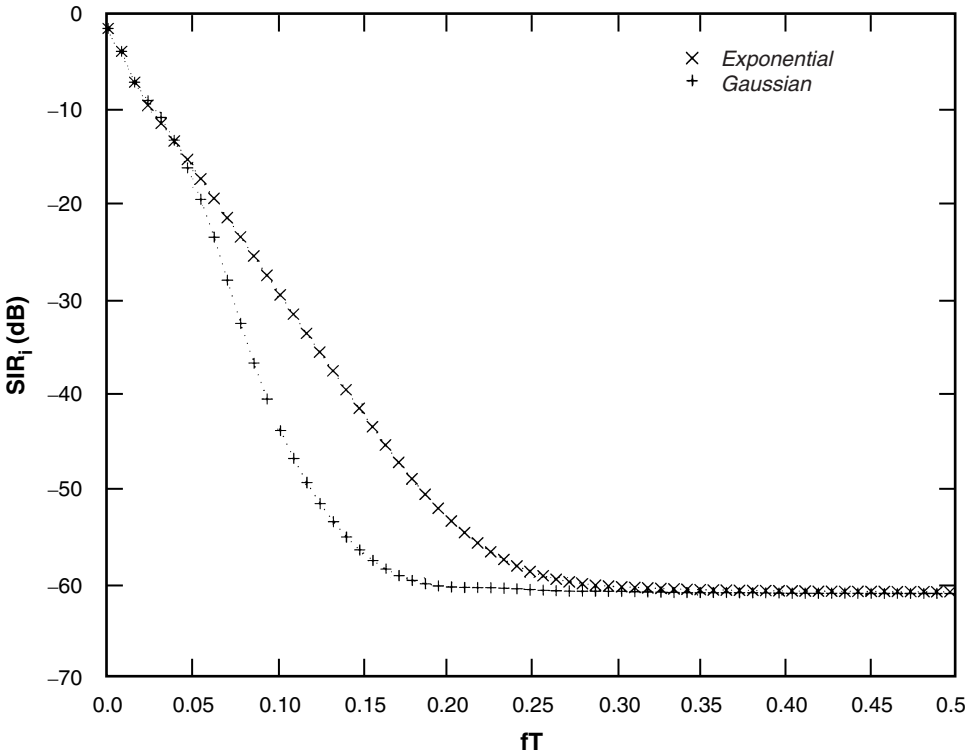

FIGURE 6.27 Comparison of X-band visibility curves (1-D case) showing SIR_i vs normalized Doppler offset fT (with $SIR_o = 0$ dB) for Gaussian and exponential clutter spectral shapes under breezy conditions and $N = 16$ coherent pulses. (Results provided by P. Lombardo, Univ. of Rome. After [32]; by permission, © 1997 IEE.)

Figure 6.30 shows L-band visibility curves for Gaussian, exponential, and power-law clutter spectral shapes under windy conditions, for integration of $N = 32$ coherent pulses. For the exponential clutter PSD, the shape parameter for windy conditions is given by $\beta = 5.7$ (see Table 6.1). The Gaussian and power-law clutter PSDs have shape parameters providing equivalent –3 dB spectral width to that of the exponential PSD. The dc/ac ratio is as specified by Eq. (6.4) for $w = 30$ mph and $f_o = 1.23$ GHz. As in the X-band results, the curve for the Gaussian-shaped clutter PSD decays much faster in Figure 6.30 than that for the more realistic exponentially-shaped clutter PSD. In the region $fT < 0.1$, performance prediction based on the exponential model requires SIR_i up to 22 dB greater than that specified by the Gaussian model. In the region $fT > 0.1$, both Gaussian and exponential PSDs are below the thermal noise level, which determines the required $SCR_i \cong -84$ dB in this region. The $n = 3$ power-law clutter PSD has a much higher spectral tail than the Gaussian or exponential PSDs (see Figures 6.44 and 6.55), resulting in much greater SCR_i being required over the complete range $0 < fT < 0.5$ to ensure the same detection performance. Performance prediction based on the $n = 3$ power-law clutter PSD is excessively pessimistic, compared to that based on the more realistic exponential clutter PSD. The $n = 4$ power-law prediction in Figure 6.30 is less pessimistic but still results in significant performance mismatch.

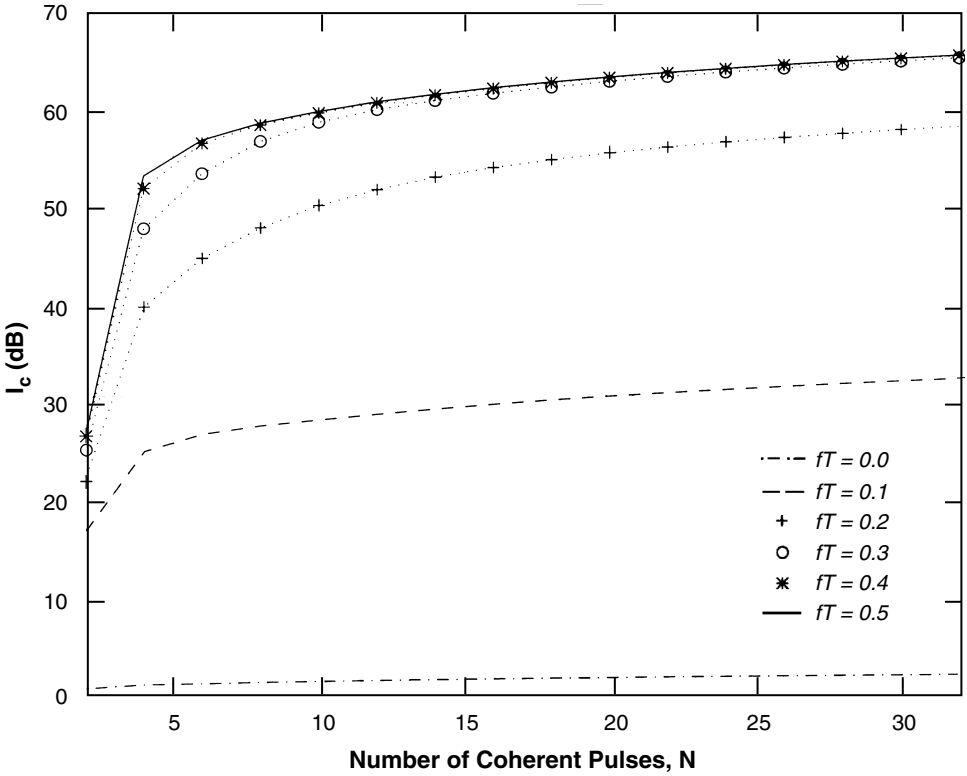

FIGURE 6.28 X-band improvement factor plots (1-D case) showing I_c vs N for breezy exponential clutter, parameterized by fT. (Results provided by P. Lombardo, Univ. of Rome. After [32]; by permission, © 1997 IEE.)

Figure 6.31 shows L-band improvement factor plots for clutter of exponential spectral shape under windy conditions (i.e., corresponding to the exponential curve of Figure 6.30) but here showing variability with number of integrated pulses N; the results are parameterized by fT. It is apparent that for high target Doppler frequencies, a small number of pulses is sufficient to yield the best performance achievable, namely, $I_c|_{\mathrm{MAX}} = CNR|_{\mathrm{dB}} + 10 \log_{10}(N)$; whereas for lower Doppler frequencies, larger numbers of pulses are necessary to converge to the same condition. Figure 6.32 compares improvement factor plots at $fT = 0.5$ and $fT = 1/16$, assuming corresponding Gaussian, exponential, and $n = 3$ power-law clutter PSDs. Unlike I_c for the Gaussian and exponential clutter PSDs, I_c for the power-law clutter PSD does not converge to the ideal performance, even at high Doppler frequencies.

6.5.3 Impact on STAP Performance

Consider an AEW radar equipped with an array of antennas with digital beam-forming capability. The detection problem is analyzed in the two-dimensional (2-D) plane of Doppler f and direction-of-arrival (DOA) θ (i.e., space-time approach [3, 4]). Assume that K channels demodulate and filter the incoming narrowband waveform received by either K antennas or K subarrays of antennas. Each channel samples the N returning pulses, thus obtaining N complex K-dimensional vectors $\{\mathbf{z}_k[i]\}_{i=0}^{N-1}$ spaced by T seconds. The N vectors are assembled into the NK-dimensional vector, $\mathbf{z} = [\mathbf{z}_1^{\mathrm{T}}, \ldots, \mathbf{z}_K^{\mathrm{T}}]^{\mathrm{T}}$. Again, the detection problem is to determine, after the vector $\mathbf{z}$ has been received, whether it consists

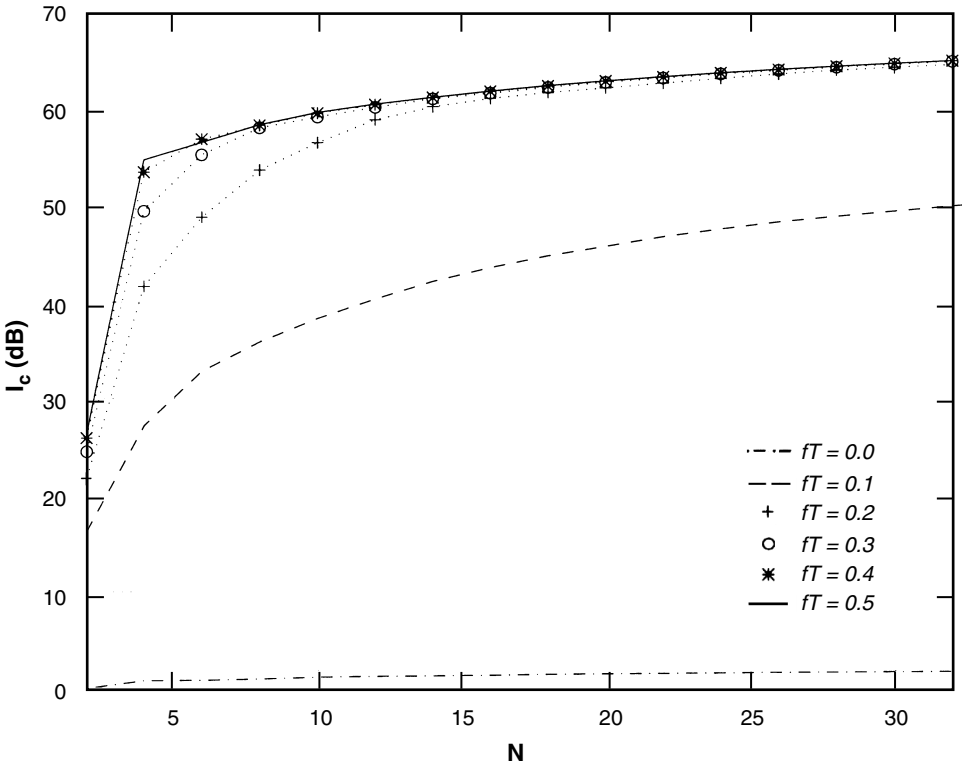

FIGURE 6.29 X-band improvement factor plots (1-D case) for breezy Gaussian clutter, parameterized by *fT*. (Results provided by P. Lombardo, Univ. of Rome. After [32]; by permission, © 1997 IEE.)

only of disturbance **d**, or, in addition to **d**, a 2-D target signal vector **s** is also received. The $(N\times K)\times 1$ target signal vector with Doppler frequency = f, DOA = θ, and complex amplitude = α is now defined as:

$$\mathbf{s}(f,\theta) = \alpha\,\mathbf{p} = \alpha[\mathbf{p}^{\mathrm{T}}{}_1(f,\theta), \mathbf{p}^{\mathrm{T}}{}_2(f,\theta), \ldots \mathbf{p}^{\mathrm{T}}{}_K(f,\theta)]^{\mathrm{T}}$$

where

$$\mathbf{p}_k(f,\theta) = e^{\,j2\pi(2d/\lambda\,\sin\theta)k}\,[1,\, e^{\,j2\pi fT}, \ldots, e^{j2\pi fT(N-1)}]^{\mathrm{T}},$$

where d is the antenna spacing. The normalized clutter covariance matrix $\mathbf{M}_c$ is a block Toeplitz matrix with blocks related to the antenna array elements. The elements of $\mathbf{M}_c$ are obtained from the space-time clutter correlation coefficient, which is usually expressed as:

$$\rho(\Delta t, \Delta s) = \rho_t(\Delta t) \quad \cdot \quad \rho_s\left(\Delta t + \frac{\Delta s}{2V}\right) \tag{6.15}$$

where for simplicity the antenna spacing is set such that $d = \lambda/2 = 2VT$ where V is the platform velocity [47, 48]. In Eq. (6.15), $\rho_t(\Delta t)$ is the temporal correlation coefficient, which depends on the temporal displacement Δt of two sequential clutter echoes. This is the only term that depends on clutter internal motion, i.e., on the clutter spectral behavior under analysis herein, which is assumed to be of either Gaussian, exponential, or power-law

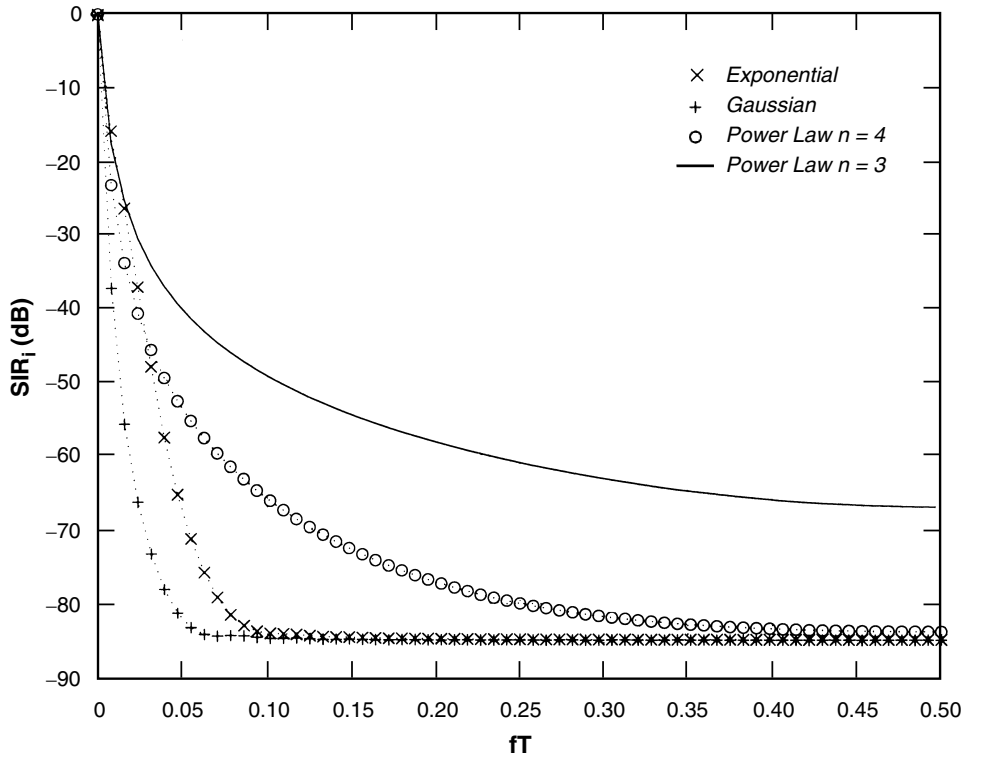

FIGURE 6.30 Comparison of L-band visibility curves (1-D case) showing SIR_i vs normalized Doppler offset fT (with $SIR_o = 0$ dB) for Gaussian, exponential, and power-law ($n = 3,4$) clutter spectral shapes under windy conditions and $N = 32$ coherent pulses. (Results provided by P. Lombardo, Univ. of Rome. After [33]; by permission, © 2001 IEEE.)

shape. The term $\rho_s(\Delta t + \Delta s/(2V))$ is the spatial correlation coefficient, which encodes the decorrelation due to the combined effect of: (i) the motion of the radar platform (and thus of the different viewing angles over the scene) and (ii) the antenna pattern. Since this term depends on the spatial position of the receivers, it is a function of both the temporal displacement Δt (which follows from the differing sequential positions of the platform in flight) and the spatial displacement Δs of the antennas in the array. The optimum detector for the signal **s** embedded in correlated Gaussian-distributed interference is given by the same matched filter as for the 1-D case that now operates in the 2-D Doppler-DOA plane with corresponding 2-D definition of target vector and interference covariance matrix [33]. As is well known, the presence of multiple receivers, corresponding to displaced phase centers, makes it possible through space-time adaptive processing (STAP) to compensate for spectral spreading due to the platform motion, thus providing a significant improvement in detection performance [3, 4, 47].

As for the 1-D case, the optimum detector for the radar target **s** embedded in Gaussian distributed clutter with zero mean value and covariance matrix **M** is given by the filter weight vector $\mathbf{M}^{-1}{}_{n}\mathbf{p}$, utilizing the 2-D definition of target vector and clutter covariance matrix. The performance parameter of interest is still I_c as specified by Eq. (6.14), which in the 2-D case is dependent on DOA θ as well as f. This same expression for I_c also characterizes the performance of a well-known adaptive detector [46] applicable to both

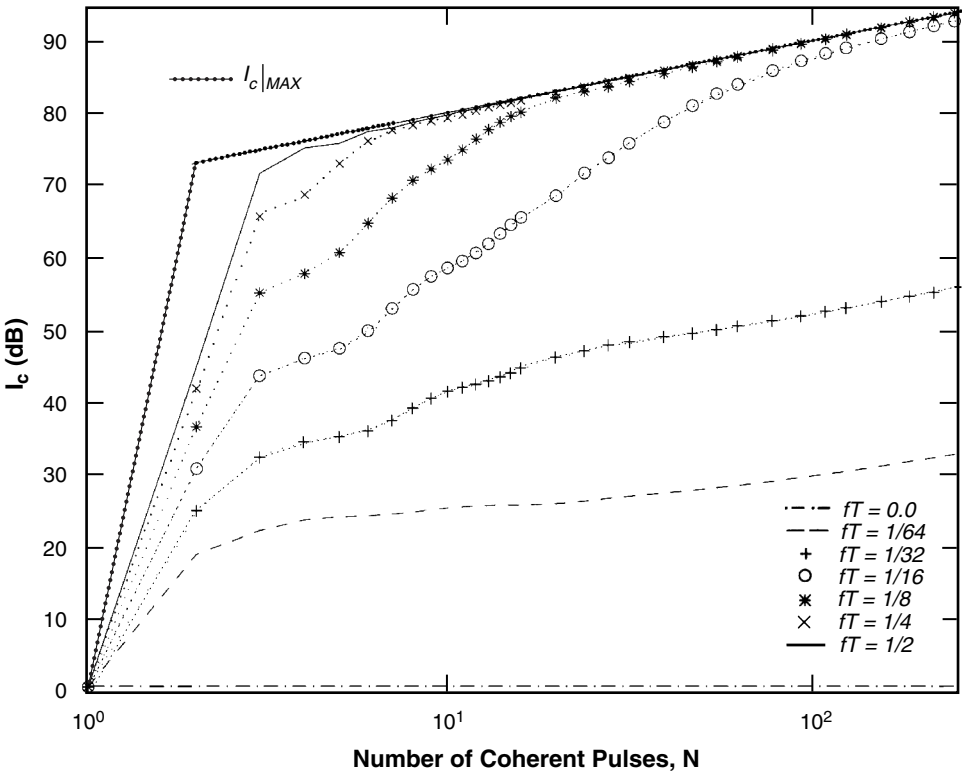

FIGURE 6.31 L-band improvement factor plots (1-D case) showing I_c vs N for windy exponential clutter, parameterized by fT. Dotted curve indicates best performance theoretically achievable, given by $I_c|_{\text{MAX}} = CNR|_{\text{dB}} + 10 \log_{10} N$. (Results provided by P. Lombardo, Univ. of Rome. After [33]; by permission, © 2001 IEEE.)

ground-based and airborne surveillance radar designed to work in nonhomogeneous and nonstationary clutter environments [33].

For simplicity, results to follow are presented for detection of a target at antenna broadside aspect (DOA = $\theta = 0$). Compared to the 1-D case of ground-based radar, the 2-D case of airborne radar has an extra parameter that influences detection performance, namely, the number of receivers K. In consequence, the two kinds of results, i.e., visibility curves and improvement factor plots described in Section 6.5.2, now each replicate for all possible values of K. However, it is usual in space-time processing to consider detection performance as a function of the number of degrees of freedom (DOF) given by the product $N \times K$ [3, 33, 47–49]. This product corresponds to the number of parameters that can be arbitrarily selected in the detection filter, this number having direct implication on the complexity of the required signal processor. Therefore, the results to follow compare the effect of different clutter spectral shapes on radar performance, assuming $N \times K = 64$. As in the 1-D case, two sets of plots are also used to represent system performance in the 2-D case:

(i) *visibility curves*: inverse of I_c as a function of the Doppler frequency f for given N (with constant $N \times K = 64$ and $\theta = 0$);

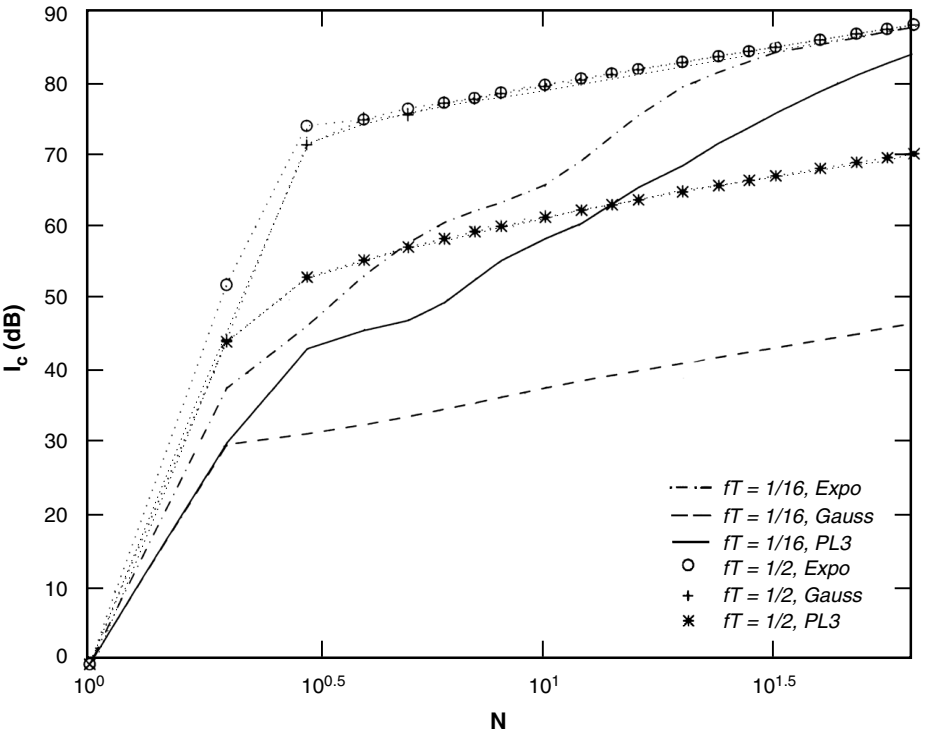

FIGURE 6.32 Comparison of L-band improvement factor plots (1-D case) for Gaussian, exponential, and power-law ($n = 3$) clutter spectral shapes under windy conditions, at $fT = 1/16$ and 1/2. (Results provided by P. Lombardo, Univ. of Rome. After [33]; by permission, © 2001 IEEE.)

(ii) *improvement factor plots*: I_c as a function of N (with constant $N \times K = 64$ and $\theta = 0$), for given Doppler frequency f.

In the generation of these plots for the airborne (2-D) case, it is necessary to quantify the spatial correlation coefficient ρ_s. This term is independent of clutter spectral behavior and depends mainly on the along-track antenna pattern. The results to follow assume a transmitter antenna pattern with a Gaussian main lobe and two Gaussian sidelobes, 25 and 40 dB, respectively, below the peak, and at normalized angles of 0.2 and 0.4, respectively, on both sides of the peak. These five antenna lobes are characterized by the same width, which corresponds to a one-lag spatial correlation coefficient of 0.995 [47].

6.5.3.1 X-Band Results (2-D)

The X-band results to follow compare STAP system performance (i.e., 2-D case) for corresponding Gaussian and exponential windblown ground clutter spectral shapes under breezy conditions. The same methodology for modeling the clutter spectra and the same values of radar parameters are utilized as specified at the beginning of Section 6.5.2.1 in the 1-D X-band case. Figures 6.33 and 6.34 show visibility plots for exponential and Gaussian clutter PSDs, respectively, under breezy conditions with dc/ac ratio r = unity. Various curves are shown in these two figures for different combinations of N and K, thus exchanging temporal DOF for spatial DOF. The optimum number of pulses is on the order of $N = \sim 16$, which provides the lowest SIR_i value needed to achieve assigned values of P_D

for fixed values of P_{FA}. The undulations of the curve for $N = 64$ are caused by the two antenna sidelobes in this degenerate case of $K = 1$. Such undulations appear when the number of spatial DOF is so low as to allow little cancellation to be possible. Comparison

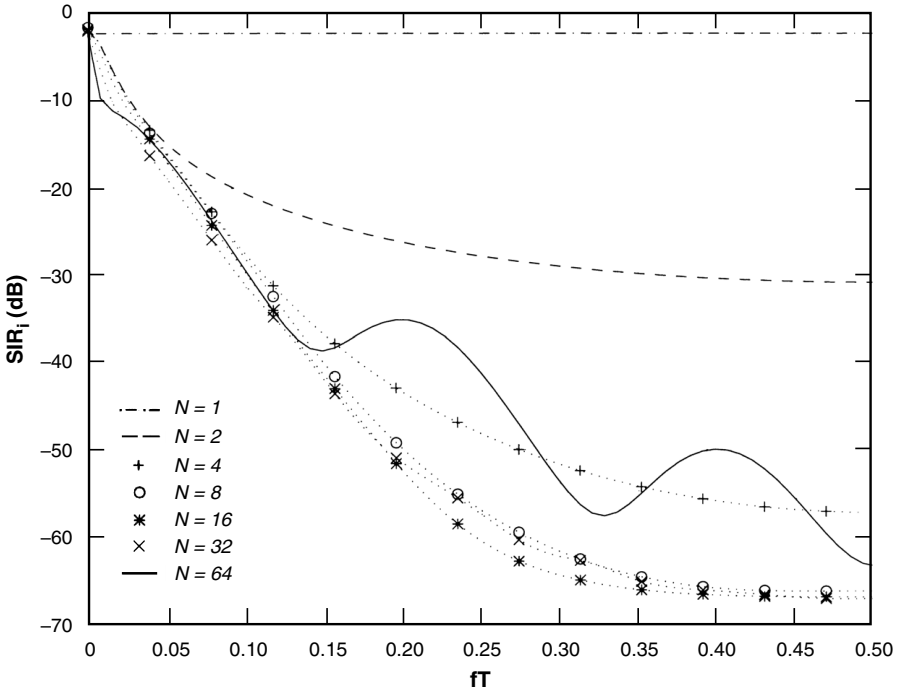

FIGURE 6.33 X-band visibility curves (2-D case) showing SIR_i vs fT (with $SIR_o = 0$ dB) for breezy exponential clutter, parameterized by number of coherent pulses N (where $N \times K = 64$, $\theta = 0$). (Results provided by P. Lombardo, Univ. of Rome. After [32]; by permission, © 1997 IEE.)

between the results of Figures 6.33 and 6.34 reveals that the detection loss incurred by the airborne MTI processor in this 2-D example under the realistic assumption of an exponential clutter PSD as opposed to the more common assumption of a Gaussian clutter PSD can be as much as 10 dB.

Figures 6.35 and 6.36 show improvement factor plots assuming exponential and Gaussian clutter PSDs, respectively, corresponding to the visibility curves of Figures 6.33 and 6.34. These figures indicate that for target Doppler frequencies well within the main clutter spectral region, i.e., for $fT = 0.1$ or 0.2, the MTI performance assuming Gaussian clutter significantly exceeds that assuming exponential clutter by amounts on the order of 8 to 10 dB for various numbers N of pulses integrated. In addition, the improvement factor I_c is much less sensitive to the number of temporal DOF N with the exponential spectrum than with the Gaussian spectrum, indicating that selection of the optimum ratio of temporal to spatial DOF depends on the assumed shape of the clutter spectrum. As in the 1-D case, in passing from breezy to windy conditions, the achievable improvement factor significantly degrades (i.e., under the assumption of an exponential PSD, and close to zero-Doppler at $fT = 0.1$, the loss in 2-D improvement factor in passing from breezy to windy is ≈10 dB [32]).

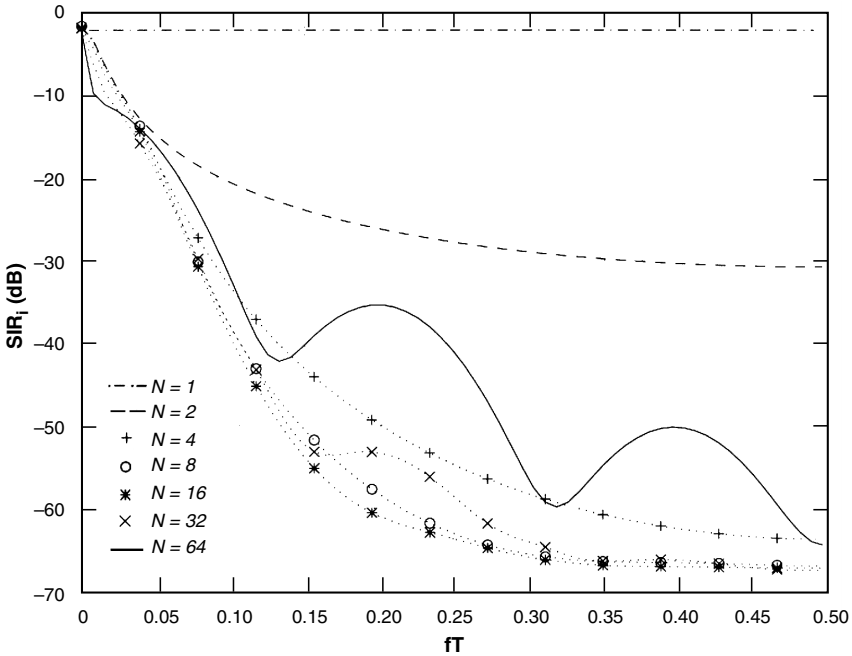

FIGURE 6.34 X-band visibility curves (2-D case) for breezy Gaussian clutter, parameterized by N (where $N \times K = 64$, $\theta = 0$). (Results provided by P. Lombardo, Univ. of Rome. After [32]; by permission, © 1997 IEE.)

6.5.3.2 L-BAND RESULTS (2-D)

The 2-D L-band results to follow compare STAP system performance for different assumed shapes of clutter spectra using the same methodology for modeling the clutter spectra and using the same values of radar parameters as specified at the beginning of Section 6.5.2.2 for the 1-D L-band case. Figures 6.37, 6.38, and 6.39 show 2-D L-band visibility plots for exponential, Gaussian, and $n = 3$ power-law clutter PSDs, respectively, under windy conditions and for various numbers N of coherently integrated pulses as processed by the optimum space-time processor. In all three figures, the undulations in the curve for $N = 64$ are caused by effects of the two antenna sidelobes in this single-antenna-element case, as mentioned in the previous subsection. For the Gaussian and exponential clutter PSDs, the optimum number of pulses to provide the lowest SIR_i needed to achieve assigned values of P_D for fixed values of P_{FA} is $N = 8$. In contrast, for the $n = 3$ power-law clutter PSD, the optimum number of pulses is $N = 32$.

Figure 6.40 compares the Gaussian, exponential, and $n = 3$ power-law visibility plots for $N = 8$ and $N = 32$ together in one figure. At $N = 32$, the results for Gaussian and exponential clutter still show residuals of the space-time cancelled sidelobes. It is apparent in these results that a significant loss in performance (i.e., as much as 10 dB) occurs over a wide range in target Doppler frequencies (i.e., $0 < fT < 0.3$) when using the realistic exponential spectrum compared to the more commonly used Gaussian spectrum. However, the additional loss in performance that occurs in utilizing an $n = 3$ power-law clutter spectrum is generally very much greater (i.e., as much as 30 dB) and extends over all available Doppler frequencies (i.e., $0 < fT < 0.5$). That is, the predictions based on the power-law model require a very much higher SIR_i at the system input to obtain the same

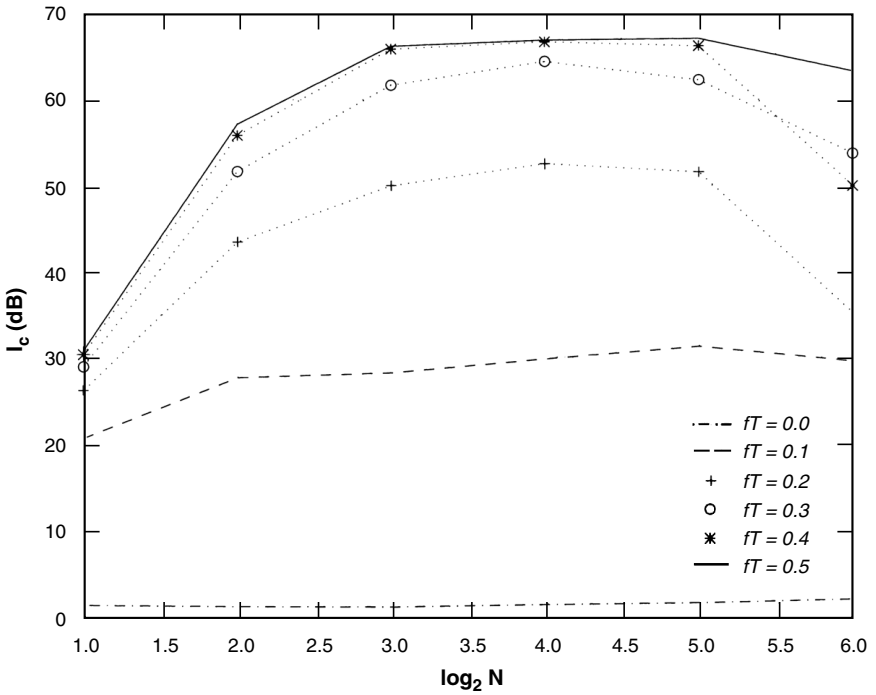

FIGURE 6.35 X-band improvement factor plots (2-D case) showing I_c vs $\log_2 N$ for breezy exponential clutter, parameterized by fT (with $N \times K = 64$, $\theta = 0$). (Results provided by P. Lombardo, Univ. of Rome. After [32]; by permission, © 1997 IEE.)

detection performance as with the Gaussian or exponential models, and the impact of the space-time cancellation is very much lower for the power-law model due to the very slow decay of the power-law spectral tails. This slow decay also masks the effects of the antenna sidelobes at $K = 2$ using the power-law model, such effects being clearly evident in the corresponding results using the other two models.

Figure 6.41 shows 2-D L-band improvement factor plots for windy exponential clutter PSD corresponding to the visibility plots for exponential clutter shown in Figures 6.37 and 6.40. Since clutter PSD modeled to be of exponential shape most closely matches the measured spectral clutter data as discussed elsewhere throughout Chapter 6 (e.g., see Figures 6.5, 6.21, 6.54), the modeled results for I_c under windy conditions shown in Figure 6.41 are the best estimate of actual L-band clutter cancellation performance to be expected. The data indicate that the optimum number of integrated pulses N to maximize I_c for the various parameterized values of target Doppler frequency fT shown is usually such that $N \cong K$, in agreement with approximate theoretical expectations discussed elsewhere [48, 49] in this regard.

Figure 6.42 compares 2-D L-band improvement factor plots for windy Gaussian, exponential, and $n = 3$ power-law clutter PSDs at two values of fT, viz., $fT = 1/32$ and $1/2$. At $fT = 1/32$ (i.e., well within the main region of clutter Doppler extent and, in fact, quite close to zero-Doppler), the prediction based on Gaussian clutter significantly overestimates I_c (by 13 dB for $N = 8$ pulses) and the prediction based on $n = 3$ power-law clutter significantly underestimates I_c (by 10 dB at $N = 8$ pulses) compared to the more realistic prediction based on exponential clutter PSD. At $fT = 1/2$ (i.e., at the highest target Doppler

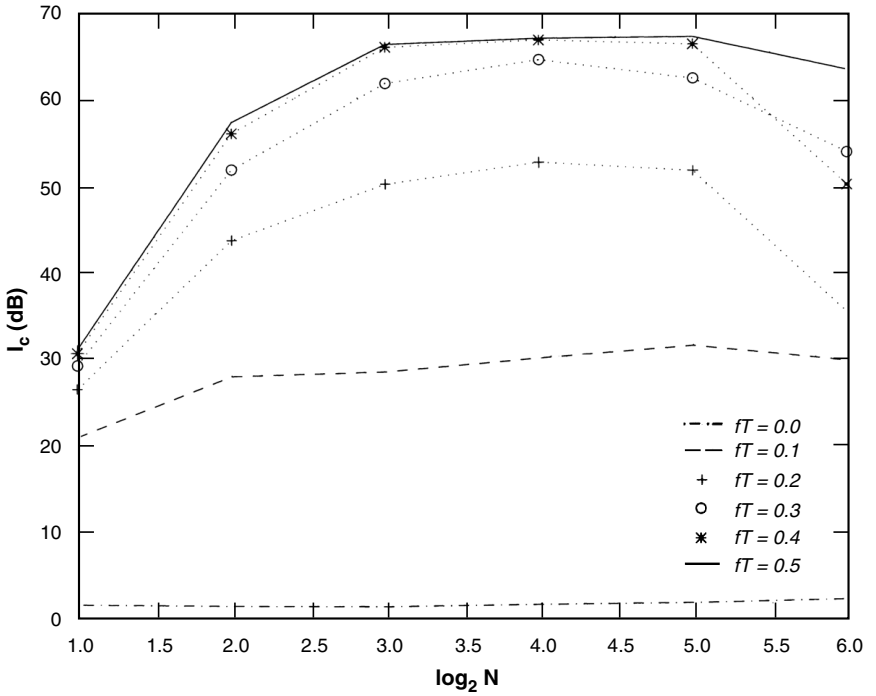

FIGURE 6.36 X-band improvement factor plots (2-D case) for breezy Gaussian clutter, parameterized by fT (with $N \times K = 64$, $\theta = 0$). (Results provided by P. Lombardo, Univ. of Rome. After [32]; by permission, © 1997 IEE.)

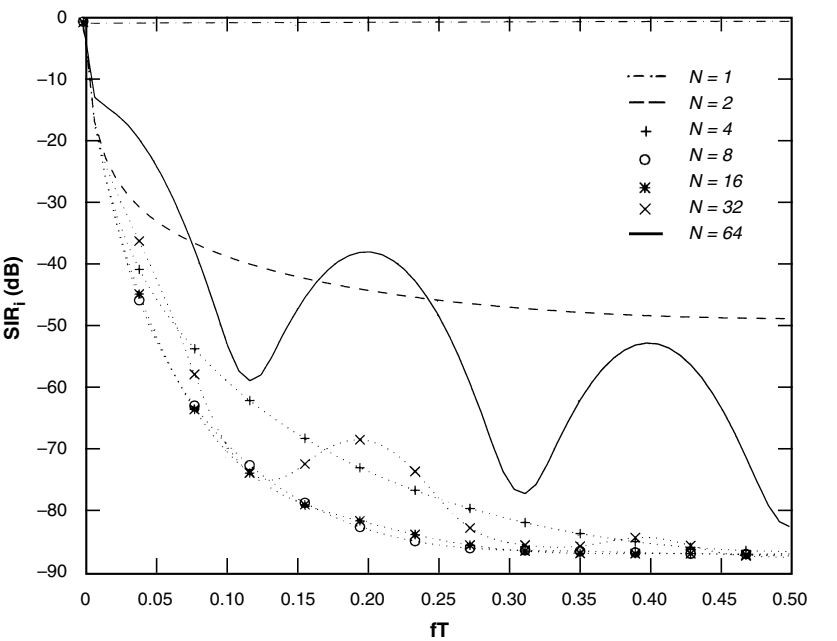

FIGURE 6.37 L-band visibility curves (2-D case) showing SIR_i vs fT (with $SIR_o = 0$ dB) for windy exponential clutter, parameterized by number of coherent pulses N (where $N \times K = 64$, $\theta = 0$). (Results provided by P. Lombardo, Univ. of Rome. After [33]; by permission, © 2001 IEEE.)

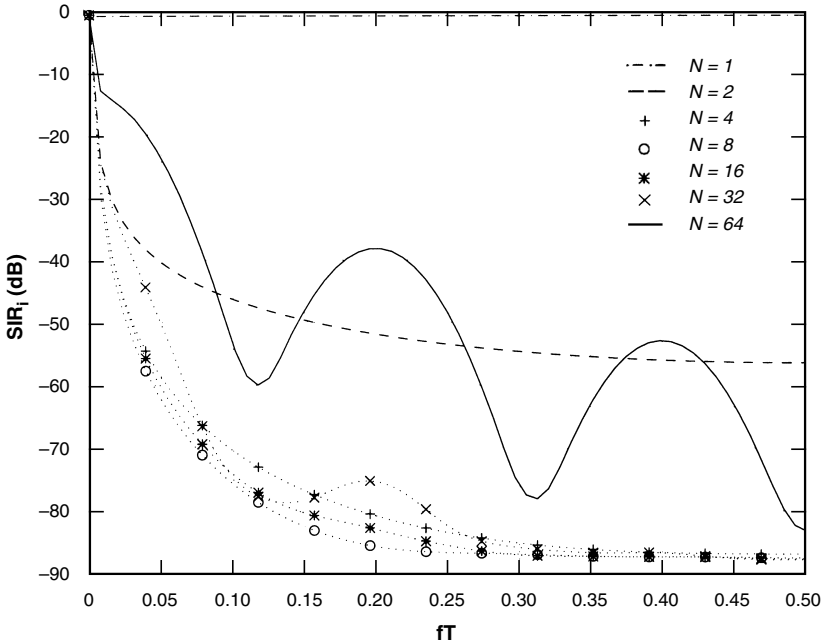

FIGURE 6.38 L-band visibility curves (2-D case) for windy Gaussian clutter, parameterized by N (where $N \times K = 64$, $\theta = 0$). (Results provided by P. Lombardo, Univ. of Rome. After [33]; by permission, © 2001 IEEE.)

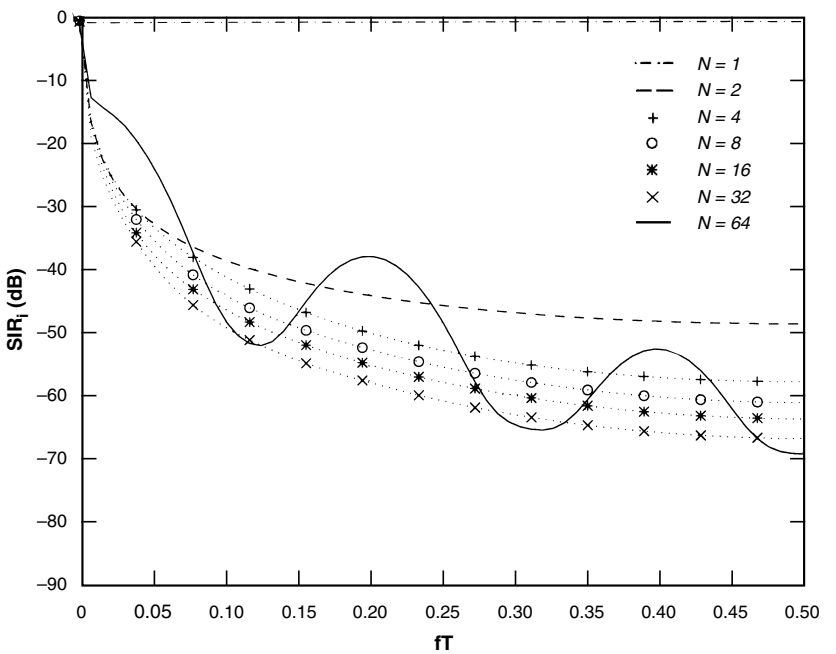

FIGURE 6.39 L-band visibility curves (2-D case) for windy power-law ($n = 3$) clutter, parameterized by N (where $N \times K = 64$, $\theta = 0$). (Results provided by P. Lombardo, Univ. of Rome. After [33]; by permission, © 2001 IEEE.)

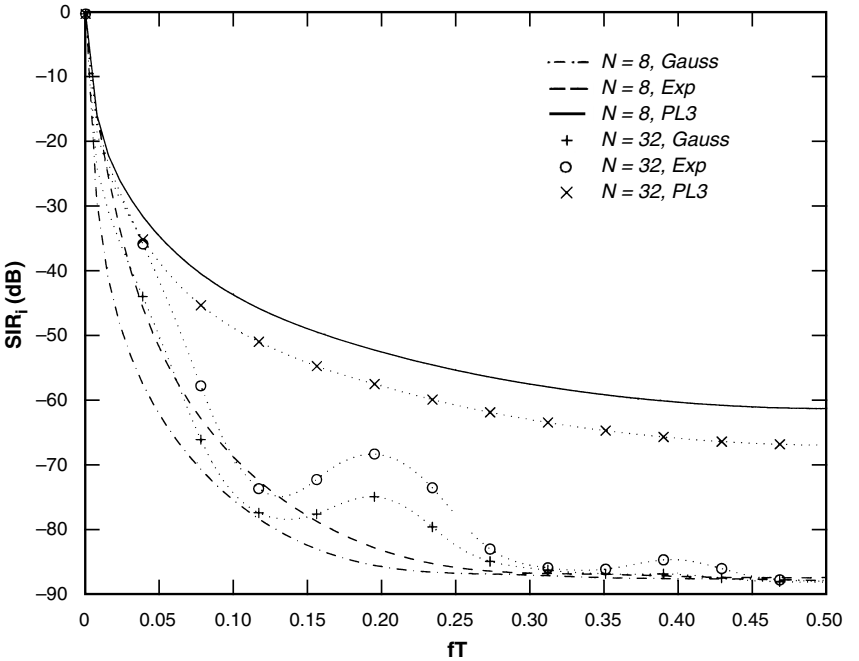

FIGURE 6.40 Comparison of L-band visibility curves (2-D case) for Gaussian, exponential, and power law ($n = 3$) clutter spectral shapes under windy conditions, for $N = 8$ and 32 coherent pulses (where $N \times K = 64$, $\theta = 0$). (Results provided by P. Lombardo, Univ. of Rome. After [33]; by permission, © 2001 IEEE.)

frequency), the predictions for I_c based on the Gaussian and exponential models are essentially identical since the clutter for both these models is well below thermal noise at such high Doppler, with the result that the performance for these two models at $fT = 1/2$ is dependent only on thermal noise. In contrast, the estimated clutter cancellation performance using the $n = 3$ power-law clutter PSD model at $fT = 1/2$ is much poorer (i.e., is far too pessimistic, by 25 dB for $N = 8$ pulses) since the power-law clutter spectral tail is still well above thermal noise even at such high Doppler.

6.5.4 Validation of Exponential Clutter Spectral Model

Elsewhere, Chapter 6 (e.g., Figures 6.5, 6.21, 6.54) shows that measured shapes of windblown ground clutter Doppler spectra appear to be much more closely matched by an exponential approximation than by Gaussian (too narrow) or power-law (too wide) approximations. The preceding subsections in Section 6.5 show that large differences exist in predictions of MTI clutter improvement factor I_c between that based on what appears to be a realistic exponential clutter spectral shape and those based on more traditional Gaussian and power-law clutter spectral shapes. Compared to the exponential shape, the Gaussian shape substantially underpredicts the effects of clutter, and the power-law shape substantially overpredicts the effects of clutter. This section validates the exponential spectral model for windblown foliage by showing that the differences in improvement factor performance prediction between using actual measured I/Q data as input to the clutter canceller, and modeled clutter data of Gaussian, exponential, or power-law spectral shape, are minimized when the spectral model employed is of exponential shape.

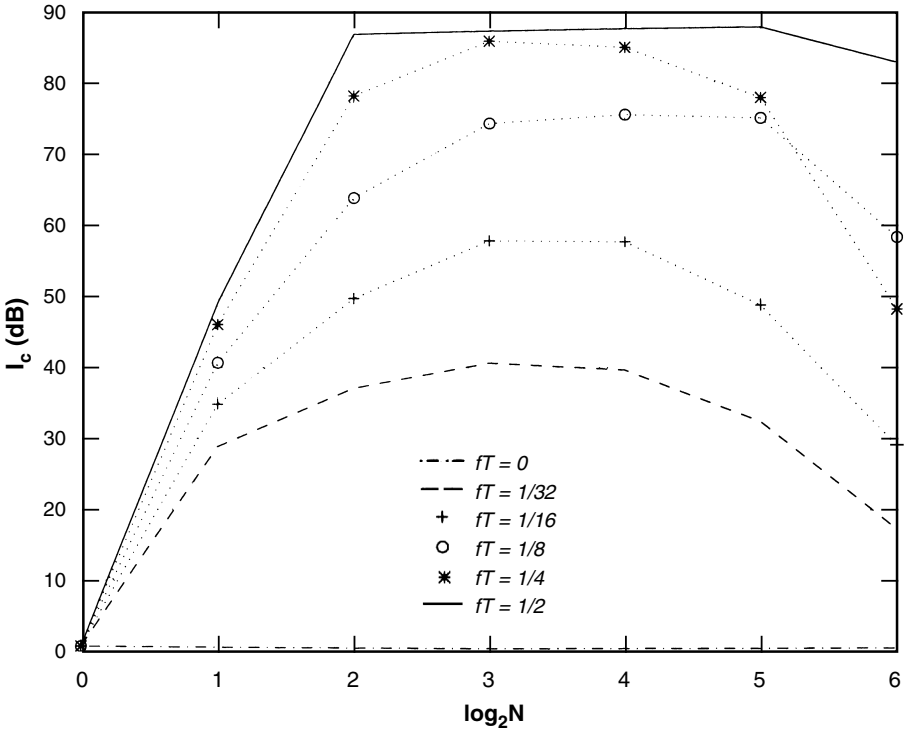

FIGURE 6.41 L-band improvement factor plots (2-D case) showing I_c vs $\log_2 N$ for windy exponential clutter, parameterized by fT (where $N \times K = 64$, $\theta = 0$). (Results provided by P. Lombardo, Univ. of Rome. After [33]; by permission, © 2001 IEEE.)

To compare performance predictions obtained by using each of the three clutter spectral models (i.e., Gaussian, exponential, and power-law) to the performance actually obtained using measured I/Q clutter data, the following procedure is established. First, within the database of long-time-dwell clutter measurements from windblown trees, a typical experiment is selected, within which a typical clutter cell (i.e., range gate) is further selected such that the temporally-varying I/Q data from the cell are Gaussian-distributed (i.e., the clutter amplitude is Rayleigh-distributed—see Figure 5.A.16—indicative of purely windblown foliage within the cell, without significant contributions from stationary discrete sources embedded within the trees which would lead to Ricean-distributed clutter amplitudes—see Figure 4.22). The clutter Doppler spectrum from the selected cell is generated from the measured I/Q data for that cell. This measured clutter spectrum is then best-fitted [i.e., utilizing a minimum least squares (MLS) procedure] by each of the three clutter spectral models in turn, resulting in three sets of fit parameters defining theoretical clutter models of Gaussian, exponential, and power-law spectral shape. The parameters for each theoretical clutter model are used to define a corresponding clutter covariance matrix for each model. Each theoretical clutter model is then used to specify an optimum MTI matched filter such that the covariance matrix of the theoretical clutter at the filter input and the filter design covariance matrix are identical. Next, the actual measured I/Q ground clutter data from the cell under consideration is input to each of these three filters in turn, and the measured improvement factor I_m is determined for each filter as the ratio between input and output clutter power. Note that, in each of the three cases, I_m is based on a mismatch between the actual measured I/Q input data (which do not provide perfect Gaussian, exponential, or

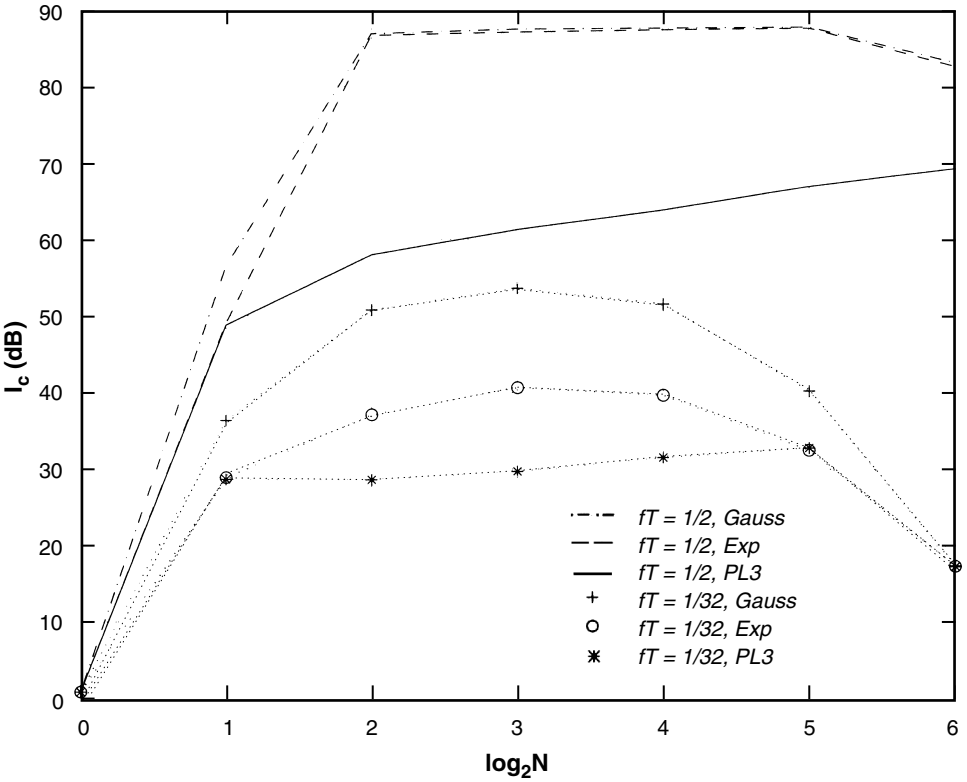

FIGURE 6.42 Comparison of L-band improvement factor plots (2-D case) for Gaussian, exponential, and power-law ($n = 3$) clutter spectral shapes under windy conditions, for $fT = 1/32$ and 1/2 (where $N \times K = 64$, $\theta = 0$). (Results provided by P. Lombardo, Univ. of Rome. After [33]; by permission, © 2001 IEEE.)

power-law spectral shape) and the filter (which is specified based on a theoretical clutter model of perfect Gaussian, exponential, or power-law spectral shape).

It is now necessary, in each of the three cases, to compare the measured value of I_m obtained as described above using the actual measured I/Q clutter data as input to the filter with the theoretical value I_c that applies, assuming the filter is perfectly matched; i.e., assuming that the input data are synthetic data such as to give the perfect Gaussian, exponential, or power-law spectral shapes obtained by best-fitting each to the measured spectrum. Also assumed is that the temporal variation is Gaussian. In each of the three cases, I_c is given by Eq. (6.14), which assumes that the covariance matrix of the theoretical clutter at the filter input and the filter design matrix are the same. In each case, the appropriate figure of merit is the ratio ΔI of the measured improvement factor I_m in the mismatched case to the theoretical improvement factor I_c in the matched case. Thus, in each case, $\Delta I = I_m/I_c$; and, in turn, $\Delta I|_{\text{Gaussian}}$, $\Delta I|_{\text{exponential}}$, and $\Delta I|_{\text{power-law}}$ are computed for the particular clutter cell under consideration. For the specific technical details involved in carrying out these computations, refer to the original technical journal articles [30, 31, 33].

The figure of merit ΔI indicates the error in MTI filter performance resulting from the mismatch between the actual measured I/Q data and the assumption that the data are of

either Gaussian, exponential, or power-law in spectral shape. The closer ΔI is to unity (i.e., 0 dB), the better that the particular clutter spectral model (Gaussian, exponential, or power-law) represents the measured clutter data in terms of the impact of the clutter data on the clutter canceller. If ΔI = unity (i.e., 0 dB), it indicates that the input I/Q clutter data provide a clutter spectral shape that is perfectly Gaussian, exponential, or power-law.

Figure 6.43 shows typical results for $\Delta I|_{\text{Gaussian}}$, $\Delta I|_{\text{exponential}}$, and $\Delta I|_{\text{power-law}}$, for one particular clutter cell containing windblown trees, utilizing $N = 8$ coherently integrated

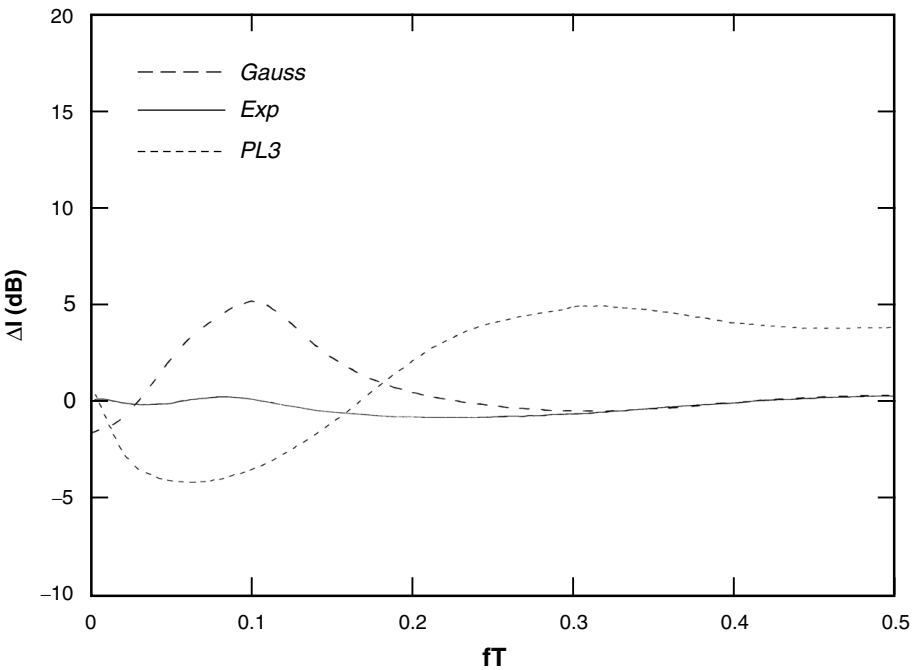

FIGURE 6.43 Differences in improvement factor (i.e., ΔI) between using measured X-band I/Q clutter data (35th range cell) as input to processor (1-D case), and theoretical clutter data of Gaussian, exponential, and power-law ($n = 3$) spectral shapes (each best fitted to the measured spectrum), vs normalized Doppler frequency fT, for $N = 8$ coherent pulses. (Results provided by P. Lombardo, Univ. of Rome, and F. Gini and M. Greco, Univ. of Pisa. After [33]; by permission, © 2001 IEEE.)

pulses. The measurement cell utilized is the 35th range cell in an X-band experiment (of HH-polarization) that was conducted at Katahdin Hill under windy conditions (20 to 30 mph). It is clearly evident in Figure 6.43 that the exponential model exhibits the lowest ΔI; i.e., for the exponential model, the predicted improvement factor I_c and the actual improvement factor I_m (as obtained using the measured I/Q clutter data to feed the clutter canceller) are very nearly equal. The errors ΔI for the Gaussian model occur, as expected, at lower values of fT; at higher values of fT, the predictions based on both Gaussian and exponential clutter models transition to limitations caused by thermal noise. Also as expected, the errors in ΔI for the power-law model (of power-law exponent $n = 3$) occur over the full range $0 < fT < 0.5$ due to the slow decay of the power-law spectral tails.

The results for ΔI shown in Figure 6.43 are generally representative of similar results for other numbers N of integrated pulses, and for data from other tested range cells and other tested experiments at L-band as well as X-band. Such results validate the exponential clutter spectral model as described in Section 6.2 as being most realistic with which to model windblown radar ground clutter spectra, and indicate that the more commonly used Gaussian and power-law models (as described hereafter in Section 6.6) are comparatively unsatisfactory. The ramifications of improvement factor prediction error ΔI to prediction error in P_D and P_{FA} are discussed in the references [30, 31, 33].

6.6 Historical Review

6.6.1 Three Analytic Spectral Shapes

In comparing different analytic forms for the shape of the ac component of the windblown clutter Doppler velocity spectrum $P_{ac}(v)$ [see Eq. (6.1)], it is necessary to base the comparison on equivalent total ac spectral power, and it is convenient to maintain total ac spectral power at unity. Such normalization is seldom implemented in representations of clutter spectra. Figure 6.44 shows examples of the three forms for $P_{ac}(v)$ to be discussed subsequently, namely Gaussian, power law, and exponential, in each of which

$$\int_{-\infty}^{\infty} P_{ac}(v)dv = 1 \quad .$$

As a result, the power density levels at any value v for these three spectral shapes as shown in Figure 6.44 are directly comparable on an equivalent total ac power basis.

The ac spectral shape function $P_{ac}(v)$ may be decomposed as

$$P_{ac}(v) = K_\eta \cdot k_\eta(v) \tag{6.16}$$

where η is a shape parameter, K_η is a normalization constant set so that

$$\int_{-\infty}^{\infty} P_{ac}(v)dv = 1 \quad ,$$

and $k_\eta(v)$ is the unnormalized shape function with $k_\eta(0) = 1$. Often, historically, K_η is omitted and only $k_\eta(v)$ is shown in plots such as Figure 6.44 with the zero-Doppler peak at 0 dB. In such cases, at best the shape parameter η of each individual spectral representation is all that remains for adjustment to equivalent total ac spectral power, where in fact it is the shape parameter that should be used to match to experimental data, or at worst (often the case) no attempt is made to compare spectra on an equivalent total ac spectral power basis at all. In short, in comparing different analytic spectral representations, it is not rigorously proper to simply set their zero-Doppler peaks each at unity (i.e., 0 dB).

In the examples shown in Figure 6.44, spectral extent of the exponential representation lies between that of the Gaussian (narrow) and that of the power law (wide). The following subsections consider the origins of these three analytic expressions that have been used in the past to represent the shape of the Doppler frequency or velocity spectrum of windblown ground clutter, and in particular the rate of decay with increasing Doppler in the tail of the spectrum. It is evident in Figure 6.44 that the historical Gaussian and power-law representations match the Lincoln Laboratory-based exponential representation reasonably

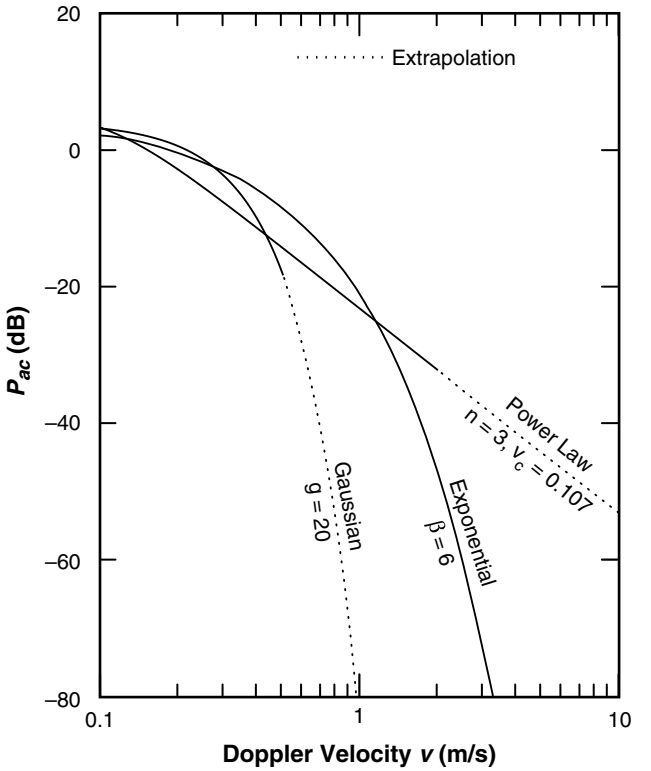

FIGURE 6.44 Three analytic spectral shapes, each normalized to unit spectral power. The $g = 20$ Gaussian curve corresponds to Barlow's [7] measurement. The $n = 3$ power-law curve corresponds to Fishbein et al.'s [10] measurement. The $\beta = 6$ exponential curve represents much of the Phase One and LCE data.

well (i.e., at least to within an order of magnitude) over the upper levels of clutter spectral power that lie within the dynamic ranges (solid lines) of these historical measurements; but that extrapolations of the historical representations (dotted lines) to much lower levels of spectral power differ by many orders of magnitude from the Lincoln Laboratory measurements at these low levels.

6.6.1.1 Gaussian Spectral Shape

Radar ground clutter power spectra were originally thought to be of approximately Gaussian shape [6–9]. The Gaussian spectral shape may be represented analytically as

$$P_{ac}(v) = \sqrt{\frac{g}{\pi}} \cdot \exp(-gv^2), \quad -\infty < v < \infty \tag{6.17}$$

where g is the Gaussian shape parameter, $K = \sqrt{g\pi}$ is the normalization constant, $k(v) = \exp(-gv^2)$, and

$$\int_{-\infty}^{\infty} P_{ac}(v)dv = 1 \quad .$$

To convert to $P_{ac}(f)$ in Eq. (6.17) where f is Doppler frequency, i.e., $P_{ac}(f)\,df = P_{ac}(v)dv$, replace v by f and g by $(\lambda/2)^2 g$. The standard deviation of the Gaussian spectrum of Eq. (6.17) is given by $\sigma_g = 1/(\sqrt{2}g)$ in units of m/s. In a much-referenced [1, 27, 50] early paper, Barlow [7] presents measured L-band ground clutter power spectra approximated by the Gaussian shape to a level 20 dB below the peak zero-Doppler level and to a maximum Doppler velocity of 0.67 m/s. Figure 6.45 shows Barlow's ground clutter spectra $k(v)$ as plotted originally, except here vs Doppler velocity v rather than Doppler frequency f. Recall that $k(v)$ is the unnormalized ac shape function such that $k(0) = 1$, so the spectra plotted in Figure 6.45 are not shown on an equivalent total ac power basis.

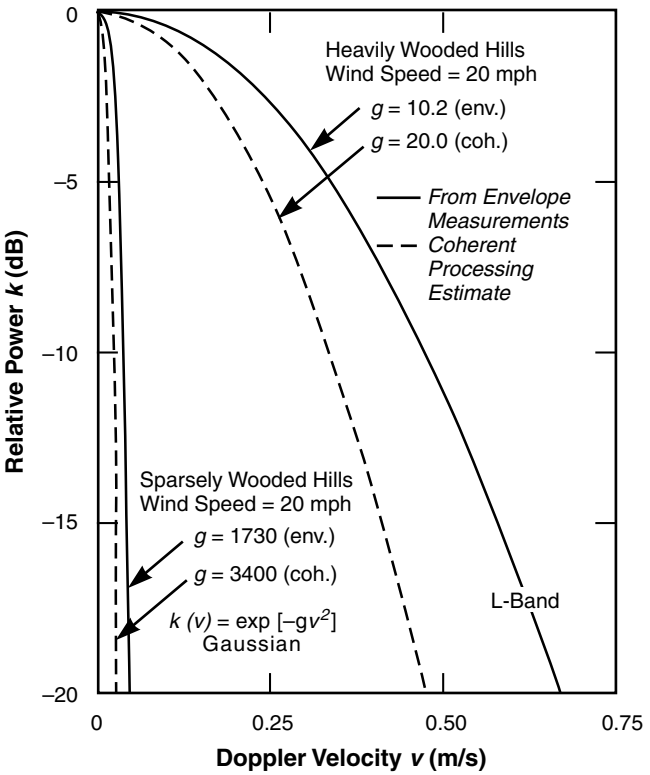

FIGURE 6.45 Measurements of radar ground clutter power spectra by Barlow. (After [7]; by permission, © 1949 IEEE.)

Barlow's spectral results were obtained from radar envelope measurements as opposed to coherent processing. For a Gaussian-shaped spectrum, the width of the envelope spectrum is approximately 1.4 times the width of the coherent spectrum [51,52]. That is, in Eq. (6.17), $g_{\text{coherent}} \approx (1.4)^2\, g_{\text{envelope}}$. On this basis, estimates of the shapes of the coherent spectra corresponding to Barlow's envelope spectra are also shown in Figure 6.45. The resulting g = 20.04 coherent-spectrum $k(v)$ curve shown in Figure 6.45 for heavily wooded hills under 20 mph winds corresponds to the Gaussian $g = 20$ $P_{ac}(v)$ curve shown in Figure 6.44.

Early observations at the MIT Radiation Laboratory [8, 9] were that the shapes of power spectra from precipitation, chaff, and sea echo were "roughly Gaussian" and that the shape of the spectrum from land clutter was "roughly similar" but with differences from Gaussian

shape "somewhat more pronounced." The explanation for clutter spectra of approximately Gaussian shape is loosely based on the idea that windblown vegetation consists fundamentally of a random array of elemental moving scatterers, each with a constant translational drift velocity. If the distribution of radial velocities of such a group of scatterers were approximately Gaussian, they would generate an approximately Gaussian-shaped power spectrum. However, consider if the motion of the scatterers also were to include an oscillatory component to represent branches and leaves blowing back and forth in the wind. It is well known [53] that simple harmonic angle modulation (frequency or phase) generates an infinite series of sidebands so that an array of oscillating scatterers would be expected to generate a wider spectrum than an array of scatterers each with only a constant drift velocity.

Indeed, in 1967 Wong, Reed, and Kaprielian [29] provided an analysis of the scattered signal and power spectrum from an array of scatterers, each with random rotational (oscillatory) motion as well as a constant random drift velocity. Under assumptions of Gaussianly distributed drift and rotational velocities, Wong et al. [29] showed that the power spectrum of the scattered signal is the sum of six components. Li [19] subsequently provided further interpretation of these six components, as follows. If scatterer rotation is absent, the Wong et al. expression for the clutter spectrum degenerates to Barlow's simple Gaussian expression, i.e., Eq. (6.17). However, with scatterer rotation present, five additional Gaussian components arise, all of which decay more slowly and all but one of which are offset from zero-Doppler (by ± 2 and ± 4 times the rotational velocity). As a result, these five additional Gaussian terms that come into play with scatterer rotation act to "spread" the spectrum beyond that of the simple Gaussian of Eq. (6.17). Narayanan et al. [42] returned to Wong's formulation of offset Gaussians in modeling some later-acquired X-band windblown clutter spectral measurements.

In 1965, two years before the publication of the Wong et al. paper [29], Bass, Bliokh, and Fuks [54] also provided a theoretical study of scattering from oscillating reradiators to model scattering from windblown vegetation. In the Bass et al. paper, the reradiators were modeled to be decaying oscillators randomly positioned on a planar surface. In their analysis, Bass et al. showed that the power spectrum of the scattered radiation from the oscillating reradiators consists of a doubly infinite sum of offset Gaussian functions, but when the reradiators do not oscillate, the power spectrum simplifies to a sum of simple non-offset Gaussians. It is evident that these results have some degree of similarity with those of Wong et al. [29] in that both represent the power spectrum from a group of oscillating random scatterers as sums of Gaussians, the peaks of which are offset from zero-Doppler and for which the offsets collapse in the absence of oscillation.

Some years following both the Wong et al. [29] and the Bass et al. papers [54], Rosenbaum and Bowles [55] derived theoretical expressions for windblown clutter spectra based on a physical model in which the backscattering was associated with random permittivity fluctuations superimposed on a lossy background slab. Again with overtones of similarity to both the Wong et al. and the Bass et al. analyses, Rosenbaum and Bowles modeled scatterer motion two ways, first, as a Gaussian process, and second, assuming scatterer motion to be quasi-harmonic, so that the scatterers behave as decaying simple-harmonic oscillators. It has been observed that the Rosenbaum and Bowles spectral results "are . . . too complex for radar engineers to use in design practice" [19].

Status (Gaussian Spectral Shape). As will be shown, essentially all measurements of ground clutter spectra from 1967 on, of increased sensitivity compared with those of Barlow and the other early investigators, without exception show spectral shapes wider in their tails than Barlow's simple Gaussian. Also, as indicated in the preceding discussion, it had become theoretically well understood, also from 1965–67 on, that scatterer rotational and/or oscillatory motion generates spectra wider than Gaussian. Nevertheless, Barlow's simple Gaussian representation continues to be how clutter spectra are usually represented in radar system engineering, at least as a method of first-approach in representing the effects of intrinsic clutter motion. Thus many of the standard radar system engineering and phenomenology textbooks continue to reference Barlow's early results [1, 27, 50].

Also, Nathanson [28] characterizes ground clutter spectral width in a scatter plot of data from many different sources in which the standard deviation in the best fit of each data source to a Gaussian shape is plotted vs wind velocity. Although it is stated in Nathanson that these results are not intended as a recommendation for the use of Gaussian spectral shape in any system design in which the detailed shape of the spectrum is of consequence, nevertheless Nathanson's results continue to be referenced as justification for the "common assumption . . . " [4] that the internal-motion clutter spectral shape is Gaussian (see also [56] for a similar remark). This continuing representation is understandably based on reasons of simplicity, i.e., "the clutter spectrum is often modeled as Gaussian for convenience, but is usually more complex" [57], and analytic tractability, e.g., the Gaussian function is its own Fourier transform [51].

6.6.1.2 Power-Law Spectral Shape

MTI system performance predicted by the assumption of a Gaussian-shaped clutter spectrum was not achieved in practice. In a much referenced later report, Fishbein, Graveline, and Rittenbach [10] introduced the power-law clutter spectral shape. The power-law spectral shape may be generally represented analytically as

$$P_{ac}(v) = \frac{n\sin(\pi/n)}{2\pi v_c} \cdot \frac{1}{1+\left[\frac{|v|}{v_c}\right]^n} \quad , -\infty < v < \infty \tag{6.18}$$

Equation (6.18) has two power-law shape parameters—*n,* the power-law exponent, and v_c, the break-point Doppler velocity where the shape function is 3 dB below its peak zero-Doppler level. The normalization constant K is equal to $n\sin(\pi/n)/(2\pi v_c)$; $k(v) = 1/[1 + (|v|/v_c)^n]$; and

$$\int_{-\infty}^{\infty} P_{ac}(v)dv = 1 \ .$$

To convert to $P_{ac}(f)$ in Eq. (6.18), i.e., $P_{ac}(f)df = P_{ac}(v)\,dv$, replace v by f and v_c by $f_c = (2/\lambda)v_c$. For velocities $v >> v_c$, Eq. (6.18) simplifies to $P_{ac}(v) = (K \cdot v_c^n)v^{-n}$, which plots as a straight line in a plot of 10 log P_{ac} vs log v. In such a plot, n defines the slope of the straight-line v^{-n} power-law spectral tail (slope = dB/decade = 10 n). Because of its two shape parameters, the power-law shape function of Eq. (6.18) has an additional degree of freedom for fitting experimental data compared with the single-parameter Gaussian and exponential shape functions of Eqs. (6.17) and (6.2), respectively. For any power of n, the power-law shape function may be made as narrow as desired by making v_c small

enough. Still, whatever the values of n and v_c, ultimately at low enough power levels (i.e., as $10\log P \rightarrow -\infty$) the power-law shape always becomes wider than Gaussian or exponential.

Fishbein et al. [10] indicate that measured clutter rejection ratios up to 40 dB are matched under the assumption of a theoretical power-law spectral shape with $n = 3$. They also made one actual X-band clutter spectral measurement in 12 knot winds verifying that an $n = 3$ spectral tail did exist down to a level 35 dB below the zero-Doppler level and out to a maximum Doppler velocity of 1.6 m/s. The graph of these results, shown in Figure 6.46, appears to very convincingly show the clutter spectrum to be an $n = 3$ power law, as opposed to Gaussian, and it is widely referenced [27, 28].

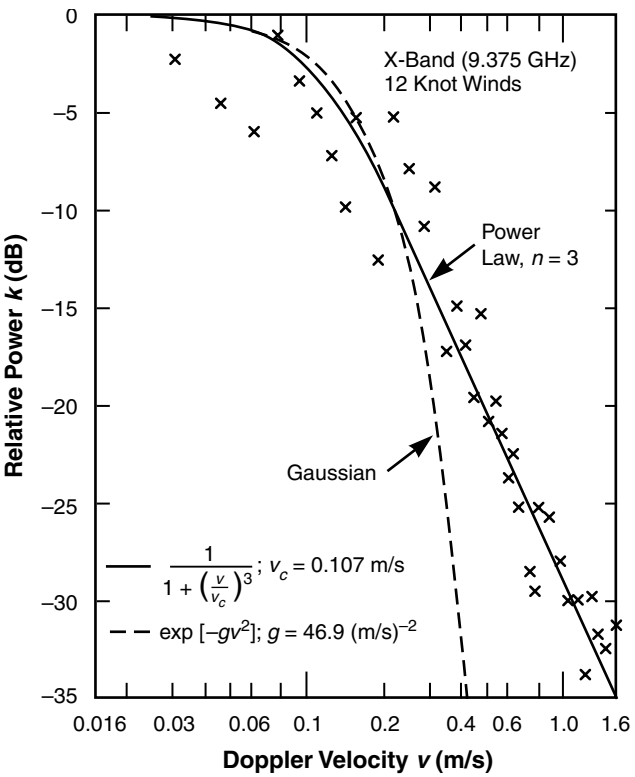

FIGURE 6.46 A measured radar ground clutter power spectrum by Fishbein, Graveline, and Rittenbach of the U. S. Army Electronics Command. After [10], 1967.

The Gaussian and power-law curves in Figure 6.46 are $k(v)$ curves as originally presented by Fishbein et al. [10] with their zero-Doppler peaks at 0 dB. Such $k(v)$ curves are generally not of equivalent total ac power. However, the particular Gaussian curve shown in Figure 6.46 is the one resulting when its shape parameter g is adjusted to the necessary value, viz., $g = 46.9$, to provide equivalent power (not unity) to that contained by the power-law curve of Figure 6.46. That is, the Gaussian curve in this figure did not arise from direct fitting to measured data. In contrast, Barlow's Gaussian curves of Figure 6.45 did arise from direct fitting to measured data. It is more fair to compare the Fishbein et al. $n = 3$ power-law curve of Figure 6.46 with Barlow's $g = 10$ and 20 Gaussian curves of Figure 6.45, all as P_{ac} curves normalized to unit total ac spectral power for whatever values of shape parameter

were required to fit to measured data. The $g = 20$ Gaussian curve and $n = 3$, $v_c = 0.107$ power-law curve shown in Figure 6.44 are Barlow and Fishbein et al. curves, respectively, plotted as P_{ac} functions, each properly normalized to equivalent unit total ac spectral power. It is evident that Barlow's $g = 20$ Gaussian curve would be considerably wider than (i.e., would lie to the right of) the $g = 46.9$ Gaussian plotted in Figure 6.46, with the result that the data in Figure 6.46 become somewhat less convincingly power law.

The Fishbein et al. [10] results were important in establishing the existence of low-level tails wider than Gaussian in ground clutter spectra. Other ground clutter spectral measurements followed in which power-law spectral shapes were observed. For example, shortly after publication of the Fishbein et al. report, Warden and Wyndham [11] briefly mentioned two S-band measurements of clutter spectra, shown in Figure 6.47. The first was a clutter spectrum for a wooded hillside in 14- to 16-knot winds. The shape of this spectrum, to –29 dB at a maximum Doppler velocity of 0.82 m/s, is wider than Gaussian but narrower than an $n = 3$ power law. The second was a clutter spectrum for a bare hill in 10- to 12-knot winds. This spectrum is slightly narrower than the first, although still wider than Gaussian in the tail. The authors concluded that an $n = 3$ power law best fitted their data overall.

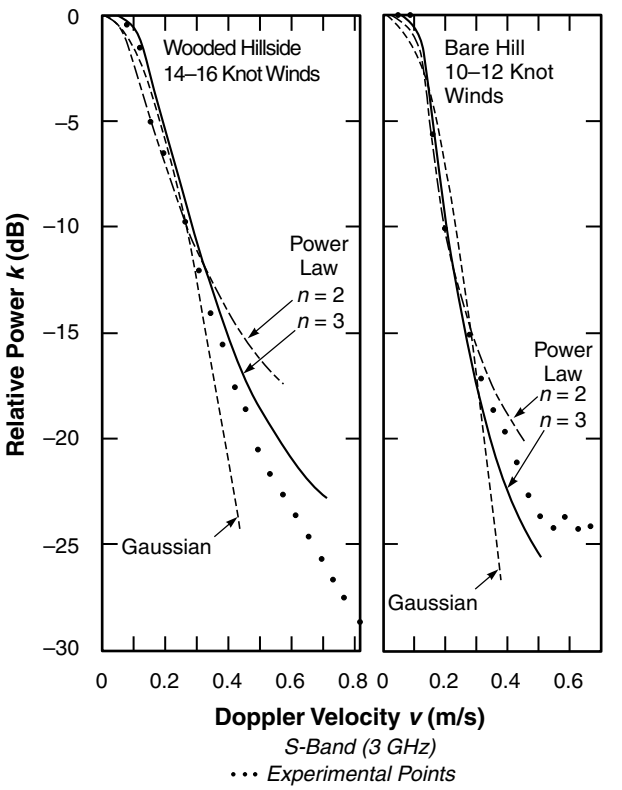

FIGURE 6.47 Two measurements of radar ground clutter power spectra by Warden and Wyndham of the Royal Radar Establishment (U. K.). After [11], 1969.

Several years later, Currie, Dyer, and Hayes [12] provided measurements of noncoherent clutter spectra from deciduous trees under light air and breezy conditions over a spectral

dynamic range of 20 dB at frequencies of 9.5, 16, 35, and 95 GHz. Over this limited spectral dynamic range, they also found their results to be well fitted with power laws of $n = 3$ in the lower bands and $n = 4$ at 95 GHz. At both 9.5 and 16.5 GHz, maximum spectral extents under breezy 6- to 15-mph winds at the –20-dB level were ~0.8 m/s, which is a close match both to the Fishbein et al. results and to the Phase One and LCE measurements and exponential model (see Figure 6.1) of Chapter 6 over similar spectral dynamic ranges and under similar breezy conditions—especially if the Currie et al. spectral widths are reduced by a factor of ~1.4 to account for the fact that their measurements were noncoherent. At 35 and 95 GHz, maximum spectral extents under breezy conditions at the –20-dB level were ~0.5 m/s, that is, ~40% narrower than at the lower X- and K_u-band frequencies. These narrower upper-band spectra appear to indicate that the frequency invariance, VHF to X-band, of Doppler-velocity ac spectral shape of the current exponential model may not extend to frequencies as high as 35 GHz (K_a-band) and 95 GHz (W-band). The Currie et al. [12] results are also discussed in Long [27] and in Currie and Brown [58]; in the latter discussion, Currie remarks that "curve-fitting is an inexact science" and raises the possibility that other spectral shapes might also have been used to equally well fit these data.

A set of papers in the Russian literature [13–16] from the same time period included power law among various analytic representations used in fitting experimental data in different Doppler regimes. Results taken from these Russian papers are shown in Figures 6.48, 6.49, and 6.50. In these Russian studies, spectral power was observed to decay at first according

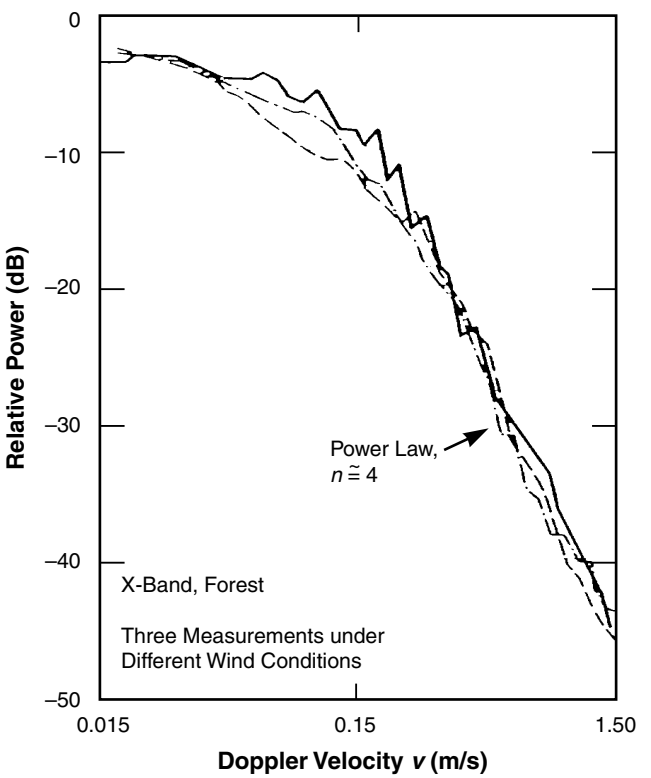

FIGURE 6.48 Measurements of radar ground clutter power spectra by Kapitanov, Mel'nichuk, and Chernikov of the Russian Academy of Sciences. After [13], 1973.

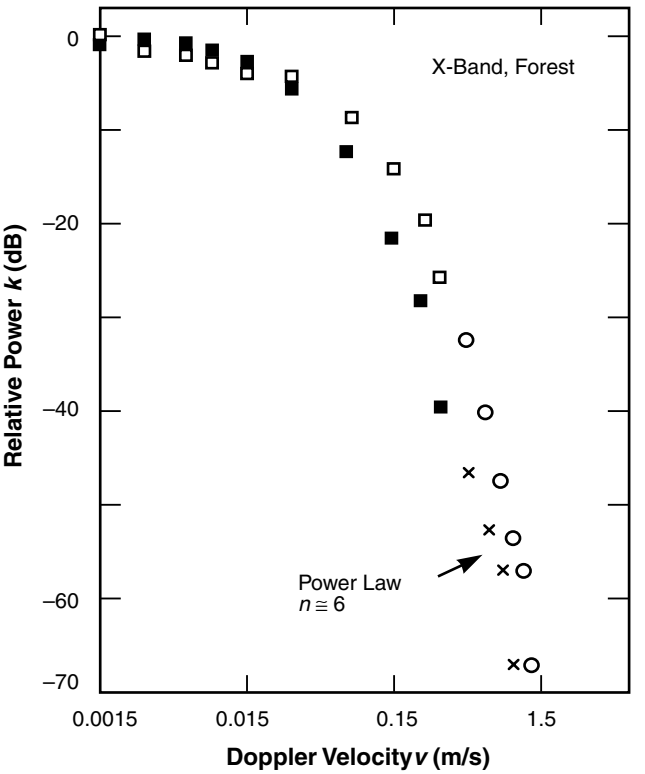

Measurement Interval	Amplifier Bandwidth (Hz)
□ —— 1	0 – 2000
■ —— 2	0 – 2000
× —— 3	20 – 2000
○ —— 4	20 – 2000

FIGURE 6.49 Measurements of radar ground clutter power spectra by Andrianov et al. of the Russian Academy of Sciences. After [15], 1976.

to Gaussian [13] or exponential [16] laws to spectral power levels down 10 to 20 dB from zero-Doppler. This initial region of decay was followed by subsequent power-law decay to lower levels and higher Doppler velocities. Spectral widths in these Russian measurements closely match those measured by the Phase One and LCE radars near their limits of sensitivity (down ~ 70 dB).

The Russian investigations included theoretical [13,14] as well as empirical characterizations of windblown clutter spectra. The theoretical studies concluded that shadowing effects (of background leaves and branches by those in the foreground under turbulent wind-induced motion) were important in determining the shapes of spectral tails, over and above oscillatory and rotational effects. A physical model of windblown vegetation was initially discussed by Kapitanov et al. [13], which included random oscillation of elementary reflectors (leaves, branches) causing phase fluctuation of returned signals and shadowing of some elementary reflectors by others causing amplitude

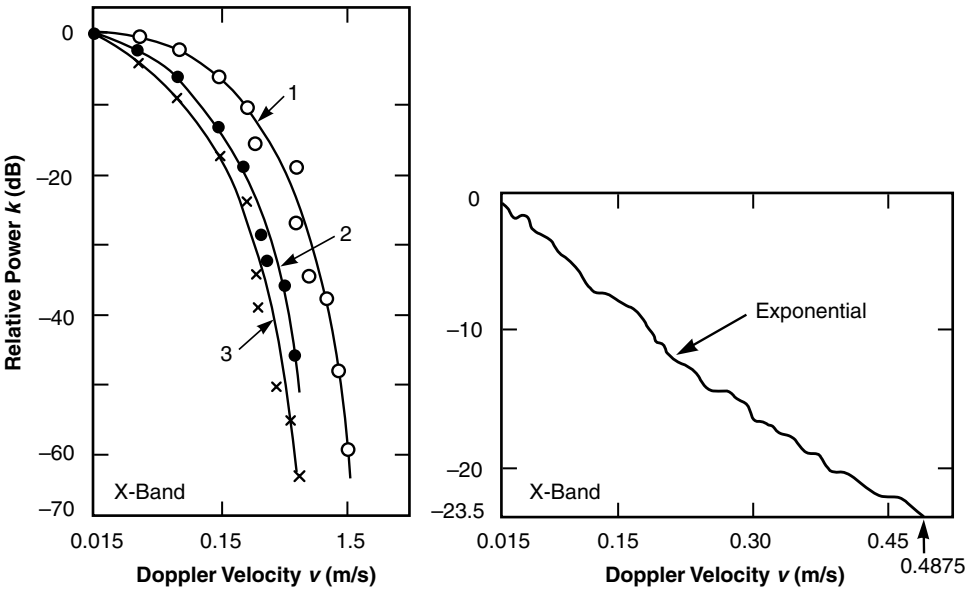

Curve	Tree Species	Wind Speed (mph)
1	Birch	6
2	Alder	11
3	Pine	13

Tree Species	Wind Speed (mph)
Birch	4

FIGURE 6.50 Measurements of radar ground clutter power spectra by Andrianov, Armand, and Kibardina of the Russian Academy of Sciences. After [16], 1976.

fluctuation of returns. An expression for the clutter spectrum was obtained based on the correlation properties of the returned signals. This expression consisted of four terms—the first dependent on the initial positions of the reflectors, the second representing the spectrum of the amplitude fluctuations, and the third describing the spectrum of the phase fluctuations; the fourth term was the convolution of the amplitude and phase fluctuations of the elementary signals and was said to determine "the behavior of the wings [i.e., tails] of the spectrum"[13]. It was believed in this study that the interaction of foliage with turbulent wind flow was beyond the scope of accurate mathematical description, so the authors resorted to experimental measurement of the oscillatory motion of branches in winds through photographic methods. These measurements of branch oscillatory motion led to the prediction of an $n = 4$ power-law clutter spectral decay associated with phase fluctuation up to a Doppler velocity of $\sim$ 0.5 m/s, with a faster phase fluctuation-induced rate of decay expected at higher Doppler velocities. Since their measurements indicated an $n = 4$ power-law decay to higher Doppler velocities (i.e., to 1.5 to 3 m/s near their system limits of –36 to –40 dB down from zero-Doppler peaks), they concluded that shadowing-induced amplitude fluctuation must have caused the $n = 4$ power-law decay continuing to be observed beyond $\sim$ 0.5 m/s.

Armand et al. [14] further developed the Kapitanov et al. [13] physical model by assuming that the elemental scatterers at X-band were primarily leaves and modeling them as metal disks. These elemental scatterers introduced phase fluctuation in returned signals due to oscillatory motion, and amplitude fluctuation due to rotational motion and shadowing effects. A mathematical model of wind-induced scatterer motion including these effects was assumed. The resultant tail of the clutter spectrum was shown to be describable by a negative power series in Doppler frequency f, including both integer and fractional powers. In the absence of shadowing effects, this expression simplified considerably, leaving only a single dominant power-law term of $n \cong 5.66$. Since the authors observed experimental power-law spectral decay of $n \cong 3$, they also concluded that shadowing effects had to be at work in determining the shape and extent of windblown clutter spectral tails.

Other results in which power-law spectral decay was observed are those of Simkins, Vannicola, and Ryan [17]. These measurements of ground clutter spectra were obtained at L-band at Alaskan surveillance radar sites as shown in Figure 6.51. In these results, power-law shapes with exponents n of 3 and 4 were attributed to the measured data which exist to levels 40 to 45 dB below the zero-Doppler peaks. In Figure 6.51, the "partially wooded hills" power law (given by $n = 4$, $v_c = 0.058$ m/s) provides spectral widths comparable with those measured by other investigators, but the "heavily wooded valley" power law (given by $n = 3$, $v_c = 0.34$ m/s) for which the bounding envelope is shown to reach 10.6 m/s at the –45 dB point provides spectral widths very much wider than any other known ground clutter spectral measurement at equivalent spectral power levels.

The particular four points in the "heavily wooded valley" data that show excessive spectral width for windblown forest in 20 knot winds are indicated as a, b, c, and d in Figure 6.51; they deviate from the general rule as determined by the vast preponderance of other measurements reported in the literature of the subject. The position of the widest LCE-measured clutter spectrum is also shown in Figure 6.51 for comparison. These results of Simkins et al. were subsequently extrapolated as $n = 3$ and $n = 4$ power laws to lower levels in clutter models (see subsequent discussion in Section 6.6.3.4).

In the 1980s, several research institutes in China investigated backscattering power spectra from windblown vegetation in various microwave radar bands, including X, S, and L [18, 19]. In all plots presented, spectral dynamic ranges were $\leq$ 30 dB below zero-Doppler peaks. The focus of interest in these Chinese investigations was on the fact that power spectra from windblown vegetation over such limited spectral dynamic ranges are typically well approximated by power laws, but that no simple physical model or underlying fundamental principle is known that requires spectral shapes to be of power-law form. Thus they wished to bring the power-law basis for spectral decay into better understanding and onto firmer theoretical footing.

Jiankang, Zhongzhi, and Zhong [18] presented a first-principles theoretical model for backscattering from vegetation to represent the intrinsic motion or time variation of σ° that occurs in microwave surface remote sensing. This model was based on representing the vegetation as a random medium in which the dielectric constant varied with space and time. A general formulation for the backscattering power spectrum was obtained based on the assumed leaf velocity distribution. Assumptions that the wind was an impulse function and that the leaves were Rayleigh-distributed elemental masses led to a leaf velocity distribution that was shown to be closely similar in form (but not exactly equal) to an $n = 3$

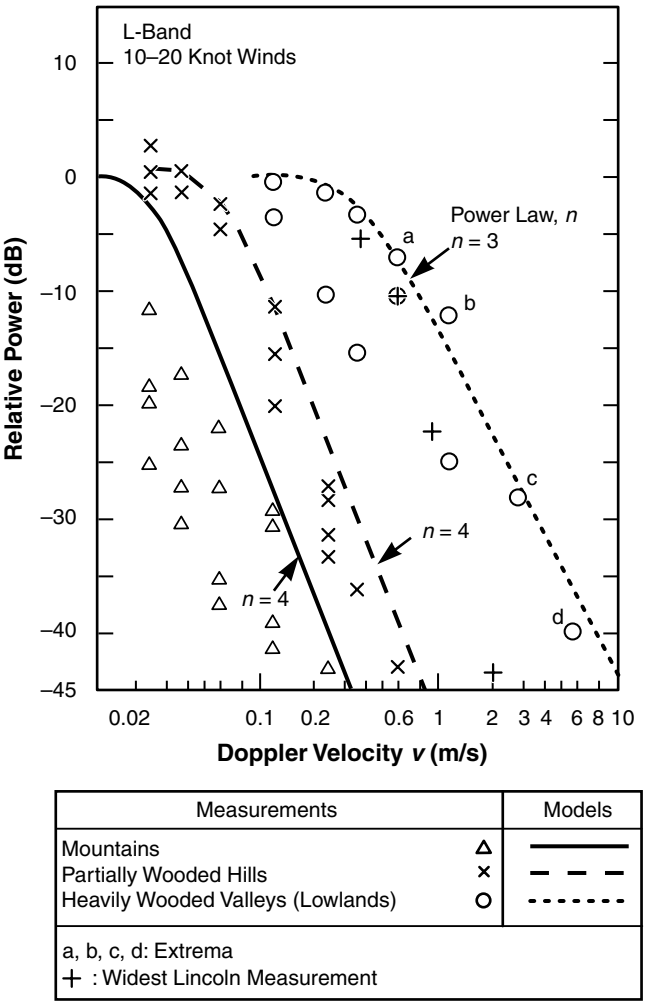

FIGURE 6.51 Measurements of radar ground clutter power spectra by Simkins, Vannicola, and Ryan of the USAF Rome Air Development Center. After [17], 1977.

power law. However, the resulting backscattering power spectrum was of "quite complex form" [18]. Its numerical evaluation and comparison with three measured spectra indicated $n = 3$ power-law spectral decay over spectral dynamic ranges reaching 30 dB down from zero-Doppler peaks. A further assumption restricting the originally specified elliptic spatial distribution of leaf motion to motion only along the wind direction reduced the complex expression for backscattering power spectrum to the same $n = 3$ quasi-power-law form as the leaf velocity distribution. This expression was compared with the Fishbein $n = 3$ power-law results and found to be in good agreement. The authors concluded by claiming that their model provides a theoretical basis for power-law spectral decay and, in addition, allows generalization of parametric effects such as wind speed on spectral shape. What their model appears to show, however, is less far-reaching—only that a postulated $n = 3$ quasi-power-law distribution of leaf velocities results in similar $n = 3$ quasi-power-law clutter spectral shapes.

In a later paper, Li [19] summarized L-band investigations at the Chinese Airforce Radar Institute to characterize Doppler spectra from windblown vegetation to improve design and performance of MTI and MTD (moving target detector) clutter filters. According to Li, the common position reached by Chinese researchers from several research institutes in China was that the radar land clutter spectrum could be represented as a power law with n ranging from < 2 to > 3, but that no direct physical explanation for the power-law spectral shape was available in published papers.

To help provide such an explanation, Li started with the complex theoretical formulation for the power spectrum from an assemblage of randomly translating and rotating scatterers expressed as a sum of offset Gaussian functions as derived much earlier by Wong et al. [29], and argued heuristically that the rotational components that spread the spectrum resulted in power-law spectral shapes. To illustrate this hypothesis, Li numerically evaluated Wong et al.'s expression for three different cases in which Wong et al.'s statistical parameters were changed to ostensibly show effects of varying wind speed and for two different cases in which the statistical parameters were changed to ostensibly show effects of changing radar frequency. For all five cases, Li showed that the changing spectral shapes resulting from such parameter variations in Wong et al.'s formula could be well tracked by changing n in a simple power-law approximation. All such comparisons were shown over spectral dynamic ranges reaching 30 dB below zero-Doppler peaks.

Li finally showed that two of his power-law approximations closely fit, respectively, two spectral measurements taken from the much earlier Rosenbaum and Bowles paper [55]. These two measurements were at UHF and L-band and were available to Rosenbaum and Bowles (who were Lincoln Laboratory investigators) from a 1972-era Lincoln Laboratory clutter spectral measurement program [59] to be discussed later. Li selectively showed the Rosenbaum and Bowles data only over upper ranges of spectral power (i.e., to –30 dB and –20 dB, respectively, or only over about one-half the spectral dynamic ranges of the original data), and Li also converted the Rosenbaum and Bowles data from a logarithmic to a linear Doppler frequency axis. Li's resulting plots show results, including both Rosenbaum and Bowles' experimental data and the power-law approximations to them, which are very linear on 10 log P vs f axes—that is, all would be reasonably matched with exponential functions, although Li matched them with power-law functions.

Measurements of decorrelation times [40], bistatic scattering patterns [41], and power spectra [42] of continuous-wave X-band backscatter from windblown trees were obtained by Narayanan and others at the University of Nebraska. These measurements were of individual trees (1.8-m-diameter illumination spot size on the tree crown) of various species at very short ranges (e.g., 30 m). Radar system noise is evident in these spectral data at levels 35 to 45 dB below the zero-Doppler spectral peaks and for Doppler frequencies f corresponding to Doppler velocities $v \leq \sim 1$ m/s [42].

Over these relatively limited spectral dynamic ranges and corresponding low Doppler velocities, many of the measured spectral data appear to closely follow power-law behavior (i.e., the spectral data are very linear as presented on 10 log P vs log f axes), although this apparent near-power-law behavior was not commented upon in the paper. As with Li [19], the Narayanan et al. starting point in modeling these data was the Wong et al. [29] formulation of the power spectrum for a group of moving scatterers, each with random rotational as well as translational motion. As previously discussed, Wong et al.'s spectral

result consists of six Gaussian terms of which four are offset from zero-Doppler. Wong et al.'s expression depends on three parameters, the standard deviation σ_d of the translational drift velocity components, and the mean $\overline{\omega_r}$ and standard deviation σ_r of the rotational components. Thus in Wong et al.'s expression σ_d determines the spectral width of the central Gaussian peak at zero-Doppler arising just from translation; $\overline{\omega_r}$ determines the locations of the four offset peaks at $\pm 2\,\overline{\omega_r}$ and $\pm 4\,\overline{\omega_r}$, respectively; and σ_d and σ_r together determine the slower-decaying spectral widths of all five additional Gaussians (four offset and one not offset from zero-Doppler) arising from rotation.

In modeling his measured power spectral data from windblown trees using Wong et al.'s theoretical expression, Narayanan postulated each of the three parameters σ_d, $\overline{\omega_r}$, and σ_r to be linearly dependent on wind speed and specified the coefficients of proportionality for each specifically by tree type based on least-squared fits to measured autocovariance data. Narayanan et al. also provided extensive conjectural discussion associating σ_d with branch translational motion and $\overline{\omega_r}$ and σ_r with leaf/needle rotational motion, although their results do not appear to be dependent on the validity of these associations. In this manner, Narayanan et al. arrived at a six-term Gaussian expression for the power spectrum from windblown trees based on three coefficients of proportionality to wind speed for which the coefficients are empirically specified for six different species of trees. This expression provided reasonable matches to measured clutter spectral data from individual trees over spectral dynamic ranges reaching 35 to 45 dB below the zero-Doppler peaks.

Narayanan et al. also derived an expression for the MTI improvement factor for a single delay-line canceller based on their six-term Gaussian expression for the clutter power spectrum from windblown vegetation, and provided numerical results showing significant degradation in tree-species-specific delay-line canceller performance using their six-term (i.e., with rotation) spectral expression compared with the corresponding single-Gaussian (i.e., without rotation) spectral expression. In both spectral and improvement factor results, there is considerable variation in these results between different tree species. These short-range small-spot-size deterministic results applicable to specific tree species are in major contradistinction to the Phase One and LCE statistical results, which are applicable to larger cells at longer ranges and over greater spectral dynamic ranges, each cell containing a number of trees, often of mixed species.

A limited set of coherent X-band measurements of ground clutter spectra were obtained by Ewell [20] utilizing a different Lincoln Laboratory radar unrelated to the Phase One and LCE radars. This radar (1° beamwidth and 1-μs pulsewidth) was not specifically designed for measuring very-low-Doppler clutter signals—e.g., it used a cavity-stabilized klystron as the stable microwave oscillator, which is less stable at low Doppler frequencies than modern solid state oscillators. The available ac spectral dynamic range provided by this radar for measuring clutter signals at low Doppler offsets was ~40 to 45 dB. Measurements were made of three desert terrain types at ranges for the most part from 3 to 12 km on three different measurement days under winds gusting from 9 to 12 mph. Results were provided for both circular and linear polarizations.

Over the available ~40-dB spectral dynamic range, these measured data appeared to follow power-law spectral shapes, although with occasional hints in the data of faster decay at lower levels. Table 6.6 shows the resulting power-law shape parameters, averaged over a number of measurements within each of the three terrain types. These three desert clutter

spectral shapes are quite similar; that is, when each is normalized to equivalent unit spectral power as per Eq. (6.18) and the set of three is plotted together, they form a relatively tight cluster to levels ~40 dB down. For example, all three curves reach the –30-dB level at $v \cong$ 1 m/s, which point is very closely matched by the $\beta = 8$ exponential shape factor provided by the spectral model of Section 6.2 for similar breezy wind conditions (see Figure 6.1).

Also included for comparison in Table 6.6 are Fishbein et al.'s original power-law spectral shape parameters. The Fishbein et al. power law is wider than the three desert power laws in Table 6.6 (e.g., the Fishbein et al. power law reaches the –30-dB level at v = 1.7 m/s), although part of the reason for the wider Fishbein et al. data is that they were noncoherent. Besides corroborating gross spectral extents of Phase One and LCE clutter spectra measured at upper ranges of spectral power under breezy conditions, the results of Ewell's spectral measurements shown in Table 6.6 also tend to substantiate the Phase One and LCE findings that ac clutter spectral shape, at least to first-order, tends to be approximately independent of terrain type and that clutter spectral shape tends to be largely independent of polarization.

TABLE 6.6 Comparison of Ewell [20] and Fishbein et al. [10] Power-Law Clutter Spectral Shape Parameters

Clutter Spectrum	Power-Law Spectral Shape Parameters	
	n	v_c (m/s)
Ewell [20] [a]		
1) Scrub/brush	4.1	0.11
2) Mountain slopes (sparse vegetation/rocks)	3.7	0.10
3) Low-growing cedar trees	3.3	0.07
Fishbein et al. [10] [b]	3.0	0.11

a. Spectral shape parameters shown are valid for approximating clutter spectra over ac spectral dynamic ranges reaching ~40 to 45 dB down from the zero-Doppler peak.
b. Valid to ~ 35 dB down

Status (Power-Law Spectral Shape). Many measurements of windblown clutter spectra obtained following the very early measurements of Barlow and others provide spectral dynamic ranges typically reaching ~ 30 or ~ 40 dB below zero-Doppler peaks. Such measurements, as reviewed in the preceding discussion, provide clutter spectral shapes that are frequently well represented as power laws.

In contrast to the Gaussian spectral shape which theoretically arises from a random group of scatterers each of constant translational drift velocity, there is no simple physical model or fundamental underlying reason requiring clutter spectral shapes to be power law. All

theoretical investigations of clutter spectra based on physical models that include oscillation and/or rotation in addition to translation of clutter elements provide expressions for clutter spectra that are to greater or lesser degree of complex mathematical form [14, 18, 29, 39, 54, 55], although one such expression [14] is derived to be a negative power series in f (i.e., as a sum of elemental power laws) which at least does have a general power law-like behavior.

Because the preponderance of the empirical evidence in spectral measurements to levels 30 or 40 dB down from zero-Doppler peaks has been for simple power-law spectral shapes, there has been some motivation by theoreticians either to reduce an initially derived complex formulation for clutter spectral shape to a simpler, approximately power-law formulation [18] or to show that numerical evaluation of the complex formulation provides results that closely match a simple power law [19]. However, the evidence that clutter spectra have power-law shapes over spectral dynamic ranges reaching 30 to 40 dB below zero-Doppler peaks is essentially empirical, not theoretical.

6.6.1.3 Exponential Spectral Shape

Phase One and LCE ground clutter spectral measurements to levels 60 to 80 dB down indicate that the shapes of the spectra decay at rates often close to exponential [21, 25]. The two-sided exponential spectral shape is given by Eq. (6.2), repeated here as:

$$P_{ac}(v) = \frac{\beta}{2} \cdot \exp(-\beta|v|) \,, -\infty < v < \infty \tag{6.19}$$

where β is the exponential shape parameter, $K = \beta/2$ is the normalization constant, $k(v) = \exp(-\beta|v|)$, and

$$\int_{-\infty}^{\infty} P_{ac}(v)dv = 1 \quad .$$

To convert to $P_{ac}(f)$ in Eq. (6.2), i.e., $P_{ac}(f)df = P_{ac}(v)\,dv$, replace v by f and β by $(\lambda/2)\beta$. The standard deviation of the exponential spectrum of Eq. (6.2) is given by $\sigma_\beta = \sqrt{2}/\beta$ in units of m/s. The exponential shape is wider than Gaussian, but in the limit much narrower than power law whatever the value of the power-law exponent n. Like the Gaussian, the exponential is simple and analytically tractable. For example, the Fourier transform of the exponential function is a power-law function of power-law exponent $n = 2$ [8, 51]. The exponential shape is easy to observe as a linear relationship in a plot of 10 log P_{ac} vs v. Figure 6.21 shows four cases of measured Phase One and LCE spectra that are remarkably close to exponential over most of their Doppler extents, and other examples of Phase One and LCE exponential or quasi-exponential clutter spectral decay are provided elsewhere in Chapter 6. There is no known underlying fundamental physical principle requiring clutter spectra to be of exponential shape. Rather, the exponential shape is a convenient analytic envelope approximating the shapes of many of the Phase One and LCE measurements to levels 60 to 80 dB down.

In Eq. (6.2), the independent variable v may itself be raised to a power, say n, as: $\exp(-\beta|v|^n)$ to provide an additional degree of freedom in curve-fitting to measured data. When $n > 1$, this results in convex-from-above spectral shapes on 10 log P vs v axes, that is, in shapes that decay faster than exponential (e.g., when $n = 2$ the shape becomes Gaussian). On the other hand, $n < 1$ (i.e., fractional) results in concave-from-above spectral shapes on 10 log P

vs v axes, which is the direction away from purely exponential that measured Phase One and LCE spectra usually tend towards, especially at lower wind speeds. Provision of a more complex exponential-like expression to possibly enable improved curve-fitting capability to particular empirical data sets is not further pursued here since the simple exponential form (i.e., $n = 1$) satisfactorily captures the general shapes and trends in the data.

The Phase One clutter data were shared with the Canadian government. Chan of Defence Research Establishment Ottawa (DREO) issued a report [22] and subsequent paper [23] on the spectral characteristics of ground clutter as determined largely from his investigations of the Phase One data, but also including measured ground clutter spectra from a DREO rooftop S-band phased-array radar. Figure 6.52 shows some of Chan's results comparing clutter spectra from the same two resolution cells under windy and breezy conditions. In the main, Chan's results agree with those of Lincoln Laboratory. In arriving at these results, Chan used a different set of the Phase One data than the long-time-dwell experiments used at Lincoln Laboratory in spectral processing. That is, to obtain a larger set of measurements, Chan used repeat sector Phase One data (see Chapter 3) which provided more spatial cells but shorter dwells, and performed maximum entropy spectral estimation on these data to obtain the necessary spectral resolution. Thus with different data, different processing, and, in the case of the DREO phased-array instrumentation, a different radar, Chan also arrived at exponential spectral decay for what he calls the "slow-diffuse" component of the ground clutter spectrum. Indeed, the spectra from the DREO radar shown in Figure 6.52 appear for the most part to be highly exponential in spectral shape. Stewart [43] has also shown a measured ground clutter spectral shape of relatively wide spectral extent that appears highly exponential.

The empirical observations of exponential decay in the Phase One and LCE clutter spectra motivated White [39] to develop a new first-principles physical model for radar backscatter from moving vegetation that also provides exponential spectral decay to conform in this respect with the experimental evidence. White's model assumes that an important element of the scattering arises from the tree branches. The key feature of the model is the representation of each branch as a cantilever beam clamped at one end. Distributions of branch lengths is Gaussian. Distribution of branch angles with respect to horizontal is uniform over π radians. Scattering centers are distributed uniformly over an outer (specifiable) portion of each branch. A mathematical expression for the Doppler spectrum of the radar return from such an assemblage of branches under a distributed wind forcing function is derived. This expression is a complex five-part multiple integral requiring numerical evaluation. When numerically evaluated, the resultant Doppler spectrum is shown to very closely provide exponential decay with increasing Doppler frequency.

In addition, the sensitivity of White's exponential spectral shape to a number of his model assumptions was tested numerically. It was found that the exponential shape was not very sensitive to a number of underlying assumptions concerning the beam modes of oscillation, but much faster than exponential decay occurred when the beams were not clamped (i.e., simple translation), when a nondistributed wind force was used, and when branch lengths were uniformly (as opposed to Gaussianly) distributed. Besides this exponential spectral component arising from branch motion, the model also postulates a rectangular wideband background spectral component at lower power levels arising from leaf motion (see Section 6.6.3.3). Although White's main thrust was the development of a theoretical clutter spectral model, he also provided a small amount of measured radar clutter spectral data acquired

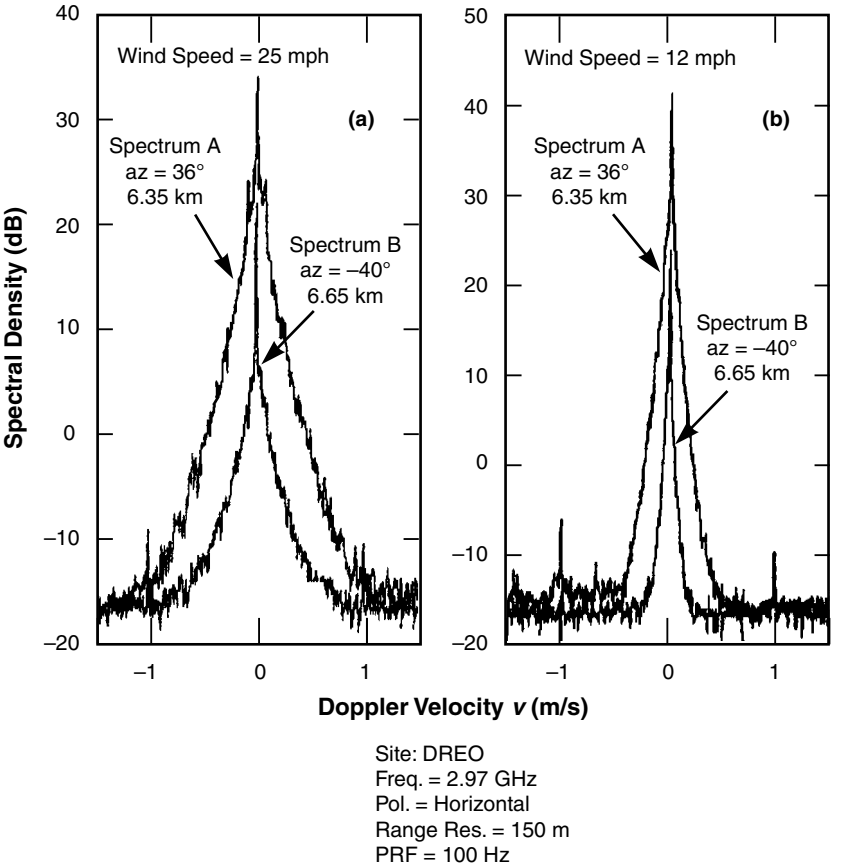

FIGURE 6.52 Measurements of radar ground clutter power spectra by Chan of DREO (Canada) showing results from the same two resolution cells under windy conditions (a), and breezy conditions (b). After [22], 1989.

using a rooftop C-band radar of spectral dynamic range reaching ≈30 to 40 dB below zero-Doppler peaks. White concluded from curve-fitting studies comparing power-law with exponential approximations to his measured data that " . . . the exponential model is the better fit" [39].

Using a different method of analysis than that of White, Lombardo [60] presents a mathematical formulation for ground clutter spectral shape derived from a phenomenologically representative negative binomial probability distribution of scatterer velocities that also can yield an exponential decay characteristic in the tail.

Measured results very similar to those of Phase One and LCE but over less wide, 40- to 60-dB dynamic ranges were obtained in a much earlier set of Lincoln Laboratory measurements of ground clutter spectra at UHF and L-band [59]. Clutter spectra from this earlier program averaged over a number (e.g., 5) of range cells and displayed on log-Doppler velocity axes typically show an increasing rate of downward curvature (convex from above) as in the LCE and Phase One measurements. By coincidence, this early Lincoln Laboratory program [59] of 1972 and the Russian X-band investigations [13] going forward in very nearly the same time period (1973) both developed first-principles physical models of clutter spectra from forest. In

both studies, the tree was modeled as a mechanical resonator excited by a turbulent wind field of known spectral content. Both programs involved measurements of tree motion. In both programs, the spectral content of tree motion decayed at low frequencies below a resonance maximum according to an $n = 5/3$ power law; at higher frequencies above the resonance maximum, the decay was faster. The slightly later (1974), largely theoretical paper by Lincoln Laboratory authors [55] concerning electromagnetic scattering from vegetative regions included three measured clutter spectra from the 1972-era measurement program.

Shoulders before the onset of faster decay, such as those shown in some of the LCE- and Phase One-measured clutter spectra (e.g., see Figures 6.22, 6.24, and 6.25), are similar to those observed previously in the earlier Lincoln Laboratory program [59] and explained as local resonance maxima associated with the natural resonant frequency of trees. The resonance shoulder was more pronounced at lower frequencies and lower wind speeds, and tended to diminish at higher frequencies and higher wind speeds. The reason is that, at lower wind speeds and longer wavelengths, the motion of the tree is a small fraction of a radar wavelength. Thus under these conditions the tree motion superimposes a phase modulation with low index of modulation, and as a result the clutter spectrum directly corresponds with that of the tree's physical motion. At higher frequencies and under stronger winds, the degree of phase modulation increases and the clutter spectrum no longer simply replicates that of the tree motion. These observations tend to be corroborated in LCE and Phase One results. In addition, the LCE and Phase One data tend to have resonance shoulders to somewhat higher frequencies in measurements from partially open or open terrain (desert, farmland, rangeland) in which there is a significant dc component; the measurements from forested terrain tend to have distinct resonance shoulders only at the lower radar frequencies (VHF and UHF). The earlier Lincoln Laboratory program observed, in passing, that the shapes of some measured spectra beyond the resonance shoulder were highly exponential, but this observation was not elaborated upon.

Another early, more explicit, observation of exponential spectral shape is in the results of Andrianov, Armand, and Kibardina [16] (see Figure 6.50). In these results, exponential decay was initially observed from the maximum zero-Doppler level down to –20 dB, followed by power-law decay thereafter to –70 dB with reported values of n equal to 3.4, 3.8, and 5.6 for pine, alder, and birch, respectively. The equipment used was ostensibly of 70-dB dynamic range [15] although, to use their words translated to English, two dynamic range intervals were "sewn together" [16], as shown in Figure 6.49, to provide the full 70-dB range. In terms of gross spectral extent (e.g., 1.5 m/s, 70 dB down; 0.4 m/s, 20 dB down), these results of Andrianov et al. [15, 16] fall closely within the range of measured LCE and Phase One spectral extents over similar spectral dynamic ranges. The earlier results of Kapitanov, Mel'nichuk, and Chernikov [13], as shown in Figure 6.48, were said to exhibit Gaussian decay down 10 to 15 dB, followed by power-law decay with $n = 4$ down to –40 dB. The initial Gaussian decay was later stated to be erroneous by Andrianov et al. [16] because of early equipment limitations and that initial exponential decay as reported by them (see Figure 6.50) was more correct.

The exponent n of the power law is easy to estimate in measured spectral data as simply one-tenth the slope of the approximating straight line on 10 log P vs log v axes in dB/decade. In Figure 6.50, the three measured spectral curves for pine, alder, and birch shown to the left do not exhibit decay anything like the quoted power-law slopes of $n = 3.4$, 3.8, and 5.6, respectively. These three curves are stated by the authors to be three particular examples of

measured spectra, whereas their quoted values of n are averages over all measurements in which the value of n varies from 2.6 to 6.8. The rates of decay in the spectral tails of the data to the left in Figure 6.50 are much greater than any of these quoted values of n and, at least in qualitative appearance (increasing downward curvature), appear to be more exponential than power law. The data of Figure 6.49 appear to be more credibly of power-law behavior ($n \approx 6$) in their tails, but the data plotted at the –68-dB level indicate slightly increasing curvature (rate of decay > $n \approx 6$) at the lowest power levels shown. The data of Figure 6.48 closely match the $n = 4$ power law attributed by the authors to these data.

Some confusion may arise because these Russian investigators [13–16] associate power-law shapes with lower ranges of spectral power in their measured data, whereas other investigators [10–12, 17–20] match their data to power-law shapes over upper ranges of spectral power. Measured clutter data in any particular regime of spectral power may be fitted with a power law, but the danger lies in extrapolating the power law beyond its regime of applicability.

An additional, somewhat more significant, past use of the exponential function to characterize clutter spectra from windblown vegetation occurred in experimental work performed at the Laboratoire Central de Telecommunications in France [38]. These French measurements were also performed during the 1970s using coherent-on-receive radars, spectrum analyzers with limited (i.e., 50 dB) dynamic range, and a limited number of vegetation clutter types. In this work, the MTI filter cutoff frequency was adjusted so as to be just sufficient to remove the clutter to the –40-dB level. It was found that the cutoff frequency just sufficient to remove the clutter was best predicted by hypothesizing an exponential spectral clutter model. The cutoff frequency predicted by a Gaussian spectral model was too low (i.e., optimistic—if there was even a light wind, significant clutter was passed by the filter); whereas the cutoff frequency predicted by a power-law spectral model was too high (i.e., pessimistic—at X-band, all targets with radial speed < 50 km/h were missed). In contrast, cutoff frequencies in the range predicted by an exponential spectral model were successfully used as the standard specification for many service radars in the French military and elsewhere.

Status (Exponential Spectral Shape). The significantly increasing rate of downward curvature (i.e., convex from above) observed in the general shapes of Phase One- and LCE-measured windblown ground clutter Doppler spectra on 10 log P vs log v axes over spectral dynamic ranges reaching 60 to 80 dB below zero-Doppler peaks points to a general exponential characterization rather than a power-law characterization that plots linearly on such axes. Increasing rate of downward curvature in such plots has always been observed without exception in all measurements examined of clutter spectra from windblown trees and other vegetation under breezy or windy conditions taken from these extensive databases. Other investigators [22, 24] have corroborated that the exponential shape factor is generally representative of these data and is not the result of processing-specific particulars.

In early studies, theoretical investigators attempted to reduce complex mathematical formulations of clutter spectra based on physical models incorporating oscillation and/or shadowing of elemental scatterers to simple power-law forms to conform with the experimental evidence then available at upper levels of spectral power (down 30 or 40 dB from zero-Doppler peaks). Subsequent awareness of investigators of the Lincoln Laboratory clutter spectral results provided motivation to develop theoretical bases for the

observed exponential spectral shapes. Thus there exist the interesting works of White [39] and Lombardo [60] in which formulations are developed for the clutter Doppler spectrum, that, although mathematically complex, provide close to exponential decay under numerical evaluation. In addition, White observed that "the series solutions produced by Bass et al. [54], Armand et al. [14], and Wong et al. [29] probably have sufficient degrees of freedom to produce a function that would be a close approximation to . . . exponential . . . " [39]. Nevertheless, as for the power law for spectral dynamic ranges 30 to 40 dB down, the evidence of exponential clutter spectral shape for spectral dynamic ranges reaching 60 to 80 dB down is essentially empirical.

The only known measurements of windblown clutter spectra of spectral dynamic ranges equal to or exceeding those of the Phase One and LCE instruments are the Russian measurements of the 1970s [13–16], for which the results over lower ranges of spectral power were approximated as power laws. However, these results are power law only in a piece-part sense; the upper range of spectral power was concluded to be exponential. Hence these results are not very useful or analytically tractable, in that no single simple analytic function was provided to describe the complete clutter spectral shape over its full measured spectral dynamic range. Furthermore, little actual measurement data were shown in these papers, thus restricting possibilities for independent assessment of the data and conclusions by present-day readers.

Like the Gaussian function, the exponential function is simple and analytically tractable. The exponential function provides spectral shapes that are wider than Gaussian, as required by all the empirical evidence and by theoretical constructs involving oscillation, rotation, and shadowing of clutter elements; that are very much narrower at lower power levels (60 to 80 dB down) than extrapolations to lower levels of power-law representations of measurements accurate at higher levels of spectral power (30 to 40 dB down); and that are reasonably equivalent to the measurement data at high and low levels of spectral power.

6.6.2 Reconciliation of Exponential Shape with Historical Results

6.6.2.1 Current vs Historical Clutter Spectral Measurements

Figure 6.5 (Section 6.3.2.1) shows a measured LCE clutter spectrum from windblown trees and compares it with several exponential shape functions (dotted lines) of various values of exponential shape parameter β. In Figure 6.5, the measured data closely follow the exponential curve of shape parameter $\beta = 5.2$ over the full spectral dynamic range shown. Also shown in Figure 6.5 is a narrower Gaussian spectral shape function (dashed line) corresponding to Barlow's much-referenced historical measurement [7] (see Figure 6.45). The Gaussian curve in the figure is shown extrapolated to low spectral power levels much below Barlow's measured spectral dynamic range, which reached only 20 dB below the zero-Doppler peak. The overall rate of decay in the LCE data of Figure 6.5 is much more exponential than Gaussian in character. Spectral tails wider than Gaussian are theoretically required by branches and leaves in oscillatory motion [19, 29] (see Section 6.6.1).

Figure 6.53 shows another LCE windblown-tree clutter spectrum different from that of Figure 6.5. The spectrum of Figure 6.53 was measured at vertical polarization on 11

September at Wachusett Mt. at range = 8.0 km. Also shown in the figure is the $n = 3$, $v_c = 0.107$ power-law curve introduced by Fishbein et al. [10] to match their data (Figure 6.46). This Fishbein et al. power-law curve is shown dashed in Figure 6.53 to a level 35 dB down from the zero-Doppler peak, which is the region for which Fishbein et al. had data; at lower levels in Figure 6.53 the Fishbein et al. power-law curve is shown dotted to indicate extrapolation to levels below Fishbein et al.'s noise floor. The LCE data in Figure 6.53 provide a remarkably close match to the Fishbein et al. power-law curve at upper levels (viz., down 35 dB) over which Fishbein et al. had data. That is, these LCE spectral data confirm the historic Fishbein et al. spectral measurement with modern measurement instrumentation. However, it is also very clear in Figure 6.53 that the Fishbein et al. power-law curve cannot be extrapolated to lower levels. At lower levels, the LCE measured spectrum in this figure decays much more rapidly than at upper levels. In overall shape, the LCE data of Figure 6.53 are not very different from Figure 6.5 and are better modeled as exponential over their complete range than as any power law.

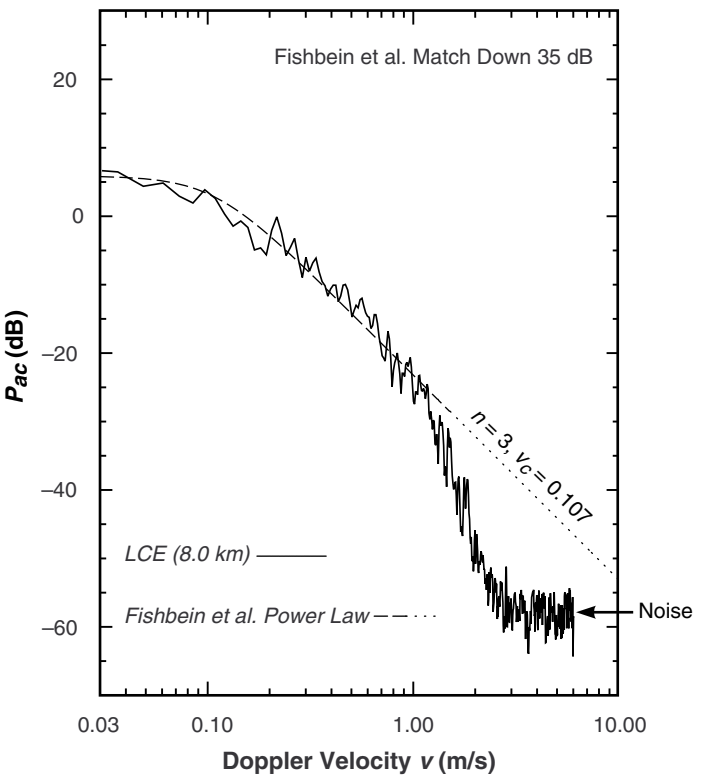

FIGURE 6.53 Comparison of an LCE windblown forest clutter spectrum with the Fishbein et al. power-law model [10].

The Fishbein et al. measurement (Figure 6.46) was made with noncoherent instrumentation; thus the Fishbein et al. power-law approximation shown in Figure 6.53 is ~1.4 times wider than would be expected if the measurement had been coherent (see Section 6.6.1.1; the 1.4 factor is specifically applicable to spectra of Gaussian shape, but a similar factor is expected to apply to spectra of power-law shape). The LCE coherent measurement shown in Figure 6.53, although of similar relative shape to what would be expected if Fishbein et al. had made

a coherent measurement, is thus wider in absolute terms at upper power levels (> –35 dB) than what would be expected in such a measurement. Even so, the narrower Fishbein et al. coherent measurement, if modeled as an $n = 3$ power law, would still extrapolate at lower levels (<< –35 dB) to spectral extents much broader than any LCE measurement at these lower levels, including LCE narrower measurements selected to match the coherent Fishbein et al. measurement at upper power levels.

Figure 6.21 (Section 6.4.2) shows measured LCE and Phase One clutter spectra as 10 log P_{tot} vs v from cells containing windblown trees on breezy and windy days. These results are among the widest windblown clutter spectra measured by these instruments. In contrast with most of the other historical spectral measurements discussed in Section 6.6.1, the measurements of Figure 6.21 over greater spectral dynamic ranges than were available in most of the other measurements have spectral shapes that are accurately representable as exponential. This accurate exponential representation is indicated by the good fits of the data to the straight lines drawn through the right sides of the spectra in Figure 6.21.

Figure 6.54 shows the right sides of Figures 6.21(a), (b), respectively, plotted as 10 log P_{tot} vs log v. Recall that the power-law spectral shape [Eq. (6.18)] plots as a straight line in the spectral tail region $v >> v_c$ using a log-Doppler velocity axis as in Figure 6.54. Certainly no single power-law straight line fits either of the spectral data traces in Figure 6.54, both of which exhibit strong downward curvature (convex from above) over their complete spectral extents. Even though the measurement data in Figure 6.54 exhibit strong downward curvature, a local power-law rate of decay can be defined for such data in a small Doppler interval δv as the value of power-law exponent n corresponding to the slope of the straight line tangent to the data curve in the region δv. The local power laws that thus fit the upper levels over historic dynamic range intervals in Figure 6.54 ($n = 3$ or 3.5) cannot be extrapolated to lower levels. Much faster decaying local power laws ($n = 7$, 8, or 10.5) fit the lower levels.

In both Figures 6.53 and 6.54, the more sensitive Phase One and LCE measurement instruments confirm measured rates of spectral power decay reported by other investigators at upper power levels, but in addition find that much faster local power-law rates of decay occur at lower power levels. Close examination of the spectral data in Figures 6.53 and 6.54 appear to indicate, in fact, two or more distinct rates of decay in the spectra, perhaps indicating different phenomenological regimes with different sets of scatterers and/or different mechanisms of scatter dominating at different spectral power levels. On the basis of these results, it is not surprising that many previous investigators have characterized the rate of ground clutter spectral decay at relatively high spectral power levels (i.e., 35 to 45 dB down) as $n = 3$ or $n = 4$ power laws.

In Figure 6.54, exponential fits to the data are shown lightly dotted. The exponential shape $\beta = 7.1$ closely fits the Phase One data of Figure 6.54(b) over its full ac spectral range away from its quasi-dc region (i.e., $|v| > \approx 0.2$ m/s), including both regions of local power-law fits; similarly, the exponential shape $\beta = 5.2$ closely fits the LCE data of Figure 6.54(a) over its full ac range (i.e., $|v| > \approx 0.1$ m/s). In Figure 6.44, the exponential $\beta = 6$ curve lying between Barlow's $g = 20$ Gaussian curve and the Fishbein et al. $n = 3$ power-law curve is now seen as reasonably representative of the data shown in Figure 6.54 from two different instruments at two different sites across more than six orders of magnitude of diminishing spectral power.

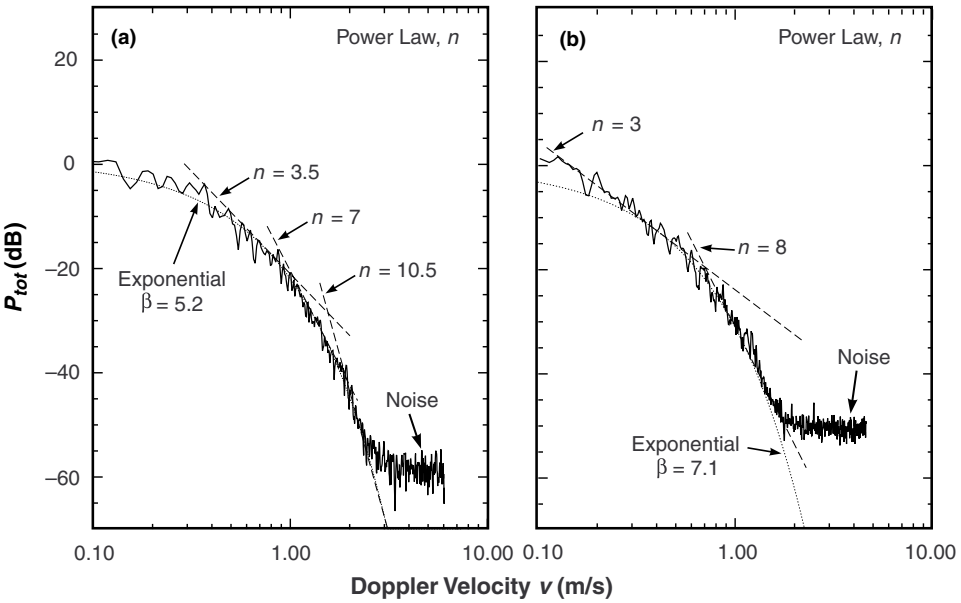

Figure 6.54 Two windblown forest clutter spectra for which exponential fits are compared with power-law fits: (a) LCE data, Wachusett Mt. (September) and (b) Phase One (L-band) data, Katahdin Hill (May).

6.6.2.2 Matching Measured Clutter Spectra with Analytic Shapes

Figure 6.55 compares the $\beta = 6$ exponential shape with $v_c = 0.1$; $n = 3, 4, 5$ power-law shapes both on 10 log P vs v axes [Figure 6.55(a)] and on 10 log P vs log v axes [Figure 6.55(b)]. Each of the four spectral shapes shown is normalized to equivalent unit spectral power as per Eqs. (6.2) and (6.18). Figure 6.55(a) uses a linear Doppler velocity axis, making evident how all power-law shapes become slowly decaying at low levels of spectral power, whatever the value of n. Given that the maximum Doppler velocities observed in Phase One- and LCE-measured clutter spectra were in the 3- to 4-m/s range at levels 60 to 80 dB down, the power-law parameters v_c and n can certainly be adjusted to provide similar spectral extents at similar power levels. However, the resultant power-law shapes will not match Phase One- and LCE-measured data at higher levels of spectral power and will rapidly extrapolate to excessive spectral width at lower levels.

As plotted against the logarithmic Doppler velocity axis in Figure 6.55(b), the $\beta = 6$ exponential shape demonstrates the increasing downward curvature (convex from above) with increasing Doppler velocity and decreasing power level that characterizes all the Phase One- and LCE-measured clutter spectra when plotted on such axes. In contrast, the power-law shapes in Figure 6.55(b) have little curvature. That is, on 10 log P vs log v axes, power-law shapes are asymptotic to two straight lines with a maximum departure in curvature below these asymptotes of only 3 dB at the $v = v_c$ breakpoint between them. This rapid rotation from near-horizontal to straight line spectral tails in which rapidly increasing downward curvature is constrained to a very narrow $v \cong v_c$ Doppler regime is not generally characteristic of the Phase One- and LCE-measured clutter spectral shapes.

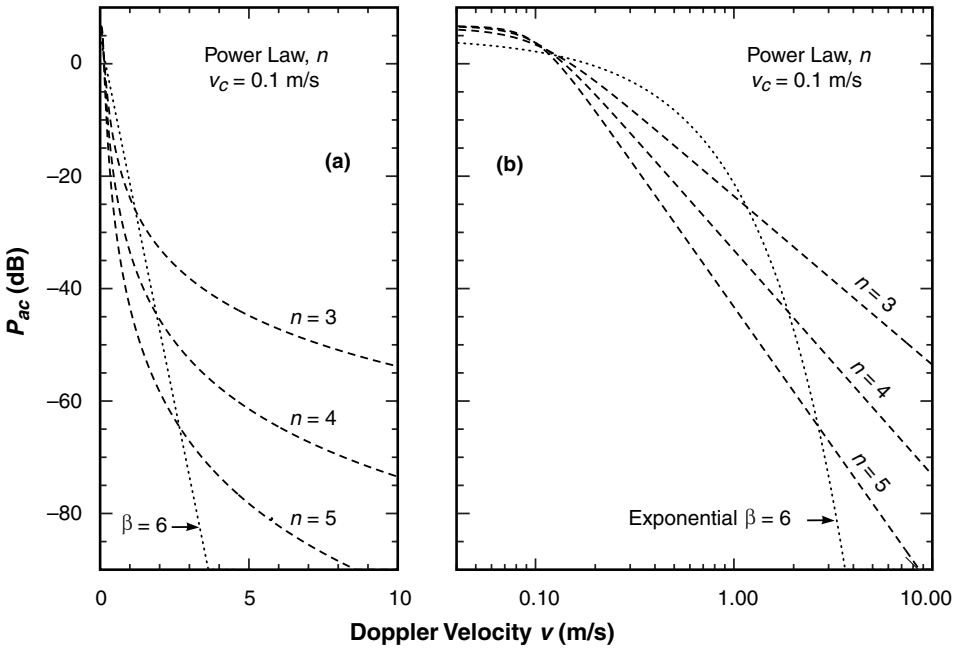

FIGURE 6.55 Comparison of exponential and power-law spectral shapes: (a) linear and (b) logarithmic Doppler velocity axes.

6.6.2.3 SUMMARY

The Phase One and LCE measurements of ground clutter spectra presented in Chapter 6 are displayed on both linear and logarithmic Doppler velocity axes. What is clear in these presentations, and what has not been generally recognized, is that if the clutter ac spectral shape P_{ac} is represented as a power law, the power-law exponent n is not constant but gradually increases from $n = 3$ or 4 when P_{ac} is 35 or 40 dB down from its maximum to $n = 5$ or 6 or even higher when P_{ac} is 60 to 80 dB down from its maximum. Uncertainty about whether "the law" of spectral decay is "$n = 3$ or $n = 6$ (or even exponential)" is abetted by the additional lack of general recognition that the shape of the spectrum to levels 60 to 80 dB down is usually not precisely representable by any single analytic expression. In the results presented herein, slight upward curvature (concave from above) often occurs on the 10 log P_{ac} vs v plots, hence the shape can be slightly broader than exponential; whereas strong downward curvature (convex from above) almost always occurs on the 10 log P_{ac} vs log v plots, hence the shape is much narrower than constant power law.

Thus there is no argument with Andrianov, Armand, and Kibardina that "It is [usually] impossible to [precisely match] the spectral density of the scattered signal by a single analytical function in the entire range of [Doppler] frequencies" [16]. However, much of the potentially ensuing difficulty in the general modeling of clutter spectra is overcome in Chapter 6 not just by utilizing exponential shapes, but also by introducing the concept of a quasi-dc region and absorbing excess power in this region into the dc delta function term of the model (see also [31]). However the spectrum is modeled, the Phase One and LCE results support the general existence of windblown clutter Doppler velocities only as great as ~ 3 to 4 m/s for 15- to 30-mph winds to levels 70 to 80 dB down.

The evidence for both power-law and exponential clutter spectral shapes is essentially empirical. The concern in Chapter 6 is not which of these two forms fits the data best over spectral dynamic ranges of –30 or –40 dB, or even whether such a question can be definitively answered. Chapter 6 provides good examples of both power-law and exponential fits to measured clutter spectral data to levels 30 or 40 dB down, and in reviewing the technical literature finds it to be similarly bipartite on this matter. The concern is, however, in determining an appropriate functional form to describe clutter spectra over greater spectral dynamic ranges. The main observation in this regard, based on the Phase One and LCE databases, is that no matter how good the power-law fits are over spectral dynamic ranges extending 30 to 40 dB below zero-Doppler peaks, they cannot be extrapolated to lower levels. That is, power-law shapes extrapolate rapidly to excessive spectral width. In contrast, the exponential form generally represents the Phase One and LCE measurements not only over their upper ranges of spectral power but also over their complete spectral dynamic ranges extending to levels 60 to 80 dB below zero-Doppler peaks. Thus radar system design for which ground clutter interference is of consequence at such low levels of spectral power is much more accurately based on an exponential clutter spectral shape approximation than on an extrapolated power-law approximation. The validity of the exponential shape on the basis of best matching coherent detection system performance to that obtained using actual measured I/Q clutter data as input to the clutter processor is demonstrated in Section 6.5.4.

6.6.3 Reports of Unusually Long Spectral Tails

Several historical reports of spectral tails in ground clutter at unusually high power levels and/or extending to unusually high Doppler velocities are considered in the following subsections.

6.6.3.1 Total Environment Clutter

There exists significant concern with how to characterize the clutter residues left in Doppler filter banks in high sensitivity radars after MTI cancellation that might cause false targets for subsequent multitarget tracking algorithms. Thus there is interest in specifying an overall environment clutter model that would include the Doppler interference from such things as aurora, meteor trails, cosmic noise, windblown material (leaves, dust, spray), birds and insects, rotating structures, rain and other precipitation, lightning, clear air turbulence, fluctuations of refractive index, etc. Often such phenomena are highly transient as they occur in measurements of radar Doppler spectra, so that it is difficult to causally and quantitatively associate unusual spectral artifacts directly with their sources. It is not suggested here that a specific program dedicated to measuring any one of these phenomena would not be successful—rather, that in a general database of spectral measurements collected from spatial ensembles of remote ground clutter cells, the occasional occurrence of causative agents different from windblown vegetation is difficult to determine. The main focus of interest in the Phase One and LCE spectral measurements is the general and continuous spectral spreading that occurs in ground clutter due to wind-induced motion of tree foliage and branches or other vegetative land cover. These clutter databases have not been very extensively used for systematic searching for infrequent, spatially unusual, narrowband, or transient spectral features resulting from other causative agents in the total clutter environment because of their ephemeral nature and uncertain signature characteristics, although occasional evidence of birds, airplanes, automobiles, and other anomalies has been encountered in the spectral analyses of these data. The one concrete example encountered by the LCE radar of clutter from the total environment over land with

atypical spectral behavior was strong Bragg resonance at small, but nonzero Doppler frequencies in the returns from a small inland body of water [34, 35]. Some of the unusually long spectral tails attributed to windblown clutter in the following discussions may have originated from external sources other than windblown vegetation or from internal instrumentation or data processing effects of which the investigators were unaware.

6.6.3.2 Chan's "Fast-Diffuse" Component

In addition to a "slow-diffuse" exponential component in ground clutter spectra, Chan [22, 23] also introduced a "fast-diffuse" component at a relatively weak but constant power level out to a higher Doppler frequency cutoff than the slow-diffuse component. Both components are indicated in Chan's idealized diagram of a composite ground clutter model shown in Figure 6.56. The fast-diffuse component is based on the observation of very infrequent or narrowband spectral features usually observed in isolated cells and for short-duration time intervals. The amplitude and cutoff frequency of the fast-diffuse component are not specified by Chan; however, for all his fast-diffuse examples, the maximum, or cutoff Doppler velocity, although greater than the slow-diffuse component present, was ≤ 2.5 m/s. Such occasional spectral features may often be caused by total environment clutter (birds, etc.).

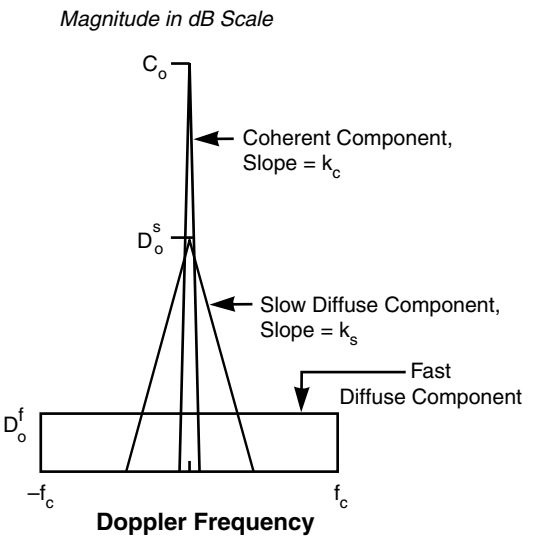

Figure 6.56 Chan's conceptual composite clutter model, including a fast-diffuse component. From [22], 1989. See also [23].

Transient, isolated, narrowband spectral features at low Doppler that do not exist symmetrically to either side of zero-Doppler can often, with some degree of confidence, be attributed to birds. Chan speculated that "regular oscillatory motion of [crop] vegetation, arising from restricted freedom of travel and natural elasticity" [22] might explain some unusual symmetrical features. Similar features have not been observed at Lincoln Laboratory, although Chan was using different Phase One data (repeat sector) and different processing (maximum entropy). Nonlinear superresolution processing techniques (such as maximum entropy) usually require large S/N ratios—not available at low levels in measured clutter spectra—to avoid spurious results. Spectral contaminants from the measurement instrument or from external RF sources of interference may also be present.

Spectral features that are not isolated but exist in all spatial resolution cells, and/or that exist symmetrically to either side of zero-Doppler, are likely to be instrumentation or processing contaminants.

Probabilities of occurrence, which would be difficult to determine, would eventually be required in a model for fast-diffuse spectral features. In any event, experience has indicated that Chan's fast-diffuse spectral component is easily misunderstood to imply the existence of a long, continuous, low-level, uniform amplitude spectral tail in ground clutter that is always there for all cells and all times. In fact, the fast-diffuse component was based on the observation of infrequent spectral artifacts.

6.6.3.3 White's Wideband Background Component

White's physical model [39] for windblown trees, which provides an exponential spectral component, also provides a rectangular wideband background spectral component at lower power levels. White essentially postulated the existence of his background component on the basis of Chan's fast-diffuse component [22, 23]. In so doing, White—as others have done—appears to have misinterpreted Chan's fast-diffuse component in the manner discussed above. Thus, whereas Chan's fast-diffuse component was based on the observation of infrequent spectral artifacts out to a maximum observed Doppler velocity of 2.5 m/s, White took this as the basis for postulating a wideband noise-like spectral component with ". . . a uniform spread of spectral power over all [Doppler] frequencies up to about 1 kHz" [39]. A cutoff frequency of 1 kHz corresponds to Doppler velocities of 15 and 50 m/s for the X- and S-band radars, respectively, that White was considering, which is well beyond Chan's observed cutoff.

White provided heuristic argument for the existence of a wideband background spectral component based on leaf (as opposed to branch) motion. In particular, he argued that rapid decorrelation in the returned signal resulting from the shadowing of one leaf by another and by leaf rotation can be expected to give rise to a wideband noise component. White did not derive a mathematical expression for the wideband component, and its absolute level was not specified.

White attempted to provide some experimental evidence for the wideband background spectral component in his limited set of C-band measured ground clutter data. This experimental evidence is unconvincing. The spectral dynamic range of the measurement radar was not shown or specified, but it was stated that the radar had a ". . . reasonably high radar noise floor" [39]. Results were provided for a quiet day and a windy day. In both sets of results, what was claimed to be the wideband background component also has the appearance of a system or processing noise floor. In both sets of results, cells with significantly spread clutter spectra, cells with little, and cells with no clutter Doppler spread were separately combined to provide averaged clutter spectra with wide, some, and no clutter spread.

It was observed that the noise-like background component was somewhat higher in spectral power level for the wide averaged spectrum than for the other two averaged spectra with little or no spread. In the quiet-day results, this difference in background level was small, and it was concluded that "the apparent white noise component . . . is due to . . . Fourier sidelobes and system noise" [39]. In the windy-day results, the difference was somewhat greater. It was argued that in this case this difference indicates "a real white-noise scatterer

motion within the band limits of the radar" [39]. In White's plotted results, what was claimed to be the white-noise spectral component occurs about 38 dB below the zero-Doppler peak.

The Phase One and LCE databases of clutter spectral measurements provide no evidence for the existence of a noise-like wideband background spectral component within the spectral dynamic ranges of these instruments, which reach 60 to 80 dB below the zero-Doppler spectral peaks. The Armand et al. [14] measured clutter spectral data (discussed subsequently in Section 6.6.3.6) at 4-mph wind speed show a noise-like component at a constant level of ~ –115 dB extending over the range $2.5 < v < 20$ m/s. At the higher wind speeds of 13 and 31 mph, the Armand et al. data decay continuously and reach the –115-dB level only at the limit of the measured data as v reaches ~20 m/s. No convincing evidence is provided by Armand et al. that the –115-dB level in these data is not a noise level. The bare-hill data of Warden and Wyndham [11] show a hint of a possible constant noise-like tail beginning at the –24-dB level ($0.55 < v < 0.65$ m/s), which is almost certainly a noise level or other corruptive influence (see Figure 6.47). In a private communication, White agreed that some degree of skepticism was warranted concerning his postulated wideband noise-like background component [61].

6.6.3.4 Simkins' "Lowland" Data of Wide Spectral Extent

This discussion concerns the L-band measurements of clutter spectra by Simkins, Vannicola, and Ryan [17] shown in Figure 6.51. Modeling information for spectral shape derived from these measurements was based on upper-bound approximations to worst-case spectra.These worst-case spectra came from resolution cells causing false alarms in a three-pulse-canceller MTI channel. These cells causing false alarms led to v^{-3} and v^{-4} power-law estimates of spectral shape. Spectra from adjacent cells with similar intensity but which did not cause false alarms were narrower, with v^{-5} or exponential shape.

Relative frequencies of occurrence of false alarm cells compared with non-false alarm cells were not specified. False alarms can be caused by transient events in the total clutter environment other than generally pervasive windblown vegetation. False alarms that moved measurable distances over several PPI scans were called angels; possible associations of angels, primarily with birds, but also with insects, clear air turbulence, and aurora, were discussed. Other false alarms were due to anomalous propagation, for which no spectral data were taken. Stationary false alarm cells were assumed to be caused directly by area-extensive ground clutter (as opposed to having less direct total environment origins) and used to develop ground clutter spectral modeling information.

Consider first the Simkins et al. ground clutter spectral data for "partially wooded hills" in 10- to 20-knot winds. The v^{-4} power-law shape attributed to these data in Figure 6.51 is an approximate upper-bound to an underlying scatter plot of data points. These data points, as typified by ≈–30 dB at 0.25 m/s and ≈–40 dB at 0.5 m/s, are not out of line with Phase One and LCE data. It is not the characterization of the bounding shape of these data as v^{-4} over the indicated 45-dB dynamic range that leads to difficulty, but the extrapolation of a constant v^{-4} power-law shape to power density levels significantly lower than –45 dB. Phase One and LCE also often show v^{-3} and v^{-4} rates of decay 35 to 40 dB down, but these become v^{-5} and v^{-6} rates of decay 60 to 80 dB down.

Consider next the Simkins et al. ground clutter spectral data for "heavily wooded valleys" or "lowlands" in 10- to 20-knot winds also shown in Figure 6.51. A wider v^{-3} power-law shape was attributed as an upper bound approximation to these data. These heavily-wooded-valley data, as typified by ~ –7 dB at 0.5 m/s and ~ –15 dB at 1 m/s, are significantly wider than Phase One- and LCE-measured spectra (the widest LCE spectrum is ~ – 20 dB at 0.5 m/s and ~ –30 dB at 1 m/s). The maximum measured Doppler velocity among the heavily-wooded-valley spectral data points is 5.8 m/s, 40 dB down; 5.8 m/s is almost twice the maximum Doppler velocity of ~ 3 m/s for windblown trees consistently seen by LCE in 15- to 30-mph winds, 70 to 80 dB down, and almost four times the Doppler velocity of 1.5 m/s seen in the widest LCE spectrum, 40 dB down. No other known measurement of a ground clutter spectrum approaches such high spectral power at such high Doppler velocity as given by the 5.8 m/s, –40-dB point of the Simkins et al. heavily-wooded-valley data.

On the basis of the many Phase One and LCE results in 15- to 30-mph winds, attributing Doppler velocities of 5.8 m/s, 40 dB down, to windblown trees would conjecturally require wind velocities much greater than the nominal 10 to 20 knots associated with the heavily-wooded-valley data. The only other known measurements of ground clutter spectra in which spectral power decays as slowly with increasing Doppler velocity as in the Simkins et al. heavily-wooded-valley data are early results reported by Goldstein [9] for trees in gale-force winds, discussed next in Section 6.6.3.5; however, these measurements only extend to a maximum Doppler velocity of 1 m/s. The only other known measurements of ground clutter Doppler velocities approaching or exceeding the 5.8 m/s maximum Doppler velocity shown at the –40-dB spectral power level in the Simkins et al. heavily-wooded-valley data (besides White's improbable wideband noise-like component) are the highly questionable results of Armand et al. [14] discussed in Section 6.6.3.6; however, spectral extent ≥ 5.8 m/s in the Armand et al. data is at dubiously low spectral power levels in the range of –90 to –120 dB. Otherwise, the Phase One and LCE measurements and the rest of the published literature [7, 10–13, 15, 16, 18–20, 22, 38, 42, 43, 45], including the other Simkins et al. data [17] and the Armand et al. data [14] at higher, less questionable spectral power levels, are in general agreement in terms of gross spectral extent (as opposed to details of spectral shape), measured over equivalent spectral dynamic ranges.

Since these high Doppler-velocity heavily-wooded-valley or lowland data are worst-case results from occasional false alarm cells, they are probably caused by some phenomenon other than windblown trees. The fact that a v^{-3} power-law spectrum at low Doppler frequencies typically results from poor stability in a radar (in particular, the oscillator) might suggest possible equipment limitations. Simkins, Vannicola, and Ryan [17] discuss efforts to quantify the spectral contamination contributed by their measurement instrumentation, including spreading of observed spectra due to oscillator instability. Further assurance that the heavily-wooded-valley data were indeed of external origin and important consequence would be provided if they could be confirmed through routine replication in independent measurements. In any event, whether internally or externally caused, these high Doppler-velocity heavily-wooded-valley data should not be misconstrued as generally representative of clutter spectra from windblown trees. The further extrapolation of these heavily-wooded-valley data as an upper bound, v^{-3} constant power-law dependency to levels significantly below –40 dB (e.g., to Doppler velocities of 30 m/s, 60 dB down), while retaining their general association with windblown trees, is highly unrealistic on the basis of the LCE and Phase One measurements.

6.6.3.5 Goldstein's Spectral Measurements in Gale Winds

Goldstein [9] describes three measurements in "gale winds or higher."[37] The actual maximum Doppler velocities to which spectral power was measured in these results are low (≤ 1 m/s), but the corresponding power levels are very high. The first two measurements were at X- and K-bands for which the power spectra are shown much as originally plotted in Figure 6.57 on linear scales of normalized spectral power density (0 to 1) vs Doppler velocity. The two spectra are quite similar; both are typical bell curves. The X-band spectrum is slightly wider than the K-band spectrum. At 0.5 m/s, the power levels in those spectra are 0.36 (–4.4 dB) and 0.28 (–5.5 dB) for X- and K-bands, respectively. At higher Doppler velocities, power levels in these bell-curve spectra diminish: at 0.85 m/s, the K-band curve is shown to reach zero power (–∞ dB); and at 1 m/s the X-band curve is at power level = 0.04 (–14 dB), this latter point being the maximum Doppler velocity provided in Goldstein's gale force spectral results. This point is nearly equivalent to corresponding points provided by the exponential spectral model of Section 6.2 for gale force winds at 1 m/s (i.e., –15.4 and –13.7 dB for $\beta = 4.3$ and 3.8, respectively; see Section 6.2).

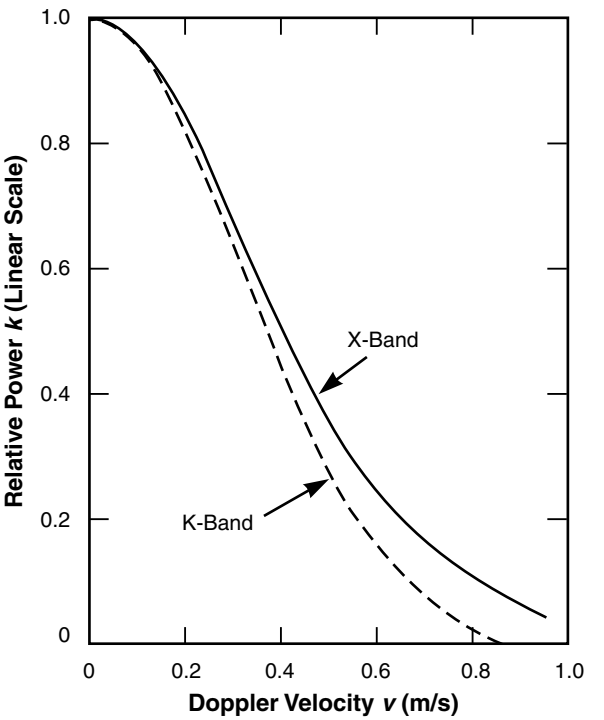

Figure 6.57 Measurements of radar ground clutter power spectra by Goldstein under gale winds. (After Goldstein [9]; by permission, The McGraw-Hill Companies, Inc.)

37. The Beaufort scale of wind velocities covers 13 Beaufort force numbers [from (0) Calm and (1) Light air to (12) Hurricane], including the following "gale force" numbers: (7) Moderate gale, winds from 32 to 38 mph; (8) Fresh gale, 39 to 46 mph winds; (9) Strong gale, 47 to 54 mph winds; and (10) Whole gale, 55 to 63 mph winds.

Goldstein's third measurement was at S-band in "winds of whole gale force." This spectrum, reported by Goldstein to be of "strange shape" and "markedly out of line with the others" [9], was not shown, although three measured points[38] were provided, viz., –1 dB at 0.1 m/s, –3 dB at 0.2 m/s, and –10 dB at 0.7 m/s. However, the autocorrelation function for this measurement was provided by Goldstein and shows a long, slowly diminishing tail plotted on linear scales. Subsequently, Wong, Reed, and Kaprielian [29] computed a corresponding power spectrum as the Fourier transform of a theoretical autocorrelation function incorporating scatterer rotational motion that was a very close match to Goldstein's unusual experimental autocorrelation function.

Wong, Reed, and Kaprielian's computed spectrum is reproduced in Figure 6.58 together with the three actual spectral points specified by Goldstein. The computed spectrum shows a long, slowly diminishing tail. Initially, it rapidly drops to power level = 0.2 (–7 dB) at 0.5 m/s, and thereafter slowly diminishes at a rate approximated by a power law of $n = 3.3$

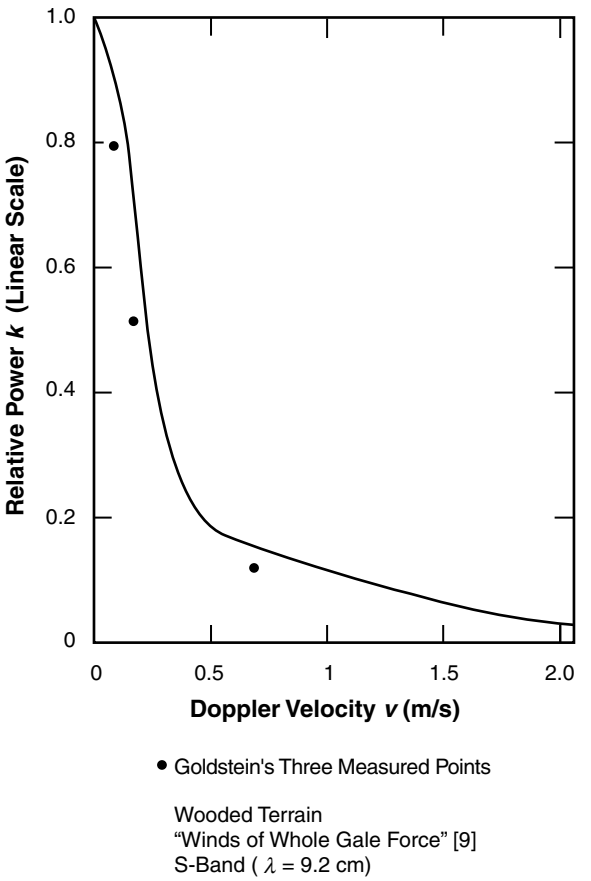

FIGURE 6.58 A radar ground clutter power spectrum computed from Goldstein's measured correlation function by Wong, Reed, and Kaprielian showing a long spectral tail under winds of whole gale force. (Computed spectrum (solid curve) after [29]; by permission, © 1967 IEEE. Three plotted points from Table 6.8 in Goldstein [9]; by permission, The McGraw-Hill Companies, Inc.)

38. Labelled as occurring at wind speed of 50 mph in Goldstein's Table 6.8 [9].

to power level = 0.02 (–17 dB) at 2 m/s. In comparison, at 2 m/s the widest measured LCE spectrum is at –53 dB. In discussing these curves of correlation function and power spectrum, Wong, Reed, and Kaprielian noted that they "deviate significantly from the usual expected Gaussian shape. Instead, they drop very slowly toward zero" [29]. Thus these data have contributed to the concept of a long spectral tail, here at an usually high power level.

Some reservations must be accorded to Goldstein's results, due to their very early origin. Goldstein was attempting to establish only the most basic general characteristics and, indeed, just the very existence of spectral spreading of ground clutter in these early results. Conversion of values from near the limits of Goldstein's plots on linear scales to decibel quantities for comparison with modern measurements to much lower power levels where the concern is with detailed behavior of spectral tails is using Goldstein's data out of historical context. In particular, Goldstein's unusual S-band gale force data and their further elaboration by Wong, Reed, and Kaprielian [29] now appear to be best regarded as an anomalous occurrence in an isolated measurement. No modern measurements of windblown tree clutter spectra under gale force winds are known to exist.

6.6.3.6 Armand's Long, Low-Level Clutter Spectral Tail

Armand et al. [14] ostensibly measured X-band clutter spectra from windblown trees to very low levels of spectral power (–120 dB) and correspondingly very high Doppler velocities (20 m/s). Their results are reproduced in Figure 6.59. Armand et al. stated that these ground clutter spectra were measured with CW equipment in which the power received from the sidelobes of the transmitter was an order of magnitude higher than that reflected from the trees. Instabilities were reported to be eliminated through use of klystrons stabilized by cooling with liquid helium. Results were obtained in the 40- to 2,500- Hz Doppler frequency band (i.e., not near the carrier). Spectral results are shown for three wind speeds—4, 13, and 31 mph—over the range from 40 to ~ 1,300 Hz (0.6 to ~ 20 m/s). Over this range, the spectral power density levels are between –50 and –120 dB (i.e., are much lower than any other known spectral measurements).

For the 4-mph spectrum, the power drops to –120 dB at 2.5 m/s, and thereafter stays at ~ –120 dB all the way out to 20 m/s (i.e., exhibits a long spectral tail at a uniform low level, like White's [39] conceptual wideband noise-like spectral component). The 13- and 31-mph spectra drop gradually from –63 and –52 dB, respectively, at 0.6 m/s to ~ –115 dB at 20 m/s. At power levels 80 dB down, Doppler velocities in the Armand et al. results of Figure 6.59 are ~ 0.9, 1.4, and 2.5 m/s for 4-, 13-, and 31-mph winds, respectively; these spectral widths are a very close match to those measured by Phase One and LCE at similar levels of spectral power (i.e., near their limits of sensitivity).

Armand et al. [14] claimed that their spectral shapes were power-law, with an average value of power-law exponent $n = 3$ in the 110- to 2,500-Hz band averaged over all tests and with n varying inversely with wind velocity between 3 and 6 in the 40- to 110-Hz band. The authenticity of these very long, very low-level clutter spectral tails is open to question; what was measured may have been effects of sidelobes, internal system instabilities, etc. Before undue credibility is ascribed to these results, they need to be confirmed by independent and consistent replication using modern measurement instrumentation. However, these results arguably keep open the possibility of long spectral tails at very low power levels below Phase One and LCE sensitivities. As previously discussed, spectral power at large Doppler velocities is theoretically accounted for by Armand et al. through amplitude modulation via

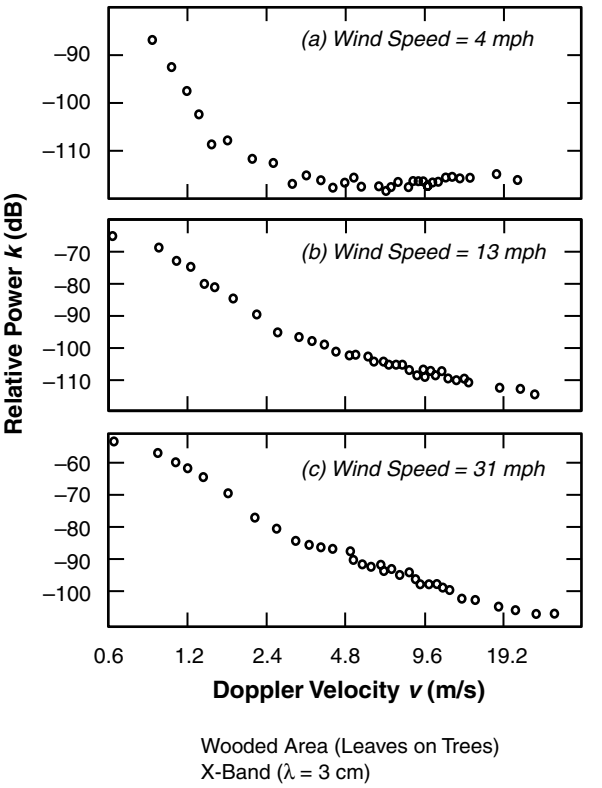

Figure 6.59 Measurements of radar ground clutter spectra by Armand et al. of the Russian Academy of Sciences showing very long, low-level spectral tails. After [14], 1975.

leaf rotation and shadowing of one leaf by another, in addition to phase modulation caused by leaf oscillatory motion in the direction of the radar. Note that the Russian spectral measurements [15, 16] that followed those of Armand et al. [14] were performed specifically to obtain information close to the carrier. Although the Phase One and LCE results do not agree with this series of Russian results [13–16] in their assessments of spectral shape as power-law, none of these Russian measurements show inordinately wide spectra over the ranges of spectral power measured by the Phase One and LCE instruments.

6.6.3.7 Instrumentation and Processing Effects

Internal effects from the measurement radar often have contaminated and corrupted attempted measurements of clutter frequency spectra to low spectral power levels. The fact that the shape of the spectrum resulting from oscillator instability is an $n = 3$ power law can raise suspicion of measured clutter spectra with $n = 3$ power-law characteristics. For example, the Simkins et al. [17] heavily-wooded-valley data of unusually wide spectral extent follow an $n = 3$ power-law shape, as do the Armand et al. [14] data at very low power levels (70 to 120 dB down) and high Doppler velocities (1.65 to 37.5 m/s). Care must be taken to isolate and avoid spectral contamination from system instabilities.

Quantification of spectral contamination is required for every measurement at the actual range at which the clutter measurement is performed, since instability of the stable local oscillator (STALO) produces a greater effect at longer ranges (the phase has more time to

change when the STALO is used to upconvert on transmit and downconvert on receive). If the STALO is not used on receive, but the signal is merely envelope-detected prior to spectral analysis (as in the results of Goldstein [9] and Fishbein et al. [10]), the full STALO instability spectrum or that of the transmitter is impressed on the received clutter signal. Goldstein's [9] early measurements were undoubtedly made using a klystron or magnetron as the transmitter, resulting in relatively poor stability.

In the Armand et al. [14] results, transitions are observable in the spectral data at low power levels (at 1.5 m/s Doppler velocity for 4-mph wind speed, and at 2.4 m/s Doppler velocity for 13-mph wind speed). For Doppler velocities greater than those of these transition points, it is conceivable that the data result from system instabilities. Note that the results of Armand et al. were obtained using a CW transmitter; use of pulsed radar can introduce additional instability due to noise contamination of trigger pulses. Nonlinearities in circuitry or processing (e.g., lin-limit amplifier) can also limit and spread the frequency spectrum, especially under strong signal (strong clutter) conditions. Data in saturation result in significant spectral spreading caused by the actual spectrum convolving with itself in such circumstances. Discounting this possibility for the stationary false alarm cells underlying the Simkins et al. heavily-wooded-valley data is the reported fact that spectra from adjacent non-false alarm cells of similar intensity were narrower. Unwanted antenna motion caused mechanically, and/or by the wind, can also spread the frequency spectrum by modulating the clutter signal. This modulation may go unobserved if stability testing is performed in low-wind conditions.

A few cases of long spectral tails extending to Doppler velocities >> 3 m/s were observed during the course of examining the Phase One database of spectral measurements. In every case, the long spectral tail was isolated to some sort of instrumentation problem (e.g., sticking bits on the A/D converter generating minute sample-and-hold stairsteps on the temporal signal, occasional saturations, external interference). One excessively wide Phase One spectral measurement caused by undetected saturation was inadvertently included in a set of "windy" spectra in a previous publication (spectrum 4, Figure 6.9, in [21]). Thus any unusually wide measured spectra should always be very carefully examined in the time domain before accepting the wide frequency domain result.

Attempts to improve Phase One stability by sampling the transmitted signal and correcting (i.e., subtracting) transmitted phase variations in the received signal were unsuccessful (i.e., proved to be not simple to implement). The LCE radar was a spectrally purer system than the Phase One radar and was never observed to generate an excessively wide spectral tail due to system or processing contamination. A number of windblown clutter spectral measurements by other investigators reviewed from time to time by the author have at first contained obviously corrupted clutter spectral tails of excessive width and extremely slow (e.g., $n \cong 3$) decay; subsequent investigation has always found these long spectral tails to be caused by errors in instrumentation or processing. In considering all the possible ways in which instrumentation limitations or processing errors can broaden measured clutter spectra, it is well to bear in mind that of two measured spectra—one narrow and one wide—ostensibly characterizing the same clutter phenomenon, the narrower spectrum is always more credible since all corruptive influences due to instrumentation limitations or processing errors can only broaden the spectrum, not narrow it.

Because of all the potential uncertainties (i.e., potential contaminants of internal and external origin) in radar ground clutter spectral measurements as exemplified in the

preceding discussions of Section 6.6.3, the use of such data requires the exercise of judgment. Ground clutter spectral models should reflect, for the most part, central repeatable trends in measured data, not unusual or isolated artifacts or aberrations.

6.7 Summary

Accurate characterization of radar ground clutter spectral shape is important in radar technology applications in which target signals compete with strong ground clutter returns. Ground clutter spectral spreading can limit the performance of MTI/Doppler processors, including both conventional one-dimensional fixed-parameter designs [1, 2] and modern two-dimensional displaced phase-centered antenna or space-time adaptive techniques [3–5] for detecting and tracking moving targets in clutter backgrounds. Internal clutter motion can also cause defocusing in SAR processing [62] and indeed can degrade any radar processing technique that assumes the clutter to be stationary. Such reasons provide motivation to obtain a proper understanding of clutter spectral spreading and to obtain an accurate characterization of the shapes of clutter spectra to very low levels of spectral power. Historically, the state of knowledge of windblown ground clutter spectral shape has been rather poor, and considerable disagreement has existed concerning the extent to which Doppler spreading occurs in such spectra.

Lincoln Laboratory measurement data indicate that ground clutter power spectra over spectral dynamic ranges reaching 60 to 80 dB below the zero-Doppler peaks are relatively narrow and reasonably characterized as of exponential shape. First observation of exponential spectral decay in the clutter studies discussed herein occurred in the early examination of windblown foliage clutter spectra obtained with the Phase One clutter measurement radar at western Canadian sites. These first observations of exponential decay remained valid in the general representation of a much more complete set of L-band spectral measurements over various regimes of wind speed obtained with the Phase One radar at the Lincoln Laboratory measurement site of Katahdin Hill in eastern Massachusetts [21].

Exponential decay was also concluded to be the best overall characterization of windblown ground clutter spectral shape covering Phase One measurements at other frequencies (i.e., VHF, UHF, S-, and X-bands), from other sites, and over several thousand spectral observations taken from the extensive L-band database of clutter spectral measurements subsequently obtained with the LCE clutter measurement radar [25]. The LCE radar was a major L-band-only upgrade of the five-frequency Phase One radar with new, much improved receiver and data recording units, lower phase noise levels, and very clean and reliable spectral response. Analyses of Phase One clutter data in Canada [22, 23] and in the U. K. [24] also concluded that ground clutter spectra were generally best-fitted with exponential shapes.

On the basis of the Phase One and LCE clutter data, two different first-principles theoretical models [39, 60] were independently developed for the windblown clutter Doppler spectrum that, although mathematically complex, in both cases provide close to exponential decay under numerical evaluation. Other previous references to exponential (or quasi- or partially-exponential) clutter spectral decay exist in a much earlier Lincoln Laboratory measurement program [59] of the 1970s, and in Russian measurements [13–16] and French measurements [38] of the same early time period.

The very earliest indications were that windblown ground clutter spectra were of Gaussian spectral shape [6–9]. Many subsequent measurements to lower power levels 30 to 40 dB below the peak zero-Doppler level indicated spectral shapes that were significantly wider than Gaussian in their tails and that appeared to be well approximated with power-law functions [10–20]. The Phase One and LCE ground clutter spectral measurements, over such limited spectral dynamic ranges, also can be adequately modeled as of power-law shapes. However, the Phase One and LCE measurement data also clearly indicate that the power-law rates of decay at upper levels of spectral power do not continue to lower levels of spectral power reaching 60 to 80 dB down from the zero-Doppler peak. The measured power-law rates of decay at lower power levels are always much faster than at the upper levels.

An exponential representation generally captures, at least approximately and occasionally highly accurately, the major attributes of the windblown clutter ac spectral shape function over the entire range from near the zero-Doppler peak to measured levels 60 to 80 dB down. In contrast, the windblown clutter ac spectral shape is not at all representable by any power law over such a wide spectral dynamic range. The maximum Phase One- and LCE-measured Doppler velocity spectral extents from windblown foliage at levels 60 to 80 dB down are ≈3 to 4 m/s. Power-law models can extrapolate data of 40-dB spectral dynamic range to spectral extent as great as 30 m/s, 60 dB down. Such extreme windblown foliage spectral extents have never been corroborated by any results in the extensive Phase One and LCE databases of windblown clutter spectral measurements.

Chapter 6 provides a new empirical model for windblown ground clutter Doppler spectra based on many clutter spectral measurements obtained with the Lincoln Laboratory LCE and Phase One five-frequency (VHF, UHF, L-, S-, and X-band) radars. This model is complete, including both ac and dc components of the spectrum. The important parameters incorporated in the model are wind speed and radar carrier frequency. Ac spectral shape is specified as exponential, with the Doppler-velocity exponential shape factor strongly dependent on wind speed but independent of radar frequency, VHF to X-band. The fact that ac spectral spreading occurs at VHF in windblown clutter Doppler-velocity spectra more or less equivalently as at X-band is illustrated through representative measurement results; many other examples of VHF-measured clutter spectra with similar spectral spreading exist in the Phase One and LCE databases.

The major difference between VHF and X-band clutter spectra is that a much larger dc spectral component exists at VHF compared with X-band. The ratio of dc to ac spectral power in the model is determined by an analytic expression empirically derived from the measurements that captures the strong dependencies of dc/ac ratio on both wind speed and radar frequency. Chapter 6 includes both a complete specification of the clutter spectral model and a thorough comparison of model predictions with many examples of measured windblown clutter spectra under various combinations of radar parameters and measurement circumstances. Besides wind speed and radar frequency, other parameters that might be thought to significantly influence clutter spectra, but that appear to be largely subsumed within general ranges of statistical variability in the measurement data, include tree species, season of the year, wind direction, cell size, polarization, range, and grazing angle. The exponential model is explicitly derived to be applicable to windblown trees, but examples are also provided of measured clutter spectra from scrub desert, cropland, and rangeland that indicate the model can also perform adequately for other windblown vegetation types by suitably adjusting its dc/ac term.

Although it is now generally accepted that radar ground clutter spectral shapes are wider than Gaussian in their tails, the simple Gaussian continues to be how clutter spectra are usually represented in radar system engineering (at least as a method of first approach in representing effects of intrinsic clutter motion) because of its simplicity and analytic tractability. The Gaussian spectral shape is theoretically generated by a group of moving scatterers, each of random translational drift velocity [19]. Theory also suggests that the origin of the increased spreading observed in measured ground clutter spectra beyond that predicted by Gaussian is largely due to the random oscillatory motion of leaves and branches, in contrast to simple random translational motion [19, 29, 42]. Like the Gaussian spectral shape, the exponential spectral shape is also simple and analytically tractable and has the advantage of being wider than Gaussian as required by experiment and supported by theory.

There is no underlying fundamental physical principle requiring clutter spectra to be precisely of exponential shape. Many of the Phase One and LCE clutter spectral measurements, particularly many of the narrower spectra occurring at lower wind speeds, are less exponential overall than some of the wider measured spectra. To be clear on this matter, almost none of the Phase One- and LCE-measured clutter spectra can be accurately represented by any single simple analytic function, including exponential [31], over their complete spectral dynamic ranges, from the point of view of passing rigorous statistical hypothesis tests. Use of the exponential shape in Chapter 6 is as a convenient analytic bounding envelope that empirically approximates, occasionally very accurately, many of the LCE and Phase One measurements over most of their spectral dynamic ranges, including the lowest power levels measured. The resulting model overcomes much of the difficulty in modeling clutter spectra not only by using exponential shapes, but also by introducing the concept of a quasi-dc region and absorbing the excess power measured in the quasi-dc region into the dc delta function term of the model. This approach allows the model the flexibility of using the exponential representation to optimally match the measured spectral spreading in the spectral tail regions without regard to the narrow near-zero-Doppler quasi-dc region, which often displays a different rate of decay than occurs in the broad spectral tail [31].

In addition to showing that measured shapes of windblown ground clutter Doppler spectra appear to be much more closely matched by an exponential approximation than by Gaussian (too narrow) or power-law (too wide) approximations, Chapter 6 also investigates the impact of assigning the correct clutter spectral shape on MTI and STAP coherent target detection. Compared to the exponential shape, the Gaussian shape substantially underpredicts the effects of clutter on detection, and the power-law shape substantially overpredicts the effects of clutter on detection. The exponential spectral model for windblown foliage is validated by showing that the differences in clutter improvement factor performance prediction between using actual measured I/Q data as input to the clutter canceller, and modeled clutter data of Gaussian, exponential, or power-law spectral shape, are minimized when the spectral model employed is of exponential shape.

It is evident on the basis of the Phase One and LCE measurements that the current state of knowledge regarding the extent of spectral spreading in windblown ground clutter has been advanced to the point where it is relatively incontrovertible that clutter spectra from windblown vegetation, although wider than Gaussian, are still generally relatively narrow and spread to Doppler velocities $< \approx 3$ or 4 m/s over spectral power levels reaching to 80 dB below zero-Doppler peaks for wind speeds in the 15- to 30-mph range. Investigators

who may wish to continue to argue for much wider clutter spectra from windblown foliage over such ranges are faced with proving spectral purity in their wider measurements, since unknown corruptive instrumentation or processing effects can only widen spectra, not narrow them. Presumably, most of the spectral spreading that occurs in the Phase One and LCE data is caused by the velocity distribution (translational and/or oscillatory) of the foliage, that is, by the radial motion of individual scatterers (leaves and branches) toward and away from the radar causing phase modulation in the returned signal. To whatever extent other effects are also at work in the Phase One and LCE data, such as leaf rotation or the shadowing of one leaf by another causing more complex amplitude modulation effects, such effects are also constrained to cause limited spreading to levels 80 dB down.

Chapter 6 also provides a relatively thorough review of the available literature of clutter spectral measurements, which generally brings it and the Phase One and LCE results into conformity and agreement. There remain hints in the literature, however, not only from theoretical reasoning but also in various poorly substantiated measurement results, of long spectral tails existing in ground clutter data to Doppler velocities greatly exceeding the maximum ≈3 to 4 m/s observed in the Phase One and LCE data. Arguments for the existence of such wide tails often are based on postulated leaf-rotation and leaf-shadowing effects. Such long tails have never been observed, whether as slowly decaying power laws or as uniform-amplitude wideband noise-like components, in any of the several thousand spectra that have been examined from the extensive Phase One and LCE databases of ground clutter spectral measurements to levels reaching 60 to 80 dB below zero-Doppler peaks. What might occur at lower levels remains conjectural.

References

1. M. I. Skolnik, *Introduction to Radar Systems,* 3rd ed., New York: McGraw-Hill (2001).

2. J. A. Scheer and J. L. Kurtz (eds.), *Coherent Radar Performance Estimation*, Boston, MA: Artech House, Inc. (1993).

3. R. Klemm, *Space-Time Adaptive Processing: Principles and Applications*, IEE Press, Radar, Sonar, Navigation and Avionics Series, 1999.

4. J. Ward, "Space-Time Adaptive Processing for Airborne Radar," Lexington, MA: MIT Lincoln Laboratory, Technical Rep. 1015 (13 December 1994), DTIC AD-A293032.

5. P. Richardson, "Relationships between DPCA and adaptive space-time processing techniques for clutter suppression," *Proc. International Conf. Radar,* SEE 48 rue de la Procession, 75724 Paris Cedex 15 (May 1994), pp. 295–300.

6. L. N. Ridenour (ed.), *Radar System Engineering*, Vol. 1 in the MIT Radiation Laboratory Series, New York: McGraw-Hill (1947). Reprinted, Dover Publications (1965).

7. E. J. Barlow, "Doppler Radar," *Proc. IRE* 37, 4 (1949).

8. J. L. Lawson and G. E. Uhlenbeck (eds.), *Threshold Signals*, Vol. 24 in the MIT Radiation Laboratory Series, New York: McGraw-Hill (1950).

9. H. Goldstein, "The Fluctuations of Clutter Echoes," pp. 550–587, in D. E. Kerr (ed.), *Propagation of Short Radio Waves*, Vol. 13 in the MIT Radiation Laboratory Series, New York: McGraw-Hill (1951).

10. W. Fishbein, S. W. Graveline, and O. E. Rittenbach. "Clutter Attenuation Analysis," Fort Monmouth, NJ: U.S. Army Electronics Command, Technical Rep. ECOM-2808 (March 1967). Reprinted in *MTI Radar*, D.C. Schleher (ed.), Boston, MA: Artech House, Inc. (1978).

11. M. P. Warden and B. A. Wyndham, "A Study of Ground Clutter Using a 10-cm Surveillance Radar," Royal Radar Establishment, Technical Note No. 745, Malvern, U. K. (1969). DTIC AD 704874.

12. N. C. Currie, F. B. Dyer, and R. D. Hayes, "Radar Land Clutter Measurements at Frequencies of 9.5, 16, 35, and 95 GHz," Engineering Experiment Station, Georgia Institute of Technology, Technical Report No. 3, United States Army, Contract DAAA-25-73-C-0256, April 1975. DTIC AD-A012709.

13. V. A. Kapitanov, V. Mel'nichuk, and A. A. Chernikov, "Spectra of radar signals reflected from forests at centimeter waves," *Radio Eng. and Electron. Phys.,* 18, 9 (1973).

14. N. A. Armand, V. A. Dyakin, I. N. Kibardina, A. G. Pavel'ev, and V. D. Shuba, "The change in the spectrum of a monochromatic wave when reflected from moving scatterers," *Radio Eng. and Electron. Phys.,* 20, 7 (1975).

15. V. A. Andrianov, I. S. Bondarenko, I. N. Kibardina, V. K. Prosshin, and D. Y. Shtern, "Characteristics of measurement of spectra of radio signals scattered by an underlying surface," *Radio Eng. and Electron. Phys.,* 21, 2 (1976).

16. V. A. Andrianov, N. A. Armand, and I. M. Kibardina, "Scattering of radio waves by an underlying surface covered with vegetation," *Radio Eng. and Electron. Phys.,* 21, 9 (1976).

17. W. L. Simkins, V. C. Vannicola, and J. P. Ryan, "Seek Igloo Radar Clutter Study," Rome Air Development Center, Technical Rep. RADC-TR-77-338 (October 1977). Updated in FAA-E-2763b Specification, Appendix A (May 1988). See also FAA-E-2763a (September 1987), FAA-E-2763 (January 1986, July 1985).

18. J. Jiankang, Z. Zhongzhi, and S. Zhong, "Backscattering power spectrum for randomly moving vegetation," *Proc. IGARSS Symposium*, Zurich (August 1986), pp. 1129–1132.

19. N. J. Li, "A study of land clutter spectrum," *Proc. 1989 International Symp. on Noise and Clutter Rejection in Radars and Imaging Sensors,* T. Suzuki, H. Ogura, and S. Fujimura (eds.), *IEICE*, Kyoto (1989), pp. 48–53.

20. G. W. Ewell, private communication (December 1995).

21. J. B. Billingsley and J. F. Larrabee, "Measured Spectral Extent of L- and X-Band Radar Reflections from Windblown Trees," Lexington, MA: MIT Lincoln Laboratory, Project Rep. CMT-57 (6 February 1987), DTIC AD-A179942.

22. H. C. Chan, "Spectral Characteristics of Low-Angle Radar Ground Clutter," Ottawa, Canada: Defence Research Establishment Ottawa, Report No. 1020 (December 1989), DTIC AD-A220817.

23. H. C. Chan, "Radar ground clutter measurements and models, part 2: Spectral characteristics and temporal statistics," *AGARD Conf. Proc. Target and Clutter Scattering and Their Effects on Military Radar Performance,* Ottawa, AGARD-CP-501 (1991), AD-P006374.

24. G. C. Sarno, "A model of coherent radar land backscatter," *AGARD Conf. Proc. Target and Clutter Scattering and Their Effects on Military Radar Performance,* Ottawa, AGARD-CP-501 (1991), AD-P006375.

25. J. B. Billingsley, "Exponential Decay in Windblown Radar Ground Clutter Doppler Spectra: Multifrequency Measurements and Model," Lexington, MA: MIT Lincoln Laboratory, Technical Report 997, 29 July 1996; DTIC AD-A312399.

26. J. B. Billingsley, "Windblown radar ground clutter Doppler spectra: measurements and model," submitted to *IEEE Trans. AES*, May 2000, accepted subject to minor revision, October 2000.

27. M. W. Long, *Radar Reflectivity of Land and Sea*, 3rd ed., Boston: Artech House, Inc. (2001).

28. F. E. Nathanson, *Radar Design Principles*, 2nd ed., New York: McGraw-Hill (1991). Reprinted, SciTech Publishing, Inc., 1999.

29. J. L. Wong, I. S. Reed, and Z. A. Kaprielian, "A model for the radar echo from a random collection of rotating dipole scatterers," *IEEE Trans. AES* 3, 2 (1967).

30. M. V. Greco, F. Gini, A. Farina, and J. B. Billingsley, "Analysis of clutter cancellation in the presence of measured L-band radar ground clutter data," in *Proceedings of IEEE International Radar Conference (Radar 2000)*, Alexandria, VA, May 8–12, 2000.

31. M. V. Greco, F. Gini, A. Farina, and J. B. Billingsley, "Validation of windblown radar ground clutter spectral shape," *IEEE Trans. AES,* vol. 37, no. 2, April 2001.

32. J. B. Billingsley, A. Farina, F. Gini, M. V. Greco, and P. Lombardo, "Impact of experimentally measured Doppler spectrum of ground clutter on MTI and STAP," in *Proceedings of IEE International Radar Conference (Radar '97)*, IEE Conf. Pub. No. 449, pp. 290-294, Edinburgh, 14–16 October 1997.

33. P. Lombardo, M. V. Greco, F. Gini, A. Farina, and J. B. Billingsley, "Impact of clutter spectra on radar performance prediction," *IEEE Trans. AES*, vol. 37, no. 3, July 2001.

34. J. B. Billingsley and J. F. Larrabee, "Bragg Resonance in Measured L-band Radar Clutter Doppler Spectra from Inland Water," Lexington, MA: MIT Lincoln Laboratory, Technical Rep. 1019 (1 August 1995), DTIC AD-A297680.

35. J. B. Billingsley, "Measurements of L-band inland-water surface-clutter Doppler spectra," *IEEE Trans AES*, Vol. 34, No. 2, April 1998, pp. 378–390.

36. R. L. Ferranti, "Very low phase noise in a pulsed 10-kw L-band triode power amplifier," Santa Clara, CA: *Proc. RF Expo West*, 59-66 (February 1991).

37. F. J. Harris, "On the use of windows for harmonic analysis with the discrete Fourier transform," *Proc. IEEE* 66, 51–83 (January 1978).

38. R. Basard, "Vegetation clutter Doppler spectrum models," *International Conference on Radar,* (Session II), Paris, pp. 28-31, 4–8 December 1978.

39. R. G. White, "A model for MTI radar clutter," *Proc. SEE Int. Radar Conf.*, Paris (May 1994), pp. 540–545.

40. R. M. Narayanan, D. W. Doerr, and D. C. Rundquist, "Temporal decorrelation of X-band backscatter from wind-influenced vegetation," *IEEE Trans. Aerosp. Electron. Syst.* 28, 2 (1992), pp. 404–412.

41. R. M. Narayanan, S. E. Nelson, and J. P. Dalton, "Azimuthal scattering pattern of trees at X-band," *IEEE Trans. Aerosp. Electron. Syst.* 29, 2 (1993), pp. 588–593.

42. R. M. Narayanan, D. W. Doerr, and D. C. Rundquist, "Power spectrum of wind-influenced vegetation backscatter at X-band," *IEE Proc.-Radar, Sonar Navig.*, 141, 2 (1994), pp. 125–131.

43. N. A. Stewart, "Use of crosspolar returns to enhance target detectability," in J. Clarke (ed.), *Advances in Radar Techniques*, IEE Electromagnetic Wave Series 20, Peter Peregrinus, Ltd., London, U.K., 1985, pp. 449–454.

44. J. B. Billingsley and J. F. Larrabee, "Multifrequency Measurements of Radar Ground Clutter at 42 Sites," Lexington, MA: MIT Lincoln Laboratory, Technical Rep. 916, Volumes 1, 2, 3 (15 November 1991), DTIC AD-A246710.

45. G. P. de Loor, A. A. Jurriens, and H. Gravesteijn, "The radar backscatter from selected agricultural crops," *IEEE Trans. on Geoscience Electronics*, 12, 70–77 (April 1974).

46. E. J. Kelly, "An adaptive detection algorithm," *IEEE Trans. on Aerospace and Electronic Systems*, Vol. 22, No. 2, pp. 115–127, March 1986.

47. A. Farina, P. Lombardo, M. Pirri, "Non-linear space-time processing for airborne early warning radar," *IEE Proc. on Radar, Sonar and Navigation*, Vol. 145, No. 1, pp. 9–18, February 1998.

48. R. Klemm, "Adaptive clutter suppression for airborne phased-array radars," *IEE Proceedings-F*, Vol. 130, No. 1, pp. 125–132, February 1983.

49. S. Barbarossa and A. Farina, "Space-time-frequency processing of synthetic aperture radar signals," *IEEE Trans. on Aerospace and Electronic Systems*, Vol. 30, No. 2, pp. 341–358, April 1994.

50. D. K. Barton, *Modern Radar System Analysis*, Boston, MA: Artech House, Inc. (1988), p. 246.

51. A. Papoulis, *The Fourier Integral and Its Applications*, New York: McGraw-Hill (1962).

52. W. B. Davenport, Jr., and W. L. Root, *An Introduction to the Theory of Random Signals and Noise*, New York: McGraw-Hill (1958).

53. S. Goldman, *Frequency Analysis, Modulation, and Noise,* New York: McGraw-Hill (1948). Reprinted, Dover Publications (1967).

54. F. G. Bass, P. V. Bliokh, and I. M. Fuks, "Statistical characteristics of a signal scattered from randomly moving reradiators on a plane section," translated from *Radiotechnika i Electronika* (USSR), 10, 5 (May 1965), pp. 731–739.

55. S. Rosenbaum and L.W. Bowles, "Clutter return from vegetated areas," *IEEE Trans. Ant. Propag*., AP-22, 2 (March 1974), pp. 227–236.

56. D. C. Schleher, *MTI and Pulsed Doppler Radar*, Norwood, MA: Artech House, 1991, p. 127.

57. J. A. Scheer, "Coherent Radar Performance Estimation," IEEE National Radar Conference, Tutorial Notes, Atlanta (1994).

58. N. C. Currie and C. E. Brown, eds., *Principles and Applications of Millimeter-Wave Radar*, Norwood, MA: Artech House, Inc. (1987).

59. L. Cartledge, M. Labitt, J. H. Teele, and R. D. Yates, "An Experimental UHF Ground Surveillance Radar, Volume 2," Lexington, MA: MIT Lincoln Laboratory, Technical Rep. 497 (12 October 1972), DTIC AD-757565.

60. P. Lombardo and J. B. Billingsley, "A new model for the Doppler spectrum of windblown radar ground clutter," in *Proceedings of 1999 IEEE Radar Conference*, Boston, MA, 20-22 April 1999, pp. 142–147.

61. R. G. White, private communication (11 September 1995).

62. C. Elachi and D. D. Evans "Effects of random phase changes on the formation of synthetic aperture radar imagery," *IEEE Trans. on Antennas and Propagation*, Vol. AP-25, No. 1, pp. 149–153, January 1977.

INDEX

C

D

E

F

G

H

I

K

L

M

N

O

P

Q

R

S

T

U

V

W

X

Z